NASA CONTRACTOR REPORT

NASA CR-1500

POTASSIUM TURBOALTERNATOR (KTA) PRELIMINARY DESIGN STUDY

Volume III - Phase II KTA Final Design

Prepared by
GARRETT CORPORATION
Phoenix, Ariz.
for Lewis Research Center

NATIONAL AERONAUTICS AND SPACE ADMINISTRATION • WASHINGTON, D. C. • APRIL 1970

1. Report No. NASA CR-1500	2. Government Accession No.	3. Recipient's Catalog No.
4. Title and Subtitle POTASSIUM TURBOALTERNATOR (KTA) PRELIMINARY DESIGN STUDY III - PHASE II KTA FINAL DESIGN		5. Report Date April 1970 6. Performing Organization Code
7. Author(s)		8. Performing Organization Report No. APS-5317-R
9. Performing Organization Name and Address AiResearch Manufacturing Company Phoenix, Arizona		10. Work Unit No. 11. Contract or Grant No. NAS 3-10934 13. Type of Report and Period Covered Contractor Report
12. Sponsoring Agency Name and Address National Aeronautics and Space Administration Washington, D.C. 20546		14. Sponsoring Agency Code

15. Supplementary Notes

Edited by R. A. Rackley

16. Abstract

The NASA is engaged in a research and technological investigation of high-temperature potassium Rankine cycle space power systems. As part of this program, AiResearch Manufacturing Company has performed a comprehensive analysis and preliminary design study of the potassium turboalternator component. The study was performed in two phases-a component performance and conceptual design analysis (Phase I) and a preliminary design study (Phase II). AiResearch was assisted by two subcontractors - Westinghouse Aerospace Electrical Division, which was responsible for the alternator design, and Westinghouse Astronuclear Laboratories, which provided technical assistance in the areas of turbine aerothermodynamic analysis and turbine material support. The report is presented in three volumes. Volume I covers the turbine and bearing parametrics, Phase I conceptual analysis and complete turboalternator configurations of Phase I. Volume II covers the Phase I alternator conceptual design. Volume III covers the detailed evaluation of the selected turboalternator assembly, which incorporates a ten-stage turbine and an alternator, each of which is straddle-mounted on potassium bearings with a flexible coupling between units. The KTA rotates at 19,200 rpm and produces 428 KWe, 480V, 3 phase, 1600 hz electrical power.

17. Key Words *(Suggested by Author(s))*	18. Distribution Statement
Potassium turboalternator design Alternator, high temperature Refractory materials Rankine cycle	Unclassified - unlimited

19. Security Classif. (of this report)	20. Security Classif. (of this page)	21. No. of Pages	22. Price*
Unclassified	Unclassified	545	$3.00

*For sale by the Clearinghouse for Federal Scientific and Technical Information Springfield, Virginia 22151

FOREWORD

This report was prepared by the AiResearch Manufacturing Company of Arizona, A Division of The Garrett Corporation, and was issued as APS-5317-R. The activities discussed herein were conducted under NASA contract NAS 3-10934; Mr. E. E. Kempke of the Lewis Research Center Space Power Systems Division was the project manager for NASA, and Mr. R. A. Rackley directed the program at AiResearch.

The study was performed in two phases, a component performance and conceptual design analysis (Phase I) and a preliminary design study (Phase II). AiResearch was assisted by two subcontractors: Westinghouse Aerospace Electrical Division (WAED), which was responsible for the alternator design, and Westinghouse Astronuclear Laboratories (WANL), which provided technical assistance in the areas of turbine aerothermodynamic analysis and turbine material support. The report was issued in three volumes. Volume I covers the turbine and bearing Phase I conceptual analysis and complete turboalternator configurations of Phase I. Volume II covers the Phase I alternator conceptual design. Volume III covers the detailed evaluation of the turboalternator that resulted from the study.

The following individuals contributed to this program as specified: alternator design (WAED): Mr. T. C. Allen, Mr. A. E. King, Mr. C. C. Kouba, and Mr. J. L. McCabria; bearings and rotor dynamics (AiResearch): Mr. D. R. Chivens and Dr. L. A. Matsch; turbine aerodynamic and mechanical design (AiResearch): Dr. K. E. Boyd, Dr. C. S. Chang, Mr. C. A. Larson, and Mr. E. A. Mock; turbine aerothermodynamic and materials support (WANL): Mr. W. D. Pouchot and Mr. G. G. Lessman.

It should be noted that many of the bearing configurations, alternator variables, and turbine materials were initially identified during the analytical and experimental SNAP 50/SPUR program.

TABLE OF CONTENTS

TABLE OF CONTENTS (Contd.)

TABLE OF CONTENTS (Contd.)

TABLE OF CONTENTS (Contd.)

TABLE OF CONTENTS (Contd.)

LIST OF FIGURES

LIST OF FIGURES (Contd.)

LIST OF FIGURES (Contd.)

LIST OF FIGURES (Contd.)

LIST OF FIGURES (Contd.)

LIST OF FIGURES (Contd.)

LIST OF FIGURES (Contd.)

LIST OF FIGURES (Contd.)

LIST OF FIGURES (Contd.)

LIST OF TABLES

LIST OF TABLES (Contd.)

POTASSIUM TURBOALTERNATOR (KTA) PRELIMINARY DESIGN STUDY

III - PHASE II KTA FINAL DESIGN

1. INTRODUCTION AND SUMMARY

This report, submitted by The AiResearch Manufacturing Company of Arizona, A Division of The Garrett Corporation, presents the analysis and final results of a program conducted under NASA-Lewis Research Center contract NAS 3-10934, "Potassium Turboalternator Preliminary Design". The program was conducted in two phases; a component performance and conceptual design analysis (Phase I) and a preliminary design study (Phase II).

During the Phase I analysis, the individual turbine, alternator, bearings, and seals subcomponents were separately optimized. At the conclusion of the Phase I analyses at least four turboalternator configurations comprised of the optimized components were to be submitted to NASA for their approval and selection. The Phase II effort was a detailed preliminary design of the turboalternator configuration(s) selected by NASA at the end of Phase I.

Assisting AiResearch in the performance of the study were two subcontractors. Westinghouse Aerospace Electrical Division was responsible for the alternator electrical and mechanical design and analysis (exclusive of bearings). Westinghouse Astronuclear Laboratory supplied technical support in the analysis of condensate formation and blade moisture collection, executed a detailed erosion analysis of the final turbine configuration, and provided the complete turbine materials support.

This report is in three volumes. Volume I contains the Phase I turbine, bearing, and rotor dynamic analysis as well as a definition of the KTA configurations defined at the end of Phase I. Volume II

contains the alternator conceptual design and analysis for Phase I. Volume III presents the final KTA configuration and the supporting analyses on the individual components.

The priorities observed in the component optimization were ranked in decending order:

(a) High reliability
(b) Ease of development
(c) Maximum energy conversion efficiency
(d) Minimum weight

1.1 Phase II Guidelines and Specifications

NASA selected only one KTA configuration for evaluation during Phase II. This was Configuration 3 from the six KTA arrangements prepared by AiResearch at the end of Phase I. This configuration of the KTA featured interspool moisture removal and utilized potassium bearings in both turbine and alternator. In addition, the turbine was specified to include interstage moisture removal via a slot in the casing at the next to last rotor blade row. Table 1 gives the final Phase II design specifications for the KTA.

The significant changes reflected by these Phase II specifications over those of Phase I are:

(a) The flow rate is specified for the turbine to match a 2-Mw thermal power reactor. This specified flow rate is 16.7 percent lower than that selected by AiResearch to meet the 450-kw_e output specified in Phase I. Power level rather than flow rate had been specified by NASA during Phase I.
(b) The turbine exit pressure and temperature was reduced below the values specified in Phase I (a second reduction since program initiation). This reduction was consistent with the

TABLE 1

PHASE II DESIGN SPECIFICATIONS SUMMARY

	Aerodynamic Design Point	Mechanical Design Point
Turbine inlet temperature, °F	2100	2150
Turbine inlet pressure, psia	165	190
Turbine exit temperature, °F	1220	1220
Turbine exit pressure, psia	5.44	5.44
Turbine mass flow rate, lb/sec	2.05	Undefined
Shaft speed, rpm	19,200	
Alternator maximum continuous load rating, kw_e	450 at 0.75 lagging pf	
Frequency, Hz	1600	
Voltage	480 line to neutral 3 phase	
Overload rating, kva	900, 0.9 pf for 5 sec	
Alternator coolant and bearing lubricant	Potassium at 700°F	

NASA intention to increase the power plant overall efficiency. NASA also requested consideration of adding stages to the turbine to increase efficiency.

(c) The maximum continuous rating of the alternator was reduced from 550 to 450 kw_e to save weight by decreasing the margin between alternator rating and turbine design power output. The final design power output from the KTA of 427 kw_e was not determined until late in Phase II.

(d) The reduction in alternator rotor and stator coolant temperatures from 800° to 700°F resulted in more stress safety margin in the rotor.

(e) The bearing potassium lubricant supply temperature for the turbine was not specified but was jointly selected by NASA and AiResearch to be 900°F. This higher (than Phase I value

of 800°F) temperature reduced thermal gradients in the bearing area.

The contractual requirements for Phase II included one conceptual design layout and the results of analysis of the following areas:

(a) Turbine pitch line velocity diagrams
(b) Moisture extraction effects
(c) Alternator design computation
(d) Rotor dynamics, critical speeds, effects of shaft coupling
(e) Bearing and seal losses
(f) Detailed thermal and stress analysis of turbine rotor, tie bolt and bearing and seal areas

These results are included herein. Section 2 contains the summary details of the turboalternator and Sections 3, 4, and 5 contain the detailed design analysis of the turbine, bearings, and alternator, respectively.

2. KTA DESIGN SUMMARY

2.1 Overall KTA Design

The final KTA preliminary design has been completed and is shown in artist's conception in Figure 1 and as a layout drawing in Figure 2. The overall weight and size of the unit and its performance are given in Table 2.

The major features of the AiResearch KTA design are:

(a) High Reliability - This is due, in part, to the extreme simplicity of the design and, in part, to the conservatism used in all stressed area calculations. Impact erosion is not expected to occur in the turbine. Alternator rotor stresses and temperatures are low enough to eliminate creep as a limiting design criterion.

(b) Ease of Development - Development is based on the use of proven techniques and demonstrated subcomponents and material where possible. No basic questions of feasibility exist regarding any feature of the design. Only three basic blade designs are required for the entire turbine. One for Stage 1, one for Stages 2 through 5, and one for Stages 6 through 10. Blade designs are generated for the longest length blade of a set, and the tip is cut back for the other blade rows. Turbine disks are identical in Stages 6 through 9 (and 10 except for a reduced curvic diameter on the rear side). Identical inserted blade dovetail details will be used on Stages 6 through 10. All these simplifying features contribute to the ease of development of the KTA turbine. In the alternator, use of a simple rotor design with a single central coolant hole and the use of slotted one-piece rotor pole tips, rather than separately attached laminated pole tips, have assured

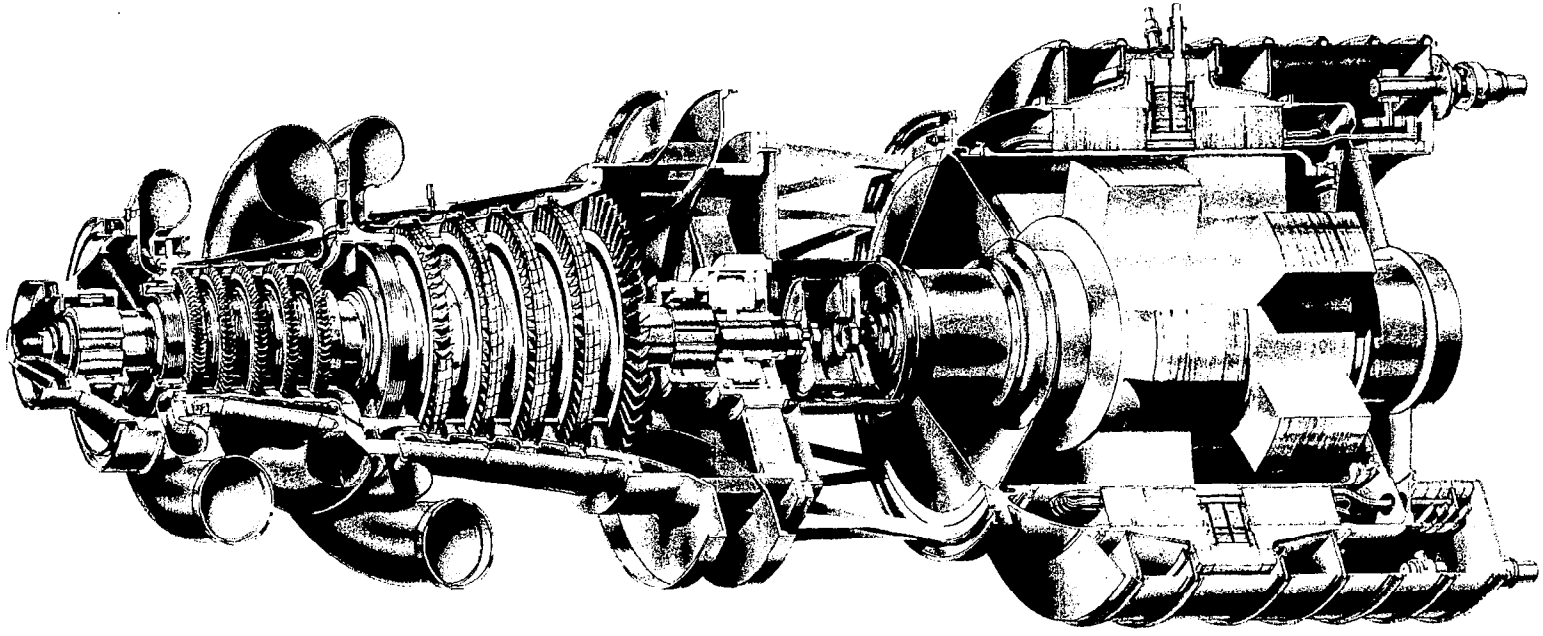

MS 1811-0

POTASSIUM TURBOALTERNATOR (KTA) ARTIST'S CONCEPT

FIGURE 1

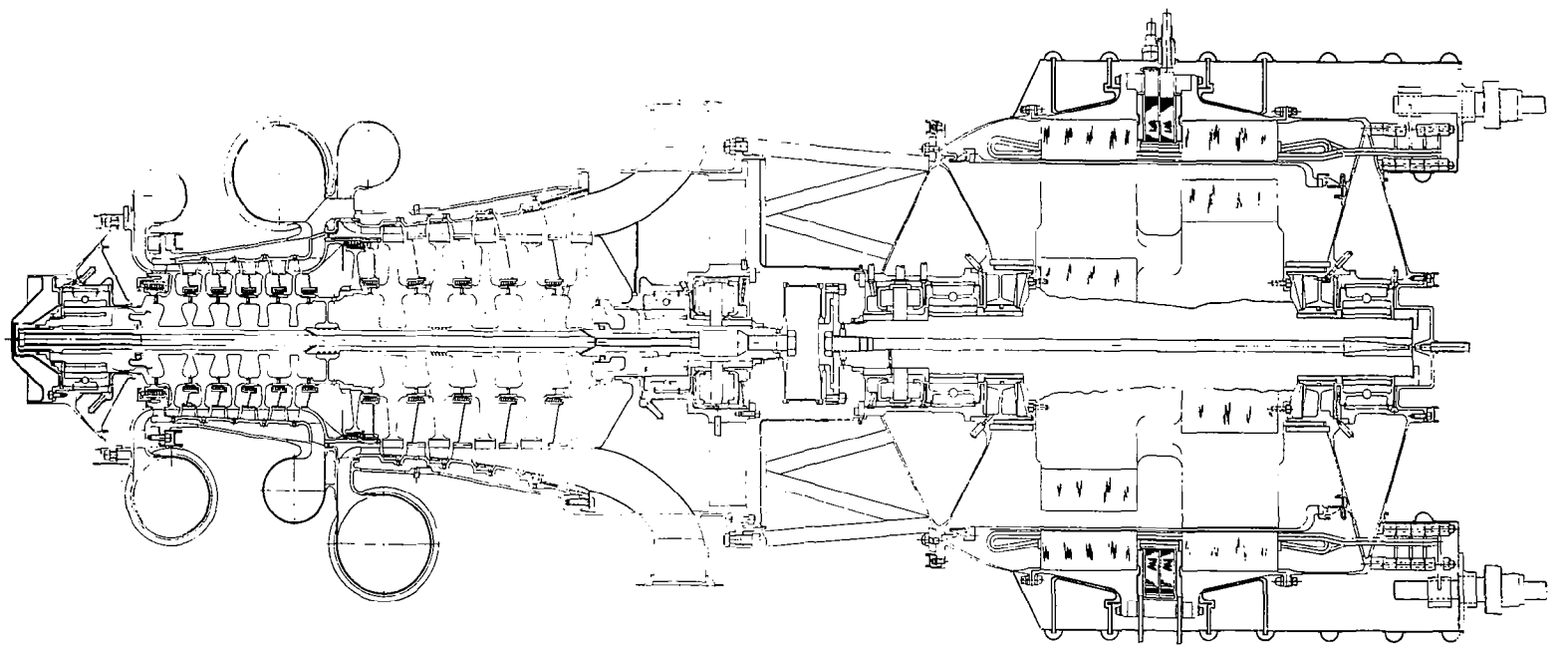

POTASSIUM TURBOALTERNATOR CROSS-SECTION LAYOUT

FIGURE 2

TABLE 2

KTA PERFORMANCE, SIZE, AND WEIGHT SUMMARY

Turbine		
Total to total efficiency including effects of labyrinth seal leakages, tip clearance losses and moisture losses		0.813
Turbine shaft power, kw		481.3
Losses	**Kilowatt**	
Turbine wheel windage	1.75	
Turbine journal bearings	2.50	
Turbine thrust bearing	10.15	
Turbine seals	1.07	
Turbine front end churning	0.43	
		15.90
Alternator journal bearings	5.00	
Alternator thrust bearing	7.29	
Alternator seals	1.35	
		13.64
Total losses		29.5
Alternator net input shaft power		451.8
Alternator electrical efficiency		0.945
Net output power, kw_e		427

KTA WEIGHT AND SIZE	
Turbine weight, lb	437
Alternator weight, lb	861
Connecting structure, lb	18
Total	1316
Overall length, in.	67.1
Maximum diameter (at alternator), in.	24.7

ease of development of the rotor. A simple, more reliable and more readily developed bore seal end member and bimetallic transition joint has been disclosed.

(c) High Efficiency - Both alternator and turbine have been optimized for maximum efficiency within the constraints of high reliability, ease of development, and minimum power plant system weight.

(d) Minimum Weight - The compact, close-coupled nature of the design favors the achievement of low weight. The use of circumferentially split rather than axially split turbine and alternator housings also favors low weight in flanges.

Minimum weight for the KTA has been interpreted as minimum system weight penalty due to the KTA. That is, the effect of increasing the component weight of the KTA will tend to be offset if component efficiency is simultaneously increased. At an assumed specific weight of 50 lb of system weight, an increase of 1 kw_e in output power is, to a first approximation, equivalent to reducing the system weight by 50 lb. From this simple analysis, it is clear that the KTA should be optimized to gain maximum practical efficiency consistent with moderate component weight increases (i.e., less than 50 lb gained per kw_e output gained). This philosophy has resulted in the selection of designs with high efficiency for both the turbine and alternator.

2.2 Turbine Design Summary

2.2.1 General Arrangement

The KTA turbine as shown in Figure 3 is a 10-stage axial flow unit straddle-mounted on pivoted-pad journal bearings lubricated by 900°F liquid potassium. A pivoted-pad thrust bearing is sized to carry the aerodynamic thrust load and the weight of the turbine rotor. The turbine housing is of one-piece design without an axial split line. This feature assures uniform thermal growth and structural integrity without

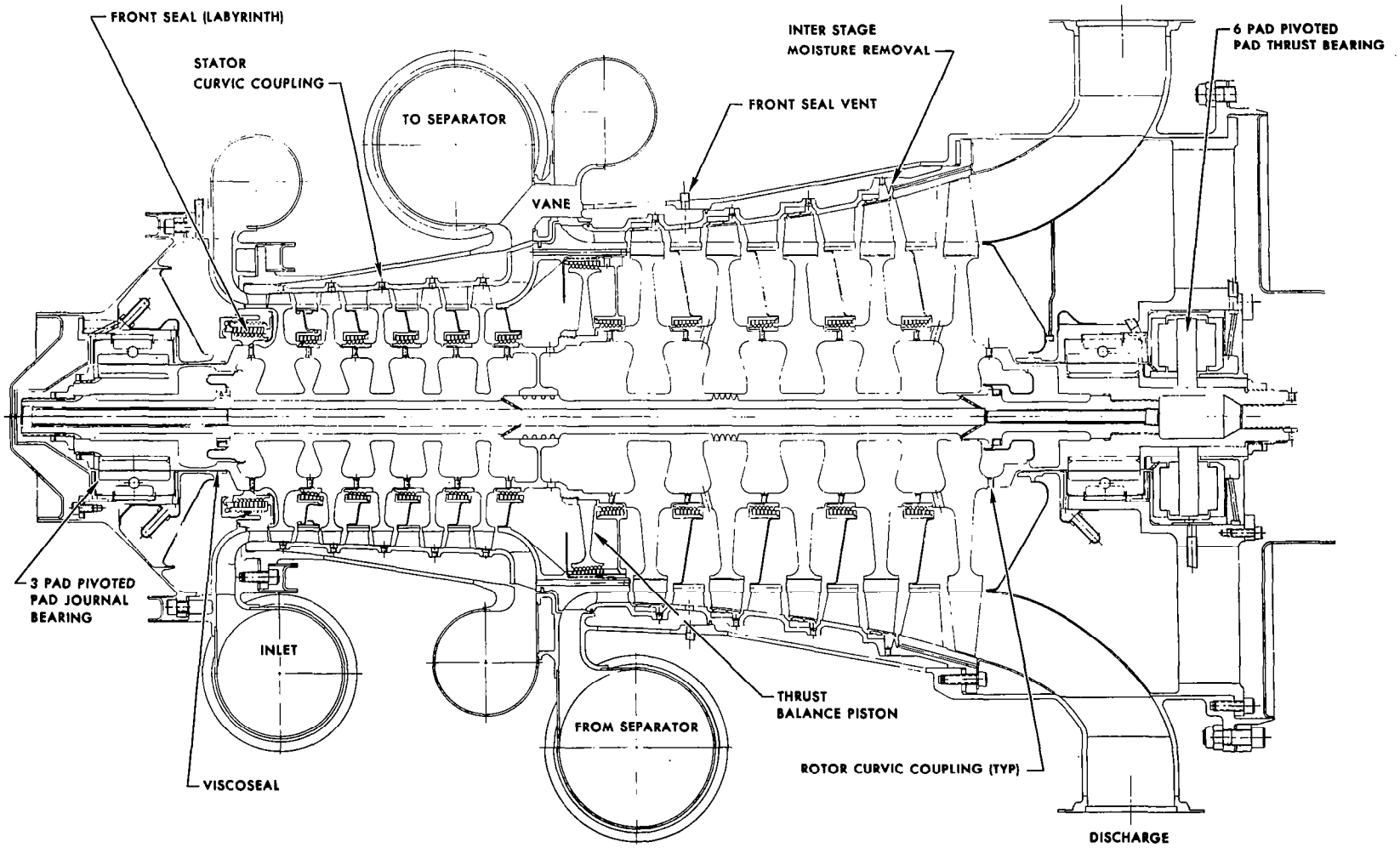

KTA TURBINE DESIGN LAYOUT

FIGURE 3

heavy longitudinal flanges. Interspool moisture removal is accomplished by collecting all the flow exiting the fifth-stage rotor in a single scroll duct. The flow is ducted to an external separator device (not considered part of this study) where 90 percent of the moisture droplets are assumed to be collected. A quantity of vapor equal to 10-weight percent of the removed moisture is also assumed to be lost in the separator. The flow is returned to the turbine in a single duct and scroll and is reintroduced into the turbine, passing through the remaining turbine stages. The turbine stages prior to the interspool duct constitute the high-pressure turbine and the turbine stages after the interspool duct constitute the low-pressure turbine. The high-pressure turbine will operate completely dry due to supersaturation of the potassium working fluid. Reversion to near-equilibrium conditions occurs in the ducting just downstream of the fifth-stage rotor. The low-pressure turbine operates with wet vapor. Interstage moisture removal is accomplished by a collection slot at the trailing edge of the ninth-stage rotor blade shroud.

An erosion analysis of the KTA turbine has been performed by WANL and, according to this analysis, the combination of droplet size and impact velocity expected in the KTA is below the threshold level at which erosion damage is significant.

2.2.2 Turbine Materials

The construction materials for the turbine (exclusive of the bearings) are all refractory alloys. The use of a minimum number of different materials is an advantage in minimizing possible mass transfer interactions between materials in the closed-liquid metal loops required in this system.

The rotating components of the turbine are TZM except for the rear bearing stub shaft which is T-111. The TZM alloy chosen for this application is KDTZM-1175, as originally developed for the SNAP 50/SPUR

program at AiResearch. This alloy possesses an outstanding advantage over other material candidates for the KTA rotor in that forging and heat-treating schedules have already been developed for this material, and sample disk forgings were made during the SNAP 50/SPUR program. Creep samples from KDTZM disk forgings have been tested during the NASA-TRW creep program with test times up to 10,000 hr. Confidence is high in the ability of this material to meet the KTA requirements. The predicted rim radial growth of the first-stage turbine disk is 0.002 in. in 30,000 hr of operation at the mechanical design condition.

The KTA turbine housing materials are T-111 and Cb-1Zr. T-111 is used at the hot end of the turbine housing, including the front bearing housing and inlet scroll and outer housing up to the interspool duct. This material is readily fabricated by welding and has the required level of strength at the maximum turbine inlet temperature of 2150°F. Cb-1Zr, also a fabricable alloy, has been chosen for the lower temperature, lower stressed regions in the turbine, beginning at the interspool duct and including the remainder of the rear-half of the turbine. Cb-1Zr has approximately one-half the density of T-111 (0.31 versus 0.604 $lb/in.^3$) and, thus, provides a substantial weight saving. The Cb-Ta-W alloys FS-85 (density 0.383 $lb/in.^3$) may be considered in the final design in areas where a higher working stress level would be beneficial (such as the interspool area). A complete discussion of the turbine materials provided by WANL is found in Appendix A of this volume.

2.2.3 Turbine Rotor Construction

The turbine rotor is held in alignment by curvic couplings on each separate rotor disk and stub shaft. A TZM tie-bolt provides a compressive load to secure the rotating assembly. Each rotor is an individual TZM forging with integral blades used in the first five stages of the turbine (high-pressure rotor) and inserted blades in the last five

stages (low-pressure rotor). The use of inserted individual blades on the low-pressure rotor allows each blade to be designed with an individual tip shroud in Stages 6, 7, 8, and 9. Stage 10 is not shrouded because the increase in dovetail stresses due to shrouding is not worth the very small increases in turbine efficiency gained in the comparatively long tenth-stage blades. The shrouds used on Stages 6, 7, 8, and 9 result in a one-point gain in overall turbine efficiency over an unshrouded design, and the shroud on the ninth stage facilitiates moisture removal after the ninth rotor. Moisture removal after all wet stages is an AiResearch and WANL recommendation for the final design of the KTA, and tip shrouding of Stages 6 through 9 will help implement this feature.

The tie-bolt operates at conservative stress levels for KDTZM-1175 at the predicted tie-bolt temperatures and will have negligible creep elongation. A mid-span bumper supports the tie-bolt at the interspool transition area. This bumper assures that the tie-bolt will not experience excessive vibration at any turbine speed, since it increases the tie-bolt critical bending frequency to above the overspeed condition for the turbine.

A thrust balancing piston is incorporated in the turbine between the fifth and sixth stages in the interspool transition area. Without the balancing piston, the turbine aerodynamic thrust load is 1344 lb at the aerodynamic design point. The balancing piston provides 961 lb net reduction in thrust. The thrust bearing shown is sized to carry the full aerodynamic load at the overpressure conditions of the mechanical design-point plus the weight of the rotor acting in either fore or aft direction. The balance piston, as shown, would allow a smaller thrust bearing to be used. The balance piston leakage losses and the large thrust bearing losses have both been incorporated in the overall losses calculated for the turbine. Both the large thrust bearing and the thrust balancing piston should be included in the prototype test

turbine, when built, and if the balance piston leakage and condensation problems prove to have been solved by this design, the thrust bearing size and its attendant losses could be reduced substantially. A gain in electrical output of up to 4 kw might be realized by reducing the thrust bearing size.

2.2.4 Turbine Stator Construction

The stator design utilizes T-111 and Cb-1Zr individual stator blades with integral inner-ring platform segments. These blades are inserted in the continuous one-piece stator rings through electrically machined blade-contour-matching holes in the rings and are welded on the outside of the stator rings. The individual blade inner-ring platform segments will then form a completed inner-ring which is then welded to the stator labyrinth seal diaphragm outer-ring to complete the assembly. Each completed stator assembly will then have curvic coupling teeth machined on the outer-ring. The stator assemblies will pilot one to another, held in precise alignment by the curvic couplings. The stator stack, comprising all ten stator rings and the interspool stator transition ring will form one assembly piloting into the outer housing at only two points at the first and tenth stages. The entire stator assembly alignment will then be virtually unaffected by any distortions of the outer housing. The outer housing will be placed in tension by the bolts holding the stator stack at the rear of the turbine, and the entire stator stack will be in compression. Piston rings are used to seal between the stator rings and outer-housing at the interspool location.

2.2.5 Seal Configurations

Noncontacting-type seals are used throughout the turbine. Viscoseals are used to contain the liquid potassium in each bearing compartment. Labyrinth seals are used for each interstage seal and for sealing

between the front bearing compartment and the first turbine rotor disk. The leakage from this seal is vented via an external pipe and reintroduced in the stator of the seventh stage. This allows the leakage flow to do work in Stages 7 through 10. Each of the labyrinth seals is fabricated from multiple T-111 foil rings (as described in Section 3.6.5). This design should tolerate minor rubs, should they occur, without serious damage.

2.2.6 Turbine Assembly

The KTA turbine is assembled by first completing the rotor and stator assembly and sliding it into the outer housing. Assembly would begin with the rear stub shaft held vertical in a fixture. The tie-bolt would be tightened into the stub shaft, and a seal weld made on the rear seal diaphragm between the stub shaft and tie-bolt. Next the tenth-stage rotor and the tenth-stage stator assembly would be slipped over the tie-bolt. A simple holding fixture would be required to support the stator ring relative to the rear stub shaft. The ninth-stage rotor and stator would next be stacked over the tie-bolt with stator and rotor parts each engaging mating curvic coupling teeth on the stator and rotor of the previously positioned stage. This procedure continues until Stage 1 has been completed. The front stub shaft is positioned over the tie-bolt and engaged with the first rotor curvic coupling. Tension is applied with a calibrated pull rig and the tie-bolt nut secured without applying a twist to the tie-bolt. This technique assures proper tie-bolt tension with lowest stresses. Locking the tie-bolt nut with an antirotation device completes the major rotor/stator assembly.

The outer housing can next be lowered over the vertical rotor/stator assembly and mated with the stator pilot diameters at Stages 1 and 10 stator rings. The bolts at the rear of the tenth stage turbine stator ring are inserted and tightened to place the outer housing in

tension and the stator rings in compression. This compression assures that the stator rings, which pilot one to another by curvic couplings, will remain in good alignment. Alignment of the entire assembly of static parts can be assured by final assembly machining of all parts. The stator assembly can be assembled without the turbine rotors and all the interstage and front labyrinths line-bored concentric with the geometric turbine centerline. This operation would best be done with a single setup on a vertical jig grind machine. The front bearing compartment can also be final match-machined to assure bearing concentricity using the same final grind setup as the stator labyrinth seals. Excellent concentricity and alignment of the rotating and stationary hardware is assured by this final machining technique. Marking the parts before disassembly and reassembly with the same relative positions assures the accuracy of the final build.

2.3 Alternator Design Summary

2.3.1 General Arrangement

The KTA alternator, as shown in Figure 4, is a 10-pole radial-gap unit straddle-mounted on pivoted-pad journal bearings which are lubricated by 700°F potassium. The maximum continuous load rating is 600 kva (450 kw_e at 0.75 load power factor) at 480 v (L-N). The stator is also cooled by 700°F potassium.

Significant improvements were realized in the Phase II alternator design. Relative to the basic conceptual design derived in Phase I, electrical efficiency was increased nearly two points to over 94 percent while the electrical weight decreased from 1.14 to 1.08 lb/kva. With these reduced electrical losses, the cooling configuration selected in Phase II was more than adequate and limited the stator hot-spot temperature to only 902°F for the 700°F inlet coolant.

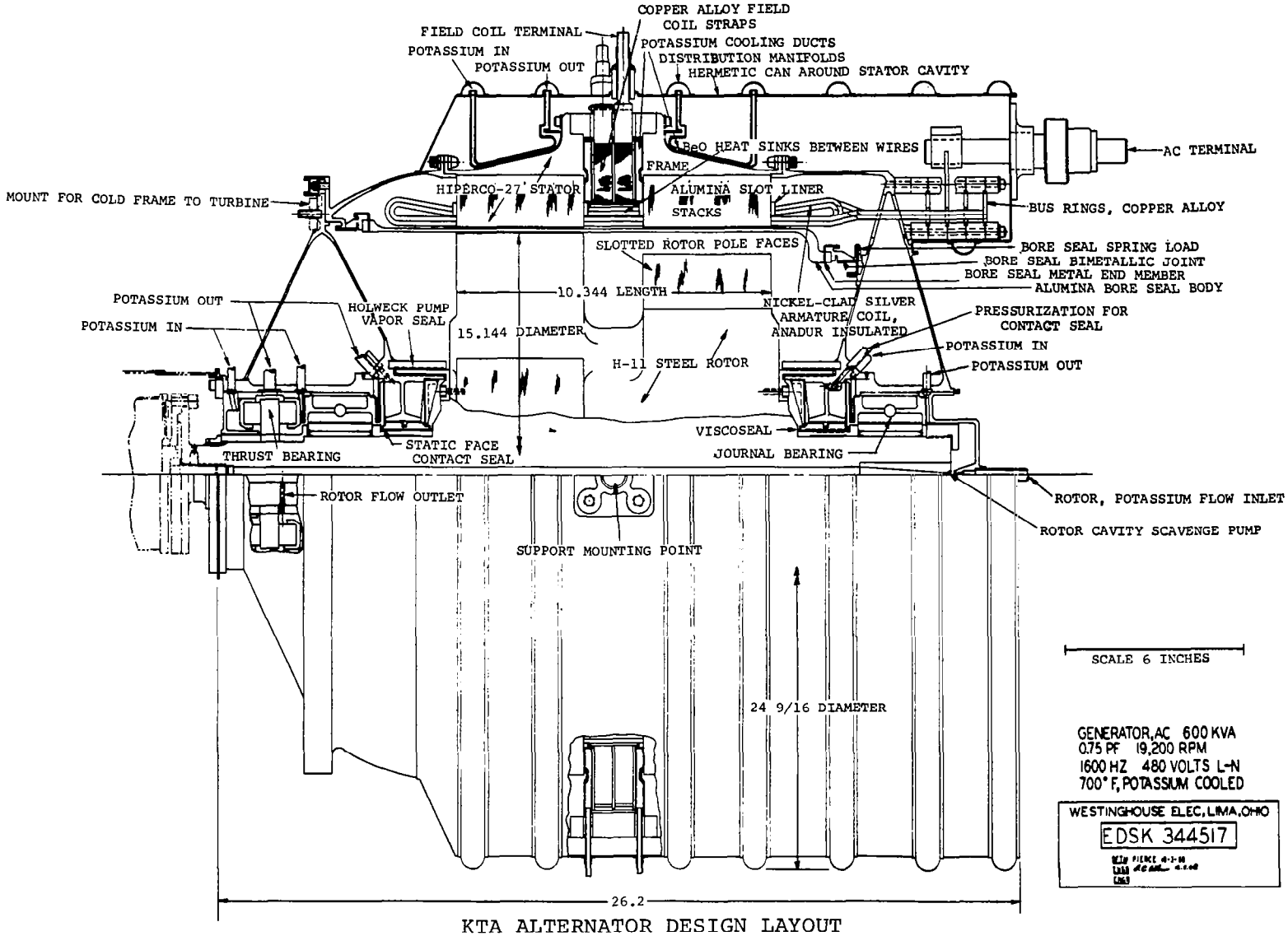

KTA ALTERNATOR DESIGN LAYOUT

FIGURE 4

As part of the stator design studies, special efforts were concentrated upon reduction of weight of the inert structural hardware. As a result, over 200 lb of weight were trimmed from the structure while still minimizing structural stresses to less than 30,000 psi.

The impact of reducing the rotor coolant temperature to 700°F was very significant to the reliability of the design. Laminated pole tips were no longer needed, and slotted pole faces became more than adequate to minimize pole face losses that limited pole tip temperatures to less than 900°F. The combined temperatures and stresses of the rotor were sufficiently low to eliminate rotor creep strain as a limiting design criteria.

Relative to the third major area of the alternator (the bore seal), a simpler, more reliable configuration was evolved for the end members and bimetallic transition joints. This was possible as a result of extensive analyses and consultations with experts in the area of bimetal joints. The resulting design integrates the requirements and desired features of the bimetallic joint with those previously defined for the ceramic-to-metal joint. However, the bore seal must be considered as lagging the development of the other major alternator components--rotor and stator.

The significant features of the alternator electrical and structural design are found in the rotor, stator, and bore seal configurations of Figures 4 and 5. The bearing designs were furnished by AiResearch.

As seen on Figure 4, the basic alternator is made up of the rotor, the magnetic frame, the Hiperco-27 stacks, the armature coils, and the field coils. The rest of the configuration around these fundamental components is to transfer the coolant in and out, transfer the power out, and support the stator and rotor as an integrated unit. The endbells mounting the bearing housings to the stator frame are mechanically

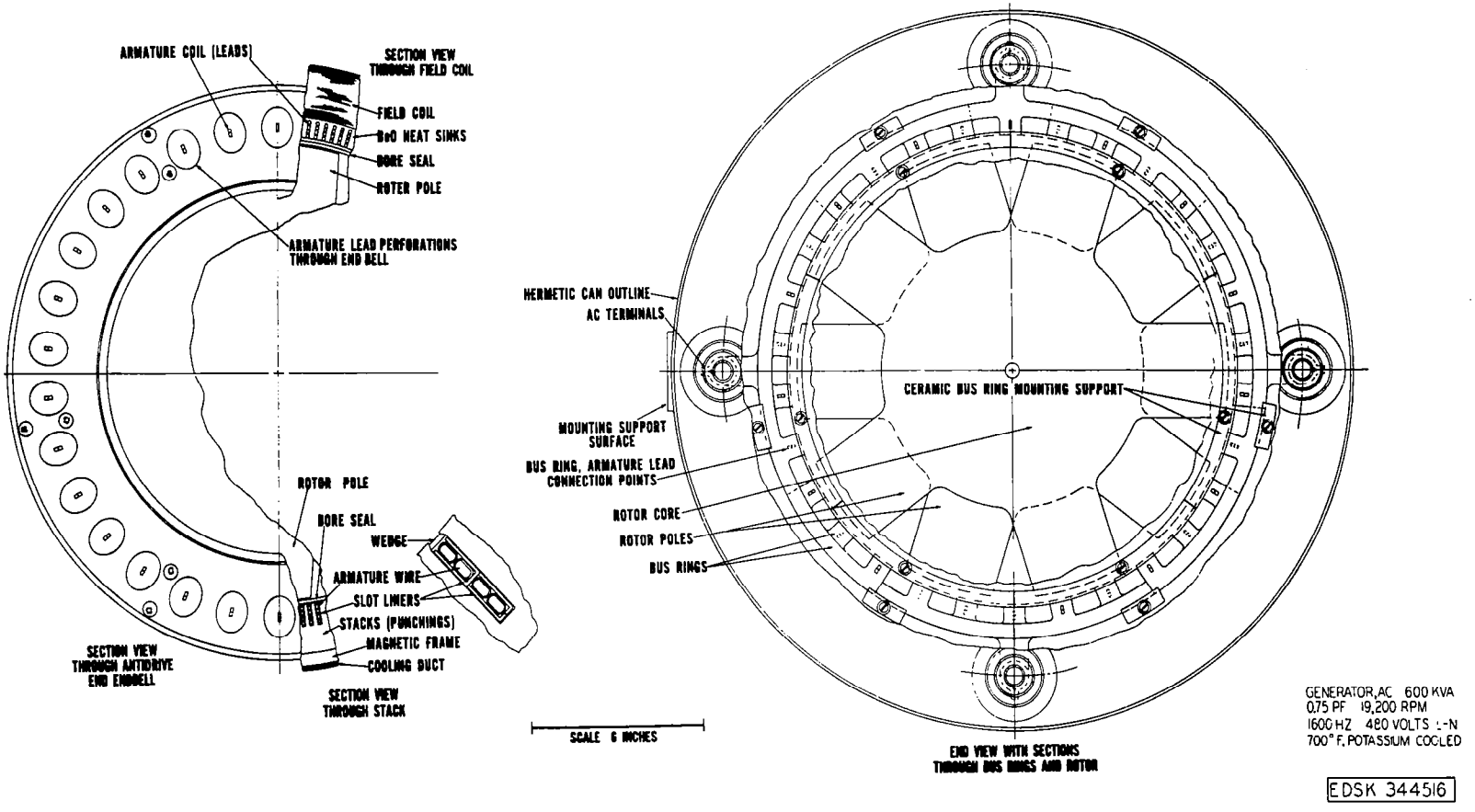

KTA ALTERNATOR CROSS-SECTIONS

FIGURE 5

fastened directly to the magnetic frame to utilize the structural rigidity associated with the relatively large magnetic frame. Because of the armature coil leads passing through the antidrive end-bell to the bus rings, the end-bell becomes a permanent part of the electrical assembly upon completion of the electrical winding. In passing through this end-bell, 1/2-in. spacing is allowed around each lead. This is to minimize eddy current heating due to the high-frequency alternating flux surrounding the lead. This spacing is adhered to as a general rule for all the electrical leads of the ac armature coil.

2.3.2 Alternator Stator

The stators are hermetically sealed to permit operation without subjecting the stator components to corrosion damage by either air or moisture external to the alternator or by potassium vapor internal to the rotor cavity. The ambient of this hermetically sealed cavity is a hard vacuum, or in flight, a space vacuum. The hermetic shroud is a thin-wall reinforced can with a thickness of 30 to 40 mils. There are reinforcing rings around the can that also double as coolant distribution manifolds for the stator coolant. The stator coolant enters and leaves through these toroidal shaped manifolds. These distribution manifolds feed the toroidal-shaped cooling ducts that are bonded directly to the Hiperco-27 frame. It should be pointed out that the stator cooling ducts bonded to the frame shown are only meant to be schematic. Thermal cooling analyses indicate there are at least a half-dozen different ways these cooling ducts can be configured to the frame; the actual details are, therefore, left to the final hardware stage and the manufacturing engineer's selection. The field coil cooling ducts must be according to the configuration shown, i.e., basically on the side of the two bundles of coil straps and bonded to the frame sides. The various cooling ducts are in parallel flow with each other to minimize the temperature rise through the stator and, therefore, minimize the temperature gradients.

The stator punchings are 0.004-in.-thick Hiperco-27 magnetic alloy, have a semiclosed slot to reduce pole face losses, and are assembled into an unwelded stack to reduce iron losses. A 0.0004-in.-thick layer of plasma arc-sprayed alumina constitutes the interlaminar insulation. The small block of material shown on the ends of the stacks are small tabs on the ends of the slot liners. Those hold and align the unwelded stacks preventing the thin teeth from flaring excessively. As seen on Figure 5 in the section view through the stack, the bottom slot liner must be slit into an L-shape in order to assemble the slot liner into the semiclosed slot. The upper slot liners are U-shaped and can be assembled from the ends of the stack at the time of winding. The segmented BeO heat-sink between the stacks acts as a spacer to serve the same function of preventing excessive flair between the stacks. As the name implies, the BeO heat-sinks carry the armature coil heat from between the stacks into the cooling sink of the copper field coil above it. The size of the segment will be determined by manufacturing economies. The field coil is wound into two (series-connected) toroids of flat straps. They are electrically insulated from each other and the cooling ducts. There is a flat-to-round transition section between each coil bundle and terminal.

There are four bus rings on the antidrive end of the alternator. The parallel phase groups of the armature are connected to each bus ring in such a manner that the bus ring I^2R losses are held to a minimum that, in turn, permits the rings to be cooled by radiation to the stator cavity walls. The maximum bus-ring temperature can be expected to be less than 900°F with a 700°F sink-temperature. The bus rings are supported by ceramic insulation and a mechanical mount, as illustrated in the end view of Figure 5. The rings are not continuous rings, but are partial arcs that allow thermal expansion without diametral growth. The insulation pieces are quite widely spaced on the OD of the rings to permit a good field of view for radiation cooling. The tabs on the rings are held by the continuous (segmented) inner ceramic-mounting

rings. Bonded to these tabs are the leads of the armature coils. These leads come straight off the armature coil into bus rings (Figure 4). This is important to the design of the alternator since it will be necessary to bake out the Anadur and fire it prior to assembly of the windings. This prebake is to obtain a better slot fit-up at assembly by accounting for the 35-percent Anadur shrinkage prior to winding. As previously mentioned, there are only 30 wire ends that are to be attached to the bus rings and as seen by the figures, these are in readily accessible areas. This minimizes bonding problems.

The Anadur prebake and shrinkage problem could be alleviated somewhat by using segmented slot liners that would not be completely inserted until after winding and baking processes. These would be similar to the configuration of the segmented PBN insulation pieces being tested on Contract NAS3-10941 at Westinghouse. The PBN material being evaluated on that contract was not selected for the KTA slot insulation because of the lack of need for the specialized higher temperature capabilities of the PBN material and the economies that result with the more readily available alumina. Nevertheless, these PBN evaluations are being closely followed because of the impact any adversely low slot conductance (measured conductance) would have on the assumptions used in the stator cooling design.

There is one terminal for each bus ring, centrally located about the armature connections. Because of the temperatures brought on by the high current density and because of the limited space, special terminal studs are required. They are sized rather large to have sufficient cross-sectional area to permit them to be self-cooled by radiation. Nickel plating is used to obtain an emmisivity of 0.4 on the outer surfaces. They can be cooled by radiation alone to less than 900° for a 700°F ambient.

2.3.3 Alternator Rotor

The features of the rotor design are found in the slotted pole faces and in the central cooling hole and scavenge system. The material is solid H-11 steel, heat-treated to 45 $\pm 1 R_C$. The slotted pole faces have 0.006 wide by 0.100-in. deep slots, approximately 30/in., that are cut with gangs of carbide cutoff wheels. The process for doing this has previously been developed by Westinghouse.

The central hole in the rotor core serves a number of functions, the first of which is for heat treatment to obtain the 45 R_C hardness and the second of which is for rotor cooling. Also, with the center of the forging drilled out, reliability should be enhanced by eliminating any center line inclusions. The coolant flow coming into the rotor is jetted through impulse-turning vanes, passes along the coolant hole to the drive-end stub shaft, and is dumped into the drive-end bearing cavity.

2.3.4 Assembly

The basic assembly sequence of the alternator is as follows:

(a) Wind the field coil and assemble the frame (with bonded coolant duct assemblies) around the field coil.

(b) Assemble the frame cap to form the magnetic frame structure. The frame cap is split into two half-moon sections and forms a mechanical connection between the two frames over the stacks. This has the undesirable feature of, once the field coil is assembled, being difficult to disassemble the stator to repair the field coil without losing concentricity between stacks. However, this may be overcome with proper tooling to hold the assembled alternator stacks concentric. Also, this feature is not too bad in light of the high reliability expected of the rather simple field coil configuration.

(c) With the frame assembled, mount the stacks into the frame and the armature coils are wound into the slots with the rigid ceramic insulation.

(d) Mount the antidrive end-bell and the drive-end frame extensions to mechanically lock the unwelded punchings into the frame.

(e) Grind the various mounting diameters and running clearance diameters concentric as an assembly. These would consist of the mounting diameter for the drive-end end-bell, the stack ID's and the bearing housing ID's on the antidrive-end.

(f) Assemble the bus rings and terminals onto the ends of the assembly of the hermetic shroud around the stator cavity with its field coil terminals and reinforcing/coolant manifold rings.

(g) Insert the bore seal, placing the bore seal preload spring in proper compression and making the seal welds between the bore seal end member assemblies and the steel frame or end-bells.

(h) Assemble the bearing components at the same time inserting these plus the rotor into the stator assembly. The sequence for this will be to insert the rotor and assemble the anti-drive end-bearing at the same time. This will be followed by attaching the drive-end end-bell and inserting that bearing at the same time.

(i) Cap the two ends of the bearing housings to complete the total alternator assembly.

(j) Disassemble in the reverse direction.

The stator can be assembled as a unit separate from the rotor and bearing stub shaft assemblies. This is an important feature for disassembly capability after tests with potassium or for general maintenance.

The alternator is attached to the turbine through the "Mount For Cold Frame". A pilot fit and studs are provided to mechanically attach the frame. Just above that fit is the drive-end end-bell connection. Because this joint must be hermetically sealed, it appears to require a second pilot fit and bolt circle over that already used for the cold frame to turbine. Since combination of these two fits would save weight, it is recommended that this area of the design be re-evaluated in the next phase.

Most of the tubing for bearing flows, etc., is not shown precisely because of the lack of definition of the test assembly setup; the tubing configuration will more than likely be influenced by it. Where a penetration in the end-bells is required to bring out any particular tube, it will be general practice to bring out two tubes (one possibly a dummy) through penetrations located 180 deg apart to equalize or balance the effects of the penetrations on the end-bell.

2.4 KTA Reliability Analysis

A Failure Mode, Effect, and Criticality Analysis has been carried out for both the turbine and the alternator. The purpose of this analysis is to identify the potentially critical failure areas so that efforts can be made to reduce the probability of these failures to an absolute minimum. This analysis has been done separately by the turbine designers at AiResearch and by the alternator designers at WAED. Tables 3 and 4 show the results of these analyses. Bearing failure modes shown for the turbine also apply to the alternator.

TABLE 3

TURBINE FAILURE MODE ANALYSIS

Subsystem or Component	Failure Mode	Failure Effect	Criticality	Remarks
1. Flexible coupling	Fatigue	Immediate - zero power	Critical	Designed for stresses below endurance limit. Should have unlimited life.
2. Rotor blade and tip shroud	Erosion	Very gradual reduction in output power	Noncritical	Analysis indicates erosion will not be significant.
3. Rotor blade	Rub due to creep	Variable, from no effect to major	Noncritical	Calculated to occur after exceeding design life. May be accelerated by excessive overtemperature.
4. Rotor blade	Nick due to foreign particle ingestion or boiler liquid slugging	Variable - Slight to serious vibration	Noncritical	May be prevented by separator device or screen.
5. Rotor blade	Fatigue break due to bending	Variable - Serious vibration or punctured turbine case	Critical	Design for low bending stress in blades.
6. Turbine disks	Excessive or non-uniform creep	Cause blade rub	Noncritical	Accelerated by overtemperature.
7. Turbine disks	Burst	Immediate - Zero power	Critical	Caused by overspeed.
8. Turbine disks	Rim cracking due to low cycle fatigue	Variable, no effect to serious rim loss	Noncritical	Due only to hundreds of rapid start cycles unexpected in this application.
9. Tie-bolt loosening	Creep relaxation	Loss of rotor assembly alignment	Noncritical	Overtemperature result.
10. Labyrinth seal (typical)	Rub	Increased leakage	Noncritical	Designed to tolerate minor rubs.
11. Viscoseal	Cavitation erosion	Internal leakage of bearing lubricant	Noncritical	Must be eliminated during development by design or material selection.

TABLE 3 (Continued)

TURBINE FAILURE MODE ANALYSIS

Subsystem or Component	Failure Mode	Failure Effect	Criticality	Remarks
12. Front stub shaft (hot end)	Excessive or nonuniform creep	Loss of rotor assembly alignment, vibration	Noncritical	Little creep expected. Avoid overtemperature.
13. Front bearing support (hot end)	Cracking due to low-cycle fatigue	Loss of potassium	Critical	Result only after hundreds of starts.
14. Front bearing compartment heat baffle	Cracking due to temperature cycling	Internal leakage - heating of bearing compartment	Noncritical	Temperature cycling eliminated by preventing liquid condensate impingement.
15. Interstage stator diaphragm	Excessive deflection	Rub	Noncritical	Low stress in part.
16. Bearings	Pivot wear - increased clearance	Lower load capacity	Noncritical	Highly wear resistant pivot material.
17. Bearings	Cavitation erosion	Lower load capacity	Noncritical	High compartment pressures will suppress cavitation potential.
18. Bearings	Wear due to foreign particles in lubricant	Increased bearing clearance resulting in lower load capacity	Noncritical	Bearing lubricant inlet filters should be used.
19. Bearings	Seizure due to lube supply failure	Immediate - zero power	Critical	Lube supply system must be designed for minimum failure potential.

TABLE 4

ALTERNATOR FAILURE MODE, EFFECT AND CRITICALITY ANALYSIS

Mode of Failure	Probable Causes of Failure	Immediate Effect on Operation	Long Range Effect on Operation	Effect on Power System
		ROTOR		
Nonuniform creep rate or yield	Due to nonuniform properties	Increased vibration	---	---
Stub shaft rubs seals	Due to loss of concentricity	Increased vibration	Wear or seizure	Loss of system
Stub shaft fatigue	Abnormal bearing whirl	Breaks off	---	Loss of system
Crack propagation in rotor core	Due to embrittling and high stress	Increased strain	Rotor disintegrates	Loss of system
Mass transfer, stress corrosion and galvanic corrosion	All due to mass transfer	Added solids into coolant	Increased stress, strain, and possible loss of rotor	Shorten life, loss of system
MHD and plasma erosion on bore seal	Due to corona and $\overline{U} \times \overline{B}$ in plasma	Reduce output	Loss of bore seal	Loss of output
Major loss of concentricity	Due to loss of bearing	Rub and/or loss of rotation	---	Loss of system
Material property change	Embrittlement, creep, resistivity, permeability	Minor change in power output	Excessive creep or yield	Shorten life
		ROTOR COOLANT		
Excessive coolant temperature	Due to system malfunction	Possible plastic yield or rupture	Excessive creep or yield	Loss of system or shorten life
Loss of cavity vacuum control	Due to seal failure or vent plugging	Increased cavity pressure and windage	Excessive rotor creep rate, failure of bore seal members	Loss of system
		BORE SEAL ASSEMBLY		
Loss of hermetic seal	Due to fatigue in joint, tube, bellows or end member; stress corrosion, mass transfer or plasma erosion, instability of braze alloy	---	Stator shorts	Loss of output

TABLE 4 (Continued)

ALTERNATOR FAILURE MODE, EFFECT AND CRITICALITY ANALYSIS

Mode of Failure	Probable Causes of Failure	Immediate Effect on Operation	Long Range Effect on Operation	Effect on Power System
BORE SEAL ASSEMBLY (Continued)				
Loss of assembly structural integrity	---	Allows rub	---	Loss of system
Seal ID shorts with conductive film	Due to excessive potassium	Increased losses	Increased thermal stress on bore seal	Loss of system
Fretting wear	Contact with stator or rotor	---	Loss of hermetic seal	Shorten life or loss of system
Abnormal temperature excursion	System malfunction	Excessive thermal stress	Loss of hermetic seal or assembly	Loss of output or system
STATOR AND STATOR COOLANT				
Leak in cooling duct	Due to fatigue stress corrosion mass transfer	Stator shorts, increased stator cavity pressure to induce corona	---	Loss of output or system
Flow blockage decreased or stopped	Due to solids accumulation or system malfunction	Excessive temperatures and losses	Accelerate insulation deterioration	Shorten life
Duct separating from frame	Due to bond or contact pressure loss	Excessive temperatures and losses	Accelerate insulation deterioration	Shorten life
Stack clamps fatigue	Due to mechanical or electrical fatigue	Separation of stack, loss of power	Fretting wear on bore seal	Noise, loss of system
Excessive coolant temperature	Due to system malfunction	Excessive losses, loosen stack fits	Accelerated deterioration or increased vibration	Shorten life
Fatigue of teeth	Due to mechanical or electrical vibration	Breaks off, flux unbalance	Decrease output, wears through bore seal	Shorten life or loss of system

TABLE 4 (Continued)

ALTERNATOR FAILURE MODE, EFFECT AND CRITICALITY ANALYSIS

Mode of Failure	Probable Causes of Failure	Immediate Effect on Operation	Long Range Effect on Operation	Effect on Power System
		WINDINGS AND INSULATION		
Extended short circuit operation	System malfunction	Armature conductors open	---	Loss of output
Slot cell insulation fatigue	Due to mechanical and electrical vibration	Loss of slot liner or wedges, increased temperatures	Stator shorts	Reduces output
Anadur frets away	Due to mechanical and electrical vibration	Loosening of windings, increased temperatures	Accelerated insulation deterioration	Shorten life
Cladding breaks	Due to handling abuse, electrical stress, poor manufacturing	Silver migrates out of wire	Shorts insulation or opens wire	Reduced output
Joint cladding instability	Due to plating or cladding breaks or chemical reaction	Loss of solid bond	Silver evaporation	Reduced output or loss of output
Armature conductor opens	Due to mechanical or electrical failure	Reduction in output, phase unbalance	---	Reduced output or loss of output
Field conductor opens	Due to mechanical or electrical failure	Loss of output-overspeeds	---	No output
Excessive coolant temperatures	Due to system malfunction	Increased losses, bus rings, and wires sag	Accelerated deterioration, possible short	Shorten life, loss of output
Bus rings and leads fatigue	Due to mechanical and electrical vibration	Open circuits	---	Reduced output or loss of output
Electrical shorts	Due to vibration	Excessive temperatures and loss of or reduced output	Accelerates insulation deterioration	Shorten life, reduced output

TABLE 4 (Continued)

ALTERNATOR FAILURE MODE, EFFECT AND CRITICALITY ANALYSIS.

Mode of Failure	Probable Causes of Failure	Immediate Effect on Operation	Long Range Effect on Operation	Effect on Power System
		INERT HARDWARE		
Loss of rotor cavity hermetic seal	Due to joint failure or fatigue crack	Lower cavity pressure, less windage	Loss of potassium	Shorten life
Excessive coolant temperature	Due to system malfunction	Thermal stress and distortions	Creep rate loosens fits, lose concentricity	Shorten life or loss of system
Fatigue of housings, end-bells, etc.	Due to excessive vibration	---	Loss of potassium	Shorten life
Reduction of emissivity on stator ID	Due to evaporation of coating	Armature temperatures increase loss	Accelerate insulation deterioration	Shorten life
Mounting flange loosens	Due to vibration	Increased vibration, loss of concentricity, loss of stack compression	Accelerated fatigue and breaking	Shorten life, loss of system

2.5 KTA Conclusions and Recommendations

The overall preliminary design of the potassium turboalternator has now been completed and practical design approaches now exist for every critical area in the unit.

2.5.1 Primary Development Areas

From the standpoint of relative level of development risk or design uncertainty still existing in the various subcomponents of the KTA, two areas stand out. These are the turbine rotors and the alternator bore seal assembly.

2.5.1.1 Turbine Rotors

Turbine rotors for the first and last stage of the turbine encompass the two extreme requirements of the KTA turbine rotating assembly. The first-stage rotor has the highest temperature level ranging from 2005 at the bore to 2040°F at the rim. Average tangential stress is 10,160 psi with a maximum bore tangential stress of 16,690 psi. The design of this rotor is creep-strength limited. The last-stage rotor disk will operate at less than 1300°F but has a much higher average tangential and maximum bore tangential stress (35,700 and 59,000 psi, respectively). Creep will not be a problem here but high yield strength is required and has been demonstrated in limited testing.

A single specimen of the selected KTA rotor material, KDTZM-1175, is still undergoing long-time creep testing at TRW under NASA Contract NAS3-2545. Test temperature is 2000°F and stress level is 22 ksi, conditions obviously quite appropriate to the KTA. Total time on this specimen is now 14,000 hr. This single specimen has been used to define the Larson-Miller curve for TZM in the high-temperature region. Thus, the desired properties have been demonstrated but with only a single long-time test specimen.

Creep and yield strength of TZM is developed during forging using particular high-temperature thermal-mechanical processing schedules. It is necessary to demonstrate that the desired properties can be achieved in complex disk forgings. The central portion of the disks are critical since stresses are highest there, but the ability to work this portion of the disk during processing is most difficult. Assuming an adequate forging schedule is developed in terms of thermal-mechanical processing history, there will remain a considerable doubt about the performance of the optimum disk under the complex three-dimensional stress state within the turbine. The best correlation between design and destructive test results can be achieved by running a hot-spin test of both first and last KTA rotors. This would provide realistic loading and a definition of the effects of directionality in the forging which could not be achieved by conducting individual uniaxial tests. Proper conduct of this test would seem to dictate the use of a vacuum or potassium vapor environment. Consequently, potassium bearing tests could be performed simultaneously as a portion of the same test.

2.5.1.2 Alternator Bore Seal

The alternator bore seal assembly is the most underdeveloped of the three major electrical subassembly components. As indicated in the report, the bore seal assembly or "bore seal" must be a coordinated design of all the critical components. These include the alumina body, the ceramic-to-metal joint, the bimetallic transition joint assembly and the refractory-to-refractory and steel-to-steel seal welds at assembly. The most development is required on the ceramic-to-metal joint and on the bimetallic joint. Such a development program must be geared around the specific KTA alternator requirements and be based on the actual KTA dimensions, stresses, strains, coefficients of expansion, material properties, etc. It will require close coordination of the KTA design with the materials and process development programs to arrive at a successful configuration the first time it is assembled and tested.

The bore seal assembly must be put through a very comprehensive analysis and test program simulating the variety of conditions the alternator will encounter prior to risking the assembly in an actual test alternator.

2.5.2 Normal Development Areas

The following brief sections describe the status of the various design areas in turbine and alternator:

(a) Fluid Expansion Behavior - Supersaturation of the potassium vapor is predicted to occur throughout the first five stages of the KTA (these will be dry). The analytical methods for predicting the extent of supersaturation should be confirmed in the existing NASA turbine test rig if possible. Interstage moisture removal taps added to the existing three-stage test rig should disclose where moisture has formed. This type of data would confirm or alter the existing WANL condensation analysis used in the design of the AiResearch KTA.

(b) Turbine Aerodynamics - The aerodynamic design of the turbine is essentially finalized and a preliminary definition of blade contour has been completed. A complete analysis of the ducting for inlet, interspool, and discharge areas, and the separator is required to verify or further reduce the pressure loss values used in the preliminary design analysis. A final analysis of the blading would then be required and would include a boundary layer analysis.

(c) Bearings - Bearings for both turbine and alternator are selected and the basic design is completed. Final designs would be expanded to include the detailed design of thermal compensators for the journal bearings to take up differential expansion between carbide-bearing parts, shafts, and housings. Load leveling or self-aligning features for the thrust bearings must also be designed. The pivoted-pad journal and

thrust bearings for the KTA are considered ahead of the development status of most of the KTA since bearings of thi same design were being developed for the SNAP 50/SPUR. Two journal bearings and a thrust bearing were successfully ope ated for 2000 hr in 600°F potassium at 24,000 rpm in the AiResearch turbodynamic test rig.

(d) Rotor Dynamics - The KTA is conservatively designed to oper ate far from shaft or bearing critical frequencies. The dynamic effects of coupling the separately supported turbir and alternator have been minimized in this design. A roto dynamics simulator test rig should be built and tested pri to initiation of final KTA hardware procurement. This rig should simulate with dummy masses the entire KTA rotating assembly, including both turbine and alternator rotors and bearing compartments.

Such a test rig has become an AiResearch standard uni for new gas turbine engine development. Many unexpected dynamic problems have been identified and corrected on thi type of rig, thereby avoiding costly redesigns later. In case of the KTA, water could be substituted for potassium the bearing lubricant, thereby eliminating rig complicati and long turnaround time on builds and generally reducing costs. Testing of all viscoseals and static seals should included in the test objectives of this rig.

(e) Turbine Housing Fabrication - The turbine housing will be fabricated from T-111 by making extensive use of welding. Underbead cracking tendencies have been recently observed multipass manual GTA weldments in thick plate of this all Since this joining process offers the greatest flexibilit for repair as well as fabrication, this problem requires resolution. Perhaps it can be resolved through the subst tution of ASTAR-811C. If this does not work, then some further development will be required. Alternately, the

turbine housing would have to be designed for single-pass EB welding, but repair techniques would still be required. For minimum weight, the rear low-temperature sections of the housing will be Cb-1Zr requiring evaluation of the structural weld between T-111 and Cb-1Zr. Satisfactory welds between these materials have been made.

(f) Alternator Stator - The stator electrical design can be assumed as relatively fixed at this stage of the design. Further analyses to seek electrical design refinements may not yield sufficient return to warrant the effort required. Should sample tests ever show that the slot conductance is much less than the 0.2 $w/in.^2-°C$ used in the design, a change might be necessary. There is at least a 5:1 safety margin in the design now to obviate, if possible, the need for any later redesign. The slot conductance must be measured in a simulated stator to determine if the 5:1 margin is adequate.

The stator structural design concepts are basically fixed but are subject to final design refinements in the hardware design stage. Final selection of the structural material must be made.

There are several minor developments to be resolved in the stator design that are amendable to resolution during fabrication of the first stator assembly. They include:

(1) Development of the bonding of the L-605 cooling manifolds to the Hiperco-27 magnetic frame.

(2) Development of the detail process techniques for even (0.0004 +0.0000, -0.0002 in. thick) application of the interlaminar plasma-sprayed insulation.

(3) Development of the fabrication techniques for electrical coil winding with prebaked Anadur insulation.

(4) Development of the bonding of the electrical winding joints at the bus rings and terminals.

(g) Alternator Rotor - The rotor electrical and mechanical design can also be assumed relatively fixed at this stage. A change might be anticipated if H-11 stability tests indicate long term decay of magnetic properties leading to a reduced rating or a required increase in the rotor (and alternator) size.

(h) Alternator Seals - Viscoseal and Holweck pump vapor seal design may be considered firm, except for the hardware drawing state--determination of fits, tolerances, clearances, etc. A more detailed temperature distribution of the entire alternator should be determined in that stage so that necessary allowance for relative thermal expansion may be made not only in the seal assembly components but also in other areas of the alternator as well.

The static contact seal is subject to further design refinement primarily because of lack of definition of a specific start-up procedure. After the design is finalized, a model of the static seal and a test fixture should be built, and the design subjected to design verification tests.

2.5.3 Complete KTA Assembly

The next major step in the design of the complete KTA should continue into hardware design drawings and fabrication planning. The selected component development tasks, previously described in this section, should proceed prior to, or in parallel with, the hardware design phase in order to furnish information for the final design. At the time of completion of the final hardware fabrication drawings and the selected component programs previously described, the KTA would be ready to proceed with a normal development program leading to an operational potassium turboalternator.

3. TURBINE DESIGN ANALYSIS

3.1 Turbine Design Specifications

The turbine cycle state-points were redefined for the Phase II effort by NASA. The Phase I and II turbine design specifications are as follows:

		Phase I	Phase II
(a)	Turbine aerodynamic design		
	Inlet temperature, °F	2100	2100
	Inlet pressure, psia	165	165
	Exit temperature, °F	1280	1220
	Exit pressure, psia	7.80	5.44
	Mass flow, lb/sec	Required to produce 450 kw_e net output	2.05
(b)	Turbine mechanical design		
	Inlet temperature, °F	2150	2150
	Inlet pressure, psia	190	190
	Exit temperature, °F	1280	1220
	Exit pressure, psia	7.80	5.44

An interspool moisture removal configuration was chosen by NASA for the KTA turbine. Interstage moisture removal was required at the next to last stage of the turbine. Shaft speed will be 19,200 rpm.

As a basis for comparison with the turbines designed at the Phase I and II conditions, Figures 6 and 7 were prepared using design input alike except for the reduced flow and back-pressure of the new conditions. Both of these figures are for a nine-stage turbine with

MULTISTAGE RANKINE CYCLE TURBINE DESIGN — SUPERSATURATED FLUID PROPERTIES WITH REVERSION IN ROTOR NO 4

NO STAGES	TURBINE EFFICIENCY	SHAFT POWER (KILOWATTS)	SHAFT SPEED (RPM)	THRUST LOADING (LBS)	TOTAL REHEAT ENERGY (KW)
9	0.7817	524.673	19200	667.007	0.000

THERMODYNAMIC CONDITIONS

	TEMPERATURE (R)	DEGREES OF SUPERHEAT (F)	QUALITY	ENTHALPY (BTU/LB)	FLOW RATE (LBS/SEC)
INLET	2560.00	71.00	1.000	1237.55	2.539
DISCHARGE WITHOUT REMOVED MOISTURE	1739.60	0.00	0.897	1096.15	2.318
DISCHARGE WITH REMOVED MOISTURE	1740.00	0.00	0.832	1041.22	2.539

STAGE DIMENSIONS AND THERMODYNAMIC CONDITIONS

STAGE NUMBER	1	2	3	4	5	6	7	8	9	10	11	12
STATOR												
TIP RAD (IN)	3.603	3.664	3.743	3.847	4.017	4.220	4.447	4.738	5.111	0.000	0.000	0.000
MEAN RD (IN)	3.490	3.520	3.560	3.612	3.697	3.798	3.912	4.057	4.244	0.000	0.000	0.000
HUB RAD (IN)	3.377	3.377	3.377	3.377	3.377	3.377	3.377	3.377	3.377	0.000	0.000	0.000
RAD HT (IN)	0.226	0.287	0.366	0.470	0.640	0.843	1.070	1.361	1.734	0.000	0.000	0.000
P2S HUB (PSIA)	126.087	90.968	64.320	44.804	31.954	21.948	15.739	11.186	7.859	0.000	0.000	0.000
ROTOR												
TIP RAD (IN)	3.619	3.683	3.767	3.903	4.061	4.276	4.528	4.857	5.290	0.000	0.000	0.000
MEAN RD (IN)	3.498	3.530	3.572	3.640	3.719	3.826	3.952	4.117	4.333	0.000	0.000	0.000
HUB RAD (IN)	3.377	3.377	3.377	3.377	3.377	3.377	3.377	3.377	3.377	0.000	0.000	0.000
RAD HT (IN)	0.242	0.306	0.390	0.526	0.684	0.899	1.151	1.480	1.913	0.000	0.000	0.000
RAD RAT	0.933	0.917	0.896	0.865	0.832	0.790	0.746	0.695	0.638	0.000	0.000	0.000
TIP VEL (FPS)	606.381	617.030	631.150	653.862	680.370	716.424	758.612	813.799	886.257	0.000	0.000	0.000
P3S HUB (PSIA)	120.149	86.974	61.711	43.861	31.128	21.565	15.537	11.084	7.810	0.000	0.000	0.000
STAGE												
FLOW (LBS/SEC)	2.539	2.539	2.539	2.539	2.539	2.318	2.318	2.318	2.318	0.000	0.000	0.000
HIN (BTU/LB)	1237.547	1216.625	1194.756	1172.114	1149.506	1190.088	1166.023	1142.318	1119.020	0.000	0.000	0.000
TIN (R)	2560.000	2400.364	2246.595	2098.178	2100.488	2007.540	1937.449	1870.567	1806.366	0.000	0.000	0.000
DSHIN (F)	71.000	14.176	-39.523	-90.997	0.000	0.000	0.000	0.000	0.000	0.000	0.000	0.000
XIN	1.0000	1.0000	1.0000	1.0000	0.9368	0.9933	0.9676	0.9430	0.9194	0.0000	0.0000	0.0000
HEX (BTU/LB)	1216.629	1194.754	1172.113	1149.506	1127.165	1166.014	1142.318	1119.020	1096.150	0.000	0.000	0.000
TEX (R)	2400.520	2245.427	2097.759	2100.487	2018.658	1937.407	1870.566	1806.365	1744.326	0.000	0.000	0.000
DSHEX (F)	14.395	-40.244	-91.191	0.000	0.000	0.000	0.000	0.000	0.000	0.000	0.000	0.000
XEX	1.0000	1.0000	1.0000	0.9368	0.9144	0.9676	0.9430	0.9194	0.8968	0.0000	0.0000	0.0000
ETA AERO	0.8108	0.8256	0.8426	0.8613	0.8851	0.9051	0.9199	0.9318	0.9402	0.0000	0.0000	0.0000
ETA TIP	0.8629	0.7058	0.7457	0.7832	0.8250	0.8573	0.8809	0.8998	0.9141	0.0000	0.0000	0.0000
ETA WET	0.8629	0.7058	0.7457	0.7515	0.7728	0.8516	0.8523	0.8465	0.8404	0.0000	0.0000	0.0000
PWR STG (KW)	56.832	58.586	60.654	59.796	59.842	58.876	57.975	56.961	55.931	0.000	0.000	0.000
MOISTURE (LB/SEC)	0.000	0.000	0.000	0.000	0.221	0.000	0.000	0.000	0.000	0.000	0.000	0.000
HMOIST (BTU/LB)	0.000	0.000	0.000	0.000	464.497	0.000	0.000	0.000	0.000	0.000	0.000	0.000
STR COL (LB/SEC)	0.000000	0.000000	0.000000	0.000000	0.001643	0.000087	0.000365	0.000720	0.001142	0.000000	0.000000	0.000000
RTR COL (LB/SEC)	0.000000	0.000000	0.000000	0.000558	0.003123	0.000337	0.000765	0.001251	0.001867	0.000000	0.000000	0.000000
TOT COL (LB/SEC)	0.000000	0.000000	0.000000	0.000558	0.003324	0.000424	0.001544	0.002445	0.003285	0.000000	0.000000	0.000000

NINE-STAGE TURBINE DESIGN WITH
INTERSPOOL MOISTURE REMOVAL AT PHASE I DESIGN CONDITIONS

FIGURE 6

MULTISTAGE RANKINE CYCLE TURBINE DESIGN — SUPERSATURATED FLUID PROPERTIES WITH REVERSION IN ROTOR NO 3 — 07/01/68 12:10:42

NO STAGES	TURBINE EFFICIENCY	SHAFT POWER (KILOWATTS)	SHAFT SPEED (RPM)	THRUST LOADING (LBS)	TOTAL REHEAT ENERGY (KW)
9	0.7607	450.379	19200	749.126	0.000

THERMODYNAMIC CONDITIONS

	TEMPERATURE (R)	DEGREES OF SUPERHEAT (F)	QUALITY	ENTHALPY (BTU/LB)	FLOW RATE (LBS/SEC)
INLET	2560.00	71.00	1.000	1237.55	2.050
DISCHARGE WITHOUT REMOVED MOISTURE	1679.97	0.00	0.890	1085.84	1.861
DISCHARGE WITH REMOVED MOISTURE	1680.00	0.00	0.822	1027.85	2.050

STAGE DIMENSIONS AND THERMODYNAMIC CONDITIONS

STAGE NUMBER	1	2	3	4	5	6	7	8	9	10	11	12
STATOR												
TIP RAD (IN)	3.698	3.752	3.826	3.947	4.094	4.305	4.549	4.871	5.296	0.000	0.000	0.000
MEAN RD (IN)	3.612	3.639	3.676	3.736	3.810	3.915	4.037	4.198	4.410	0.000	0.000	0.000
HUB RAD (IN)	3.525	3.525	3.525	3.525	3.525	3.525	3.525	3.525	3.525	0.000	0.000	0.000
RAD HT (IN)	0.173	0.227	0.301	0.422	0.569	0.780	1.024	1.346	1.770	0.000	0.000	0.000
P2S HUB (PSIA)	122.855	85.147	57.581	39.069	26.387	17.348	11.959	8.155	5.479	0.000	0.000	0.000
ROTOR												
TIP RAD (IN)	3.713	3.770	3.862	3.978	4.138	4.362	4.634	5.002	5.502	0.000	0.000	0.000
MEAN RD (IN)	3.619	3.648	3.694	3.752	3.831	3.944	4.080	4.264	4.514	0.000	0.000	0.000
HUB RAD (IN)	3.525	3.525	3.525	3.525	3.525	3.525	3.525	3.525	3.525	0.000	0.000	0.000
RAD HT (IN)	0.187	0.245	0.337	0.453	0.612	0.837	1.109	1.477	1.977	0.000	0.000	0.000
RAD RAT	0.950	0.935	0.913	0.886	0.852	0.808	0.761	0.705	0.641	0.000	0.000	0.000
TIP VEL (FPS)	622.035	631.726	647.058	666.543	693.270	730.830	776.407	838.081	921.913	0.000	0.000	0.000
P3S HUB (PSIA)	115.628	80.285	54.645	37.413	25.492	16.954	11.764	8.064	5.439	0.000	0.000	0.000
STAGE												
FLOW (LBS/SEC)	2.050	2.050	2.050	2.050	2.050	1.861	1.861	1.861	1.861	0.000	0.000	0.000
HIN (BTU/LB)	1237.547	1216.277	1193.471	1168.689	1144.660	1187.763	1161.635	1135.901	1110.624	0.000	0.000	0.000
TIN (R)	2560.000	2389.305	2223.099	2157.095	2062.222	1962.605	1888.275	1817.714	1750.167	0.000	0.000	0.000
DSHIN (F)	71.000	14.923	-40.140	0.000	0.000	0.000	0.000	0.000	0.000	0.000	0.000	0.000
XIN	1.0000	1.0000	1.0000	0.9575	0.9332	0.9929	0.9653	0.9388	0.9135	0.0000	0.0000	0.0000
HEX (BTU/LB)	1216.284	1193.469	1168.697	1144.667	1120.606	1161.641	1135.907	1110.629	1085.845	0.000	0.000	0.000
TEX (R)	2389.442	2222.644	2157.112	2062.239	1974.354	1888.285	1817.722	1750.174	1684.948	0.000	0.000	0.000
DSHEX (F)	15.102	-40.565	0.000	0.000	0.000	0.000	0.000	0.000	0.000	0.000	0.000	0.000
XEX	1.0000	1.0000	0.9575	0.9333	0.9094	0.9653	0.9388	0.9135	0.8894	0.0000	0.0000	0.0000
ETA AERO	0.7940	0.8084	0.8260	0.8499	0.8728	0.8966	0.9148	0.9294	0.9396	0.0000	0.0000	0.0000
ETA TIP	0.6055	0.6613	0.7118	0.7648	0.8068	0.8460	0.8746	0.8973	0.9141	0.0000	0.0000	0.0000
ETA NET	0.6055	0.6613	0.6987	0.7323	0.7530	0.8400	0.8442	0.8424	0.8351	0.0000	0.0000	0.0000
P4R STG (KW)	45.988	49.327	51.003	51.953	52.021	51.290	50.519	49.623	48.655	0.000	0.000	0.000
MOFLOW (LB/SEC)	0.000	0.000	0.000	0.000	0.189	0.000	0.000	0.000	0.000	0.000	0.000	0.000
HMOIST (BTU/LB)	0.000	0.000	0.000	0.000	456.310	0.000	0.000	0.000	0.000	0.000	0.000	0.000
STR COL (LB/SEC)	0.000000	0.000000	0.000000	0.000312	0.000449	0.000038	0.000113	0.000209	0.000319	0.000000	0.000000	0.000000
RTR COL (LB/SEC)	0.000000	0.000000	0.001575	0.000724	0.000938	0.000132	0.000267	0.000402	0.000545	0.000000	0.000000	0.000000
TOT COL (LB/SEC)	0.000000	0.000000	0.001575	0.002611	0.003998	0.000169	0.000549	0.001160	0.002024	0.000000	0.000000	0.000000

NINE-STAGE TURBINE DESIGN WITH
INTERSPOOL MOISTURE REMOVAL AT PHASE II DESIGN CONDITIONS

FIGURE 7

interspool moisture removal after the fifth stage. The resulting basic changes are:

(a) A larger hub radius throughout that reflects increased work per stage required to extract the isentropic work available from the potassium due to lower back-pressure.
(b) Lower blade heights in the front stages resulting primarily from the reduced turbine mass flow specified by the NASA work statement.
(c) Nominally a two-point drop in turbine efficiency over the old conditions due primarily to lower blade heights.

The Phase II parametric design effort was then directed toward regaining or surpassing the efficiency level defined for the Phase I design conditions. Among the higher efficiency design approaches were:

(a) Increasing the number of stages over the previous nine-stage design
(b) Designing for less work in the front stages to reduce the hub diameter and the axial velocity, thereby increasing blade height
(c) Incorporating more reaction in the blade design

In addition, turbine tip shrouds were used in the stages between the separator and the last stage. This results in increased stage efficiency and facilitates interstage moisture removal. The last stage is not shrouded since interstage moisture removal is not utilized, the stage efficiency increase is not appreciable, and the blade stresses are, thus, reduced in the region of maximum blade stress.

3.2 Parametric Evaluation

The first step toward increasing the efficiency was to increase the number of turbine stages to 10. Since the Phase II isentropic

turbine work was increased due to the lower back-pressure, the 10-Stage design has about the same work per stage as the Phase I selected nine-stage. Thus, the hub radius and disk stresses are similar.

3.2.1 Work Coefficient and Hub Design Selection

The previous turbine parametric evaluations utilized an impulse reference blade design (work coefficient, $\lambda_2 = 2.0$). The stage aerodynamic efficiency was determined from an efficiency map as a function of the hub/tip ratio. This map was for a particular blade design as calculated by an existing AiResearch blade efficiency computer program (briefly described in Appendix B). Figure 8 shows a typical variation in the blade aerodynamic efficiency with the work coefficient and rotor hub/tip ratio calculated by the blade efficiency program.* These results are for a particular stator discharge angle, chord length, trailing edge thickness, and loading coefficient and the potassium fluid properties of a typical last stage. The blade efficiency program was added to the turbine parametric program so that the myriad turbine designs could be readily evaluated. Since the hub/tip ratio varies for each stage, a cursory review of Figure 8 suggests that the work coefficient of each stage should be slightly larger than the previous stage. However, the axial thrust associated with the lower work coefficient also affects the final efficiency.

Selection of the first-stage work coefficient is influenced by the disk material allowable design stress, which is a function of the stator discharge total relative gas temperature. Since the first stage is operating very close to the maximum allowable disk temperature, the first-stage work coefficient was selected as 2.0. This allows the

*These results do not include the effects of tip clearance, moisture, or shroud curvature and secondary flow that are evaluated separately.

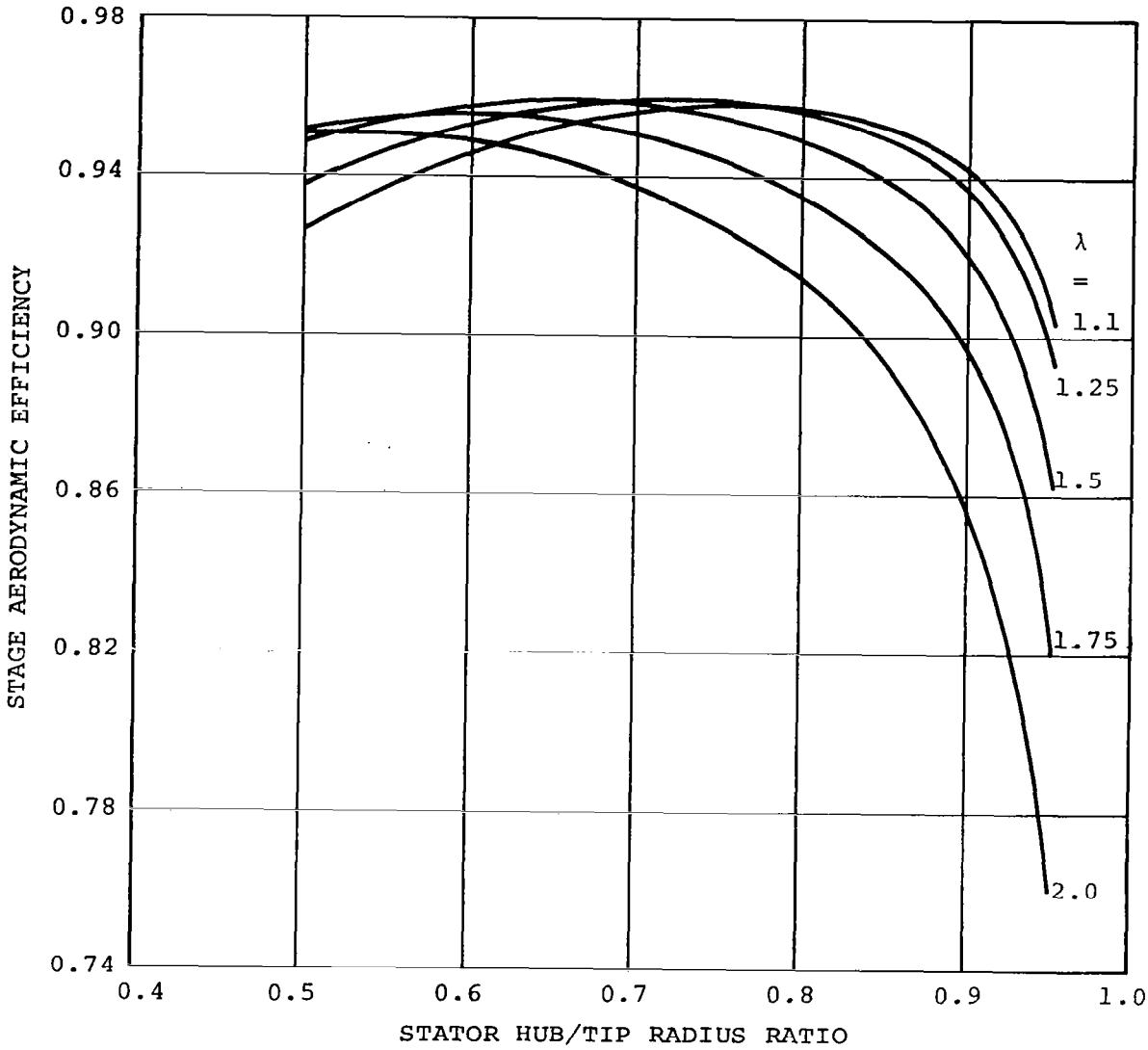

EFFECT OF HUB/TIP RADIUS RATIO AND WORK COEFFICIENT ON STAGE AERODYNAMIC EFFICIENCY

FIGURE 8

maximum temperature drop to occur in the stator and results in the minimum total relative gas temperature achievable for a free-vortex turbine design without exit swirl (highest efficiency turbine design).

3.2.1.1 Variable Hub Radius Front End

The turbine configuration first evaluated with the revised turbine parametric program was a 10-stage design with a first-stage work coefficient of 2.0. The first stage was maintained at a hub radius of approximately 2.90 in., so that the blade height exceeded 0.250 in. and a reasonable disk design could be obtained. The stage hub radius increased from Stages 1 through 4 with a constant hub radius for Stages 5 through 10. A work coefficient range of 1.2 to 1.8 for Stages 2 through 4 was investigated with the last six stages at work coefficients of 1.2 to 2.0. Figures 9 and 10 show the results of this investigation. If turbine efficiency were the selection criterion without regard for axial thrust, the best turbine configuration would utilize a work coefficient of 1.2 for all stages. However, the axial thrust variation shown in Figures 9 and 10 will reduce the overall efficiency. Figure 11 shows the results of a thrust bearing evaluation in which the thrust bearing power loss is a function of the bearing load capacity for a constant bearing operating clearance. When the turbine output shaft power is reduced by this thrust bearing power loss, a lower turbine efficiency is defined as shown in Figures 9 and 10. The effect of the work coefficient on the last-stage tip speed and blade stress is shown in Figures 9, 10, and 12.

The work coefficient selected for the latter stages is 1.6. Nearly maximum turbine effective efficiency is realized by this selection with a significantly lower blade stress than the indicated optimum of 1.4. Since the axial thrust is lower, this selection is more amenable to thrust balancing. Any method that reduces the thrust bearing power losses will reduce the system low-temperature radiator heat rejection

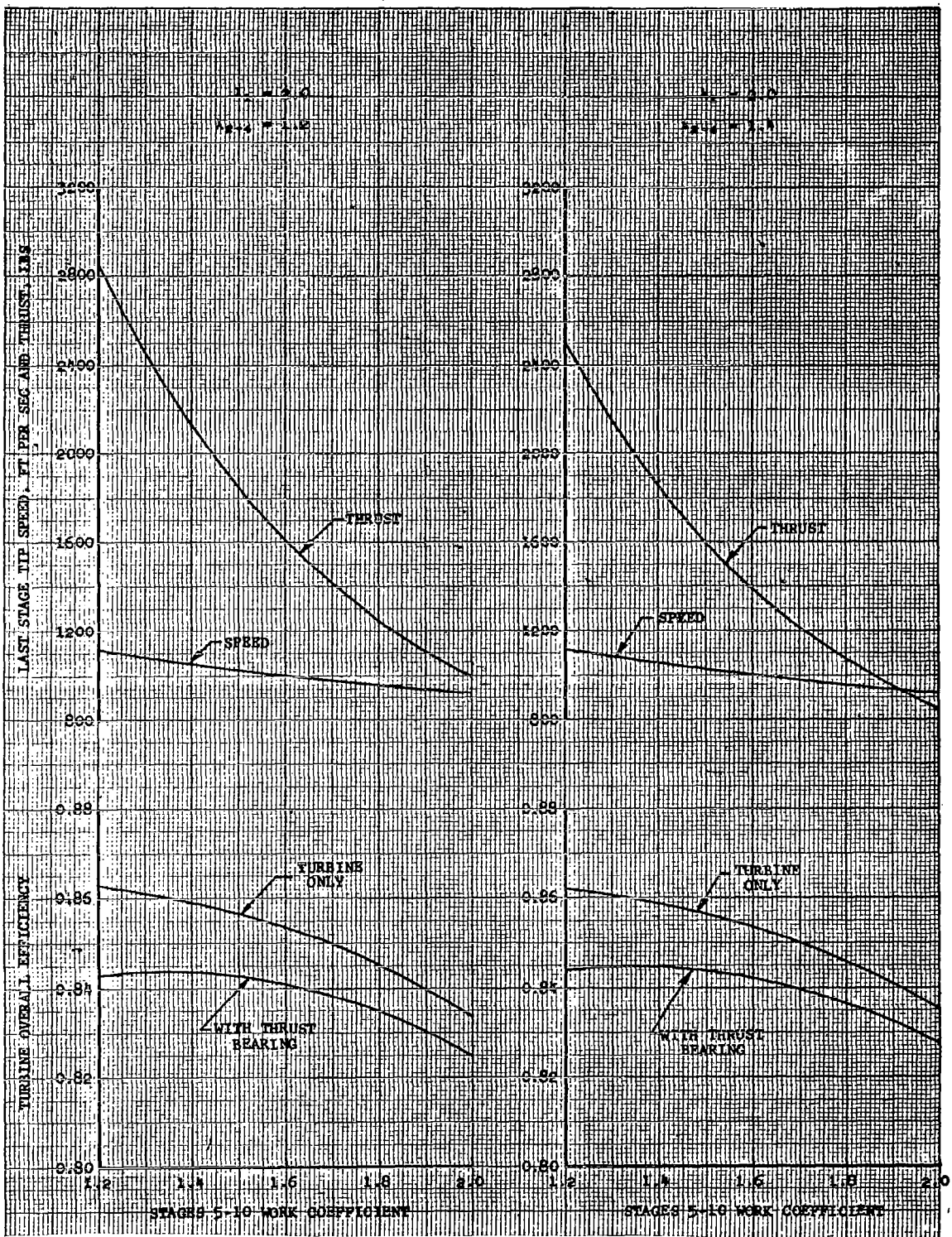

EFFECT OF WORK COEFFICIENT ON

VARIABLE HUB TURBINE DESIGNS

FIGURE 9

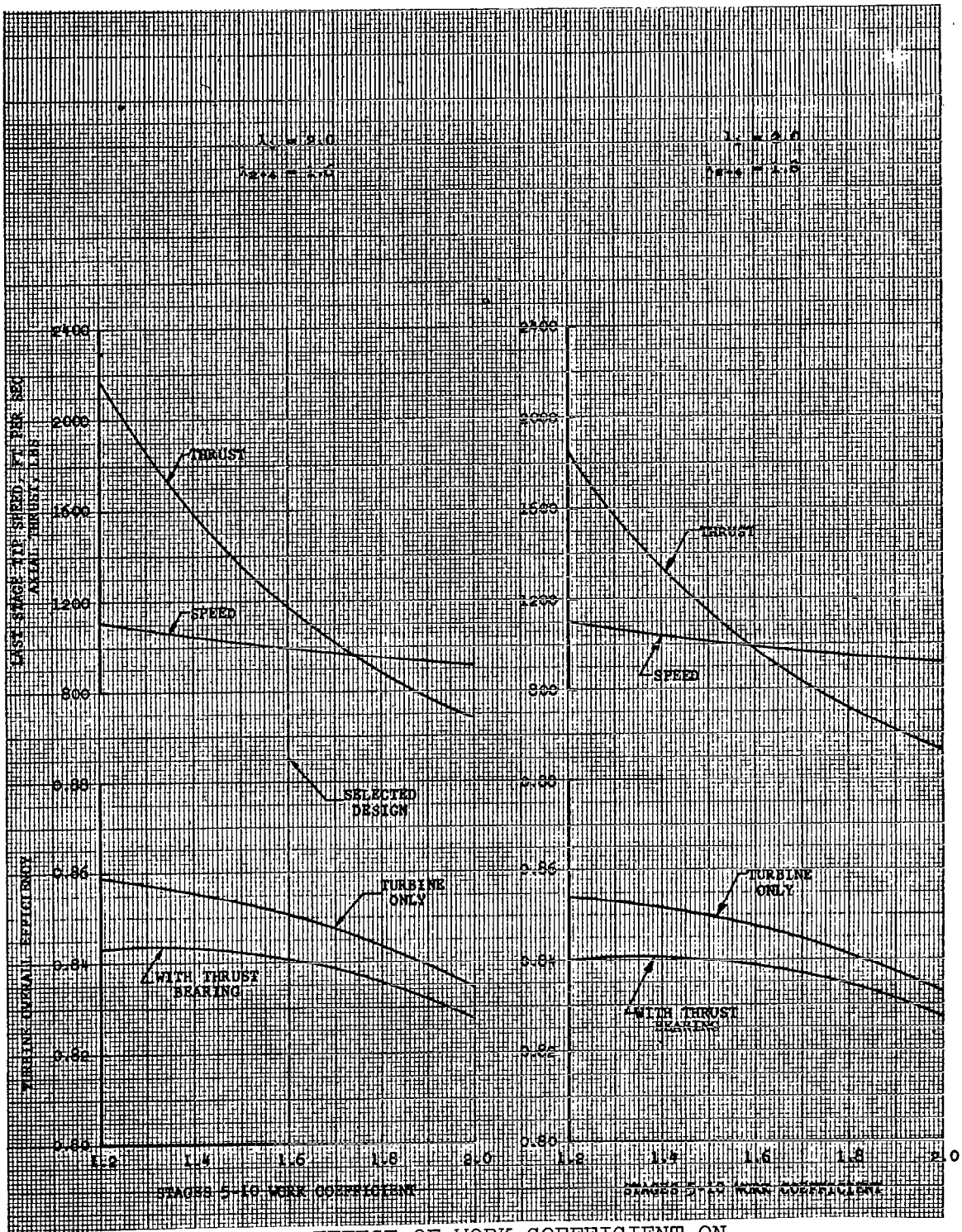

EFFECT OF WORK COEFFICIENT ON

VARIABLE HUB TURBINE DESIGNS

FIGURE 10

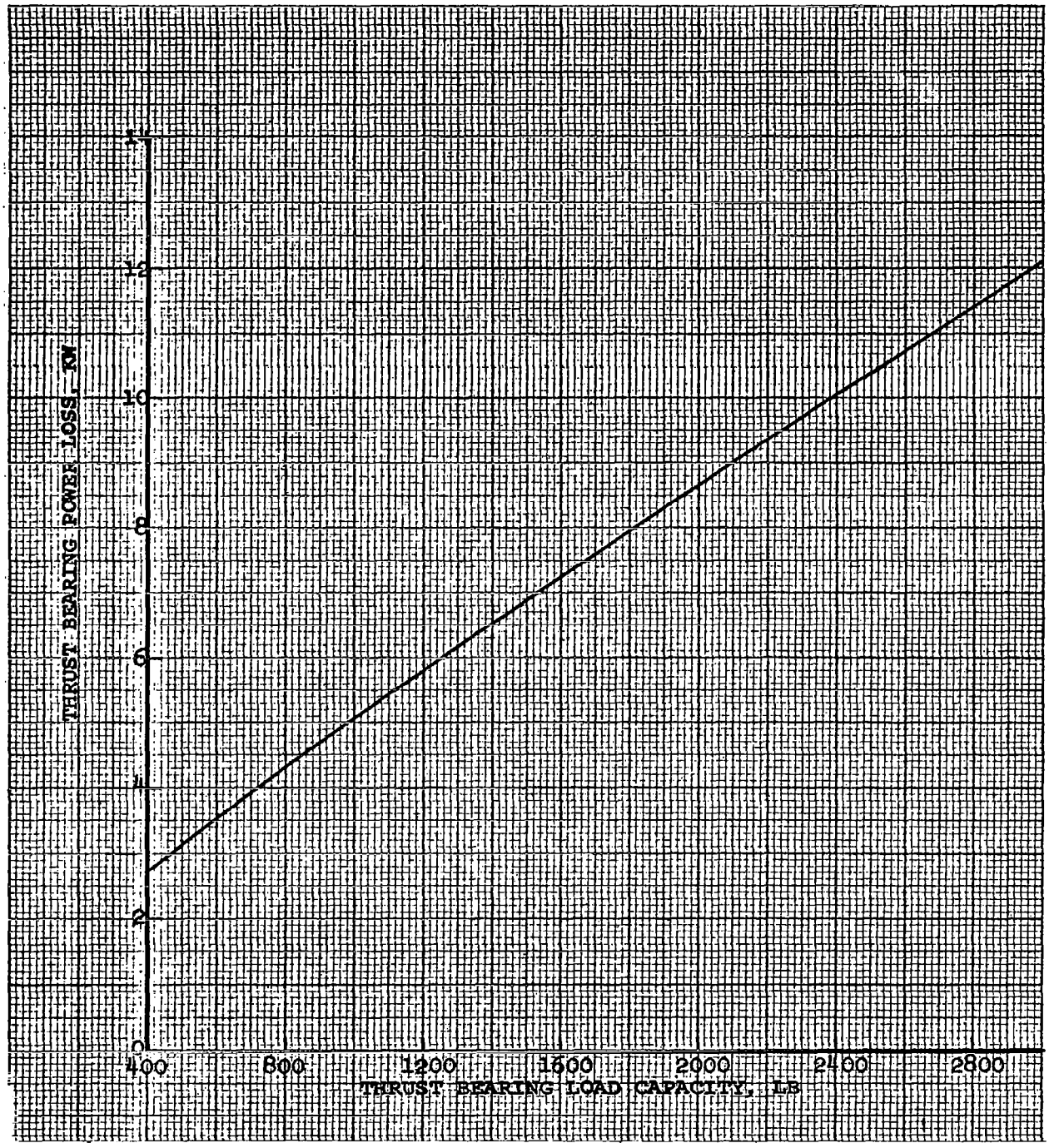

KTA TURBINE THRUST BEARING

PARAMETRIC PERFORMANCE

FIGURE 11

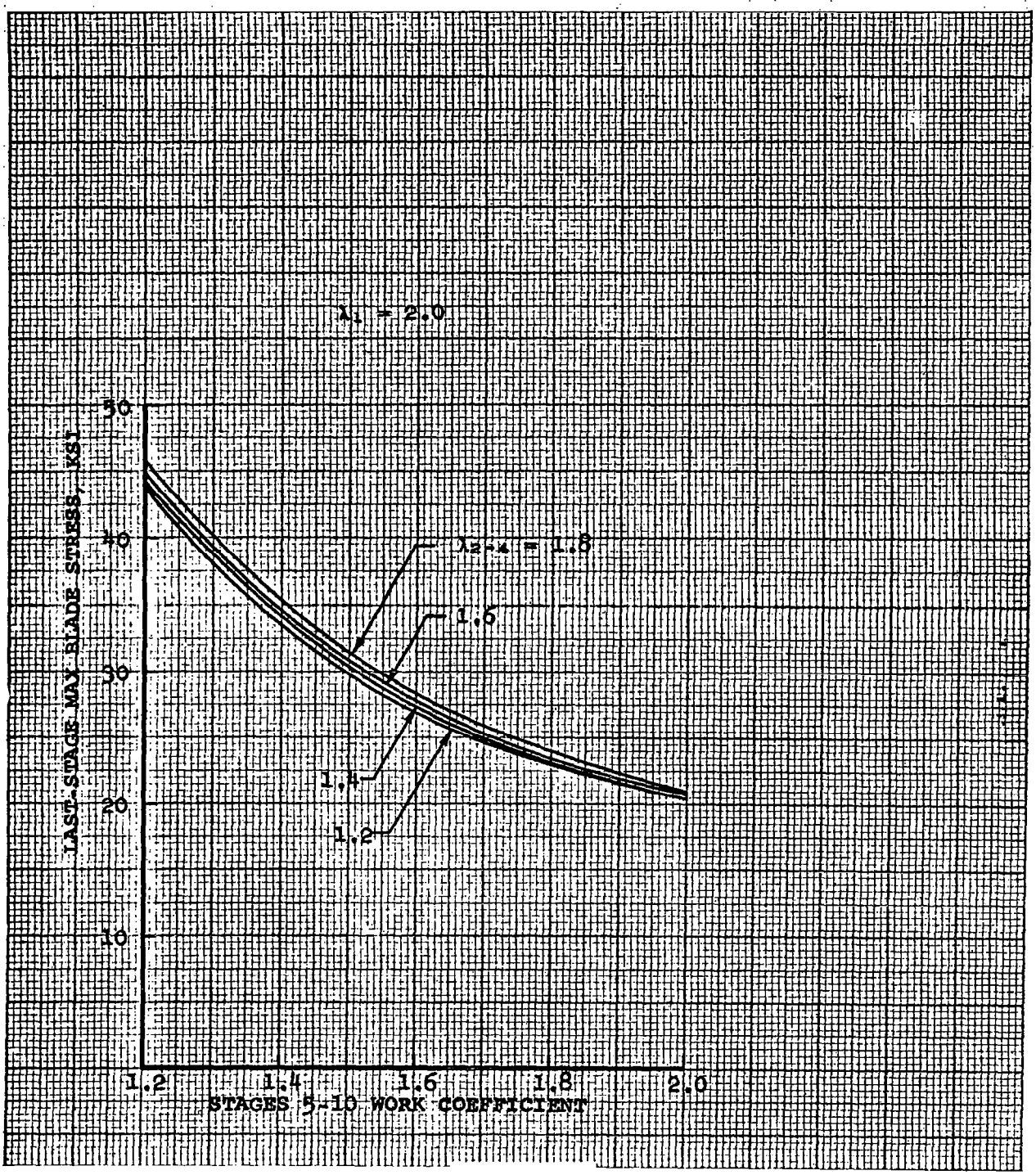

EFFECT OF WORK COEFFICIENT ON

VARIABLE HUB TURBINE DESIGNS

FIGURE 12

weight penalty. Selection of the front-stages work coefficient at 1.6 follows essentially the same rationale as discussed above. Figure 13 shows the parametric computer program output for the selected configuration.

A complete conical turbine design in which each stage hub radius is greater than the previous stage was first considered but rejected. In this design, the last stage would be accomplishing the largest percentage of the total work at the lowest stage efficiency. The ETA WET column of Figure 13 shows the stage efficiency which includes the aerodynamic losses, tip-clearance correction, and the effects of moisture. This stage efficiency indicates that the middle stages should be loaded the same as or more than the rear stages. The combined conical/cylindrical design thus accomplishes the more desirable stage loading.

3.2.1.2 Constant Hub Radius Front End

The constant hub radius front-end design was then evaluated with the first-stage radius maintained at approximately 2.90 in. Based on the evaluation of the variable hub radius front-end designs, the work coefficient of the rear stages was maintained at 1.6 with the work coefficient of the front stages varied from 1.2 to 2.0. Figure 14 shows the results of the analysis.

The front-end work coefficient was selected at 1.6. This selection results in the maximum effective turbine efficiency with no significant tip-speed penalty. A value of 1.8 could be considered but only at a thrust bearing penalty decrease associated with 140 lb of thrust. Figure 15 shows the turbine parametric program output for this constant hub diameter turbine design.

MULTISTAGE RANKINE CYCLE TURBINE DESIGN — SUPERSATURATED FLUID PROPERTIES WITH REVERSION IN STATOR NO 5 — 07/31/68 22:02:10

NO STAGES	TURBINE EFFICIENCY	SHAFT POWER (KILOWATTS)	SHAFT SPEED (RPM)	THRUST LOADING (LBS)	TOTAL REHEAT ENERGY (KW)
10	0.8507 0.8408	493,780 5.73	19200	1178,849	0,000

THERMODYNAMIC CONDITIONS

	TEMPERATURE (R)	DEGREES OF SUPERHEAT (F)	QUALITY	ENTHALPY (BTU/LB)	FLOW RATE (LBS/SEC)
INLET	2560,00	71,00	1,000	1237,55	2,010
DISCHARGE WITHOUT REMOVED MOISTURE	1680,40	0,00	0,828	1032,83	1,902
DISCHARGE WITH REMOVED MOISTURE	1680,00	0,00	0,794	1004,28	2,010

STAGE DIMENSIONS AND THERMODYNAMIC CONDITIONS

STAGE NUMBER	1	2	3	4	5	6	7	8	9	10	11	12
STATOR												
TIP RAD (IN)	3,095	3,365	3,649	3,945	4,472	4,579	4,730	4,943	5,246	5,678	0,000	0,000
MEAN RD (IN)	2,978	3,224	3,510	3,801	4,314	4,368	4,443	4,550	4,701	4,917	0,000	0,000
HUB RAD (IN)	2,860	3,082	3,371	3,656	4,156	4,156	4,156	4,156	4,156	4,156	0,000	0,000
RAD HT (IN)	0,235	0,283	0,278	0,289	0,316	0,423	0,574	0,787	1,090	1,522	0,000	0,000
P2S HUB (PSIA)	136,664	117,423	93,820	70,863	48,149	32,809	22,042	14,574	9,454	5,992	0,000	0,000
ROTOR												
TIP RAD (IN)	3,102	3,376	3,663	3,963	4,500	4,620	4,792	5,040	5,402	5,935	0,000	0,000
MEAN RD (IN)	2,981	3,229	3,517	3,810	4,328	4,388	4,474	4,598	4,779	5,045	0,000	0,000
HUB RAD (IN)	2,860	3,082	3,371	3,656	4,156	4,156	4,156	4,156	4,156	4,156	0,000	0,000
RAD HT (IN)	0,242	0,294	0,292	0,307	0,344	0,464	0,636	0,884	1,246	1,779	0,000	0,000
RAD RAT	0,922	0,913	0,920	0,923	0,924	0,900	0,867	0,825	0,769	0,700	0,000	0,000
TIP VEL (FPS)	519,679	565,671	613,732	663,999	753,955	774,075	802,842	844,450	905,177	994,391	0,000	0,000
P3S HUB (PSIA)	134,770	112,702	89,150	66,447	44,195	30,117	20,224	13,354	8,641	5,454	0,000	0,000
STAGE												
FLOW (LBS/SEC)	2,010	2,010	2,010	2,010	1,902	1,902	1,902	1,902	1,902	1,902	0,000	0,000
HIN (BTU/LB)	1237,547	1220,820	1205,026	1186,153	1201,046	1171,157	1142,003	1113,598	1085,943	1059,026	0,000	0,000
TIN (R)	2560,000	2444,857	2343,025	2225,328	2198,196	2102,024	2010,815	1924,130	1841,376	1761,924	0,000	0,000
DSHIN (F)	71,000	22,663	-19,480	-65,765	0,000	0,000	0,000	0,000	0,000	0,000	0,000	0,000
XIN	1,0000	1,0000	1,0000	1,0000	0,9966	0,9641	0,9333	0,9044	0,8771	0,8514	0,0000	0,0000
HEX (BTU/LB)	1220,816	1205,029	1186,152	1163,884	1171,164	1142,009	1113,604	1085,948	1059,031	1032,832	0,000	0,000
TEX (R)	2444,787	2342,937	2225,339	2092,808	2102,038	2010,827	1924,141	1841,385	1761,931	1685,159	0,000	0,000
DSHEX (F)	22,645	-19,580	-65,763	-115,016	0,000	0,000	0,000	0,000	0,000	0,000	0,000	0,000
XEX	1,0000	1,0000	1,0000	1,0000	0,9641	0,9334	0,9044	0,8771	0,8514	0,8273	0,0000	0,0000
ETA AERO	0,8895	0,9355	0,9397	0,9387	0,9247	0,9347	0,9431	0,9500	0,9552	0,9583	0,0000	0,0000
ETA TIP	0,8109	0,8664	0,8694	0,8712	0,8944	0,9115	0,9257	0,9369	0,9454	0,9510	0,0000	0,0000
ETA WET	0,8109	0,8664	0,8694	0,8712	0,8914	0,8788	0,8640	0,8473	0,8292	0,8097	0,0000	0,0000
PWR STG (KW)	35,480	33,486	40,022	47,224	59,978	58,504	57,000	55,496	54,016	52,576	0,000	0,000
MOFLOW (LB/SEC)	0,000	0,000	0,000	0,108	0,000	0,000	0,000	0,000	0,000	0,000	0,000	0,000
HMOIST (BTU/LB)	0,000	0,000	0,000	499,183	0,000	0,000	0,000	0,000	0,000	0,000	0,000	0,000
STR COL (LB/SEC)	0,000000	0,000000	0,000000	0,000000	0,000184	0,001257	0,002680	0,003794	0,004366	0,004428	0,000000	0,000000
RTR COL (LB/SEC)	0,000000	0,000000	0,000000	0,000000	0,000934	0,002595	0,004309	0,005436	0,005848	0,005745	0,000000	0,000000
TOT COL (LB/SEC)	0,000000	0,000000	0,000000	0,000000	0,001118	0,004970	0,011958	0,021189	0,031403	0,041576	0,000000	0,000000

A34852

TEN-STAGE TURBINE DESIGN WITH VARIABLE HUB RADIUS
AND INTERSPOOL MOISTURE REMOVAL AFTER STAGE 4

FIGURE 13

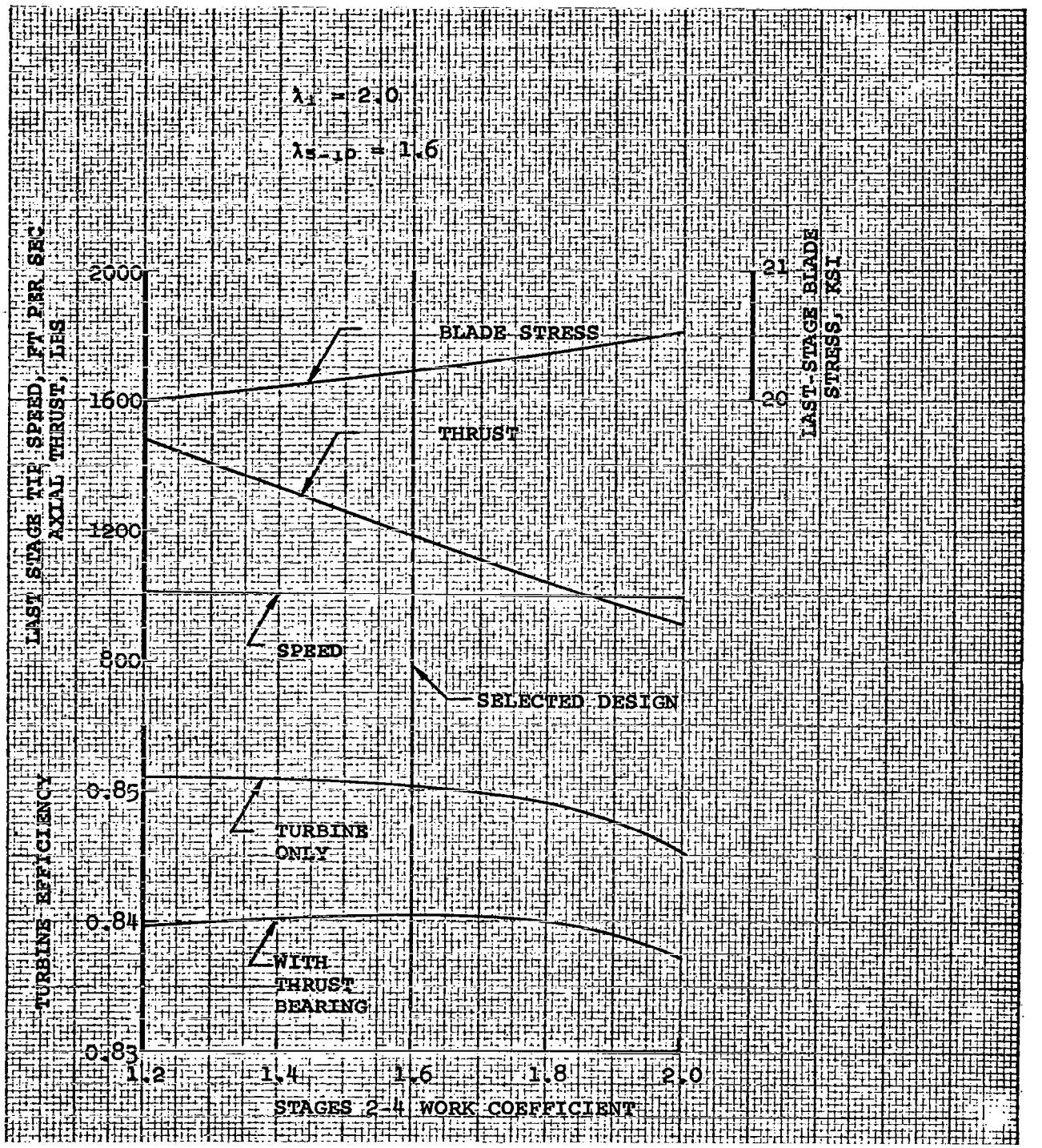

EFFECT OF WORK COEFFICIENT ON

CONSTANT HUB TURBINE DESIGNS

FIGURE 14

MULTISTAGE RANKINE CYCLE TURBINE DESIGN — SUPERSATURATED FLUID PROPERTIES WITH REVERSION IN STATOR NO 5 — 08/02/68 11:31:09

NO STAGES	TURBINE EFFICIENCY	SHAFT POWER (KILOWATTS)	SHAFT SPEED (RPM)	THRUST LOADING (LBS)	TOTAL REHEAT ENERGY (KW)
10	0.8504 0.8405	493.613 5.76	19200	1183.712	0.000

THERMODYNAMIC CONDITIONS

	TEMPERATURE (R)	DEGREES OF SUPERHEAT (F)	QUALITY	ENTHALPY (BTU/LB)	FLOW RATE (LBS/SEC)
INLET	2560.00	71.00	1.000	1237.55	2.010
DISCHARGE WITHOUT REMOVED MOISTURE	1679.99	0.00	0.819	1025.68	1.928
DISCHARGE WITH REMOVED MOISTURE	1680.00	0.00	0.795	1004.59	2.010

STAGE DIMENSIONS AND THERMODYNAMIC CONDITIONS

STAGE NUMBER	1	2	3	4	5	6	7	8	9	10	11	12
STATOR												
TIP RAD (IN)	3.209	3.256	3.294	3.338	4.556	4.652	4.792	4.996	5.295	5.734	0.000	0.000
MEAN RD (IN)	3.082	3.103	3.122	3.144	4.425	4.473	4.543	4.645	4.794	5.014	0.000	0.000
HUB RAD (IN)	2.955	2.950	2.950	2.950	4.294	4.294	4.294	4.294	4.294	4.294	0.000	0.000
RAD HT (IN)	0.254	0.306	0.344	0.388	0.262	0.359	0.498	0.702	1.001	1.440	0.000	0.000
P2S HUB (PSIA)	135.356	117.488	98.715	82.339	56.678	37.543	24.487	15.694	9.851	6.023	0.000	0.000
ROTOR												
TIP RAD (IN)	3.216	3.268	3.307	3.354	4.580	4.689	4.849	5.087	5.446	5.992	0.000	0.000
MEAN RD (IN)	3.086	3.109	3.129	3.152	4.437	4.491	4.571	4.690	4.870	5.143	0.000	0.000
HUB RAD (IN)	2.955	2.950	2.950	2.950	4.294	4.294	4.294	4.294	4.294	4.294	0.000	0.000
RAD HT (IN)	0.261	0.318	0.357	0.404	0.286	0.395	0.555	0.793	1.152	1.699	0.000	0.000
RAD RAT	0.919	0.903	0.892	0.880	0.937	0.916	0.886	0.844	0.788	0.717	0.000	0.000
TIP VEL (FPS)	538.895	547.474	554.132	561.924	767.422	785.630	812.394	852.287	912.453	1004.011	0.000	0.000
P3S HUB (PSIA)	133.515	113.279	95.101	79.219	51.553	34.172	22.285	14.269	8.934	5.439	0.000	0.000
STAGE												
FLOW (LBS/SEC)	2.010	2.010	2.010	2.010	1.928	1.928	1.928	1.928	1.928	1.928	0.000	0.000
HIN (BTU/LB)	1237.547	1219.568	1205.016	1190.355	1203.792	1172.083	1141.138	1110.998	1081.677	1053.171	0.000	0.000
TIN (R)	2560.000	2437.126	2344.119	2253.245	2248.876	2141.534	2040.424	1944.989	1854.512	1768.153	0.000	0.000
DSHIN (F)	71.000	19.006	-19.714	-56.225	0.000	0.000	0.000	0.000	0.000	0.000	0.000	0.000
XIN	1.0000	1.0000	1.0000	1.0000	0.9972	0.9628	0.9303	0.8996	0.8709	0.8439	0.0000	0.0000
HEX (BTU/LB)	1219.561	1205.019	1190.354	1175.590	1172.090	1141.145	1111.005	1081.683	1053.176	1025.689	0.000	0.000
TEX (R)	2437.097	2344.033	2253.275	2165.209	2141.549	2040.439	1945.002	1854.523	1768.161	1685.113	0.000	0.000
DSHEX (F)	19.042	-19.811	-56.213	-90.326	0.000	0.000	0.000	0.000	0.000	0.000	0.000	0.000
XEX	1.0000	1.0000	1.0000	1.0000	0.9628	0.9303	0.8997	0.8709	0.8439	0.8189	0.0000	0.0000
ETA AERO	0.8956	0.9418	0.9465	0.9488	0.9159	0.9284	0.9383	0.9469	0.9533	0.9574	0.0000	0.0000
ETA TIP	0.8223	0.8773	0.8885	0.8970	0.8799	0.9015	0.9185	0.9324	0.9428	0.9422	0.0000	0.0000
ETA WET	0.8223	0.8773	0.8885	0.8970	0.8775	0.8680	0.8545	0.8388	0.8210	0.7952	0.0000	0.0000
PWR STG (KW)	38.142	36.853	31.091	31.310	64.486	62.931	61.295	59.630	57.973	55.903	0.000	0.000
MOFLOW (LB/SEC)	0.000	0.000	0.000	0.082	0.000	0.000	0.000	0.000	0.000	0.000	0.000	0.000
MMOIST (BTU/LB)	0.000	0.000	0.000	508.151	0.000	0.000	0.000	0.000	0.000	0.000	0.000	0.000
STR COL (LB/SEC)	0.000000	0.000000	0.000000	0.000000	0.001566	0.010736	0.014628	0.015597	0.015067	0.013907	0.000000	0.000000
RTR COL (LB/SEC)	0.000000	0.000000	0.000000	0.000000	0.007601	0.020353	0.023197	0.023474	0.021826	0.019511	0.000000	0.000000
TOT COL (LB/SEC)	0.000000	0.000000	0.000000	0.000000	0.009167	0.040257	0.078082	0.117154	0.154047	0.187465	0.000000	0.000000

A34854

TEN-STAGE TURBINE DESIGN WITH CONSTANT HUB RADIUS
AND INTERSPOOL MOISTURE REMOVAL AFTER STAGE 4

FIGURE 15

3.2.1.3 Hub Design Selection

The two turbine designs discussed above were compared and the stepped-constant hub design was selected. Both designs have the same efficiency and axial thrust loads. However, the constant hub radius design has a lower maximum last-stage blade stress even though the last-stage tip speed is greater. Both blades are the same double taper design, but the longer blade of the variable radius front-end design has its maximum blade stress region displaced from the hub radius.

The most important difference between the two designs, however, is the uncertainty of predicting the blade efficiency of the climbing-out front-end stages. These stages have more shroud curvature and a greater secondary flow potential. Shown below is a simplified graphical representation of this problem for some typical stator and rotor sets.

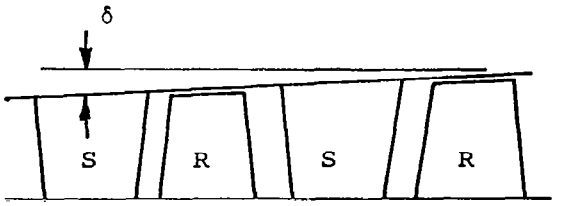

CONSTANT HUB

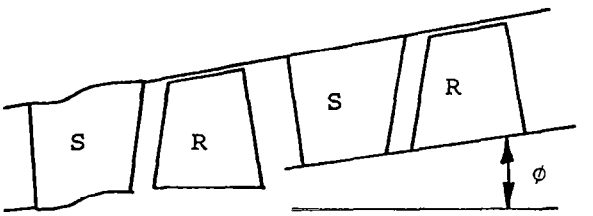

VARIABLE HUB

Without regard for how the transition is made, the through-flow of the variable hub design must conform to the angle ϕ. The resultant secondary flow is in addition to that caused by the angle δ that the constant hub turbine must have. The turbine performance shown in Figures 13 and 15 is without the evaluation of shroud curvature and secondary flow.

AiResearch has correlated actual test data for the constant hub design to evaluate this added turbine loss. However, to correlate the losses for the variable hub designs would require that the radius rate of change (ϕ) must be included. This correlation has not been accomplished to our satisfaction for a climbing-hub radius turbine and thus the actual blade efficiency of a variable hub radius design is open to some question. The shroud curvature and secondary flow correlation was applied to the selected constant-hub radius design as discussed in Section 3.2.3.

3.2.2 Reference Design Configuration

A more critical review of Figure 15 shows that the blade height of Stage 5 is quite small. Reversion from supersaturated to near-equilibrium flow is accomplished in the duct prior to the separator located between Stages 4 and 5. The blade height of Stage 5 could be increased if the hub radius were dropped to the hub radius of Stage 4. As in the Phase I reference design, short-chord blades with small leading and trailing edges are utilized in those stages prior to reversion. If reversion still occurs in the duct leading to the separator after Stage 5, then the hub diameter may be reduced and the blade height and stage efficiency increased. Figure 16 shows the results of reducing Stage 5 to the hub radius of Stage 4. A slight reduction in the axial thrust and last-stage blade stress was realized with an increase in the overall turbine efficiency. Reversion still occurs in the duct prior to the separator, so the transition between the two hub radii may be accomplished between Stages 5 and 6. When this procedure was extended to drop the sixth-stage radius, reversion occurred in that stage which precludes the use of the short-chord blades in Stage 6.

The Phase II reference design, thus selected, consists of a 10-stage turbine with five stages before and five after the separator. The first stage has a work coefficient of 2.0 with 1.6 utilized in the remainder.

MULTISTAGE RANKINE CYCLE TURBINE DESIGN SUPERSATURATED FLUID PROPERTIES WITH REVERSION IN STATOR NO 6 08/06/68
********** 17:32:18

NO STAGES	TURBINE EFFICIENCY	SHAFT POWER (KILOWATTS)	SHAFT SPEED (RPM)	THRUST LOADING (LBS)	TOTAL REHEAT ENERGY (KW)
10	0.8531	495.199	19200	1158.793	0.000

THERMODYNAMIC CONDITIONS

	TEMPERATURE (R)	DEGREES OF SUPERHEAT (F)	QUALITY	ENTHALPY (BTU/LB)	FLOW RATE (LBS/SEC)
INLET	2560.00	71.00	1.000	1237.55	2.010
DISCHARGE WITHOUT REMOVED MOISTURE	1680.06	0.00	0.829	1033.79	1.897
DISCHARGE WITH REMOVED MOISTURE	1680.00	0.00	0.794	1003.60	2.010

STAGE DIMENSIONS AND THERMODYNAMIC CONDITIONS

STAGE NUMBER	1	2	3	4	5	6	7	8	9	10	11	12
STATOR												
TIP RAD (IN)	3.207	3.253	3.291	3.335	3.386	4.811	4.932	5.117	5.399	5.832	0.000	0.000
MEAN RD (IN)	3.080	3.099	3.118	3.140	3.166	4.670	4.731	4.823	4.964	5.181	0.000	0.000
HUB RAD (IN)	2.952	2.946	2.946	2.946	2.946	4.529	4.529	4.529	4.529	4.529	0.000	0.000
RAD HT (IN)	0.255	0.307	0.345	0.389	0.440	0.281	0.403	0.587	0.870	1.303	0.000	0.000
P2S HUB (PSIA)	135.411	117.564	98.855	82.505	68.338	45.098	28.309	17.418	10.463	6.095	0.000	0.000
ROTOR												
TIP RAD (IN)	3.214	3.264	3.304	3.350	3.405	4.841	4.980	5.196	5.536	6.081	0.000	0.000
MEAN RD (IN)	3.083	3.105	3.125	3.148	3.175	4.685	4.755	4.863	5.033	5.305	0.000	0.000
HUB RAD (IN)	2.952	2.946	2.946	2.946	2.946	4.529	4.529	4.529	4.529	4.529	0.000	0.000
RAD HT (IN)	0.262	0.318	0.358	0.404	0.459	0.312	0.451	0.666	1.007	1.552	0.000	0.000
RAD RAT	0.919	0.903	0.892	0.879	0.865	0.936	0.910	0.872	0.818	0.745	0.000	0.000
TIP VEL (FPS)	538.488	546.890	553.537	561.311	570.427	811.106	834.389	870.525	927.598	1018.945	0.000	0.000
P3S HUB (PSIA)	133.575	113.393	95.249	79.390	65.689	40.537	25.466	15.665	9.387	5.442	0.000	0.000
STAGE												
FLOW (LBS/SEC)	2.010	2.010	2.010	2.010	2.010	1.897	1.897	1.897	1.897	1.897	0.000	0.000
HIN (BTU/LB)	1237.547	1219.688	1205.087	1190.465	1175.738	1200.091	1164.771	1130.426	1097.100	1064.803	0.000	0.000
TIN (R)	2560.000	2437.354	2344.603	2253.963	2166.108	2196.563	2081.820	1974.377	1873.298	1777.428	0.000	0.000
DSHIN (F)	71.000	19.092	-19.537	-55.967	-89.997	0.000	0.000	0.000	0.000	0.000	0.000	0.000
XIN	1.0000	1.0000	1.0000	1.0000	1.0000	0.9955	0.9573	0.9215	0.8881	0.8570	0.0000	0.0000
HEX (BTU/LB)	1219.593	1205.089	1190.465	1175.740	1160.919	1164.779	1130.434	1097.108	1064.809	1033.793	0.000	0.000
TEX (R)	2437.325	2344.502	2253.994	2166.147	2080.909	2081.838	1974.393	1873.312	1777.438	1685.700	0.000	0.000
DSHEX (F)	19.128	-19.636	-55.955	-89.996	-121.954	0.000	0.000	0.000	0.000	0.000	0.000	0.000
XEX	1.0000	1.0000	1.0000	1.0000	1.0000	0.9573	0.9215	0.8881	0.8570	0.8284	0.0000	0.0000
ETA AERO	0.8956	0.9419	0.9466	0.9489	0.9511	0.9171	0.9305	0.9416	0.9498	0.9556	0.0000	0.0000
ETA TIP	0.8224	0.8775	0.8886	0.8971	0.9049	0.8835	0.9064	0.9246	0.9380	0.9391	0.0000	0.0000
ETA WET	0.8224	0.8775	0.8886	0.8971	0.9049	0.8795	0.8677	0.8520	0.8330	0.8047	0.0000	0.0000
PWR STG (KW)	38.074	30.772	31.008	31.225	31.425	70.658	68.706	66.668	64.613	62.049	0.000	0.000
MOFLOW (LB/SEC)	0.000	0.000	0.000	0.000	0.113	0.000	0.000	0.000	0.000	0.000	0.000	0.000
MMOIST (BTU/LB)	0.000	0.000	0.000	0.000	498.587	0.000	0.000	0.000	0.000	0.000	0.000	0.000
STR COL (LB/SEC)	0.000000	0.000000	0.000000	0.000000	0.000000	0.001605	0.009972	0.013471	0.013667	0.012338	0.000000	0.000000
RTR COL (LB/SEC)	0.000000	0.000000	0.000000	0.000000	0.000000	0.007019	0.018109	0.020700	0.019851	0.017299	0.000000	0.000000
TOT COL (LB/SEC)	0.000000	0.000000	0.000000	0.000000	0.000000	0.008624	0.036704	0.070875	0.104393	0.134030	0.000000	0.000000

A34855

TEN-STAGE TURBINE DESIGN WITH CONSTANT HUB RADIUS
AND INTERSPOOL MOISTURE REMOVAL AFTER STAGE 5

FIGURE 16

3.2.3 Reference Design Performance Factors

The reference design configuration shown in Figure 16 does not include the following:

(a) Losses due to shroud line curvature and secondary flow
(b) Losses due to labyrinth seal leakage
(c) Effect of interstage moisture removal
(d) Losses due to accelerating the blade collected moisture

The shroud line curvature and secondary flow loss correlation, developed by AiResearch for constant hub diameter turbine designs, was incorporated into the turbine parametric design program. The correlation modifies the aerodynamic efficiency predicted by the two-dimensional flow blade efficiency program (discussed in Appendix B).

3.2.3.1 Labyrinth Seal Leakage

Labyrinth seals will be used in the KTA turbine between each turbine rotor and between the first-stage rotor and the front bearing compartment. The turbine design summarized in Figure 16 is based on a flow rate of 2.01 lb/sec instead of the 2.05 valve specified for the Phase II KTA evaluation. The difference was taken as the first-stage labyrinth seal leakage. Losses due to the seal leakage of the other interstage seals were not included.

In order to minimize seal leakage, the running clearance of the seal must be reduced to the minimum practical value consistent with the shaft run-out, shaft-to-seal assembly tolerance stack-up, and shaft-to-seal differential thermal growth. If the seal does rub at any time during operation, the rub must not result in catastrophic damage to the seal or shaft. The design chosen to meet the KTA turbine seal requirements is shown in Figure 17 in an enlarged view. The labyrinth

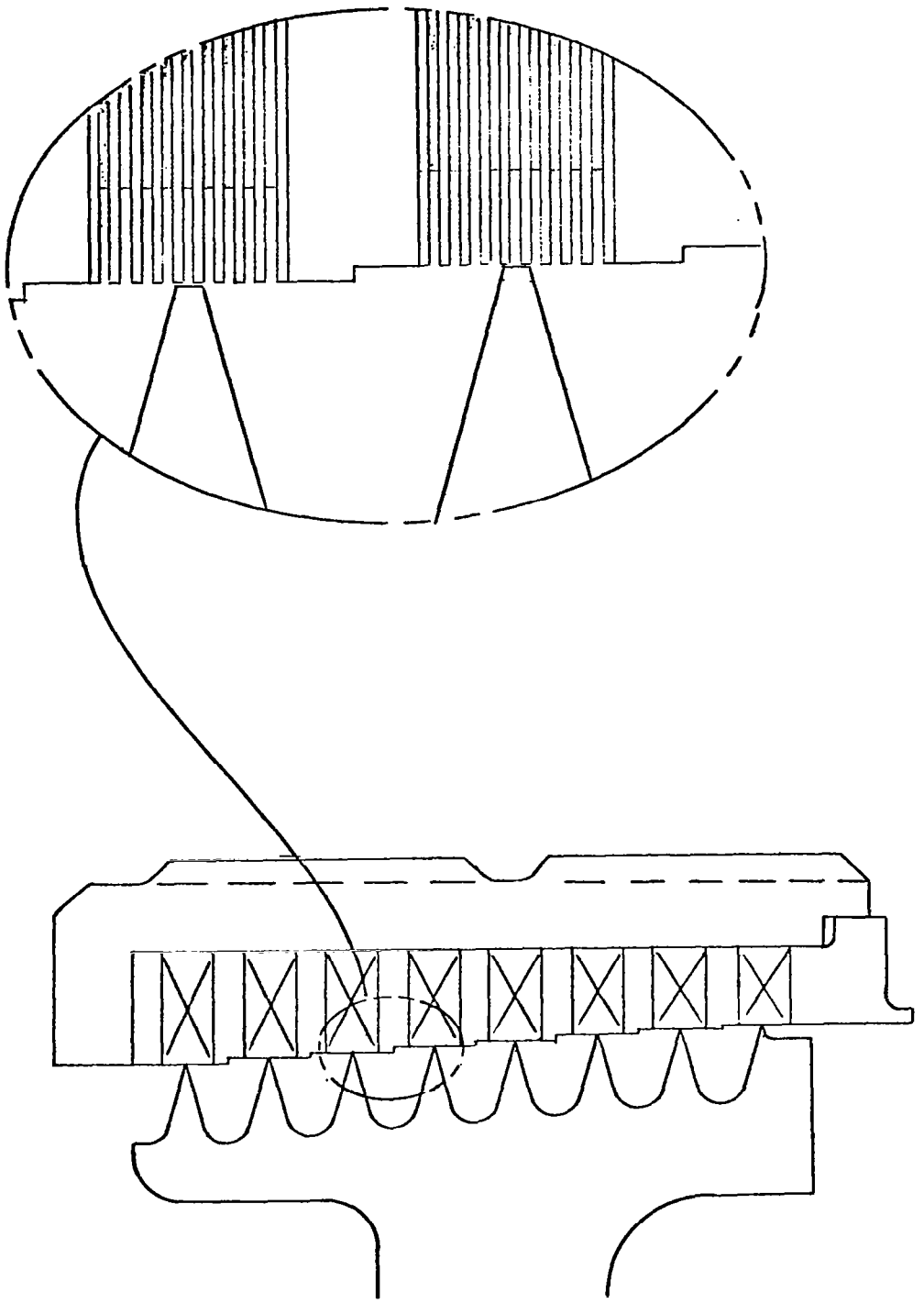

TYPICAL LABYRINTH SEAL

CONFIGURATION

FIGURE 17

knife edges are mounted on the shaft as a replaceable part. This arrangement is preferred over one in which fixed-knives run adjacent to a smooth shaft since, in the advent of a rub, shaft heating and attendant shaft damage is minimized in the selected configuration.

The stationary seal member design shown was chosen in order to present the knives with a surface which is easily deformable and somewhat tolerant to a rub. This stationary seal member is constructed of foil with a thickness of 0.002 to 0.004 in. Rings of the foil are cut with the same outer diameter, but the inner diameter of 50 percent of the rings is increased approximately 0.030 in. The rings are stacked alternately large and small inside diameters. This results in a resilient sealing surface which may be deformed.

Each rotating knife edge is stepped in diameter approximately 0.005 in. with respect to the preceding knife edge to eliminate "carry-over" effects which result in increased leakage in straight-through-type designs. The stepped-design plus adequate spacing between knife edges should ensure that complete dissipation of kinetic energy occurs in each stage of the labyrinth.

Assuming negligible pressure recovery between the teeth, the flow through an unchoked segment can be estimated from the equation (see Appendix C for the derivation):

$$w = CA \sqrt{\frac{2\,gn}{n-1}\,\frac{P_1}{V_1}\left[\left(\frac{P_2}{P_1}\right)^{2/n} - \left(\frac{P_2}{P_1}\right)^{(n+1)/n}\right]} \qquad (1)$$

where

w = mass flow rate, lb/sec

C = discharge coefficient

A = geometric flow area, ft^2

P_1 = upstream total pressure, lb/ft^2

P_2 = downstream total pressure, lb/ft^2

V_1 = upstream gas specific volume, ft^3/lb

n = isentropic exponent = $- \frac{V}{P} \left(\frac{\partial P}{\partial V}\right)_s$

Equation 1 is based on the assumption that the pressure-specific volume relationship during expansion can be described by the relationship: PV^n = constant.

If the last tooth is choked, the corresponding mass flow rate is:

$$w = CA \sqrt{\frac{gn\ P_1}{V_1} \left(\frac{2}{n+1}\right)^{(n+1)/(n-1)}} \qquad (2)$$

The orifice is assumed to be choked when:

$$\frac{P_2}{P_1} \leq \left(\frac{2}{n+1}\right)^{n/(n-1)} \qquad (3)$$

The discharge coefficient [1] is a function of Δ/δ and P_2/P_1 as depicted in Figure 18 where

Δ = tooth thickness, in.

δ = radial clearance, in.

For best results, Δ/δ should be less than 2.0. The discharge coefficient continues to increase even when P_2/P_1 drops below the value corresponding to choked-flow.

The assumption of negligible pressure recovery is valid, provided that the teeth are radially staggered or separated by a distance equal to at least 12 radial clearances. A pocket depth-to-width ratio of 1:1 is nearly optimum.

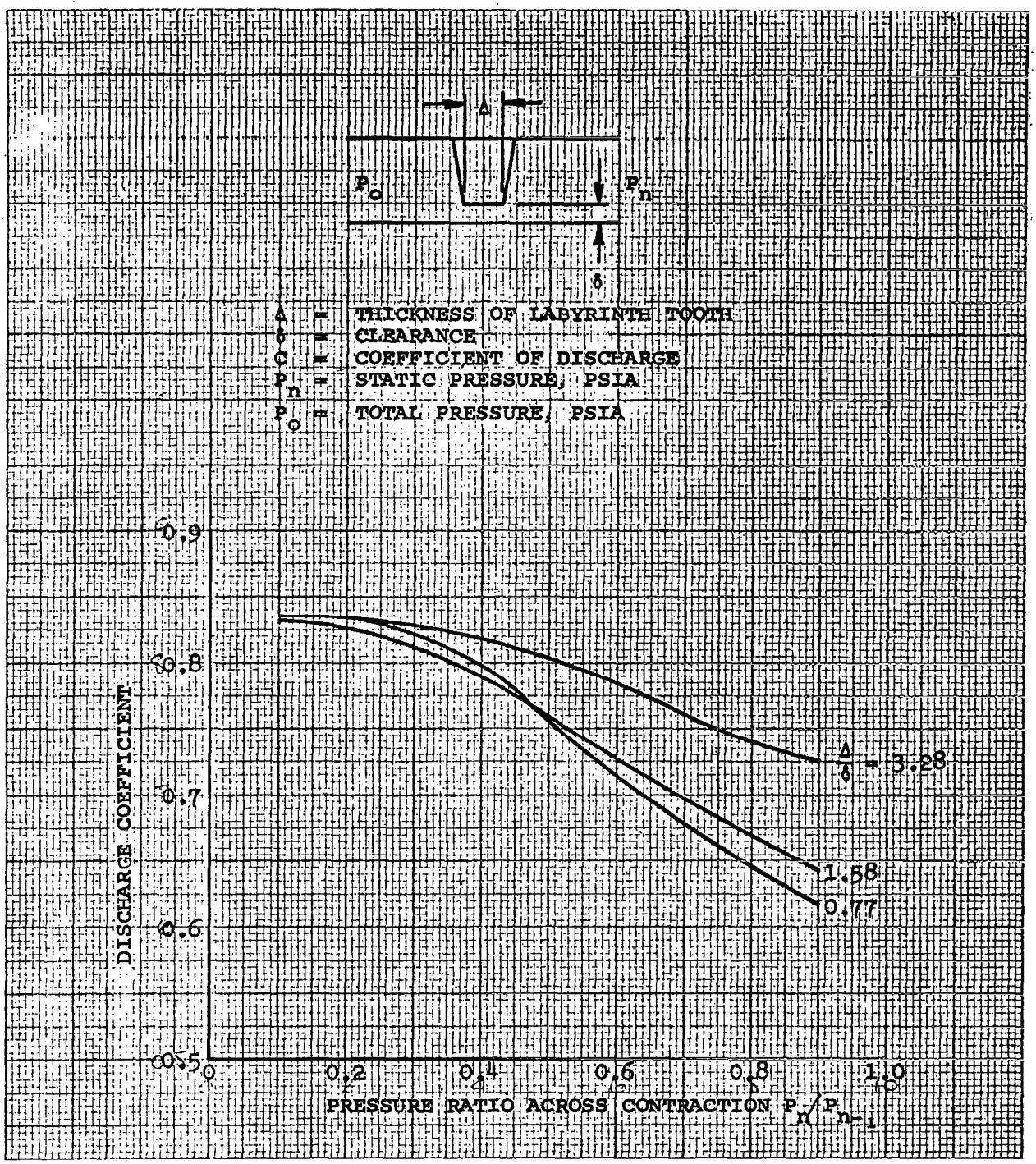

COEFFICIENT OF DISCHARGE FOR CONTRACTIONS

FROM KEARTON AND KER

FIGURE 18

In the absence of pressure recovery, the vena contracta static pressure of one stage becomes the upstream total pressure of the next stage.

It is interesting to note that potassium vapor throttled from the KTA inlet conditions exhibits a pronounced cooling effect. Figure 19 shows gas temperature versus pressure for potassium throttled adiabatically from 2100°F and 165 psia. This departure from ideal gas performance (an ideal gas shows no change in temperature with reduced pressure) requires a stage-by-stage analysis of the flow process using real gas rather than ideal gas properties.

A computer program was available to facilitate the solution of Eq.1 and 2 for a labyrinth seal having any number of teeth. The isentropic exponent and discharge coefficient are functionally related to local pressure level and tooth pressure ratio, respectively. Seal leakage calculations reported in the literature generally do not account for local discharge coefficient variations through the seal. The computer program was incorporated into the parametric turbine program so that the interstage labyrinth seal leakages and performance penalty could be calculated directly. The performance penalty is discussed in Volume I, Section 2.2.2.1.

The first-stage labyrinth seal leakage was calculated for a range of seal discharge cavity pressures. Figure 20 shows the labyrinth seal leakage for a first-stage seal diameter of 4.40 in. The discharge cavity pressure is determined by the venting location selected for this cavity. If the seal leakage is vented to a stator inlet part way through the turbine, some of the loss charged to the first-stage seal may be recovered. Figure 21 shows the effect of introducing the first-stage labyrinth seal leakage after Stages 5 through 10. The upper curve shows the turbine efficiency without the thrust bearing losses. Thrust bearing losses increase as the

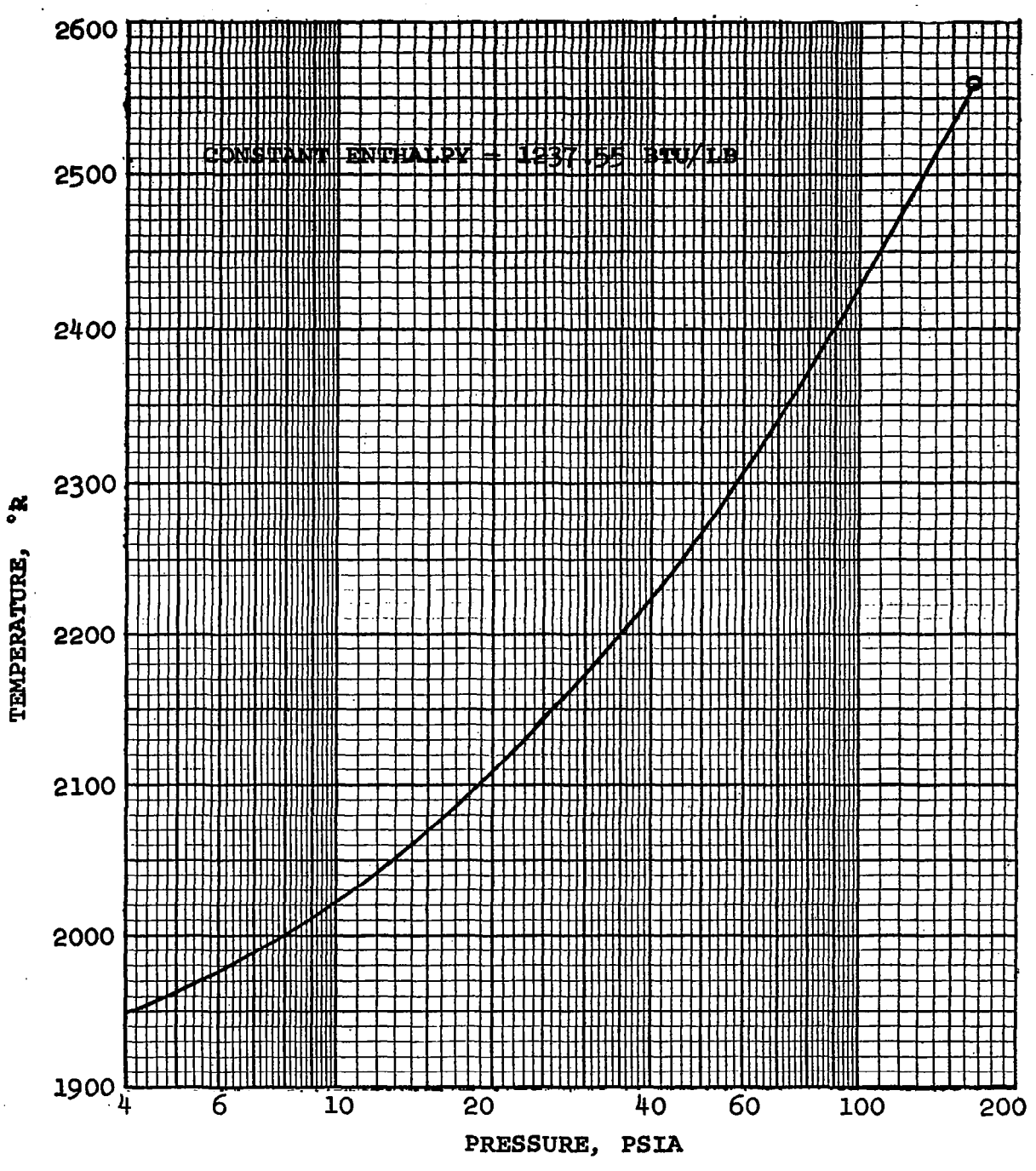

POTASSIUM VAPOR THROTTLING

FROM KTA INLET CONDITIONS

FIGURE 19

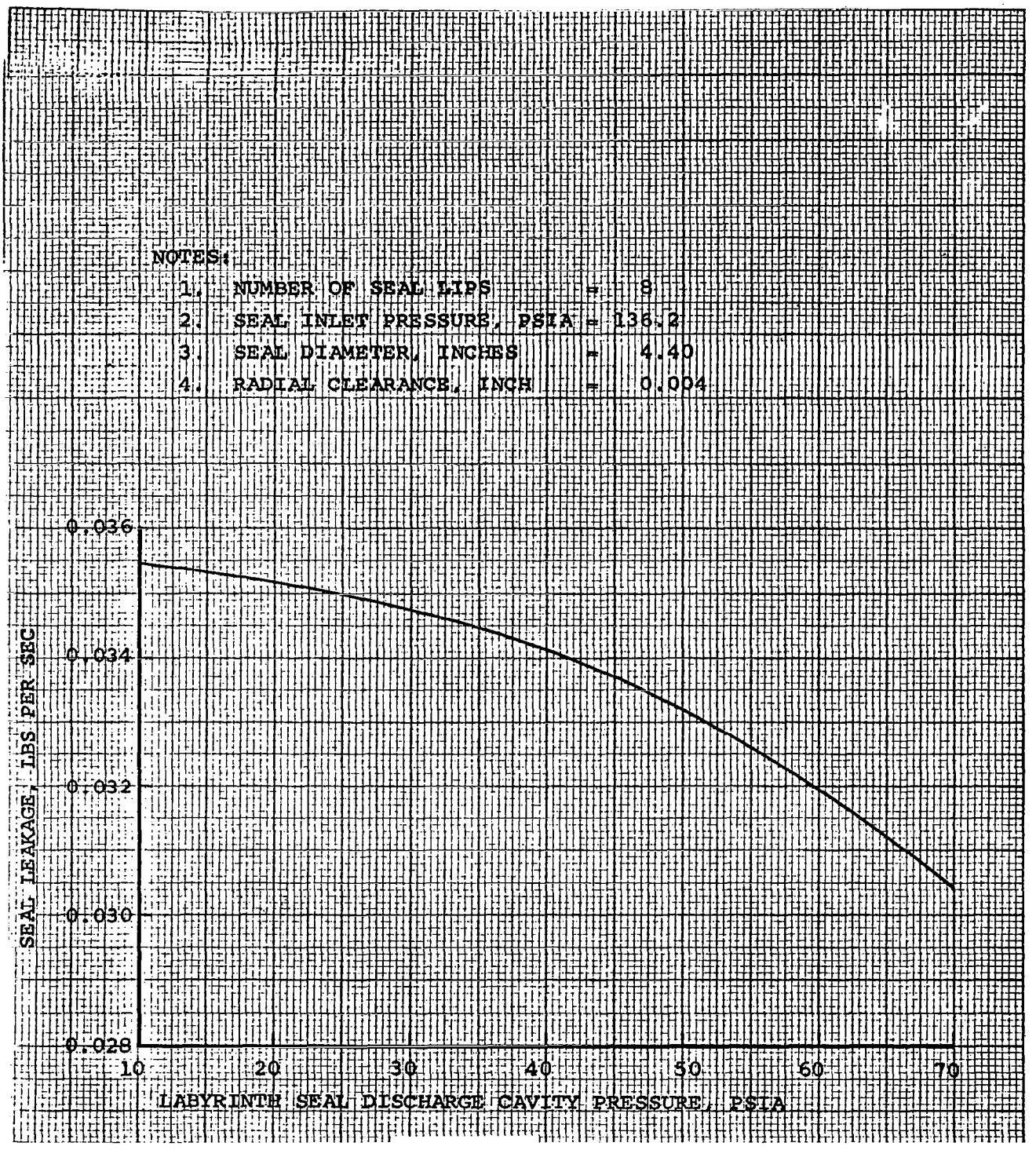

KTA TURBINE FIRST-STAGE

LABYRINTH SEAL LEAKAGE

FIGURE 20

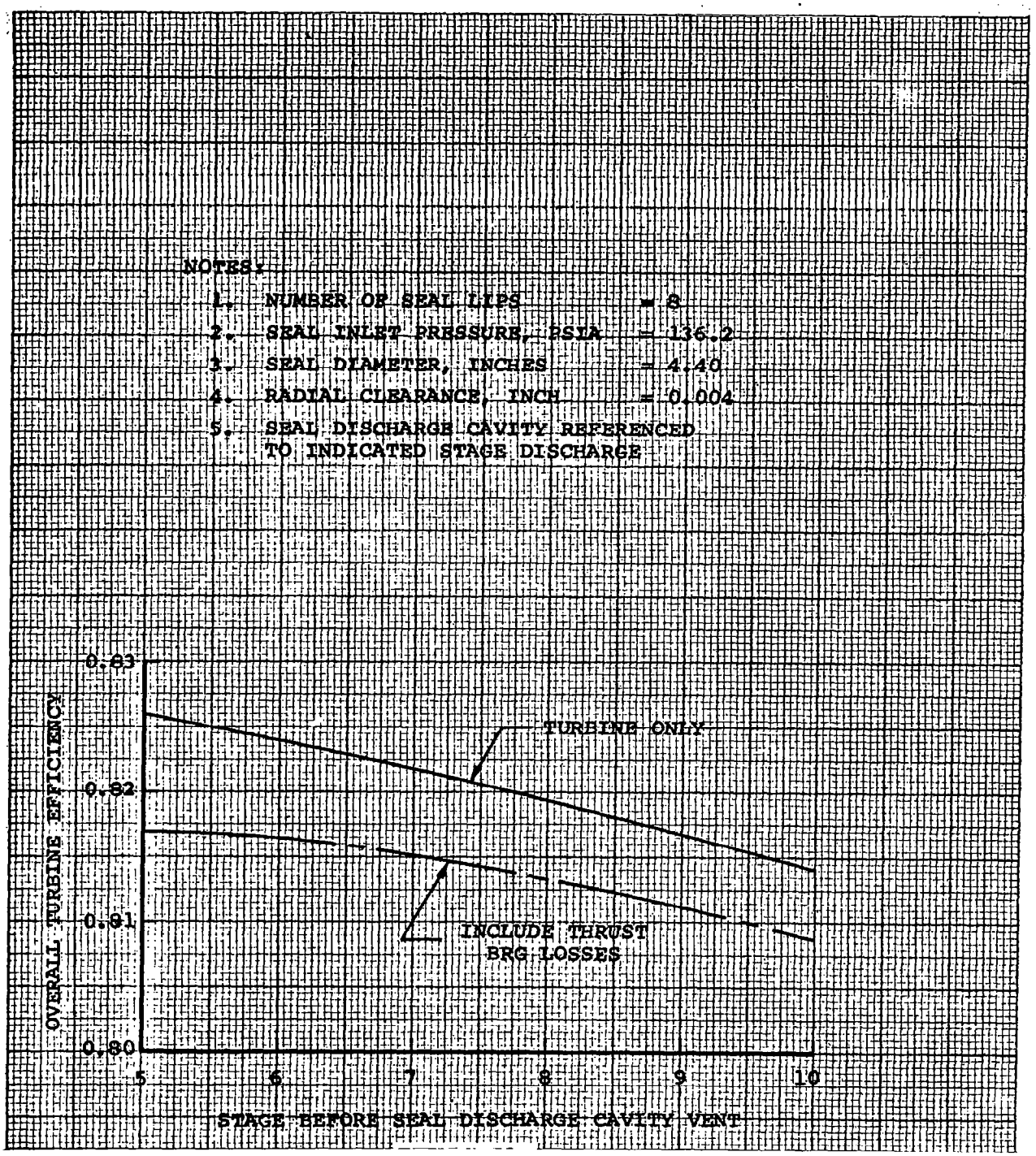

EFFECT OF LABYRINTH SEAL LEAKAGE VENT

LOCATION ON TURBINE PERFORMANCE

FIGURE 21

seal leakage is vented to higher pressures. The lower curve includes the thrust bearing losses as shown in Figure 11, page 47. The optimum vent location for the first-stage labyrinth seal leakage would be the discharge of Stage 5 or the separator inlet. However, the results of the thermal analysis showed that this vent location would result in too high a pressure for the viscoseal liquid-vapor interface. Thus the seal vent location was selected as the sixth-stage rotor discharge. The first-stage stator is sized to pass the total inlet flow (2.05 lb/sec) with the rotor and subsequent stages sized to pass the reduced flow. No additional penalty is charged to this seal leakage. Since no work has been extracted from the leakage flow, its total energy is taken as the turbine inlet total energy for the mixing process.

A thrust balancing piston is included in the KTA turbine reference design between the fifth and sixth stages. The effect is to add two additional labyrinth seals that are vented to a lower pressure in the turbine. The vent location was selected as the rotor inlet of the seventh stage. This results in a 38.8-psi pressure drop across the balance piston and a total thrust bearing load of 383 pounds which is sufficient for stable thrust bearing operation. The total thrust balance piston seal leakage is 0.053 lb/sec which must be accelerated to wheel speed since it is vented through the tie-bolt and to the seventh-stage rotor inlet. This performance penalty is also included in the reference design.

3.2.3.2 Interstage Moisture Removal

Interstage moisture removal is incorporated after the ninth stage of the 10-stage KTA turbine design. The total stator- and rotor-collected moisture at the removal location is to be removed. See Vol. I Sections 2.2.2.3 and 2.3.7 for a discussion of blade-collected moisture and interstage moisture removal.) A vapor removal penalty of 0.25 lb of vapor per pound of removed moisture was assumed for the evaluation.

The turbine must first be designed so that the collected moisture may be determined before the interstage moisture removal is evaluated. For this reason only the final turbine reference design was evaluated for interstage moisture removal.

3.2.3.3 Moisture Performance Penalty

The moisture performance penalty utilized in the evaluation of the KTA turbine consists of two parts:

(a) No liquid entering a stage may do work on the rotor. Thus, the stage-enthalpy drop is reduced by the stage-inlet quality. This is the larger performance penalty.
(b) Liquid collected by the stator, which is stripped from the stator and hits the rotor, and the rotor-collected moisture must be accelerated to rotor wheel speed.

The first part of the moisture performance penalty can be directly calculated and, thus, this penalty is normally imposed on the turbine design. The turbine must first be designed so that the collected moisture may be determined before the second moisture penalty is evaluated.

3.2.4 Phase II Turbine Reference Design Summary

The KTA Phase II reference turbine design incorporates the following features and performance factors:

(a) A 10-stage design with five stages before and five after the interspool moisture removal scroll. The high- and low-pressure spools have a constant hub radius.
(b) A first-stage work coefficient of 2.0 for maximum stator temperature drop. The remaining nine stages have a work coefficient of 1.6 for nearly optimum turbine efficiency.

(c) Rotor tip clearance equals 0.010 in.

(d) Stage inlet moisture can do no work, and the moisture collected by the stage must be accelerated to turbine wheel speed.

(e) Interstage labyrinth seal leakage can do no work and is accelerated to wheel speed.

(f) The first-stage labyrinth seal leakage is vented to the seventh-stage stator inlet and does work in Stages 7, 8, 9, and 10.

(g) A thrust balance piston is included between Stages 5 and 6, and its leakage is vented to the seventh-stage rotor inlet. This leakage does work in Stages 8, 9, and 10.

(h) Interspool moisture removal between Stages 5 and 6 incorporates the following losses:

(1) Two velocity heads pressure loss (1.5 psi)
(2) Ninety-percent removal of the moisture present.
(3) One-tenth pound of vapor removed per pound of liquid.

(i) Interstage moisture removal after the ninth-stage rotor with the following losses:

(1) One hundred-percent of the prior collected moisture removed.
(2) One-quarter pound of vapor removed per pound of liquid.

(j) Tip shrouds are utilized in Stages 6, 7, 8, and 9 to facilitate interstage moisture removal and improve the turbine efficiency.

(k) A turbine discharge pressure loss of one velocity head (0.15 psi).

Figure 22 presents the final turbine parametric program output for the KTA reference design. Reversion from supersaturated to near-equilibrium flow occurs in the separator inlet duct. The turbine output power is the shaft power before the bearing, viscoseal, and disk windage losses have been taken into account.

The contract requires that the KTA Phase II turbine design "incorporates interstage moisture removal via a slot in the casing at the next-to-last rotor blade row". The reference design summarized in Figure 22 answers this contractual requirement. However, based on the erosion analysis presented in Section 3.4, it is recommended that interstage moisture removal be incorporated after Stages 6, 7, 8, and 9 of the 10-stage reference design. Figure 23 presents the summary of the reference design with the interstage moisture removal after the four stages. No other departure from the reference design is included.

3.3 Turbine Aerodynamic Design

At the initiation of the KTA study, two turbine evaluation procedures (computer programs) were in use at AiResearch; a turbine parametric program and a turbine design program.

The turbine parametric program was usually used to investigate a multitude of turbine designs in preparation for selecting one configuration for a particular application. Both the aerodynamic flow passages and the blade and disks were sized for a prediction of the turbine performance, size, weight, and disk life.

The turbine design program was capable of analyzing a more general aerodynamic design. No mechanical design analysis such as disk stress and life was performed. In addition, the turbine design program was used to provide input to a series of blade aerodynamic design and efficiency prediction procedures.

MULTISTAGE RANKINE CYCLE TURBINE DESIGN
****

SUPERSATURATED FLUID PROPERTIES WITH REVERSION IN STATOR NO 6

01/15/69
02:28:03

NO STAGES	TURBINE EFFICIENCY	SHAFT POWER (KILOWATTS)	SHAFT SPEED (RPM)	THRUST LOADING (LBS)	TOTAL REHEAT ENERGY (KW)
10	0.8131	481.355	19200	1246.413	0.000

THERMODYNAMIC CONDITIONS

	TEMP, R	SUPERHEAT, F	QUALITY	ENTHALPY, BTU/LB	FLOW, LBS/SEC
INLET	2560.00	71.00	1.000	1237.77	2.050
EXIT WITHOUT MOISTURE	1679.51	0.00	0.935	1124.80	1.685
EXIT WITH MOISTURE	1680.00	0.00	0.807	1014.81	2.050

DIMENSIONS AND PERFORMANCE	1	2	3	4	5	6	7	8	9	10	11	12
STATION 1 TIP RAD, IN	3.140	3.194	3.228	3.267	3.314	4.751	4.848	5.006	5.240	5.586	0.000	0.000
HUB RAD, IN	2.901	2.901	2.901	2.901	2.901	4.539	4.539	4.539	4.539	4.539	0.000	0.000
RAD HT, IN	0.239	0.293	0.327	0.366	0.413	0.211	0.309	0.467	0.701	1.047	0.000	0.000
STATION 2 TIP RAD, IN	3.169	3.217	3.254	3.297	3.348	4.810	4.939	5.147	5.452	5.857	0.000	0.000
HUB RAD, IN	2.901	2.901	2.901	2.901	2.901	4.539	4.539	4.539	4.539	4.539	0.000	0.000
RAD HT, IN	0.268	0.316	0.353	0.396	0.447	0.270	0.399	0.608	0.913	1.318	0.000	0.000
STATION 3 TIP RAD, IN	3.171	3.227	3.266	3.312	3.366	4.841	5.003	5.236	5.610	6.089	0.000	0.000
HUB RAD, IN	2.901	2.901	2.901	2.901	2.901	4.539	4.539	4.539	4.539	4.539	0.000	0.000
RAD HT, IN	0.270	0.326	0.365	0.411	0.465	0.302	0.464	0.697	1.071	1.550	0.000	0.000
STATOR TIP CHORD, IN	0.473	0.434	0.443	0.454	0.466	0.688	0.722	0.778	0.863	0.980	0.000	0.000
HUB CHORD, IN	0.401	0.359	0.359	0.359	0.359	0.618	0.618	0.618	0.618	0.618	0.000	0.000
ROTOR TIP CHORD, IN	0.463	0.402	0.394	0.386	0.376	0.749	0.716	0.667	0.604	0.532	0.000	0.000
HUB CHORD, IN	0.535	0.479	0.479	0.479	0.479	0.825	0.825	0.825	0.825	0.825	0.000	0.000
ETA AERO	0.8891	0.9370	0.9391	0.9410	0.9429	0.8910	0.8989	0.9092	0.9133	0.9191	0.0000	0.0000
ETA TIP	0.8197	0.8746	0.8828	0.8905	0.8977	0.8571	0.8754	0.8933	0.9024	0.9034	0.0000	0.0000
ETA WET	0.8197	0.8746	0.8828	0.8905	0.8977	0.8446	0.8234	0.8068	0.7849	0.8490	0.0000	0.0000
ETA STAGE	0.8197	0.8623	0.8718	0.8807	0.8891	0.8306	0.7841	0.8006	0.7809	0.8464	0.0000	0.0000
OUTPUT POWER, KW	37.059	29.595	29.855	30.098	30.325	67.723	64.430	66.859	64.920	60.491	0.000	0.000
MO FLOW, LBS/SEC	0.000	0.000	0.000	0.000	0.103	0.000	0.000	0.000	0.262	0.000	0.000	0.000
HMOIST, BTU/LB	0.000	0.000	0.000	0.000	499.718	0.000	0.000	0.000	510.548	0.000	0.000	0.000
NO COND NUCLEI	0.00+000	0.00+000	0.00+000	0.00+000	0.00+000	4.05+011	2.70+011	1.66+011	1.11+011	8.27+010	0.00+000	0.00+000
DROP RADIUS, FT	0.00+000	0.00+000	0.00+000	0.00+000	0.00+000	4.78-006	8.58-006	1.04-005	1.12-005	1.14-005	0.00+000	0.00+000
STR COL, LBS/SEC	0.000000	0.000000	0.000000	0.000000	0.000000	0.005296	0.018367	0.023365	0.022254	0.016333	0.000000	0.000000
RTR COL, LBS/SEC	0.000000	0.000000	0.000000	0.000000	0.000000	0.023784	0.040808	0.048643	0.048377	0.039681	0.000000	0.000000
TOT COL, LBS/SEC	0.000000	0.000000	0.000000	0.000000	0.000000	0.029080	0.088255	0.160263	0.230894	0.056015	0.000000	0.000000
INPUT STAGE VARIABLES												
DEL TAP, VEL HDS	0.000	0.000	0.000	0.000	2.000	0.000	0.000	0.000	0.000	0.000	0.000	0.000
MOIST REMOVED	0.000	0.000	0.000	0.000	0.900	0.000	0.000	0.000	0.790	0.000	0.000	0.000
VAPOR FRACTION	0.000	0.000	0.000	0.000	0.100	0.000	0.000	0.000	0.250	0.000	0.000	0.000
REHEAT CONDITION	0.000	0.000	0.000	0.000	0.000	0.000	0.000	0.000	0.000	0.000	0.000	0.000
WORK SPLIT	0.511	0.408	0.408	0.408	0.408	1.000	1.000	1.000	1.000	1.000	0.000	0.000
STATOR ALPHA, DEG	76.000	74.000	74.000	74.000	74.000	74.000	74.000	74.000	74.000	74.000	0.000	0.000
WORK COEFFICIENT	2.000	1.600	1.600	1.600	1.600	1.600	1.600	1.600	1.600	1.600	0.000	0.000
TIP COEFFICIENT	2.000	2.000	2.000	2.000	2.000	1.000	1.000	1.000	1.000	2.000	1.000	2.000
TIP CLEARANCE	0.010	0.010	0.010	0.010	0.010	0.010	0.010	0.010	0.010	0.010	0.010	0.010
SEAL DIA, IN	4.400	4.000	4.000	4.000	4.000	4.800	4.800	4.800	4.800	4.800	4.800	4.800
SEAL LEAKAGE, LBS/SEC	0.031	0.017	0.015	0.014	0.012	0.072	0.013	0.008	0.005	0.003	0.000	0.000
ACC LIQUID FRACTION	0.0000	0.0000	0.0000	0.0000	0.0000	0.0151	0.0284	0.0347	0.0339	0.0349	0.0000	0.0000

PARAMETRIC TURBINE OUTPUT FOR KTA PHASE II REFERENCE DESIGN

FIGURE 22

STAGE THERMODYNAMIC AND MECHANICAL CONDITIONS

01/15/69
02:28:03

STATION 1	1	2	3	4	5	6	7	8	9	10	11	12
FLOW, LBS/SEC	2.050	2.019	2.019	2.019	2.019	1.863	1.894	1.947	1.947	1.685	0.000	0.000
STOT, BTU/LB R	1.0293	1.0309	1.0318	1.0327	1.0336	1.0525	1.0564	1.0613	1.0657	1.1200	0.0000	0.0000
HTOT, BTU/LB	1237.769	1220.370	1206.476	1192.460	1178.330	1200.696	1167.414	1135.936	1103.390	1158.838	0.000	0.000
TTOT, R	2560.000	2441.564	2351.535	2262.693	2175.369	2202.846	2083.900	1972.560	1868.396	1768.894	0.000	0.000
DSHT, F	71.000	21.545	-15.944	-51.646	-85.736	0.000	0.000	0.000	0.000	0.000	0.000	0.000
XTOT	1.000	1.000	1.000	1.000	1.000	0.996	0.960	0.928	0.896	0.969	0.000	0.000
PTOT, PSIA	165.713	135.871	115.800	97.714	81.711	66.477	42.025	26.003	15.759	9.245	0.000	0.000
HSTAT, BTU/LB	1236.596	1219.377	1205.483	1191.467	1177.337	1198.265	1164.983	1133.505	1100.959	1156.407	0.000	0.000
TSTAT, R	2552.613	2435.695	2345.579	2256.843	2169.699	2195.704	2077.150	1966.194	1862.350	1763.733	0.000	0.000
DSHST, F	67.235	18.808	-18.631	-54.298	-88.237	0.000	0.000	0.000	0.000	0.000	0.000	0.000
XSTAT	1.000	1.000	1.000	1.000	1.000	0.993	0.958	0.926	0.894	0.967	0.000	0.000
PSTAT, PSIA	164.044	134.612	114.624	96.694	80.823	64.765	40.880	25.257	15.282	8.978	0.000	0.000
SPVST, CU FT/LB	3.717	4.301	4.825	5.444	6.182	8.026	11.644	17.420	26.798	47.911	0.000	0.000
STATION 2 (HUB ONLY)												
FLOW, LBS/SEC	2.019	2.019	2.019	2.019	2.019	1.863	1.894	1.947	1.947	1.685	0.000	0.000
STOT, BTU/LB R	1.0297	1.0311	1.0320	1.0329	1.0339	1.0531	1.0571	1.0620	1.0664	1.1208	0.0000	0.0000
HTOT, BTU/LB	1237.769	1220.370	1206.476	1192.460	1178.330	1200.696	1167.414	1135.936	1103.390	1158.838	0.000	0.000
TTOT, R	2557.535	2440.273	2350.016	2261.223	2173.921	2198.722	2080.035	1968.940	1864.968	1765.979	0.000	0.000
DSHT, F	71.376	21.924	-15.649	-51.496	-85.559	0.000	0.000	0.000	0.000	0.000	0.000	0.000
XTOT	1.000	1.000	1.000	1.000	1.000	0.996	0.961	0.929	0.896	0.970	0.000	0.000
PTOT, PSIA	164.403	135.199	115.146	97.196	81.254	65.485	41.366	25.577	15.487	9.094	0.000	0.000
HSTAT, BTU/LB	1217.724	1207.299	1193.405	1179.389	1165.259	1168.698	1135.416	1103.938	1071.392	1126.839	0.000	0.000
TSTAT, R	2433.332	2360.825	2272.612	2185.828	2100.469	2106.792	1993.248	1886.948	1786.851	1698.892	0.000	0.000
DSHST, F	12.448	-14.522	-49.986	-83.883	-116.349	0.000	0.000	0.000	0.000	0.000	0.000	0.000
XSTAT	1.000	1.000	1.000	1.000	1.000	0.961	0.926	0.895	0.864	0.936	0.000	0.000
PSTAT, PSIA	136.221	118.665	100.383	84.160	69.922	46.092	28.544	17.299	10.224	6.118	0.000	0.000
SPVST, CU FT/LB	4.236	4.694	5.291	6.004	6.865	10.491	15.584	23.912	37.847	66.870	0.000	0.000
STATION 3												
FLOW, LBS/SEC	2.019	2.019	2.019	2.019	1.966	1.863	1.947	1.947	1.947	1.685	0.000	0.000
STOT, BTU/LB R	1.0303	1.0313	1.0322	1.0331	1.0341	1.0547	1.0585	1.0633	1.0677	1.1219	0.0000	0.0000
HTOT, BTU/LB	1218.898	1205.273	1191.379	1177.363	1163.232	1163.737	1130.455	1098.977	1066.431	1121.879	0.000	0.000
TTOT, R	2436.437	2347.301	2259.507	2173.016	2088.095	2083.896	1972.555	1868.392	1769.560	1684.515	0.000	0.000
DSHT, F	16.577	-19.715	-54.920	-88.562	-120.827	0.000	0.000	0.000	0.000	0.000	0.000	0.000
XTOT	1.000	1.000	1.000	1.000	1.000	0.956	0.922	0.891	0.860	0.932	0.000	0.000
PTOT, PSIA	135.807	115.633	97.742	81.845	67.960	42.024	26.002	15.759	9.280	5.596	0.000	0.000
HSTAT, BTU/LB	1217.724	1204.280	1190.386	1176.369	1162.239	1161.306	1128.024	1096.546	1064.000	1119.448	0.000	0.000
TSTAT, R	2429.471	2341.745	2253.614	2167.233	2082.722	2077.113	1966.143	1862.309	1763.740	1679.481	0.000	0.000
DSHST, F	13.350	-22.309	-57.578	-91.100	-123.051	0.000	0.000	0.000	0.000	0.000	0.000	0.000
XSTAT	1.000	1.000	1.000	1.000	1.000	0.953	0.919	0.888	0.857	0.929	0.000	0.000
PSTAT, PSIA	134.305	114.568	96.710	80.934	67.188	40.873	25.251	15.279	8.979	5.422	0.000	0.000
SPVST, CU FT/LB	4.293	4.813	5.428	6.159	7.029	11.589	17.296	26.643	42.472	74.455	0.000	0.000
BLADE STRESS, PSI	2742.59	3221.04	3563.32	3953.64	4399.21	9725.88	11974.60	15138.53	19557.55	19705.95	0.00	0.00
BLADE TEMP, R	2502.931	2425.339	2372.659	2319.795	2266.959	2156.792	2043.242	1936.948	1836.851	1748.881	0.000	0.000
BLADE CRIT RD, IN	2.901	2.901	2.901	2.901	2.901	4.539	4.539	4.539	4.539	4.539	0.000	0.000
NO OF STR-RTR BLADES	28 77	36 64	36 64	36 64	36 64	33 59	33 59	32 59	32 59	32 59	0 0	0 0
BLADE CG RAD, IN	3.030	3.053	3.070	3.090	3.113	4.766	4.849	4.965	5.131	5.179	0.000	0.000
BLADE WEIGHT, LBS	0.224	0.155	0.170	0.188	0.208	0.821	0.993	1.226	1.533	1.530	0.000	0.000
BLADE INERTIA, LB IN2	2.053	1.446	1.609	1.797	2.015	18.644	23.368	30.288	40.527	41.293	0.000	0.000
DISK LIFE, HRS	1.36+004	3.00+004	3.00+004	3.00+004	3.00+004	3.00+004	3.00+004	3.00+004	3.00+004	3.00+004	0.00+000	0.00+000
DISK STRESS, PSI	16805.83	23870.06	30046.89	37604.03	46500.00	46500.00	46500.00	46500.00	46500.00	46500.00	0.00	0.00
DISK TEMP, R	2502.931	2425.339	2372.659	2319.795	2266.959	2156.792	2043.242	1936.948	1836.851	1748.881	0.000	0.000
PLATFORM THICK, IN	0.145	0.130	0.130	0.130	0.130	0.559	0.559	0.559	0.559	0.559	0.000	0.000
DISK HUB WIDTH, IN	0.100	0.100	0.100	0.100	0.100	0.141	0.149	0.160	0.175	0.175	0.000	0.000
DISK ROOT WIDTH, IN	1.500	1.155	0.563	0.173	0.105	0.882	0.920	0.974	1.050	1.053	0.000	0.000
DISK HOLE RAD, IN	0.600	0.600	0.600	0.600	0.600	0.600	0.600	0.600	0.600	0.600	0.000	0.000
ROTOR WEIGHT, LBS	3.213	2.765	2.217	1.692	1.564	10.246	10.659	11.231	12.012	12.025	0.000	0.000

TURBINE WEIGHT, LBS = 213.0 DESIGN LIFE, HRS = 30000.0 DISK DELTA TEMP, F = 50.0 BLADE DELTA TEMP, F = 50.0

FIGURE 22 (CONTD.)

VELOCITY DIAGRAM AT STATION 2 HUB

01/15/69
02:28:03

V2X, FT/SEC	242.382	223.011	223.011	223.011	223.011	348.924	348.924	348.924	348.924	348.924	0.000	0.000
V2U, FT/SEC	972.143	777.733	777.733	777.733	777.733	1216.843	1216.843	1216.843	1216.843	1216.843	0.000	0.000
V2, FT/SEC	1001.903	809.075	809.075	809.075	809.075	1265.881	1265.881	1265.881	1265.881	1265.881	0.000	0.000
U2, FT/SEC	486.071	486.083	486.083	486.083	486.083	760.527	760.527	760.527	760.527	760.527	0.000	0.000
W2U, FT/SEC	486.071	291.650	291.650	291.650	291.650	456.316	456.316	456.316	456.316	456.316	0.000	0.000
W2, FT/SEC	543.152	367.143	367.143	367.143	367.143	574.432	574.432	574.432	574.432	574.432	0.000	0.000
W3, FT/SEC	-543.152	-534.800	-534.800	-534.800	-534.800	-836.749	-836.749	-836.749	-836.749	-836.749	0.000	0.000
ALPHA, DEG	76.000	74.000	74.000	74.000	74.000	74.000	74.000	74.000	74.000	74.000	0.000	0.000
BETA2, DEG	63.497	52.597	52.597	52.597	52.597	52.597	52.597	52.597	52.597	52.597	0.000	0.000
BETA3, DEG	63.497	65.355	65.355	65.355	65.355	65.355	65.355	65.355	65.355	65.355	0.000	0.000

VELOCITY DIAGRAM AT STATION 2 MEAN

V2X, FT/SEC	242.382	223.011	223.011	223.011	223.011	348.924	348.924	348.924	348.924	348.924	0.000	0.000
V2U, FT/SEC	929.293	737.614	733.155	728.018	722.065	1161.637	1165.551	1140.480	1105.639	1062.589	0.000	0.000
V2, FT/SEC	960.383	770.590	766.323	761.409	755.720	1232.077	1216.659	1192.662	1159.390	1118.411	0.000	0.000
U2, FT/SEC	508.484	512.521	515.639	519.277	523.558	783.186	793.995	811.449	837.020	870.931	0.000	0.000
W2U, FT/SEC	420.810	225.093	217.516	208.741	198.507	398.450	371.557	329.031	268.620	191.658	0.000	0.000
W2, FT/SEC	485.623	316.861	311.524	305.462	298.562	529.633	509.708	479.593	440.346	398.097	0.000	0.000
W3, FT/SEC	-563.298	-558.938	-561.798	-565.140	-569.075	-857.397	-867.281	-883.288	-906.835	-938.226	0.000	0.000
ALPHA, DEG	75.382	73.178	73.081	72.969	72.837	73.549	73.334	72.989	72.485	71.821	0.000	0.000
BETA2, DEG	60.058	45.266	44.285	43.107	41.673	48.791	46.799	43.319	37.591	28.779	0.000	0.000
BETA3, DEG	64.514	66.485	66.612	66.758	66.928	65.986	66.277	66.732	67.370	68.167	0.000	0.000

VELOCITY DIAGRAM AT STATION 2 TIP

V2X, FT/SEC	242.382	223.011	223.011	223.011	223.011	348.924	348.924	348.924	348.924	348.924	0.000	0.000
V2U, FT/SEC	890.062	701.432	693.410	684.277	673.834	1148.410	1118.409	1073.135	1013.059	943.044	0.000	0.000
V2, FT/SEC	922.475	736.030	728.390	719.700	709.779	1200.248	1171.574	1128.436	1071.465	1005.525	0.000	0.000
U2, FT/SEC	530.896	538.959	545.194	552.471	561.033	805.846	827.463	862.372	913.512	981.335	0.000	0.000
W2U, FT/SEC	359.166	162.472	148.216	131.806	112.802	342.565	290.946	210.763	99.547	-36.291	0.000	0.000
W2, FT/SEC	433.301	275.919	267.773	259.050	249.917	448.977	454.310	407.639	362.846	351.019	0.000	0.000
W3, FT/SEC	-583.609	-583.276	-589.042	-595.784	-603.731	-878.143	-898.021	-930.287	-977.882	-1041.521	0.000	0.000
ALPHA, DEG	74.767	72.363	72.171	71.949	71.688	73.100	72.673	71.988	70.995	69.696	0.000	0.000
BETA2, DEG	55.987	36.075	33.609	30.584	26.831	44.473	39.823	31.134	15.923	-6.263	0.000	0.000
BETA3, DEG	65.461	67.521	67.753	68.018	68.322	66.588	67.136	67.971	69.095	70.427	0.000	0.000

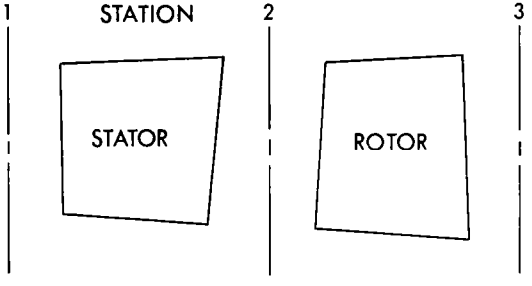

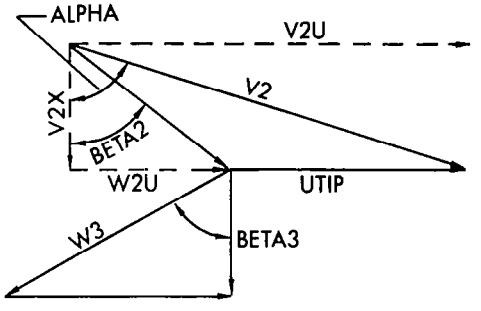

FIGURE 22 (CONTD.)

MULTISTAGE RANKINE CYCLE TURBINE DESIGN — SUPERSATURATED FLUID PROPERTIES WITH REVERSION IN STATOR NO 6 — 01/29/69 22:11:16

NO STAGES	TURBINE EFFICIENCY	SHAFT POWER (KILOWATTS)	SHAFT SPEED (RPM)	THRUST LOADING (LBS)	TOTAL REHEAT ENERGY (KW)
10	0.8214	486.277	19200	1260.229	0.000

THERMODYNAMIC CONDITIONS

	TEMP, R	SUPERHEAT	QUALITY	ENTHALPY, BTU/LB	FLOW, LBS/SEC
INLET	2560.00	71.00	1.000	1237.77	2.050
EXIT WITHOUT MOISTURE	1679.86	0.00	0.941	1129.98	1.651
EXIT WITH MOISTURE	1680.00	0.00	0.803	1011.85	2.050

DIMENSIONS AND PERFORMANCE	1	2	3	4	5	6	7	8	9	10	11	12
STATION 1 TIP RAD, IN	3.141	3.195	3.229	3.269	3.315	4.805	4.903	5.057	5.275	5.600	0.000	0.000
HUB RAD, IN	2.903	2.903	2.903	2.903	2.903	4.599	4.599	4.599	4.599	4.599	0.000	0.000
RAD HT, IN	0.238	0.293	0.326	0.366	0.413	0.206	0.304	0.458	0.676	1.001	0.000	0.000
STATION 2 TIP RAD, IN	3.170	3.218	3.255	3.299	3.351	4.865	4.994	5.194	5.469	5.869	0.000	0.000
HUB RAD, IN	2.903	2.903	2.903	2.903	2.903	4.599	4.599	4.599	4.599	4.599	0.000	0.000
RAD HT, IN	0.267	0.315	0.353	0.396	0.447	0.266	0.395	0.595	0.870	1.270	0.000	0.000
STATION 3 TIP RAD, IN	3.172	3.228	3.263	3.314	3.369	4.898	5.058	5.279	5.607	6.096	0.000	0.000
HUB RAD, IN	2.903	2.903	2.903	2.903	2.903	4.599	4.599	4.599	4.599	4.599	0.000	0.000
RAD HT, IN	0.270	0.326	0.365	0.411	0.465	0.299	0.459	0.680	1.008	1.497	0.000	0.000
STATOR TIP CHORD, IN	0.473	0.433	0.442	0.453	0.466	0.686	0.719	0.773	0.848	0.961	0.000	0.000
HUB CHORD, IN	0.401	0.359	0.359	0.359	0.359	0.618	0.618	0.618	0.618	0.618	0.000	0.000
ROTOR TIP CHORD, IN	0.463	0.402	0.394	0.385	0.375	0.751	0.718	0.672	0.614	0.543	0.000	0.000
HUB CHORD, IN	0.535	0.478	0.478	0.478	0.478	0.825	0.825	0.825	0.825	0.825	0.000	0.000
ETA AERO	0.8890	0.9370	0.9390	0.9410	0.9429	0.8886	0.8971	0.9086	0.9140	0.9174	0.0000	0.0000
ETA TIP	0.8196	0.8745	0.8827	0.8904	0.8977	0.8542	0.8734	0.8924	0.9026	0.9012	0.0000	0.0000
ETA WET	0.8196	0.8745	0.8827	0.8904	0.8977	0.8418	0.8342	0.8425	0.8545	0.8539	0.0000	0.0000
ETA STAGE	0.8196	0.8622	0.8717	0.8806	0.8891	0.8277	0.7950	0.8363	0.8504	0.8512	0.0000	0.0000
OUTPUT POWER, KW	37.102	29.628	29.889	30.131	30.360	69.463	65.849	67.650	64.876	61.330	0.000	0.000
MO FLOW, LBS/SEC	0.000	0.000	0.000	0.000	0.103	0.038	0.073	0.094	0.091	0.000	0.000	0.000
HMOIST, BTU/LB	0.000	0.000	0.000	0.000	499.654	562.271	543.616	526.568	510.928	0.000	0.000	0.000
NO COND NUCLEI	0.00+000	0.00+000	0.00+000	0.00+000	0.00+000	4.05+011	2.69+011	1.41+011	6.21+010	2.29+010	0.00+000	0.00+000
DROP RADIUS, FT	0.00+000	0.00+000	0.00+000	0.00+000	0.00+000	4.80-006	8.65-006	1.12-005	1.42-005	1.82-005	0.00+000	0.00+000
STR COL, LBS/SEC	0.000000	0.000000	0.000000	0.000000	0.000000	0.005466	0.018537	0.025558	0.026144	0.022220	0.000000	0.000000
RTR COL, LBS/SEC	0.000000	0.000000	0.000000	0.000000	0.000000	0.024471	0.041398	0.049685	0.050067	0.045216	0.000000	0.000000
TOT COL, LBS/SEC	0.000000	0.000000	0.000000	0.000000	0.000000	0.029937	0.059935	0.075243	0.076212	0.067435	0.000000	0.000000
INPUT STAGE VARIABLES												
DEL TAP, VEL RDS	0.000	0.000	0.000	0.000	2.000	0.000	0.000	0.000	0.000	0.000	0.000	0.000
MOIST REMOVED	0.000	0.000	0.000	0.000	0.900	0.362	0.490	0.590	0.630	0.000	0.000	0.000
VAPOR FRACTION	0.000	0.000	0.000	0.000	0.100	0.250	0.250	0.250	0.250	0.000	0.000	0.000
REHEAT CONDITION	0.000	0.000	0.000	0.000	0.000	0.000	0.000	0.000	0.000	0.000	0.000	0.000
WORK SPLIT	0.495	0.398	0.399	0.398	0.398	1.000	1.000	1.000	1.000	1.000	0.000	0.000
STATOR ALPHA, DEG	76.000	74.000	74.000	74.000	74.000	74.000	74.000	74.000	74.000	74.000	0.000	0.000
WORK COEFFICIENT	2.000	1.600	1.600	1.600	1.600	1.600	1.600	1.600	1.600	1.600	0.000	0.000
TIP COEFFICIENT	2.000	2.000	2.000	2.000	2.000	1.000	1.000	1.000	1.000	2.000	1.000	2.000
TIP CLEARANCE	0.010	0.010	0.010	0.010	0.010	0.010	0.010	0.010	0.010	0.010	0.010	0.010
SEAL DIA, IN	4.400	4.000	4.000	4.000	4.000	4.800	4.800	4.800	4.800	4.800	4.800	4.800
SEAL LEAKAGE, LBS/SEC	0.031	0.017	0.015	0.014	0.012	0.072	0.012	0.008	0.005	0.003	0.000	0.000
ACC LIQUID FRACTION	0.0000	0.0000	0.0000	0.0000	0.0000	0.0151	0.0284	0.0347	0.0339	0.0349	0.0000	0.0000

PARAMETRIC TURBINE OUTPUT FOR KTA PHASE II REFERENCE DESIGN
WITH INTERSTAGE MOISTURE REMOVAL AFTER STAGES 6, 7, 8, AND 9

FIGURE 23

STAGE THERMODYNAMIC AND MECHANICAL CONDITIONS

01/29/69
22;11;16

STATION 1	1	2	3	4	5	6	7	8	9	10	11	12
FLOW, LBS/SEC	2.050	2.019	2.019	2.019	2.019	1.863	1.856	1.836	1.742	1.651	0.000	0.000
STOT, BTU/LB R	1.0293	1.0309	1.0319	1.0327	1.0336	1.0526	1.0625	1.0790	1.1002	1.1229	0.0000	0.0000
HTOT, BTU/LB	1237.769	1220.351	1206.441	1192.409	1178.263	1200.674	1178.706	1168.807	1166.532	1165.180	0.000	0.000
TTOT, R	2560.000	2441.417	2351.267	2262.346	2174.928	2202.494	2080.009	1967.293	1864.860	1771.260	0.000	0.000
DSHT, F	71.000	21.493	-16.033	-51.770	-85.887	0.000	0.000	0.000	0.000	0.000	0.000	0.000
XTOT	1.000	1.000	1.000	1.000	1.000	0.996	0.975	0.969	0.973	0.977	0.000	0.000
PTOT, PSIA	165.715	135.833	115.743	97.642	81.630	66.392	41.362	25.385	15.479	9.370	0.000	0.000
HSTAT, BTU/LB	1236.594	1219.356	1205.447	1191.415	1177.269	1198.179	1176.210	1166.311	1164.036	1162.684	0.000	0.000
TSTAT, R	2552.605	2435.541	2345.525	2256.489	2169.247	2195.164	2073.205	1961.061	1859.157	1765.993	0.000	0.000
DSHST, F	67.231	18.753	-18.723	-54.424	-88.392	0.000	0.000	0.000	0.000	0.000	0.000	0.000
XSTAT	1.000	1.000	1.000	1.000	1.000	0.993	0.972	0.967	0.970	0.974	0.000	0.000
PSTAT, PSIA	164.042	134.572	114.566	96.621	80.740	64.637	40.221	24.668	15.034	9.094	0.000	0.000
SPVST, CU FT/LB	3.717	4.382	4.827	5.447	6.186	8.039	11.992	18.584	29.538	47.687	0.000	0.000
STATION 2 (HUB ONLY)												
FLOW, LBS/SEC	2.019	2.019	2.019	2.019	2.019	1.863	1.856	1.836	1.742	1.651	0.000	0.000
STOT, BTU/LB R	1.0297	1.0311	1.0320	1.0329	1.0339	1.0532	1.0632	1.0797	1.1010	1.1237	0.0000	0.0000
HTOT, BTU/LB	1237.769	1220.351	1206.441	1192.409	1178.263	1200.674	1178.706	1168.807	1166.532	1165.180	0.000	0.000
TTOT, R	2557.535	2440.124	2349.767	2260.872	2173.474	2198.236	2076.108	1963.758	1861.639	1768.285	0.000	0.000
DSHT, F	71.376	21.872	-15.737	-51.619	-85.712	0.000	0.000	0.000	0.000	0.000	0.000	0.000
XTOT	1.000	1.000	1.000	1.000	1.000	0.996	0.975	0.969	0.973	0.977	0.000	0.000
PTOT, PSIA	164.403	135.150	115.089	97.123	81.172	65.368	40.705	24.976	15.226	9.214	0.000	0.000
HSTAT, BTU/LB	1217.700	1207.264	1193.354	1179.322	1165.177	1187.826	1145.858	1135.959	1133.684	1132.332	0.000	0.000
TSTAT, R	2433.182	2366.587	2272.277	2185.399	2099.954	2103.944	1988.617	1883.404	1787.808	1699.822	0.000	0.000
DSHST, F	92.379	-14.613	-50.109	-84.037	-116.528	0.000	0.000	0.000	0.000	0.000	0.000	0.000
XSTAT	1.000	1.000	1.000	1.000	1.000	0.960	0.940	0.934	0.938	0.943	0.000	0.000
PSTAT, PSIA	136.188	118.610	100.314	84.081	69.838	45.571	27.959	16.996	10.279	6.153	0.000	0.000
SPVST, CU FT/LB	4.237	4.696	5.294	6.008	6.871	10.588	16.108	25.371	40.891	66.960	0.000	0.000
STATION 3												
FLOW, LBS/SEC	2.019	2.019	2.019	2.019	1.966	1.863	1.909	1.836	1.742	1.651	0.000	0.000
STOT, BTU/LB R	1.0303	1.0318	1.0322	1.0331	1.0341	1.0548	1.0647	1.0811	1.1022	1.1250	0.0000	0.0000
HTOT, BTU/LB	1218.874	1205.235	1191.326	1177.293	1163.148	1162.734	1140.765	1130.867	1128.592	1127.239	0.000	0.000
TTOT, R	2436.281	2347.046	2259.156	2172.573	2087.566	2060.164	1967.541	1865.136	1771.513	1684.986	0.000	0.000
DSHT, F	14.514	-19.810	-55.045	-88.720	-121.011	0.000	0.000	0.000	0.000	0.000	0.000	0.000
XTOT	1.000	1.000	1.000	1.000	1.000	0.955	0.935	0.930	0.933	0.938	0.000	0.000
PTOT, PSIA	135.769	115.575	97.670	81.764	67.875	41.388	25.413	15.500	9.383	5.612	0.000	0.000
HSTAT, BTU/LB	1217.700	1204.241	1190.331	1176.299	1162.154	1160.238	1138.270	1128.371	1126.096	1124.743	0.000	0.000
TSTAT, R	2429.307	2341.481	2253.256	2166.779	2082.188	2073.215	1961.078	1859.168	1766.000	1679.850	0.000	0.000
DSHST, F	13.284	-22.468	-57.769	-91.262	-123.237	0.000	0.000	0.000	0.000	0.000	0.000	0.000
XSTAT	1.000	1.000	1.000	1.000	1.000	0.952	0.932	0.927	0.931	0.935	0.000	0.000
PSTAT, PSIA	134.266	114.508	96.634	80.852	67.103	40.223	24.670	15.035	9.095	5.435	0.000	0.000
SPVST, CU FT/LB	4.294	4.815	5.431	6.163	7.035	11.744	17.919	28.225	45.558	74.784	0.000	0.000
BLADE STRESS, PSI	2742.00	3220.95	3563.75	3954.85	4401.30	9858.89	12137.67	15208.34	19227.23	19351.05	0.00	0.00
BLADE TEMP, R	2502.804	2425.191	2372.446	2319.567	2266.623	2153.944	2038.611	1933.404	1837.798	1749.811	0.000	0.000
BLADE CRIT RD, IN	2.903	2.903	2.903	2.903	2.903	4.599	4.599	4.599	4.599	4.599	0.000	0.000
NO OF STR-RTR BLADES	28 77	36 64	36 64	36 64	36 65	33 59	33 59	33 59	33 59	32 59	0 0	0 0
BLADE CG RAD, IN	3.031	3.055	3.072	3.092	3.115	4.824	4.907	5.019	5.167	5.217	0.000	0.000
BLADE WEIGHT, LBS	0.223	0.155	0.173	0.187	0.210	0.872	0.995	1.218	1.496	1.491	0.000	0.000
BLADE INERTIA, LB IN	2.050	1.444	1.606	1.795	2.044	19.128	23.969	30.750	40.104	40.822	0.000	0.000
DISK LIFE, HRS	1.3e+004	3.00+004	3.00+004	3.00+004	3.00+004	3.00+004	3.00+004	3.00+004	3.00+004	3.00+004	0.00+000	0.00+000
DISK STRESS, PSI	19515.55	23805.74	30974.25	37639.82	46500.00	46500.00	46500.00	46500.00	46500.00	46500.00	0.00	0.00
DISK TEMP, R	2502.804	2425.191	2372.446	2319.567	2266.623	2153.944	2038.611	1933.404	1837.798	1749.811	0.000	0.000
PLATFORM THICK, IN	0.145	0.130	0.130	0.130	0.130	0.559	0.559	0.559	0.559	0.559	0.000	0.000
DISK HUB WIDTH, IN	0.100	0.100	0.100	0.100	0.100	0.143	0.150	0.161	0.174	0.175	0.000	0.000
DISK ROOT WIDTH, IN	1.500	1.156	0.564	0.173	0.105	0.923	0.962	1.015	1.085	1.087	0.000	0.000
DISK HOLE RAD, IN	0.600	0.600	0.600	0.600	0.600	0.600	0.600	0.600	0.600	0.600	0.000	0.000
ROTOR WEIGHT, LBS	3.214	2.747	2.215	1.692	1.566	10.541	10.963	11.523	12.242	12.250	0.000	0.000

TURBINE AP DAT, LBS = [illegible] DISK DELTA TEMP, F = 50.0 BLADE DELTA TEMP, F = 50.0

FIGURE 23 (CONTD.)

01/29/69
22:11:16

VELOCITY DIAGRAM AT STATION 2 HUB

V2X, FT/SEC	242.531	223.142	223.142	223.142	223.142	353.527	353.527	353.527	353.527	353.527	0.000	0.000
V2U, FT/SEC	972.737	778.189	778.189	778.189	778.189	1232.894	1232.894	1232.894	1232.894	1232.894	0.000	0.000
V2, FT/SEC	1002.516	809.550	809.550	809.550	809.550	1282.579	1282.579	1282.579	1282.579	1282.579	0.000	0.000
U2, FT/SEC	486.368	486.368	486.368	486.368	486.368	770.559	770.559	770.559	770.559	770.559	0.000	0.000
W2U, FT/SEC	486.368	291.821	291.821	291.821	291.821	462.335	462.335	462.335	462.335	462.335	0.000	0.000
W2, FT/SEC	543.484	367.356	367.356	367.356	367.356	582.009	582.009	582.009	582.009	582.009	0.000	0.000
W3, FT/SEC	-543.484	-535.114	-535.114	-535.114	-535.114	-847.786	-847.786	-847.786	-847.786	-847.786	0.000	0.000
ALPHA, DEG	76.000	74.000	74.000	74.000	74.000	74.000	74.000	74.000	74.000	74.000	0.000	0.000
BETA2, DEG	63.497	52.597	52.597	52.597	52.597	52.597	52.597	52.597	52.597	52.597	0.000	0.000
BETA3, DEG	63.497	65.355	65.355	65.355	65.355	65.355	65.355	65.355	65.355	65.355	0.000	0.000

VELOCITY DIAGRAM AT STATION 2 MEAN

V2X, FT/SEC	242.531	223.142	223.142	223.142	223.142	353.527	353.527	353.527	353.527	353.527	0.000	0.000
V2U, FT/SEC	929.927	738.099	733.635	728.492	722.532	1198.233	1182.160	1158.013	1126.360	1083.356	0.000	0.000
V2, FT/SEC	961.033	771.091	766.820	761.901	756.204	1249.297	1233.890	1210.774	1180.537	1139.579	0.000	0.000
U2, FT/SEC	508.759	512.736	515.906	519.548	523.834	792.848	803.628	820.385	843.440	876.921	0.000	0.000
W2U, FT/SEC	421.168	225.312	217.730	208.944	198.698	405.385	378.532	337.627	282.920	206.435	0.000	0.000
W2, FT/SEC	486.005	317.109	311.767	305.696	298.787	537.883	517.946	488.849	452.797	409.385	0.000	0.000
W3, FT/SEC	-563.610	-559.233	-562.095	-565.440	-569.381	-868.095	-877.952	-893.316	-914.534	-945.500	0.000	0.000
ALPHA, DEG	75.383	73.179	73.062	72.970	72.838	73.562	73.351	73.023	72.575	71.927	0.000	0.000
BETA2, DEG	60.064	45.277	44.297	43.118	41.684	48.909	46.956	43.682	38.670	30.282	0.000	0.000
BETA3, DEG	64.512	66.483	66.610	66.757	66.927	65.968	66.255	66.687	67.259	68.043	0.000	0.000

VELOCITY DIAGRAM AT STATION 2 TIP

V2X, FT/SEC	242.531	223.142	223.142	223.142	223.142	353.527	353.527	353.527	353.527	353.527	0.000	0.000
V2U, FT/SEC	890.726	701.936	693.907	684.761	674.305	1165.468	1135.437	1091.707	1036.773	966.169	0.000	0.000
V2, FT/SEC	923.154	736.551	728.903	720.202	710.267	1217.907	1189.200	1147.521	1095.390	1028.816	0.000	0.000
U2, FT/SEC	531.149	539.204	545.443	552.728	561.299	815.137	836.697	870.212	916.321	983.283	0.000	0.000
W2U, FT/SEC	359.577	162.732	148.464	132.033	113.006	350.331	298.739	221.495	120.451	-17.114	0.000	0.000
W2, FT/SEC	433.724	276.178	268.019	259.276	250.126	497.707	462.846	417.182	373.483	353.941	0.000	0.000
W3, FT/SEC	-583.901	-583.552	-589.322	-596.071	-604.027	-888.499	-908.319	-939.262	-982.154	-1044.905	0.000	0.000
ALPHA, DEG	74.769	72.565	72.174	71.951	71.689	73.126	72.706	72.057	71.171	69.902	0.000	0.000
BETA2, DEG	56.001	36.202	33.637	30.613	26.859	44.740	40.199	32.068	18.815	-2.772	0.000	0.000
BETA3, DEG	65.458	67.518	67.750	68.016	68.320	66.554	67.095	67.890	68.903	70.225	0.000	0.000

FIGURE 23 (CONTD.)

These two programs were modified for the KTA study as follows:

(a) The parametric program utilizes approximate fluid properties in the form of polynominal expressions. Minor modification to the program logic was required to include the capability of utilizing supersaturated fluid properties. The blade moisture collection analysis, utilized by Westinghouse in their erosion analysis[14] was refined and included in the mechanical blade evaluation. This modified program was utilized in the KTA turbine parametric design analysis and is described in Section 2.2 of Volume I.

(b) The turbine design program utilizes the exact equations of state for the two phase working fluid. The condensation analysis utilized in the Westinghouse erosion model was incorporated into the program so that supersaturated vapor flow could be precisely evaluated as well as a precise prediction of the reversion location.

With respect to a fully designed vapor turbine, the total turbine design procedure is as follows:

(a) Determine the preliminary turbine performance with the use of the turbine parametric program utilizing the built-in condensation model. The approximate blade efficiency, sizing, and number of blades are output.

(b) Evaluate the preliminary design with the use of the turbine design program. The condensation history obtained gives a more rigorous evaluation with approximate blade shapes.

(c) Evaluate the blade-collected moisture with the turbine parametric program and the use of the condensation history output of Step (b).

(d) Evaluate the revised turbine design with the turbine design program and submit the vector diagram requirements for a detailed blade design.

(e) Evaluate the mechanical aspects of the preliminary blade design and design the required disks.

(f) Evaluate the preliminary blade-shape designs with the turbine design program to check the condensation history for possible differences.

(g) Repeat Step (c) but with the condensation history of Step (f).

(h) Evaluate the revised turbine design with the turbine design program and submit the new velocity diagrams to the blade design procedure. If changes are required of the preliminary blade shapes, make the necessary changes and repeat the procedure starting at Step (e). If no changes are required continue to Step (i).

(i) Finalize the blade and disk designs and prepare detailed drawings for manufacturing.

The KTA turbine design has been completed through Step (g) on the first pass. This was sufficient information to determine the performance of the turbine, establish the initial blade and disk designs and conduct an erosion analysis. Section 3.2.4 gives the final parametric design program output as defined by Step (g). This section describes the turbine design program and the blade design procedures and summarizes the preliminary blade shapes as generated in Step (d).

3.3.1 Turbine Design Program

3.3.1.1 Condensation Model

Westinghouse Astronuclear Laboratory has developed an erosion analysis[2,3] to evaluate vapor turbine designs. A portion of this analysis is a condensation analysis in which the formation of condensate (droplet quantity and droplet size, as a function of axial location) is rigorously predicted. In this analysis, the flow equations consisting of the one-dimensional continuity, energy, and momentum equations

as well as the fluid-state equations are solved along the mean line of a turbine design being analyzed for condensation.

The nucleation rate (j) is a function of the thermodynamic state only, and it is possible to determine at any point in the flow path if liquid has formed. If j is less than or equal to some critical value (j_{crit}), any liquid formed is immediately evaporated. When $j > j_{crit}$, stable liquid droplets are formed at a rate according to the Katz, Saltsburg, and Reiss model[4]. Once stable droplets exist, the nucleation rate increases rapidly since nucleation sites are readily available. When sufficient nucleation sites are present to absorb the condensate, the nucleation rate decreases. The point at which j reaches a maximum is, by definition, where the expansion crosses the Wilson line. Once the Wilson line is passed, any further condensation potential results in the immediate formation of condensate. When the amount of condensate exceeds some percentage (90 percent as used for the KTA) of the equivalent equilibrium moisture, reversion from supersaturated to equilibrium flow is assumed to have occurred. This assumption is a good approximation since the deviation in fluid properties is negligible between the actual process and the assumed equilibrium process.

This condensation model was incorporated into the turbine design program in subroutine form. In this form, the precise definition of condensation is used to design the turbine instead of evaluating an existing turbine design, as is the case for the Westinghouse utilization. The use of the Westinghouse condensation subroutine directly with the AiResearch turbine design program resulted in an entropy decrease across an ideal blade row. Investigation showed that there were slight inconsistencies between the property equations as used by AiResearch and the flow equations as written by Westinghouse. This discrepancy was rectified by rewriting the flow equations. Both the property and flow equations are included as Appendix D. The property equations are consistent with the NRL[5] potassium properties as required by the contract.

When the flow equations in the Westinghouse code were made to conform to those given in Appendix D, the entropy was unchanged across an ideal (100-percent efficient) blade row.

3.3.1.2 Aerodynamic Design Procedure

The turbine inlet and discharge conditions are used to define the isentropic work and inlet conditions for the first stage. The work coefficients and flow angles specified for the stage are used to define the required vector diagram at the hub radius and the flow for a given stator blade radial increment. Successive stator blade radial increments are stacked until the flow matches the specified stage flow for a free vortex stage design. The overall stage aerodynamic efficiency utilized by the program is an input item normally obtained from the turbine parametric computer program described in Volume I, Section 2.2. The fraction of stage inlet liquid flow that is collected by the stator and rotor and the labyrinth seal leakage rates are additional input items obtained from the parametric program. Both programs determine the losses due to tip clearance, moisture, and seal leakages as described in Volume I, Section 2.2.2.1. Once the losses have been evaluated, the inlet conditions to the next stage have been defined.

If the initial thermodynamic state is superheated or saturated, the initial stages are designed with supersaturated fluid properties. At the completion of the sizing of a particular stage, the thermodynamic state and nucleation rate (j) are computed. For all values of j less than a critical value (j_{crit}), the use of the equilibrium superheat (supersaturated) properties is continued. However, when $j \geq j_{crit}$, spontaneous condensation has occurred somewhere along the flow path formed by the prior blade row. This triggers the code to call the condensation model for an analysis of that blade row. Thus, across a blade row where condensation is occurring, the row is resized during an integration of the condensation along the flow path. Supersaturated fluid

properties are used but with a quality as defined by the amount of condensate formed. The moisture is assumed to be in kinetic equilibrium with the vapor and homogeneously distributed through the flow passage. However, the liquid is not in thermodynamic equilibrium with the vapor, and the temperature difference between the liquid and vapor phases is a result of the condensation calculation.

After the Wilson line has been passed and the condensed moisture reaches a required fraction of the equilibrium moisture for a particular thermodynamic fluid state, reversion to equilibrium thermodynamics occurs. All subsequent calculation stations are computed with the use of equilibrium properties.

Major iterations are performed by adjusting the hub radii until the discharge conditions of the last stage agree with the required conditions.

3.3.1.3 Program Output

The turbine design program output is split into three areas. No sample output is included herein due to the large volume of output data. Up to 50 pages of printout may be required for a single design point.

The first section of the output is a step-by-step history of the condensation formation as the program steps from stage-to-stage. This history allows the determination of the actual moisture level at any axial location between the point of initial condensate formation and the point of reversion to equilibrium. The reversion point may be located within less than one percent of the actual axial location in the blade row in which it occurs. The program also calculates the number of condensation nuclei and, thus, the average size of the droplets. This information may be used by the turbine parametric program for the blade-moisture-collection model.

The second section of the output is a summary of the thermodynamic conditions at the inlet and exit of each stage. A summary of the stator and rotor discharge flow path dimensions are given as well as the individual stage and overall output power and the overall turbine efficiency.

The third section of the output is a set of velocity diagrams for each blade row and a blade geometric summary for each blade. The velocity diagrams are normalized by the sonic velocity referred to total conditions for each station, so that they may be directly used in the blade design procedures as discussed in Section 3.3.2.

3.3.1.4 KTA Utilization of Turbine Design Program

The turbine design program was used for three specific purposes during the evaluation of the KTA reference design turbine.

Once the baseline turbine configuration had been selected (Section 3.2.2) the program was used to check the reversion location. The turbine parametric program forced reversion to occur in the separator inlet scroll and fixed the fifth-stage rotor discharge quality at 1.0. The turbine design program predicted that condensation would begin at the fifth-stage rotor inlet with a discharge quality of 0.998. The condensation nuclei per pound of vapor was predicted at 9.3×10^{11} for an average droplet radius of 1.06×10^{-6} ft. A second run was used to simulate the separator inlet scroll, and reversion to equilibrium conditions was predicted at a location of 6 in. down the duct leading to the separator. At reversion, the number of nuclei per pound was 4.05×10^{12} for an average droplet radius of 4.07×10^{-6} ft. Since the separator removed 90-percent of the available moisture, the number of nuclei per pound delivered to the sixth-stage stator inlet was 4.05×10^{11}. This value was used as input to the turbine parametric program for the blade-moisture-collection model so that the interstage moisture removal could be evaluated.

The second use of the turbine design program was a check of the Phase II reference design performance and flow passage size as defined by the turbine parametric program. The hub radii were the same as defined by the two programs. Small discrepancies were observed between the blade heights, with those calculated by the turbine design program being smaller. The actual blade heights are summarized in Table 5. These differences resulted in a total shaft power difference of 0.7 kw_e, due primarily to the tip clearance losses. The approximate fluid property equations used in the turbine parametric program, particularly for the vapor specific volume, caused the discrepancy. It should be noted that the close comparison between the two programs is primarily due to the fact that most of the condensation and the reversion occurs outside of the turbine flow path and in the separator inlet scroll. The agreement would not be as good for a turbine configuration in which reversion occurred in a blade row. The magnitude of the discrepancy is totally dependent upon the accuracy with which the turbine parametric program handles the condensation prior to reversion.

The third use of the turbine design program was to establish the blade velocity diagrams for each of the three different blade designs:

(a) Stage 1 stator and rotor with a work coefficient of 2.0
(b) Stage 5 stator and rotor with a work coefficient of 1.6 and axial chords of 0.522 and 0.53 in. at the hub, respectively
(c) Stage 10 stator and rotor with a work coefficient of 1.6 and axial chords of 0.734 and 0.847 in. at the chord, respectively.

These three blade sets comprise the total blade design requirements since Stages 2 through 5 and Stages 6 through 10 utilize the same blade design with each blade longer than the preceeding blade.

TABLE 5

KTA REFERENCE DESIGN BLADE SUMMARY

Stage No.	Hub Radius, in.	Trailing Edge Blade Height, in.	
		Stator	Rotor
1	2.901	0.2613	0.2648
2	2.901	0.3088	0.3199
3	2.901	0.3457	0.3592
4	2.901	0.3891	0.4049
5	2.901	0.4406	0.4600
6	4.539	0.2686	0.3009
7	4.539	0.3899	0.4456
8	4.539	0.6015	0.6929
9	4.539	0.9050	1.0643
10	4.539	1.3058	1.5425

82

3.3.2 Aerodynamic Blade Design Analysis

3.3.2.1 Aerodynamic Efficiency Prediction Procedure

The blade design procedure begins with the design of two-dimensional sections that satisfy the vector diagrams generated by the turbine design program. The objective of this design procedure is to design flow passages that will produce the flow angles and critical Mach numbers specified by the vector diagrams, have maximum efficiency, and satisfy the overall design and manufacturing requirements. The aerodynamic blading design procedure consists of the following steps:

(a) A nondimensional blade velocity distribution is assumed as a function of dimensionless blade surface length at each radial station for both stator and rotor of each stage. The blade loading is controlled by a specified value of pressure surface diffusion and the requirement that the calculated circulation about a blade profile equals that imposed by the corresponding vector diagram. The blade axial solidity is then calculated from a correlation of the axial chord to the blade surface length. The resulting axial solidity and specified axial chord then determine the number of blades for optimum solidity for the blade row.

(b) The local surface velocity distributions determined in Step (a) are then used to calculate two-dimensional compressible flow boundary-layer thickness parameters at the blade trailing edge as a function of radius. This boundary-layer calculation technique is based on the work of Whitney, Stewart, and Miser[6].

(c) Local relative total pressure losses for the stator and rotor of a stage are computed as a function of radius with use of the boundary-layer data determined in Step (b) according to the technique of Stewart[7].

3.3.2.2 Generation of Two-Dimensional Blade Sections

Once the number of blades and the passage solidity have been determined for a given radius, two-dimensional blade sections can be designed to meet the requirements of the vector diagram for that radius. At AiResearch, this procedure is incorporated into a computer program that generates two-dimensional blade sections and the corresponding velocity distributions or loadings. Several passes are made to successively adjust the blade shape parameters of the program, until a loading is obtained which has a small value for the total diffusion parameter, D_t, and satisfies the required vector diagram. The procedure utilizes direct computer plotting for accuracy and automation. This procedure for designing cylindrical sections includes the following steps:

(a) A relative critical Mach number and flow angle in the plane of the trailing edge are calculated from the specified vector diagram downstream of the blade for the required blade spacing and trailing-edge thickness. This calculation assumes one-dimensional flow and satisfies continuity and the momentum equation for either subsonic or supersonic flow in the plane of the trailing edge.

(b) The blade suction surface is generated by an involute curve which turns from the inlet flow angle specified by the upstream vector diagram to the calculated blade angle. The blade section stagger-angle is a function of the inlet-to-exit curvature ratio of the involute, which is an input number. The solidity of the passage is determined from Zweifel's[8] criterion on the basis of an input aerodynamic loading coefficient.

(c) The profile pressure surface is specified by input data.

(d) The velocity distribution for the passage formed by two adjacent profiles is calculated by the estimation of blade-to-blade velocity gradients and the adjustment of the suction

surface velocities until continuity is satisfied. The resultant velocity distribution generates a circulation that is in close agreement with the required value imposed by the vector diagram.

(e) The velocity distribution for the leading-edge region is determined from a potential flow solution of incompressible flow through turbine cascades coupled with a Karman-Tsien compressible flow correction[9]. The potential flow solution is carried out by a computer program based on the work of Mortensen[10]. The patching of the passage velocity distribution with the potential flow solution is accomplished by forcing the potential flow solution to satisfy the downstream flow conditions previously calculated by the passage solution. The two solutions give excellent agreement over most of the passage and together give a loading which satisfies the required circulation precisely.

(f) A two-dimensional boundary-layer analysis based on the method of Whitney, Stewart, and Miser[6] is next calculated using the prior determined velocity distribution and profile shape. The anlysis method accounts for the effects of three-dimensional flow within the blade row in an approximate manner. That is, the specific mass flow is assumed to vary linearly with axial chord from the inlet to the exit of the blade row in order to satisfy the vector diagram at a given section radius. The analysis does not account for shock wave losses in the case of supersonic flow or for the wake losses at the trailing edge.

3.3.2.3 Blade Design Summary

The aerodynamic design procedure was used to design preliminary blade shapes for the KTA turbine. Table 6 is a summary of the blade designs for the three stages required. Since the turbine reference

TABLE 6

KTA PRELIMINARY BLADE DESIGN REQUIREMENTS

	Blade Design for Stage		
	1	5	10
Hub Radius, in.	2.901	2.901	4.462
Number of Stator Blades	30	32	38
Stator Tip Radius, in.	3.1626	3.3397	5.7904
Stator Blade Height, in.	0.2616	0.4387	1.3284
Number of Rotor Blades	78	64	58
Rotor Tip Radius, in.	3.1644	3.3594	6.0772
Rotor Blade Height, in.	0.2634	0.4584	1.6152
Stator Leading-Edge Thickness, in.	0.090	0.090	0.090
Trailing-Edge Thickness, in.	0.020	0.020	0.020
Rotor Leading-Edge Thickness, in.	0.024	0.036	0.036
Trailing-Edge Thickness, in.	0.015	0.015	0.015
Stator Hub Axial Chord, in.	0.4560	0.5226	0.7336
Rotor Hub Axial Chord, in.	0.6023	0.5302	0.8471

design uses the same blades for Stages 2 through 5 and Stages 6 through 10, only three sets of blade designs were required. Note that the blade designs for the tenth stage are for a hub radius of 4.462 in. This was the hub radius of the low-pressure spool when the blade design procedure was initiated. Minor modifications to the Stage 10 design would be required (as described on Page 75) prior to final detailing of the blade and disk designs.

Figures 24 through 35 show the hub and tip radius cylindrical sections and corresponding loading diagrams for the Phase II KTA design. These figures are direct copies of the computer program output produced by a CALCOMP plotter which is a part of the automated design procedure. Mean radius sections are also obtained but are not shown in the interest of brevity.

When the hub, mean-line, and tip design sections have been finalized to the point where the velocity distributions have minimized frictional and other losses, the sections are stacked to produce the preliminary blade shape subject to final three-dimensional loading calculations and stress analysis. For the KTA design, the stator sections were stacked about the point representing the throat midway between two adjacent sections. The rotor sections are stacked about a radial line passing through the center of gravity of each section. Several intermediate sections are then computed, faired from the three primary sections, to adequately define the blade shape for manufacturing. Figures 36 through 41 show the intermediate sections and Figures 42 through 47 show the stacked blades for the KTA Phase II design.

3.4 KTA Turbine Erosion Analysis (WANL)

Erosion in wet vapor turbines takes place locally but the condition leading to the erosion involves the total thermodynamic and fluid-dynamic history of the working fluid from the time it enters the turbine.

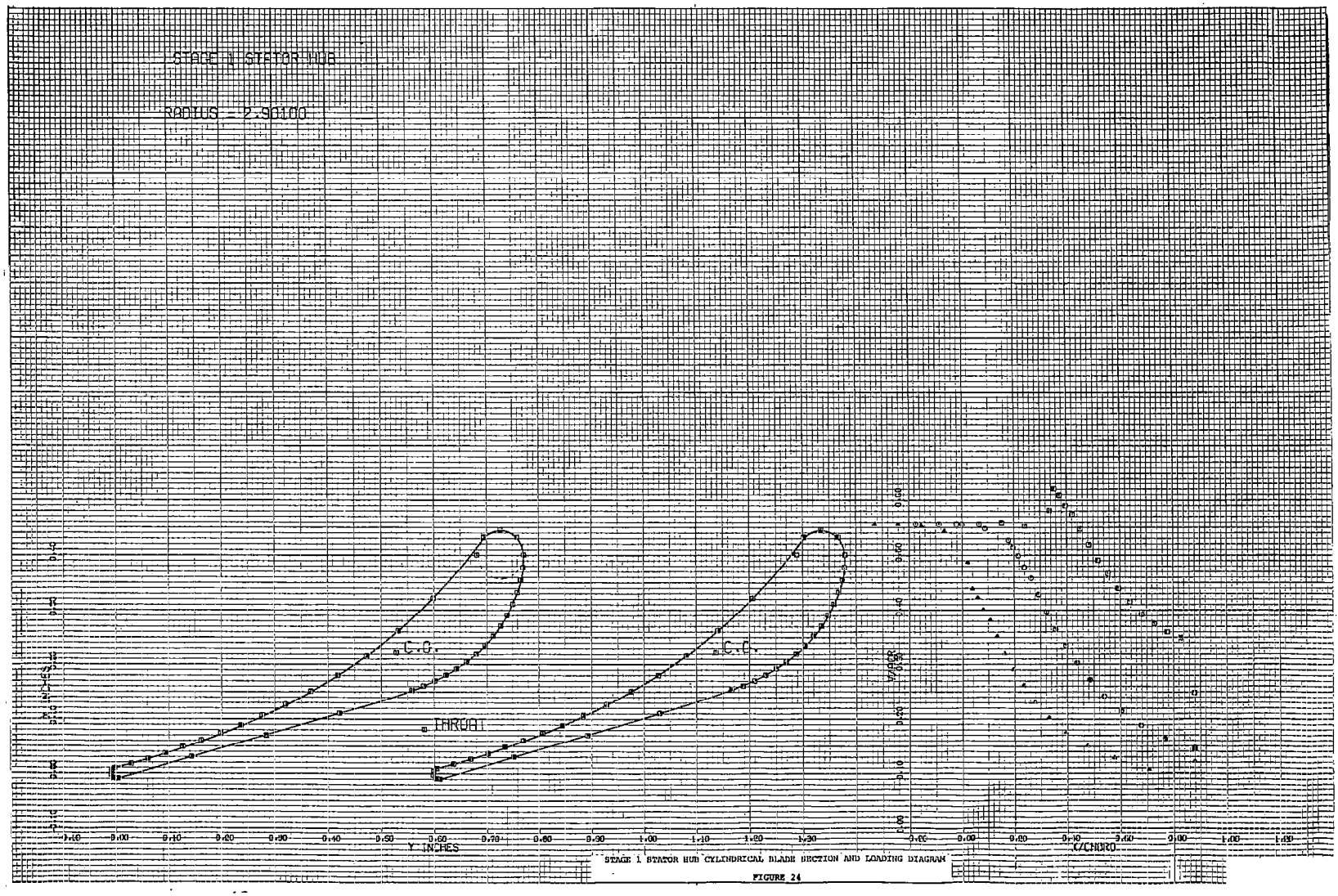

STAGE 1 STATOR HUB CYLINDRICAL BLADE SECTION AND LOADING DIAGRAM

FIGURE 24

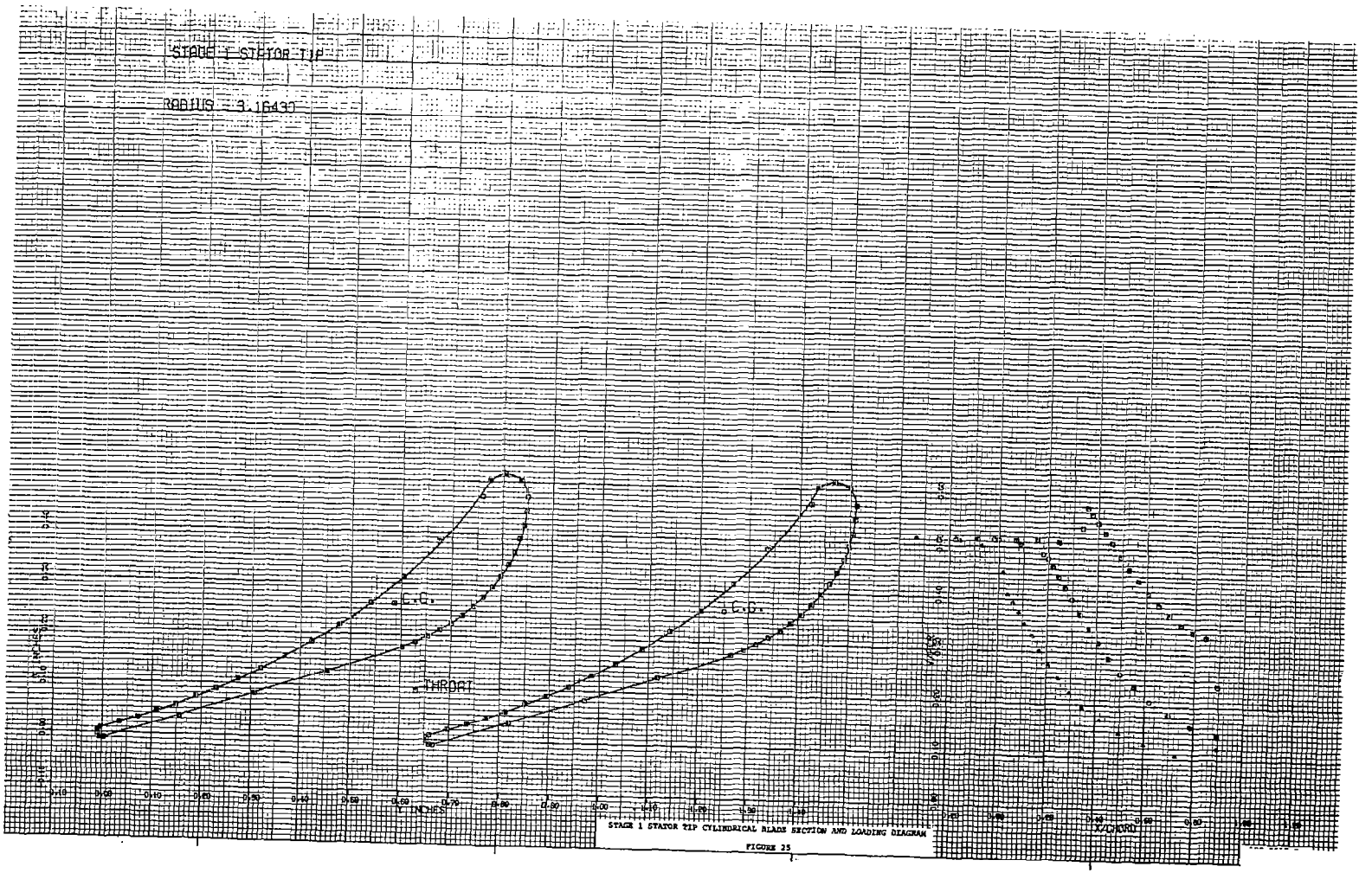

STAGE 1 STATOR TIP CYLINDRICAL BLADE SECTION AND LOADING DIAGRAM

FIGURE 25

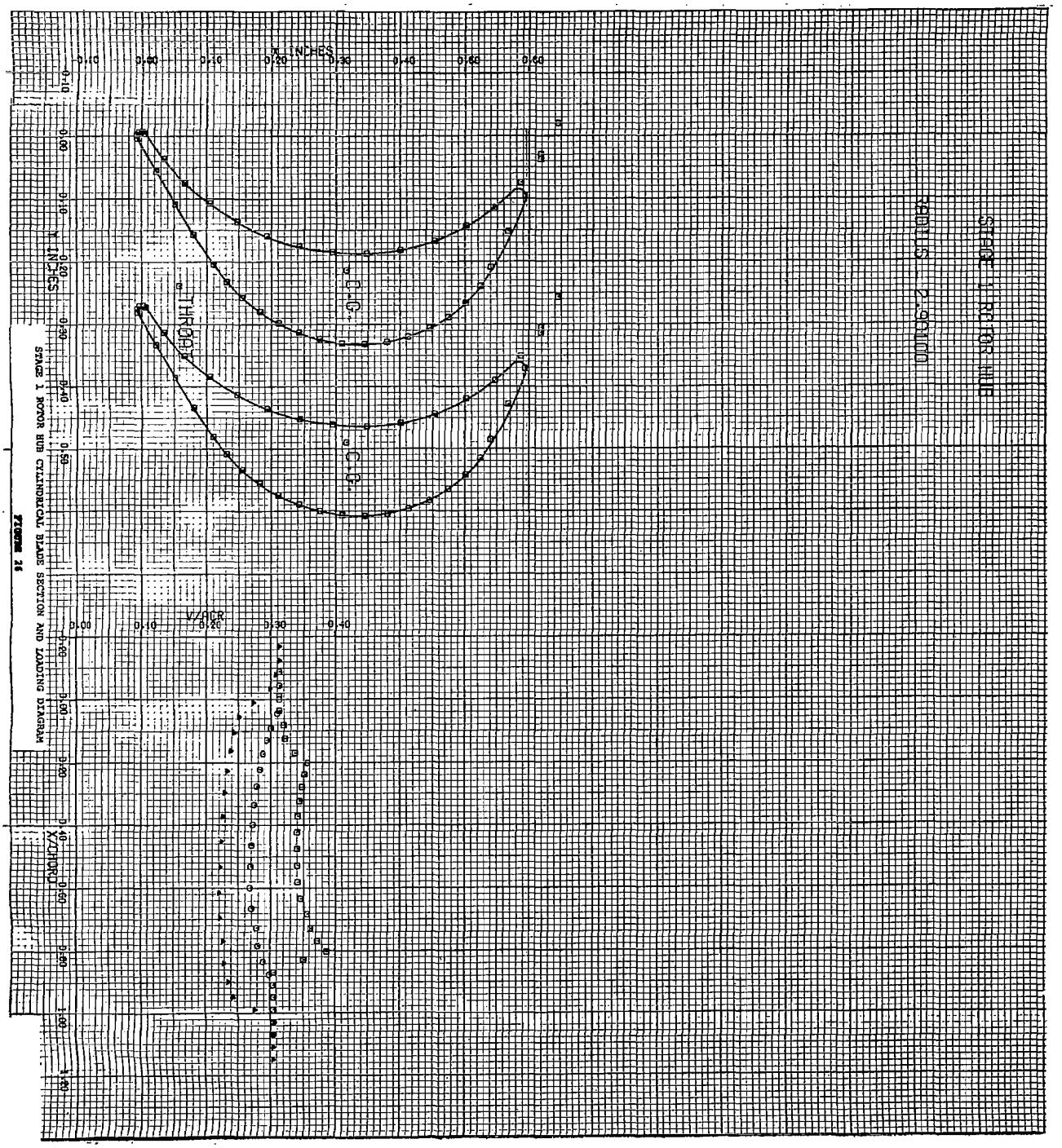
STAGE 1 ROTOR BLADE
STAGE 2 ROTOR BLADE
THROAT
C.G.
C.G.
C.G.
V/ACR
0.10
0.20
0.30
0.40
INCHES
0.10
0.20
0.30
0.40
0.50
0.60
0.70
0.80
0.90
1.00
1.10
1.20
1.30
1.40
1.50
1.60
1.70
1.80
1.90
2.00
2.10
2.20
2.30
2.40
2.50
2.60
2.70
2.80
2.90
3.00
3.10
3.20
3.30
3.40
3.50
3.60
3.70
3.80
3.90
4.00

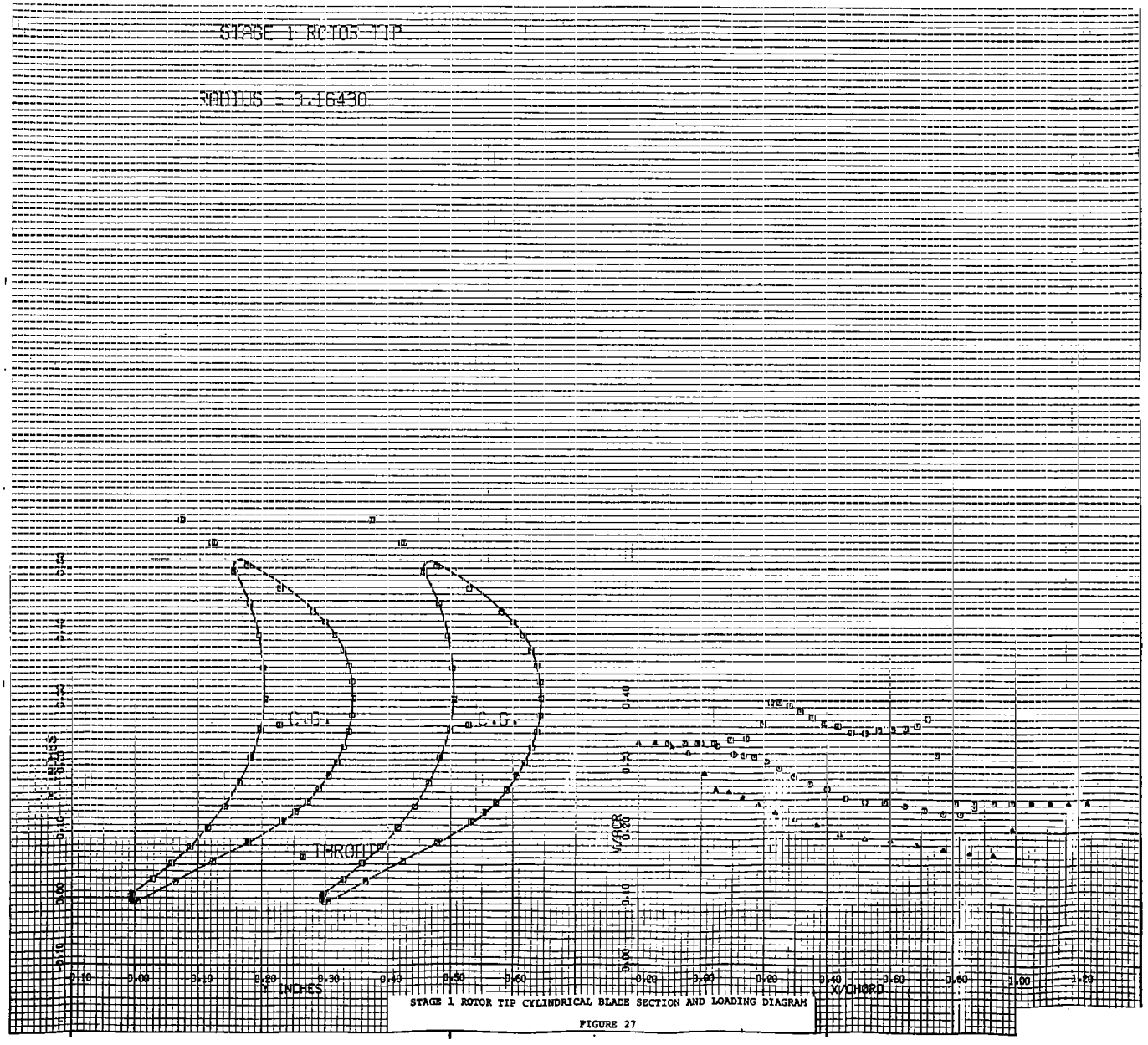

STAGE 1 ROTOR TIP CYLINDRICAL BLADE SECTION AND LOADING DIAGRAM

FIGURE 27

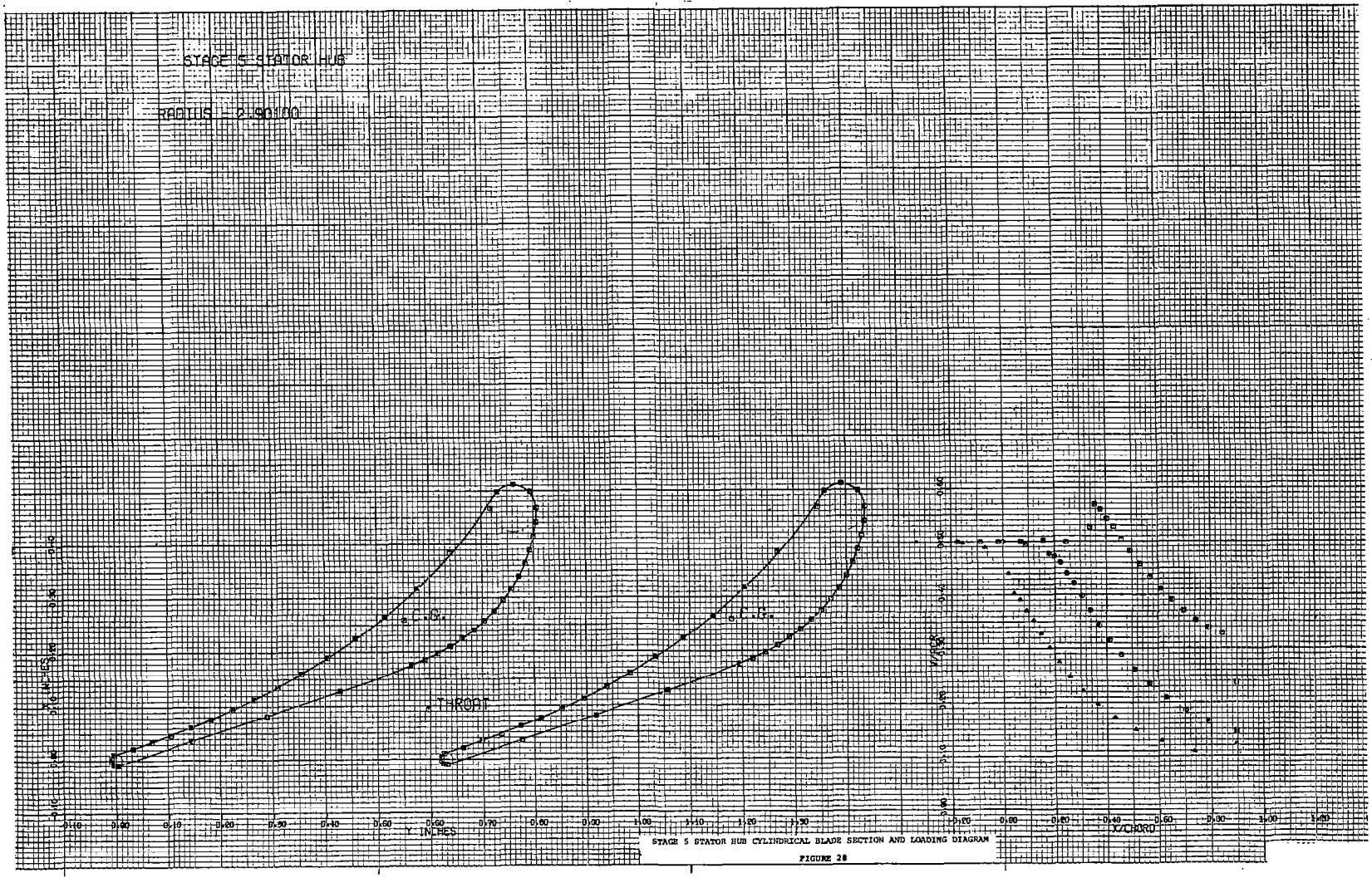

STAGE 5 STATOR HUB CYLINDRICAL BLADE SECTION AND LOADING DIAGRAM

FIGURE 28

STAGE 5 STATOR TIP CYLINDRICAL BLADE SECTION AND LOADING DIAGRAM

FIGURE 29

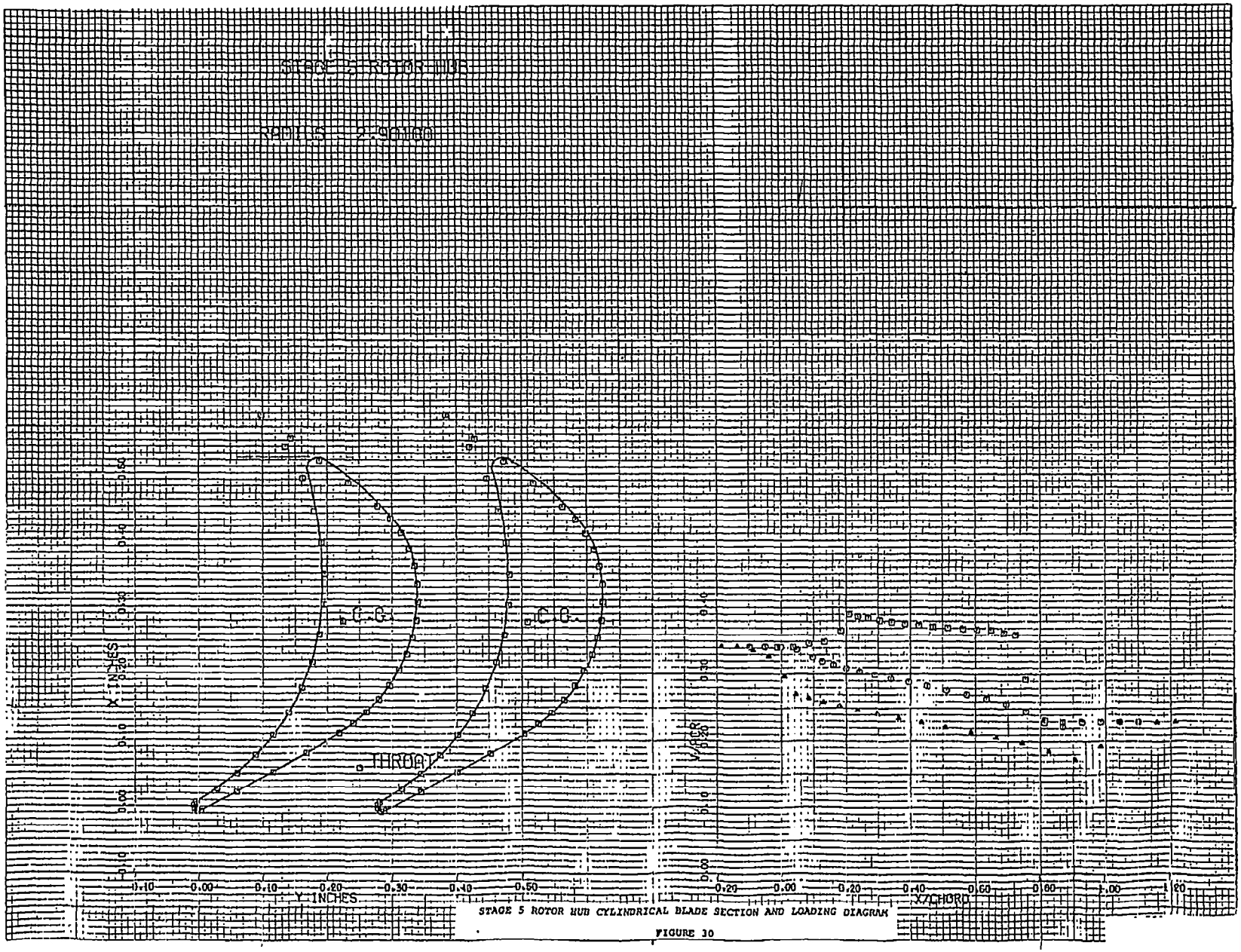

STAGE 5 ROTOR HUB CYLINDRICAL BLADE SECTION AND LOADING DIAGRAM

FIGURE 30

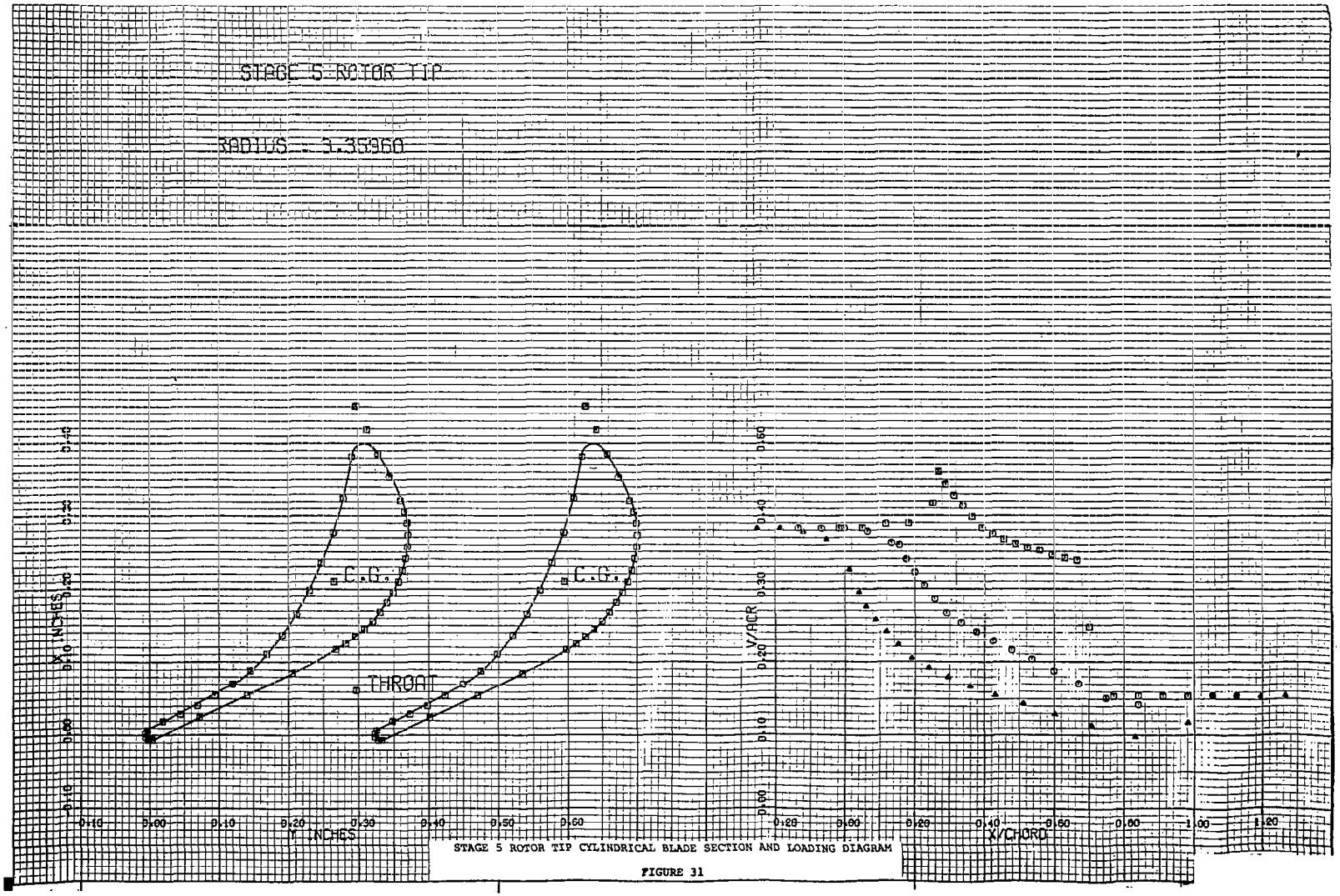

STAGE 5 ROTOR TIP CYLINDRICAL BLADE SECTION AND LOADING DIAGRAM

FIGURE 31

STAGE 10 STATOR HUB CYLINDRICAL BLADE SECTION AND LOADING DIAGRAM

FIGURE 32

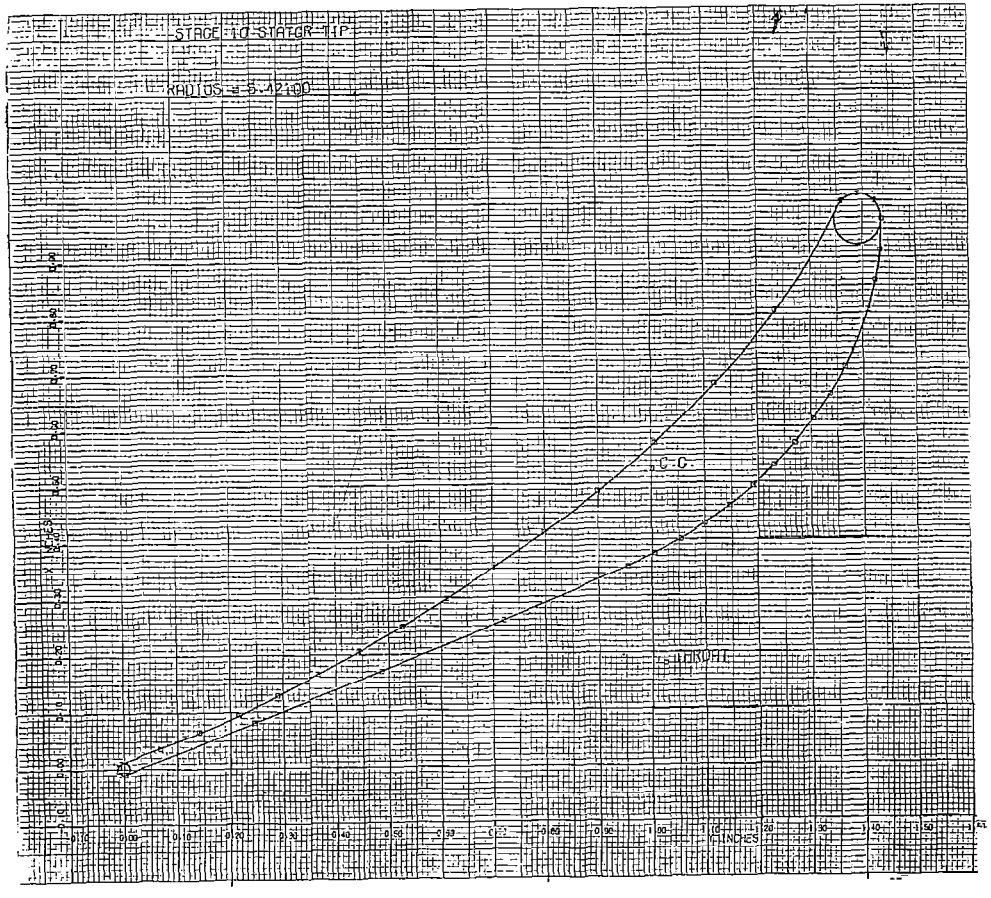

STAGE 10 STATOR TIP CYLINDRICAL BLADE SECTION AND LOADING DIAGRAM

FIGURE 33

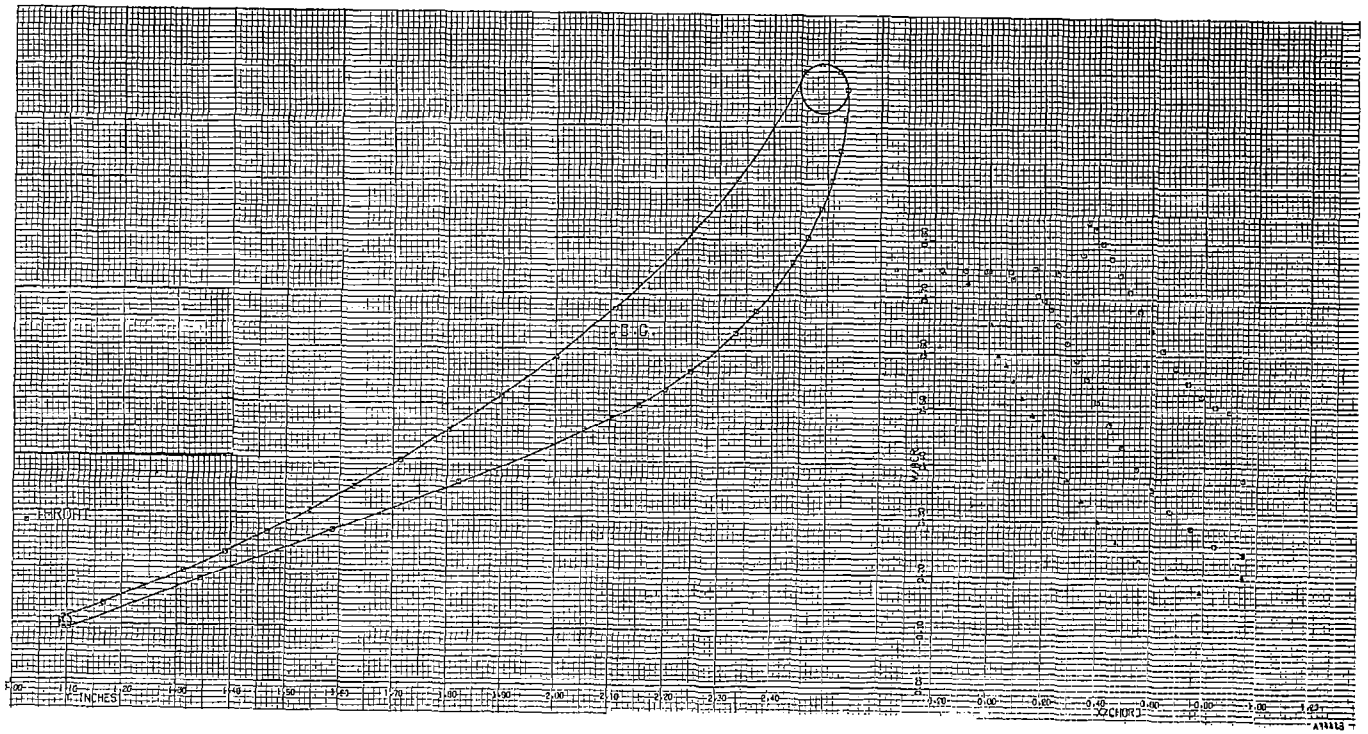

STAGE 10 STATOR TIP CYLINDRICAL BLADE SECTION AND LOADING DIAGRAM

STAGE 10 ROTOR HUB CYLINDRICAL BLADE SECTION AND LOADING DIAGRAM

FIGURE 14

STAGE 10 ROTOR TIP CYLINDRICAL BLADE SECTION AND LOADING DIAGRAM

FIGURE 35

STAGE 1 STATOR INTERMEDIATE CYLINDRICAL AND PLANE BLADE SECTIONS

FIGURE 36

STAGE 1 STATOR INTERMEDIATE CYLINDRICAL AND PLANE BLADE SECTIONS

FIGURE 36 Continued

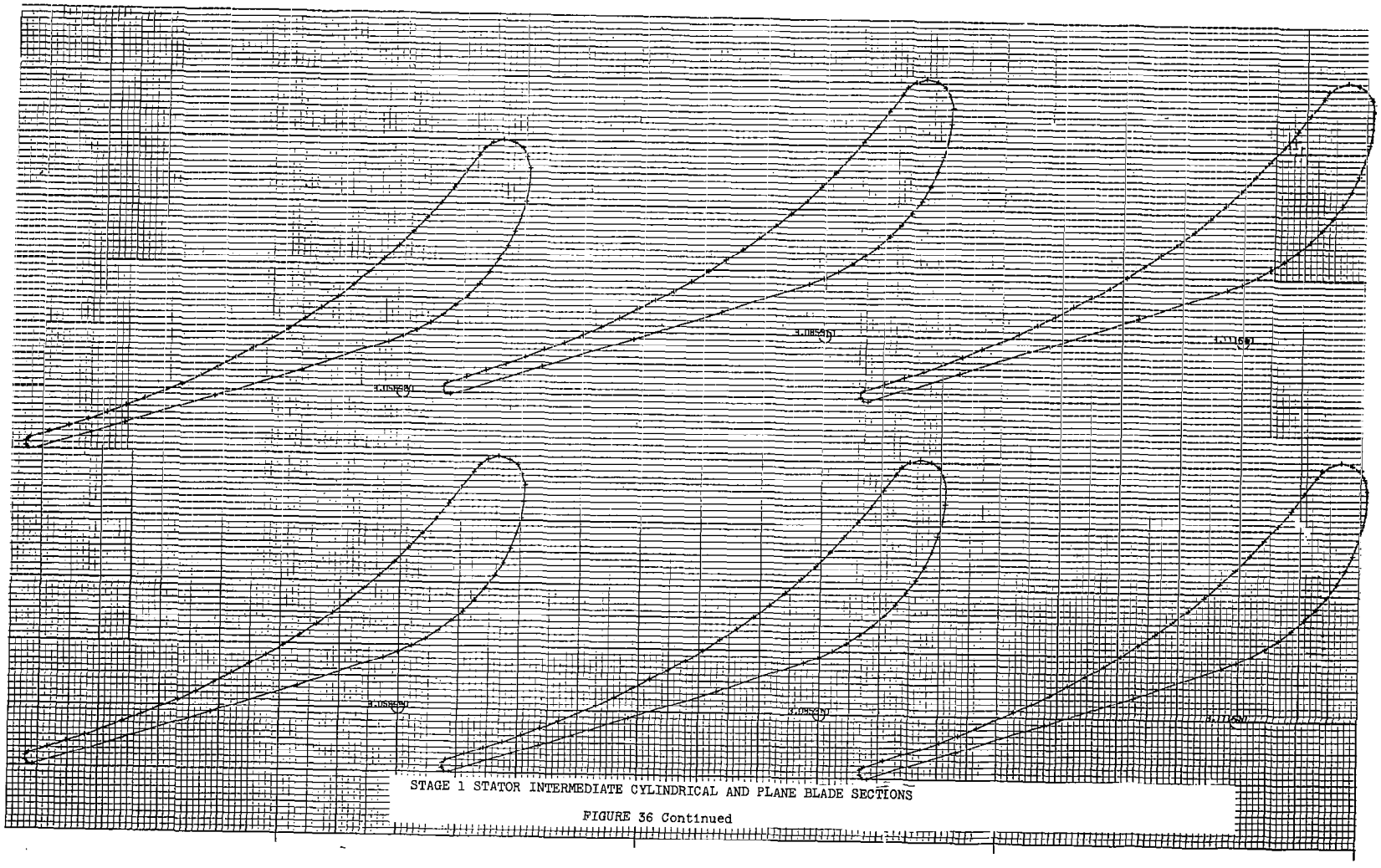

STAGE 1 STATOR INTERMEDIATE CYLINDRICAL AND PLANE BLADE SECTIONS

FIGURE 36 Continued

STAGE 1 STATOR INTERMEDIATE CYLINDRICAL AND PLANE BLADE SECTIONS

FIGURE 36 Concluded

STAGE 1 ROTOR INTERMEDIATE CYLINDRICAL AND PLANE BLADE SECTIONS

FIGURE 37

STAGE 5 STATOR INTERMEDIATE CYLINDRICAL AND PLANE BLADE SECTIONS

FIGURE 38

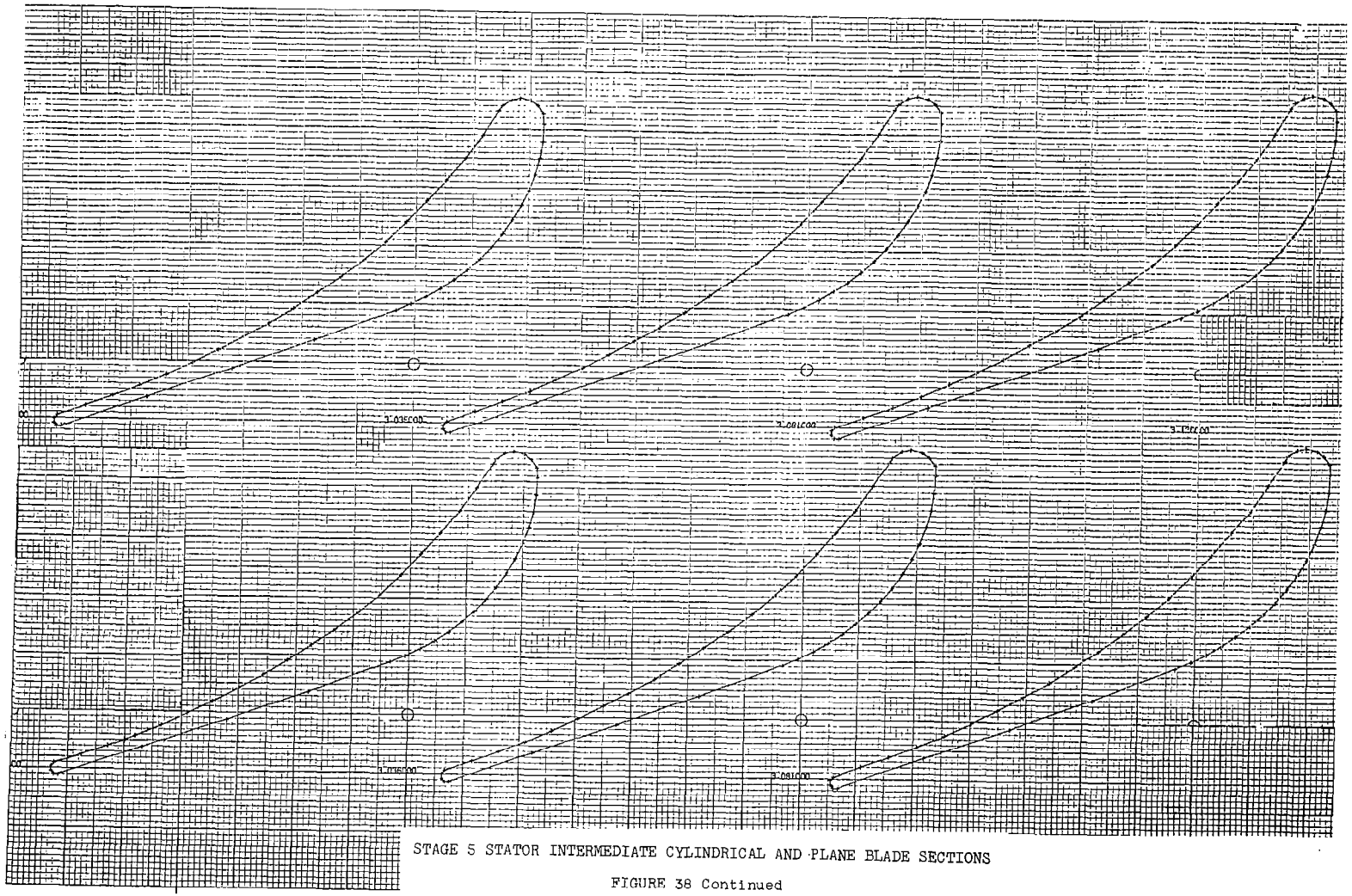

STAGE 5 STATOR INTERMEDIATE CYLINDRICAL AND PLANE BLADE SECTIONS

FIGURE 38 Continued

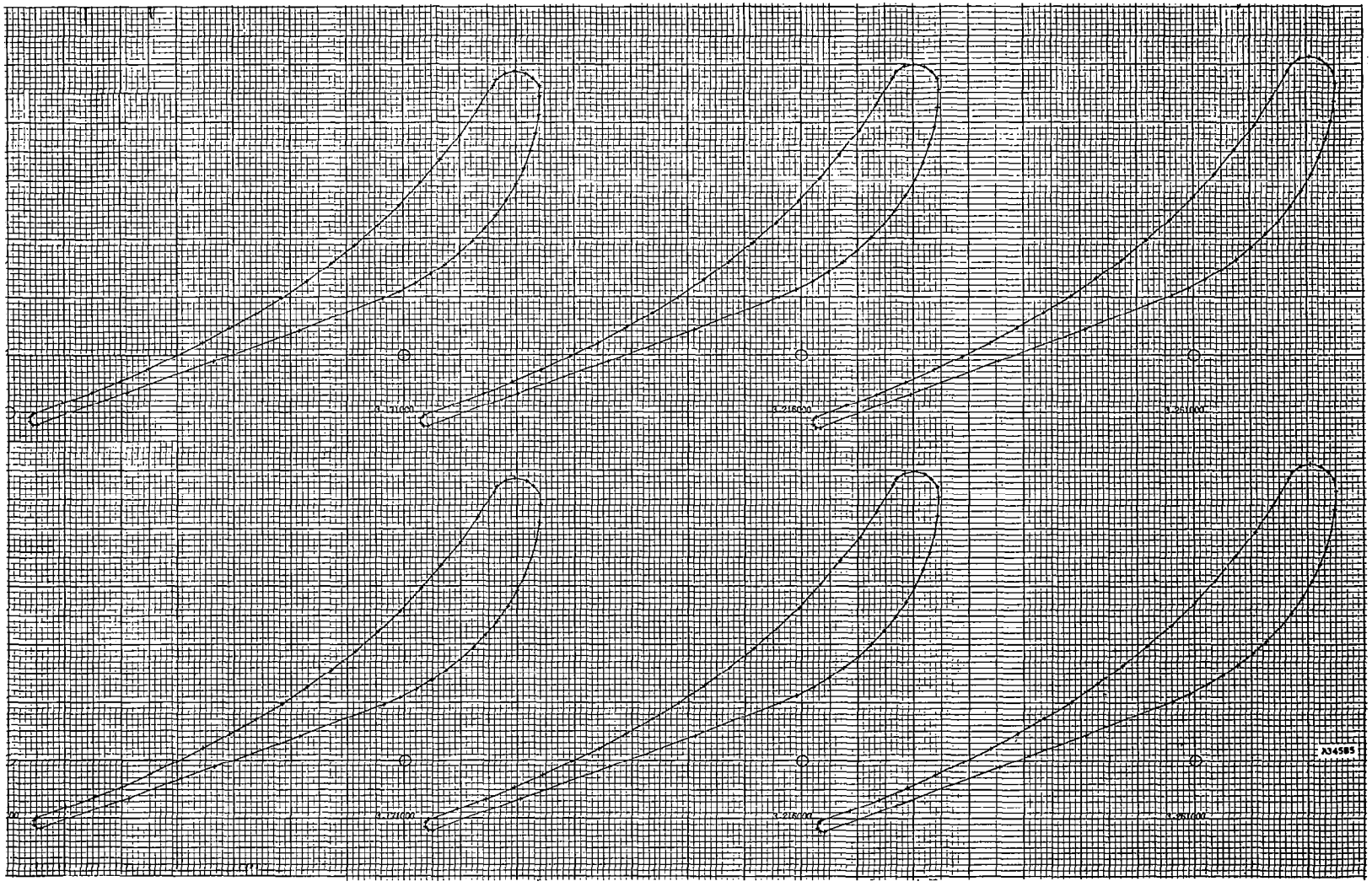

STAGE 5 STATOR INTERMEDIATE CYLINDRICAL AND PLANE BLADE SECTIONS

FIGURE 38 Concluded

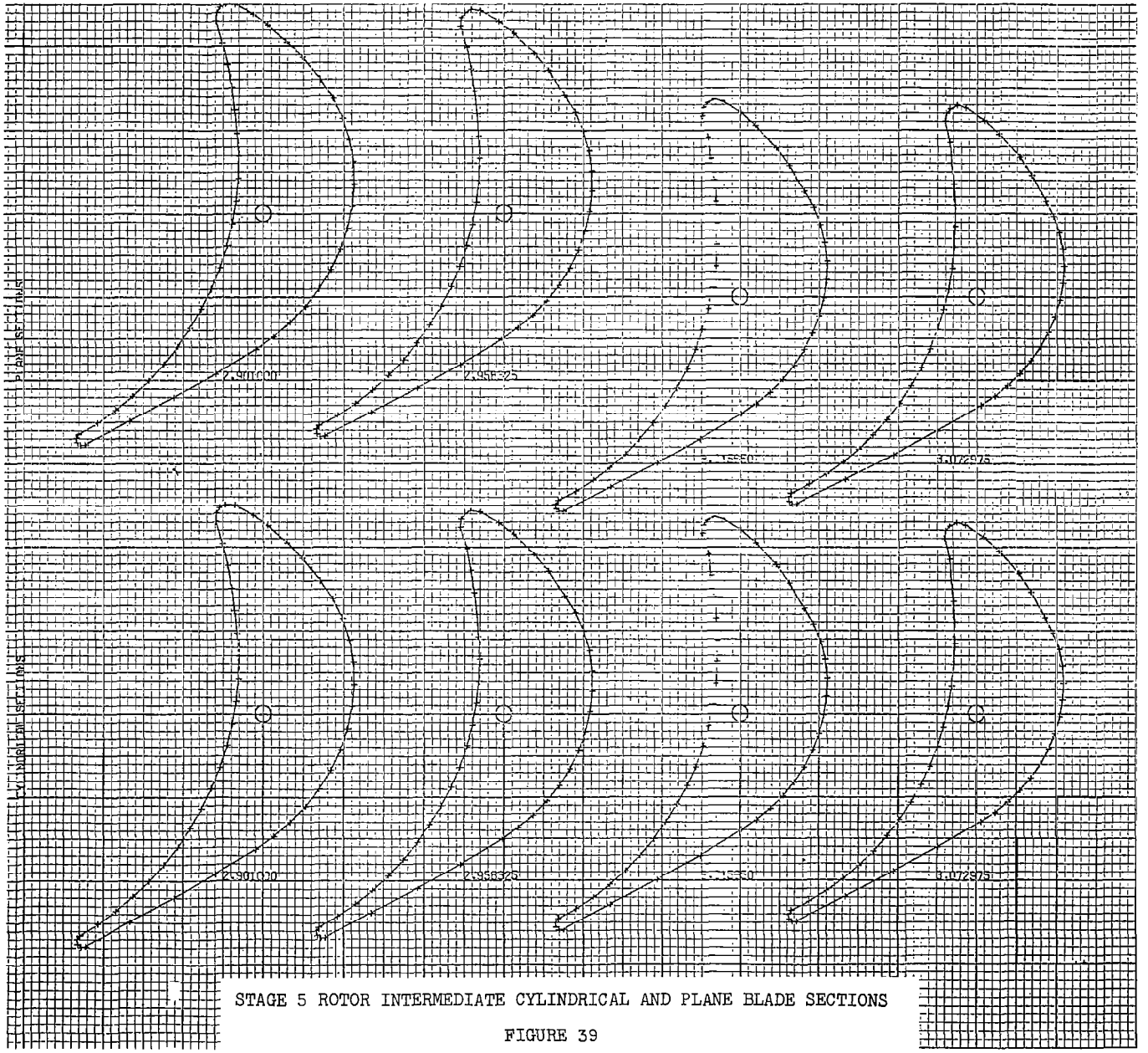

STAGE 5 ROTOR INTERMEDIATE CYLINDRICAL AND PLANE BLADE SECTIONS

FIGURE 39

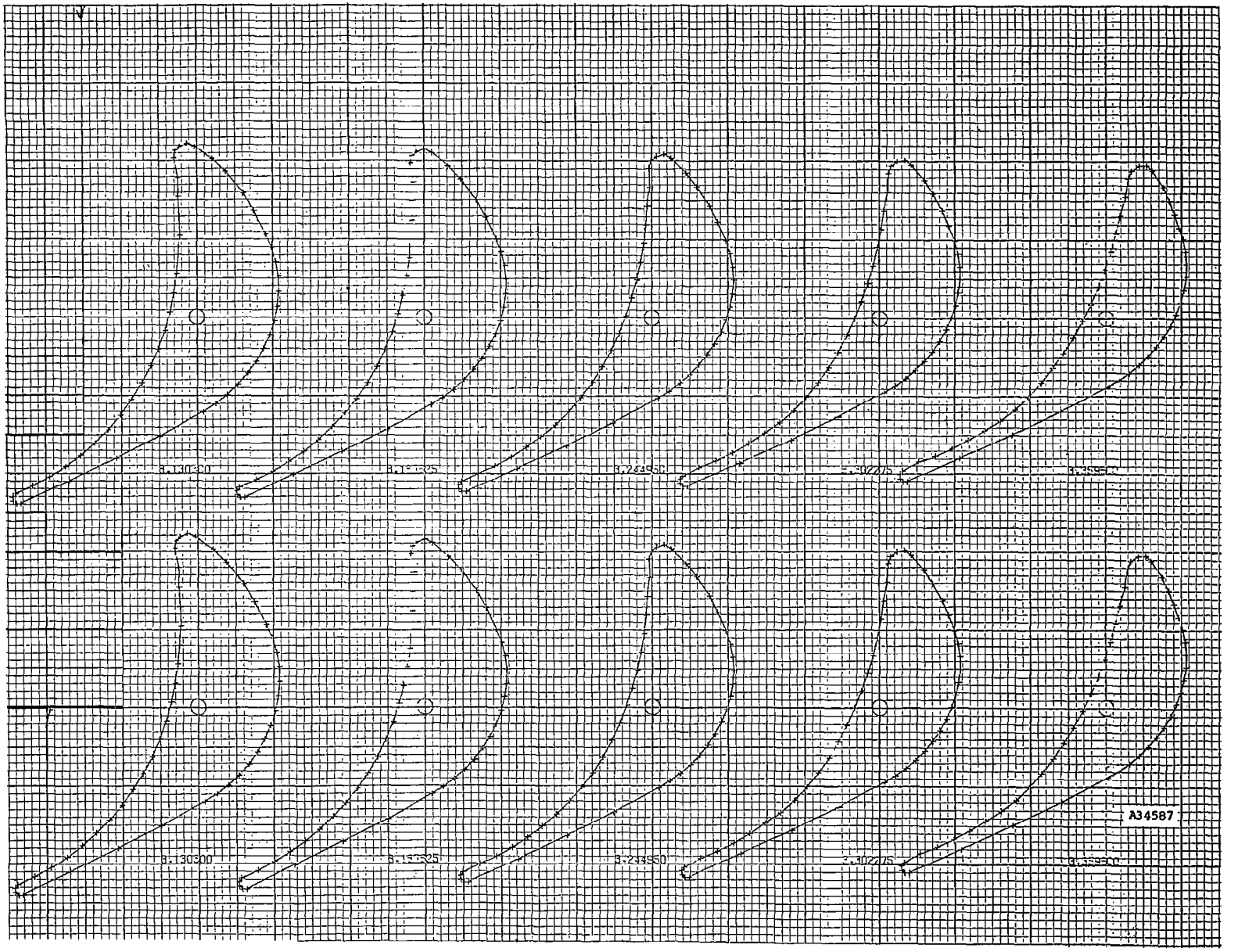

STAGE 5 ROTOR INTERMEDIATE CYLINDRICAL AND PLANE BLADE SECTIONS

FIGURE 39 Concluded

STAGE 10 STATOR INTERMEDIATE CYLINDRICAL AND PLANE BLADE SECTIONS

FIGURE 40

STAGE 10 STATOR INTERMEDIATE CYLINDRICAL AND PLANE BLADE SECTIONS

FIGURE 40 Continued

STAGE 10 STATOR INTERMEDIATE CYLINDRICAL AND PLANE BLADE SECTIONS

FIGURE 40 Concluded

STAGE 10 ROTOR INTERMEDIATE CYLINDRICAL AND PLANE BLADE SECTIONS

FIGURE 41

STAGE 10 ROTOR INTERMEDIATE CYLINDRICAL AND PLANE BLADE SECTIONS

FIGURE 41 Concluded

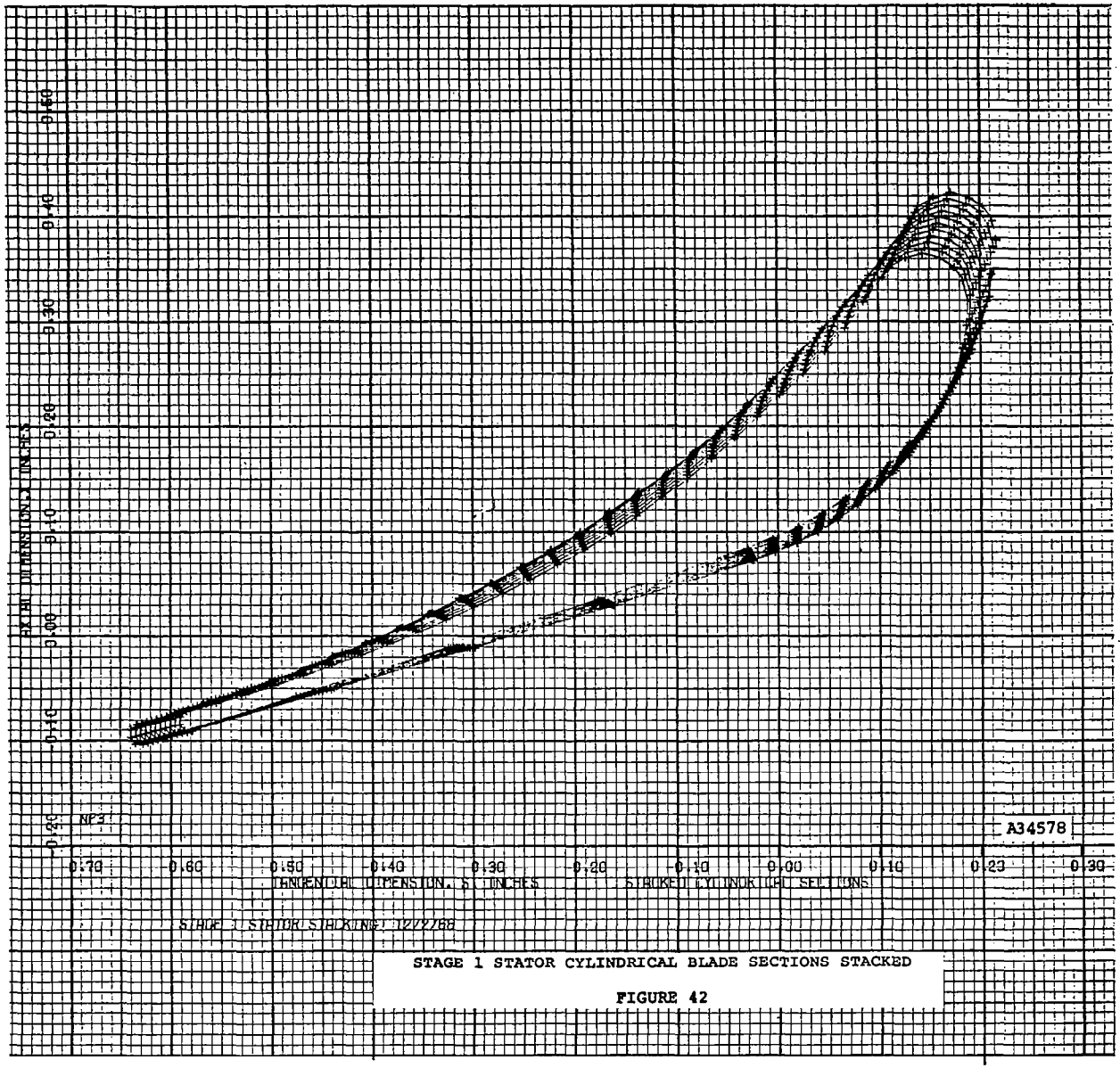

STAGE 1 STATOR CYLINDRICAL BLADE SECTIONS STACKED

FIGURE 42

STAGE 1 ROTOR PLANE AND CYLINDRICAL BLADE SECTIONS STACKED

FIGURE 43

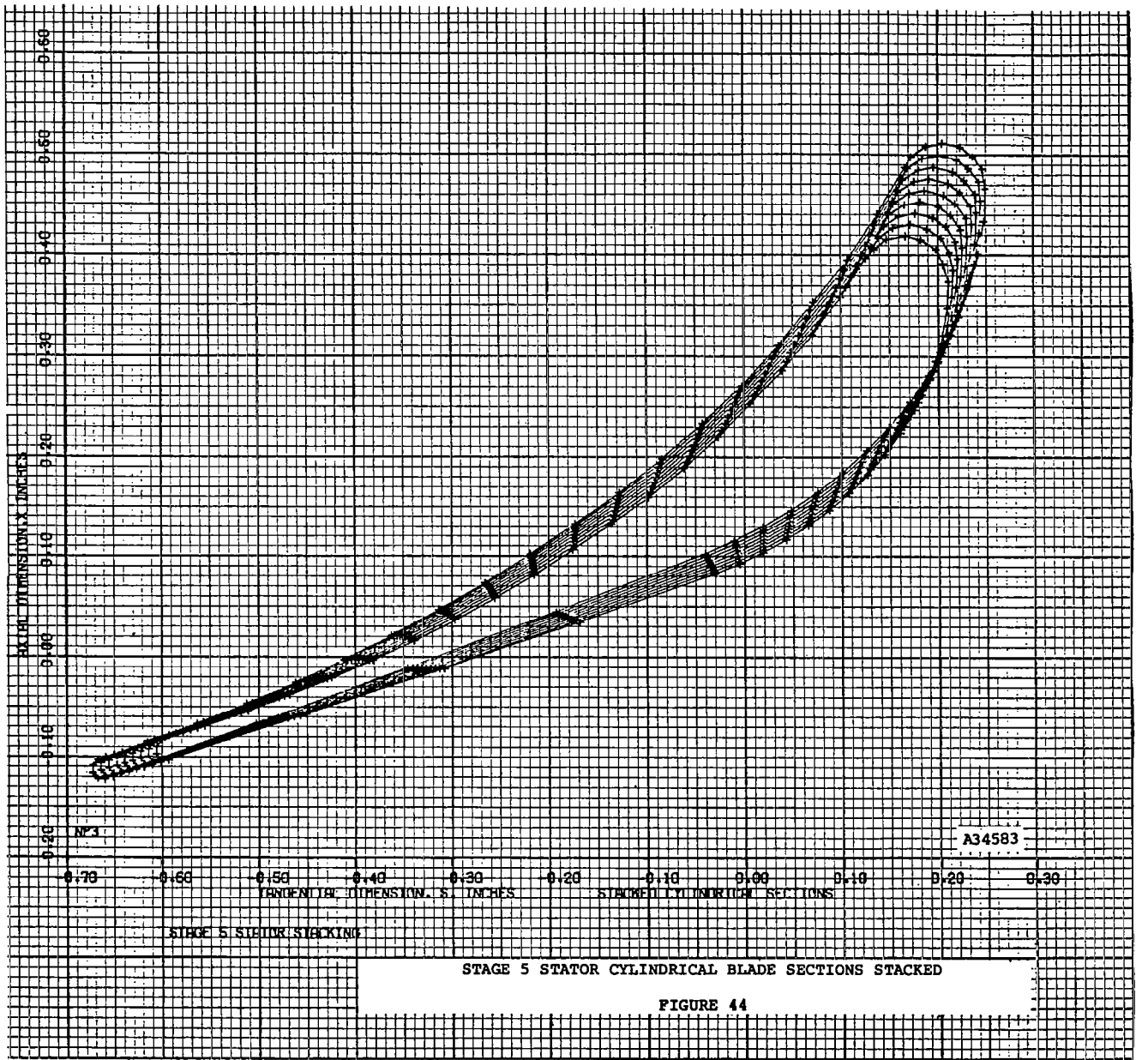

STAGE 5 STATOR CYLINDRICAL BLADE SECTIONS STACKED

FIGURE 44

STAGE 5 ROTOR PLANE AND CYLINDRICAL BLADE SECTIONS STACKED

FIGURE 45

STAGE 10 STATOR CYLINDRICAL BLADE SECTIONS STACKED

FIGURE 46

STAGE 10 ROTOR PLANE AND CYLINDRICAL BLADE SECTIONS STACKED

FIGURE 47

As a result, there are a great many steps involved in an erosion analysis. The various steps or processes analyzed are given in block diagram form in Figure 48. A reasonably complete account of this erosion model as worked out for steam is given in Reference 2. Its modification to the alkali metal vapors, potassium and cesium, is covered in Reference 3. Most of this reference material will not be repeated here. An exception to this is the introduction of empirical information on the various physical process steps as support for the analytical procedures used. Another exception is a recasting of the mathematics involved in blade material dissolution to eliminate some of the approximations previously employed.

For those process steps which are physical in nature and do not involve complex chemical reactions, such as are probably present in connection with the dissolution of turbine blade material in the liquid metal, there is empirical information to check against the analytical assumptions made. Unfortunately, this is not clearly the case when chemical removal of blade material is a possibility. The analytical assessment of chemical material removal is on the basis of what are believed to be reasonable hypotheses for dissolution of refractory metal alloys such as TZM and TZC.

During the first phase of the KTA study, the procedures used by the Westinghouse erosion model in the analysis of vapor condensation and condensate particle collection was refined, and incorporated into the AiResearch turbine design program and the turbine parametric program, respectively. The erosion analysis interface between AiResearch and Westinghouse, during the erosion analysis of the turbine design resulting from the KTA study, was located between process steps as indicated by the dashed line of Figure 48. AiResearch analyzed those steps above the dashed line. Westinghouse conducted an analysis which deals with those steps below the dashed line.

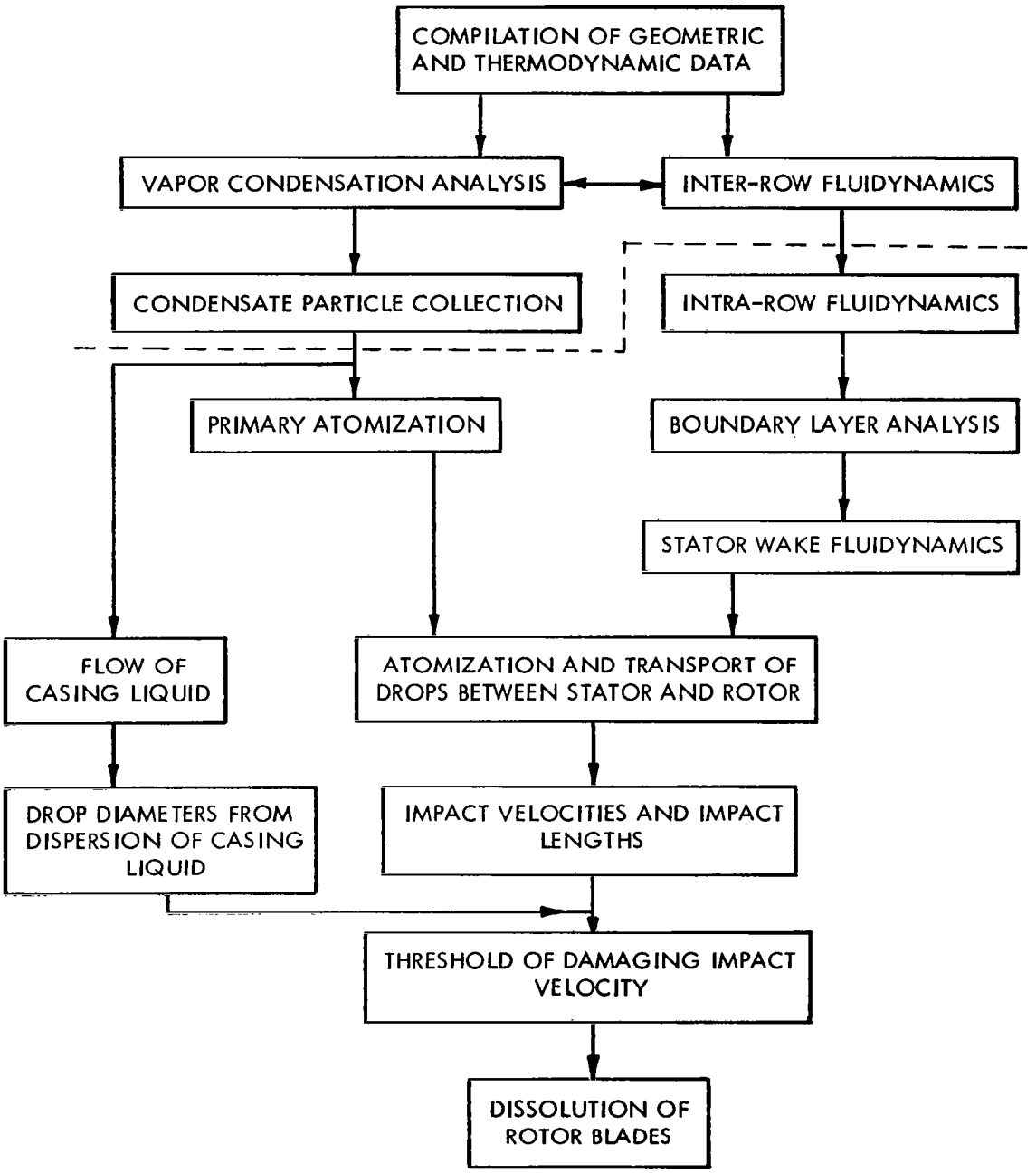

WANL TURBINE BLADE EROSION MODEL

FIGURE 48

The KTA study turbine is essentially two turbines. There is a 5-stage high-pressure spindle, called hereafter the forward turbine that exhausts to an external moisture separator. The flow then enters the 5-stage low-pressure spindle, hereafter called the aft turbine, where expansion is completed. The state conditions as supplied by AiResearch at each row of the forward and aft turbines are given in Figure 49.

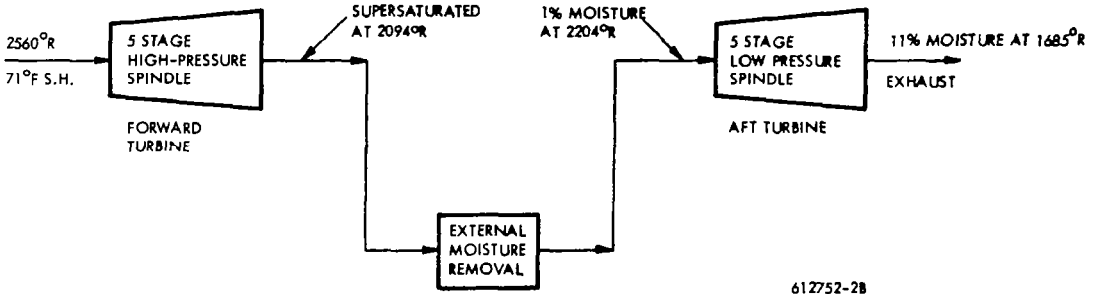

AiResearch designed the forward turbine so that the vapor will remain supersaturated until turbine exit with reversion to wet thermodynamic equilibrium in the piping leading to the external moisture separator. The absence of moisture, of course, eliminates the possibility of liquid material removal. The extent of the Westinghouse examination of the forward turbine was to carry out an independent condensation reversion calculation using a slightly higher value for surface tension of liquid potassium than that used by AiResearch. Reversion calculations are sensitive to the value of liquid surface tension used and this was a check on the sensitivity of the design.

MULTISTAGE RANKINE CYCLE TURBINE DESIGN — SUPERSATURATED FLUID PROPERTIES WITH REVERSION IN STATOR NO 6 — 10/07/68 09:46:45

NO STAGES	TURBINE EFFICIENCY	SHAFT POWER (KILOWATTS)	SHAFT SPEED (RPM)	THRUST LOADING (LBS)	TOTAL REHEAT ENERGY (KW)
10	0.8198	485.328	19200	1225.256	0.000

THERMODYNAMIC CONDITIONS

	TEMPERATURE (R)	DEGREES OF SUPERHEAT (F)	QUALITY	ENTHALPY (BTU/LB)	FLOW RATE (LBS/SEC)
INLET	2560.00	71.00	1.000	1237.55	2.050
DISCHARGE WITHOUT REMOVED MOISTURE	1680.09	0.00	0.887	1083.60	1.798
DISCHARGE WITH REMOVED MOISTURE	1680.00	0.00	0.804	1012.60	2.050

STAGE DIMENSIONS AND THERMODYNAMIC CONDITIONS

STAGE NUMBER	1	2	3	4	5	6	7	8	9	10	11	12
STATOR												
TIP RAD (IN)	3.170	3.217	3.255	3.298	3.348	4.808	4.929	5.118	5.431	5.862	0.000	0.000
MEAN RD (IN)	3.037	3.060	3.079	3.101	3.126	4.670	4.730	4.825	4.981	5.197	0.000	0.000
HUB RAD (IN)	2.904	2.904	2.904	2.904	2.904	4.532	4.532	4.532	4.532	4.532	0.000	0.000
RAD HT (IN)	0.267	0.313	0.351	0.394	0.445	0.276	0.397	0.587	0.899	1.331	0.000	0.000
P2S HUB (PSIA)	136.349	119.077	100.543	84.344	70.312	46.379	29.072	17.636	10.421	6.099	0.000	0.000
ROTOR												
TIP RAD (IN)	3.173	3.229	3.268	3.314	3.368	4.839	4.982	5.208	5.594	6.102	0.000	0.000
MEAN RD (IN)	3.038	3.066	3.086	3.109	3.136	4.685	4.757	4.870	5.063	5.317	0.000	0.000
HUB RAD (IN)	2.904	2.904	2.904	2.904	2.904	4.532	4.532	4.532	4.532	4.532	0.000	0.000
RAD HT (IN)	0.269	0.325	0.364	0.410	0.464	0.307	0.450	0.677	1.062	1.570	0.000	0.000
RAD RAT	0.915	0.899	0.888	0.876	0.862	0.937	0.910	0.870	0.810	0.743	0.000	0.000
TIP VEL (FPS)	531.553	540.972	547.548	555.202	564.264	810.730	834.686	872.670	937.220	1022.428	0.000	0.000
P3S HUB (PSIA)	134.723	114.715	96.881	81.218	67.472	41.596	25.751	15.554	9.132	5.443	0.000	0.000
STAGE												
FLOW (LBS/SEC)	2.050	2.015	2.015	2.015	2.015	1.908	1.908	1.908	1.943	1.798	0.000	0.000
HIN (BTU/LB)	1237.547	1220.163	1206.228	1192.128	1177.925	1200.673	1167.239	1133.554	1103.277	1116.253	0.000	0.000
TIN (R)	2560.000	2441.575	2351.423	2263.203	2177.715	2204.263	2088.133	1976.810	1871.874	1772.151	0.000	0.000
DSHIN (F)	71.000	20.582	-16.545	-51.822	-84.930	0.000	0.000	0.000	0.000	0.000	0.000	0.000
XIN	1.0000	1.0000	1.0000	1.0000	1.0000	0.9958	0.9600	0.9252	0.8956	0.9186	0.0000	0.0000
HEX (BTU/LB)	1220.114	1206.225	1192.169	1177.954	1163.648	1167.247	1133.562	1100.821	1071.357	1083.602	0.000	0.000
TEX (R)	2441.290	2351.133	2263.241	2177.691	2094.335	2088.151	1976.826	1871.887	1772.495	1685.373	0.000	0.000
DSHEX (F)	20.481	-16.609	-51.668	-84.802	-115.937	0.000	0.000	0.000	0.000	0.000	0.000	0.000
XEX	1.0000	1.0000	1.0000	1.0000	1.0000	0.9600	0.9252	0.8927	0.8652	0.8868	0.0000	0.0000
ETA AERO	0.8976	0.9299	0.9384	0.9401	0.9416	0.9130	0.9004	0.9064	0.9088	0.9418	0.0000	0.0000
ETA TIP	0.8273	0.8675	0.8819	0.8894	0.8962	0.8789	0.8767	0.8900	0.8977	0.9259	0.0000	0.0000
ETA WET	0.8273	0.8675	0.8819	0.8894	0.8962	0.8719	0.8314	0.8108	0.7907	0.8368	0.0000	0.0000
PWR STG (KW)	37.060	29.631	29.889	30.130	30.351	67.268	67.774	65.875	65.418	61.931	0.000	0.000
MOFLOW (LB/SEC)	0.000	0.000	0.000	0.000	0.107	0.000	0.000	0.000	0.145	0.000	0.000	0.000
HMOIST (BTU/LB)	0.000	0.000	0.000	0.000	499.978	0.000	0.000	0.000	511.048	0.000	0.000	0.000
GAMMA	1.461	1.465	1.462	1.460	1.448	1.276	1.239	1.200	1.169	1.153	0.000	0.000
GAS R (FT LB/LB R)	33.673	32.865	32.340	32.271	32.040	33.499	33.421	33.224	33.023	34.521	0.000	0.000
TOT COL (LB/SEC)	0.000000	0.000000	0.000000	0.000000	0.000000	0.011560	0.045194	0.083507	0.119172	0.039317	0.000000	0.000000

KTA STATE CONDITIONS AS USED FOR THE EROSION ANALYSIS

FIGURE 49

10/07/68
09146145

VELOCITY DIAGRAM AT HUB RADIUS

V2X (FPS)	242.609	223.217	223.217	223.217	223.217	348.395	348.395	348.395	348.395	348.395	0.000	0.000
V2U (FPS)	972.961	778.388	778.388	778.388	778.388	1214.897	1214.897	1214.897	1214.897	1214.897	0.000	0.000
V2 (FPS)	1002.752	809.761	809.761	809.761	809.761	1263.864	1263.864	1263.864	1263.864	1263.864	0.000	0.000
URAD (FPS)	486.481	486.492	486.492	486.492	486.492	759.311	759.311	759.311	759.311	759.311	0.000	0.000
W2U (FPS)	486.481	291.895	291.895	291.895	291.895	455.586	455.586	455.586	455.586	455.586	0.000	0.000
W2 (FPS)	543.620	367.463	367.463	367.463	367.463	573.531	573.531	573.531	573.531	573.531	0.000	0.000
W3 (FPS)	-543.620	-535.258	-535.258	-535.258	-535.258	-835.423	-835.423	-835.423	-835.423	-835.423	0.000	0.000
ALPHA (DEG)	76.000	74.000	74.000	74.000	74.000	74.000	74.000	74.000	74.000	74.000	0.000	0.000
BETA2 (DEG)	63.495	52.595	52.595	52.595	52.595	52.595	52.595	52.595	52.595	52.595	0.000	0.000
BETA3 (DEG)	63.495	65.354	65.354	65.354	65.354	65.354	65.354	65.354	65.354	65.354	0.000	0.000
WORK COEFF	2.0000	1.6000	1.6000	1.6000	1.6000	1.6000	1.6000	1.6000	1.6000	1.6000	0.0000	0.0000

VELOCITY DIAGRAM AT TIP RADIUS

V2X (FPS)	242.609	223.217	223.217	223.217	223.217	348.395	348.395	348.395	348.395	348.395	0.000	0.000
V2U (FPS)	891.107	702.556	694.423	685.294	675.015	1145.137	1117.073	1075.671	1013.766	939.161	0.000	0.000
V2 (FPS)	923.542	737.164	729.418	720.732	710.965	1196.961	1171.141	1130.684	1071.961	1001.699	0.000	0.000
URAD (FPS)	531.167	539.003	545.315	552.580	560.994	805.567	825.805	857.590	909.958	982.243	0.000	0.000
W2U (FPS)	359.939	163.554	149.108	132.715	114.021	339.570	291.268	218.081	103.808	-43.082	0.000	0.000
W2 (FPS)	434.069	276.723	268.439	259.691	250.653	486.504	454.110	411.021	363.531	351.048	0.000	0.000
W3 (FPS)	-583.950	-583.395	-589.232	-595.962	-603.772	-877.677	-896.288	-925.656	-974.373	-1042.200	0.000	0.000
ALPHA (DEG)	74.771	72.375	72.182	71.959	71.703	73.079	72.679	72.055	71.035	69.648	0.000	0.000
BETA2 (DEG)	56.020	36.231	33.743	30.734	27.059	44.266	39.897	32.046	16.592	-7.049	0.000	0.000
BETA3 (DEG)	65.453	67.505	67.740	68.005	68.304	66.413	67.127	67.892	69.051	70.472	0.000	0.000
WORK COEFF	1.6776	1.3034	1.2734	1.2402	1.2032	1.4215	1.3527	1.2543	1.1141	0.9561	0.0000	0.0000

INPUT STAGE VARIABLES

DEL TAP (VH)	0.000	0.000	0.000	0.000	2.000	0.000	0.000	0.000	0.000	0.000	0.000	0.000
MOIST REMOVED	0.000	0.000	0.000	0.000	0.900	0.000	0.000	0.000	0.434	0.000	0.000	0.000
VAPOR FRACT	0.000	0.000	0.000	0.000	0.100	0.000	0.000	0.000	0.250	0.000	0.000	0.000
REHEAT COND	0.000	0.000	0.000	0.000	0.000	0.000	0.000	0.000	0.000	0.000	0.000	0.000
WORK SPLIT	0.513	0.410	0.410	0.410	0.410	1.000	1.000	1.000	1.000	1.000	1.000	1.000
VEL COEFF	0.980	0.980	0.980	0.980	0.980	0.980	0.980	0.980	0.980	0.980	0.980	0.980
TIP COEFF	2.000	2.000	2.000	2.000	2.000	1.000	1.000	1.000	1.000	2.000	1.000	2.000
TIP CLEARANCE (IN)	0.010	0.010	0.010	0.010	0.010	0.010	0.010	0.010	0.010	0.010	0.010	0.010
SEAL DIA (IN)	4.400	4.000	4.000	4.000	4.000	4.800	4.800	4.800	4.800	4.800	4.800	4.800
SEAL LEAK (LB/SEC)	0.035	0.016	0.014	0.012	0.011	0.059	0.012	0.006	0.005	0.003	0.000	0.000
ACC LIQUID FRACT	0.0000	0.0000	0.0000	0.0000	0.0000	0.0054	0.0167	0.0196	0.0193	0.0173	0.0000	0.0000

STAGE WEIGHT AND LIFE PARAMETERS

BLADE LIFE (HR)	4.02+007	2.47+008	1.98+009	1.70+010	1.57+011	2.45+009	3.38+010	4.06+011	3.63+012	2.01+014	0.00+000	0.00+000
BLADE STRESS (PSI)	2738.51	3212.58	3557.46	3946.76	4389.90	9971.86	12089.22	15228.50	20018.23	19900.41	0.00	0.00
BLADE TEMP (R)	2518.91	2427.38	2338.69	2252.63	2168.92	2177.03	2065.01	1957.56	1856.19	1762.82	0.00	0.00
BLADE CRIT RD (IN)	2.904	2.904	2.904	2.904	2.904	4.532	4.532	4.532	4.532	4.532	0.000	0.000
NO OF STR-RTR BLADES	28 78	36 65	36 65	36 65	36 65	33 59	33 59	32 59	32 59	32 59	0 0	0 0
BLADE CG RAD (IN)	3.032	3.055	3.072	3.092	3.115	4.763	4.840	4.954	5.130	5.180	0.000	0.000
BLADE WEIGHT (LBS)	0.224	0.156	0.172	0.189	0.209	0.841	1.004	1.235	1.568	1.544	0.000	0.000
BLD INERT (LB IN2)	2.064	1.456	1.621	1.811	2.029	19.094	23.534	30.374	41.453	41.685	0.000	0.000
DISK LIFE (HR)	9.59+003	3.00+004	3.00+004	3.00+004	3.00+004	3.00+004	3.00+004	3.00+004	3.00+004	3.00+004	0.00+000	0.00+000
DISK STRESS (PSI)	15594.47	22825.30	28810.70	35937.69	44394.60	46500.00	46500.00	46500.00	46500.00	46500.00	0.00	0.00
DISK TEMP (R)	2519.08	2435.41	2382.39	2330.60	2279.64	2177.06	2065.04	1957.58	1856.20	1762.82	0.00	0.00
PLAT THICK (IN)	0.145	0.116	0.116	0.116	0.116	0.500	0.500	0.500	0.500	0.500	0.000	0.000
DISK HUB WD (IN)	0.100	0.100	0.100	0.100	0.100	0.130	0.137	0.148	0.164	0.164	0.000	0.000
DISK ROOT WD (IN),	1.500	1.121	0.614	0.270	0.105	0.908	0.843	0.897	0.979	0.977	0.000	0.000
DISK HOLE RD (IN)	0.600	0.600	0.600	0.600	0.600	0.600	0.600	0.600	0.600	0.600	0.000	0.000
ST ROTOR WT (LBS)	3.215	2.656	2.192	1.775	1.482	9.278	9.666	10.237	11.087	11.050	0.000	0.000

TURBINE WEIGHT, LBS = 139.4 DESIGN LIFE, HRS = 30000.0 DISK DELTA TEMP, F = 50.0 BLADE DELTA TEMP, F = 50.0

AiResearch designed the aft turbine, supplied to Westinghouse for analysis, for full thermodynamic wet vapor equilibrium throughout the turbine. Under these conditions, the highest moisture level and highest relative velocities between collected liquid and rotor blades occur in the last stage. Because of this, the last stage of a wet vapor turbine is the one most likely to suffer erosion damage. Westinghouse analysis of this aft turbine was confined to the last stage.

3.4.1 Areas and Mechanisms of Erosion

In wet vapor turbines most of the material removal by liquid is from the turbine rotor blades. This damage is not done directly by the condensate particles in the vapor. The condensate particles are small enough, being submicronic-diameter particles, that only a very small percentage ever impinge upon a surface. The impingement of this small percentage does, however, allow concentrations of liquid to build up on the various turbine surfaces, and it is this liquid which can do damage.

Principal locations of material removal from rotor blades are illustrated in Figure 50. This figure shows forward and aft views of a shrouded turbine blade and points out four types of material removal by liquid that are likely to be obtained on the rotors of wet vapor turbines.

In steam turbines, where chemical dissolution of blade material does not occur to any extent, the material removal mechanism is largely that of mechanical removal by the force of liquid impingement as at locations (1) and (2) or by cavitation induced by the circulating eddies as at (4). In potassium vapor turbines the impingement removal can be compounded by dissolution effects either directly in the impingement areas or by rivulations such as illustrated at location (3). These

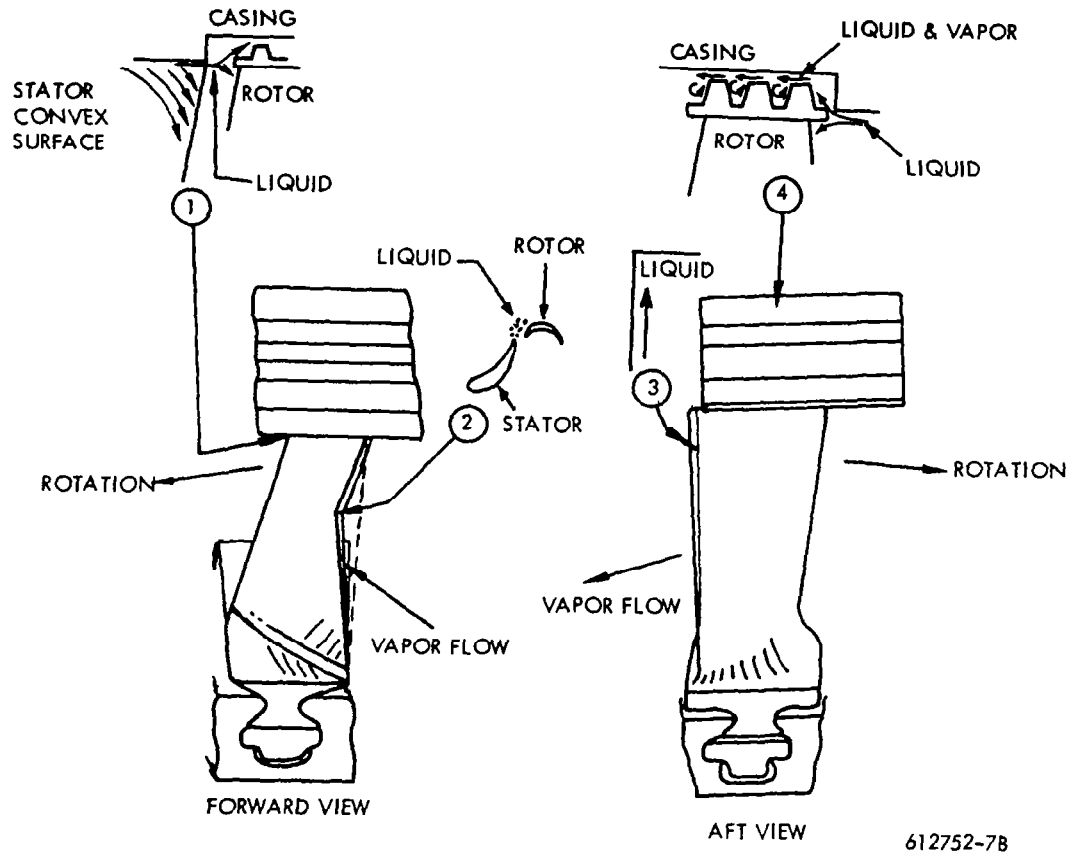

ROTOR BLADE MATERIAL REMOVAL LOCATIONS

FIGURE 50

rivulets can occur at other locations on the rotor blades as well as the trailing edge. They are nearly radial lines because the centrifugal force component on the liquid deposited on the rotors is much higher than the vapor shear force.

Liquid reaches the turbine casing primarily by being slung from the turbine rotors. It can also reach the casing under urging of the vapor secondary flow from the pressure (concave) surface over the casing to the suction (convex) surface of the adjacent stator vane. Other mechanisms (of little importance) are impingement and condensation from the bulk flow.

The casing-collected liquid, in addition to causing damage to shrouds and seals as indicated in Figure 50, also tends to flow down over the stators on the convex side, as illustrated at location (1) of Figure 50. This augments the liquid discharged from the stators that impacts the leading edges of the rotor blades[11]. Since the highest normal impact velocities of collected liquid are with the leading edge of the rotor blades, increases in this liquid supply rate are obviously undesirable.

The classic means of controlling the damage which can be caused by the casing-collected liquid, as used by the steam turbine industry, is to remove this liquid periodically through suitable ports in the casing. A casing flow analysis of a potassium turbine of similar diameter and blade dimensions to those of the KTA study turbine and with similar operating state points was carried out under Contract NAS7-390[3]. The conclusion of the NAS7-390 analysis was that such removal will be required in potassium turbines if major erosion damage to shrouds and seals is to be avoided. This casing flow analysis has not been repeated for the KTA study turbine because it is not felt that the differences between the conditions of the NAS7-390 study and this study are

great enough to reverse the NAS7-390 study conclusion. It is, therefore, recommended that there be provisions for periodic removal of the casing liquid in the KTA turbine.

Even if all the casing liquid is removed, liquid which collects on the stator rotor blades of a given stage can cause material removal damage. The stator-collected liquid can discharge from the stator blade trailing edges into the path of the rotor blades, causing rotor blade edge damage as at location (2) in Figure 50. The rotor blade-collected liquid can run up the rotor blades, causing dissolution damage as indicated in Figure 50, location (3).

In principle, this potentially damaging liquid can be removed as is recommended for the casing-collected liquid. However, control of damage from this liquid without removal is possible and is a more practical solution than sucking it off the stator and rotor blades. For this reason, the erosion analysis of the KTA study turbine has been mostly concerned with providing a critique of the design with respect to control of the potential damage that can be self-inflicted through the liquid collected by the individual stage.

3.4.2 Analysis of Forward Turbine

As previously mentioned, AiResearch designed this forward turbine to retain the expanding vapor in a supersaturated state until just before turbine exit. Westinghouse checked this analysis using somewhat higher values of liquid surface tension than those used by AiResearch.

Information supplied by AiResearch on the forward KTA turbine (Figure 49) was input into a one-dimensional turbine condensation analysis computer code. Pertinent calculated values at the fifth rotor exit are given in Table 7.

TABLE 7

CONDENSATION ANALYSIS OF THE KTA FIFTH STAGE ROTOR EXIT

KA	KB	STEP SIZE H	Z	Z/L		ROW 1
90	40	1.8125000E-03	.0725	1.0000		
P	T	SP. VOL.-V	W	U-AXIAL	Z-COMPRESS	PSAT
6.82544E+01	2.07497E+03	6.85993E+00	5.94131E+02	2.32527E+02	8.22325E-01	4.06723E+01
DP	DT	DV	DW	-(DP/DT)/P	AREAA	DA/A
-1.79085E+04	-1.13728E+03	6.83941E+00	5.98663E+03	4.23681E+02	8.59217E+00	-9.07926E+00
DELTAT	TLIQUID	LAMBDAO	LAMBDA1	JDOT	RCRITICAL	DN/DZ
1.35041E+02	2.07497E+03	5.17694E-01	4.24952E-01	6.11377E+12	5.78309E-09	0.
K2	K4	CPL	PRANO	CPVO	CPV	SIGMA
5.00245E-02	3.01442E-04	2.13516E-01	2.36770E-01	1.27004E-01	4.10248E-01	3.97912E-03
TOTAL MOISTURE	PARTIAL P1	QUALITY	MEAN RADIUS	TOTAL DROPS	NEUV	SINBETA
0.	7.87857E+03	1.00000E+00	0.	0.	9.54465E-05	3.91374E-01
Y-EQUILIB	HG	HL	HFG	DELO	DELW	1-M**2
7.23222E-02	1.15634E+03	3.90315E+02	7.66022E+02	2.69828E+07	2.71886E+08	9.01052E-01
YB Y BLADE	YBO Y CASE	YABS YATOMIZED	YSURFACE	NATOMIZE	MACH	
0.	0.	0.	0.	0.	3.14559E-01	

The code used is essentially the same as that reported in Reference 12 and also as that incorporated as a subroutine by AiResearch in their turbine design code. The principal differences between the code used here and the other two is the treatment of the physical property values for thermal conductivity, viscosity, liquid surface tension, and liquid specific heat. In the latter two codes thermal conductivity, viscosity, and liquid specific heat are input as constants. The present code incorporates these variables in subroutines which give their values as functions of temperature. The most important difference between the present code and the other is in the expression used to evaluate potassium liquid surface tension. The present code incorporates an expression recommended by Hoffman and Cox[13] in their recently published review of the physical properties of potassium. The other two codes use an expression suggested by Reference 12.

At the temperatures present in the fifth stage of the KTA, the Hoffman and Cox recommended expression yields surface tension values approximately 15 percent higher than the Reference 12 expression. The use of the higher surface tension values has the effect of reducing the predicted nucleation rates for a given degree of vapor supersaturation. For example, the value of nucleation rate predicted at 90 percent of the fifth rotor chord by the present calculation is 4×10^{11} nuclei/sec, whereas AiResearch calculated values under the same flow and thermodynamic conditions are 2×10^{16} nuclei/sec. This is not as large a difference as it might seem. In the fifth rotor, the nucleation rate is rising exponentially with distance along the blade chord. The present calculation implies that all the condensation of the vapor flow will take place in the piping leading to the external moisture separator. The AiResearch (previous) calculation implies that a great deal but not all the condensation of the vapor flow will take place in the piping leading to the external moisture separator.

The purpose of this analysis was to appraise the KTA turbine designers of the effect of the uncertainties in the values of potassium

surface tension on condensation calculations. As far as picking the turbine stage at which to go to external moisture separation is concerned, the two calculations are in substantial agreement. In addition, it should be pointed out (1) that surface tension is hard to measure accurately and (2) that condensation calculations using values of surface tension obtained from Reference 8 (the AiResearch case) give good agreement with the nozzle experiments of Goldman and Nozek (see Volume I, Section 2.1.2.2).

3.4.3 Analysis of Aft Turbine

As mentioned previously, AiResearch has designed the aft turbine for full thermodynamic wet vapor equilibrium throughout the turbine. Under these conditions, the highest moisture level and highest relative velocities between collected liquid and rotor blades occur in the last stage. Because of this, the last stage of a wet vapor turbine is the one most likely to suffer erosion damage. Westinghouse analysis of this aft turbine was confined to the last stage. This analysis is conveniently broken into two categories, the analysis for mechanical erosion and the analysis for chemical dissolution. It is believed that if the blade materials are of refractory alloys such as TZM and TZC, there is not much interaction between mechanical and chemical effects. This belief is supported by the results from a single test and is discussed in Section 3.4.3.2.

3.4.3.1 Mechanical Erosion

To establish the potential level of mechanical erosion damage to the last (tenth) rotor blades of the KTA study turbine, it is first necessary to establish the quantity, particle diameters, and velocities of the liquid impacting the rotor blades. The damaging moisture collected by the preceding row of stator blades and discharged into the path of the rotor blades impacts in region (2) of previously mentioned Figure 50. It is only that part of the total condensate collected and

then subsequently discharged into the path of the rotors which is likely to do impact or mechanical damage. This is only a fraction of the total moisture flowing with the vapor stream; estimated by AiResearch (Figure 49) to be 0.0393 lb/sec. This is 19.4 percent of the total moisture present in the stage.

An analysis of the movement of this tenth-stage-collected moisture has been completed. According to Figure 48, this analysis consists of the steps described as: intra-row fluid dynamics, boundary layer analysis, stator-wake fluid dynamics, atomization and transport of drops between stator and rotor, and impact velocities and impact lengths (of liquid on rotor blades).

The analysis is based on the bulk-flow conditions and geometry factors as shown in Figure 49 and preliminary blade cross sections, at the hub and tip, of the tenth stator blades supplied by AiResearch. The hub section used in the analysis is shown in Figure 51. The actual calculations were carried out by use of two computer programs. The stator blade surface velocities were determined using the computer code given in NASA TND-3762[15]. The blade surface velocities were then used as input to the boundary layer, atomization, and trajectory calculations of the ADRØP[13] code originated under NASA Contract NAS7-390.

Table 8 gives the calculated boundary layer parameters at the exit of the tenth stator blades. Figures 52 and 53 are plots of the tenth stator blade surface velocities at turbine hub and tip, respectively.

Figures 52 and 53 show that surface velocities in terms of referred values are similar at hub and tip; there are two sets of velocities in each figure. The dashed line is that calculated by the surface velocity computer program[15]; the solid line is the ADRØP[16] code, collected-liquid transport code, interpretation of the surface velocity input as used by ADRØP. There are substantial differences between the two lines near

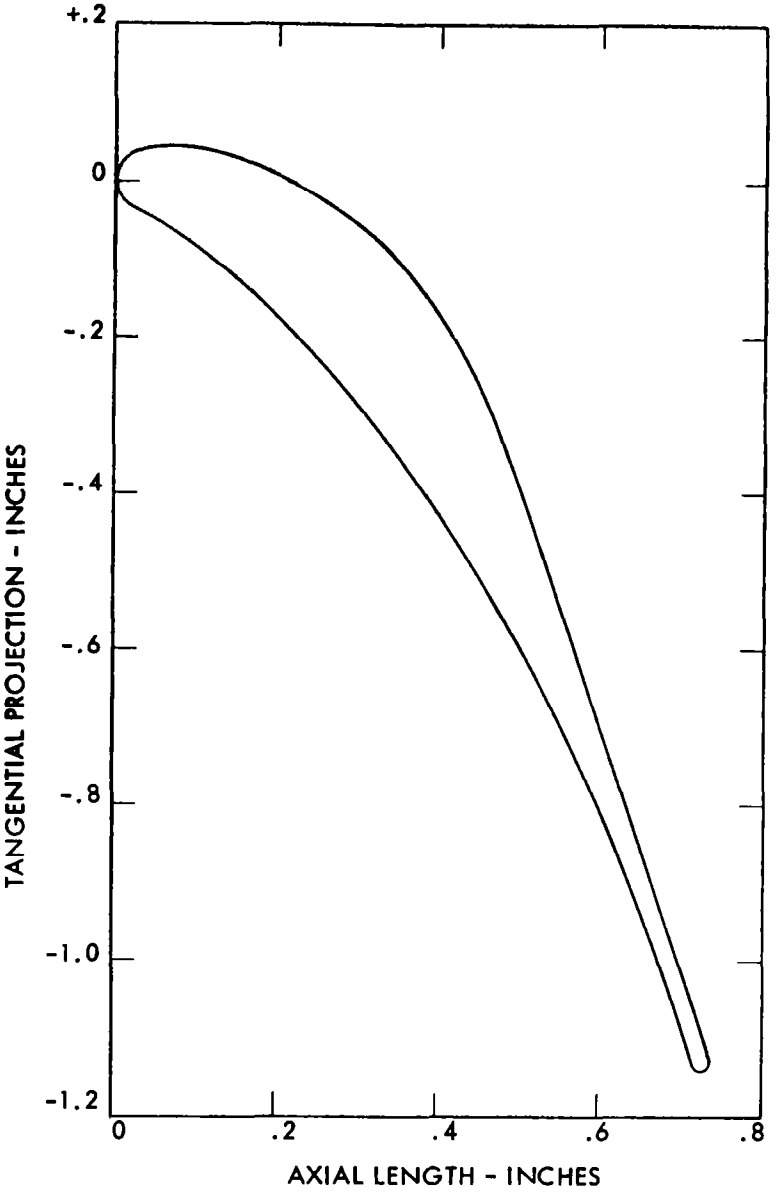

TENTH STATOR BLADE CROSS-SECTION AT ROTOR HUB

FIGURE 51

TABLE 8

KTA TURBINE – TENTH STATOR

TRAILING EDGE BOUNDARY LAYER SUMMARY

	Hub	Tip
Pressure Side		
Momentum thickness, cm	0.00287	0.00393
Displacement thickness, cm	0.00412	0.00553
Full thickness, cm	0.02315	0.03269
Suction Side		
Momentum thickness, cm	0.01163	0.01656
Displacement thickness, cm	0.01775	0.02486
Full thickness, cm	0.08518	0.12402

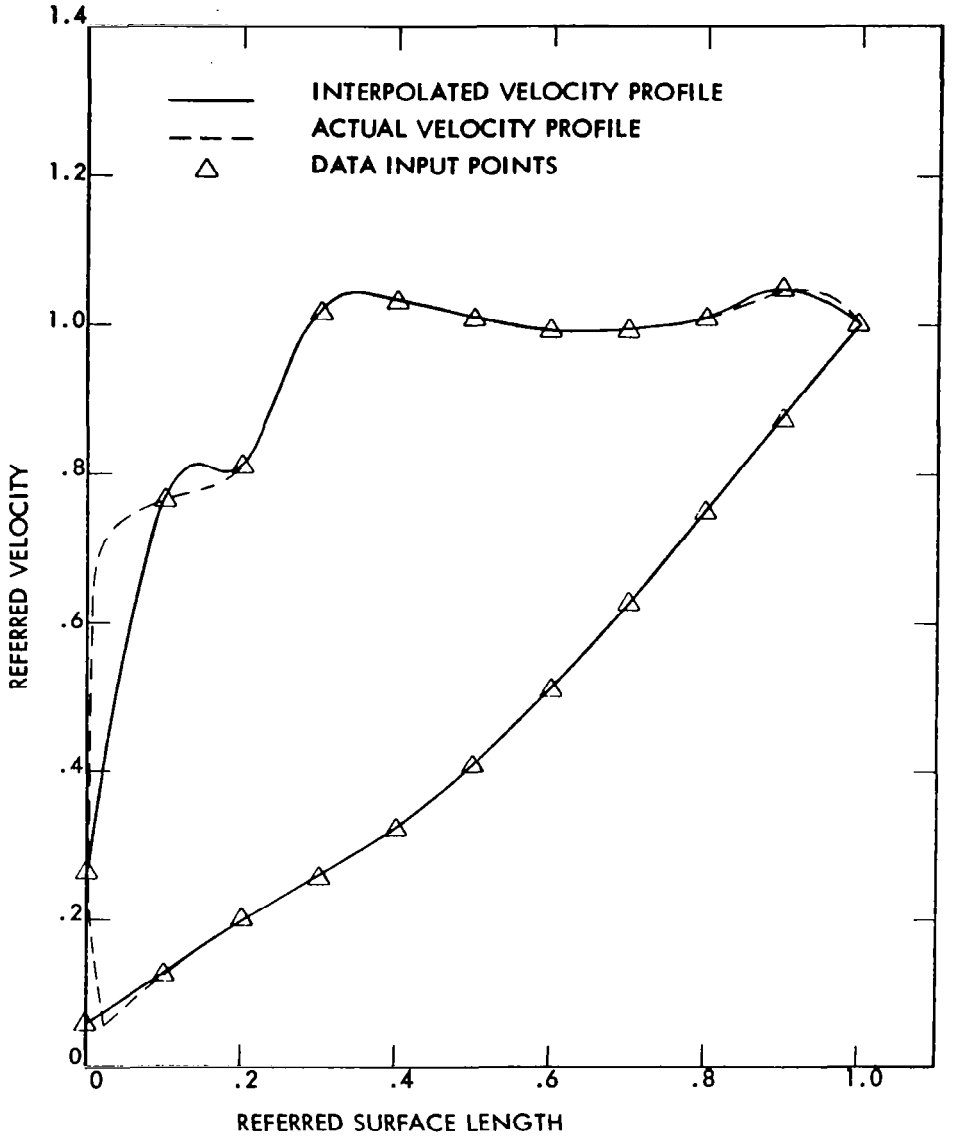

TENTH STATOR BLADE SURFACE VELOCITIES AT TURBINE HUB

FIGURE 52

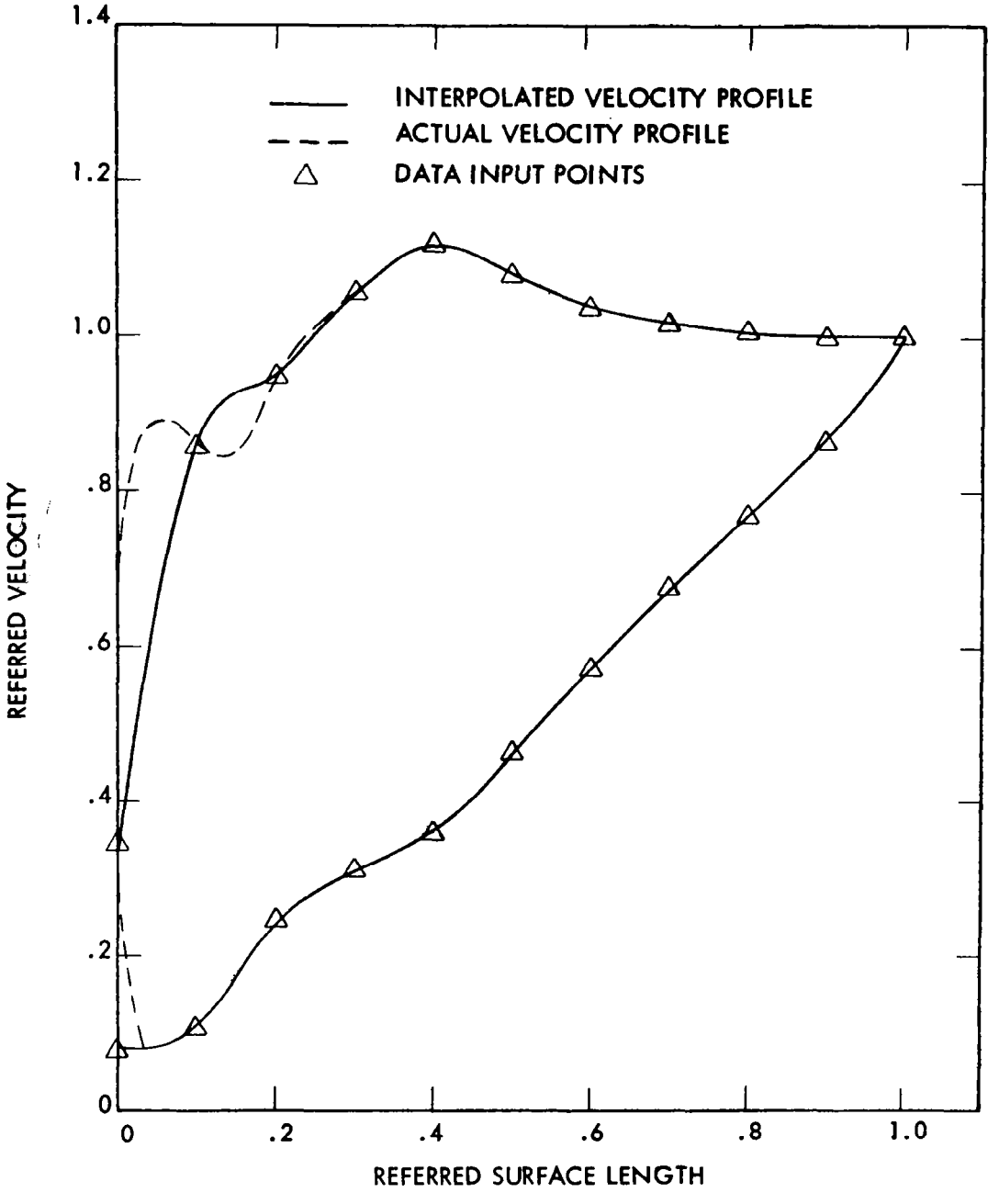

TENTH STATOR BLADE SURFACE VELOCITIES AT TURBINE TIP

FIGURE 53

the inlet of the row but little difference aft of that location. This is because there is a small region of flow separation just aft of the leading edge of the stator blades on the pressure surface (about 0.015 referred-surface length) as reported by ADRØP, using the actual surface velocities. The code does not contain provisions for analyzing a separated flow region. To allow the code to continue, the initial surface velocities were adjusted to eliminate the separated region since this region is of a very local character.

This small area of flow separation just aft of the nose of the tenth stator blades on the pressure surfaces will cause a small area of recirculation running nearly radially outward from hub to tip of the stators. It is our opinion that this area of recirculation is probably present in the same general location on the rotor blades. No numerical analysis was conducted to confirm this opinion. However, markings on both the GE2-stage[17] and 3-stage[18] potassium test turbine rotor blades show evidence of a radial stream tube in this general location.

These markings have previously been ascribed to negative-incidence on the rotor blades[17,18]. However, almost all our previous turbine analyses using the ADRØP code have shown such an area of separation at design incidence on stator blades. Since we have never analyzed the surface flows about the noses of the turbine rotor blades, we can not be absolutely sure this is also true of rotor blades. Such an area of flow separation provides a path for a stream of liquid to flow radially along the rotor blade as a result of centrifugal force. This is of no serious consequence in steam turbines. It might become so for long-time operation of potassium turbines since dissolution of the blade material may be a problem (see Section 3.4.3.2).

3.4.3.1.1 Impact Velocities of Wake Axis Drops with Tenth Rotor Blades

The information given in Figure 54 is a summary of impacting drop velocities on the tenth rotor blades at hub and tip. Velocity W_d is

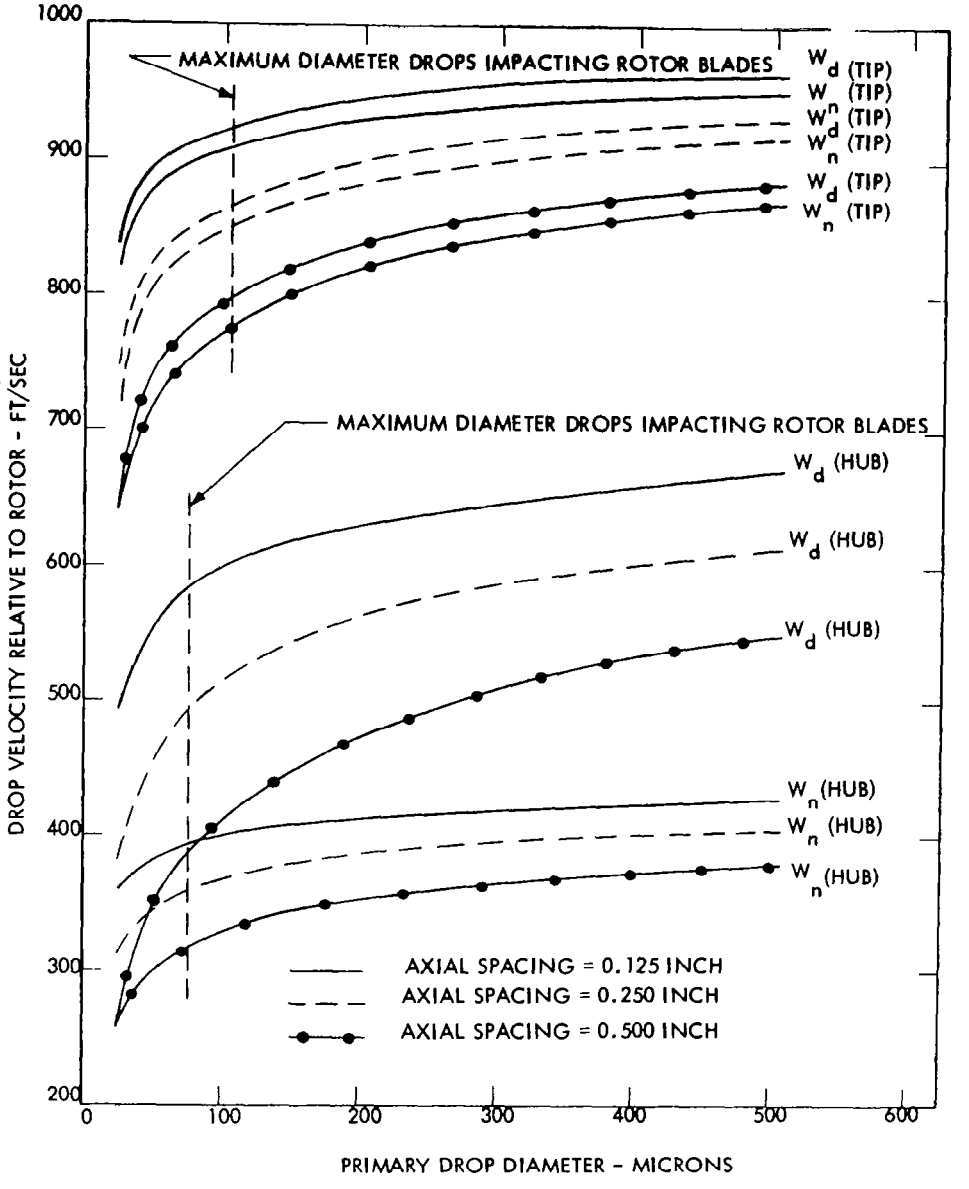

IMPACT VELOCITIES OF WAKE AXIS DROPS WITH TENTH ROTOR BLADES

FIGURE 54

the relative velocity of impact between drop and blade. Velocity W_n is the normal component relative to the rotor blade surface of velocity W_d.

Also shown in the figure are the maximum diameter drops calculated to hit the tenth rotor blades. Values are 110 μ at blade tips and 70 at blade hubs. These values are based on a wake axis critical Weber No. for drop disruption of 13. This value of 13 is consistent with past practice in Westinghouse analysis of small potassium turbines. Recently[19] a more elaborate set of dimensionless numbers was generated to predict turbine liquid drop diameters. In small potassium turbines of the type being analyzed, the more recent expression gives maximum drop diameters about 20 percent smaller than those derived from a critical Weber No. = 13.

The maximum normal velocity of impact of 110-μ drops with the tips of the rotor blades is slightly greater than 900 ft/sec for 1/8-in. stator to rotor axial spacing. The impact velocity will decrease to less than 800 ft/sec for a 1/2-in. stator to rotor axial spacing.

3.4.3.1.2 Length of Drop Impact Zone Aft of Rotor Blade Leading Edge - Tenth Rotor

Figure 55 depicts the area over which the stator blade discharged-liquid will be concentrated as it strikes the suction surface of the rotor blades. The impact length calculated is a mathematical convenience but does approximate the actual blade length over the initial 1/4 in. aft of the rotor blade nose. As can be seen, at the tip of the rotor most of the stator blade liquid will strike within 1/10-in. of the leading edge for a 1/2-in. axial spacing from stator to rotor. For a 1/8-in. spacing, the liquid will be concentrated in the first 1/20-in. aft of the leading edge at the tips of the rotor blades. Also the dispersion of the liquid at the hubs of the blades will be considerably greater than at the tips, regardless of spacing.

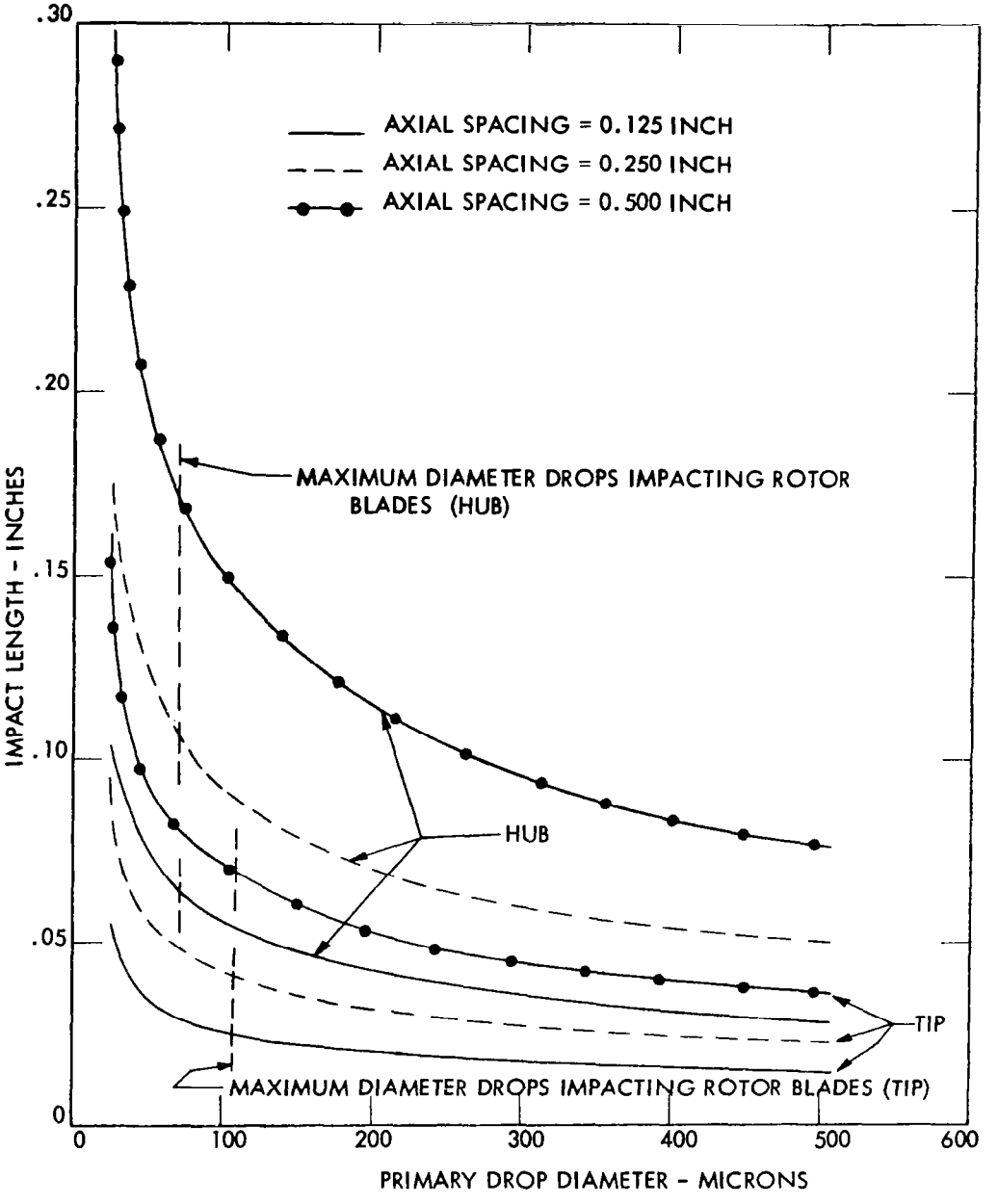

LENGTH OF DROP IMPACT ZONE AFT OF
ROTOR BLADE LEADING EDGE - TENTH ROTOR

FIGURE 55

3.4.3.1.3 Axial Spacing Required to Allow Breakup of Tenth Stator Discharged-Liquid at Blade Tips

In Figure 56, the axial spacing between stator and rotor required to allow disruption of all stator-discharged primary drops, potentially unstable under the flow conditions along the wake axis, is given. This distance is substantially independent of the values of the critical Weber Number selected. The largest of the primary drops, 500-μ diameter or so, will be broken up very quickly and only those which are nearly stable take long distances to disrupt.

3.4.3.1.4 Potential for Mechanical Erosion

If the axial spacing between stator and rotor is at least 1/8 in., the maximum diameter drops impacting the rotor will be slightly greater than 100 μ. The maximum normal impact velocities of these largest drops on the rotor blades is slightly greater than 900 ft/sec. Based on previous analytical studies[3], the threshold velocity to cause purely mechanical damage to the rotor blades by drops of this size is greater than 1300 ft/sec. Therefore, we conclude that purely mechanical erosion is unlikely in this turbine. However, interactions between mechanical erosion and dissolution erosion have not been established, at this time, and such interactions may modify the material removal picture. We are of the opinion that the refractory alloys will be only modestly affected by such combined attack in nearly oxygen-free systems on the basis of the effects on these alloys when tested as erosion inserts in the NASA-GE 2-stage potassium test turbine[17].

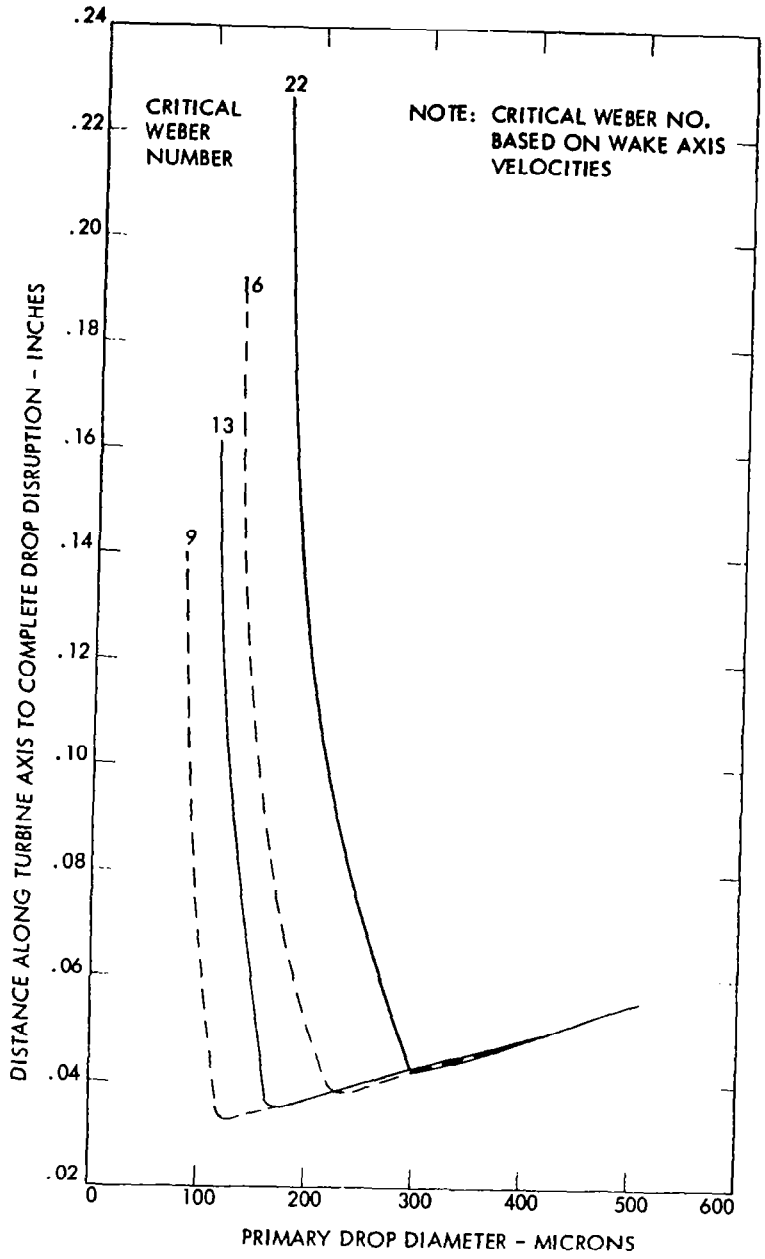

AXIAL SPACING REQUIRED TO ALLOW BREAKUP OF TENTH STATOR DISCHARGED LIQUID AT BLADE TIPS

FIGURE 56

3.4.3.2 Chemical Dissolution

3.4.3.2.1 Theory

To repeat, a fraction of the condensed moisture present in the wet vapor will be collected by the stator blades and will carry over to the subsequent rotor row in the form of atomized drops.

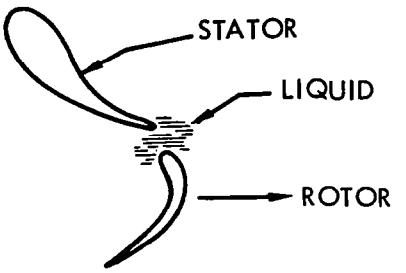

612752-4B

This liquid impacts the rotor blades along a relatively narrow portion of the leading edge of the convex surface and then flows in a nearly radial direction to discharge at the blade tips. It is assumed that the impacted moisture forms a continuous film and that the fluid impinges uniformly along the blade-impact zone. The concern of this analysis is the chemical dissolution of the blade material associated with the flow of this film.

Because the film of liquid formed on the rotor blades is at most a few micrometers thick and is violently stirred by the incoming drops, it is assumed that the rate-controlling step in the dissolution process is that of the rate of dissolution for the blade material into the liquid at the liquid-solid interface.

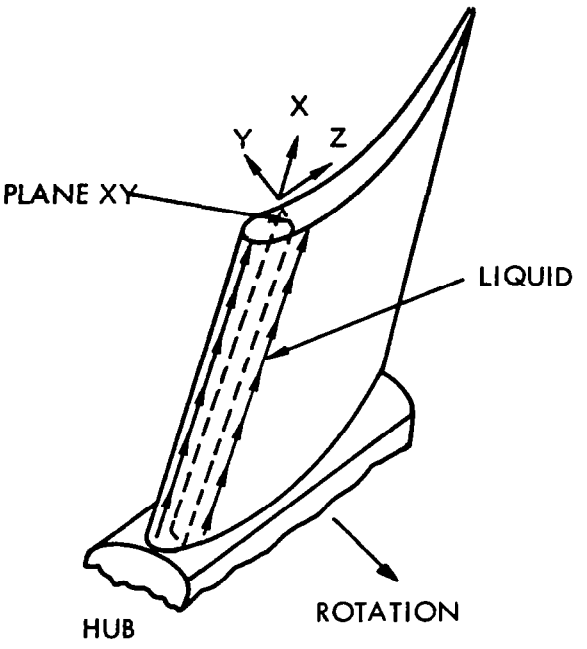

ROTOR BLADE 612752-5B

This is different from dissolution of solids into liquids in pipe flow, where the rate-controlling step is often the rate of diffusion of the dissolved solute across the solvent boundary layer into the bulk flow of solvent in the pipe.

For a turbine operating at some steady-state condition, rates of flow are a function only of position. Hence at any location x,z measured from the hub and nose, respectively, of the rotor blade, the rate flows of solute and solvent in the liquid film are time-independent,

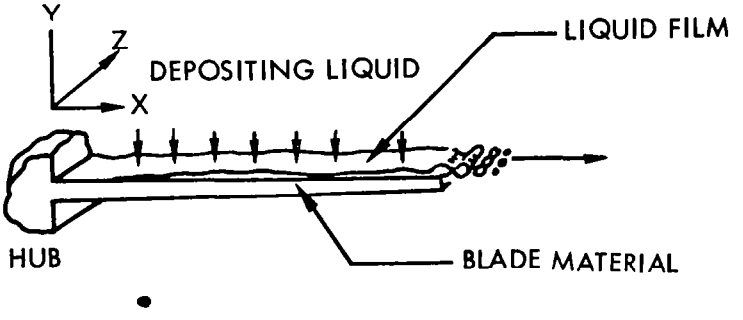

and the concentration, S, of solute in the solvent at location x,z is the ratio of the rate-flow of solute to rate-flow of solvent at this location or

$$S = \rho_\ell \frac{\dot{V}_m}{\dot{m}_\ell} \tag{4}$$

where

$\dot{V}_m$ is the rate flow of solute in the x-direction per unit width of film (z-direction) — cm^2/sec

$\dot{m}_\ell$ is the rate of solvent in the x-direction per unit width of film — gm/sec/cm

ρ_ℓ is the solvent density — gm/cm^3

According to Epstein[20], the rate of dissolution of a pure metal into a pure liquid solvent at the metal-liquid interface is given by:

$$S = S_o \left[1 - \exp\left(-\frac{\alpha A t}{V_\ell}\right)\right] \tag{5}$$

where

A is the surface area in contact with the liquid —cm^2

S_o is the saturation solubility of material in the solvent

S is the solute concentration in the solvent at time t

V_ℓ is the volume of liquid in contact with the metal for time t-cm^3

t is the contact time between liquid and metal along surface A-sec

α is the solution rate constant -cm/sec

From Eq. (5), the following differential equations may be inferred:

$$\frac{dS}{dt} = \frac{\alpha}{V_\ell} (S_o - S) A \tag{6}$$

and since $dS = 1/V_\ell \; dV_m$

$$\frac{dV_m}{dt} = \dot{V}_m = \alpha(S_o - S) A \tag{7}$$

In the case of the rotor blade film of unit width at location "x", Eq. (7) may be written:

$$\dot{V}_m = \int_o^x \alpha(S_o - S)dx \tag{8}$$

By the assumption of uniform deposition of liquid along the rotor blade-impact zone:

$$\dot{m}_\ell = \dot{m}_a \, x \tag{9}$$

where $\dot{m}_a$ is the rate of deposition per unit area per unit time—gm/cm^2/sec.
Substitutions from Eq. 8 and 9 into Eq. 4 yield, after some rearranging of terms,

$$Sx = \frac{\rho_\ell}{\dot{m}_a} \int \alpha(S_o - S)dx \tag{10}$$

Differentiation of Eq. 10 and rearrangement of terms gives

$$\frac{dS}{\frac{\rho_\ell \alpha}{\dot{m}_a} S_o - \left(1 + \frac{\rho_\ell \alpha}{\dot{m}_a}\right) S} = \frac{dx}{x} \tag{11}$$

Equation 11 is readily integrated to give

$$S = \frac{\dot{m}_a}{\dot{m}_a + \rho_\ell \alpha} \left[\frac{\rho_\ell \alpha}{\dot{m}_a} S_o - \frac{C}{x\left(\frac{1 + \rho_\ell \alpha}{\dot{m}_a}\right)} \right] \tag{12}$$

where C is a constant of integration.

Now it may be noted that when x = 0 in Eq. 12, S = $-\infty$ unless C = 0 (in which case S is indeterminate). However, a C taken equal to zero is the only reasonable physical interpretation, since the physical concentration S must fall with the limits:

$$0 \geq S \leq S_o$$

and the equation

$$S = \frac{\dot{m}_a}{\dot{m}_a + \rho_\ell \alpha} \left[\frac{\rho_\ell \alpha}{\dot{m}_a} S_o - \frac{(0)}{x\left(1 + \frac{\rho_\ell \alpha}{\dot{m}_a}\right)} \right] \tag{13}$$

satisfies these limits as $x \to 0$. Equation 12, therefore, reduces to:

$$S = \frac{\rho_\ell \alpha}{\dot{m}_a + \rho_\ell \alpha} S_o \tag{14}$$

It will be noted that the concentration S is not only time-independent but is constant throughout the liquid-flow zone along the leading edge of the rotor blades.

"S" in terms of S_o from Eq. 14 may be substituted into Eq. 6 to give

$$\dot{V}_m = \int_o^x \alpha\, S_o \left(1 - \frac{\rho_\ell \alpha}{\dot{m}_a + \rho_\ell \alpha}\right) dx = \alpha S_o \left(\frac{\dot{m}_a}{\dot{m}_a + \rho_\ell \alpha}\right) x \qquad (15)$$

The rate of material thickness removal, $\dot{\delta}_m$, therefore is

$$\dot{\delta}_m = \frac{\dot{V}_m}{x} = \alpha S_o \left(\frac{\dot{m}_a}{\dot{m}_a + \rho_\ell \alpha}\right) \qquad (16)$$

Eq. 16 presents a reasonable physical picture. If $\dot{m}_a >> \alpha$, this implies that $S \rightarrow 0$ or the rate of material thickness removal is

$$\dot{\delta}_m = \alpha[S_o - (0)] = \alpha S_o$$

The thickness removal rate is dissolution-rate constant-controlled and is independent of liquid-flow rate. If $\dot{m}_a$ is low, $\dot{m}_a << \rho\alpha$; this implies that $S \rightarrow S_o$ and

$$\dot{\delta}_m = S_o \frac{\dot{m}_a}{\rho_\ell}$$

The thickness-removal rate is then directly proportional to the liquid-flow rate and independent of the dissolution-rate constant.

Between these extremes, the thickness-removal rate is, of course, affected by both dissolution-rate constant and liquid-flow rate.

The discussion so far has assumed a pure metal dissolving into a pure liquid. The latter assumption, pure liquid, is probably reasonable since turbine system operators go to some length to keep a pure liquid in the system. However, turbine blade materials are alloys composed of materials of differing solubility and probably chemical activity. In advanced high-temperature Rankine-cycle liquid metal systems, the turbine blade materials are likely to be refractory alloys such as TZM and TZC. These are molybdenum alloys with small amounts of titanium, carbon, and zirconium. The alloying materials such as Ti and Zr are more soluable than the base material and, while present in concentrations of only 1 to 2 percent, tend to collect at the alloy grain boundaries where they may be more readily leached from the surface than if uniformly mixed. In addition if there is preferential leaching at the grain boundaries, this may so weaken the material that a considerably greater amount of material may be lost than that which simply dissolved.

At the present time, there are insufficient experimental results and/or theory to judge these factors adequately. Nonetheless, it seems worthwhile to delineate these areas of uncertainty by the application of multiplicative correction factors to Eq. 16, as:

$$\dot{\delta}_s = k_1 \dot{\delta}_m = k_1 ka\alpha S_o \left(\frac{\dot{m}_a}{\dot{m}_a + \rho_\ell ka\alpha} \right) \tag{17}$$

where

a is the activity level of a readily dissolvable constituent of the alloy in the alloyed form relative to the constituents dissolvability in pure form

k is ratio of the effective surface area from which the constituent is dissolving to the total surface area of the alloy

k_1 is the ratio of total alloy removal rate to dissolving constituent removal rate

$\dot{\delta}_s$ is the thickness removal rate for the alloy surface as a whole

In the numerical analysis on dissolution completed during this contract, it has been assumed that $k = 1/k_1$ and $a \sim 1$. Hence,

$$\dot{\delta}_s = \alpha S_o \frac{\dot{m}_a}{\dot{m}_a + \rho_\ell k \alpha} \tag{18}$$

In addition, it has been assumed that k (the effective surface area ratio) is equal to the ratio of dissolving constituent volume to total alloy volume.

3.4.3.2.2 KTA Tenth Rotor Dissolution Analysis

To our knowledge, there are no experimental values of dissolution-rate constant (α) available for TZM, TZC constituents dissolving into potassium. There are values for Fe dissolving in Na[20] and 304 SS dissolving in Li[11]. The values for 304 SS dissolving in Li are used (Figure 57). The saturation solubilities of the various materials are:

Material	S_o, ppm
Molybdenum	0.2
Zirconium	58
Titanium	68

The saturation solubilities of Zr and Ti are most uncertain[21] and may be as low as 10 ppm at tenth-rotor conditions. The values used are

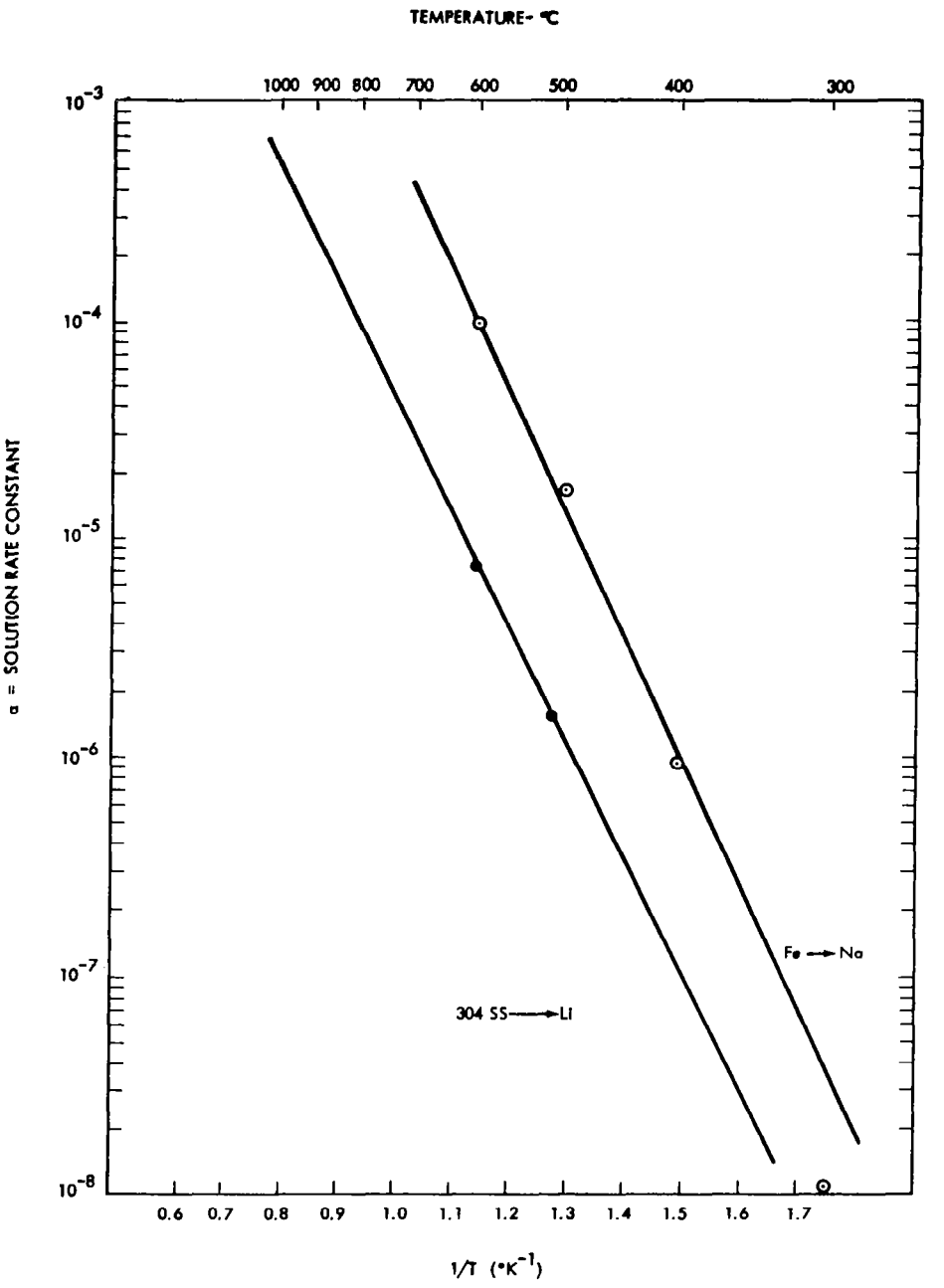

TEMPERATURE DEPENDENCE OF α

FIGURE 57

near the maximum reported in the literature for the tenth-rotor temperature. The rotor blade material was assumed to be TZM of the following composition:[22]

Constituent	Volume Fraction
Carbon	0.0009
Titanium	0.0110
Zirconium	0.0014
Molybdenum	0.9867

The fluid and geometric conditions along the leading portion of the convex surface of the tenth-rotor blades (the information comes from Figures 49 and 55, assuming a stator-to-rotor axial spacing of 1/8 in.) are as follows:

KTA Tenth-Rotor Blade Conditions

Total liquid flow, gm/sec	17.8
Number of rotor blades	59
Liquid flow/blade, gm/sec	0.302
Blade height, cm	4.03
Temperature, °C	670
Liquid density, gm/cm^3	0.685
Liquid film width, cm	0.25
Liquid film area, cm^2	1.

The information from Figure 57 and the preceding three tables on material solubilities, the composition of TZM, and the tenth-rotor blade conditions were used to calculate material-removal rates using Eq. 18. The results of this calculation follow:

KTA Tenth-Rotor Blade Dissolution Results

$\dot{m}_a$ – liquid-deposition rate/unit area, $gm/cm^2/sec$	0.302
α solution-rate constant, cm/sec	$2(10^{-5})$

KTA Tenth-Rotor Blade Dissolution Results (CONT)

k effective surface area ratio of Ti + Zr, dimensionless	0.012
S_o average saturation soluability of Ti and Zr	$63(10^{-6})$
$\rho_\ell \alpha$ k dissolution factor, gm/cm^2/sec	$1.65(10^{-7})$
$\dot{\delta}_s$ material thickness removal rate, mm/sec	$1.26(10^{-8})$
Thickness removed in 2000 hr, in.	0.0036
Thickness removed in 20,000 hr, in.	0.0356

It will be noted from the tabulation of results that the liquid-deposition rate, $\dot{m}_a$, is some two million times greater than the dissolution factor, $\rho_\ell \alpha k$. Therefore, the material loss rate is independent of the rate of liquid flow and deposition. By this model of material removal by dissolution, the liquid-flow rate will have to be reduced to about 10^{-6} of the level used here to effect a substantial reduction in material-loss rate.

3.4.3.3 Discussion of Potassium Tests Involving Erosion

Table 9 lists some coupon and turbine tests where wet potassium vapor impinged on metal coupons or turbine surfaces. In all these tests, there was some material removal.

In tests such as No. 1 and 5 where the oxygen content of the potassium is reported or suspected to have been "high" ("high" is not defined quantitatively by the various authors), the rates of material or damage are substantial in 100 to 2000 hr for TZM material. It may be concluded that TZM is oxygen-sensitive.

In tests such as No. 2, 3, 4, 7, 10, and 13 where the oxygen content of the potassium is reported to be low and impinging particle diameters are most probably submicronic, regardless of the theoretical

TABLE 9

EXPERIENCE ON MATERIAL REMOVAL BY LIQUID POTASSIUM

Agency	No. & Type of Test	Y %	V ft/sec	D Microns	Material	Oxygen Content ppm	Test Duration hr.	Material Removal	Remarks	
ORNL	1 Coupon	17	~2000	D<1	TZM	Unknown, high	1000-2000	High	Material removal attributed to oxygen attack	
ORNL	2 Coupon	17	~2000	D<1	TZM	Unknown, low	1000	Small		
ORNL	3 Coupon	17	~2000	D<1	Cb-1Zr	Unknown, low	3000	1-7 mils	Dissolution or corrosion attack	
ORNL	4 1 stage turbine	15	~2000	D<1	TZM	Unknown, low	2700	Unknown	No visual damage	
Philco-Aeronutronics	5 1 stage turbine	15	~2000	D<1	TZM	Unknown, high	100	Several mils	Liquid jet cut groove in rotors. Liquid collected in stator flow separation	
General Electric	6 2 stage turbine No. 1	10-15	~500	Large Unknown	U-700	Unknown	<50	Massive	Liquid sprayed into turbine inlet to increase wetness	
General Electric	7 2 stage turbine No. 2	4-5	~500	D<1	U-700	<20 ppm	2000-3000	Nil	Rotor blades	Simultaneous experiments during 2 stage turbine test.
General Electric	8 2 stage turbine, No.2	4-5	>770	30<D<100	U-700	<20 ppm	2000-3000	8-10 mils	Erosion inserts(coupon test)	
General Electric	9 2 stage turbine, No.2	4-5	>770	30<D<100	U-700	<20 ppm	2000-3000	Some	Shrouds, clips	
General Electric	10 2 stage turbine, No.2	4-5	<700	D<1	TZM	<20 ppm	2000-3000	2.8 mils	Rotor blades	
General Electric	11 2 stage turbine, No.2	4-5	>770	30>D>100	TZM	<20 ppm	2000-3000	Nil	Erosion inserts(coupon test)	
General Electric	12 3 stage turbine	8-12	~500	70>D>150	U-700 TZM,TZC	<20 ppm	1300	20-40 mils	Leading edges 3rd stage rotor blades, not clearly liquid removal	Simultaneous experiments during 3 stage turbine test.
General Electric	13 3 stage turbine	8-12	~500	D<1	U-700 TZM,TZC	<20 ppm	1300	1-2 mil rivulations	Rotor blades	
General Electric	14 3 stage turbine	8-12	>850	20<D<80	U-700 TZM,TZC	<20 ppm	1300	Substantial	Erosion inserts(coupon test) Not clearly liquid removal	

Y — Theoretical moisture content of bulk flow (reported values)
V — Liquid impingement velocity (Westinghouse estimates)
D — Liquid particle diameter (Westinghouse estimates)

moisture level or impact velocity or material tested, the loss rates observed were of the order of 1 mil/1000 hr or less. It may be concluded that where, because of the submicronic size of the impinging particles, impingement effects can be definitely assumed absent, material-removal rates are approximately the same as are calculated by the material-dissolution model used here in the tenth-rotor analysis. In fact, removal rates are probably lower than calculated.

During the General Electric two-stage turbine tests, those such as No. 8 and 9 had substantial material losses for U-700 material where the impinging drop velocities were of the order of 770 ft/sec and the impinging particle diameters were in the range of 30 to 100 μ. Losses were massive during Test No. 6, but an estimate of the liquid particle diameters could not be made on the basis of the information examined, and the particle diameters may have been very large. It must be pointed out that neither the impingement erosion model nor the dissolution model used during this analysis would predict the substantial degree of material removal experienced during Tests No. 8 and 9 on U-700 material. It is concluded that there was a combined interaction of chemical (dissolution) and mechanical (impingement erosion) removal taking place in the U-700 material. The erosion analysis model treats dissolution and mechanical removal as independent processes with no interaction. However, under identical conditions (and at the same time) as Test No. 8, TZM inserts, Test No. 11, did not show this interaction. This observation is the justification for the use of a "noninteraction" erosion model in this analysis.

The General Electric three-stage turbine tests, Tests No. 12, 13, and 14, resulted in substantial material removal from the three-stage rotor blades and in damage to erosion (coupons) inserts aft of the third-stage. This material removal may have been caused by liquid or it may have been mechanical damage from some blade retainer clips or pieces of third-stage shrouding, which broke loose during the course of the tests.

It is the Westinghouse opinion that most of the damage was caused by these broken pieces. It must be added, however, that the informed opinion of NASA and its contractors is divided with respect to the causes of this material removal and the significance of this test.

3.4.4 Conclusions and Recommendations

In a steady-flow expansion process (of the type occurring in axial flow turbines) into the thermodynamically wet region, dry or nearly dry potassium vapor supersaturates to an extent of 7- to 9-percent theoretical moisture level before substantial condensation occurs. This conclusion is based on well-founded theory[4] and substantial experimental observation.[14,26,27]

AiResearch proposes to utilize the supersaturation characteristics of potassium vapor to make the forward KTA turbine (first five stages) moisture free. Westinghouse confirms the AiResearch intent and design with respect to the extent of supersaturation in the forward KTA turbine.

The extent and rate of mechanical damage by liquid impingement of water drops is strongly dependent on the diameters of the impacting water drops, as well as on the impingement velocities and quantity of water. This statement is based on substantial systematic experimental observations[28,29] and Westinghouse steam turbine experience. There is also experimental evidence that this is true of potassium drops in low-oxygen systems:

(a) Potassium condensate particles do not damage TZM by impingement at up to 2000 ft/sec at vapor quality levels as low as 85 percent.[23]

(b) Potassium drops in the diameter range of 30 to 60 μm did not damage TZM test coupons at normal impact velocities of approximately 770 ft/sec.[17]

(c) Periodic passage of materials samples normal to potassium jets of 4.75- and 6.35-mm diameters caused substantial damage to a variety of turbine blade materials in 25 hr at only 212 ft/sec liquid impact velocity, and quote,[30] "Slightly more erosion could be obtained with a 1/4-in. (6.35 mm) stream than with a 3/16-in. (4.75 mm) stream at the test speed of 212 ft/sec."

The potential for massive impingement erosion in wet-vapor potassium turbines is obviously present on the basis of experimental evidence such as the Ford Aeronutronic single-stage test,[27] the initial GE two-stage potassium turbine tests,[17] and the AiResearch whirling arm tests just mentioned.[30*] Yet on the basis of experimental evidence such as the TZM test coupons in the later GE two-stage potassium turbine tests[17] and the ORNL single-stage potassium turbine test,[23] it is equally clear that such erosion can be avoided.

To recapitulate, the experimental evidence suggests that severe material removal will result from the impact of liquid potassium at apparent velocities of impact as low as 212 ft/sec if the liquid is in large chunks, and that no material removal will result for up to 15-percent moisture in the vapor and at apparent velocities of 2000 ft/sec if the liquid is very finely divided. This is in accordance with Westinghouse steam turbine experience that there are no magic tip-speed or quality numbers or combinations of the two which, except by coincidence, assure a tolerable level of material removal in wet-vapor turbines. The key to control of impingement erosion in wet-vapor turbines is in sufficient subdivision of the impinging liquid, where this can be reasonably accomplished, and through liquid removal, where sufficient

*The GE three-stage test is not included in this listing because Westinghouse is of the opinion that most of the material-removal experienced during this test was from broken pieces of the turbine interacting with the third rotor and was not the result of liquid removal.

subdivision is doubtful. In this connection, a natural conservative tendency to decrease turbine tip-speeds as a means of combating erosion through a reduction in apparent liquid impact velocities on the rotor blades can prove to be misleading. If a reduction in turbine rotor blade speed calls for an equivalent reduction in the stator spouting velocity, this would lower the aerodynamic force available for subdividing and accelerating stator discharged liquid. The resulting increase in diameter of the drops impacting the rotor can more than compensate for the reduction in apparent liquid-impact velocity.

The AiResearch KTA design is essentially two turbines, a moisture-free, or nearly so, forward turbine and an aft turbine with substantial moisture in the bulk-flow and substantial collection of that moisture on the turbine surfaces. Collected moisture traveling along the casings of the turbine, in Westinghouse opinion, will cause sufficient damage to turbine rotor shrouds and seals to warrant casing moisture removal in the aft turbine. Because of the uncertainties in the nature of the output of the external moisture separator which supplies the aft turbine, it is recommended that casing moisture removal be used after every stage of the aft turbine.

An analysis of the tenth-rotor blades for material removal by stator-discharged liquid has been carried out. Providing (1) the moisture on the casing ahead of this row is removed effectively, (2) the stage remains a clean aerodynamic design, and (3) there is greater than 1/8-in. axial spacing between stator exit and rotor inlet, the damage to refractory alloy TZM blades by mechanical removal through impinging drops is expected to be negligible. An analysis of collected-moisture discharged from the stators predicts that the largest drops impacting the leading edges of the rotor blades will be around 100-μm diameter. The maximum normal impact velocity of these drops will be approximately 900 ft/sec.

Previous calculations[3] predict that to cause appreciable mechanical material-removal damage (1 mm/year) to TZM by 100-μm diameter drops of potassium, normal impact velocities in excess of 1300 ft/sec are required. This conclusion is based on the extrapolation of systematic water-drop impingement tests on steam turbine blade materials to a potassium-TZM combination by a systematic procedure which effects a correlation and offers an explanation of the peculiarities of the water system test results.

It is recommended that systematic drop-impingement tests be carried out for potassium-refractory metal turbine blade material combinations to eliminate the need to extrapolate water-drop data on steam turbine blade materials to potassium impact on refractory alloys. This is recommended even though Westinghouse believes that the extrapolation technique used is accurate enough for the purposes of this analysis.

Proposed potassium turbine blade materials have a certain amount of solubility in liquid potassium. Material loss by dissolution of the blade material into potassium, even in the absence of serious impingement effects, is a distinct possibility. Some evidence of this is present in all the turbine test results reviewed during this study. A theoretical calculation for the leading edges of the tenth-rotor blades of the KTA predicts dissolution-material loss-rates of 0.2 to 0.4 mm per year. Not much reliance can be placed on this calculation because of theoretical and material property uncertainties.

3.5 Overall Turbine Heat Transfer Analysis

3.5.1 General

The overall turbine heat-transfer analysis was performed concurrently with the mechanical design, since much of it depends on metal temperature, temperature gradients, thermal expansion, etc. Pertinent

details of the thermal analytical study are discussed, and final results are presented in this section.

Several digital computer programs were utilized in this study, and brief descriptions of each of these analytical tools are in Appendix E. The principal tools used in the heat-transfer analysis were Programs 5688 and 5750 to produce steady-stage and transient temperatures, respectively. Each of these programs include provisions for three-dimensional heat-transfer by conduction, convection, and radiation and for heat-sources and -sinks and finite cooling flows. The relaxation method is employed with a finite number of nodes. Program 5750 is limited to 300 nodes, the limit reached in the present analysis.

The thermal analysis proceeded from the front (hot-end) to the rear of the turbine, as input data for more and more nodes were generated. This procedure was stopped at several points, and the appropriate boundary temperatures imposed so that preliminary solutions could be obtained. The result was that many configuration changes were made, and the mechanical design was well under way before the rear-end of the turbine and the limiting number of nodes was reached. The final extent of the computerized analysis includes the entire front-end of the machine to the second-stage stator and the entire turbine rotor, including bearings. Hand calculations were made to establish steady-state temperatures and heat flux in the remainder of the turbine--the stators, outer housing, exhaust pipe, and rear thrust-bearing support structure.

The results of an overall heat-transfer analysis are useful in these ways:

(a) Provide heat losses for the system which defines the thermodynamic performance penalty.
(b) Provide temperature distributions for candidate component designs and the necessary information for evaluation of

physical and mechanical properties, stresses, dimensional changes, functional performance, etc.

(c) Provide a medium for the synthesis of component parts into a compatible mechanical system.

3.5.2 Boundary Conditions

Figures 58 and 59 show the total pressure and total temperature distributions through the turbine along the main flow path. Note that the mechanical and aerodynamic design points have identical exhaust conditions but different turbine inlet conditions as shown below:

	Aerodynamic Design	Mechanical Design
Inlet temperature, °F	2100	2150
Inlet pressure, psia	165	190
Inlet superheat, °F	71	71

Since the inlet superheat is the same for both mechanical and aerodynamic design-points, it was decided to maintain this equivalence at each stage. Thus, the mechanical design-point overtemperature is 50°F at the inlet and decreases by 5°F at each succeeding stage. The inlet pressure at each stage was the saturation pressure corresponding to the aerodynamic design-point saturation temperature plus the required overtemperature. These distributions define the heat-source boundary conditions for the thermal analysis and the information necessary to compute heat-transfer coefficients and adiabatic wall temperatures. The complete pressure schedule throughout the turbine is also defined. This schedule depends on local pressure ratios predicted by the aerodynamic analysis and the total pressure distribution through the turbine for the mechanical design-point. The various cavity pressures are established by the static pressure at the locations in the flow path to which the cavities are vented.

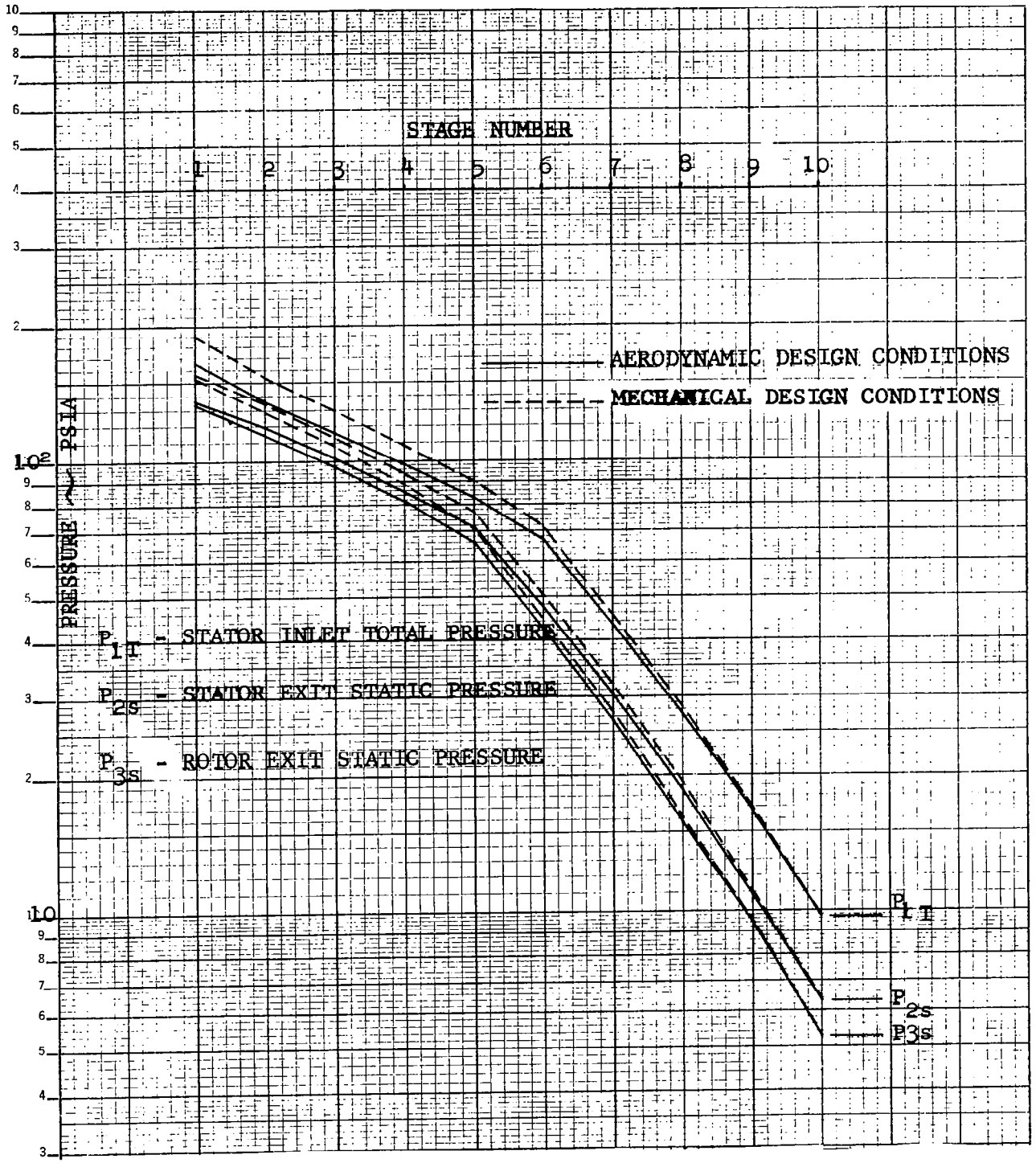

KTA DESIGN CONDITIONS, TURBINE

PRESSURE DISTRIBUTION

FIGURE 58

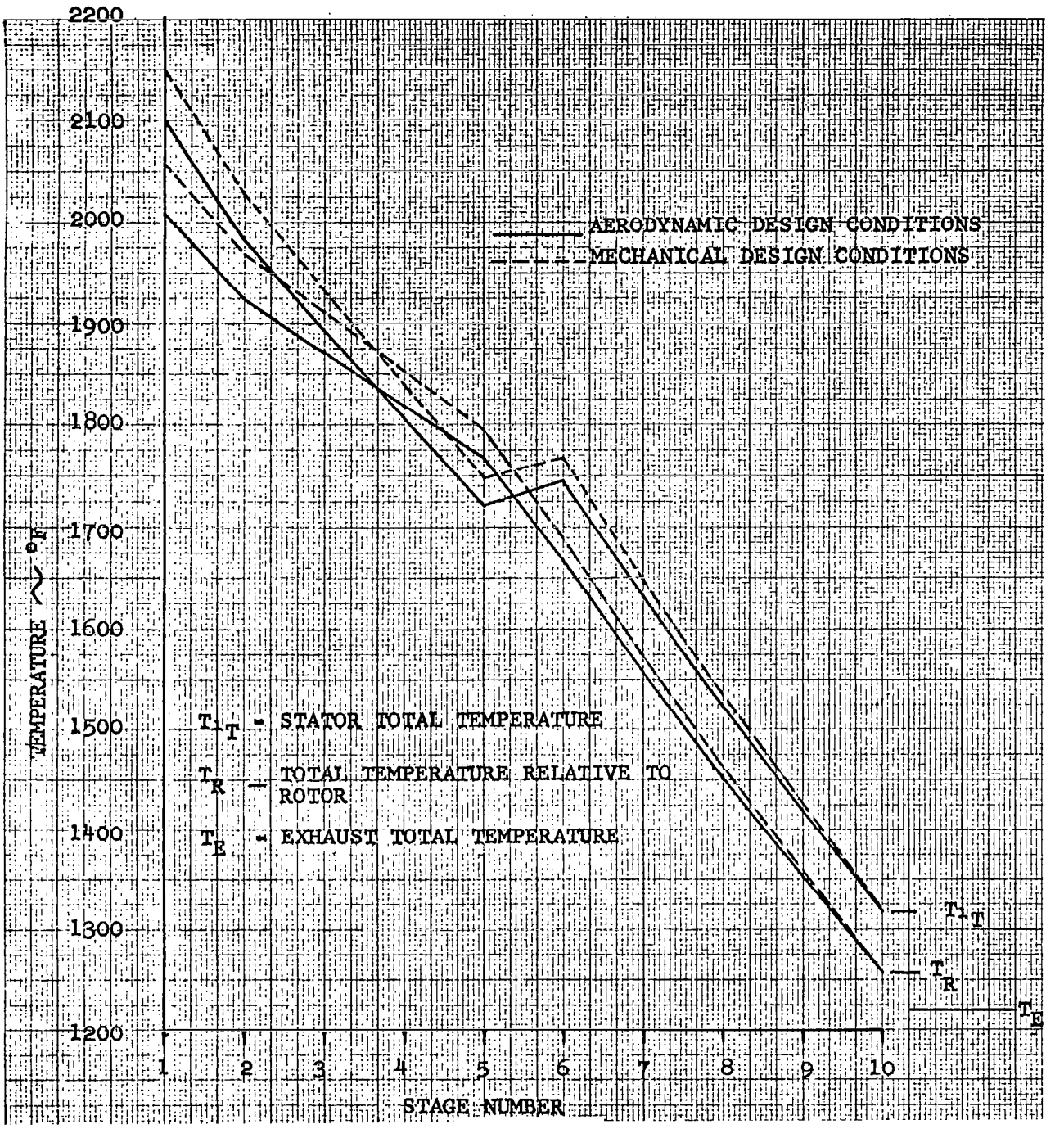

KTA DESIGN CONDITIONS, TURBINE

TEMPERATURE DISTRIBUTION

FIGURE 59

The heat-sink temperatures are defined by the inlet and exit lubricant temperatures at each bearing. These liquid potassium temperatures were selected as follows:

Bearing	Inlet Temp, °F	Exit Temp, °F
Front journal	900	950
Rear journal	940	1000
Thrust, loaded side	900	1000
Thrust, unloaded side	940	1000

The mechanical design-point is an off-design condition not necessarily possible, as defined by Figures 58 and 59. A normal approach to the problem would be to perform the thermal analysis using the aerodynamic design-point and adding a fixed amount to the resulting temperatures of critical components, thus providing a safety margin when computing stresses, creep rates, strength properties, etc., of these components. However, the present approach was taken due to contractual requirements. By setting the amount of superheat (negative when flow is supersaturated) at each stage equal to the superheat at the aerodynamic design-point, the relationship between metal and saturation temperatures at any point in the turbine will be essentially identical. This results in potassium condensation on the same surfaces and in equivalent amounts for both design-points. The metal temperature distributions for the two design-points will be similar, with only a generally higher temperature level using the mechanical design-point.

The boundary temperature at the rim of each turbine disk is determined as follows: For each turbine rotor stage operating below the saturation line (2 through 10), the rotor blades will be very close to the saturation temperature corresponding to the rotor inlet static pressure. The reasoning is that the boundary layer on the blades will be in equilibrium-flow because the relative velocity is zero at the

blade surface, regardless of the condition of the free-stream flow outside the boundary layer, supersaturated or equilibrium. Since the flow expands to a lower static pressure through each of these rotor stages, there will be heat-transfer from the leading edge toward the trailing edge regions in each. This will result in condensation near the leading edge and revaporization of the condensate as it flows toward the trailing edge. In 8 of these 9 stages, this vaporization is aided by heat conduction from the disk, so that a wet film will exist mostly in the inlet region and a dry film near the exit. Since the heat-transfer coefficient is at least two orders of magnitude greater for a wet than a dry film, the metal temperature of the blades will be much closer to the inlet saturation temperature. This approximation results in conservatively high boundary temperatures which are within a few-degrees accuracy. Thus, many man-hours are saved which could be spent computing exact boundary temperatures. This approximation could not be made in the first-stage rotor because the flow is superheated therein. In this case, it was necessary to compute the local adiabatic wall temperature and heat-transfer coefficient distributions. The rim temperatures used at each of the turbine wheels are printed in black in Figure 63, page 164.

The stator vane temperatures, where the flow is below the saturation line, are influenced by boundary layer condensation in the similar fashion. However, the first- and second-stage stators are in superheated flow, and the rest are not included in the computerized part of the thermal analysis. Only the first-, second-, and sixth-stage stators are significantly affected by heat-sinks; these effects will be described later. The temperatures of the remaining stators are dominated by the turbine through-flow so that the metal temperatures were approximated by plotting a smooth curve of temperature-versus-length through points of saturation temperature at the inlet position. The results are reflected in Figure 63, page 164.

3.5.2.1 Materials and Fluid Properties

The thermodynamic properties of potassium used in the thermal analysis were taken from Reference 5. The transport properties of potassium used are from Reference 31. The physical properties of the refractory metals used in the turbine construction are those presented in Appendix A. Some emissivity data on TZM was found in Reference 32.

3.5.2.2 Calculation of Heat-Transfer Coefficients and Adiabatic Wall Temperatures

The local heat-transfer coefficients along streamlines over vanes, blades, and shrouds in the main flow-path were computed using the modified Ambrok equation, Reference 33. A digital computer program, 5700, was used for this task and is briefly described in Appendix E. Reference 34 provided data for heat-transfer coefficients on rotating disks, and Reference 35 was used for rotating concentric cylinders. Natural convection heat-transfer coefficients in the rotating cavities inside the turbine rotor (where centrifugal forces are high) were computed using empirical equations from Reference 36. Condensation and boiling coefficients were estimated from data presented in Reference 37. Heat-transfer coefficients in other areas were estimated, using parallel plate and circular pipe flow-solutions (both fully developed flow and thermal-entry-length) as guides.

In the main flow-path, the local adiabatic wall temperatures, T_{aw}, along dry vanes and blades must be determined from the local recovery enthalpy, h_{aw}, and the local free-stream static pressure, P_{∞}.

$$T_{aw} = f\ (h_{aw},\ P_{\infty})\ \text{from Mollier Diagram}$$

where:

$h_{aw} = h_\infty + r_c U_\infty^2/2g_c$, r_c is the recovery factor

$r_c = P_r^{*1/2}$, for laminar flow in boundary layer

$r_c = P_r^{*1/3}$, for turbulent flow in boundary layer

$P_r^* = \mu^* C_p/K^*$, Prandtl number evaluated at local reference temperature

$T^* = t_\infty + 0.5(T_T - t_\infty) + 0.22(T_{aw} - t_\infty)$, reference temperature

The area of greatest importance in applying the above methods of computing T_{aw} and h_∞, the heat-transfer coefficient, is the first-stage stator, since it is the primary heat-source for vaporizing the liquid potassium passing through the front labyrinth seal. Presented in Figures 60 through 62 are the velocity, adiabatic wall temperature, and heat-transfer coefficient distributions along the first-stage stator vanes for both pressure and suction sides at the hub and tip radii. Accurate utilization of the variable boundary conditions in the first-stage stator required the use of a larger number of nodes in that area, since only a constant temperature and heat-transfer coefficient can be applied to each node.

3.5.2.3 Power Losses

The frictional power losses along the turbine rotor are converted into thermal energy; hence, they must be included as heat sources in the thermal analysis. The bearing and the viscoseal losses are given in Table 2, Page 8. The power loss in the front labyrinth seal was

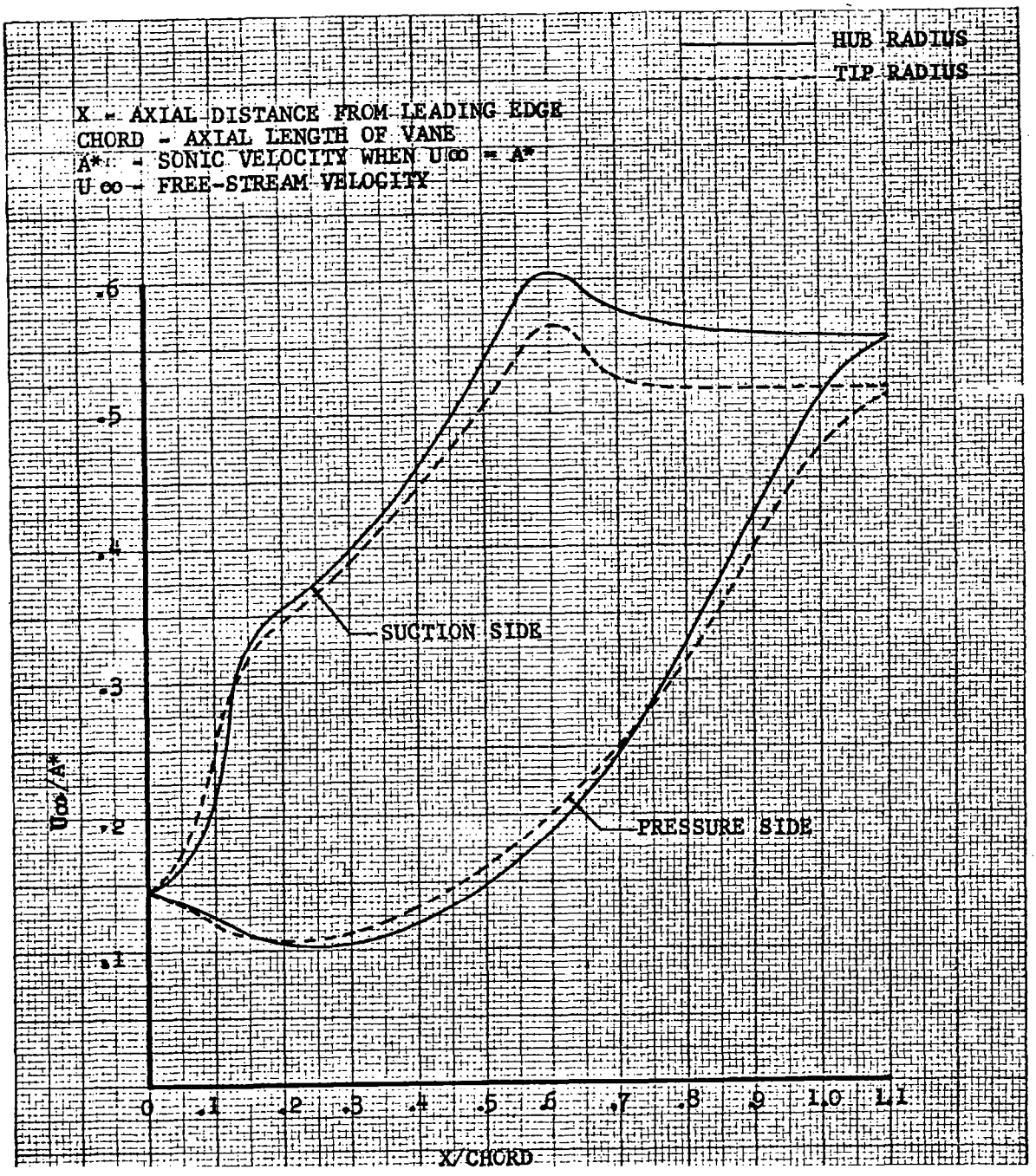

KTA FIRST-STAGE STATOR VELOCITY DISTRIBUTION

WITH AXIAL DISTANCE

FIGURE 60

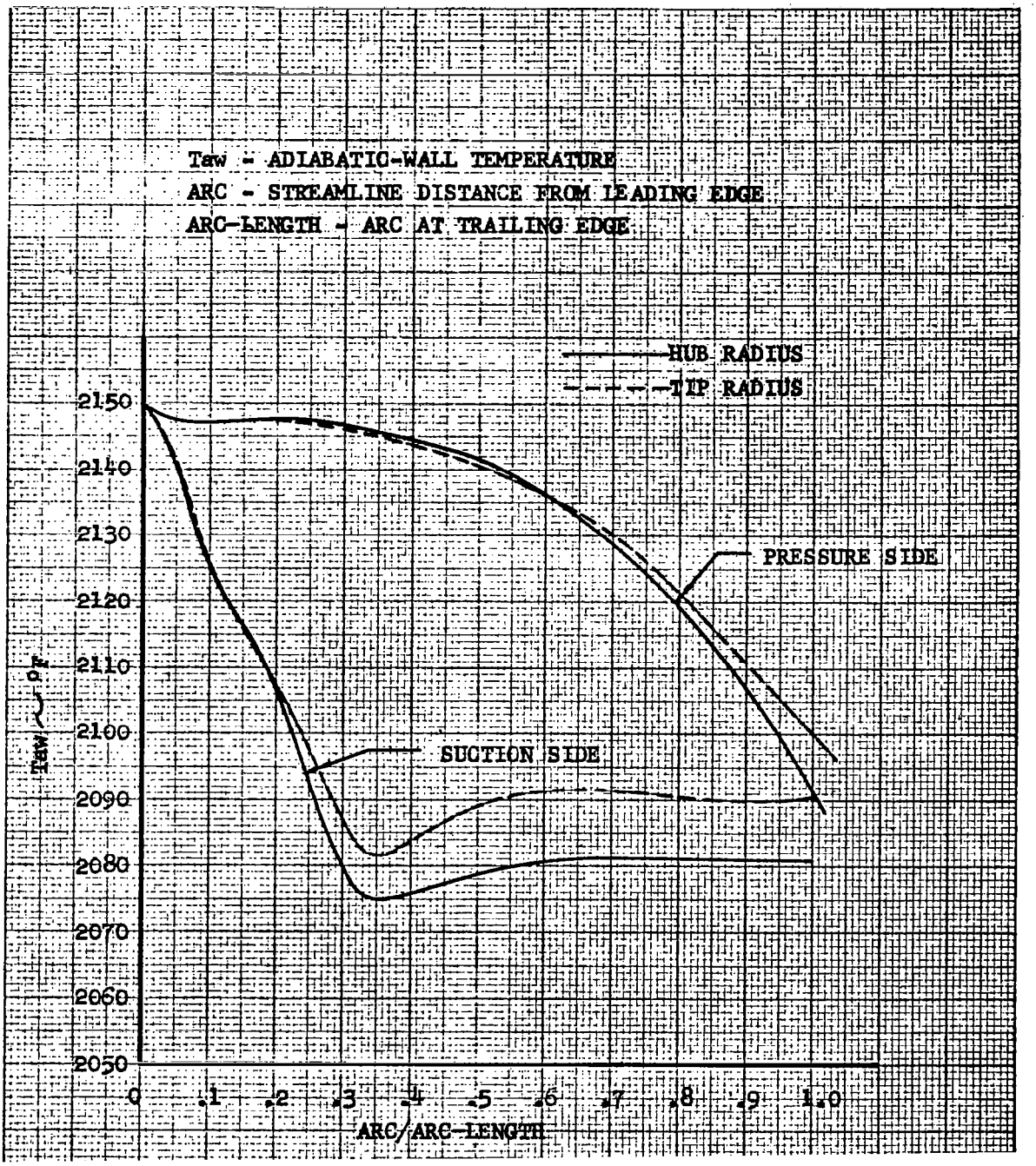

KTA FIRST-STAGE STATOR TEMPERATURE

DISTRIBUTION ALONG VANES

FIGURE 61

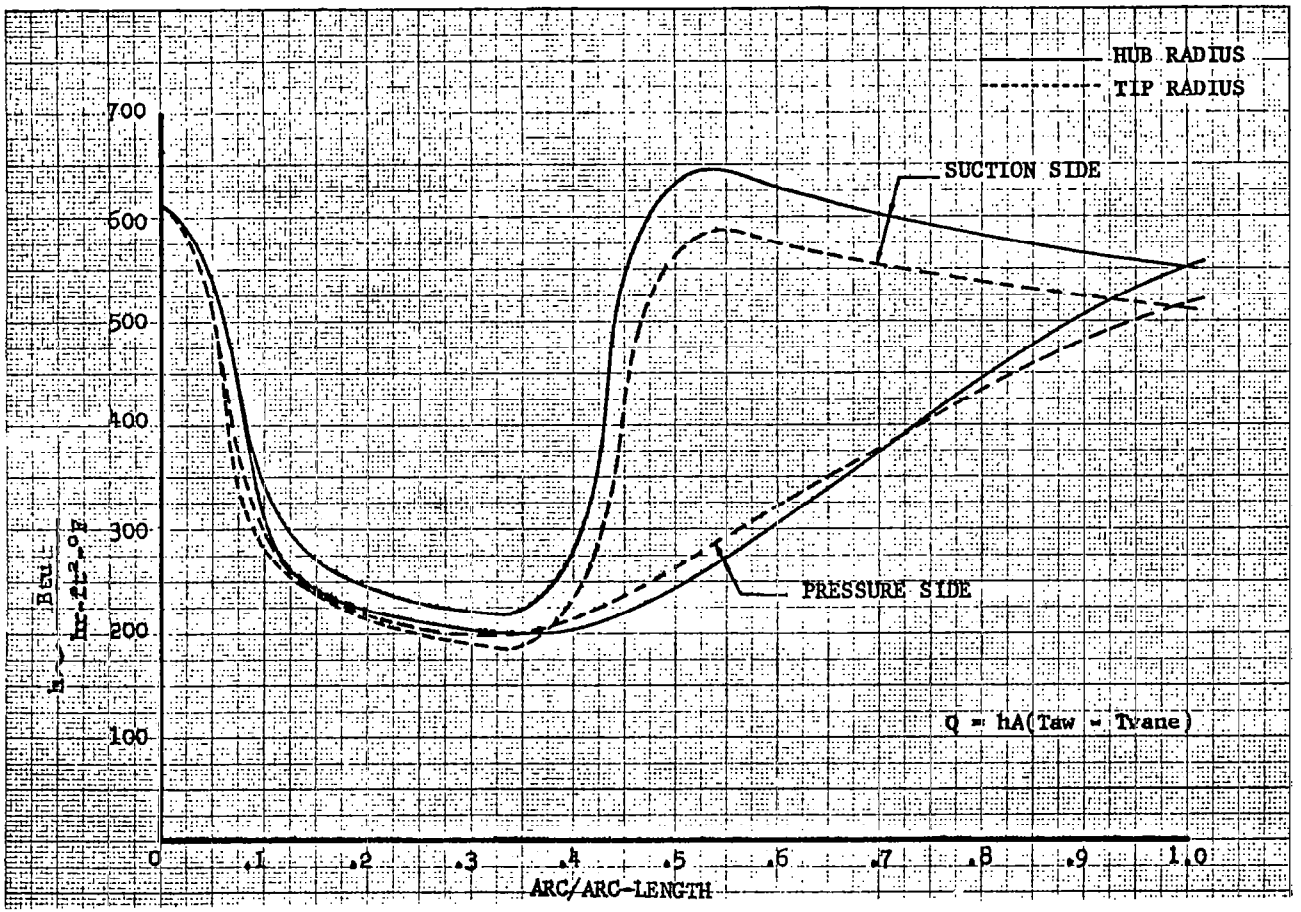

KTA FIRST-STAGE STATOR HEAT TRANSFER

COEFFICIENT DISTRIBUTION

FIGURE 62

calculated at approximately 0.03 kw; those in the rest of the seals were neglected. The windage loss on the turbine wheels was also calculated and is given in Table 2. Most of this loss occurs near the rim of the disks and is generated in the vapor boundary layer in close communication with the turbine through-flow. Therefore, the effect of this windage loss, from a thermal standpoint, was also neglected, although it was included as a shaft-power penalty.

In addition to the actual heat sources described above, it was necessary to include an "apparent heat-sink" to simulate the drop in total temperature due to throttling the leakage flow through the front labyrinth seal. The pressure drops from 155 to 48 psia, and the resultant drop in total temperature is 284°F due to adiabatic expansion. Additional temperature drop results from heat-transfer effects.

3.5.3 Steady-State Thermal Analysis

The final results of the steady-state thermal analysis are presented in Figure 63. An isothermal map (lines of constant temperature) is shown above the centerline of the turbine, and a heat-flux map is shown below the centerline. The arrows indicate the direction of heat flow with the heat quantities given in watts. The solid arrows represent heat conduction in metal parts and the dashed arrows heat-transfer by radiation. Heat-transfer by convection cannot be adequately represented by a map of this type. In interpreting the results of the steady-state thermal analysis quantitatively, it is necessary to supplement the temperatures and heat-flux values with pertinent facts regarding the thermal aspects of the mechanical design. The following data and discussion are segregated according to location in the turbine, proceeding from front (hot-end) to rear.

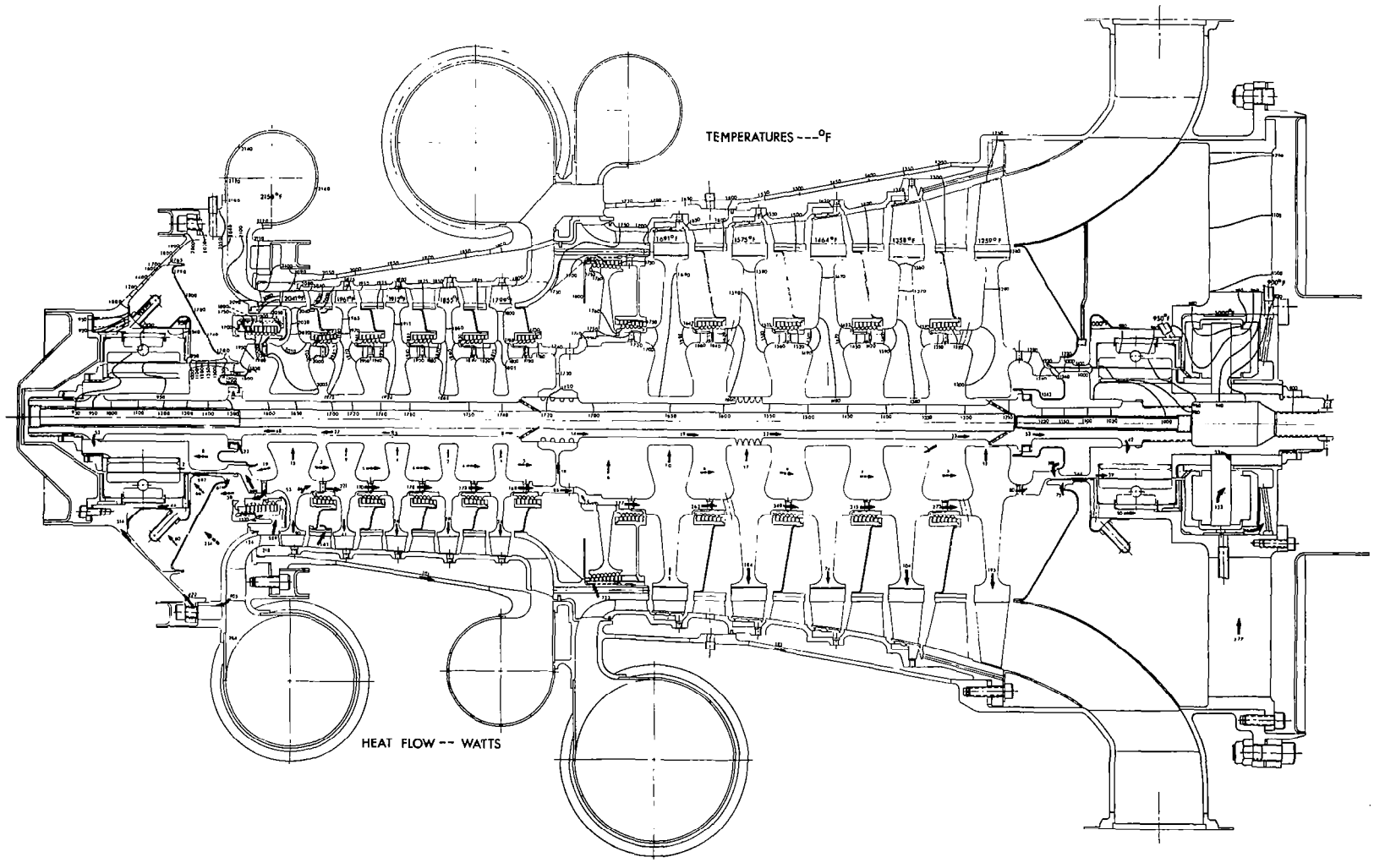

KTA TURBINE TEMPERATURE DISTRIBUTION AND HEAT FLOWS

FIGURE 63

3.5.3.1 Front Journal Bearing

The total heat-transfer into the journal bearing from the turbine inlet, first-stage stator, and tie-bolt is about 1.7 kw. When this is added to the frictional power loss in the liquid potassium of the bearing at the rotor front end and along the stub-shaft including the visco-seal, the total heat picked up by the lubricant (and coolant) is 3.8 kw. The liquid flow rate required to maintain a lubricant temperature rise of 50°F is about 4 gal/min.

Figure 64 is an enlargement of the turbine hot-end with the isothermal map. The temperature variation along the journal and the bearing pads is found to be 20° to 40°F. The resulting thermal distortion of the bearing surfaces are not severe in view of the low-expansion bearing materials and the 3 deg of freedom of the pivoted pads.

The bearing housing (containing liquid potassium) is surrounded by low-pressure cavities, two stationary and one rotating. These are labeled Regions A, B, and C in Figure 65. The stationary cavities, Regions A and B, are each vented by external lines connected to the alternator scavenge system. Region C is vented into the bearing cavity through holes in the stub-shaft under the journal sleeve. A liquid-vapor interface is positioned approximately at the bore of the journal sleeve and is established by the radial-pressure gradient in the liquid resulting from the centrifugal force of rotation at shaft speed. Radial slots are cut in the journal spacer to ensure communication between the interface and the liquid at the journal radius where the pressure is 53 psia. The pressure in Region C is the saturation pressure corresponding to the average interface temperature of about 940°F. Since all the metal surfaces in Region C are at or above this temperature, latent heat-transfer by condensation and re-evaporization is prevented. The pressure in Regions A and B is lower than the saturation pressure corresponding to 900°F, 0.44 psia, so that latent heat-transfer will

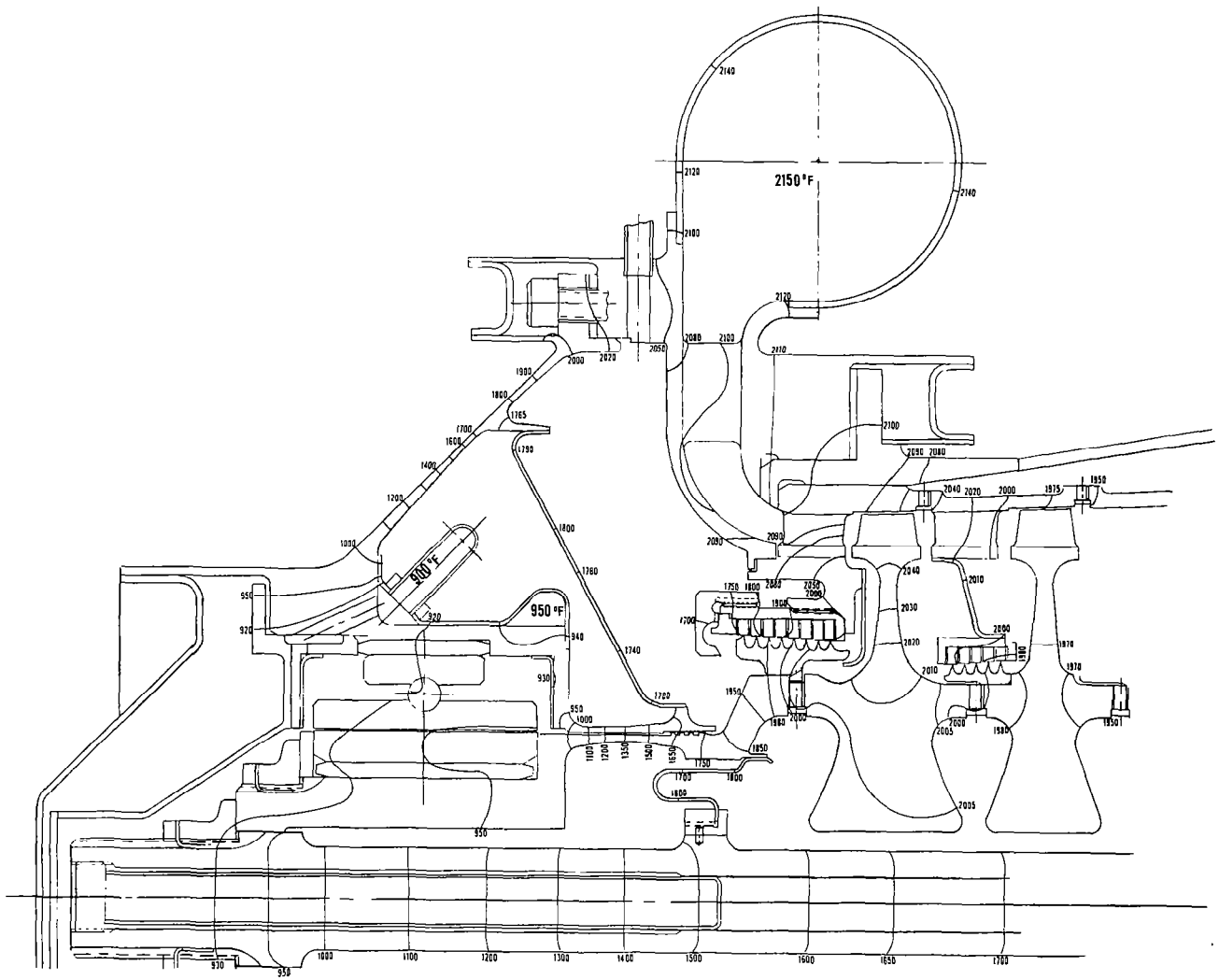

FIGURE 64

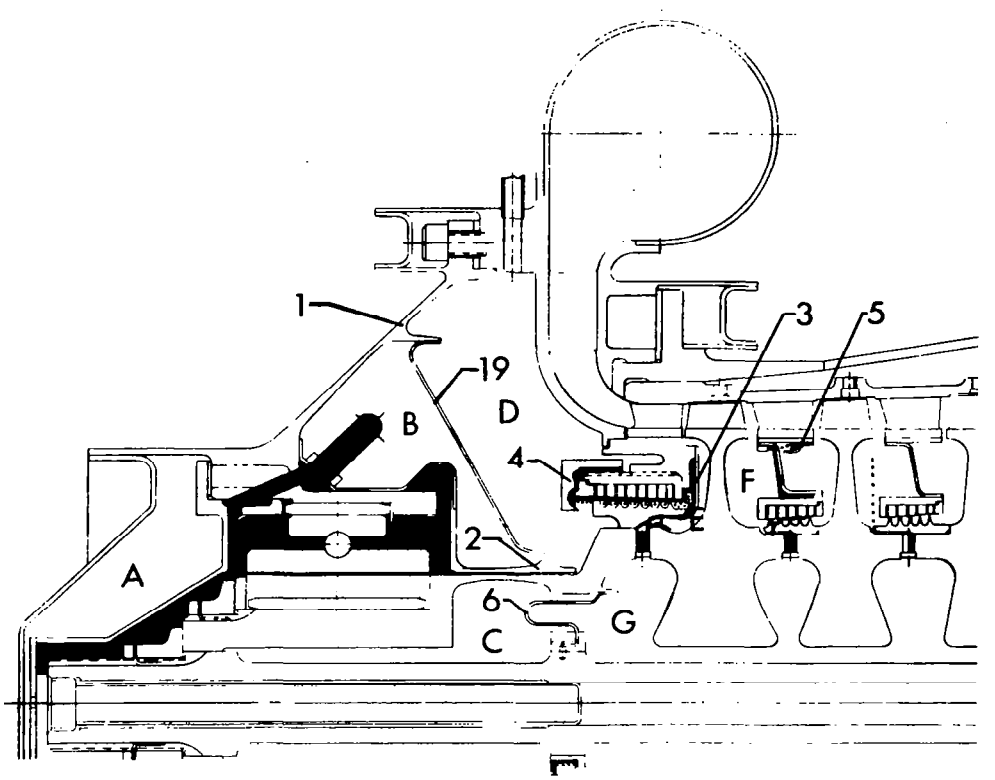

LETTERS CORRESPOND TO "REGIONS" IN TEXT
NUMBERS CORRESPOND TO "ITEMS" IN TEXT

KTA TURBINE FRONT-END, SURFACES AND
REGIONS WETTED BY POTASSIUM

FIGURE 65

not occur in these regions either. It is necessary to vent these cavities so that any potassium leakage into them will not cause pressure build-up with resulting latent heat transfer short-circuiting the heat-flow paths.

Very high-temperature gradients occur in the conical outer housing (Item 1) that supports the journal bearing, the thin-shell section of the stub-shaft, and the concentric cylinder supporting the viscoseal stator (Item 2). These parts have been carefully designed with enough flexibility to tolerate the relative thermal expansion.

3.5.3.2 Front Viscoseal

The viscoseal is designed to contain the liquid within the bearing. The pressure imposed on the liquid-vapor interface within the seal is the pressure in the cavity labeled Region D (Figure 65). This cavity is vented back to the seventh-stage inlet, where the pressure at the mechanical design-point is about 46 psia. Allowing a reasonable pressure drop in the external vent tubes, which carry the front labyrinth seal leakage flow, a cavity pressure of 48 psia was selected. The bearing pressure was selected at 5 psi above this in order to provide a pressure differential for the viscoseal to pump against. Thus the interface position is governed by the required wet-length for pumping, about 1/8-in. for 5 psi.

One of the objectives in the steady-state thermal analysis is to achieve mass equilibrium at the viscoseal interface since a net mass transfer between the working fluid loop and the bearing lubricant loop is undesirable. Mass equilibrium is satisfied with heat equilibrium since condensation or vaporization is required to transport mass across the interface. Thus, equilibrium can be approximately satisfied when the average metal surface temperature at the interface position is equal to the saturation temperature at the interface pressure; this is 1656°F at the mechanical design-point. This condition was attained in

the thermal analysis by trial and error, altering the stub-shaft configuration until the proper thermal conductance distribution was found.

The sheet-metal cone welded to the viscoseal stator and to the conical outer housing serves as a radiation shield as well as a pressure vessel. It was found that internal insulation is not required since the heat loss by radiation is only a small part of the total.

3.5.3.3 Front Labyrinth Seal

The leakage rate through the front labyrinth seal is about 0.036 lb/sec at the mechanical design-point (0.031 lb/sec at the aerodynamic design-point). The leakage flow enters the high-pressure cavity, Region E, Figure 65, at a pressure of 156 psia and 2095°F total temperature. It is notable that the total temperature has dropped 55°F due to isenthalpic expansion through the first-stage stator. As the vapor flows radially inward to the labyrinth seal inlet, the pressure drops slightly (1 psi), and it is cooled to a temperature of about 2030°F or to a superheat of about 20°F. The vapor is discharged from the seal with 75°F of superheat (1730°F) and is heated an additional 100°F as it passes through Region D and through the inlet scroll flange.

Early in the thermal analysis, it was found that, due to the liquid potassium lubricant-coolant in the front-end journal bearing acting as a heat-sink, the first-stage turbine wheel tends to be cooled to the extent that the surface temperatures in the innermost parts of the high-pressure cavity, Region E, are reduced below the equilibrium saturation temperature of the potassium in that cavity. This results in condensation on the high-pressure side of the front labyrinth seal rotor and at the first curvic coupling. The amount of condensate formed is substantial and should not be allowed to re-enter the flow path. Therefore, the problem of handling the condensate and providing for its vaporization arises.

It would be desirable to prevent condensation in the high-pressure cavity by minimizing the heat transfer to the front bearing compartment. The only means of doing this would be (1) designing a front stub-shaft with a very low thermal conductance or (2) using a very high bearing lubricant temperature (1900°F). Neither of these means is feasible due to the limitations imposed by the primary functions of these components.

The geometry of the high-pressure side of the labyrinth seal rotor is such that the condensate formed will be directed by centrifugal force into a baffle plate, Item 3, which forms a high-pressure enclosure at the labyrinth seal inlet. During terrestrial operation in the vertical attitude with the hot-end up or in a 0-g environment, the moisture collected in this enclosure cannot escape back into the high-pressure cavity due to centrifugal force, but is dragged into the seal.

Some boiling will occur in the outer part of the enclosure, where the surface temperatures are above the boiling point, 2008°F, and the rest of the liquid will eventually pass into the seal along with additional condensate which forms on the seal stator at the inlet and through the first three to six labyrinth stages. In the final stages of the seal, the pressure drops sufficiently so that the boiling point is below the seal stator metal temperatures. Since most of the liquid within the seal is maintained in contact with the seal stator by centrifugal force, vaporization will begin. Although some of the liquid within the seal will come into contact with the rotating knives and be vaporized thereon, this will merely cause more condensation on the high-pressure side of the seal rotor, and no net reduction in liquid mass rate will result. However, this will produce a larger temperature gradient in the seal rotor than that indicated by the thermal analysis, and this tends to increase the seal clearance, albeit a negligible amount.

Finally, a substantial amount of liquid is discharged from the seal entrained in the annular jet. The moisture collector-boiler, Item 4, attached to the low-pressure side of the seal stator is designed to complete the vaporization of this remaining liquid. Although the liquid will eventually be vaporized regardless of where it goes within the low-pressure cavity (Region D), it cannot be allowed to strike the conical sheet metal pressure vessel-radiation shield, Item 19, because the resulting fluctuating cold spots would eventually produce fatigue failure. The moisture is collected in the collector-boiler by jet and centrifugal force and will be vaporized as it passes through the slots around to the outer part of the seal stator.

All of the heat required to boil the liquid must come from the only heat sources available--the inlet potassium vapor passing through the first-stage stator vanes and the seal leakage flow. Since there is a large variation in total temperature as the vapor expands through the vanes, a very detailed heat-transfer analysis was required in this area as explained earlier. The heat flow to the boiler causes an axial temperature drop in the seal stator of 300°F; this has an effect on the seal clearance, decreasing it from inlet to exit.

The amount of condensate formed under the front labyrinth seal for the stub-shaft heat-source is tabulated in Table 10, with the heat and mass rates at all the condensation sites in the turbine caused by heat-transfer. The total amount of condensation throughout the turbine is also given, but the only place where heat-transfer directly increases the amount of moisture in the flow path is at the sixth-stage stator and the interspool region. This amount is about 0.0015 lb/sec, which is 0.075 percent of the turbine through-flow.

3.5.3.4 Interstage Labyrinth Shaft Seals

A significant amount of condensation will also take place at the first- to second-stage rotor curvic coupling and interstage labyrinth

TABLE 10

KTA TURBINE, RATES OF CONDENSATION
DUE TO HEAT TRANSFER

Location	Heat Rate, w	Mass Rate, lb/sec
Front Curvic Coupling and Labyrinth Seal Rotor	1186	0.00153
Interstage Curvics:		
Stages 1-2	141	0.000182
Stages 2-3	42	0.000053
Stages 3-4	32	0.000040
Stages 4-5	26	0.000033
Stage 5 - Piston	6.4	0.000008
Thrust Balancing Piston, High-Pressure Chamber	723	0.00089
Stages 6-7	89	0.000107
Stages 7-8	48	0.000056
Stages 8-9	61	0.000070
Stages 9-10	0	0
Rear Stub-Shaft (under viscoseal)	201	0.000204
Rear Viscoseal Stator	80	0.000089
Tie-Bolt, Rear-End at Sheet Metal Fastener	18	0.00002

seal. The amount condensed here is an order of magnitude smaller than the amount condensed under the front seal, but to be conservative, it should also be prevented from entering the flow-path in the liquid phase. The condensate formed under this interstage seal rotor is collected in an annular groove and injected into the first-stage of the seal through a very small hole. As this condensate passes through the seal, the boiling point drops and vaporization will be complete; the heat of vaporization being supplied by additional condensation on the outer surface of the seal stator.

This additional condensate will remain in contact with the surface due to surface tension and, when operating in a gravitational field, it will form a puddle at the lowest point, the annular space between the sheet metal and the seal stator. This space will become flooded and the overflow will migrate outward along the sheet-metal surface, assisted by the centrifugal force of the rotating vapor between the sheet metal and the first-stage disk (Region F). The liquid will also begin to rotate as it moves outward and will pass through a small hole in the sheet metal into a baffle plate (Item 5), partially enclosing a lower pressure region under the second-stage stator base. The liquid collected in this low-pressure region will be boiled away with heat supplied by the vapor passing through the second-stage stator vanes and conducted through the vanes and base. The evaporating vapor can escape around the end of the baffle plate and re-enter the flow-path at the second-stage rotor. When operating in a 0-g environment, the puddle at the seal stator will not necessarily be formed, and a small dam may be needed to prevent the condensate from migrating around the high-pressure end of the stator base and re-entering the flow path, otherwise the 0-g operation is similar to terrestrial operation in the vertical, hot-end-up position. The only differing effect expected from the two modes of operation is that the seal stator will run slightly cooler in terrestrial operation due to the subcooling of liquid under the surface of the puddle.

The remaining curvics and seals in the first five stages of the turbine will have a small amount of condensation in them. However, the amount is so small that no moisture control measures are necessary. In fact, if the interstage seal rotors in these areas were reversed so that the curvics were on the low-pressure side of the seals, there would be no condensation at all, and the metal temperatures around these curvics would be slightly lower. Therefore, this change is recommended, although it was discovered too late to change the thermal analysis on the final layout drawing.

The remaining curvic couplings on the low-pressure turbine rotor and the seals will also have a small amount of condensation in them, with the exception of the ninth- to tenth-stage curvic that is dry. However, as with the smaller rotor curvics mentioned above, the amount of condensate formed is so small that no moisture control is needed, and reversing the interstage seal rotors would prevent condensation entirely and lower the metal temperatures slightly.

3.5.3.5 Thrust-Balancing Piston

A relatively large amount of condensation occurs on the high-pressure side of the thrust balancing piston, Item 8 of Figure 66. All surfaces exposed to this high-pressure chamber, Region J, will have condensate on them to some extent, although most of the condensate will form on the piston itself. Some formed near the inner labyrinth seal inlet, Item 9, and will be dragged into the seal and vaporized due to the reduction in its boiling point, the heat of vaporization being supplied by an equivalent amount of additional condensation on the outer surface of the seal stator. All the condensate remaining in the high-pressure chamber will be slung outward by the rotating piston and evaporate in the chamber at a pressure of 71 psia.

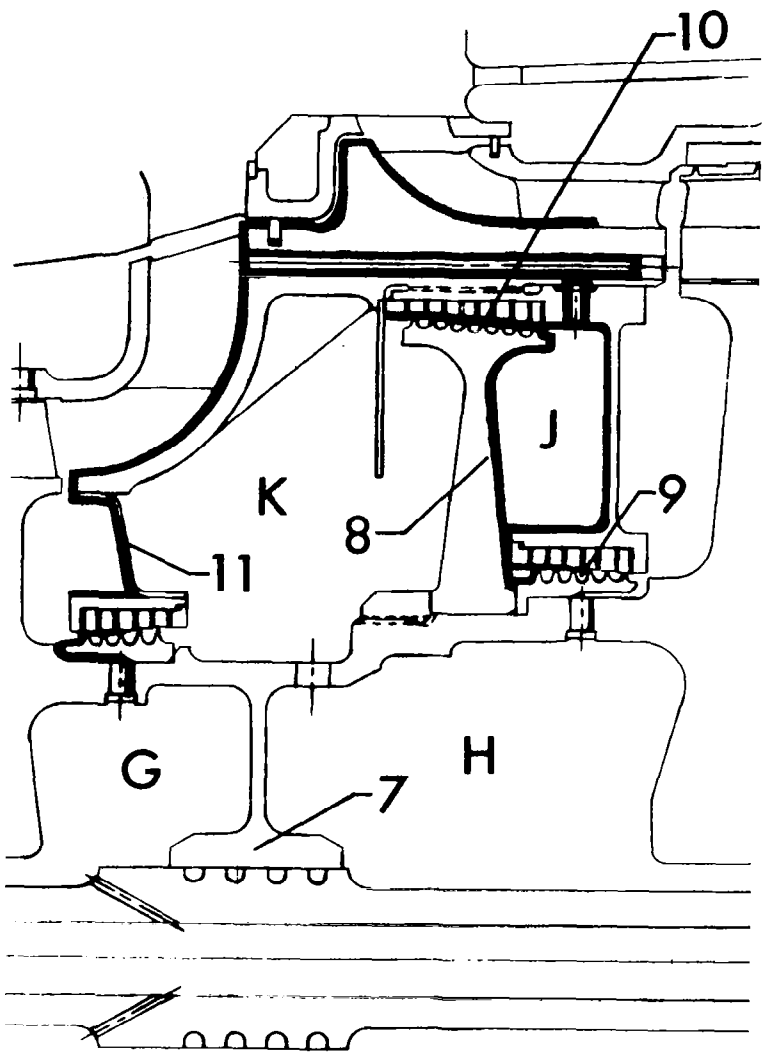

KTA TURBINE THRUST-BALANCING PISTON AND INTERSPOOL REGION, SURFACES WETTED BY POTASSIUM

FIGURE 66

When operating in a 0-g environment, all the condensate will easily be dragged into the outer labyrinth seal, Item 10, since it is forced to collect on the outermost surface of the high-pressure chamber. As the liquid passes through the outer seal, its boiling point drops with the pressure drop and vaporization begins. The heat of vaporization is supplied from the sixth-stage stator, which has an inlet pressure essentially equal to that at the outer seal inlet. The inlet vapor to the sixth-stage stator is saturated so that the heat drawn inward to vaporize the liquid within the seal will produce more condensation in the main flow-path. As the vapor expands through the stator, however, the pressure drops so rapidly that the boiling point drops below the vane metal temperatures, and some of the potassium, condensed at or before the inlet, will return to the vapor phase before reaching the stator exit. It is estimated that all of the condensate passing through the outer piston seal will be vaporized before reaching the exit. However, in case any moisture is discharged from the seal, it will be trapped behind the shroud on the low-pressure side of the piston where vaporization will be completed. The shroud also serves to reduce the windage loss by the rotating piston. It is possible that the sheet-metal shroud will develop fatigue cracks due to fluctuating thermal stresses associated with cold spots where liquid drops contact the surface. This would not be catastrophic, however, since the shroud carries no load. It is necessary to prevent this cold liquid from contacting load-carrying parts, such as the sheet-metal diaphragm, Item 11, that supports the fifth-stage shaft seal.

During terrestrial operation with the hot-end up, the condensate formed on the high-pressure side of the rotating piston will not necessarily be dragged into the outer piston seal but will tend to collect in the lower outside corner of the chamber. Therefore, a small hole is provided connecting this corner to the first-stage of the piston seal, with slots cut in the first- to second-stage foil spacer. The pressure drop across the first labyrinth is sufficient to pull liquid

out of the corner and into the seal. Otherwise, the thrust-balancing piston condensate is handled similarily to the operation described above.

The low-pressure chamber (Region K) is at a pressure of 32.7 psia, being vented through the turbine rotor cavity (Region H) to the seventh-stage rotor inlet. The corresponding saturation temperature is 1563°F, and the leakage flow entering Region K is superheated about 30 deg. Since this low-pressure chamber is virtually surrounded by regions of higher pressure (71 psia) with a saturation temperature of 1768°F, heat-transfer into the chamber will result, with condensation on the high-pressure side of the walls as indicated in Figure 66. Thus, the leakage flow passing through the low-pressure chamber is heated to about 1650°F. It picks up another 10°F passing through the rotor and, finally, is cooled to about 1645°F passing over the seventh-stage disk before re-entering the flow path with about 85°F of superheat.

3.5.3.6 Tie-Bolt

The tie-bolt is a long slender body with a heat-sink at each end, under the journal bearings. In the steady-state condition, it is heated primarily by radiation from the disk bores of the high-pressure spool. Additional tie-bolt heating of lesser magnitude occurs by natural convection, caused by the rather large centrifugal force field of the rotating cavities, Region G, which are vented to the tenth-stage rotor inlet via the hollow tie-bolt. The pressure in Region G is about 6.4 psia. A small amount of heat is conducted directly into the tie-bolt at the two points of contact with the turbine shaft, the sheet-metal static seal under the front stub-shaft (Item 6 of Figure 65), and the tie-bolt bumper in the interspool region (Item 7 of Figure 66). Some forced convection also occurs in the cavity where the thrust-balancing piston leakage is channeled through the rotor, passing under the sixth-stage disk bore and vented into the seventh-stage rotor inlet, where

the pressure is about 32 psia. This rotating cavity (Region H) is sealed by static labyrinth seals at the tie-bolt bumper and at the bore of the seventh-stage disk. The rotating cavities aft of the seventh-stage are all vented to the tenth-stage rotor inlet, 6.3 psia (labeled Region I in Figure 67). One remaining tie-bolt heat-source exists under the tenth-stage disk; condensation at the tie-bolt bore plug that maintains the temperature of 1240°F at this point.

Overall, the thermal resistance between the tie-bolt and the disks is high so that the tie-bolt temperatures are very sensitive to the cross-sectional area, which determines the thermal resistance to the heat sources. By minimizing the cross-sectional area without reducing the surface area (by using a rifle-bored configuration), the temperature level in the tie-bolt was maximized. The minimum cross-sectional area of the tie-bolt is limited by the axial load requirements. The tie-bolt load changes due to thermal expansion are, in turn, dependent on the temperature level and cross-sectional area. These effects are more fully described in a later section.

Condensation will occur at the rear plug in the tie-bolt bore, Item 12, and on the surface of the mechanical fastener for the sheet-metal pressure cap, Item 13. This condensation supplements the 33 w of sensible heat-transfer along the tie-bolt to provide the necessary 53 w in the rear section, which produces a 290°F temperature drop. This temperature drop is fixed by the saturation temperature in Region I, the rotating cavity vented to the tenth-stage rotor inlet, and the heat-sink temperature that is the rear journal bearing lubricant inlet temperature.

The condensate formed within the tie-bolt will flow out through the vent holes and be slung onto the tenth-stage disk bore. Here it will be vaporized by heat from the disk, which is about 60°F above the boiling point. A dam is provided on the disk bore to prevent liquid

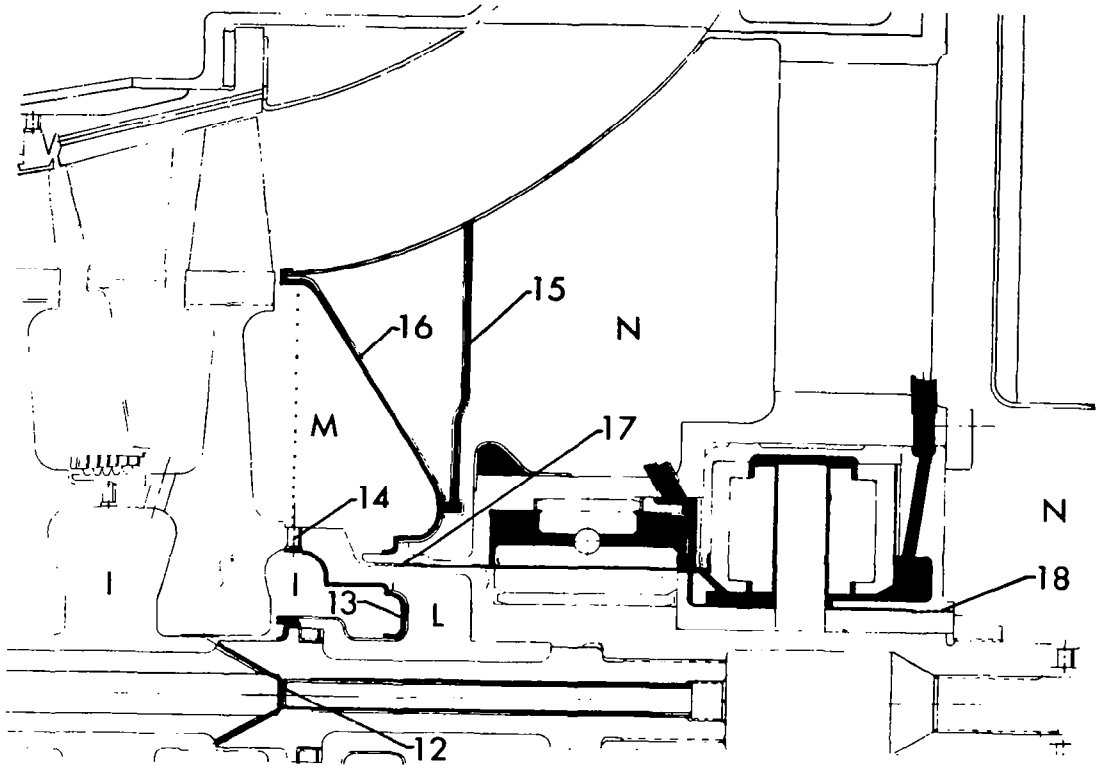

KTA TURBINE REAR-END, SURFACES AND

REGIONS WETTED BY POTASSIUM

FIGURE 67

from reaching the inlet side of the disk. The condensate formed at the sheet metal fastener is slung outward to the underside of the stub-shaft curvic coupling.

3.5.3.7 Rear Stub-Shaft and Viscoseal

Condensation on the underside of the rear stub-shaft will exist in and near the corner where the sheet-metal pressure cap is welded to the stub-shaft. The stub-shaft and sheet metal are T-111 so that this weldment is feasible. The purpose of the weld is to provide a positive seal to prevent condensate from leaking into the low-pressure rotating cavity (Region L), which is vented into the rear journal bearing cavity under the journal sleeve in a manner similar to that in the front end.

The condensation provides the necessary heat-source to supplement the heat from the tenth-stage disk so that the prescribed temperature drop across the thin-shell section of the stub-shaft is produced. The temperature drop is fixed by the 1242°F condensation and the 1000°F heat-sink temperature at the journal bearing. All the condensate which formed inside the stub-shaft and is not revaporized by the tenth-stage disk will be forced outward and collect under the 3.6-in.-diameter curvic coupling, Item 14. From here it will pass through a small hole in the curvic static seal, through the curvic teeth gaps, and out along the exhaust side of the tenth-stage disk.

Additional condensation occurs on the outer surface of the rear viscoseal stator at 1220°F, which also serves as a heat source to establish the necessary temperature gradient along the stationary cylinder supporting the stator. All the moisture entering Region M, or being formed in it, will be dumped into the turbine exhaust pipe. A gravity flow drain line, Item 15, is provided for terrestrial operation, but the condensate can enter the exhaust pipe at the tenth-stage disk rim gap also, especially during 0-g operation.

The sheet-metal shroud, Item 16, welded at the exhaust pipe inlet and at the viscoseal stator, seals the turbine exhaust pressure (5.44 psia) from the coupling area, Region N, that is at a pressure between 0.04 and 0.4 psia.

The rear journal bearing viscoseal, Item 17, is designed for a pressure rise of about 37.5 psi within a wet-pumping length of 0.26 in., corresponding to a bearing lubricant supply pressure of 43 psia at the journal radius, 10 psi below the front bearing pressure. The liquid-vapor interface in this viscoseal will be in mass equilibrium with the average metal temperature at the interface position at about 1220°F, the saturation temperature at turbine exhaust pressure. This is possible because the controlling heat source condensation inside the stub-shaft is 22°F higher by design, which is the reason for venting Region I to the tenth-stage rotor inlet. Heat transfer by liquid convection along the shaft between the viscoseal and journal bearing is effectively blocked by using a running clearance of only 0.005 in., the same as at the front end.

3.5.3.8 Rear Journal Bearing

The heat transfer into the rear journal bearing and viscoseal area is about 200 w. When this is added to the frictional power loss in the bearing and viscoseal, the total heat to be picked up by the journal bearing lubricant is 1.9 kw, which requires 1.63 gpm of lubricant with a 60°F-temperature rise.

The thermal distortion of the bearing surfaces is comparable to that in the front journal bearing and is considered within practical limits.

The bearing housing is surrounded by low-pressure cavities, Regions L and N. The pressure in each cavity is low enough so that latent heat-transfer on the surfaces of the bearing housing will not occur.

3.5.3.9 Turbine Thrust Bearing

The net heat-transfer into the thrust bearing is about 100 w. The total friction loss in the thrust bearing is 10.15 kw; 4.06 kw on the unloaded side and the remainder on the loaded side. The lubricant flow required for the unloaded side is 3.37 gpm with a 60°F-temperature rise. The journal bearing and the unloaded side of the thrust bearing have a common inlet supply which is split by properly sized orifices. Since the total flow requirement for the inlet is 5 gpm with a 60°F-temperature rise, it is necessary to mix 1 gpm of 900°F liquid with the 4 gpm of 950°F liquid from the front journal bearing, with a resultant mix temperature of 940°F at the common inlet. On the loaded side of the thrust bearing, the total heat picked up by the lubricant is 6.4 kw. This requires a lubricant flow of about 3.28 gpm with a 100°F-temperature rise. Thus, the total bearing cooling flow required is 8.28 gpm with an overall temperature rise of 100°, 900° inlet and 1000°F exit. The total heat rejection by the bearing loop is, therefore, 16.16 kw, of which 2.07 kw is due to heat-transfer.

The maximum temperature difference across the thrust bearing slider is about 40°F. This is a realistic value from a thermal distortion standpoint with the bearing materials under consideration and with the pivoted-pad bearing design.

3.5.3.10 Thrust Bearing Viscoseal

The viscoseal, Item 18, located on the loaded side of the thrust bearing (the side nearest the alternator) holds the lubricant in the thrust bearing at a pressure of about 40 psia. The pumping length required is about 0.46 in. With the configuration shown in Figure 67, Page 179, the liquid temperature in the viscoseal will be about 920°F, with a vapor pressure of 0.50 psia. The liquid-vapor interface in this viscoseal is exposed to the coupling area (Region N) which is also

exposed to the alternator viscoseal and scavenge system. The lubricant temperature in the alternator, also liquid potassium, is 200°F lower than the turbine lubricant, with a corresponding vapor pressure of about 0.05 psia. With this difference in vapor pressures, a net mass transfer by evaporation from the turbine bearing loop to the alternator bearing loops would be set up. The rate of mass transfer would be substantial so that frequent correction of the loop inventories would be necessary. If the corrections were made in the liquid phase, the turbine bearing loop would become contaminated with iron from the alternator loop.

An alternate configuration of the turbine viscoseal is shown in Figure 68, which is designed to prevent or reverse the mass transfer. A portion of the 900°F liquid from the thrust bearing supply line is passed through a closed heat-exchanger and cooled to about 750°F. The alternator bearing loop is used as the heat-sink, with an inlet temperature of 700°F. The cooled liquid is then injected through an insulated injection tube into an annular space around the viscoseal stator. From here it is passed through small holes into the gap between the shaft and stator (0.005-in. radial clearance) immediately inside the viscoseal and flows on into the thrust bearing cavity. Here it is again mixed with the 900°F liquid. The amount of liquid flow bypassed through the heat exchanger can be regulated to produce the desired amount of viscoseal cooling within certain limits. Thus, the liquid temperature in the viscoseal can be controlled to 800°F or less, possibly as low as 750°F.

In addition, a Holweck molecular pump is placed in series with the viscoseal which has the capability of pumping the vapor pressure from 0.04 to 0.16 psia (saturation pressure at 800°F) or higher. Thus, with the combination of viscoseal cooling and the Holweck pump, the mass transfer can be prevented. In fact, the mass transfer can even be automatically controlled by simply regulating the cooled liquid flow rate. An analysis of this alternate configuration is given in Appendix F.

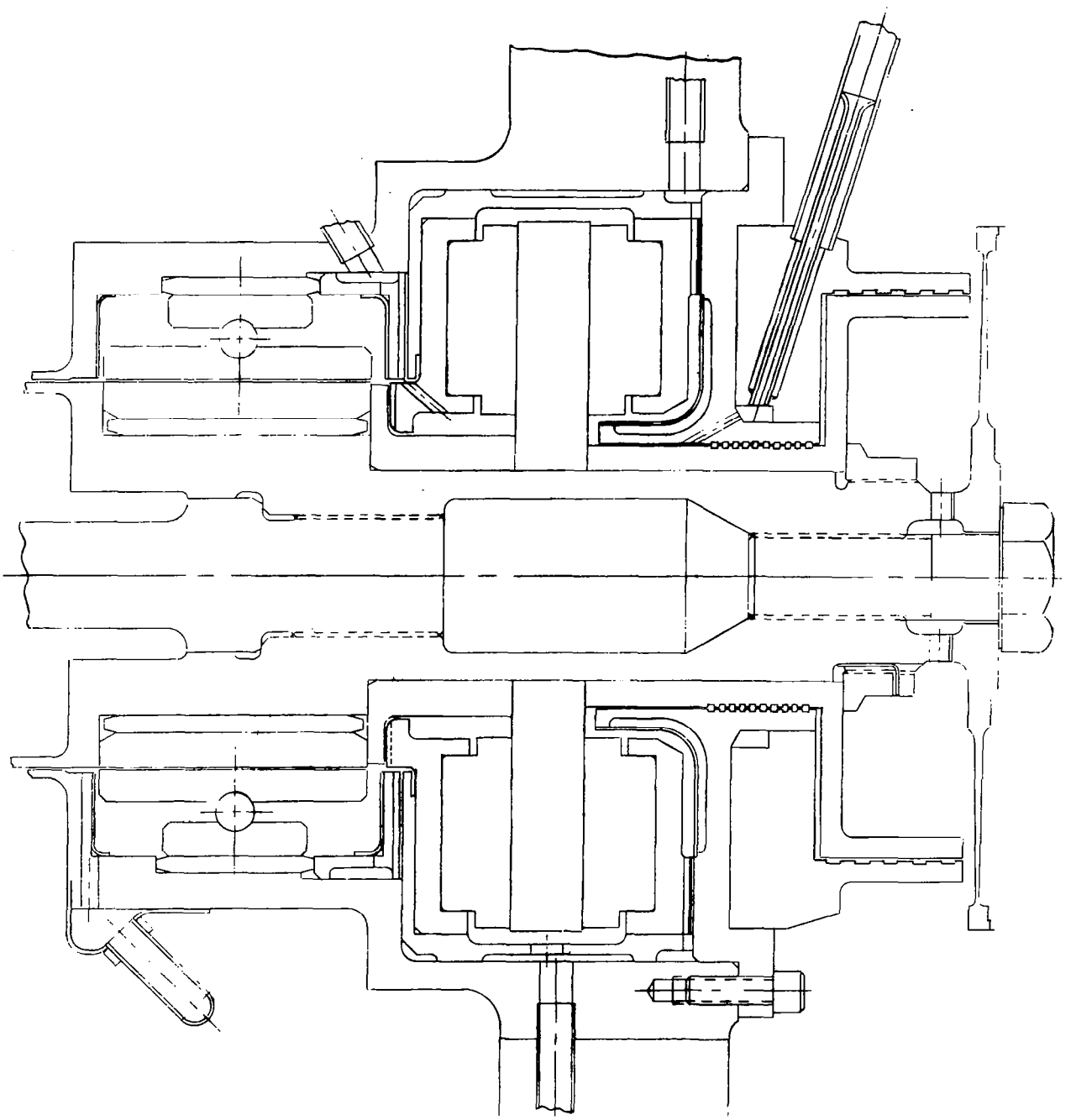

ALTERNATE KTA TURBINE REAR-END CONFIGURATION

FIGURE 68

3.5.4 Transient Temperature Analysis

Following the steady-state thermal analysis and the mechanical design of the turbine, a transient temperature analysis was performed using the same mathematical model as for the steady-state analysis. The purpose was to determine the maximum rate of increase in turbine inlet temperature that can be imposed during a start-up condition, what limits this rate of increase and the general temperature response of the turbine.

From the stress analysis of the stub-shafts, it was decided that the axial load should be limited to 20,000 lb, although the strength of these stub-shafts can be increased substantially by redesign so that a considerably higher transient load could be tolerated. With the present design of these stub-shafts and of the tie-bolt (to be described later) using a minimum preload of 12,000 lb (for seating of curvic couplings), it was found that increasing the turbine inlet temperature at a constant rate of 1.0°F/sec, from a uniform initial temperature of 900°F, produces a peak axial load of 17,800 lb, whereas the steady-state load is 14,200 lb.

Figure 69 shows the temperature response of the turbine wheel rims using the linear inlet temperature ramp of 1°F/sec, which is also plotted. It is found that temperature versus time at each of the rims is also essentially linear, indicating that the rim temperatures respond practically instantaneously to the boundary temperatures imposed by the flow path, at least when compared to the relatively slow rate of increase in these boundary temperatures, which are exactly linear with time by definition.

The temperature response at the turbine wheel bores are presented in Figure 70. Here again, the response is very fast compared to the relatively long time-scale under consideration.

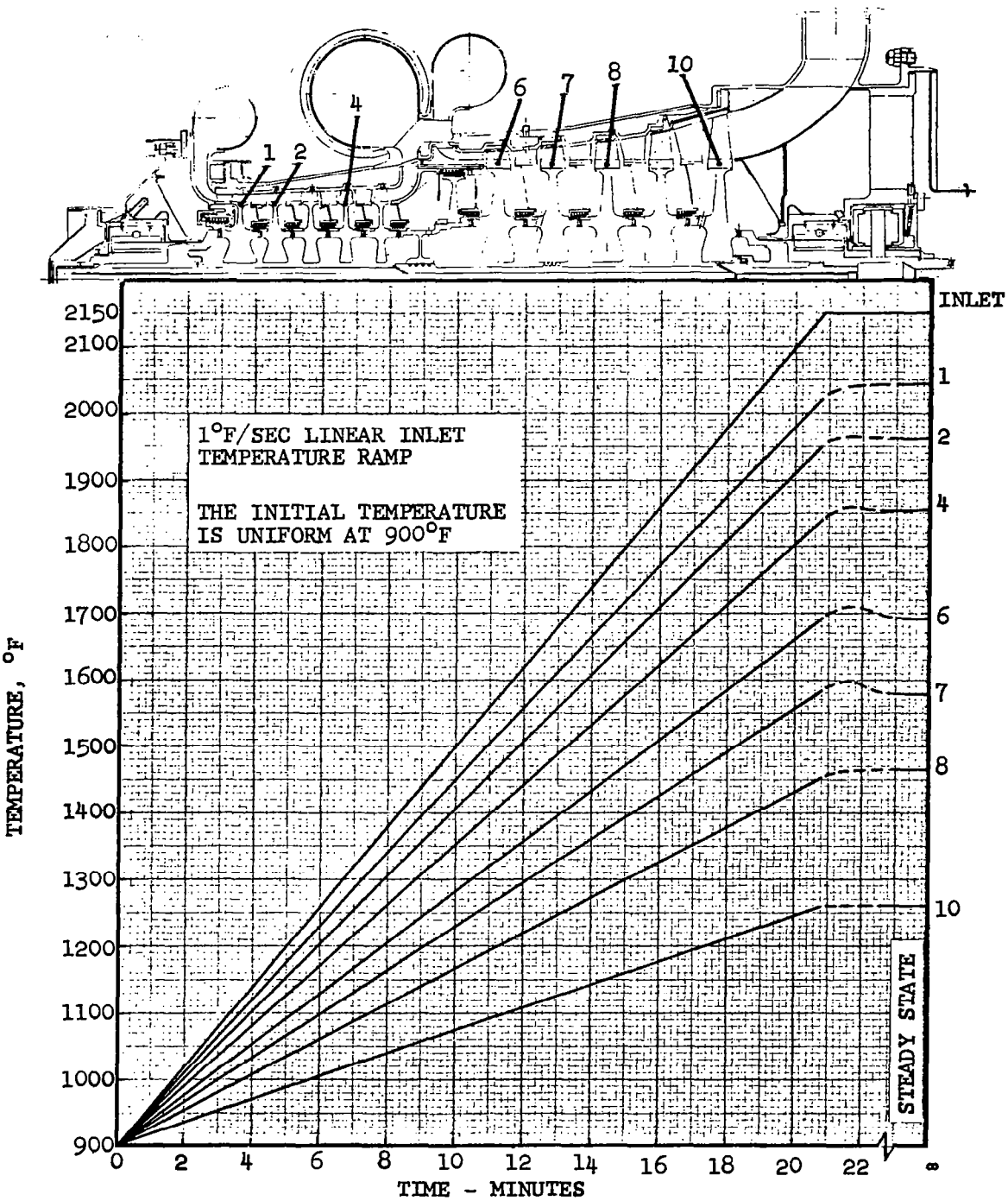

KTA TURBINE WHEEL RIMS, TEMPERATURE RESPONSE

DURING A START-UP CONDITION

FIGURE 69

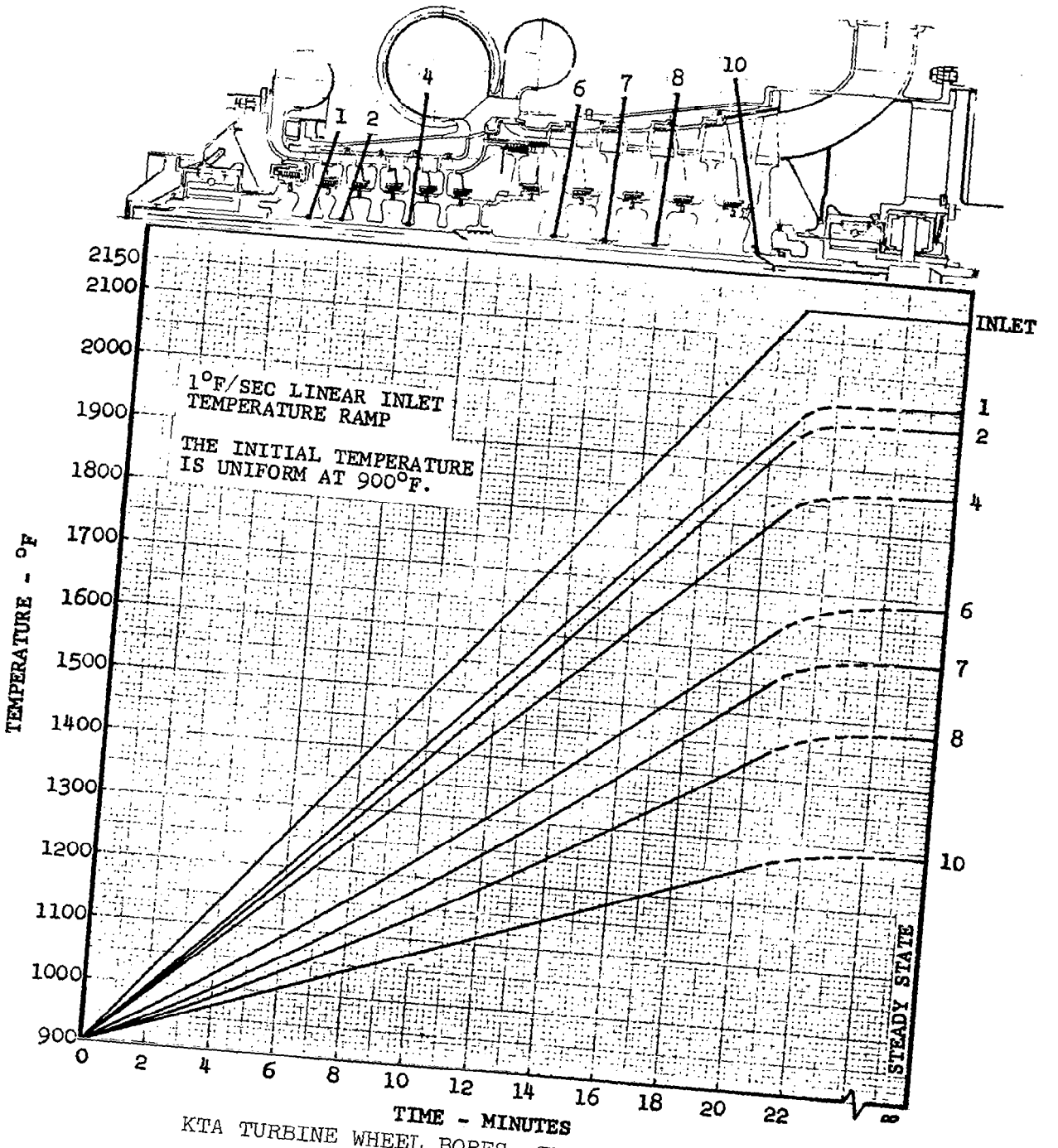

KTA TURBINE WHEEL BORES, TEMPERATURE RESPONSE DURING A START-UP CONDITION

FIGURE 70

The temperature-versus-time curves for some of the wheels in the low-pressure spool have a noticeable dip in them, indicating thermal lag. This, of course, is due to the greater mass in these wheels, but the amount of lag is still rather small.

Figure 71 shows the temperature response of certain locations in the hot-end of the turbine, and at three points in the tie-bolt. The locations labeled 1 through 4 respond very rapidly due to the close proximity to condensation sites, although 1 does indicate a slight lag. The points on the conical outer housing, C1 and C2, have quite a large thermal lag, as indicated by the marked dips in the curves. This is attributed to the rather massive inlet scroll flange. Of the points on the tie-bolt, T1 has a very large thermal lag due to its thermal isolation from the rest of the turbine. T2 also has a considerable lag, but it is not as pronounced because of the contact established at the tie-bolt bumper and the convection heat-transfer from the leakage flow channeled through the rotor around the sixth-stage disk. The temperature at T3 responds nearly instantaneously because condensation occurs at that point.

The temperature response of the turbine casing was not calculated since an insulation system has not been designed. However, the response would necessarily be much faster than the tie-bolt response due to the shorter distance between heat sources and the closer proximity to the main flow-path.

Figure 72 shows the temperatures versus length along the two stub-shafts with time as a parameter, using the 1°F/sec inlet temperature ramp. The slope of these curves represent the local temperature gradient. By inspection, it is found that the maximum temperature gradients occur at the steady-state condition. The stress analyses on the stub-shafts were made using the steady-state temperature distribution so that the worst-case of thermal stress was indeed considered.

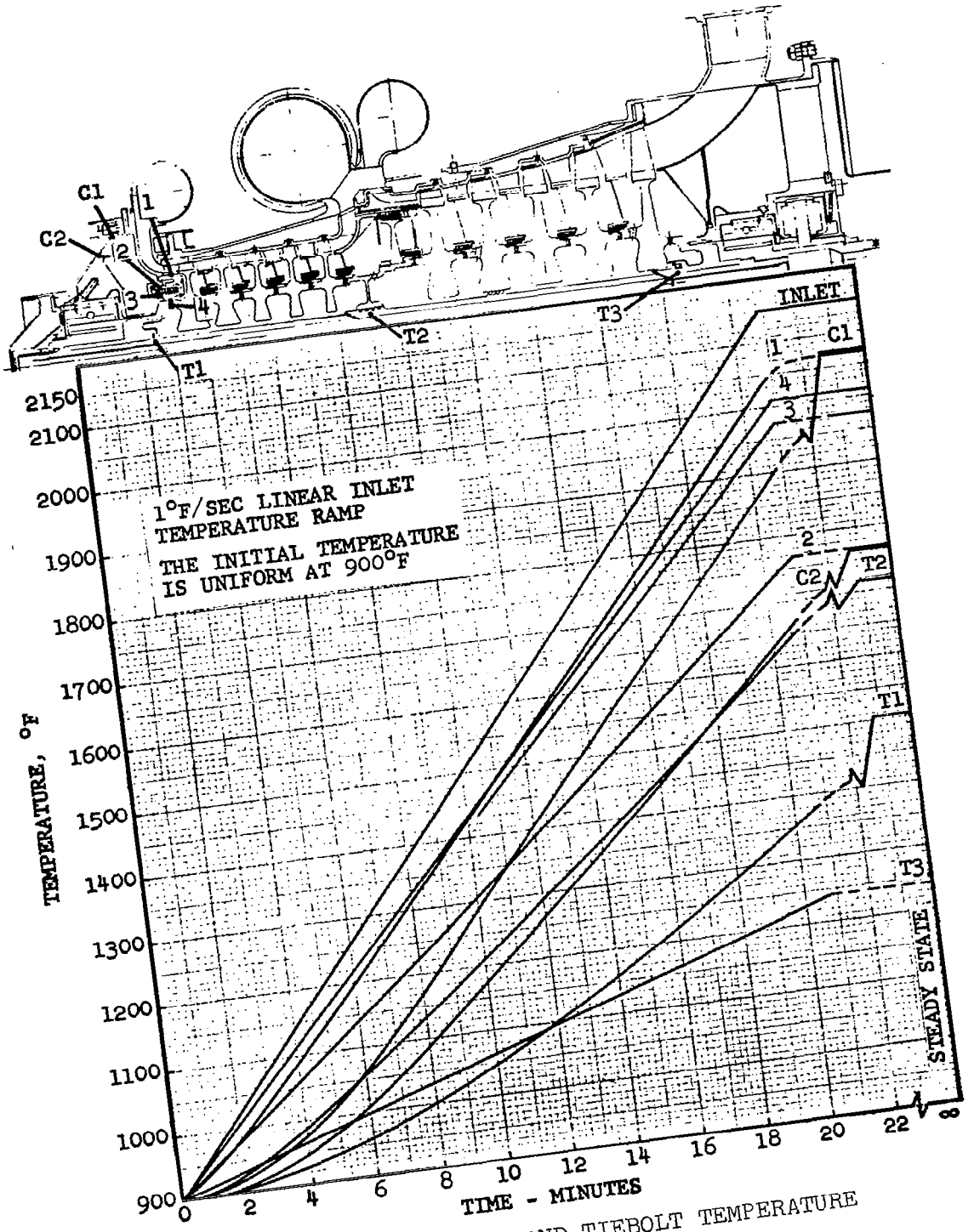

KTA TURBINE, HOT-END AND TIEBOLT TEMPERATURE RESPONSE DURING START-UP

FIGURE 71

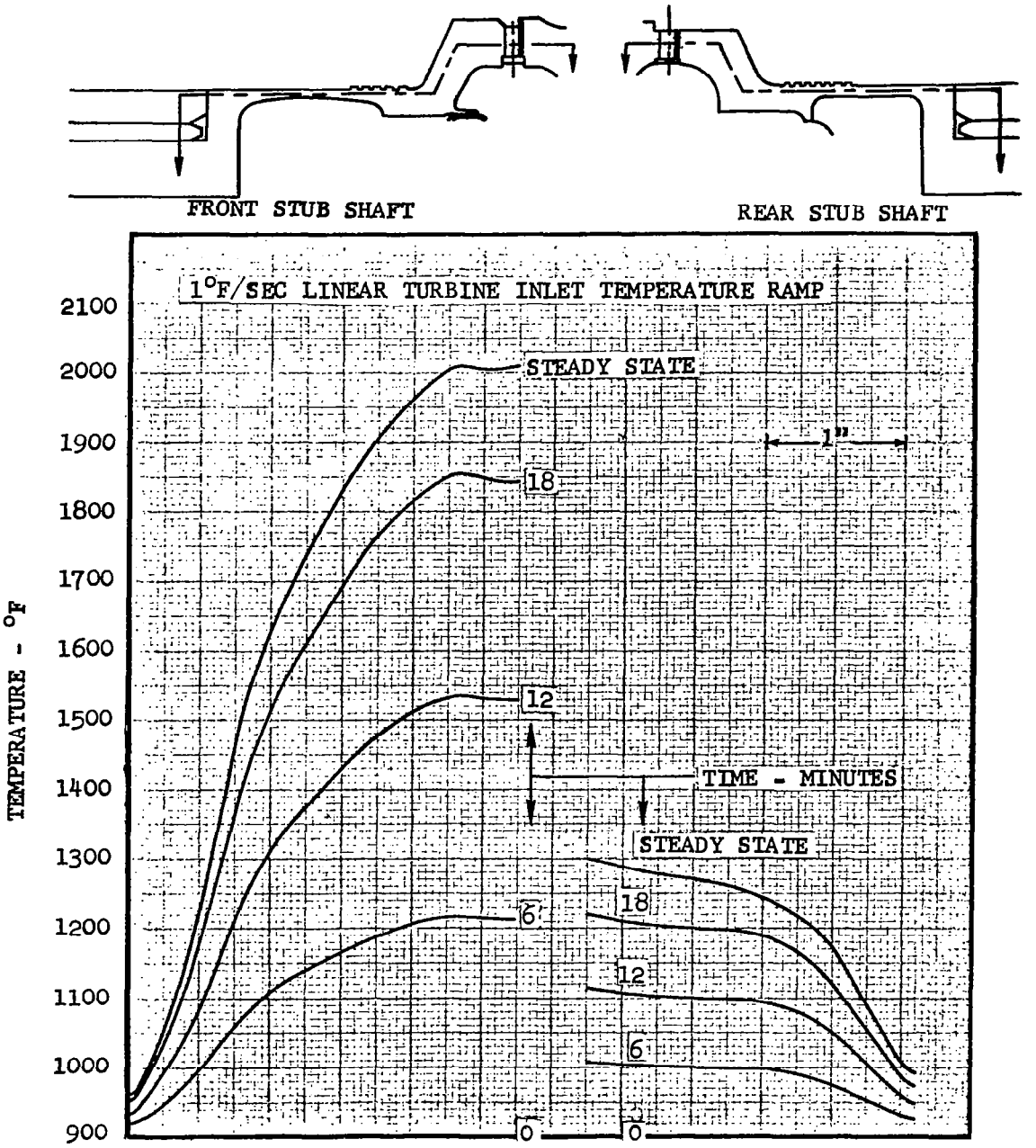

KTA TURBINE STUB-SHAFTS, TEMPERATURE ALONG STUB-SHAFT MEAN LINES DURING A START-UP CONDITION

FIGURE 72

In general, it is determined that the entire turbine has a fast temperature response when compared to the 20+ minutes required to reach the full 2150°F turbine inlet temperature, except for the tie-bolt and the front conical housing. The only adverse effect of the thermal lag in the conical housing is to increase the temperature gradient in the scroll flange, of little importance since this area is not highly stressed. Therefore, the tie-bolt load is the only critical variable peculiar to turbine thermal transients. The rate of increase in turbine inlet temperature used in the present analysis was acceptable, although an equivalent series of small step changes would be also.

3.5.5 Accuracy and Conclusions

The results of a thermal analysis of the type described herein can only be as accurate as the boundary conditions imposed on the machine, about which certain assumptions were necessary as discussed earlier. Further limitations in accuracy are as follows:

(a) Uncertainties and nonhomogeneity in physical properties of materials
(b) Uncertainties and the effect of superheat on the transport properties of potassium vapor
(c) Dimensional tolerances
(d) Uncertainties in the data used for calculation of frictional power losses
(e) Geometrical idealizations used in the mathematical model
(f) Approximations necessary in evaluation of heat transfer coefficients and radiation target factors
(g) The turbine through-flow was treated as an adiabatic process, heat-transfer effects on boundary temperatures being neglected.

Although the above uncertainties are significant, the computed temperatures are relatively accurate due to the balancing effect of satisfying the law of conservation of energy throughout the turbine.

The conclusions which can be drawn from the results of the thermal analysis are listed below:

(a) The hot-end mounted journal bearing is effectively isolated from the turbine inlet in a practical design.
(b) Neutral potassium mass equilibrium can be approached, subject to the above uncertainties, at the liquid-vapor interface in each viscoseal.
(c) Condensate formed by heat-transfer can be adequately controlled.
(d) The turbine metal temperature response is relatively fast except in the tie-bolt.

3.6 Turbine Mechanical Design

3.6.1 Turbine Wheel Design

Each of the 10-stage turbine wheels are made from TZM, heat-treat KDTZM 1175. The disk contours were established on the basis of 30,000-hr creep and yield strength data presented in Appendix A. The first five stages have wheels with integral blades, and inserted blades are used with the final five stages.

3.6.1.1 Blade Stress Analysis

The blade stresses are evaluated for the 10 turbine stages based upon the blade shapes obtained from the aerodynamic design presented in Section 3.3.2.3 and the thermal analysis presented in Section 3.5. Figure 73 shows the blade stresses due to centrifugal loading for

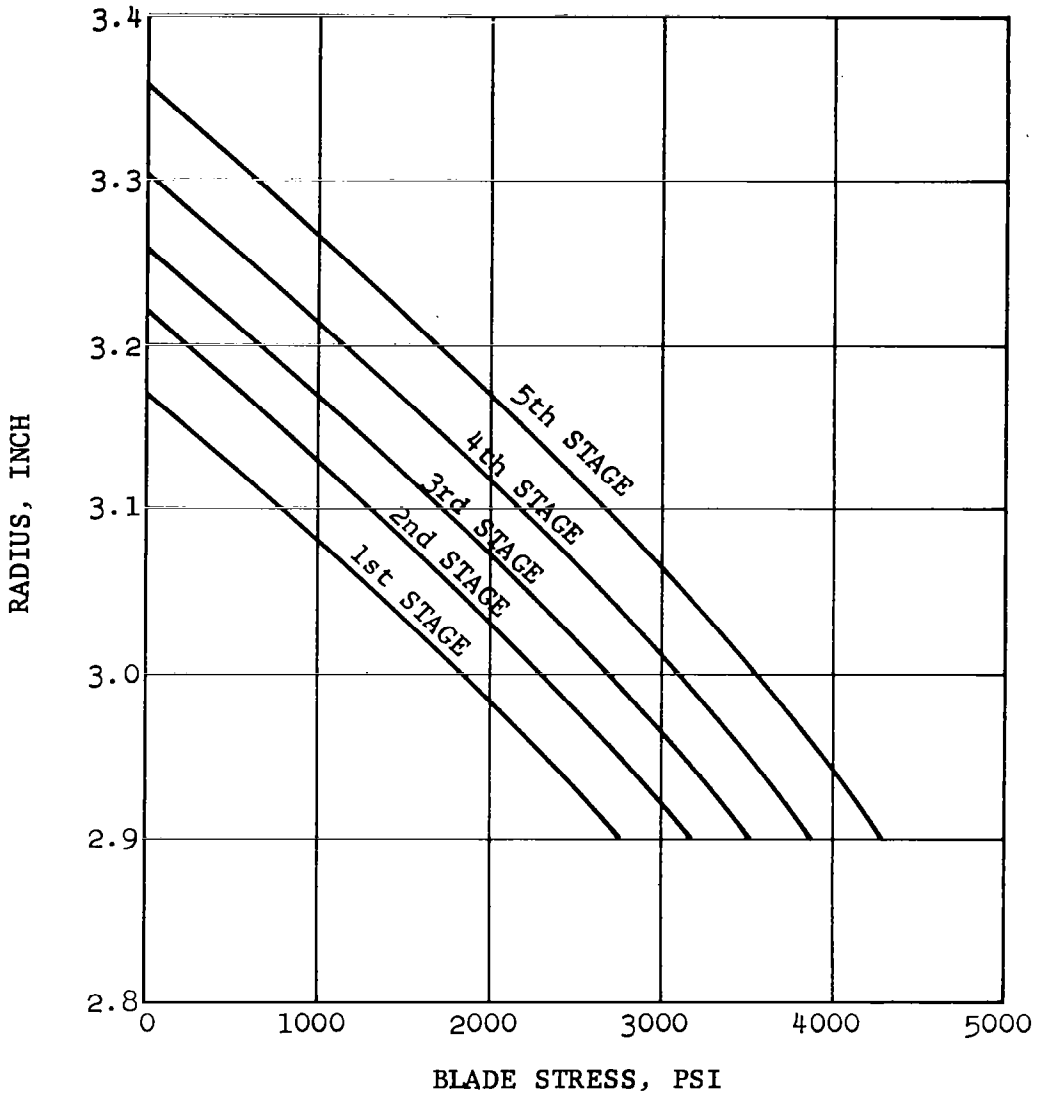

BLADE STRESSES VERSUS RADIUS FOR

KTA FIRST TO FIFTH STAGES

FIGURE 73

the first five stages. Similar results for the sixth through the tenth stages are shown in Figure 74 where the effect of the integral blade shrouds for stages six through nine are included. The three-rib blade shroud, shown in Figure 75, is used to facilitate interstage moisture removal and improve the individual stage efficiency.

A summary of the individual blade operating conditions, root stresses, and rim loads imposed on the disks is shown in Table 11.

3.6.1.2 KTA Turbine Fir-Tree Design

The fir-tree design is common for turbine wheel Stages 6 through 10 and is presented in Figure 76. The design comprises two tangs with a broach angle of 17 deg. Blade root loadings, shown in Table 11, are highest for the tenth stage. The resulting critical stresses for that stage are presented in Table 12. The maximum stress component, which is the combined fillet stress, is tabulated in Table 13 for all of the latter five stages, with respective allowable stresses and margins of safety.

3.6.1.3 Disk Design and Stress Analysis

The disk designs for all ten stages have been designed with adequate safety margin and are consistent with the physical constraints imposed, such as bore and rim radii, rim loadings, curvic coupling dimensions and maximum permissible axial dimension per stage. Disk shapes for the first through fifth stages are presented in Figure 77. The sixth- through ninth-stage disks are identically the same design. This and the tenth-stage disk design are presented in Figure 78. The thrust balancing piston design is presented in Figure 79.

The first turbine stage is life-limiting for the rotor assembly due to its more severe temperature environment. To achieve the required

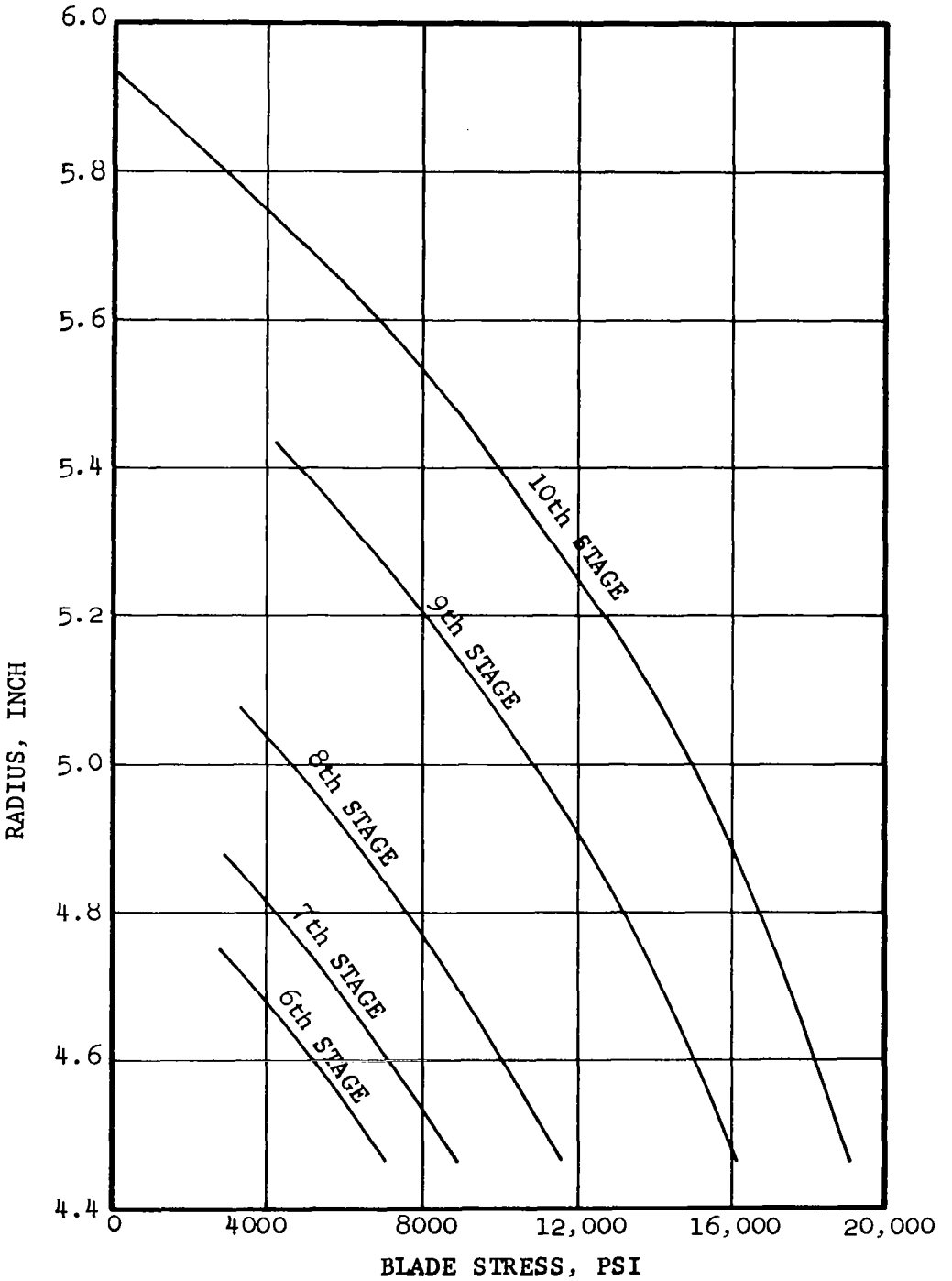

BLADE STRESS VERSUS RADIUS FOR

KTA SIXTH TO TENTH STAGES

FIGURE 74

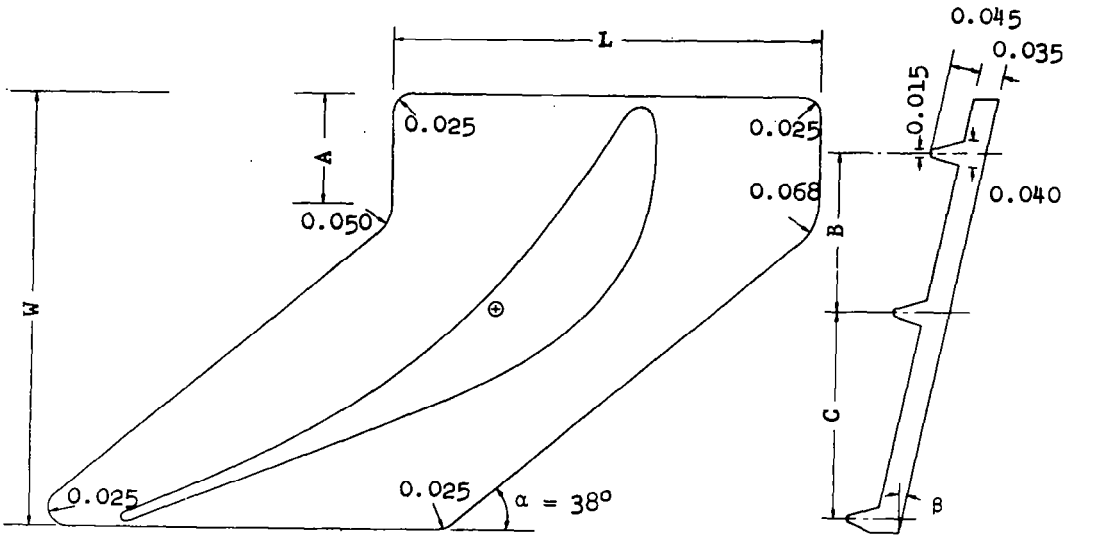

(A) NINTH STAGE BLADE SHROUD CONFIGURATION

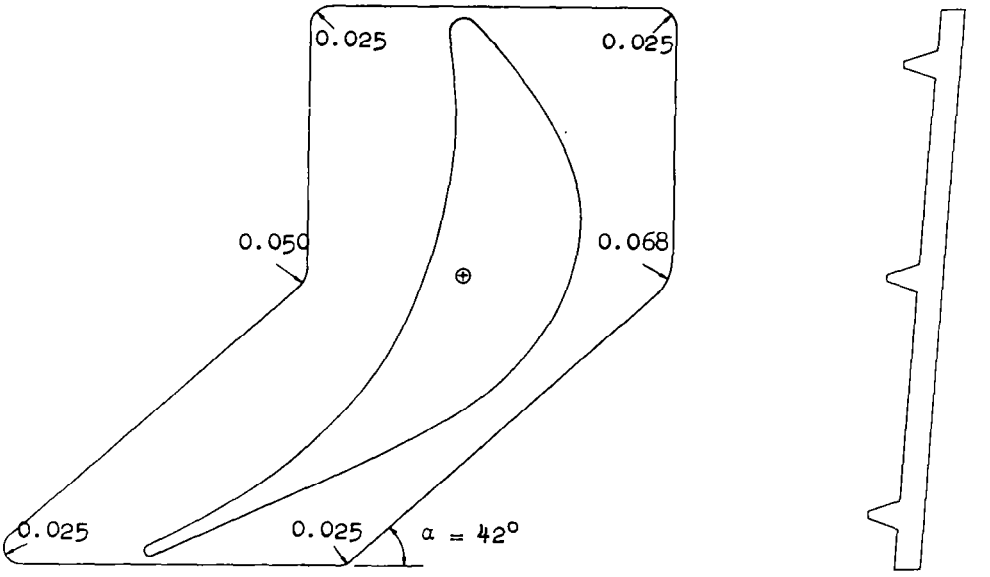

(B) SIXTH STAGE BLADE SHROUD CONFIGURATION

(C) PERTINENT DIMENSIONS FOR BLADE SHROUDS

STAGE	L, IN	W, IN	A, IN	B, IN	C, IN	α, DEG	β, DEG
NO. 6	0.515	0.81	0.37	0.31	0.34	42	3.5
NO. 7	0.528	0.78	0.33	0.29	0.31	41	4
NO. 8	0.550	0.74	0.28	0.28	0.30	40	7
NO. 9	0.588	0.63	0.16	0.23	0.30	38	15

BLADE SHROUD CONFIGURATION
FOR KTA 6TH TO 9TH STAGE

A90936

FIGURE 75

TABLE 11

SUMMARY OF ROTOR BLADE STRESS ANALYSIS
(Material TZM, 19,200 rpm)

Stage No.	Number of Blade	Operating Temperature °F	Weight per Blade, lb	Root Area, in^2	Centrifugal Force at Root, lb	Blade Stress at Root, psi
1	78	2058	0.00575	0.0661	182	2758
2	64	1955	0.00576	0.0568	180	3174
3	64	1911	0.00622	0.0568	200	3511
4	64	1852	0.00685	0.0568	221	3886
5	64	1795	0.00733	0.0568	245	4301
6	58	1689	0.01278	0.1308	923	7059
7	58	1574	0.01768	0.1308	1159	8861
8	58	1463	0.02463	0.1308	1520	11617
9	58	1359	0.03509	0.1308	2106	16100
10	58	1258	0.04687	0.1308	2494	19068

NOTE: The centrifugal force and stress at root include the effect of blade shroud.

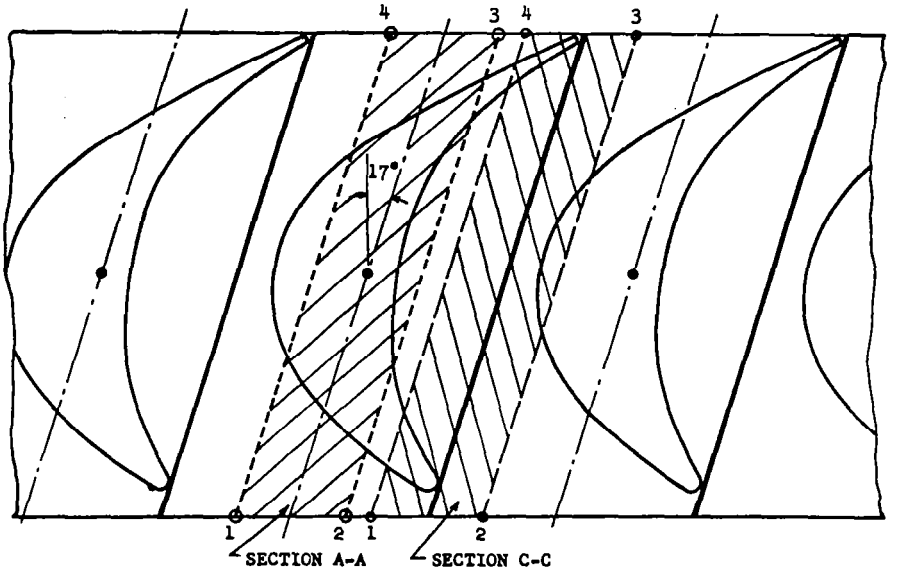

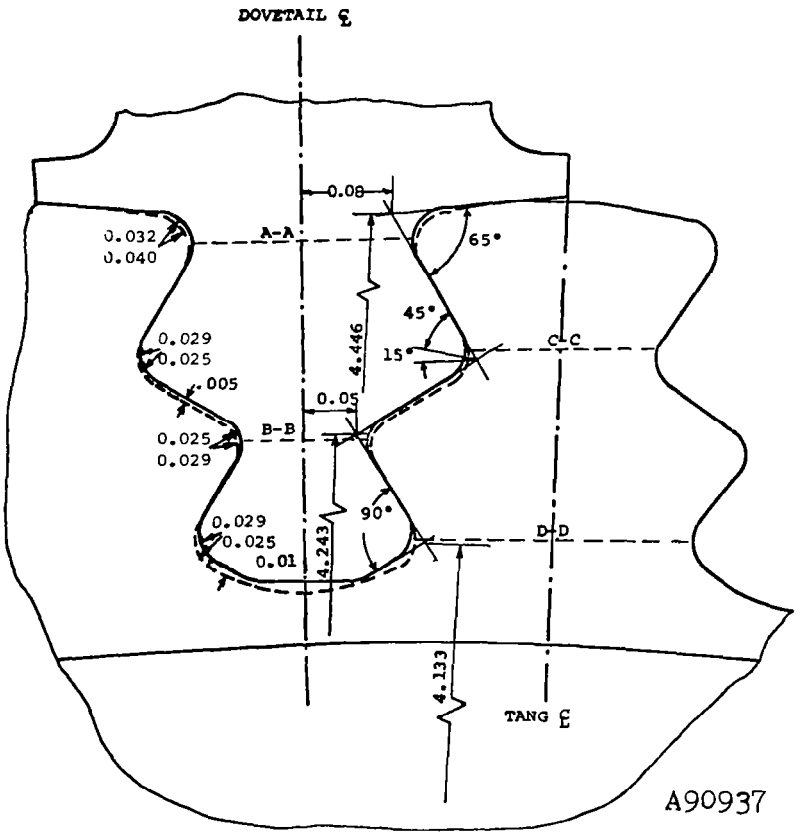

KTA TURBINE FIR TREE DESIGN

FIGURE 76

TABLE 12

FIR-TREE STRESSES FOR TENTH-STAGE TURBINE
(Material TZM, 19,200 rpm)

Item	Stress Type	Blade				Disk				Allowable*
		Upper Tang		Lower Tang		Upper Tang		Lower Tang		
		Nominal	Peak	Nominal	Peak	Nominal	Peak	Nominal	Peak	
1	Neck tension	15.8	25.8	15.5	26.2	17.1	29.2	22.1	26.3	74.5
2	Tang bending	16.0	19.9	18.1	20.7	20.7	25.8	22.7	26.1	74.5
3	Combined fillet	31.8	45.8	33.6	47.0	37.7	54.9	44.7	52.3	93.2
4	Bearing	19.6	24.4	27.7	31.8	19.6	24.4	27.7	31.8	93.2
5	Hook shear	9.6	12.0	12.1	13.9	9.0	11.2	11.7	13.4	43.2

*NOTES: (1) Allowable stress for Items 1 and 2 is 0.90 times minimum yield strength at operating temperature; in addition, a reduction of 10 percent is allowed for rate of loading and surface finish.

(2) Allowable stress for Items 3 and 4 is 1.25 times above value.

(3) Allowable shear stress is 0.58 times the value of Item 1.

(4) Stress in ksi.

TABLE 13

SUMMARY OF NOMINAL AND PEAK COMBINED FILLET STRESSES VERSUS ALLOWABLE STRESS FOR THE SIXTH- TO TENTH-STAGE FIR-TREE DESIGN**
(Material TZM, 19,200 rpm)

Stage No.	Nominal Combined Fillet Stress				Peak Combined Fillet Stress				Allowable Combined Fillet Stress	Minimum Factor of Safety*
	Blade		Disk		Blade		Disk			
	Upper Tang	Lower Tang	Upper Tang	Lower Tang	Upper Tang	Lower Tang	Upper Tang	Lower Tang		
6	17.5	19.7	24.7	29.6	26.2	28.0	35.3	34.2	89.6	2.54
7	19.7	21.8	26.7	31.9	29.2	30.9	38.3	37.0	90.4	2.36
8	23.1	25.1	29.7	35.4	33.8	35.4	42.9	41.2	91.1	2.12
9	28.5	30.4	34.7	41.2	41.3	42.6	50.4	48.1	92.1	1.83
10	31.8	33.6	37.7	44.7	45.8	47.0	54.9	52.3	93.2	1.78

*Minimum factor of safety is defined as: $\frac{\text{Allowable Stress}}{\text{Maximum Peak Stress}}$

**Stress in ksi

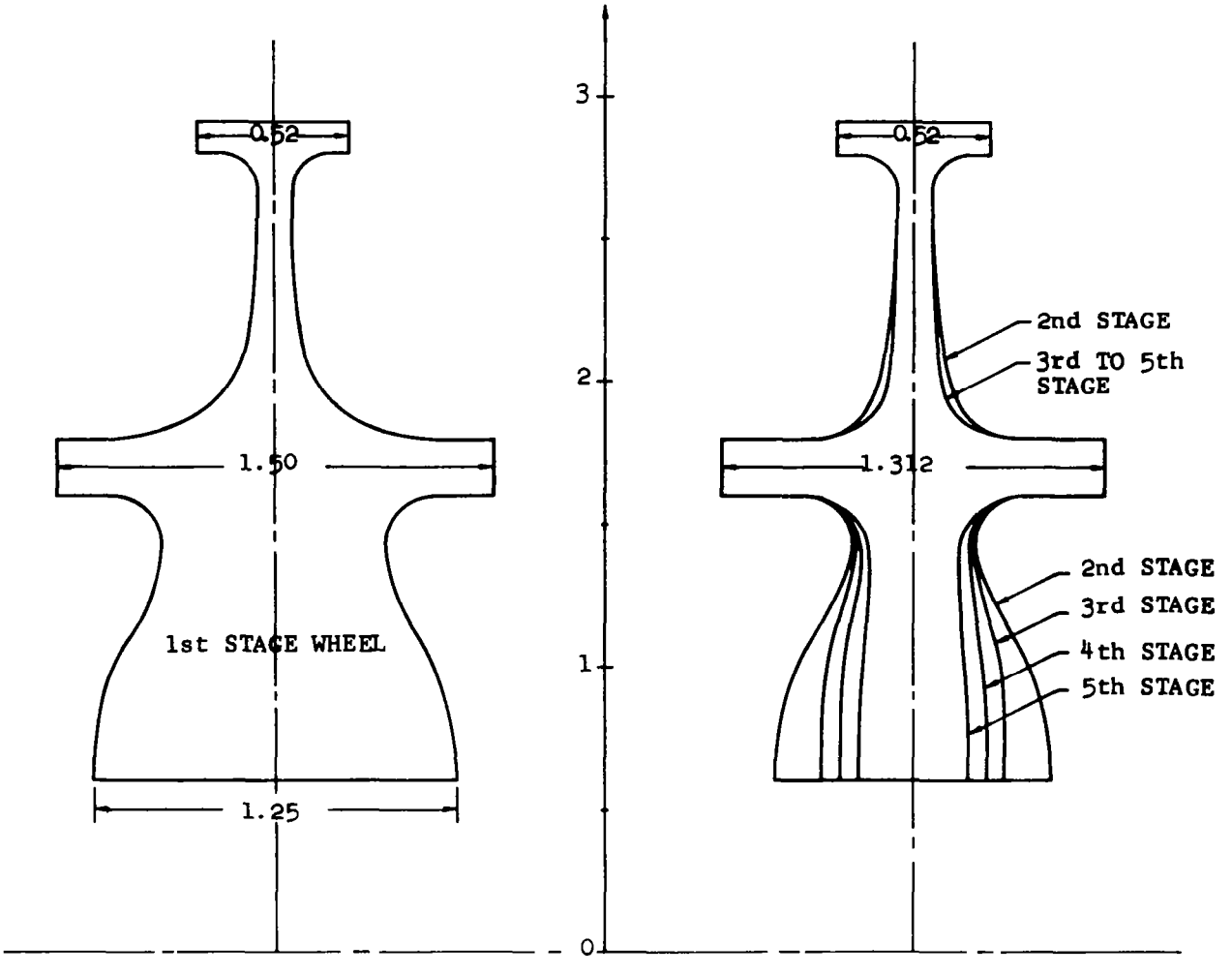

CENTER LINE OF ROTATING AXIS

TURBINE WHEEL DISK SHAPE FOR KTA FIRST TO FIFTH STAGES A90938

FIGURE 77

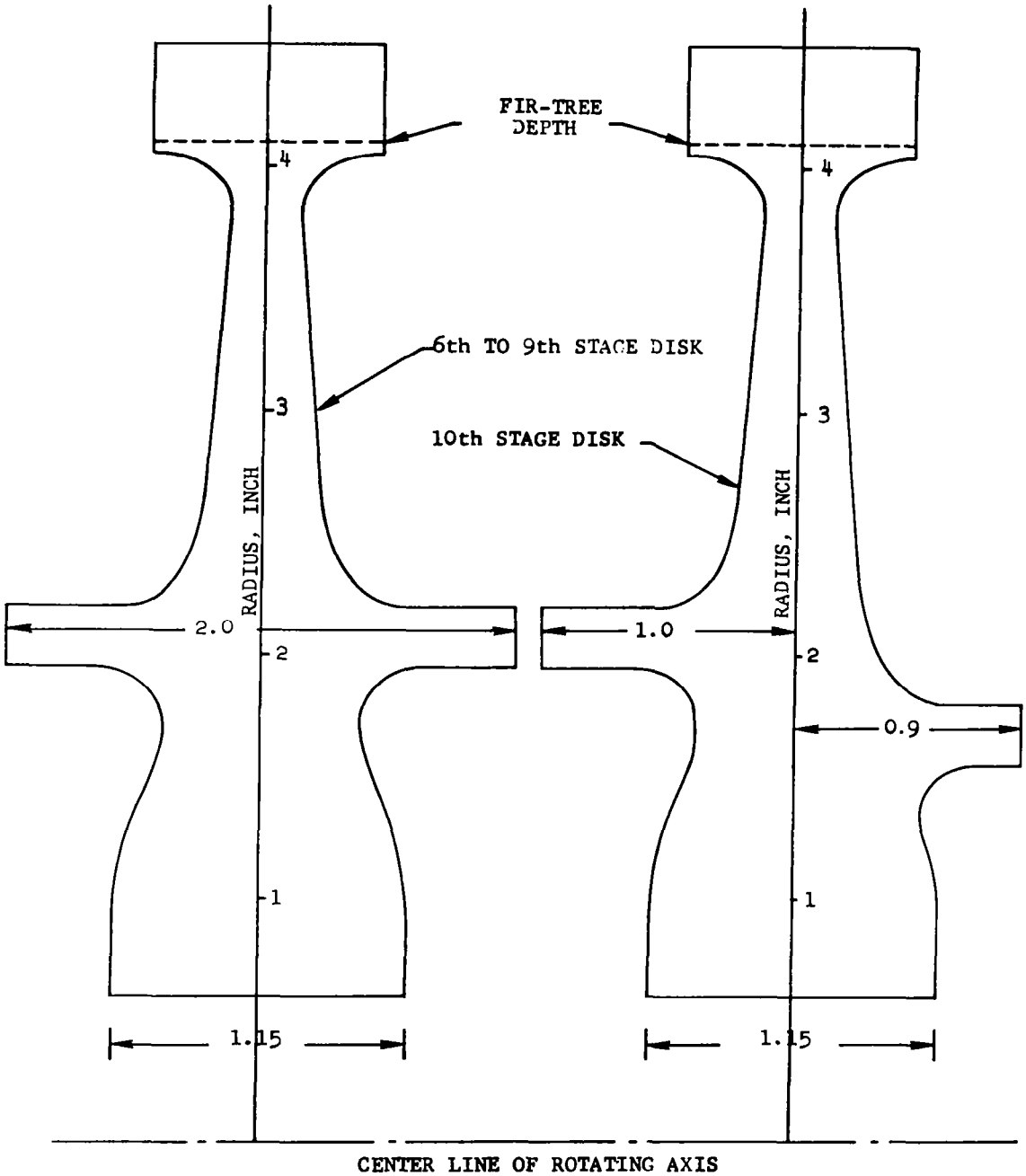

TURBINE WHEEL DISK SHAPE FOR

KTA SIXTH TO TENTH STAGES

FIGURE 78

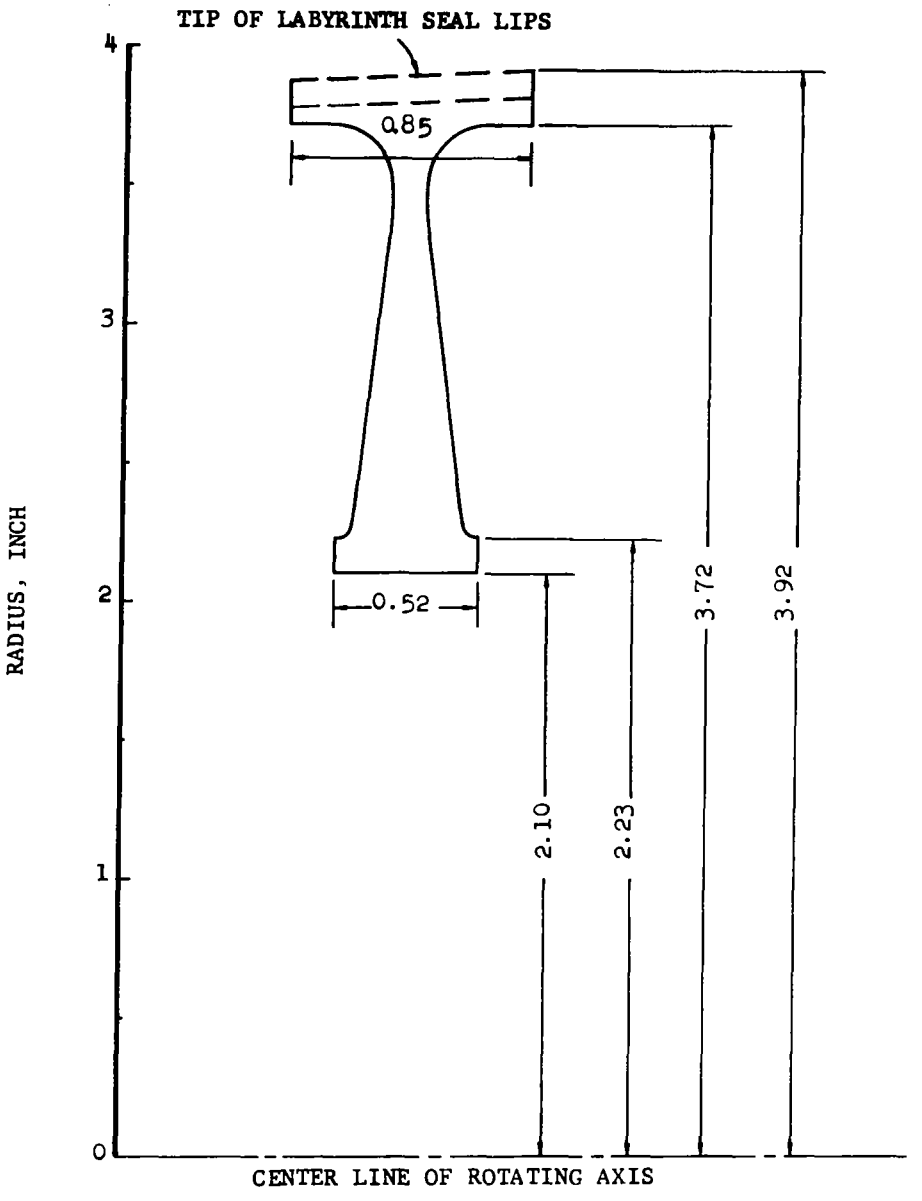

DISK SHAPE FOR KTA THRUST

BALANCING PISTON

FIGURE 79

wheel life for this stage, the following design approach was followed. As the first step, an essentially optional disk contour was defined based upon plane stress theory. The design uncertainty at this juncture was the degree of axial variation in the stress distribution from the thick disk bore to the thin neck section just beyond the curvic coupling outer radius. A three-dimensional stress analysis was, therefore, conducted using the finite element approach. Comparisons of stresses based upon the two theories are presented in Figures 80 and 81. The agreement in these results justifies the plane-stress theory as reliable. Most important, the axial variation in tangential stress is, in general, not significant.

The third phase in the design verification was to predict the disk radial growth over the period of 30,000 hr due to creep. The method of analysis used was that of M. B. Millenson and S. S. Manson.[38] This approach relies upon the assumptions of plane stress, and an empirical relationship of local strain rate with local state of stress. This relationship is based upon uniaxial stress versus strain rate data. The predicted bore and rim tangential stresses and radial growths versus time are presented in Figure 82, based upon a disk isothermal operating temperature of 2058°F. Final thermal analysis results indicate that at the bore, the steady-state operating temperature will be about 50°F less than that assumed in the creep analysis. The 0.5 percent creep strength of TZM is greater by about 5000 psi with this temperature reduction, and thereby the creep predictions are highly pessimestic. Nonetheless, the predicted plastic strains after 30,000 hr of operation are quite adequately minimal.

For the remaining stages, the design requirements of the disks are less severe due to the reduced temperature environments, in spite of the higher rim loadings, as is the case for the thrust balancing piston. A summary of pertinent disk dimensions and stresses for the 10 turbine wheel stages is presented in Table 14. Figure 83 depicts peak and

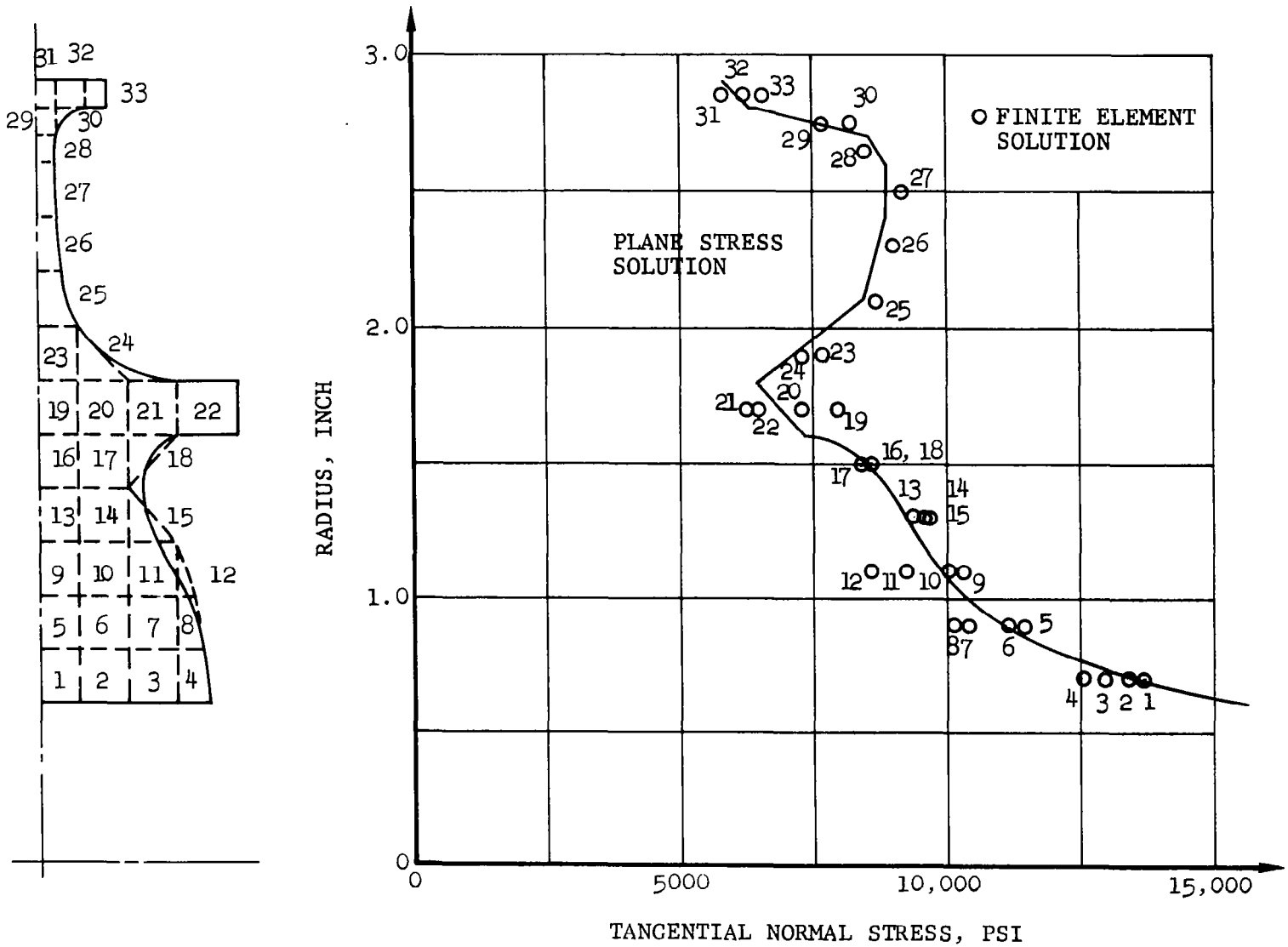

COMPARISON OF TANGENTIAL STRESSES OBTAINED BY PLANE STRESS SOLUTION AND FINITE ELEMENT METHODS

A90940

FIGURE 80

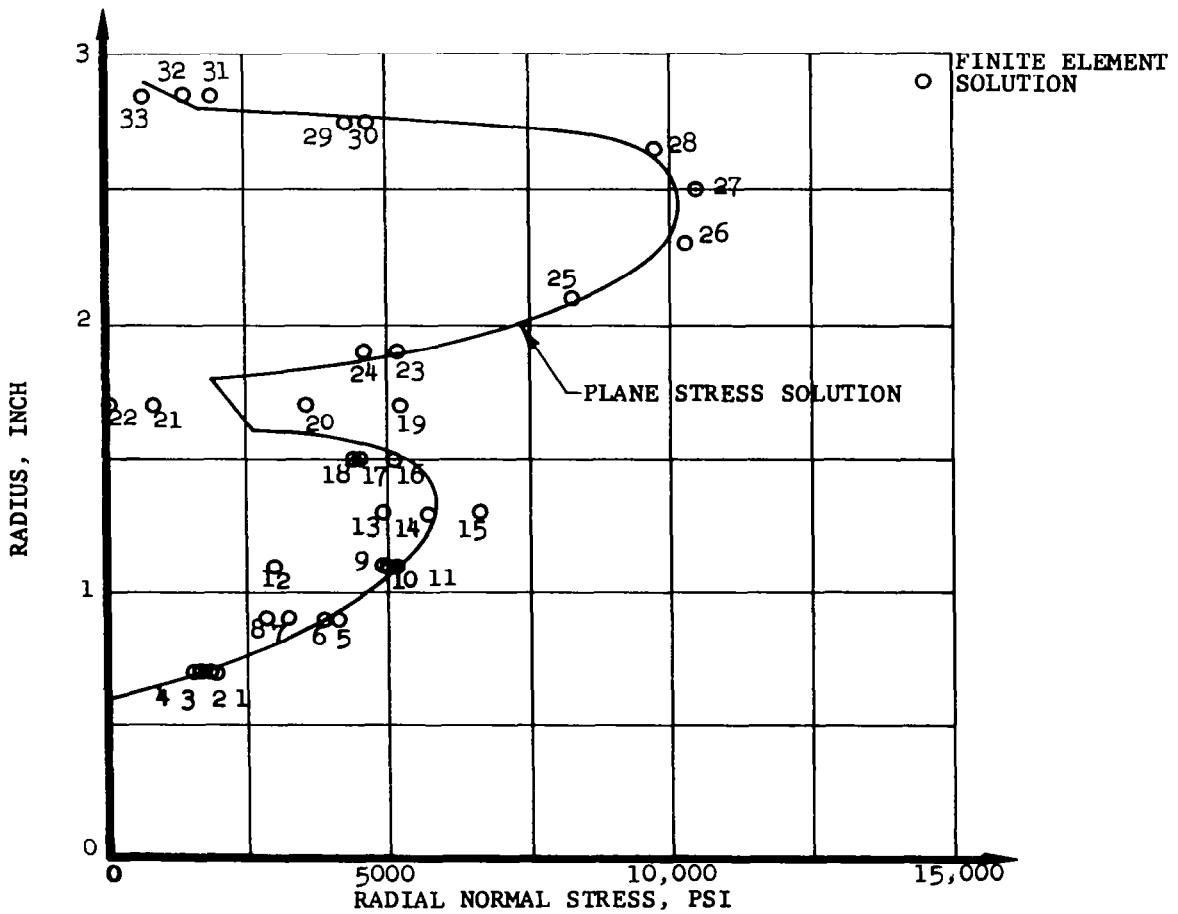

COMPARISON OF RADIAL STRESS OBTAINED BY PLANE STRESS SOLUTION AND FINITE ELEMENT METHOD

FIGURE 81

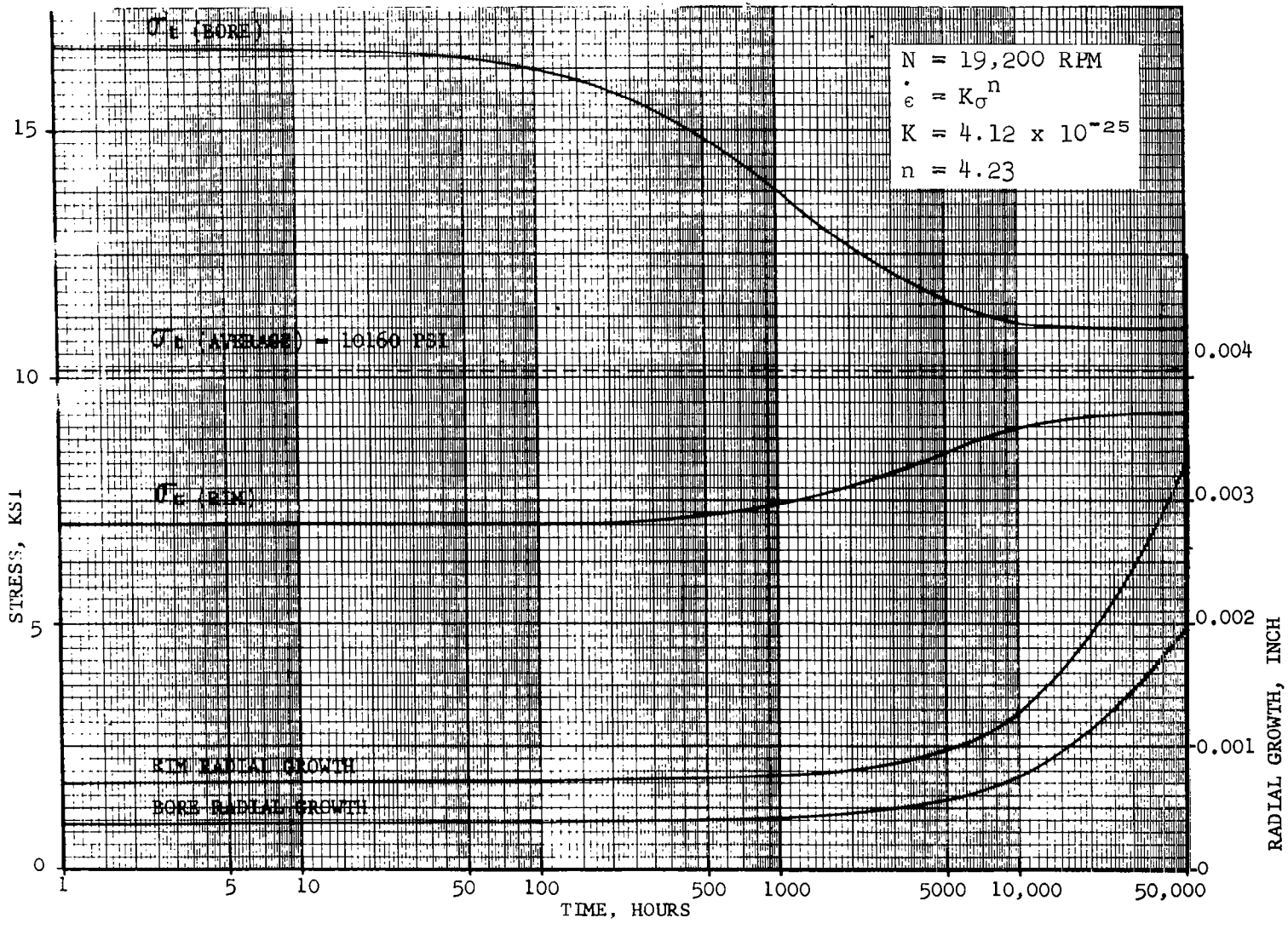

CREEP STRESS AND RADIAL GROWTH FOR FIRST WHEEL

FIGURE 82

A90942

TABLE 14

PERTINENT DIMENSIONS AND STRESSES FOR THE TEN-STAGE TURBINE WHEELS AND THRUST BALANCING PISTON DESIGN

Stage No.	Neck Thickness, in.	Bore Thickness, in.	Platform Thickness, in.	Neck Radial Stress, psi	Bore Maximum Tangential Stress, psi	Average Tangential Stress, psi	Yield Strength*. 0.2% Strain, psi	Creep Strength*, 0.5% Creep psi
1	0.120	1.250	0.520	12800	16690	10160	85800	16000
2	0.120	0.950	0.520	12470	18090	11280	86200	20000
3	0.120	0.625	0.520	13100	22270	12610	86700	30000
4	0.120	0.500	0.520	13820	25100	13840	87000	39000
5	0.120	0.375	0.520	14640	29030	15220	87200	47000
Thrust Balancing Piston	0.110	0.500	0.850	9000	48320	34910	87400	52000
6	0.280	1.150	0.900	37370	52000	30900	88000	59000
7	0.280	1.150	0.900	39280	53150	31710	88600	65000
8	0.280	1.150	0.900	42180	54890	32940	89200	--
9	0.280	1.150	0.900	46940	57740	34950	90000	--
10	0.280	1.150	0.900	49690**	59000	35700	90300	--

*The yield and creep strengths are obtained from Reference (5) based on the average temperature for each stage.

**Average stress at each position.

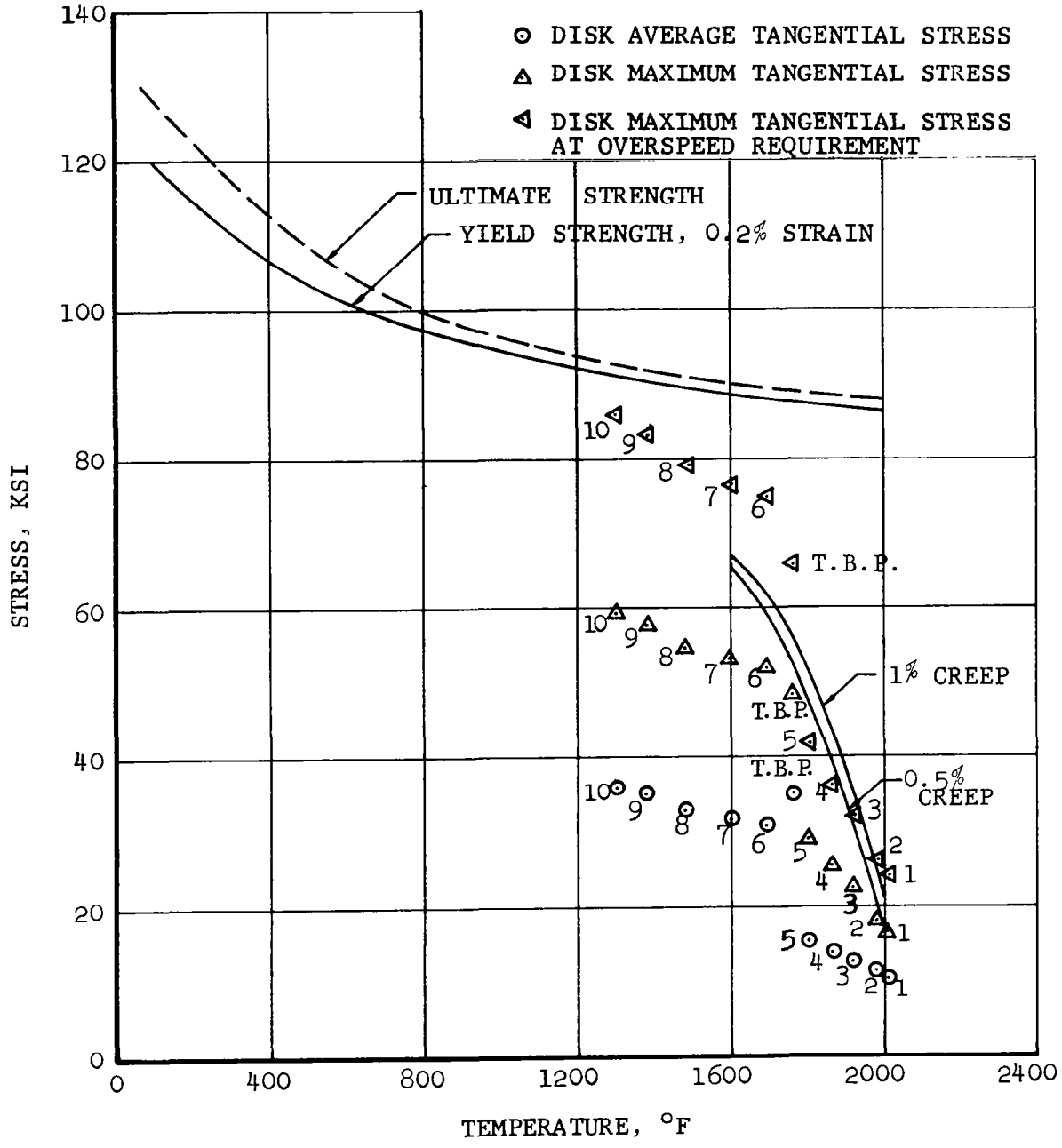

DISK STRESSES AND

DESIGN CRITERION

FIGURE 83

average tangential stresses for all 10-stage disks, as well as for the thrust balancing piston, with material strength properties. This figure shows that at the 20-percent overspeed condition, the peak tangential stress per stage is significantly below the respective material yield strength.

3.6.2 Stub-Shaft Stress Analysis

The turbine rotor stub-shafts are key components which must operate under rather severe conditions. These conditions and the functional requirements are as follows:

(a) Transmit the tie-bolt load to the turbine disks, at 3.4-in. diameter and the rotor unbalance load to the bearings
(b) Carry an axial load up to 20,000 lb in compression
(c) Rotate to 23,000 rpm (overspeed)
(d) Hot-end above 2000°F with a temperature variation in excess of 1000°F (front-end only)
(e) Provide rigid support for bearing journals
(f) Serve as viscoseal rotors
(g) Certain temperatures at the viscoseal interface locations
(h) Flexibility and length limited by critical speed requirements
(i) Rigidity limited by heat-transfer and thermal expansion requirements
(j) Pilot the front labyrinth seal rotor

The stresses are limited by the material yield strength at the lower temperatures and by creep at the higher temperatures. The stress distribution in each stub-shaft was computed using a finite element analysis, Program 5902, which is described in Appendix E. This analysis was made for the temperature distribution at the mechanical design-point, a 20,000-lb compressive axial load, and at the design speed of 19,200 rpm. The results of the analysis are presented in Figure 84 for

the front stub-shaft and Figure 85 for the rear stub-shaft. The tangential, radial, and axial stress distributions and the temperature distribution are shown in each figure.

Inspection of these results reveals that stress nodes (or relative maximums) occur at certain locations. At each of these nodes, the stress components were combined according to the minimum distortion energy theory of failure, thus obtaining peak equivalent stresses. These stresses are noted with the tangential stress distribution of each figure, but only at those locations where the peak equivalent stress exceeds the largest of the three component stresses. Also noted on each figure is the average tangential stress in the region where it is highest. In Figure 84, this value is obtained by averaging the area above the dotted line and in Figure 85, to the left of the dotted line.

In Figure 84, for the front stub-shaft, the computed stresses are all well below the short-time yield strength of TZM, even when the tangential stresses are multiplied by 1.44 to account for the 20-percent overspeed condition. The design is, therefore, conservative from a short-time standpoint but is limited by creep in the region where the tangential stress was averaged. The stress in this high-temperature region is 17.3 ksi, whereas the 0.5-percent creep strength of TZM at 2000°F for 30,000 hr is about 20 ksi. It is difficult to determine the radial growth at the stub-shaft outer diameter under these conditions, in view of the stress and temperature variations in the region. With local creep causing stress relaxation* and by using the average tangential stress of 17.3 ksi and a metal temperature of 1980°F, the amount of creep after 30,000 hr is about 0.15 percent.

The average tangential stress in the front labyrinth seal rotor is about 15.5 ksi (Figure 86) and has a temperature of about 2000°F in

*The finite element stress program is currently being revised to include plastic strain.

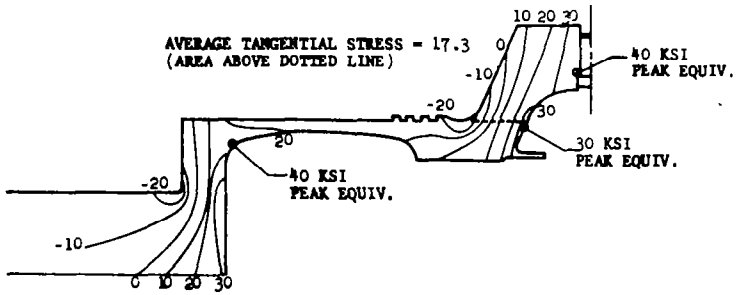

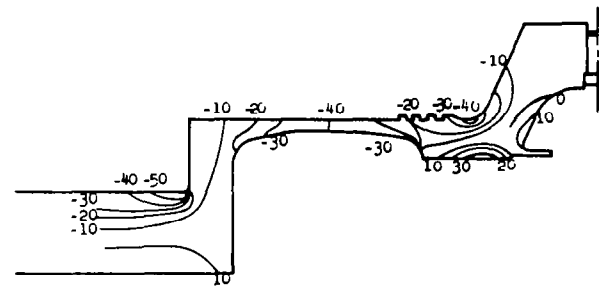

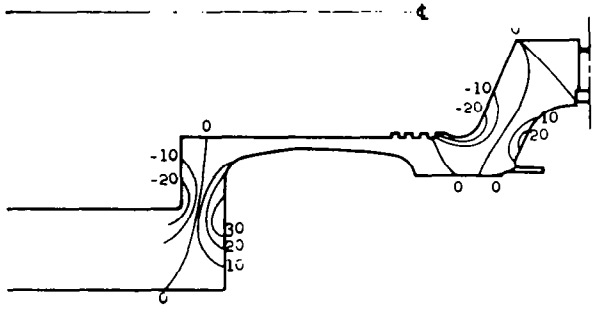

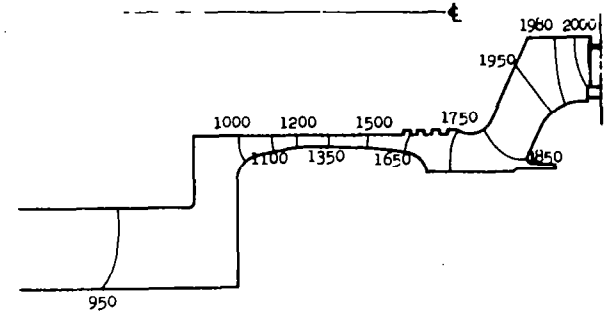

FRONT-END STUB SHAFT STRESSES

FIGURE 84

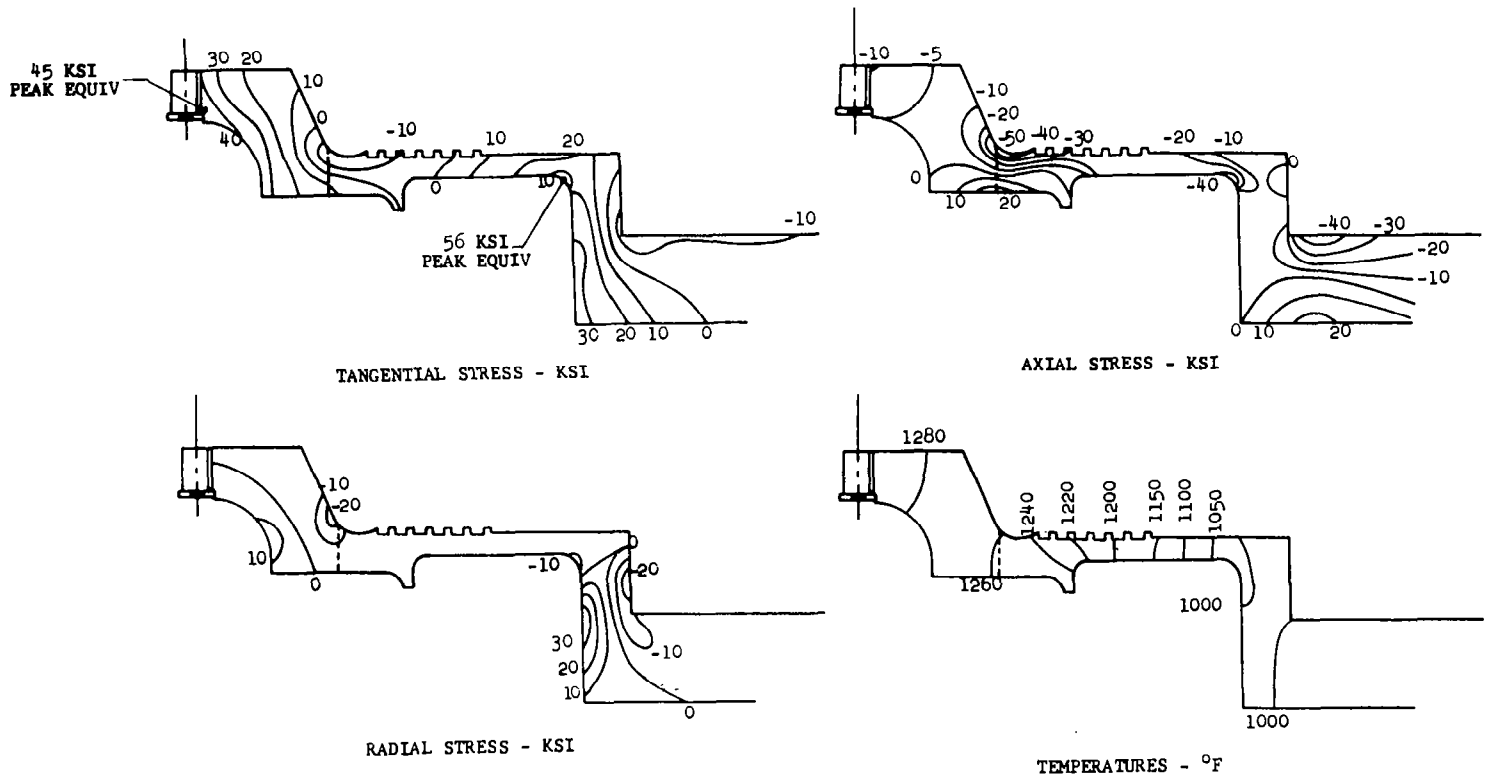

REAR-END STUB SHAFT STRESSES

FIGURE 85

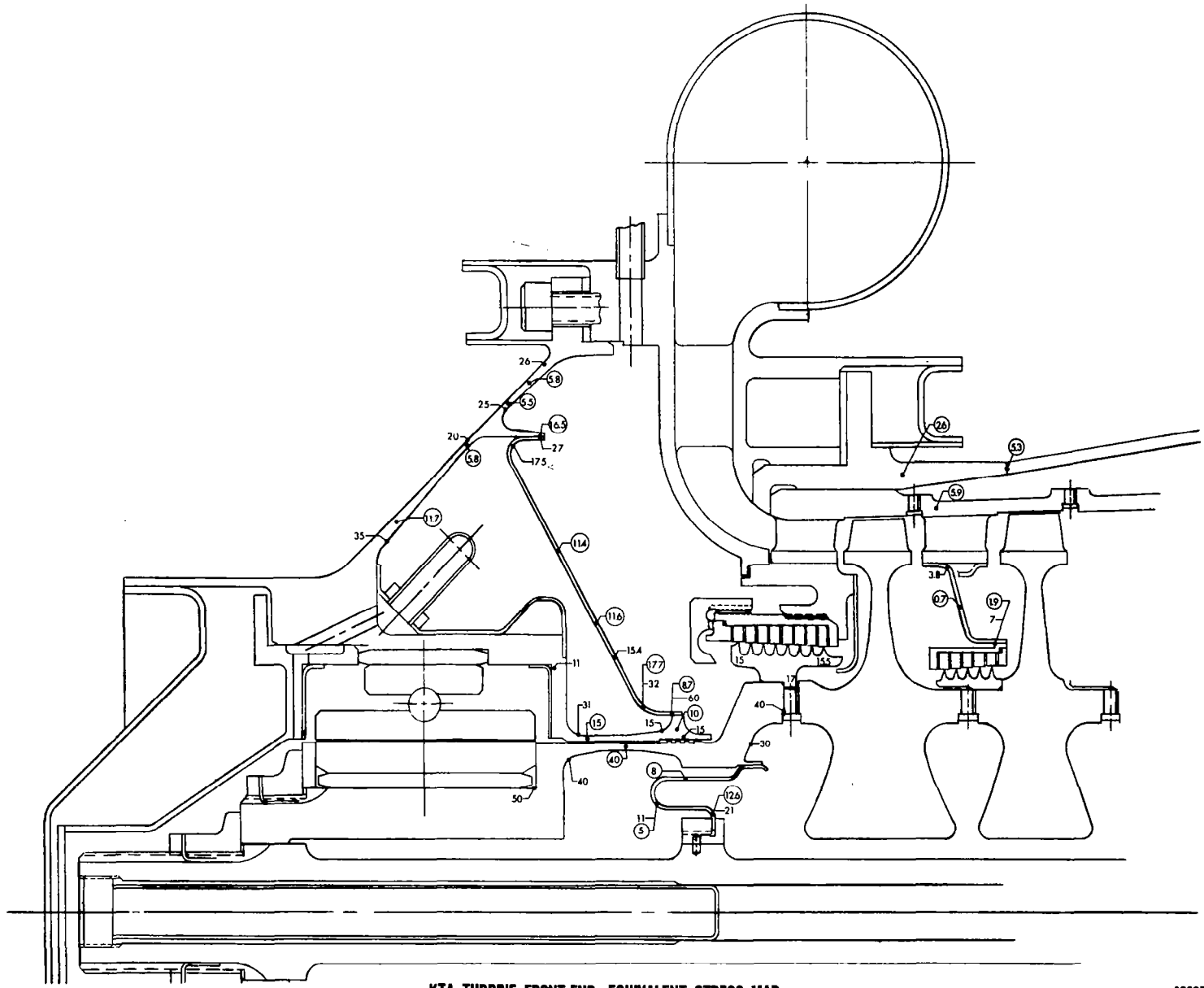

FIGURE 86

the middle. Under these conditions, the seal rotor, acting as a free ring, would creep about 0.15 percent, which indicates that the seal rotor will not separate from the stub-shaft on which it is piloted. Thus, the stub-shaft and seal rotor grow at about the same rate, and the radial growth after 30,000 hr is approximately 0.0033 in., slightly less than the initial seal-running clearance.

For the rear stub-shaft (Figure 85), one or two of the stress nodes exceed the 0.2-percent yield strength of T-111 (about 50 ksi) although none reach the ultimate strength. The bending stress in these areas is highly localized, so that local yielding will merely cause stress relaxation, until no further yielding occurs and no significant dimensional changes result. Multiplying the tangential stresses by 1.44 to represent the 20-percent overspeed condition, the tangential stresses near the curvic coupling also exceed the yield strength but do not reach the ultimate strength. Local yielding here will redistribute the tangential stress over the area in which the average value of 19.2 ksi was computed (27.7 ksi at 20-percent overspeed), and this should be conservative enough. Dimensional changes from this yield will not significantly reduce the axial load, and creep does not occur at this low-temperature level.

The calculated stress levels in both front and rear stub shafts are considered satisfactory; however, these stress levels can be reduced by further optimization of the configurations.

3.6.3 Mechanical Design of Structural Components

A summary of computed stress results are presented in Figure 86 for the turbine hot-end in the highly stressed parts of the T-111 structure. The stress in thin-shell sections was computed with Program 589, which is described in Appendix E. The stress values

shown in the figure represent the equivalent stress according to the von Mises theory of failure (minimum distortion energy), which is most applicable to ductile materials. For a biaxial stress field, as in a thin shell, the equivalent stress is defined as;

$$\sigma_{eq} \equiv \sqrt{\sigma_1^2 - \sigma_1\sigma_2 + \sigma_2^2}$$

where σ_1 and σ_2 are principal stresses. The circled numbers represent average values over the shell cross section, and the uncircled numbers are local values at the shell surface, where the stress is maximum due to bending. Also, the values are noted only at the stress nodes, i.e., where relative maximums occur along the shell length.

3.6.3.1 Conical Front-End Housing, Item 1

The functional requirements of this housing are as follows.

(a) Provide a rigid support for the front journal bearing housing
(b) Tolerate the relative thermal expansion between the bearing housing and the inlet scroll flange
(c) Carry the axial load due to pressure in Region D and in the bearing compartment
(d) Conduct a reasonably small amount of heat into the bearing compartment
(e) Support the conical sheet-metal pressure vessel, Item 19

The location of the sheet-metal pressure vessel support was determined by the temperature at that point, which must be higher than the saturation temperature of Region D but low enough to prevent creep problems in the sheet metal. The thickness distribution along the housing was optimized to achieve minimum stress and heat-transfer, while maintaining a feasible design that can be machined with reasonable

tolerances. The shell thickness is tapered linearly between 0.040 and 0.100 in. in the inner portion and between 0.050 and 0.080 in. in the outer portion, with ample fillets.

Comparison of the computed stresses with the strength data for T-111 reveals that no short-time yielding occurs, the highest stress being about 70 percent of the yield strength, although some creep will occur at the higher temperatures. Specifically, in the outer portion of the housing, the shell bending produces peak stresses which are well above the 1-percent creep strength at the corresponding temperature. However, these stresses are localized at the shell surface and, with less than 0.1 percent of local creep, stress relaxation will produce nearly uniform stress over the shell cross section. Only the average stresses are constant (fixed by the axial load), and these are all below the 0.1-percent creep strength at 30,000 hr. Most of the creep (in bending) would occur on the first temperature cycle, so that residual stresses would exist in the part after cooling. Subsequent temperature cycles would produce negligible creep.

3.6.3.2 Conical Sheet-Metal Pressure Vessel, Item 19

This part functions as a pressure container to Region D, with a near-vacuum in Region B, and as a radiation shield between the turbine inlet scroll and the front bearing housing. The sheet metal is 0.030-in. nominal thickness.

The peak stresses computed are below the material yield point with the exception of a highly localized bending stress at the inner radius of the sheet metal. This stress is below the ultimate strength of T-111, and it will be relieved by local yielding when pressure is applied. The average equivalent stress due to constant pressure loading is just under 12 ksi, which would cause about 0.1-percent creep in 30,000 hr at the maximum temperature of 1800°F. At the stress nodes,

creep will cause stress relaxation so that everywhere the stress will asymptotically approach a value of about 12 ksi as time proceeds.

At the inner radius temperature of the sheet metal, the peak stress may be relieved to as low as 20 ksi. With a computed elastic stress of 60 ksi, the peak residual stress after one temperature cycle would be 40 ksi or less in compression. Since this is well below the material yield strength at low temperature, it follows that low-cycle fatigue due to temperature cycling is not a problem, unless many thousand cycles were anticipated, which is not the case.

3.6.3.3 Miscellaneous

The stress levels in all other areas of the hot-end structure are much lower than those discussed above. These parts--viscoseal stator support, bearing housing, inlet scroll, etc.--were more conservatively designed in order to provide rigidity and dimensional stability.

The sheet-metal pressure caps inside the stub-shafts are 0.020-in. nominal thickness. At the hot-end, where the pressure seal is dependent on an interference fit between the sheet metal and the stub-shaft bore, the initial radial interference must be at least 0.001 in. in order to prevent separation at steady-state operating conditions. The bore of the stub-shaft will not creep significantly since the temperature there is sufficiently low for TZM. However, if the initial interference exceeds 0.0015 in., some creep will occur in the sheet metal due to interference at operating temperature so that the contact pressure is reduced to about 120 psi. Also, if the initial interference exceeds 0.002 in., some yielding would occur during assembly in addition to the high-temperature creep. Otherwise, the peak stresses in either of the sheet-metal caps are well below the creep strength of T-111.

The turbine stator rings are piloted by curvic couplings, similar to the rotors, which are held in place by tension in the outer casing (acting as a tie-bolt). The amount of tension needed to hold the stators in alignment has not been determined nor has a complete stress analysis been made to design for this axial load and the duct loads. Consequently, a final materials selection has not been accomplished, although T-111 and Cb-1Zr were used for the thermal analysis, seal design, and weights calculations, with the transition point where the high-pressure spool casing is welded to the interspool scroll. Some preliminary stresses were computed at the hot end based on a 12,000-lb load, which is probably higher than necessary. These are also shown in Figure 86 and are acceptable, with less than 0.5-percent creep in 30,000 hr at the hot end and decreasing to nothing within 1 in. FS-85 has a relatively high strength-to-weight ratio and would perhaps be a better selection for the interspool scroll, the low-pressure spool stator rings, and outer casing.

The rear bearing compartment support structure was designed as four 4-in. radial beams, each with a rectangular cross section of 0.5 x 1.6 in. The material selected, Cb-1Zr, has a relatively low modulus of elasticity. The axial stiffness is 10^6 lb/in. and the transverse stiffness about 5 x 10^6 lb/in. The computed thermal stress is 10.5 ksi, and the maximum bending stress under a 3000-lb axial load (20 g acceleration) is 7 ksi. These stress levels are well below the material yield strength of 25 to 30 ksi. Creep is not measurable at these low temperatures (1200°F maximum).

3.6.4 Mechanical Design of Tie-Bolt

3.6.4.1 Configuration

The tie-bolt material selected is TZM. The length between the fixed-end pilots is 26 1/2 in. supported near the middle. The sheet-metal pressure caps under each stub-shaft are connected to the tie-bolt

with mechanical fasteners, and two static labyrinth seals are positioned near the middle as described in Section 3.5. The outer diameter of the tie-bolt is 0.85 in. from the front fasteners and two static seals, and 0.75 in. from the rear fastener to the rear pilot. The tie-bolt is rifle-bored from both ends. The bore diameter is 0.45 in. between the sheet-metal fasteners, being bored from the front end, and 0.50 in. from the front end to the front fastener. From the rear end, the tie-bolt is bored to the rear fastener at a 0.40-in. diameter and under the fastener at a 0.35-in. diameter. Sheet-metal bore plugs that seal the bore directly under the fasteners are used at each end. A positive seal is assured by relative thermal expansion using T-111 sheet metal and by rolling the sheet metal in place after assembly. Vent holes are drilled into the resulting internal cavity at two locations (Section 3.5). These holes are drilled at a 30-deg angle from the axis and are located in larger cross sections so that stress concentrations will be small. The extra thread length at the front end of the tie-bolt is for the use of a puller-nut so that the tie-bolt can be pre-loaded without torsion.

3.6.3.2 Thermal Effects and Stress

Figure 87 presents the relative thermal expansion of the turbine rotor to tie-bolt for the transient start-up condition analyzed thermally, i.e., 900°F initial temperature and a 1.0-°F/sec inlet temperature ramp. The relative expansion is non-zero at zero-time because of the T-111 rear stub-shaft, which expands at a greater rate per unit length than the rest of the turbine rotor when heating from room temperature to the 900°F initial temperature. As the turbine inlet temperature increases, the tie-bolt relative expansion increases rapidly at first, then approaches a gradual constant rate of increase which continues to the end of the inlet temperature ramp. The transient thermal analysis was not carried beyond this point, but it is apparent that the relative expansion will reach a maximum soon after

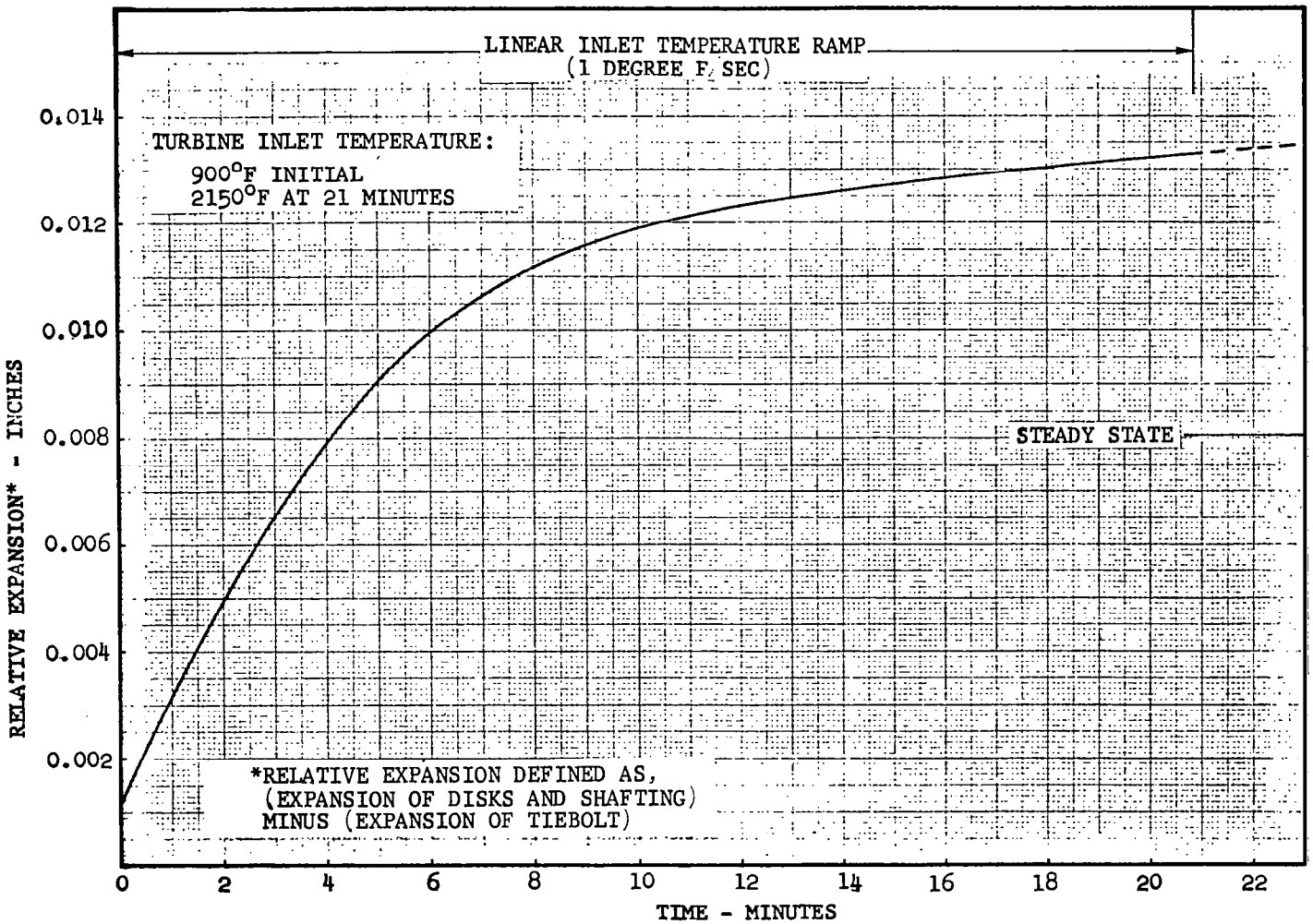

KTA TURBINE ROTOR AND TIEBOLT,

RELATIVE THERMAL EXPANSION

FIGURE 87

this and begin to decline to the steady-state value, which is shown at the right side of the figure.

Figure 88 shows the total tie-bolt axial load versus time for the same transient start-up condition. The load changes due to relative thermal expansion are superimposed on the variable preload, which is selected as 12,000 lb at 900°F. This requires an initial stretch of the tie-bolt relative to the turbine rotor of 0.0188 in., resulting in an initial preload at room temperature of 12,880 lb. The preload varies with temperature due to the opposing effects of the higher thermal expansion rate of the rear stub-shaft and the decreasing modulus of elasticity of TZM at higher temperature levels. The tie-bolt load reaches a maximum of 17,800 lb after only 11 min, which is less than half the time required to reach the relative thermal expansion maximum. This is due to the reduction in modulus of elasticity at higher temperatures. The steady-state load at the mechanical design point is 14,200 lb.

The minimum preload of 12,000 lb was selected for proper seating of the curvic couplings based on AiResearch experience. The total tie-bolt load may be allowed to drop below this temporarily during a transient shutdown condition. The lower bound on tie-bolt load is about 2000 lb--that required to prevent curvic-coupling separation at any speed. It may be inferred from Figure 88 that reducing the turbine inlet temperature at a rate of 2°F/sec would be safe. Also, a sudden stoppage in turbine flow would not unload the tie-bolt because the heat-sink effect of this flow would be removed.

A comparison of tie-bolt stress and strength is presented in Figure 89, again for the transient start-up condition. The time of 100 min is assumed essentially at steady-state. The maximum temperature in the tie-bolt at the mechanical design-point is about 1750°F and occurs under the fourth-stage disk. The axial stress at this

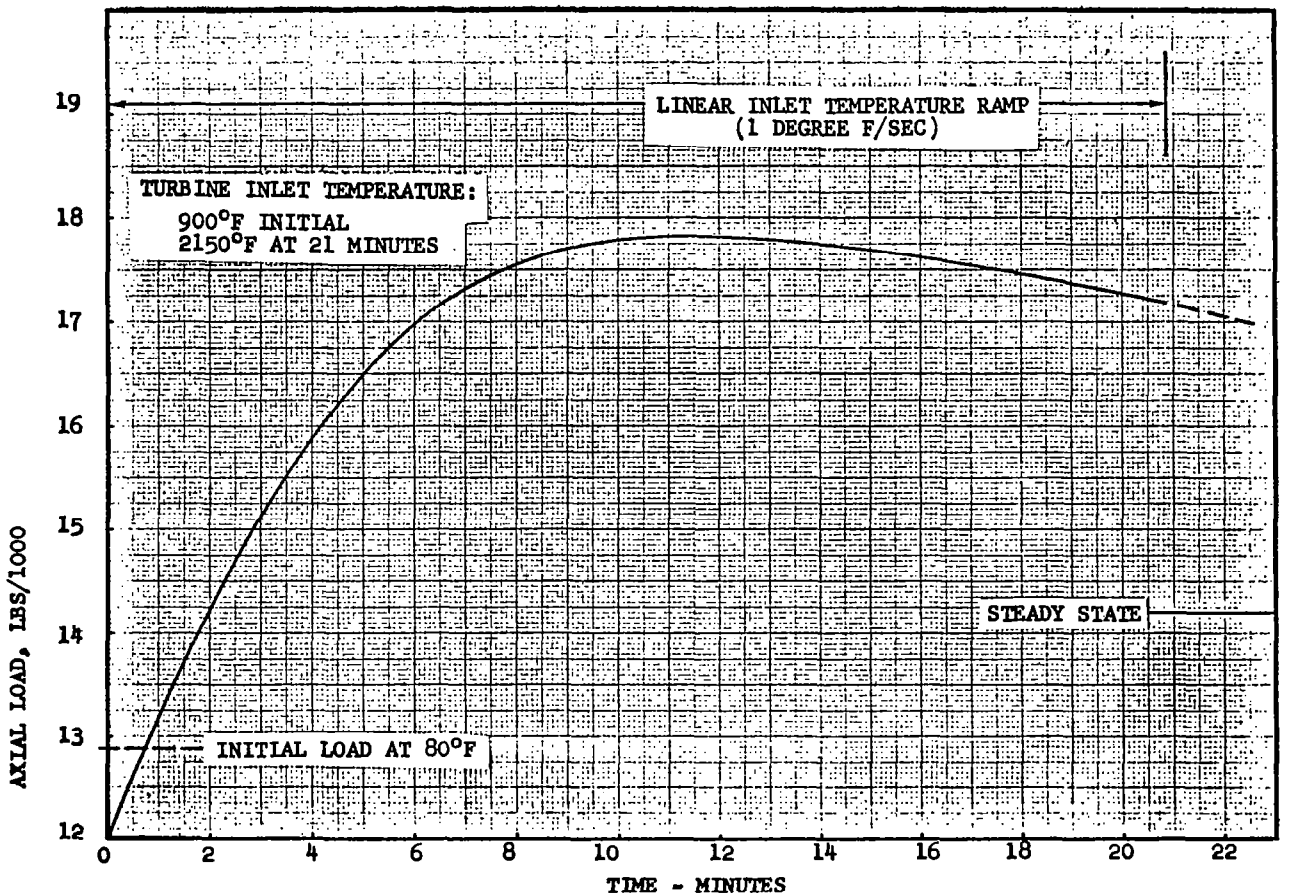

KTA TURBINE TIEBOLT,

TOTAL AXIAL LOAD

FIGURE 88

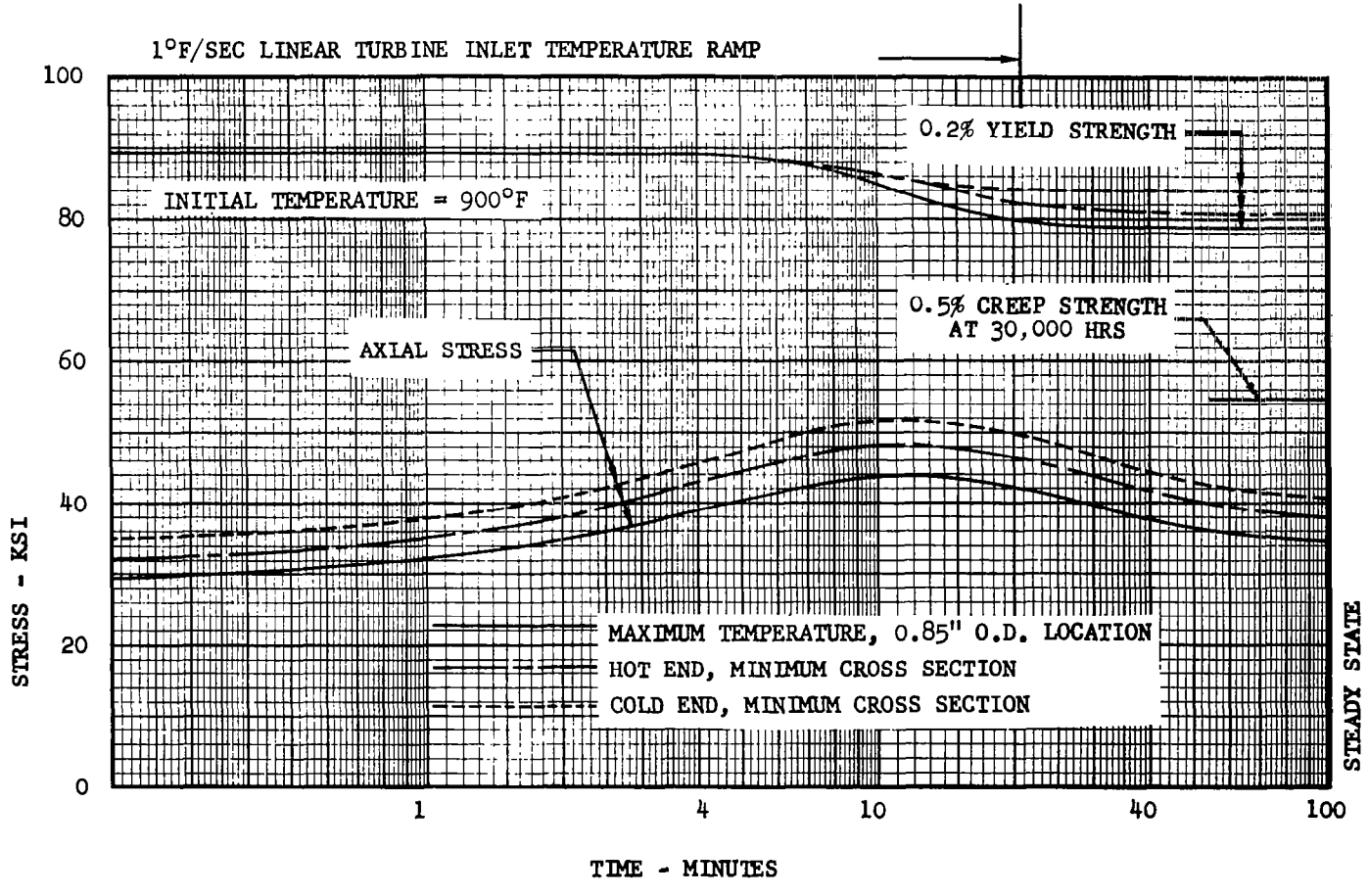

KTA TURBINE TIEBOLT, AXIAL

STRESS AND STRENGTH

FIGURE 89

point is about 35 ksi at steady-state, and the 0.5-percent creep strength at 30,000 hr is 55 ksi, so that no appreciable creep will occur. The steady-state stresses at the smaller cross sections near the tie-bolt ends are higher, but these are limited only by the yield strength due to the lower temperatures. The maximum transient stresses, also limited only by yield strength, are conservative at all points.

3.6.3.3 Tie-Bolt Critical Speeds

The influence of the tie-bolt upon the turbine rotor dynamics at operating speed will be negligible if the tie-bolt natural frequency (neglecting the center bumper) is adequately removed from operating speed. The bumper is present in order to safely transverse the critical speed, since it has been found most convenient to design the tie-bolt with a natural frequency below the operating speed of the rotor.

It was found that by the design of the intermediate supports (seals) and of the tie-bolt outer radius, the natural frequency could be located between 24,500 and 16,900 rpm. Both of these numbers are upper bounds since the tie-bolt ends were considered "built-in" and the modulus of elasticity was 40×10^6 psi (corresponding to the coldest portion of the tie-bolt). In addition, the calculation was made with the peak tension load of 20,000 lb corresponding to a transient condition.

The final configuration is that the tie-bolt natural frequency would be below 16,900 rpm under the turbine operating conditions. At room temperature, where the modulus would be about 46×10^6 psi, the natural frequency upper bound is 18,000 rpm. This would apply to the operation of a dynamic simulator test rig.

3.6.5 Mechanical Seal Design

3.6.5.1 Configurations

The front turbine viscoseal utilizes a smooth stator and a grooved rotor. Both the rear viscoseals have grooved stators and rotors. In each seal, there are 30 groove-starts at a helix angle of 14 deg, a groove depth of 0.018 in., and the ratio of channel-width to land-width of 1.5. The diameter of the lands are 2.8 in. for the two journal-bearing viscoseals and 2.0 in. for the thrust bearing viscoseal. The overall lengths and the required pumping lengths at the mechanical design-point are tabulated below. The optimization of viscoseals for this application is given in Appendix G.

Viscoseal	Wet Length, in.	Total Length, in.
Front journal bearing	0.125	0.33
Rear journal bearing	0.26	0.46
Thrust bearing	0.46	0.70

The configuration of the front labyrinth seal shown in Figure 90 is typical of the 12 labyrinth seals used along the turbine rotor, where the upper part is the stator and the lower part, the rotor. The stators are made of thin foil disks (0.004-in. thickness) of two different inner diameters stacked alternately and separated between stages by a spacer. The staggered foils are designed to tolerate seal rubs without destruction of the seal. The spacers are stepped in diameter to prevent the annular jet from one orifice from impinging directly on the succeeding one, thus minimizing carryover leakage. The rotating knives are designed as replaceable parts. Seal rubs will not cause failure in the rotors since any damage will be localized at the knife edges. The front labyrinth seal and the rotating piston rim seal each

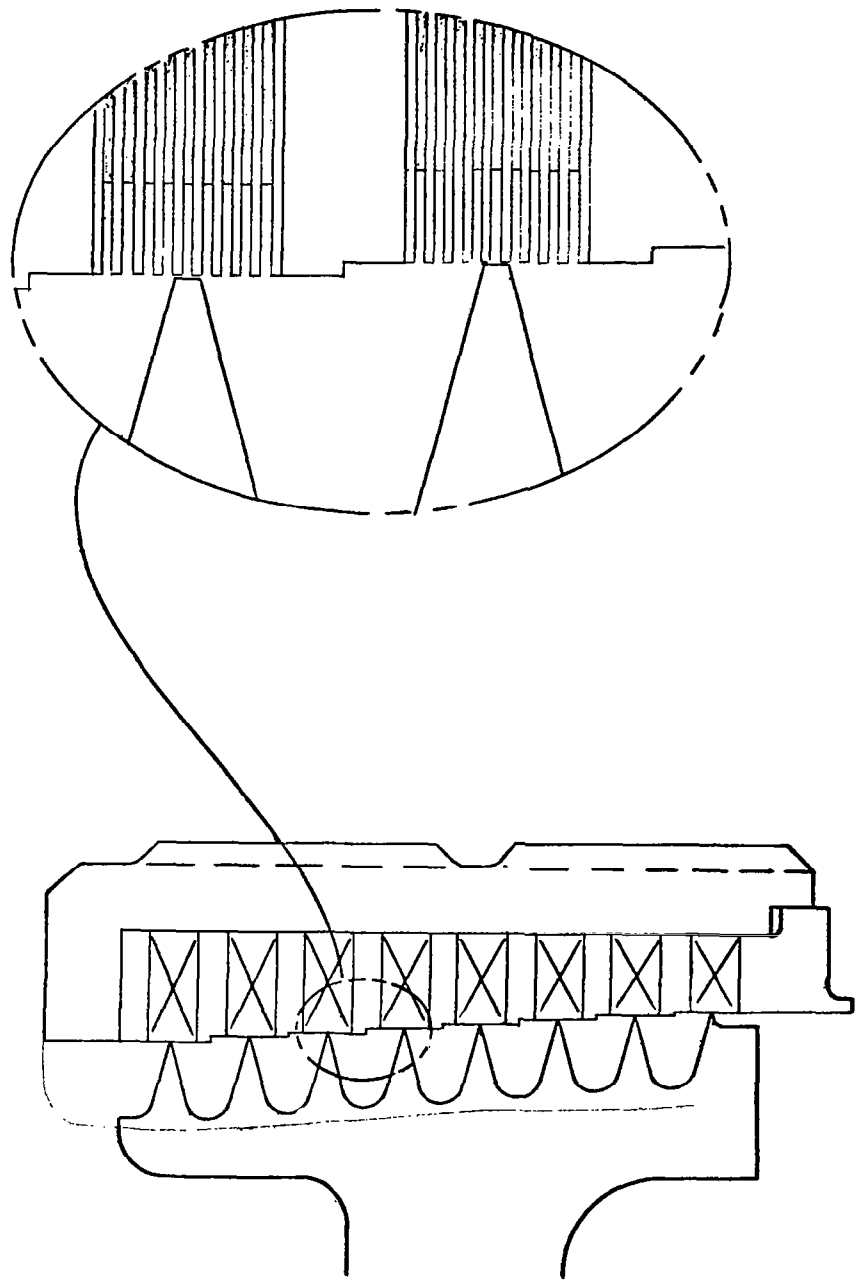

KTA TURBINE, LABYRINTH

SEAL CONFIGURATION

FIGURE 90

have eight labyrinth stages. The interstage shaft seals each have five stages except for the ones on each side of the piston that have six.

Two static seals of the labyrinth-type are located in the center portion of the tie-bolt. The one at the tie-bolt bumper will have a very small clearance (0.001 in.) and is designed to contact the bumper. The one under the seventh-stage disk will have a relatively large clearance (0.005 in.) so that contact with the disk bore will be prevented. These seals contain the pressure of the thrust-balancing piston leakage. The sheet-metal static seal under the front stub-shaft relies on an interference fit to prevent leakage into the bearing loop. The interference is maintained by the thermal expansion of the sheet metal (T-111) relative to the stub-shaft (TZM).

Three piston-ring seals are used between the turbine outer casing and the stator walls and will tolerate misalignments as well as clearance changes. These seals prevent short-circuit leakage between the openings to the flow path. They are located so that the metal temperatures are always above the saturation temperatures, thereby preventing latent heat-transfer in this area.

3.6.5.2 Clearances and Leakage

Figure 91 summarizes the leakage rates and flow paths of all the labyrinth seals. The flow rates are given for the aerodynamic design-point because these quantities directly affect turbine performance.

The leakage rates are based on certain running clearances, which are tabulated below for all seals designed to operate at finite clearances.

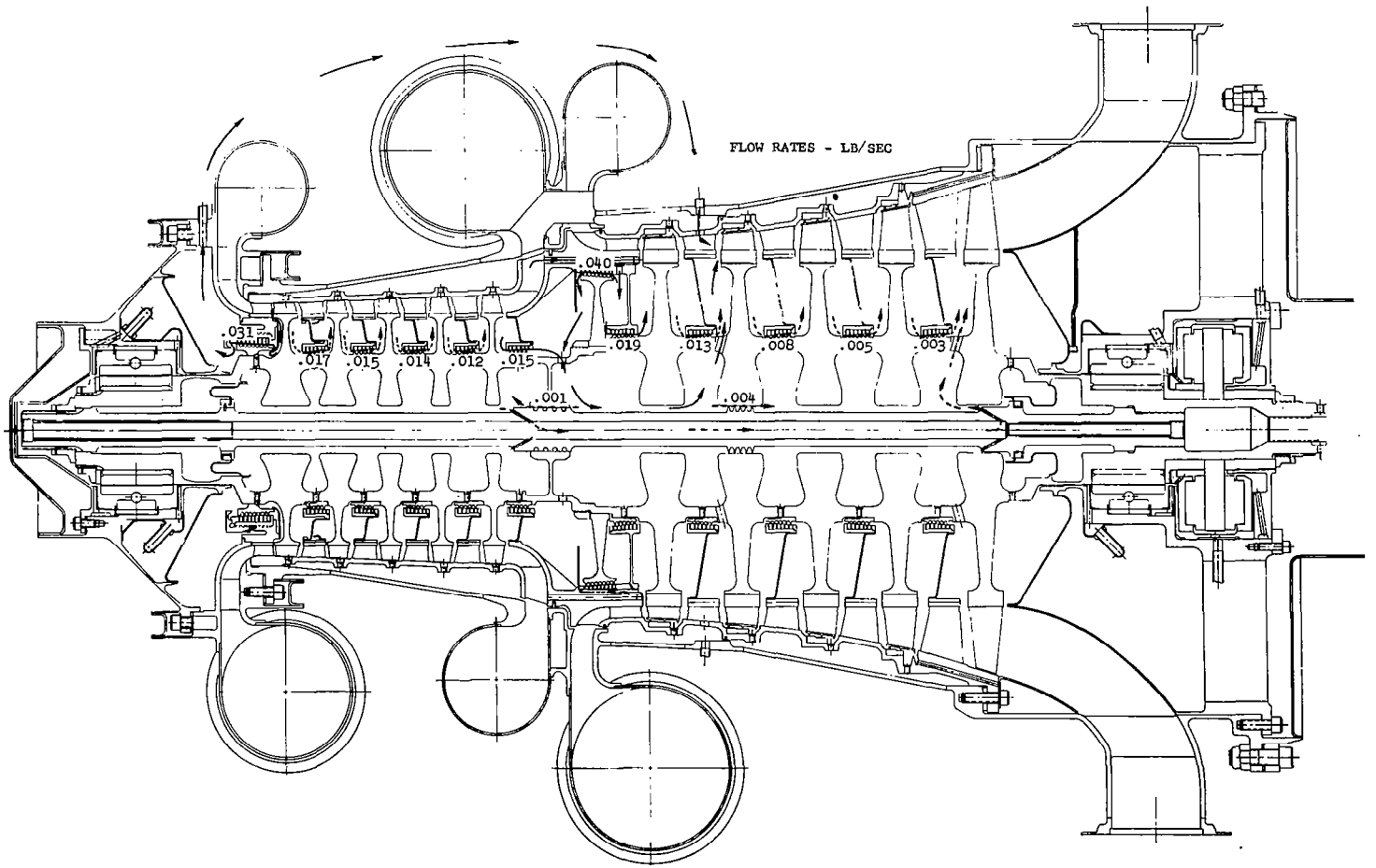

KTA TURBINE LABYRINTH SEAL LEAKAGE RATES AND SECONDARY

FLOW PATHS FOR AERODYNAMIC DESIGN POINT

FIGURE 91

Seals	Clearance, In.
Viscoseals	0.005
Labyrinth shaft	0.004
Rotating piston	0.006
Tie-bolt bumper	0.001
Tie-bolt-seventh disk bore	0.005

The clearance changes (from initial assembly clearances) due to thermal and centrifugal expansion are presented in Table 15. Values are given for a 900°F uniform temperature at design speed, the initial condition for start-up following acceleration, and for the mechanical design-point. It is notable that the clearance change goes from positive to negative along the length of the front labyrinth seal. This is due to the large temperature gradient in this seal stator, as described in Section 3.5. Subtracting the tabulated values for the mechanical design-point from the selected running clearances, it is found that the minimum initial assembly clearance must be 0.0013 in. at the interstage shaft seal between Stages 6 and 7. Adding to these differences the clearance changes at the 900°F, design-speed condition, it is found that the minimum clearance during acceleration is 0.00285 in. and occurs at the same shaft seal. About the same clearance changes occur at the Stage 5 piston shaft seal, which is a more critical seal when thrust balancing is used. Although the rotating piston has the maximum clearance change, it also has a larger running clearance, so that the assembly clearance is 0.00295 in. and the minimum clearance during acceleration is 0.00485 in. The minimum clearance change is approximately 0.0042 in. All these clearance-changes are within practical limits.

Figure 92 shows the assumed seal clearance-change response during the start-up condition — 900°F uniform initial temperature at design speed and a 1°F/sec turbine inlet temperature ramp. Only the more critical seals, with respect to turbine performance, are shown along

TABLE 15

KTA TURBINE SEALS, CHANGES IN MINIMUM RADIAL CLEARANCE

Location	900°F Design Speed, in.	Mechanical Design-Point, in.
Front Journal Bearing, Shaft Viscoseal	+0.00056	0.00105
Front Shaft Seal Labyrinth, Inlet	-0.00017	0.00053
Exit	-0.00013	-0.00125
Interstage Shaft Seals (Labyrinth)		
Stages 1-2	+0.00019	0.00069
Stages 2-3	+0.00019	0.00066
Stages 3-4	+0.00019	0.00066
Stages 4-5	+0.00019	0.00066
Stages 6-7	+0.00156	0.00271
Stages 7-8	+0.00156	0.00257
Stages 8-9	+0.00156	0.00239
Stages 9-10	+0.00156	0.00222
Stage 5 - Piston Shaft Seal (Labyrinth)	+0.00158	0.00269
Rotating Thrust Balancing Piston (Labyrinth)	+0.00189	0.00305
Piston - Stage 6 Shaft Seal (Labyrinth)	+0.00029	0.00120
Rear Journal Bearing, Shaft Viscoseal	+0.00020	0.00060
Turbine Thrust Bearing	+0.00070	0.00070

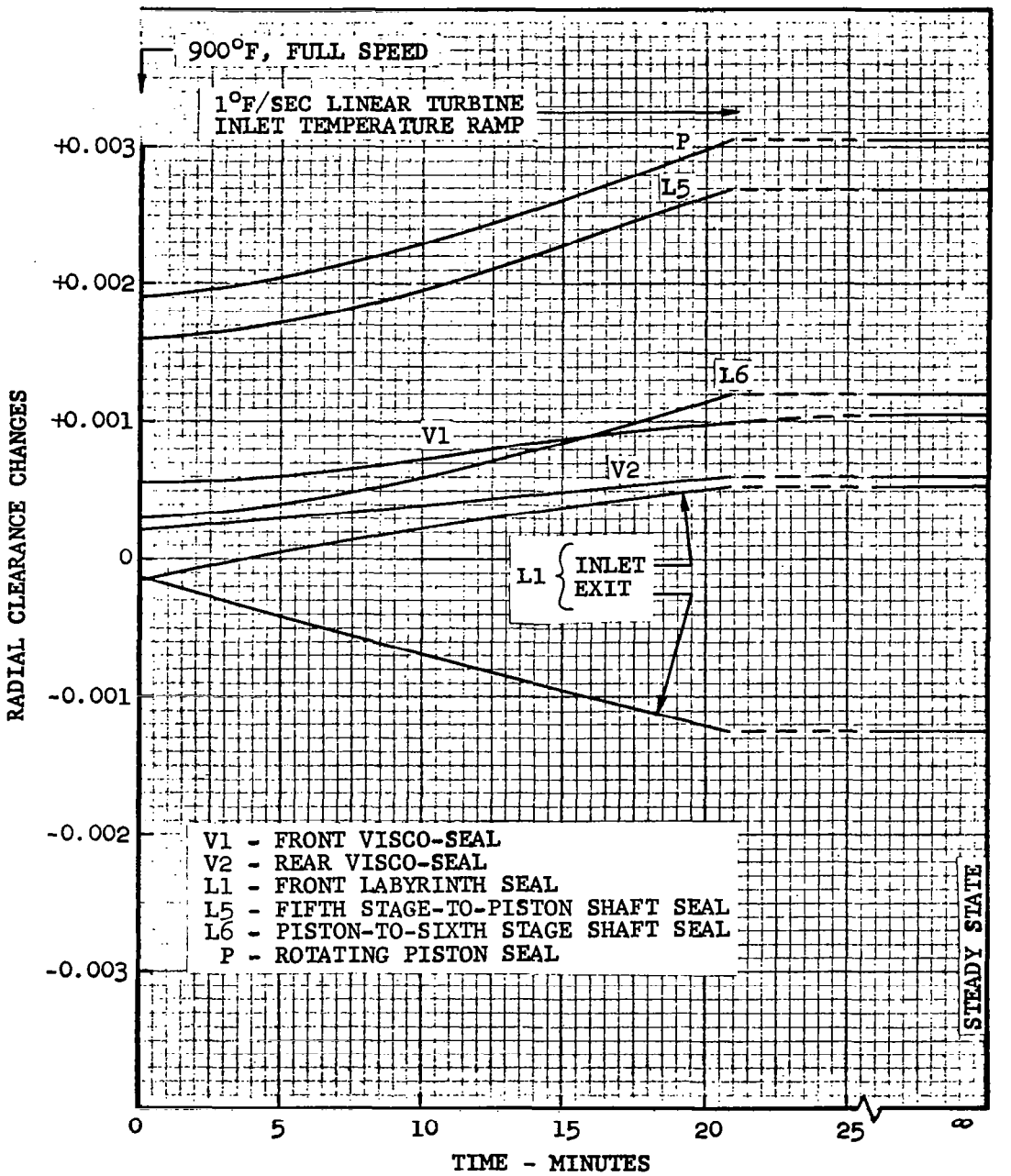

KTA TURBINE, SEAL CLEARANCE

RESPONSE DURING START-UP

FIGURE 92

with the viscoseals. Most of this information is repeated from the preceding table. As discussed in Section 3.5.4, the temperatures in these areas are almost linear with time. Therefore, the nonlinearity of these curves are due to the variable thermal expansion coefficient, which increase with temperature. Table 16 lists the clearance changes at the turbine wheel tips for the same conditions as Table 15 for the seals. Using a running clearance of 0.010 in. at all stages, it is found that the minimum initial assembly clearance is 0.0022 in. at the sixth-stage wheel, and the minimum tip clearance during acceleration is 0.0044 in.

All the temperatures and clearances computed in this study are based on the selection of Cb-1Zr alloy for all the stationary parts aft of the fifth-stage exit station and T-111 forward of that point. If T-111 were used in place of Cb-1Zr or some other alloy of lower expansion than Cb-1Zr, all the seal clearance changes in this region would be smaller so that larger assembly clearances could be used.

3.6.5.3 Axial Displacement and Diaphragm Stress

A summary of stress and deflections of the interstage shaft seals, which are supported by sheet-metal diaphragms, is presented in Table 17. The sheet-metal thickness used is 0.040 in. at all interstage seals except the one under the sixth-stage stator, which is 0.050 in.

The average equivalent stress, based on the minimum distortion energy theory, in each diaphragm is well below the material creep strength at the corresponding temperature. Some of the peak equivalent stresses exceed the material creep strength. However, these are highly localized bending stresses which will be relieved when local plastic strain begins, and no significant increase in seal deflections will result.

TABLE 16

KTA TURBINE WHEELS, TIP CLEARANCE CHANGES

Stage	900°F Design Speed, in.	Mechanical Design-Point, in.
1	+0.0006	+0.0020
2	+0.0006	+0.0019
3	+0.0006	+0.0016
4	+0.0005	+0.0017
5	+0.0006	+0.0019
6	+0.0022	+0.0078
7	+0.0025	+0.0055
8	+0.0026	+0.0059
9	+0.0027	+0.0055
10	+0.0030	+0.0048

NOTES:
1. Centrifugal growth of each disk utilizing the modulus of elasticity corresponding to the disk temperature
2. Thermal growth of each disk referenced from 80°F
3. Thermal growth of each stator shroud section referenced from 80°F

TABLE 17

KTA TURBINE INTERSTAGE SHAFT SEALS, AXIAL DEFLECTION AND STRESSES DUE TO PRESSURE DROP

Stator Stage	Material	Pressure Drop, psi	Seal Deflection, in.	Seal Stator Mounts (Sheet Metal*)		
				Temperature, °F	Average Stress, ksi	Peak Stress, ksi
2	T-111	18.7	0.0025	2000	0.7	7.0
3	T-111	16.4	0.0022	1950	0.6	5.8
4	T-111	14.5	0.0019	1890	0.5	5.1
5	T-111	12.5	0.0016	1830	0.4	4.4
Interspool removal duct	Cb-1Zr	40.3	0.0224	1770	1.4	14.1
6	Cb-1Zr	21.1	0.0122	1760	2.0	14.0
7	Cb-1Zr	14.2	0.0198	1640	3.0	21.3
8	Cb-1Zr	9.2	0.0119	1530	2.0	13.8
9	Cb-1Zr	6.1	0.0074	1420	1.3	9.2
10	Cb-1Zr	3.5	0.0040	1310	0.75	5.3

*0.040-in. thickness, 0.050 in. at sixth-stage

Figure 93 shows the axial displacements of the stationary parts relative to the rotating parts due to thermal expansion only. Curve A represents the 900°F uniform temperature and design-speed condition, and Curve B represents the mechanical design-point. The axial displacements of the interstage seal stators due to pressure drop are in the opposite direction from the displacements due to thermal expansion. Thus, the difference between the values of Table 17 and those of Figure 93 is the net axial displacements of the seal stators relative to the rotor. The axial displacements at all seals and bearings are within practical limits, provided allowances are made during assembly.

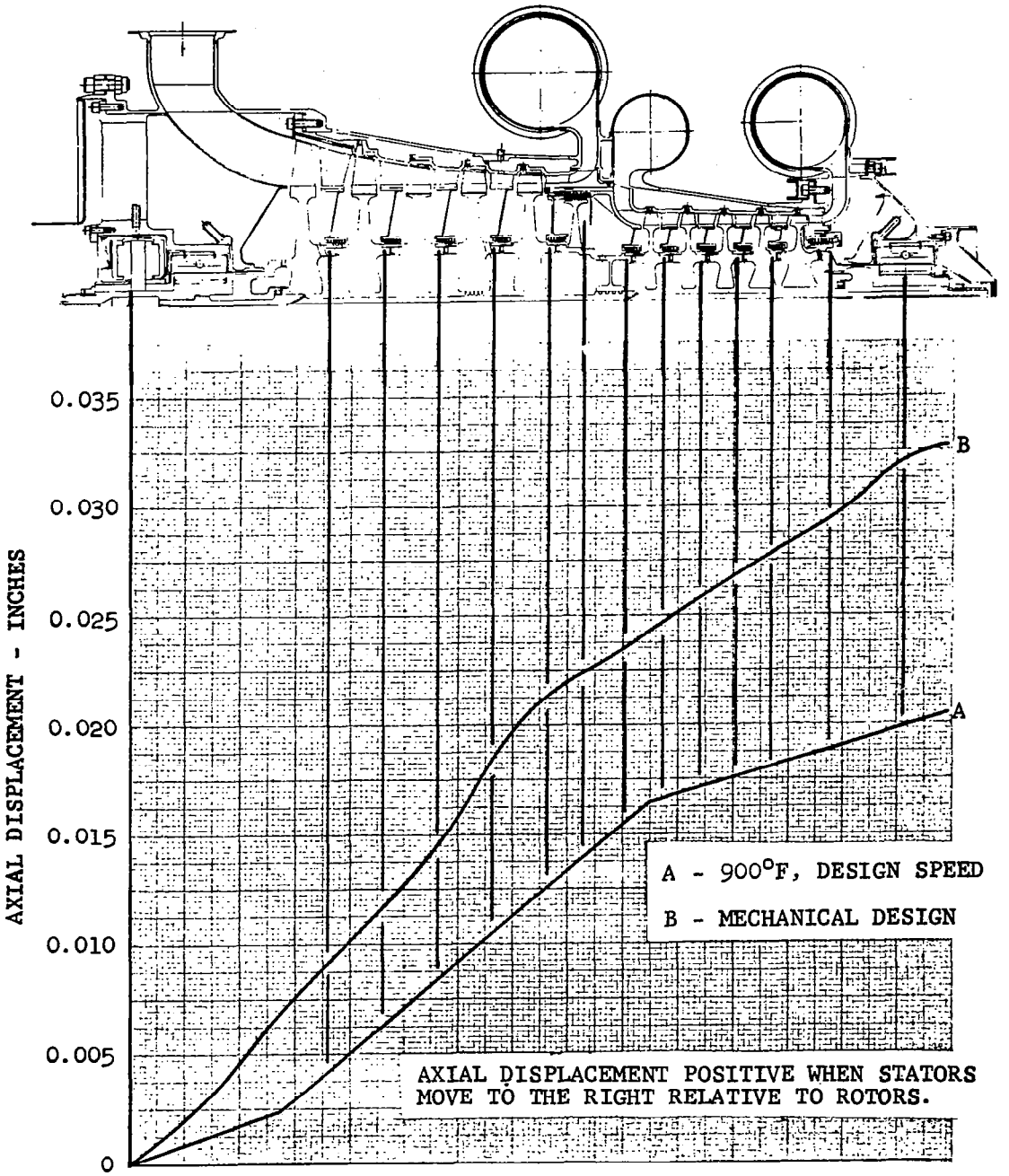

KTA TURBINE, RELATIVE AXIAL DISPLACEMENT

DUE TO THERMAL EXPANSION

FIGURE 93

4. BEARING DESIGN

4.1 Rotor System Dynamics

The dynamic rotor responses have been examined with the turbine as a unit, the alternator as a unit, and the turbine and alternator coupled, with the following bearing idealizations:

(a) Linear spring with no damping
(b) Linear spring with a constant damping coefficient
(c) A spring with a stiffness varying linearly with speed and with no damping
(d) A spring with a stiffness varying linearly with speed and with a constant damping coefficient

The case of a constant linear bearing spring-rate approximates the case of a horizontal rotor where the journal bearing load consists of the rotor weight and the dynamic forces combined. In addition, it is important to know where the critical speeds are located when the rotor is at operating speed; since the spring-rate used is for the respective bearing at 19,200 rpm, these results provide that information. A bearing spring-rate that increases linearly with speed approximates a vertical rotor above its first critical speed in that the spin is very nearly about the rotor cg. This implies a constant eccentricity ratio where the spring rate of a hydrodynamic bearing is a linear function of speed.

Figures 94 and 95 present the turbine rotor bearing loads for the two spring-rate cases and Figures 96 and 97 present the turbine rotor radial runout for the same cases. Similar information for the alternator rotor is shown in Figures 98 through 101.

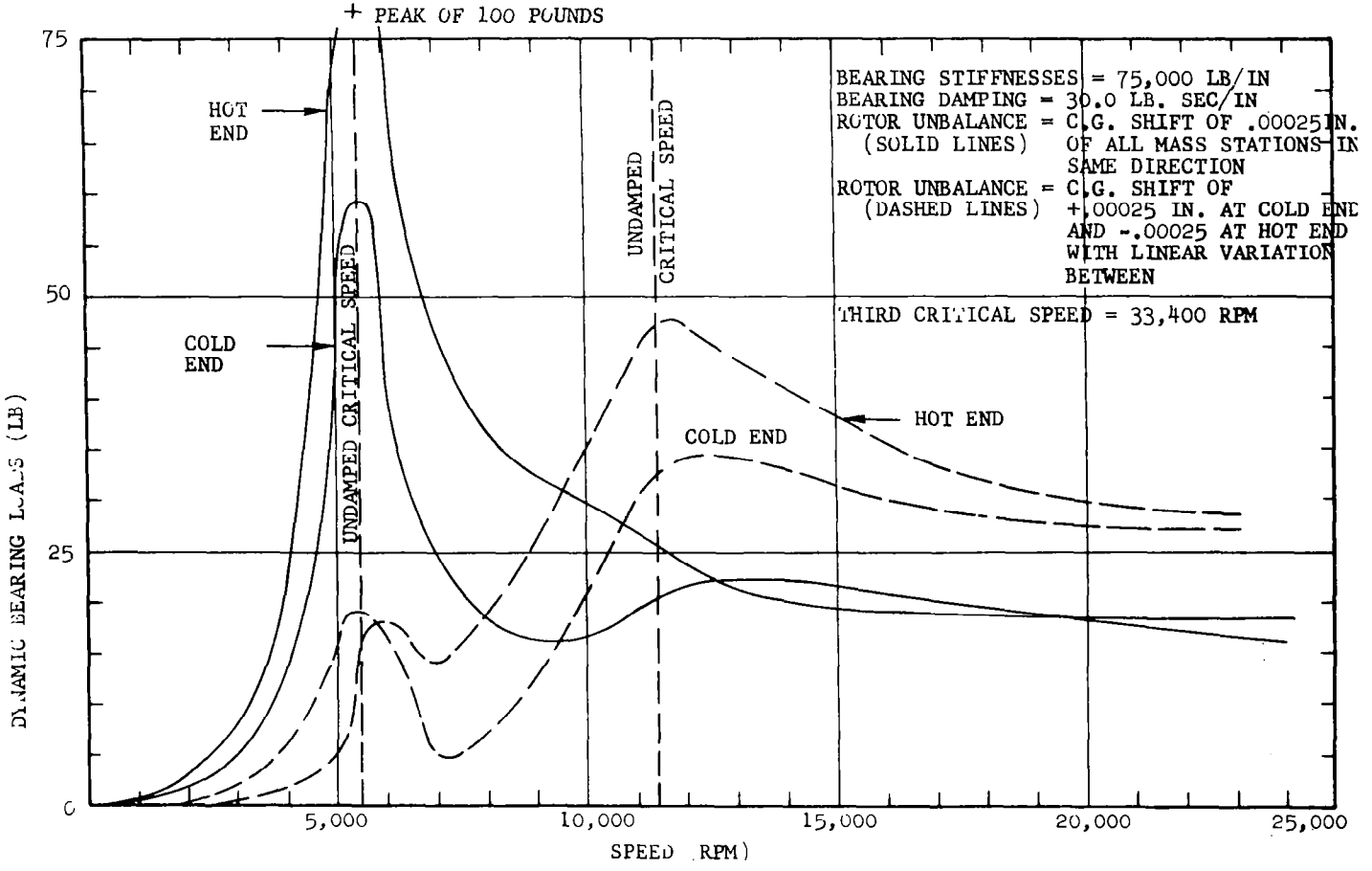

KTA TURBINE ROTOR CRITICAL SPEED ANALYSIS

(CONSTANT BEARING STIFFNESS)

FIGURE 94

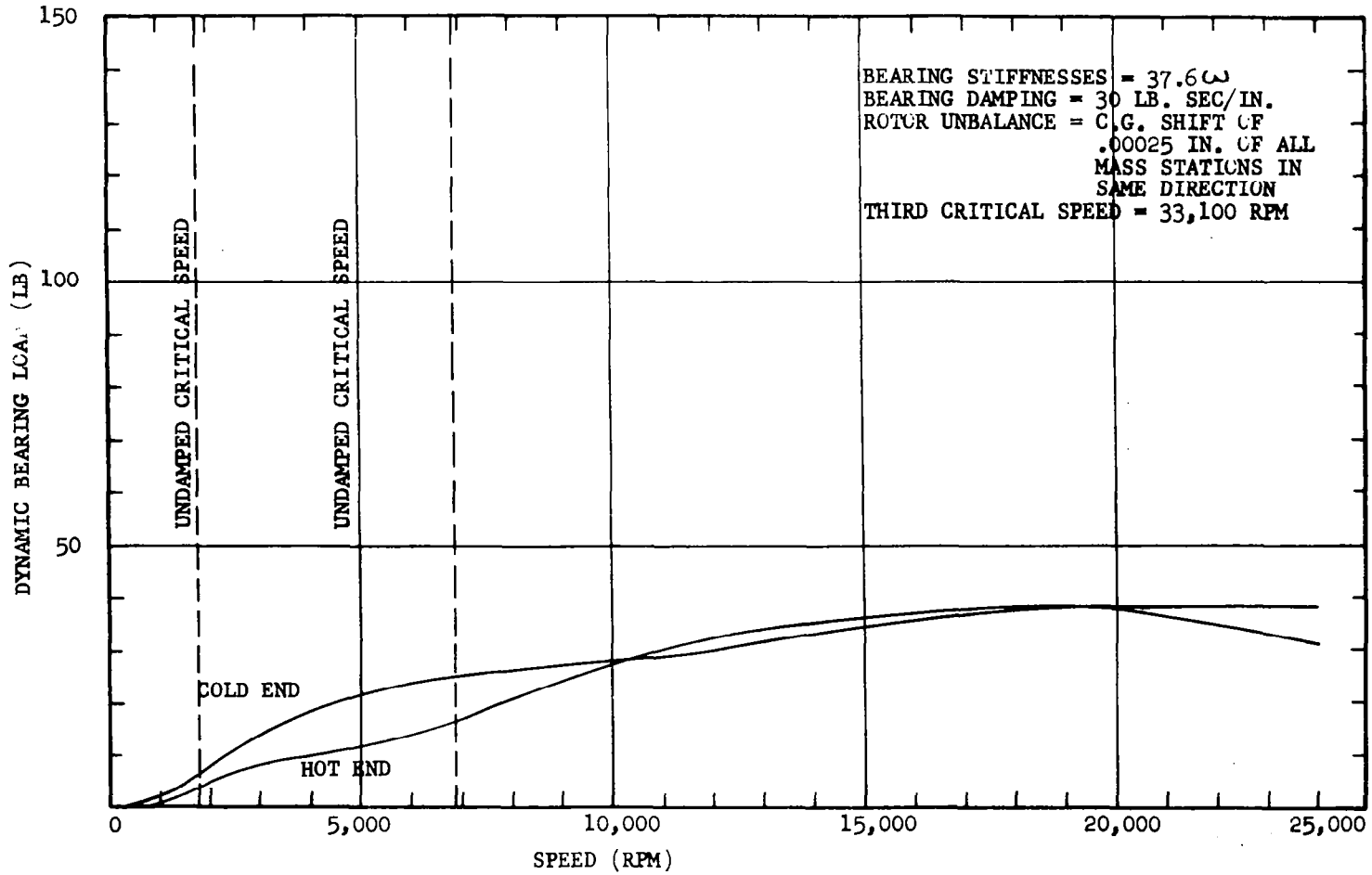

KTA TURBINE ROTOR CRITICAL SPEED ANALYSIS

(LINEAR BEARING STIFFNESS)

FIGURE 95

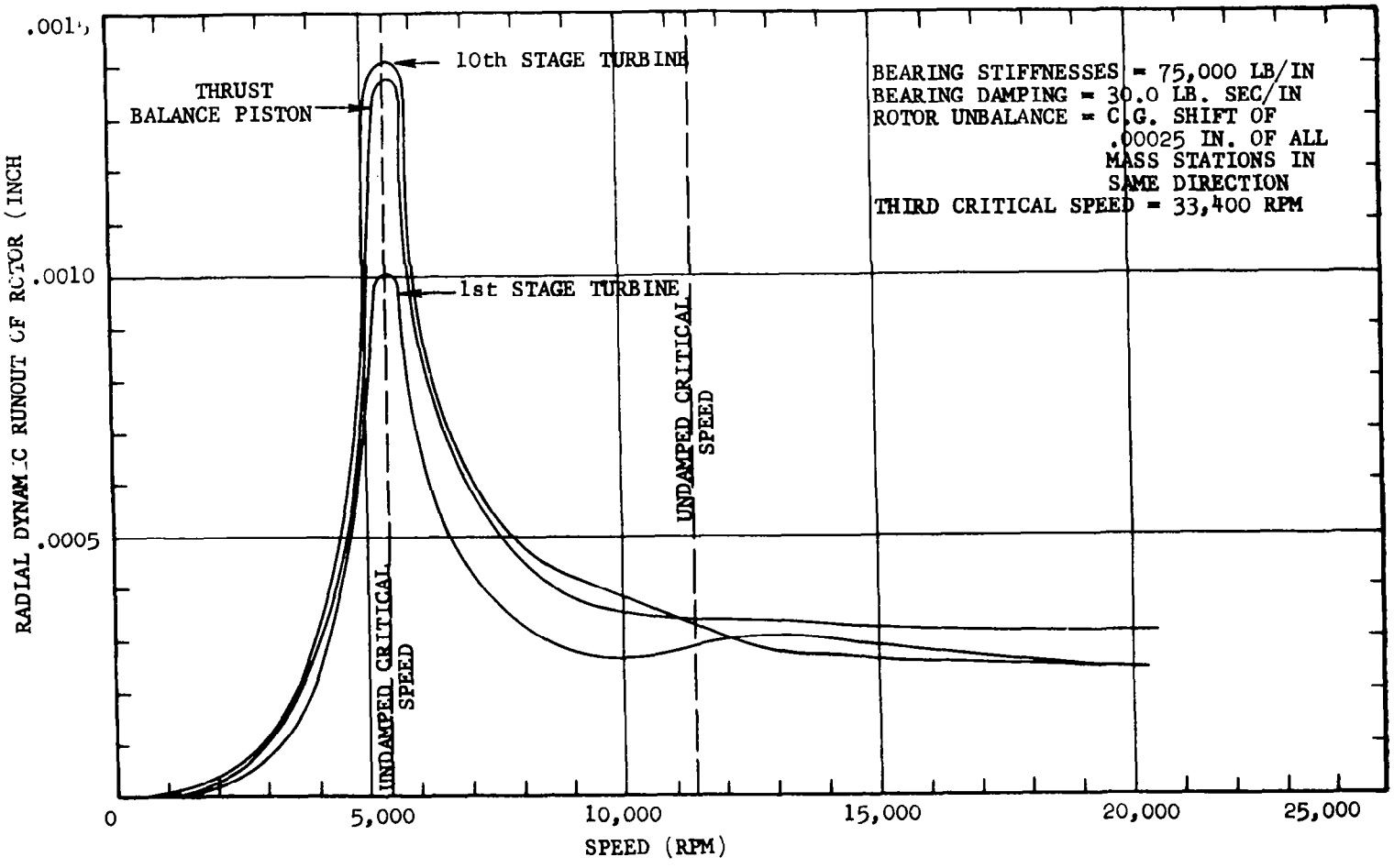

KTA TURBINE ROTOR CRITICAL SPEED ANALYSIS

(CONSTANT BEARING STIFFNESS)

FIGURE 96

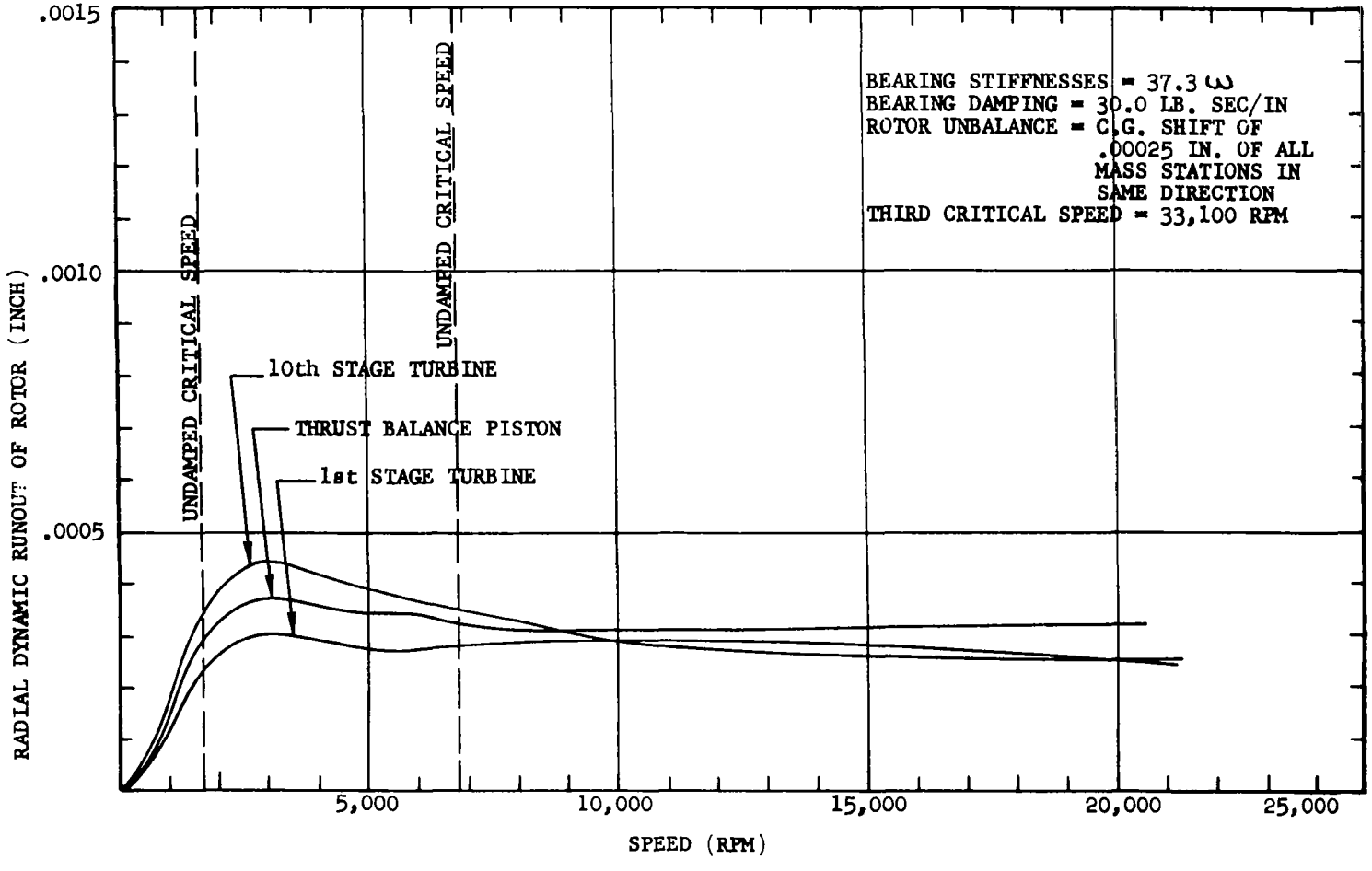

KTA TURBINE ROTOR CRITICAL SPEED ANALYSIS

(LINEAR BEARING STIFFNESS)

FIGURE 97

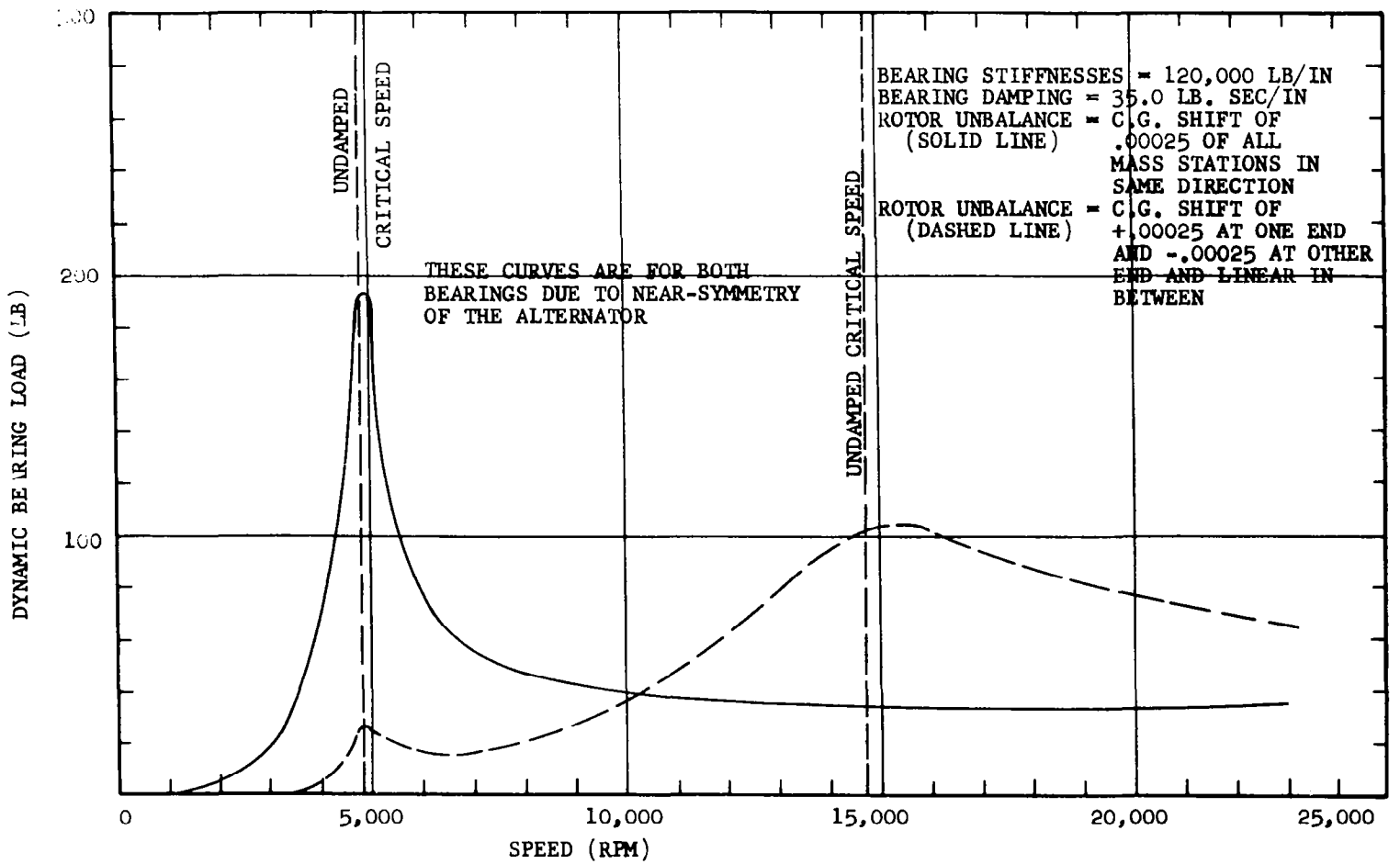

KTA ALTERNATOR ROTOR CRITICAL SPEED ANALYSIS

(CONSTANT BEARING STIFFNESS)

FIGURE 98

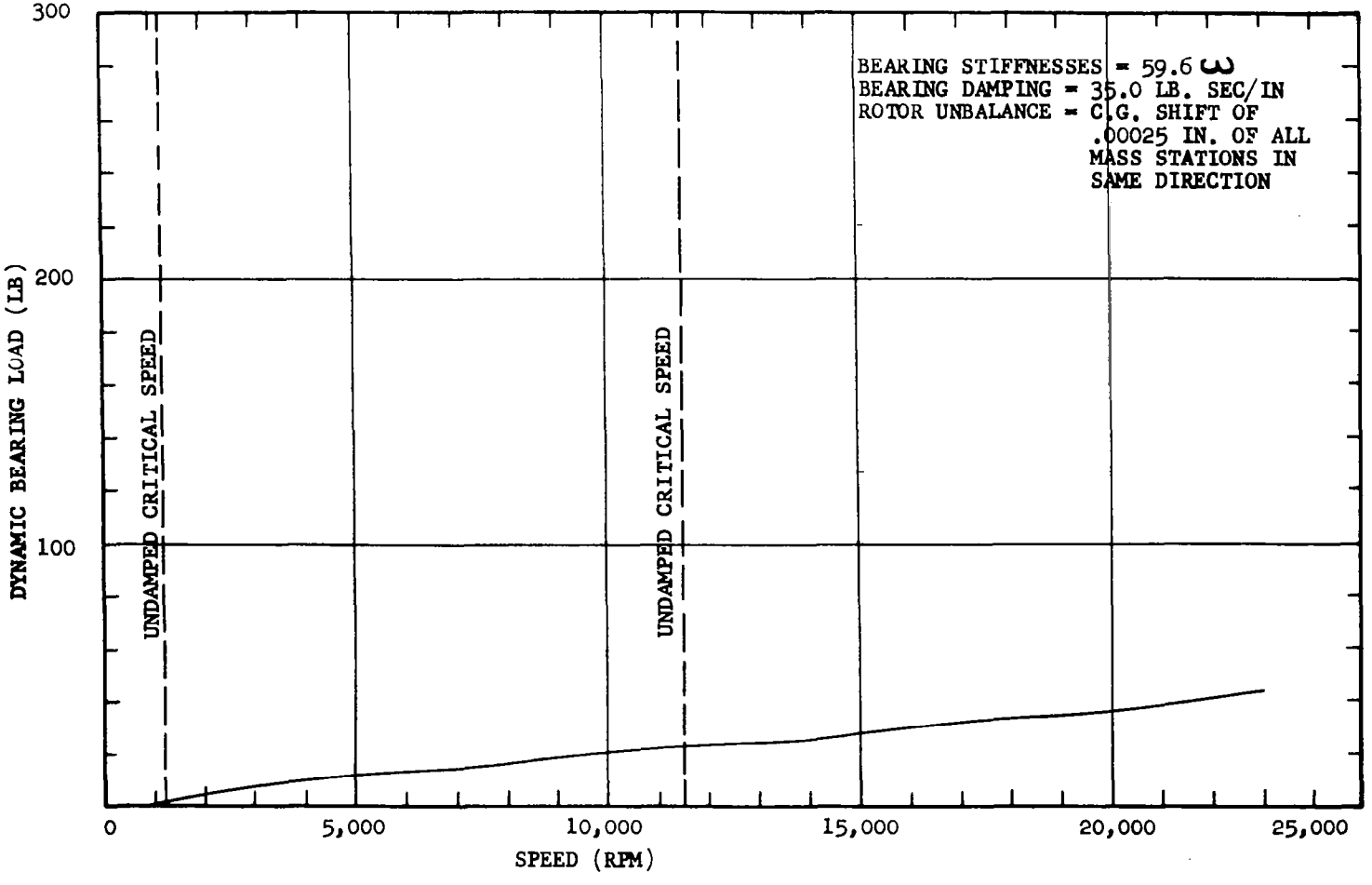

KTA ALTERNATOR ROTOR CRITICAL SPEED ANALYSIS

(LINEAR BEARING STIFFNESS)

FIGURE 99

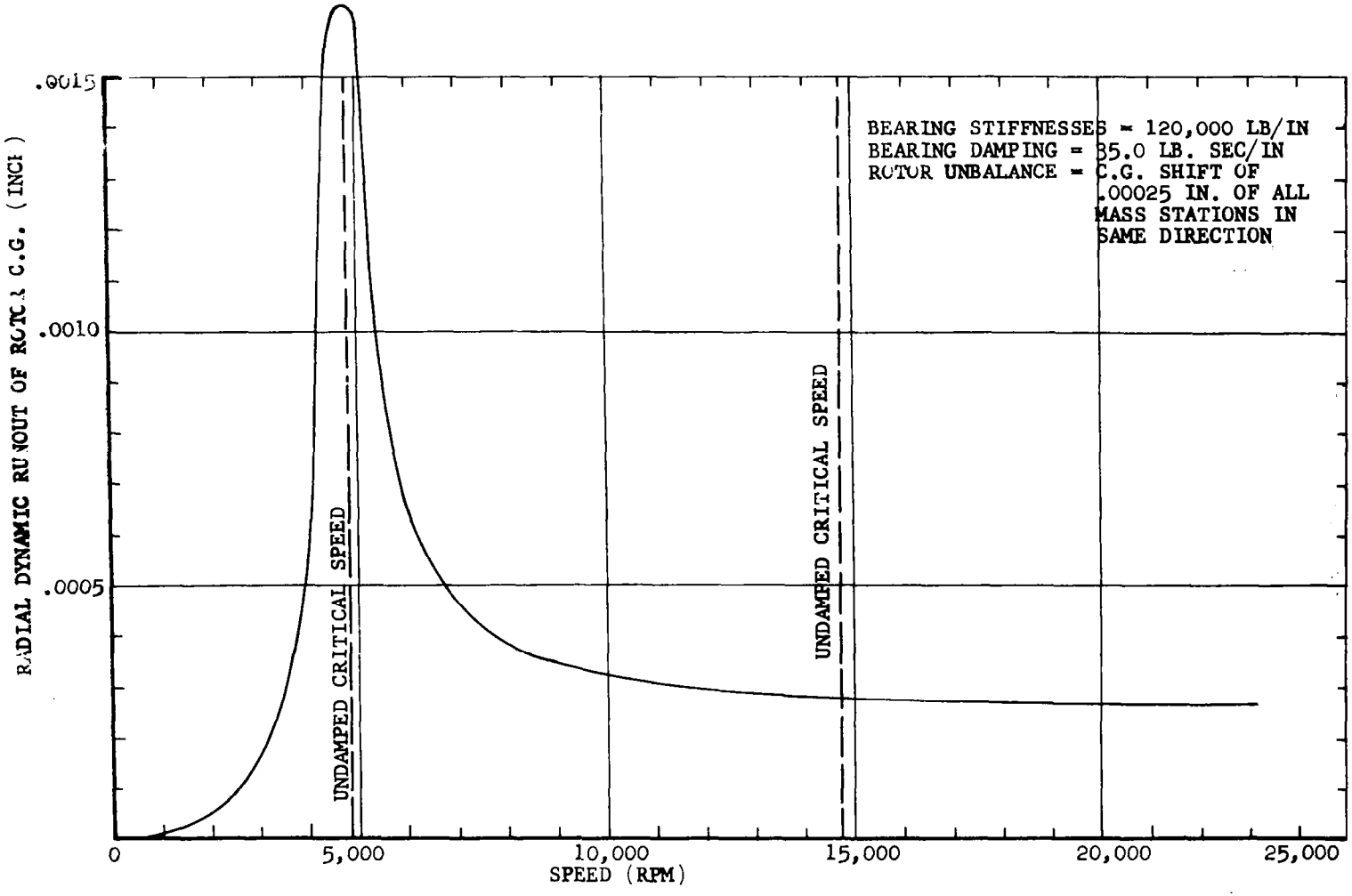

KTA ALTERNATOR ROTOR CRITICAL SPEED ANALYSIS

(CONSTANT BEARING STIFFNESS)

FIGURE 100

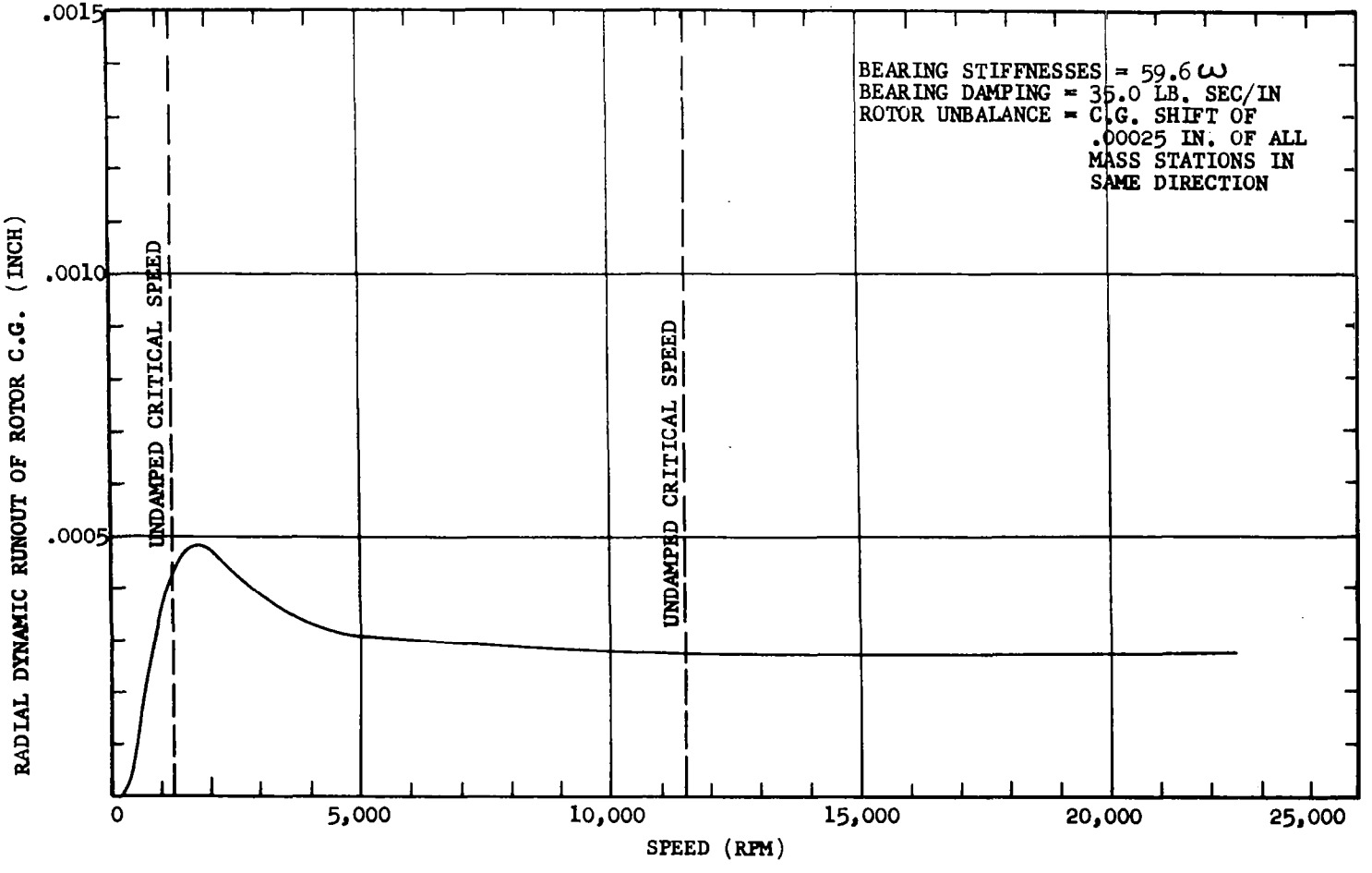

KTA ALTERNATOR ROTOR CRITICAL SPEED ANALYSIS

(LINEAR BEARING STIFFNESS)

FIGURE 101

The coupled turbine-alternator system is illustrated in Figure 102, where the critical speed-mode shapes are also shown. The geometrical information in this figure applies to the uncoupled systems if the coupling is ignored. Figure 103 presents the bearing load data for the coupled system.

All of the rotor critical speed results are summarized in Table 18. The most significant factor is that the coupling effects are so small that they are almost negligible. A comparison of Figure 103 with Figures 94 and 98 substantiates this. Since the interaction is small, the coupled system is only presented for one bearing spring-rate and unbalance configuration. All of the remaining individual results are thus applicable to the coupled system.

The preceding analytical results are intended to provide a complete description of the dynamic behavior of the final Phase II KTA turbine-alternator configuration. Emphasis has been placed on the runout of the respective rotors as functions of speed in addition to the usual attention to bearing loads. This is justified by the necessity for tight blade shroud clearances and extremely tight seal clearances in this machine. Most of the plotted results for both the turbine and alternator are for rotor unbalances that correspond to a cg shift of every mass station of 0.00025 in. in the same direction. For the turbine this is a static unbalance of 0.6 oz.-in. which experience indicates as a very realistic value for a machine of this type. A uniform cg shift produces a dynamic unbalance as well, because the mass distribution of the rotor is not uniform. It is seen from the figures that this type of unbalance accentuates the first ("cylindrical mode") critical speed, and that the dynamic unbalance component is so small that the second ("conical mode") critical speed is nearly indistinguishable from bearing loads or shaft motions. This has been, in fact, experimentally verified wherein the second critical speed of an

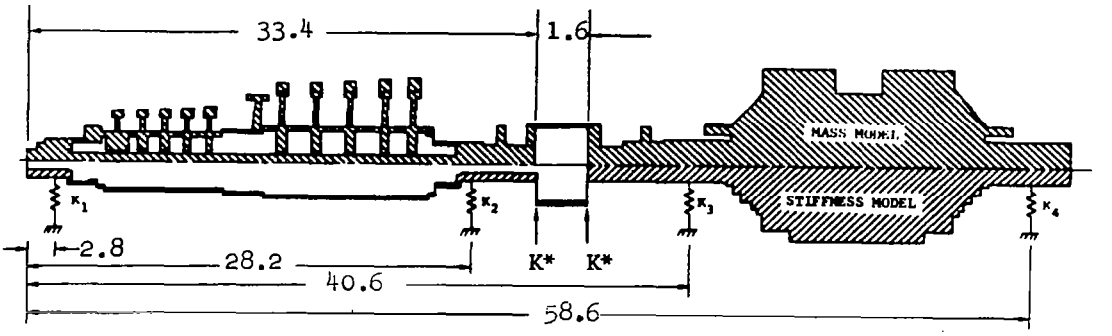

$K_1 = K_2 = 75{,}000$ LB/IN K* = 14,000 IN. LB/RAD

$K_3 = K_4 = 120{,}000$ LB/IN

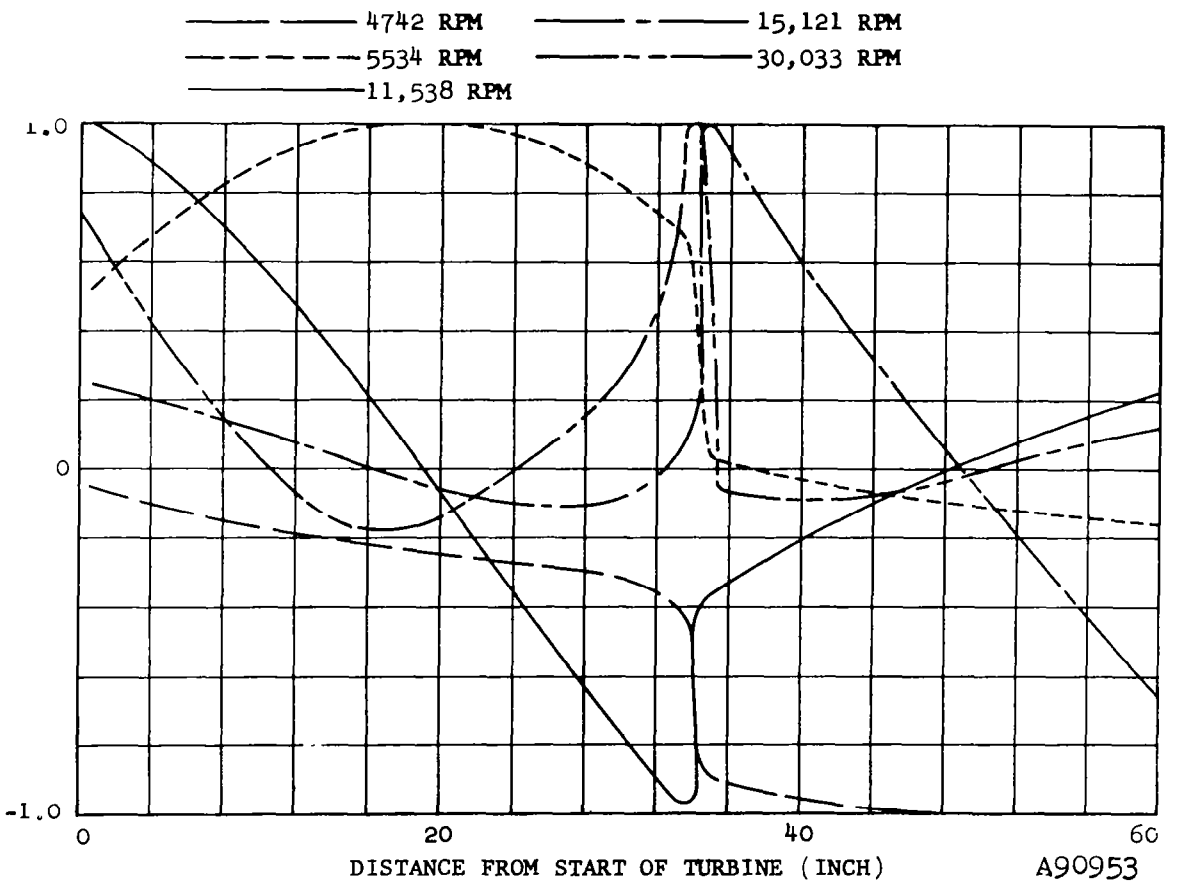

COUPLED TURBINE-ALTERNATOR CRITICAL SPEED MODE SHAPES

FIGURE 102

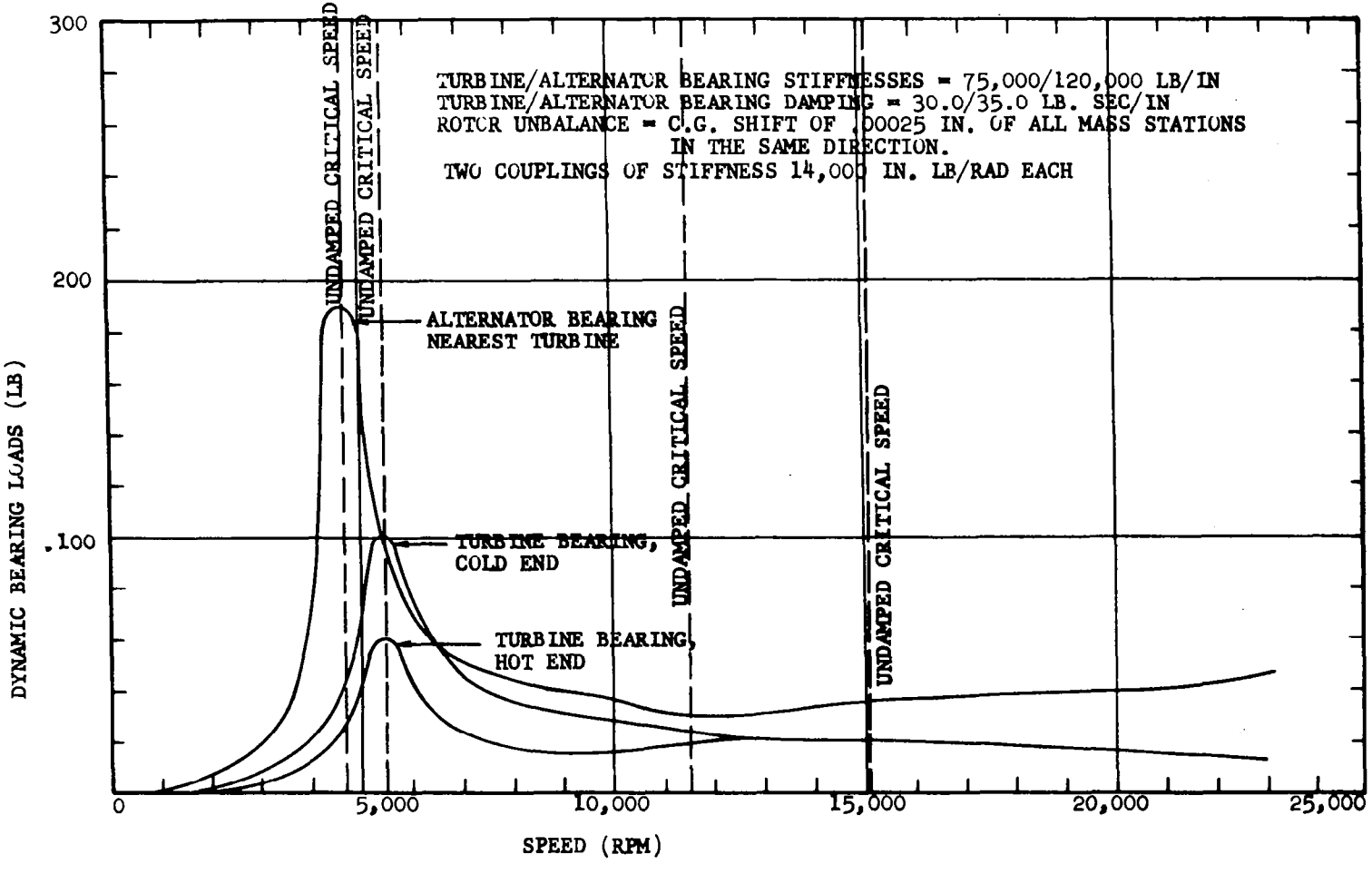

KTA TURBINE-ALTERNATOR COUPLED CRITICAL SPEED ANALYSIS

(BEARING LOADS)

FIGURE 103

TABLE 18

KTA CRITICAL SPEED SUMMARY

Unit	Bearing Spring-Rates, lb/in.	ωn_1	ωn_2	ωn_3	ωn_4	ωn_5	ωn_6
Turbine	75,000	5483	11,453	33,427	---	---	---
Turbine	37.3ω	1743	6864	33,102	---	---	---
Alternator	120,000	4850	14,735	>50,000	---	---	---
Alternator	59.6ω	1246	11,490	>50,000	---	---	---
*Turbine/Alternator	75,000/120,000	4742	5534	11,538	15,121	30,033	>50,000

*Turbine and alternator coupled with two Bendix couplings of 14,000 in.-lb/rad spring-rate each.

instrumented shaft is difficult to locate. If the unbalance distribution is such that it accentuates the second critical speed, this is no longer true, and Figures 94 and 98 illustrate this.

It is important to note that amplitude responses predicted at the critical speeds are in fact upper bounds for the prescribed unbalances in two respects. First, bearing damping is highly nonlinear, and in fact varies approximately inversely with the cube of the bearing film thickness. Therefore, for the finite displacements of the rotor, the damping forces will always be greater than the values assumed in the analysis, and actual amplitude response at critical speeds will be less than those predicted. Second, the bearing stiffness is also a function of rotor amplitude. Thus, as the rotor amplitude increases, the rotor-bearing dynamic system characteristics also change.

4.2 Rotor System Bearing Designs

4.2.1 Journal Bearings

The Phase I KTA system study led to the selection of the pivoted-pad journal bearings for both turbine and alternator sections of the rotor system. Each bearing comprises three pads per bearing, and each pad is provided with pivotal freedom about three mutually orthogonal axes. In that study, the hybrid and modified lobe journal bearings were evaluated on a comparative basis with the pivoted-pad. Of these geometries, the pivoted-pad is the only configuration that offers no quasi-static cross-coupling stiffness and on this basis is least vulnerable to rotor system self-excited instabilities. In addition, although the mechanical design of this bearing is in some respects more complicated than the others, it is also the most tolerant to misalignments and distortions. Stability studies of the alternator rotor during Phase I confirmed that the pivoted-bearing will assure system stability with a much smaller bearing size requirement than the

others evaluated. Therefore, the pivoted-pad journal bearing clearly emerged as the best selection for both the turbine and alternator rotors.

Figure 104 presents conceptually the pivoted-pad journal bearing. Geometrical parameters optimized at the outset were:

(a) Pivot angle = 55 percent of pad angle from leading edge
(b) Geometric preload = $1 - \delta/C = 0.63$

These parametric optimizations are based upon load maximization. Selection of the bearing size is dictated by the following additional considerations:

(a) Adequate bearing load capacity at reliably safe minimum film thickness
(b) Minimum size constraints imposed to insure adequate rotor stiffness
(c) System critical speeds safely removed from operating speed range
(d) Rotor system stability with respect to self-excited oscillations for gravity-free as well as terrestrial operation

Requirement (b) above was predominant for the turbine rotor section and requirement (d) for the alternator rotor section. (The system dynamic characteristics, including rotor stability, are further discussed in the following section.) The two pivoted-pad journal bearings are summarized in Table 19.

Load and power loss predictions for the turbine and alternator journal bearings at steady-state design operating conditions are presented in Figures 105 and 106. Bearing stiffnesses for the two designs are presented in Figure 107.

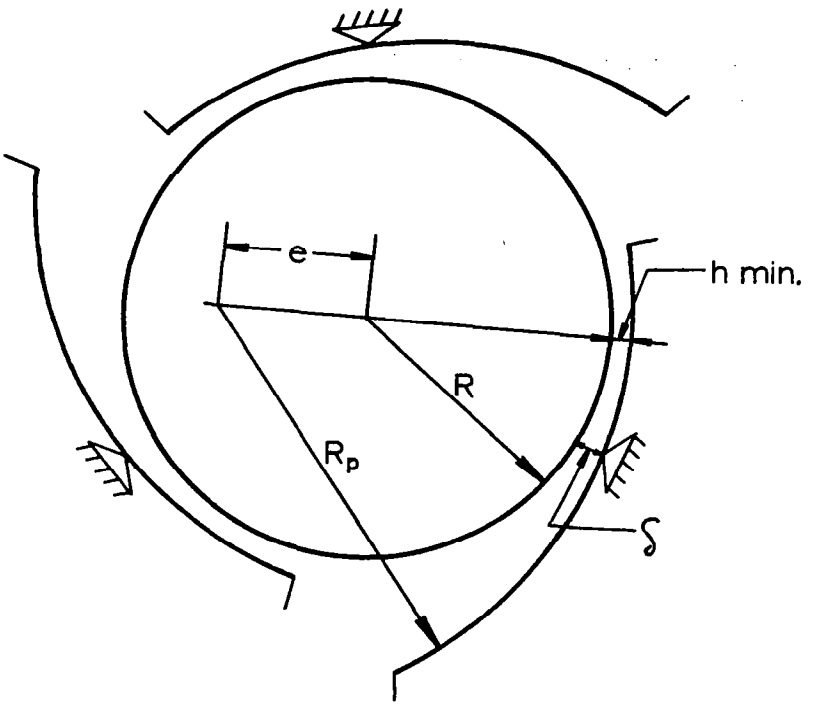

NOMENCLATURE FOR PIVOTED-PAD BEARINGS

R = JOURNAL RADIUS
R_p = PAD RADIUS
C = R_p-R (CLEARANCE)
e = DISTANCE BETWEEN JOURNAL CENTER AND PAD CENTER
δ = PIVOT FILM THICKNESS
h min. = MINIMUM FILM THICKNESS
1-δ/C = GEOMETRIC PRELOAD

PIVOTED-PAD JOURNAL BEARING

CONFIGURATION

FIGURE 104

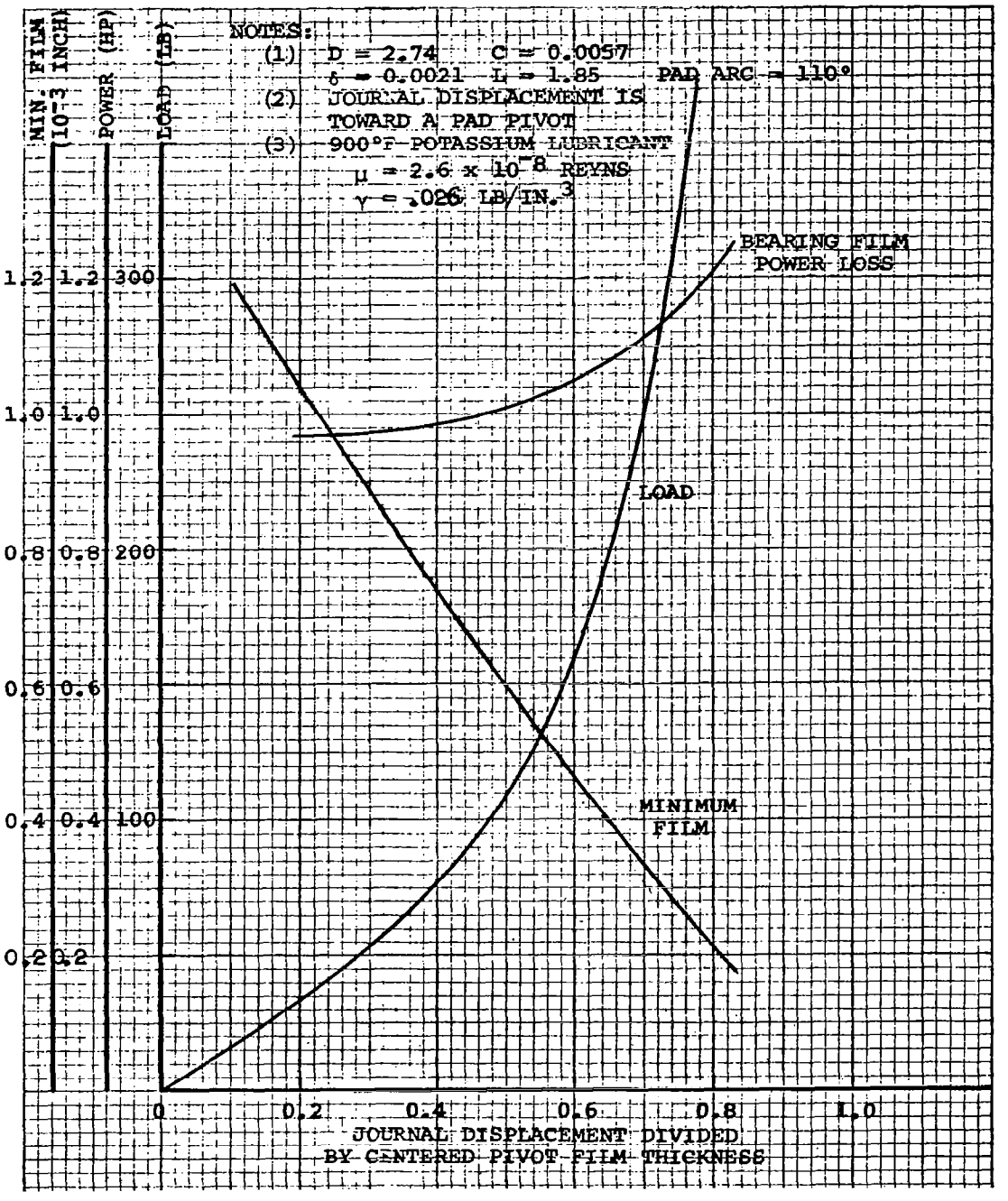

KTA TURBINE PIVOTED-PAD JOURNAL

BEARING PERFORMANCE

FIGURE 105

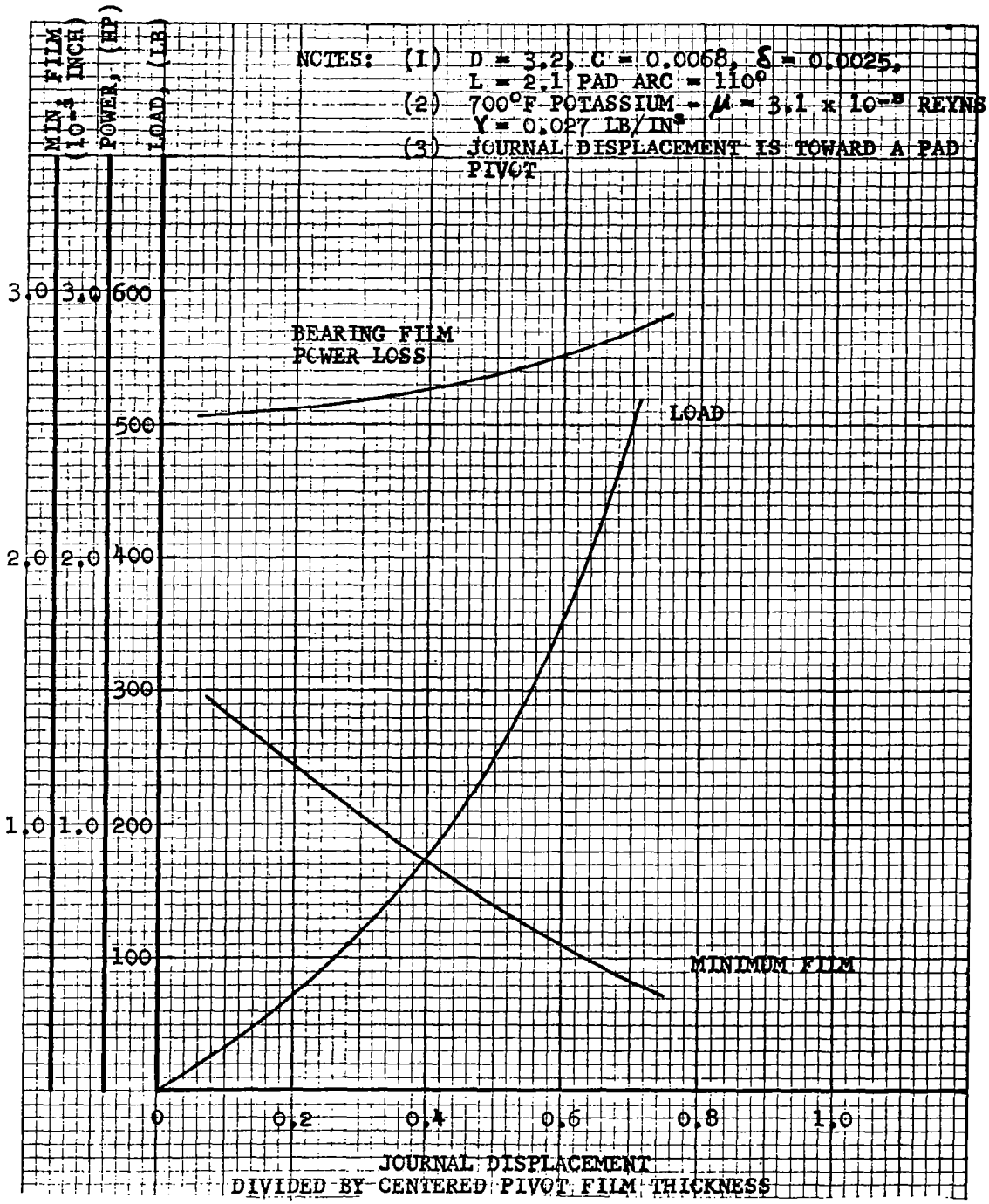

KTA ALTERNATOR PIVOTED-PAD JOURNAL

BEARING PERFORMANCE

FIGURE 106

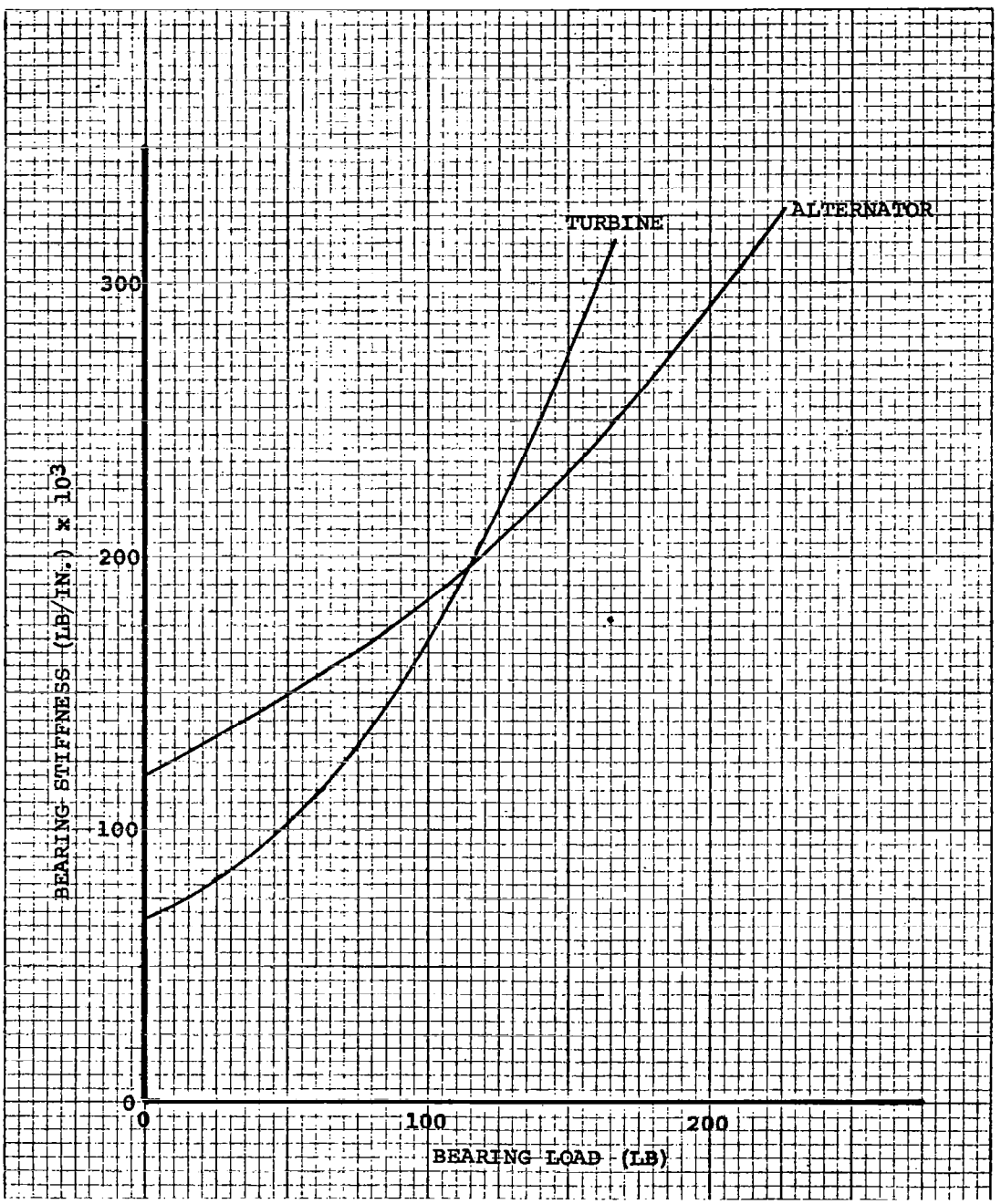

KTA JOURNAL BEARING STIFFNESS

FIGURE 107

TABLE 19

KTA TURBINE AND ALTERNATOR

JOURNAL BEARING DESIGN DETAILS

	Turbine	Alternator
Journal Radius, in.	1.370	1.600
Pad Radius, in.	1.3757	1.6068
Pad Arc, deg.	110	110
Pad Length, in.	1.850	2.100
Pad Pivot Angle, deg.	55	55
Centered Pivot Clearance, in.	0.0021	0.0025
Journal Material	Titanium carbide, TiC + 10-percent Cb	*K-96
Pad Material	Titanium carbide, TiC + 10-percent Cb	*K-94
Pivot Sphere Material	Titanium carbide, TiC + 10-percent Cb	*K-96

The selection of bearing materials for the turbine is discussed in Appendix A. Titanium-carbide with columbium binder was selected for the turbine bearings. The columbium binder eliminates any potential mass transport problems in the all refractory turbine loop due to non-refractory binder being leached from the bearing materials. Since the alternator coolant loop is completely non-refractory, refractory alloy binders should not be used. Kennemetal K-94 and K-96 with cobalt binders were selected for the alternator bearings. These materials have shown excellent wear and friction characteristics in testing for the SNAP 50/SPUR program and were used in the 2000 hour potassium bearing tests conducted at AiResearch. These materials have

*Kennametal designation K-96 (WC + 2% (Cb,Ta)C + 6% Co)
-94 (WC + 2% (Cb,Ta)C + 12% Co)

the disadvantage of high elastic modulus and brittleness. Differential thermal expansions of the bearing journal sleeve and pad outer-ring housing relative to their respective pilot surfaces may, thus, induce excessive thermal stresses unless compliance is introduced in the designs. The method by which compliance is achieved is schematically illustrated in Figure 108. Two rings of this type per bearing tend to isolate the bearing component thermal expansions.

4.2.2 Thrust Bearings

For Phase I, both taper-flat and pivoted-pad thrust bearings were studied. The taper-flat geometry was generally superior on the basis of load-to-power loss ratio. On the other hand, the pivoted-pad bearing is generally more tolerant to static misalignments and distortions. The second factor was considered predominant, and the pivoted-pad concept emerged as the selection. This decision has been reinforced by the thrust balancing-piston innovation, developed in Phase II for the turbine rotor to substantially diminish aerodynamic thrust loads. The need for a thrust bearing geometry of more nearly optimum configuration from the standpoint of load capacity is thereby lessened. In addition, the pivoted-pad thrust bearing concept has been successfully developed for liquid metal applications.

The pivoted-pad thrust bearing for the alternator rotor is presented in Figure 109. Table 20 summarizes the two thrust-bearing design parameters.

The thrust bearing for the turbine rotor is designed to be capable of supporting the rotor weight of 145 lb and the total aerodynamic load (with no thrust-balancing) at the 20-percent overpressure condition of about 1820 lb. If the thrust-balancing is totally successful, this bearing is grossly overdesigned. The performance is presented in Figure 110.

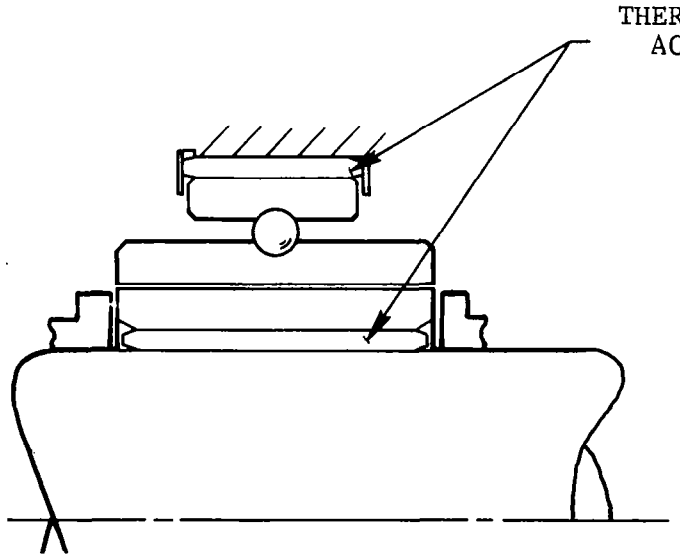

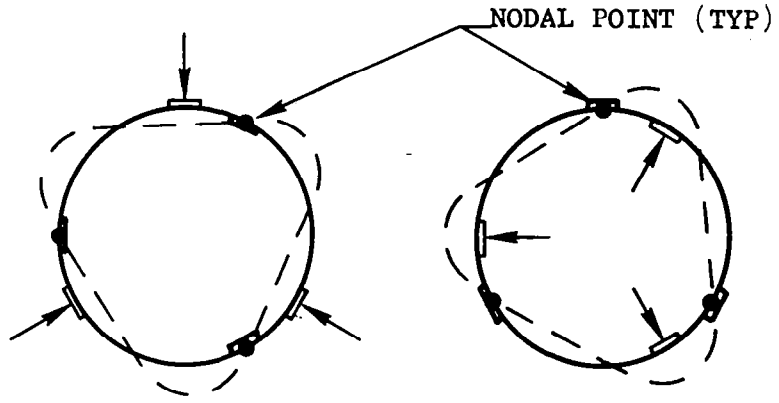

WITH COMBINED INNER AND OUTER LOADS, DEFLECTIONS SUPERIMPOSE. LANDS ON ONE SURFACE ARE POSITIONED ON NODAL POINT WITH RESPECT TO LOADS ON OTHER SURFACE.

THERMAL EXPANSION ACCOMMODATORS

FIGURE 108

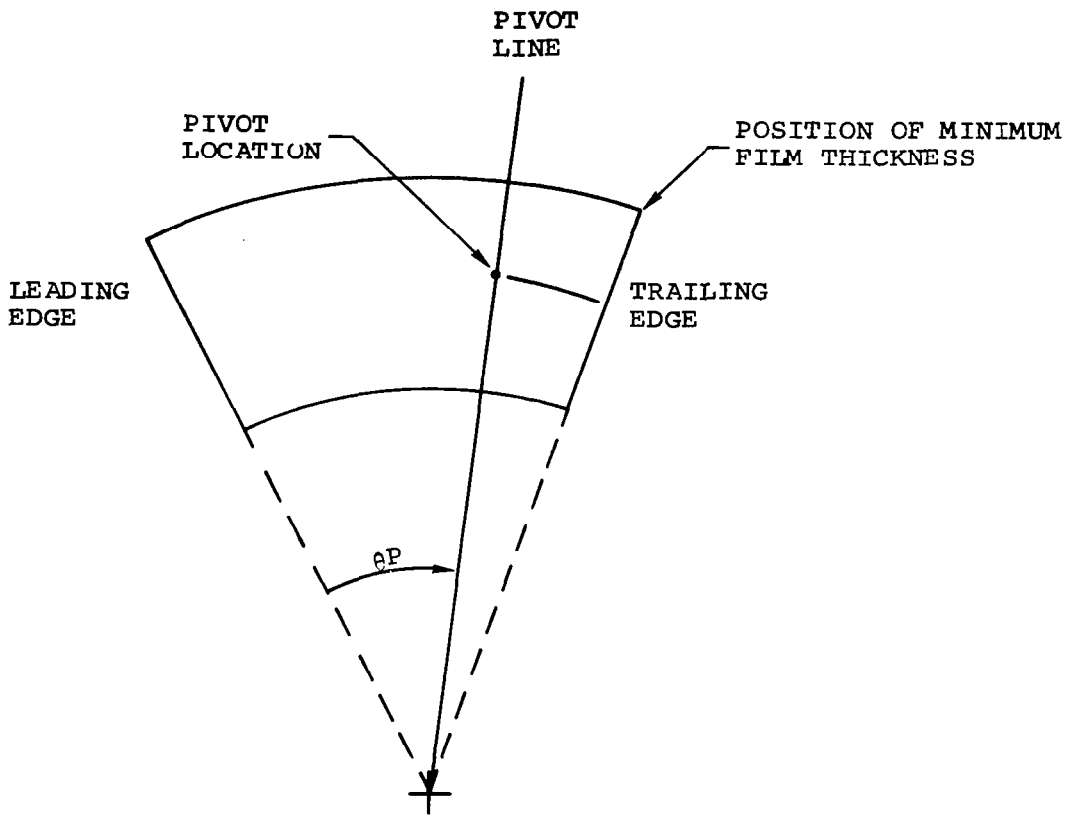

NOMENCLATURE

θ_P = ANGLE FROM LEADING EDGE TO RADIAL LINE ABOUT WHICH PAD IS PIVOTED
h_{MIN} = MINIMUM FILM THICKNESS
h_p = PIVOT FILM THICKNESS
Φ_T = TANGENTIAL SLOPE OF PAD AT PIVOT LINE

KTA PIVOTED-PAD THRUST BEARING

FIGURE 109

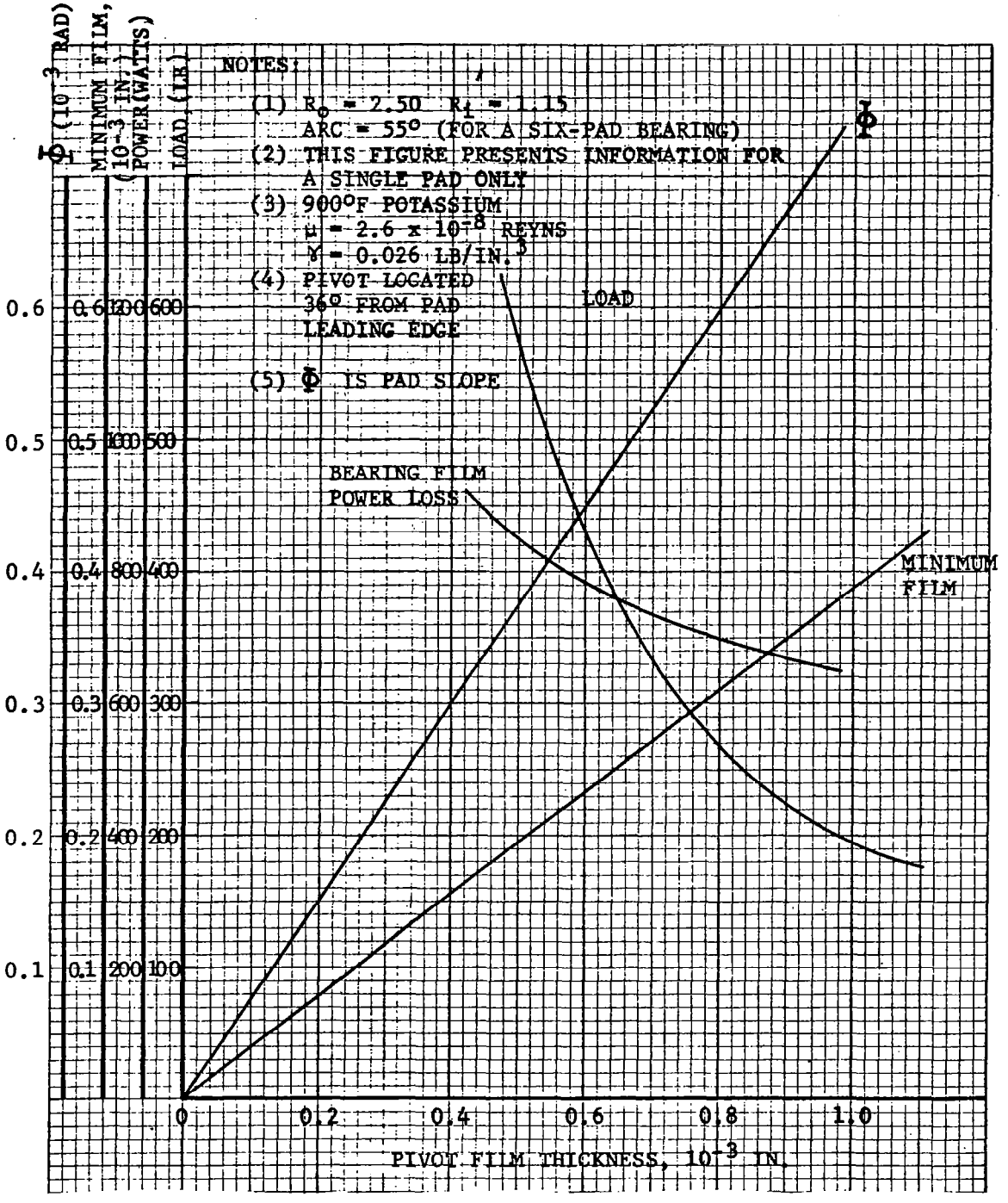

KTA TURBINE THRUST BEARING

PERFORMANCE

FIGURE 110

TABLE 20

KTA THRUST BEARING DESIGN SUMMARY

	Turbine Rotor Thrust Bearing	Alternator Rotor Thrust Bearing
Pad Outer Radius, in.	2.50	2.25
Pad Inner Radius, in.	1.15	1.55
Pad Arc Length, deg.	55	43
Pad Pivot Angle, deg.	36	29
Pad Pivot Radius, in.	1.85	1.825
Number of Pads	6	8
Bearing Pad, Slider and Pivot Materials	Titanium Carbide, 10% Cb	K-94 vs K-96

The alternator rotor thrust bearing is designed for the alternator weight of 350 lb. Its performance is presented in Figure 111.

4.3 System Power Losses

Power losses of the bearings and seals, together with churning losses of liquid potassium are summarized in Table 21.

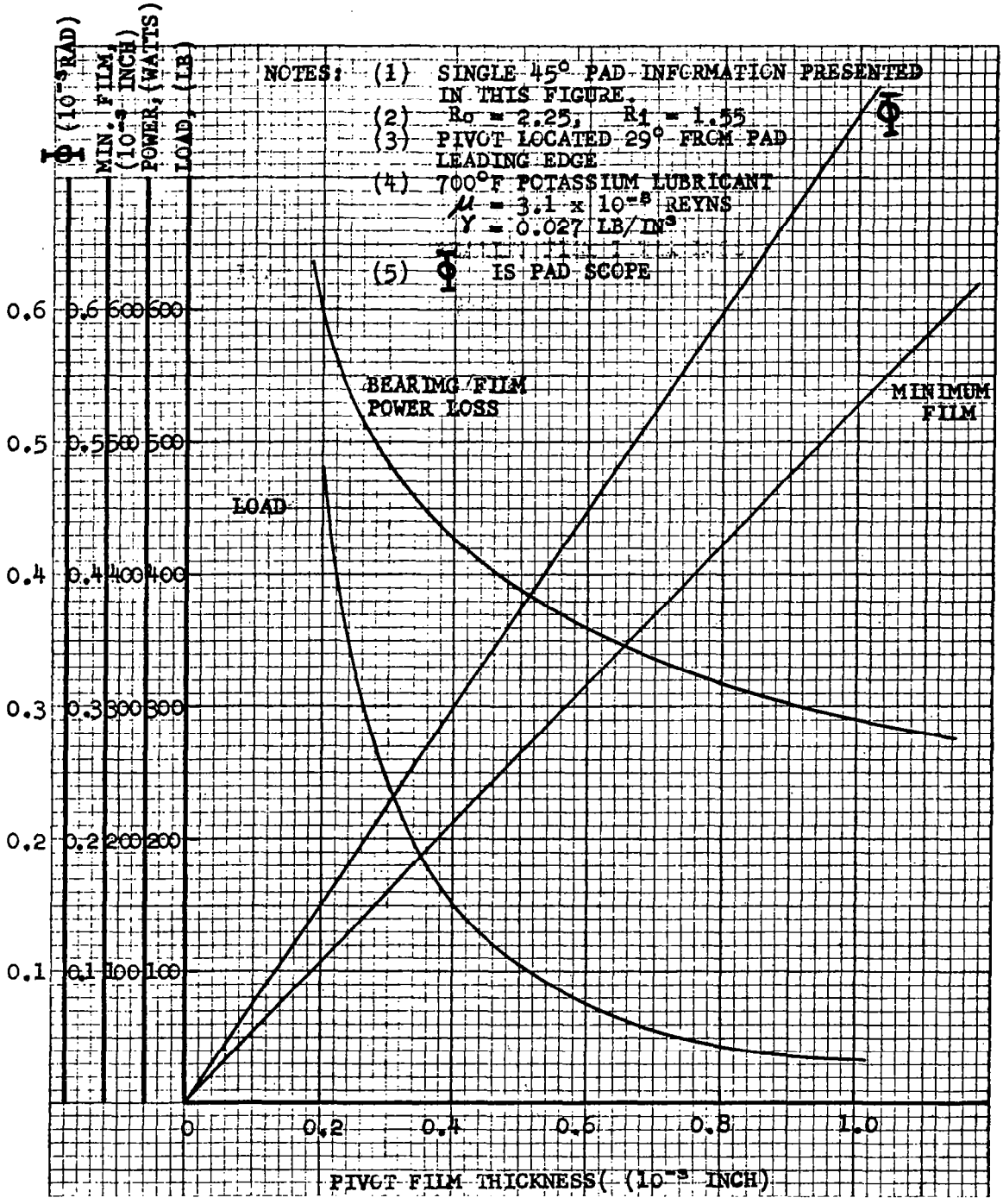

KTA ALTERNATOR THRUST BEARING

PERFORMANCE

FIGURE 111

TABLE 21

KTA BEARING, SEAL AND LIQUID POTASSIUM CHURNING POWER LOSSES

Location	Power Loss, kw
Front Turbine Rotor End	0.425
Turbine Rotor Journal Bearings (including pumping losses)	2.50
Turbine Front and Back End Viscoseals	0.446
Turbine Thrust Bearing (including pumping and churning losses)	10.150 (for assumed 2000-lb thrust load)
Alternator Journal Bearings (including pumping losses)	5.0
Alternator Thrust Bearing (including pumping and churning losses)	7.290
Alternator Viscoseals	1.350
Heat Conduction to Front and Rear Bearings	2.0

5. ALTERNATOR DESIGN ANALYSIS

This section describes the accomplishments of the Aerospace Electrical Division, Westinghouse Electric Corporation, on the second part of a design study performed to produce the KTA alternator subcomponent preliminary design(s). The design study was conducted in two phases. Phase I consisted of alternator performance and conceptual design analyses as discussed in Volume II of this report. Phase II consisted of a preliminary design study of a specific design selected by NASA from the Phase I conceptual designs.

One alternator design configuration was selected from Phase I for further study in Phase II. The configuration consisted of a 1600 Hz, 19,200 rpm, 480 v (L-N) design. The maximum continuous-load rating was reduced to 600 kva (450 kw_e at 0.75 lagging-load power factor) from the 733-kva maximum continuous-load rating design specification of Phase I. Coolants were initially specified as 800°F NaK for the stator and 700°F potassium for the rotor; however, during the Phase II study, the stator coolant was changed to potassium and the temperature reduced to 700°F. This reduction in stator coolant temperature provides benefits in rotor material strength limitations and in stator-rotor heat-transfer characteristics.

The primary tasks of the Phase II design study were

(a) Completion of a final electromechanical design configuration
(b) Supporting electromechanical design and performance analyses with related considerations regarding turbine-alternator interface

(c) Material selection

(d) Drafting of a detail preliminary alternator layout drawing

(e) Reliability and failure mode and criticality studies

These primary tasks are discussed thoroughly in the sections of this report which follow.

The preliminary alternator design derived from the Phase II Preliminary Design Study will be the basis for a final design to be established in a later study. This final design will be fabricated and tested.

5.1 Electrical Design and Performance Study

A review of the changes in specification, state points, and configuration that occurred as a result of the Phase I Conceptual Design Analysis Review was conducted, and studies were performed to verify or adjust several of the alternator internal design variables established during the Phase I studies. Sufficient design computations were performed to establish the preliminary Phase II alternator electrical design configuration. Performance calculations were made to determine the electrical performance of the established alternator configuration to verify that the performance meets the specifications and electrical load requirements.

5.1.1 Specification Change Review

As a result of conclusions of the Phase I turboalternator design study, one alternator configuration was selected by NASA for the Phase II preliminary design study. The design specifications of the selected configuration are as follows:

(a) The alternator maximum continuous-load rating shall be 450 kw_e, three-phase, at a 0.75-lagging-load power factor.

Nominal alternator-load rating shall be the same as the maximum continuous-load unless otherwise specified.

(b) The alternator design to the maximum extent feasible shall reduce to a minimum any adverse effects due to unbalanced magnetic forces.

(c) The speed (frequency) control of the alternator is presently considered the parasitic-load type, and frequency regulation is anticipated as ±1 percent of design frequency for a change in external load from 10 percent to maximum load (450 kw_e).

(d) Specification MIL-G-6099A (ASG) per the latest revision in effect on date of this contract shall apply to the following:

(1) Waveform* - Paragraph 4.5.16. In addition, the total rms harmonic content of the line-to-neutral voltage wave, when the alternator is operating into a purely resistive load, shall be less than 5 percent from 10 to 100 percent maximum load (450 kw_e)

(2) Phase balance - Paragraph 4.5.10, 4.5.10.1 and 4.5.10.2, except that 4.5.10.1 is amended to read "...the individual phase voltages shall not deviate from the average by more than 2.25, 4.5, and 9 percent, respectively"

(3) Output voltage modulation* - Paragraph 4.5.13 except that modulation shall not exceed 0.5 percent

(4) Overload - 900 kva at 0.9-lagging-load power factor for 5 sec

(5) Short-circuit capacity - Paragraph 4.5.12 for a minimum of 5 sec shall be included as a design goal

(e) Frequency - 1600 Hz

(f) Speed - 19,200 rpm ±1 percent

(g) Voltage - 480 v (L-N)

(h) Rotor coolant - liquid potassium at 700°F supply temperature

(i) Stator coolant** - liquid NaK at 800°F supply temperature

---

* To be retained as a design goal without analytical verification.

**Reduced to 700 F potassium during course of program.

The basic changes between the Phase I and Phase II requirements regarding the electrical design of the alternator are a reduction in maximum continuous rating from 733 kva (550 kw_e at 0.75 power factor, lagging) to 600 kva (450 kw_e at 0.75 power factor, lagging), a corresponding reduction in the overload requirement, and a reduction in rotor coolant temperature from 800° to 700°F. Rotor material property data for the alternator design computer program was adjusted to reflect the decrease in rotor temperature. Several alternator internal design variable studies were performed to verify or adjust the values selected in Phase I as a result of the changes listed above.

5.1.2 Alternator Internal Design Variable Review

Several alternator internal design variables were selected for study and verification because of changes occurring between Phase I and II KTA tasks. An armature current density study was performed to verify the previously selected (Phase I) current density with the lower current of the 600-kva rating. A field current density study was performed to determine the optimum field coil configuration with respect to field coil power, weight, limiting temperature, system weight, and exciter-voltage regulator requirements. A study of armature coil flux density was performed using new calculation procedures derived as a result of an experimental verification program, AEC Contract AT(04-3)-679, which indicated that armature iron losses with unwelded Hiperco-27 stacks were less than those previously calculated by a factor of 2/3 and that the amplitude of the ac circumferential flux in the armature core was also less than anticipated. These factors resulted in generally higher efficiencies and in conjunction with the lower Phase II kva rating, in lower weights compared to Phase I results. The saturated vapor pressure of potassium at 700°F was assumed for the pressure of the rotor cavity for the design variable studies, resulting in higher windage losses than those established for the final design. Study results are presented in Tables 22, 23 and 24.

TABLE 22

ARMATURE CURRENT DENSITY STUDY

Current Density, amp/in.^{2}	Alternator Electrical Weight, lb	Efficiency, %	Armature Hot Spot Temp, °F*	Alternator Weight + System Weight Penalty, lb
8645	643	92.7	1283	3113
6310	662	93.4	1130	2882
4971	766	93.7	1060	2876
3864	842	93.7	1000	2952

*Based on 300°F stator coolant temperature.

TABLE 23

ARMATURE CORE FLUX DENSITY STUDY

Flux Density, kl/in.^{2}	Alternator Electrical Weight, lb	Efficiency, %	Stator OD, in.	Alternator Weight + System Weight Penalty, lb
100	627	92.8	18.00	3057
80	640	93.1	18.30	2960
60	662	93.4	18.79	2882
40	729	93.9	19.72	2769
20	905	94.2	22.59	2835

TABLE 24

FIELD CURRENT DENSITY STUDY

Current Density, amp/in.^{2}	Alternator Electrical Weight, lb	Efficiency %	Field Power, w	Field Coil Weight, lb	Field Coil Hot-Spot Temp, °F**	Estimated* Exciter Weight, lb	Field Coil Voltage	Alternator Weight + System Weight Penalty, lb
8285	630	92.7	9888	19.6	1480	119	59.7	3100
6540	644	93.1	7904	25.1	1230	95	47.5	2974
5174	661	93.3	6341	32.2	1120	76	37.9	2911
3257	706	93.7	4142	52.8	980	50	24.4	2816
1682	823	94.1	2183	104.7	880	26	12.4	2793

*Based on 12 lb/kw specific weight.
**Based on 800°F stator coolant temperature.

In all of the studies performed, alternator weight increased as efficiency increased, necessitating the use of a trade-off criterion in the form of a system weight penalty per kilowatt of loss. From discussions with NASA, a preliminary weight penalty in the range of 59 to 79 lb/kw was determined suitable for use in the studies. A value of 70 lb/kw was chosen to determine the weight penalty associated with the alternator inefficiency.

Results of the armature current density study (Table 22) indicated an optimum current density of 5000 to 6000 amp/in.^{2} based on minimum system weight and a limiting armature hot-spot temperature of 1100°F. This compares favorably with an armature current density of 6000 amp/in.^{2} selected for the Phase I, 19,200-rpm, 800°F coolant-temperature conceptual design.

Optimum armature core flux density (Table 23) occurs in the range of 20 to 60 kilolines/in.^{2} based on minimum system weight. Accurate calculation of the penetration of the high-frequency circumferential ac wave into the depth of the armature core is exceedingly difficult, and very large core depths may not be fully utilized by the high-frequency (1600 Hz) flux wave. The stator OD increases rapidly below 60-kilolines/in.^{2} density due to an increasing armature core depth behind slot. A density of 60 kilolines/in.^{2} was chosen because this value results in near-minimum stator punching OD and near-minimum system weight.

A field current density of 4000 amp/in.^{2} (Table 24) was selected based on results of the field current-density study. The selected value results in near-minimum system weight, minimum field coil plus estimated exciter weight, and a field coil hot-spot temperature below 1100°F. A study of field coil conductor configurations performed in Phase I with regard to heat transfer characteristics has shown that a low voltage, wide strap field coil configuration with cooling manifolds

located on each side of the field coil provides the lowest field coil operating temperatures. As shown later, more detailed analysis of the temperatures revealed hot spots well below 1100°F.

A field current density of 4000 amp/in.^{2} requires a full-load field voltage of about 30 v. A preliminary review of exciter-voltage regulator (VRE) characteristics indicates a VRE efficiency of about 80 percent for the 30-v field coil configuration. Although a higher voltage, lower current field coil would provide a higher VRE efficiency, the selected configuration represents the optimum considering all of the factors previously discussed.

Reanalysis of the Phase I winding configuration with regard to the harmonic content of the armature MMF has shown that an increase in the pitch factor from 0.8 to 1.0 (full pitch) is desirable. Even harmonics can be present in the MMF distribution of 120-deg phase belt, three-phase windings when the pitch factor is other than one. The value of pitch factor for a winding is selected on the basis of reducing or eliminating the amplitudes of an objectional harmonic or series of harmonics. In this case, all even harmonics are eliminated by the choice of a full-pitch coil which is desirable from the standpoint of decreasing the load component of rotor pole face losses. Selection of a full-pitch coil for the KTA alternator does not significantly increase the harmonic content of the terminal voltage because the harmonic distribution factors are low, due to the relatively high number of slots per pole per phase.

The winding factors (product of pitch and distribution factors) for the 120-deg phase belt, full-pitch winding of the KTA alternator are identical to those that would be produced if the armature were wound for 60-deg phase belts with 2/3 coil pitch. Calculated harmonic content of the no-load voltage is 1.85 percent. A slight weight reduction (approximately 6 percent) was achieved by the increased pitch factor.

5.1.3 Final Alternator Design Configuration

A final alternator electrical design configuration was established based on results of the Phase I studies and the internal design variable studies described in Section 5.1.2. Pertinent design information regarding the final alternator electrical configuration is listed below:

Rating:	600 kva
Voltage:	480 v (L-N)
Frequency:	1600 Hz
Speed:	19,200 rpm
Type:	Radial gap inductor
Coolant:	
Stator inlet	700°F potassium
Rotor inlet	700°F potassium
Armature Windings:	Three-phase, wye-connected 180 slots 5 parallel paths 2 parallel strands 12 series turns per phase Full-pitch, 120 deg phase belts 2 conductors per slot
Field Winding:	52 turns, strap wound

Machine Dimensions, in.:*	
Stack length (each)	4.193
Length between stacks	1.956
Length over end extensions	15.010
Rotor OD	15.109
Stator OD	18.693
Frame OD over field	22.610
Rotor core OD	9.199
Linear pole width (circumferential)	3.143
Electrical Weight Breakdown, lb:	
Armature conductors	29.7
Field conductors	40.8
Armature stacks	149.0
Frame	123.9
Rotor	303.5
Total	646.9
Resistance and Reactance:	
Armature resistance per phase (hot)	0.0182 ohms
Armature leakage reactance	0.149 ohms
Field coil resistance (hot)	0.159 ohms
Direct axis synchronous reactance, Xd	0.553 per unit

*Design dimensions are at operating temperature and rated speed. Fabrication dimensions (R.T. at 0 rpm) must be worked back from these by use of calculated temperatures and strains. These fabrication dimensions and associated tolerances must then be extended back upward to off-design conditions at near-end of life (3 to 5 years) to assure fits, running clearances, etc., will remain satisfactory over the life of the machine.

Resistance and Reactance (CONT):	
Quadrature axis synchronous reactance, Xq	0.322 per unit
Transient reactance, X'd	0.240 per unit
Subtransient reactance, X"d	0.240 per unit
Quadrature subtransient reactance, X"q	0.322 per unit
Negative sequence reactance, X2	0.281 per unit
Zero sequence reactance, X0	0.013 per unit
Time Constants (hot):	
Short circuit transient, T'D1	0.067
Open circuit transient, T'DO	10.110
Armature, TA	0.0061
Materials:	
Stator frame	Hiperco-27 forging
Armature laminations	Hiperco-27 0.004-in. thick
Armature interlaminar insulation	Plasma-arc sprayed alumina
Armature conductors	Anadur insulated nickel clad silver
Field coil conductors	Bare CUBE copper
Field coil insulation	Alumina and synthetic mica sheet
Rotor	Premium quality H-11 (AMS 6487)
Slot liners and wedges	Ceramic; 99.5% alumina
Pole face configuration	Grooved

The armature winding is a 120-deg phase belt, two-conductor-per-slot windings. This configuration eliminates the need for conductor

end-extension joints with the nickel clad silver conductors. Coil ends are connected directly to the bus-rings, there being a total of 30 joints required for the complete armature winding.

Joining of clad silver conductors to the bus-rings is a much less complex procedure than making conductor-to-conductor joints in the winding end extensions. Access to the joint area is greater at the bus-ring, and the conductor ends can be embedded in the bus ring material. The latter can eliminate the need for elaborate preweld clamping procedures. Joints located at the bus-ring do not require insulation and, because the bus-rings are remote from the end extensions, the probability of damaging the armature insulation during the joining process is greatly reduced. Had 60-deg phase belts and/or four-conductor-per-slot windings been used, the number of joints would have been increased by 50 or 100 percent with joints required in the end-extensions as well as at the bus-rings.

Armature windings are often referred to as integral or fractional slot windings. The basic difference between the two types is that the number of slots per pole per phase of an integral slot winding always equals an integer, whereas the number of slots per pole per phase of a fractional winding is not an integer. The basic disadvantage of a fractional slot winding in this application is the greater number of harmonics present in the armature MMF as compared to an integral slot winding. Fractional slot windings can contain all odd harmonics, even harmonics, fractional harmonics (e.g., the order of 1.5) and in some cases subharmonics which rotate at very high speeds. The higher harmonic content of fractional slot windings can result in very high rotor pole face losses when the alternator is under load. Minimization of pole face losses is a prime goal in the design of high-speed alternators for space applications. Integral slot, 60-deg phase-belt windings contain only odd harmonics in the armature MMF and, for this reason, are well suited for high-speed alternators. Integral slot,

120-deg phase-belt windings can contain all odd and even harmonics, but even harmonics are eliminated by selecting full-pitch coils. This configuration was selected for the KTA application because end-extension interconnections are not required (as they are for 60-deg phase belts) and the selected coil distribution of the KTA armature configuration will result in low pole face losses.

For a given number of series turns per phase, the number of armature slots is directly proportional to the number of parallel paths and inversely proportional to the number of conductors per slot. A high number of slots is beneficial to machine performance with regard to lowering rotor pole face losses and providing better heat transfer of the armature winding loss from the slots. The tooth ripple (no-load) component of pole face loss is reduced because of the lower slot pitch and amplitude of the tooth flux oscillation factor. Load harmonic losses and voltage harmonic content are reduced by means of lower harmonic distribution factors achievable for high slots per pole per phase designs.

Slot heat transfer is improved by reducing the heat-flux density ($w/in.^2$) along the slot sides. The choice of five parallel paths and two conductors per slot for the armature winding attains the above-listed design benefits by providing a high number of armature slots. The use of parallel paths in the armature has the further advantage of reducing unbalanced magnetic forces on the rotor under dynamic (rotating) conditions. The advantage of a two-conductor-per-slot configuration has already been discussed.

Each slot conductor is comprised of two parallel strap wires to reduce localized eddy current losses in the conductors. The calculated eddy-current factor (a multiplier for the dc armature resistance) is 1.26 at the alternator frequency of 1600 Hz and 700°F stator coolant temperature. The use of a higher number of parallel strands would

further reduce the eddy-current factor but would result in increased alternator weight caused by a corresponding decrease in slot space factor (i.e., ratio of wire area to slot area) with Anadur insulated wire.

The per-unit direct-axis synchronous-reactance value for the Phase II KTA alternator (0.55) falls below the selected range specified in the Phase I studies (0.7 to 1.0). This results from the lower armature current of the Phase II kva rating and maintenance of the same number of armature slots, conductors per slot, etc., as the Phase I design. Increasing the Xd of the Phase II alternator would require an increase in the number of armature slots or an increase in the number of conductors per slot from two to four, which is not desirable. The number of armature slots cannot be increased arbitrarily as there are inviolable rules governing slot, pole, phase, and parallel path relationships. The next highest number of slots for the KTA alternator is 210 (an increase of 30) if an integral slot winding is to be maintained. This configuration has an Xd of 0.91, an alternator weight of 608 lb, and efficiency of 93.7 percent and compares with an alternator weight of 647 lb and efficiency of 94.4 percent for the selected 180-slot configuration. A system weight penalty of 70 lb/kw of loss results in a system weight savings of 461 lb for the selected 180-slot alternator.

The per-unit direct-axis synchronous-reactance Xd for the KTA alternator is low (0.55) relative to values normally associated with aircraft alternators (e.g., 1.8). Although a low Xd machine suffers the disadvantage of higher weight, there are many overriding advantages in this application. First, the load component of rotor pole face loss is minimized, since this component is proportional as a first approximation, to $(Xd)^2$ for a given spectrum of armature harmonics. Also, there is less effect from distorted current waveforms that may be created by nonlinear load characteristics. Unbalance of terminal

voltage between the three phases for a given load unbalance is less with a low Xd machine. Field power requirements are lessened and the ability to meet three-phase short-circuit is enhanced as Xd is decreased. Finally, the low Xd in this application allows the use of a two-conductor-per-slot winding configuration whose benefits have been previously described.

The armature stacks are built from 0.004-in. thick Hiperco-27 laminations with plasma-sprayed alumina interlaminar insulation. The stacks are not welded in order to minimize core losses. Rigid ceramic slot liners are used in the slot channels of the armature stacks. In order to ensure that the slot liners can be inserted into the slot channels and the conductor can be inserted into the slot, a clearance between the slot liner and slot channel sides and the slot liner and conductor must be allowed. These clearances are detrimental to slot heat-transfer, especially in a hard vacuum where slot heat-conduction characteristics are almost entirely dependent on contact conductance and radiation. If the space gaps in the slot are not filled with a heat conducting material (e.g., a potting compound), then the slot heat-flux density must be kept low. The best high temperature non-organic potting compounds have high shrink-rates during cure, high outgassing-rates in hard vacuums, and their dielectric power factors and electric strength at high temperatures are poor. Because of the unavailability of a suitable high-temperature inorganic potting compound for the KTA application, the armature will not be encapsulated. The low slot heat-flux density of the KTA alternator design (approximately 5 $w/in.^2$) provides for a reasonable temperature rise from conductor-to-tooth in a hard vacuum. Refer to Section 5.2 for details on thermal performance.

A low voltage, high current strap-wound field-coil configuration was selected for the KTA alternator. Results of a study performed in the Phase I portion of the KTA Program show that this configuration

provides better heat-transfer characteristics than a high-voltage, low-current field coil. A high-voltage design requires many turns of small diameter insulated wire which consequently results in a large number of insulation and contact gaps in the thermal path to the heat-sink. The high-current configuration requires a few turns of large cross-sectional area strap conductors that are oriented to provide a minimum number of insulation and contact gaps in the thermal path. Coolant manifolds are located in the frame housing on each side of the field coil to minimize temperature rise. The field conductors are CUBE copper (BeO dispersion-strengthened copper). Synthetic mica paper* will be used for turn-to-turn insulation because of its low outgassing and adequate electrical properties at the operation temperatures and voltage of the KTA alternator field coil. Alumina insulation is provided for the field-coil to cooling-manifold insulation.

Because of the requirement for a ceramic bore seal separating the rotor and stator cavities, the radial gap between the stator and rotor must be large enough to accommodate the bore seal thickness plus provide adequate running clearance. The radial gap for the KTA alternator is 0.140 in. (with the machine hot and running) and was selected based on results of the Phase I parametric studies.

The selected gap was the larger of two alternate values (0.130 and 0.140) which provided nearly equal minimum system weight. The largest was chosen to minimize magnetic unbalance forces, provide increased radial clearance, and reduce pole face losses. The selection of a large radial gap tends to transfer losses from the rotor to the stator by reducing rotor pole face losses and increasing stator field losses. Removal of loss heat from the stator field coil instead of the rotor is a much simpler design task, which provides many benefits regarding machine reliability and simplicity.

---

*Alternatively spe[illegible]ting, plasma-arc sprayed alumina may be possible.

As mentioned in Section 5.1.2, a new calculation procedure was derived as a result of an experimental verification program for determining the ac circumferential flux in the armature core. This new procedure was incorporated into the design program between Phase I and Phase II. It results in lower ac circumferential flux amplitudes than previously calculated and an approximate 10-percent corresponding weight reduction. Parametric trends for all studies performed in Phase I, except the armature core flux-density studies, are not affected by the change. A rerun of the armature core flux-density study, using the new procedure, resulted in the same trends as in Phase I with the exception of lower alternator weights. Of course, the lower rating of the Phase II KTA alternator (600 kva versus 733 kva for Phase I) also contributed to lower Phase II design weights.

5.1.4 Alternator Electrical Performance Data

Alternator electrical performance computations were made to verify that the performance meets the output and other requirements of the specification. Performance was determined at the alternator maximum continuous-load rating (450 kw_e, 0.75-lagging-power factor), which was also specified as the nominal alternator rating for purposes of alternator performance calculations. Alternator performance at a load rating corresponding to a 455-kw turbine power output was also determined where there was discernible performance differences. Waveform and output voltage modulation requirements are retained as a final design goal without analytical verification.

Figure 112 presents the no-load voltage-saturation characteristic, the load-saturation characteristic at 417 amp, 0.75-power factor and at 0-power-factor lagging, and the three-phase short-circuit characteristic. It also presents saturation characteristics at the specified overload condition, 900 kva, 0.9 power factor, lagging. Required field current to obtain rated voltage at the no-load, maximum rated-load,

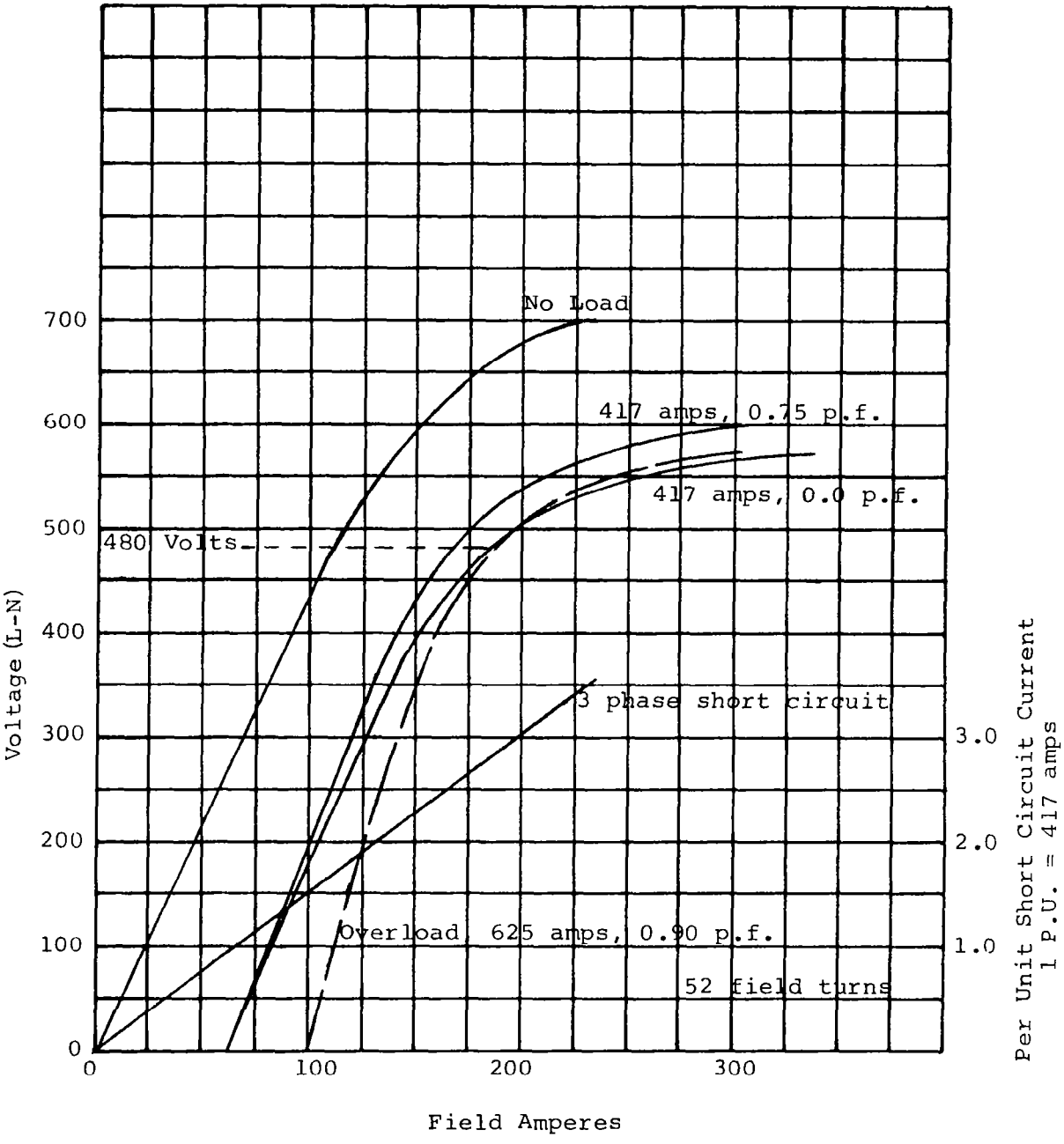

ALTER ATOR SATU ATION CURVES

FIGURE 112

overload, and three per unit short-circuit conditions are 109, 166, 187, and 189 amp, respectively. Alternator electrical efficiency, excluding terminal, bus-ring, bearing, and seal losses, is presented in Figure 113 as a function of load at rated-power factor.

The nominal rated output of the turbine was specified by AiResearch as 455 kw which corresponds to a 428 kw_e alternator load assuming an alternator efficiency of 94 percent. The load (428 kw) represents a 4.7 percent reduction from the 450 kw_e maximum continuous-rated alternator load. Table 25 presents a breakdown of electrical losses, armature and field-current densities, flux densities, and voltage unbalance for the alternator maximum continuous-load rating and the 428-kw_e (571-kva at 0.75-power factor) load condition. The load saturation characteristic at 417-amp line current, 0.75 power factor, lagging, which corresponds to 450-kw_e load (Figure 112) can be used for the 428-kw_e alternator load condition because the performance difference would be imperceptible if plotted on the same scale.

Pole face losses were calculated for a grooved pole face configuration with 0.006-in. wide grooves, 0.100 in. deep, with a groove pitch of 0.034 in. Calculated losses for this configuration are 1024 w with 527 w caused by the tooth-ripple component of surface loss and 497 w caused by the harmonics of the stator MMF when the alternator is under load. Windage losses were calculated as less than 100 w; however, the 100 are assumed for the efficiency calculation. The listed percent voltage unbalance corresponds to a single-phase unbalance current of 2/3-rated current.

5.2 Mechanical Design and Performance Study

The mechanical design studies included the final thermal analysis of the rotor and stator, the rotor stress analysis, the structural weight minimization and stress analysis, the bore seal assembly design and analysis, and the alternator seal design and performance analyses.

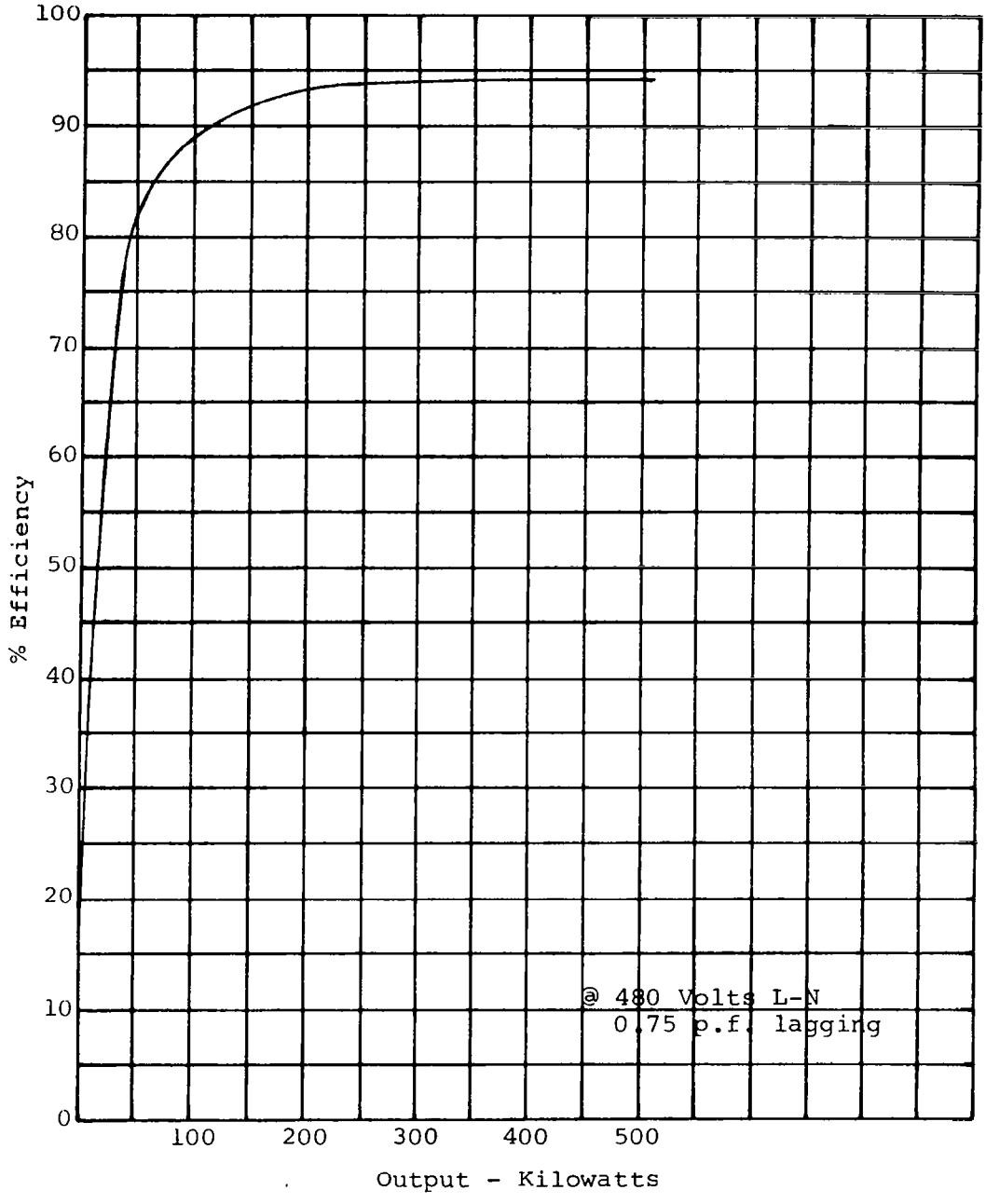

ALTERNATOR EFFICIENCY

FIGURE 113

TABLE 25

ALTERNATOR PERFORMANCE DATA

	600 kva	571 kva
Loss Breakdown, kw:		
Armature conductor	9.85	8.91
Field conductor	4.37	4.16
Armature stack loss	11.38	11.09
Pole face loss	1.02	0.96
Windage loss	0.10	0.10
	26.72	25.22
Electrical Efficiency, %:	94.4	94.5
Current Density, amp/in.^{2}:		
Armature	5650	5370
Field	4045	3960
Flux Density Under Load, kl/in.^{2}:		
Depth behind slot	60	59
Teeth	124	123
Frame	114	113
Rotor core	80	79
Rotor pole	69	68
Voltage Unbalance, 2/3 rated Amp, 1-phase, %:	5.7 (L-N)	5.6 (L-N)

The thermal analysis was based on the basic Phase I procedures as well as the cooling configuration selected from the Phase I studies. Because the Phase II electrical power loss density was lowered, the resulting temperature gradient between the hot spot and coolant was only about 200°F instead of the 300°F of Phase I. This, plus the reduction of the coolant temperature to 700°F, kept all hot spots near or below 900°F even on slotted (unlaminated) pole faces.

The rotor stress analysis was completed with a recently developed computer program based on finite element theory that determines a very accurate two-dimensional picture of the elastic/plastic stress pattern in the complete irregular rotor body. Programs and calculation routines as complex and powerful as this one have previously been unavailable, awaiting the advent of bigger and faster computers.

Structural weight minimization studies were carried out in response to NASA suggestions for Phase I design improvements. By departing from aircraft alternator frame design techniques and using aerospace structural design techniques, significant weight reductions were achieved.

The bore seal design effort concentrated upon the two tasks of becoming familiar with bimetallic joint technology and performing basic stress analyses on the selected bore seal design. The study showed that the basics are well in hand for proceeding into a major development effort to bring the bore seal assembly up to the same developmental status as the rest of the alternator. A logical plan was derived that does not take a "shot-gun" approach to achieve a high degree of developmental or operational success on the first bore seal assembly as quickly as possible.

Once the needs of the bimetallic joint were realized, it was possible to configure a simpler and more reliable bore seal assembly design in Phase II (relative to that in Phase I). More important, however, was the realization that the design and fabrication of all the components of the bore seal assembly must be closely coordinated so that each of the seemingly separate areas of the design are, in fact, complementing each other. In other words, the components of the assembly cannot be developed separately without a thorough knowledge of each of their requirements, functions or limitations.

5.2.1 Thermal Analysis

The thermal design and analysis is based on the selected cooling configuration and calculation methods of the Phase I studies. Because of this, the complete details of the studies will not be repeated. Contained below is a basic description of the analytical model, the analytical methods and finally, a summary of the results.

5.2.1.1 Stator Cooling Configuration

The stator frame cooling configuration consists of two 360-deg circumferential cooling manifolds on the outside of the stator magnetic frame sections. These manifolds are ducted to the outside of the hermetic shroud around the alternator frame for access to the coolant supply lines. Cooling is achieved by conduction from the heat generating armature windings and stacks through the stator frame and manifold walls. The end turns of the stator (armature) windings are also cooled by radiation to the surrounding end bell and conduction to the stator frame. Between stacks, BeO spacers that double as heat-sinks act to aid in transferring (by radiation and conduction) the armature losses to the field coil cooling sink.

The thermal analysis of this configuration was calculated with the use of two computer programs. The first is a digital computer program for finding the transient and/or steady-state (TØSS) temperature distributions of a three dimensional irregular body. This program, used in the Phase I studies, considers the heat transfer mechanisms of conduction between internal points, conduction between internal and surface points, radiation between surface points, and radiation, free convection, and forced convection between surface and boundary points. It also considers internal heat generation which is a function of space and time. Boundary temperatures may vary as a function of time. The second program is a modified version of TØSS.

This second program has eliminated the transient capabilities of TØSS and changed the solution of the general heat conduction equation from the explicit method used in TØSS to an implicit method, thereby allowing a larger time step and the use of less digital computer time. However, this second program (steady-state), due to its method of solution, introduces an error to the results. For our calculations though, this error is quite tolerable. In general, most of the final results were obtained through use of the steady-state program with occasional use of the TØSS program for result verification.

The calculation of a temperature distribution for the stator frame by use of these computer programs involves the establishment of a nodal grid work of the stator. For the sake of conserving computer storage space, a symmetrical axial section was taken as the analytical model. The three-dimensional section comprised one-half a stator tooth-pitch plus one-half a slot pitch for a section comprising 1.0 deg of arc circumferential volume. An axial length of one-half the total stator length was chosen for the symmetrical model. These models correspond to the basic configurations reported in Phase I as do the property data and configuration constants such as the critical 0.2 $w/in.^2/°C$ equivalent slot conductance.

5.2.1.2 Field Coil Cooling Configuration

The KTA Phase I study showed the desirability of including direct cooling of the field coil in the stator cooling configuration. The Phase II design has two separate circular-cooling ducts the full height of the field coil, one on either axial side of the coil. They are electrically isolated from the coil by ceramic insulation. The cooling ducts on the coil sides provide a short, direct thermal path to the coolant for each field coil electrical turn as well as additional cooling for the armature stack and ac windings between the stacks. These coolant ducts are ducted to the outside of the alternator hermetic

frame-shroud for access to the coolant supply. The field coil and the stator frame cooling ducts should be in parallel flow but may be arranged in series if volumetric flow requirements penalize the system-cooling configuration.

Initially, an analytical model representing a simulation of the stator frame with assumed rotor pole tip surface temperatures as fixed-boundary values was analyzed with the computer programs. The results were inconclusive due to the assumed rotor conditions. It was concluded that a new model that included the collected stator and rotor geometries should be analyzed. This analytical model better simulated the actual physical situation in one sense but because of computer storage limitations, prevented analyzing the rotor temperatures in the circumferential direction. Thus, the rotor temperatures calculated were based on an analytical model of 1.0 deg of arc off an axial plane through the center of the pole.

5.2.1.3 Rotor Cooling Configuration

The rotor cooling configuration consists of a central coolant hole with the 700°F coolant passing through the hole in series with the antidrive end-bearing lubricant. For calculation of the complete rotor-stator temperature distribution, heat-transfer mechanisms of both conduction to the coolant passage and radiation to the end bell-housing were considered. The effects of windage losses and losses for both slotted and solid rotor pole face configurations were included in the analysis.

5.2.1.4 Summary of Results

The temperature distributions shown in Figures 114 and 115 represent the computer outputs for a 700°F stator coolant and slotted rotor pole faces. An analysis for an 800°F stator coolant for slotted rotor

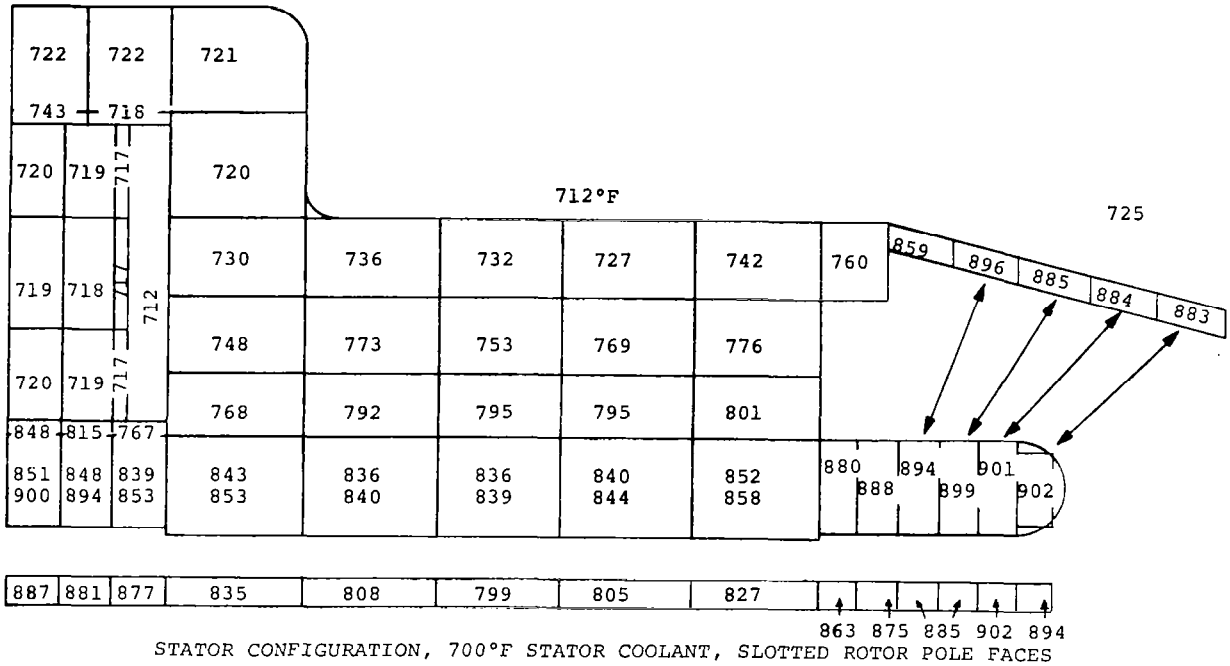

STATOR CONFIGURATION, 700°F STATOR COOLANT, SLOTTED ROTOR POLE FACES

FIGURE 114

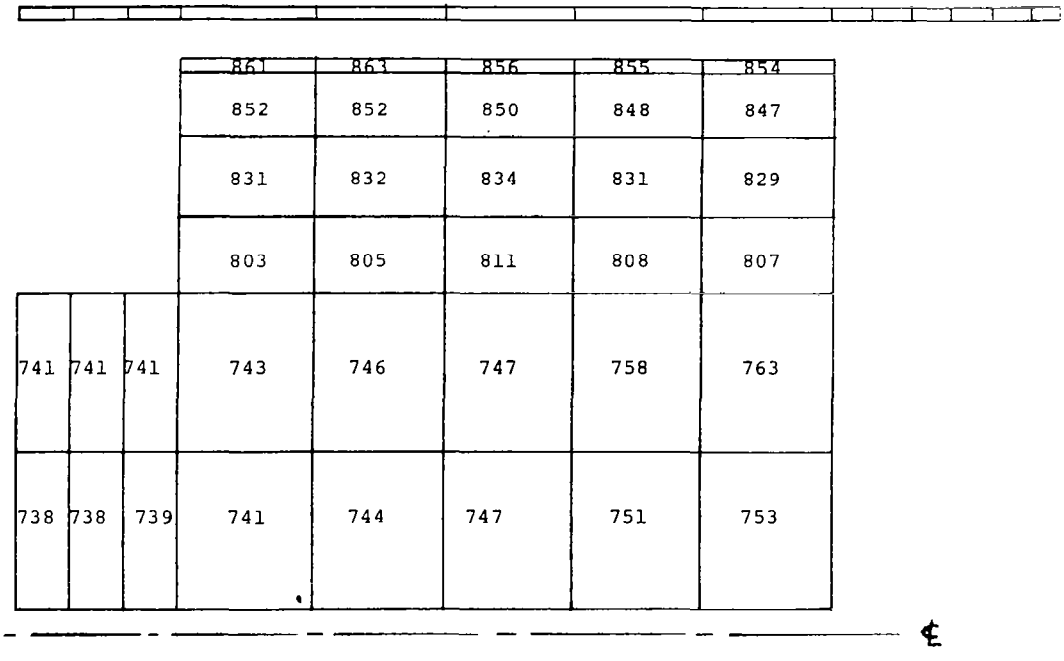

ROTOR ℄ CONFIGURATION, 700°F STATOR COOLANT, SLOTTED ROTOR POLE FACES

FIGURE 115

pole face configurations is given in Figures 116 and 117. The 800°F stator coolant models do not contain temperature distributions for the end-bell extensions above the stator end-turns, due to the late addition of this section to the main thermal analytical model. It should be noted that this addition raised the end-turn temperatures approximately 10°F over the original 700°F stator without end-bells (not shown). The relative difference in this addition is negligible to the total thermal map. The coolant and boundary temperatures shown are necessary approximations (of expected results) for computer input requirements. The coolant approximations are based on the average of inlet and outlet temperatures. The void temperatures, used as radiation heat-sinks, are based on approximations through experience with preliminary calculations.

A significant feature should also be noted in the figures in comparison of the 700° and 800°F stator coolant models. The heat-flux across the air-gap and bore seal between rotor and stator reverses itself with the reduction of coolant temperature. This is also illustrated in a comparative summary of the significant temperatures (Table 26).

One of the major conclusions resulting from the thermal analyses was that the reduction in rotor coolant temperature to 700°F obviated the need for laminated pole faces. The pole-tip temperatures will be less than 900°F with slotted pole faces; hence, reliability should be enhanced with the solid pole bodies. In fact, based on the calculated results shown on Table 26, solid pole faces should suffice. In the interests of reliability and design conservation, however, it is proposed the slotted pole face construction be used.

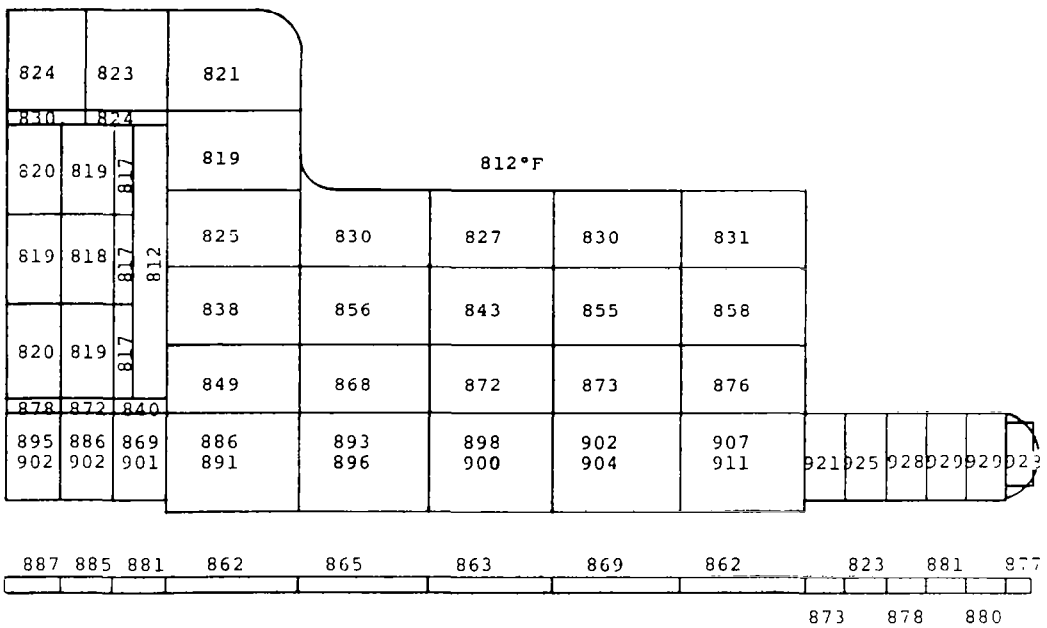

STATOR CONFIGURATION, 800°F STATOR COOLANT, SLOTTED ROTOR POLE FACES

FIGURE 116

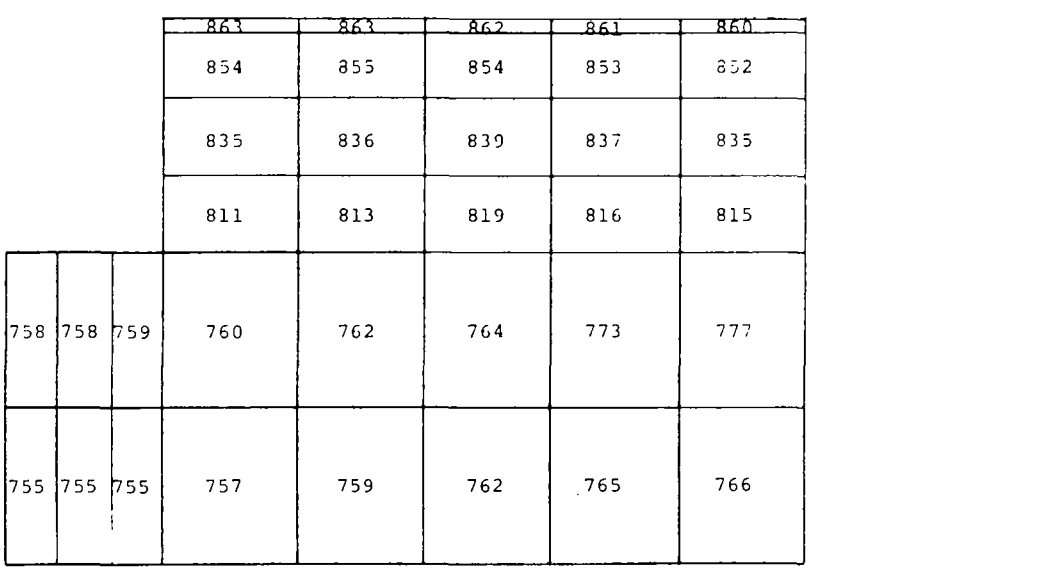

ROTOR ℄ CONFIGURATION, 800°F STATOR COOLANT, SLOTTED ROTOR POLE FACES

FIGURE 117

TABLE 26

PRELIMINARY COMPARATIVE ALTERNATOR TEMPERATURES*

	700°F Stator Coolant		800°F Stator Coolant	
	Slotted Rotor Pole Face	Solid Rotor Pole Face	Slotted Rotor Pole Face	Solid Rotor Pole Face
Hot Spot, °F	900	900	929	929
Location	Arm. Wind. Below F.C.	Arm. Wind. Below F.C.	End Turns	End Turns
End Turn Avg. Temp., °F	875	875	927	927
Armature Wind. Avg. Temperature, °F	867	867	912	912
Stator Tooth Avg. Temperature, °F	835	835	897	897
Field Coil Avg. Temperature, °F	720	720	820	820
Rotor Pole Face Avg. Temperature, °F	862	874	862	873
Heat Flux Direction Between Stator/Rotor	Rotor to Stator	Rotor to Stator	Stator to Rotor	Stator to Rotor
Calculated Pole Face Losses, w	1024	1410	1024	1410

*Excludes the effects of the end-bell between the armature end turns and the 725°F void ambient. Was done prior to including the simulated end-bell into the analytical model.

5.2.2 Structural Weight Minimization

5.2.2.1 Introduction

As a result of the review of the Phase I Conceptual Design Study, it was recognized that weight reduction of the alternator inert or structural components was desirable. The alternator structural components are the frame (housing), end-bells, and bearing and seal housings. The design of the Phase I conceptual design alternator structural components was conservative and was based on common aircraft generator frame design techniques. A weight minimization study was conducted to reduce the weight of the alternator structural components, applying aircraft structure design techniques where applicable and feasible.

The first concept adopted to reduce structural weight was to use the Hiperco-27 magnetic frame to support the end bells and the bearing and seal housings. This eliminated the steel frame around the stator used to support the magnetic frame, end-bells, and the bearing and seal housings in the Phase I designs.

Qualified personnel in aircraft minimum-weight structures-design from the Westinghouse Astronuclear Laboratories (WANL) were engaged to evolve a lighter weight end-bell configuration without sacrificing strength. As a result of the study at WANL, an end bell configuration was evolved which meets structural requirements and the weight of the end-bells was reduced from 232 to 46 lb, for an actual weight reduction of 186 lb or a real* weight reduction of 144 lb. Elimination of the Phase I configuration steel frame and the new minimum weight end-bell

*The real weight reduction takes into account the reduction in alternator rating between Phase I and Phase II. For example, Real weight reduction = 232 lb x 500 kva/733 kva - 46 lb = 144 lb.

configuration reduced the total alternator structural frame weight from 363 to 137 lb for an actual weight reduction of 226 lb or a real weight reduction of 137 lb.

It is believed that this end-bell configuration is a minimum-weight design for all practical purposes. It might be possible to reduce the weight another 20 lb by stiffening the weaker sections with some sort of sandwich structure at the expense of increasing the cost and complexity of the components by a factor of approximately 5 to 10. This potential weight reduction does not appear practical because of the additional cost and complexity required to reduce the total machine weight by such a small percentage (approximately 3 percent). The present end-bell design must be considered preliminary even though it is a minimum-weight configuration, because the design study to evolve the design did not allow any design refinement.

5.2.2.2 Design Summary

Certain ground rules were followed for the preliminary structural design. No attempt will be made to list every constraint but the more significant ones are:

(a) The end-bell material must be nonmagnetic and compatible for mounting to the Hiperco-27 stator material.
(b) The end-bells must be sufficiently rigid to prevent bearing housing deflections from exceeding 0.010 in. translation and 0.012-deg rotation while withstanding environmental shock and vibration loadings as well as design pressure and temperature as specified.
(c) The bearing housing configuration must be maintained so that the interfaces with the bearing and seal housings are not altered.

(d) Provision must be made for penetration of the antidrive end-bell by 30 electrical leads with approximately 1/2-in. clearance around each lead.

(e) The design must also provide for suitable sealing of the rotor cavity and lend itself to reasonable assembly procedures that are restricted somewhat by the requirements of the bore seal and the design of the integrated stator and rotor.

All of the above requirements were considered in arriving at the structural design. In some areas, the result is over-design; i.e., the stresses were low compared to the material allowable stress. In some areas, another limit has been reached--the stress in the sheet metal components is limited by buckling. No attempt was made to optimize the situation on a cost basis; that is, choose a cheaper, weaker material.

The choice of end-bell material is limited by certain requirements dictated by the electrical design. Basically, these are (1) the material must be nonmagnetic, (2) it must be compatible with the operating temperature of approximately 900°F, and (3) the coefficient of thermal expansion must be between 4.1 and 6.4 x 10^{-6} in./in./°F. The coefficient of a thermal expansion requirement is one of the more critical limitations because it is necessary to match as closely as possible the expansion of the Hiperco-27, the H-11, and the bore seal end-member assembly structure. Coefficients of expansion, which exceed or are much lower than the range, complicate the design problem, especially in the bore seal end-member design and can affect the reliability as a result. The primary candidate materials considered for the end-bell are listed in Table 27. Of the five materials shown, only two have coefficients of expansion which fall into the desired range. One of them, the titanium alloy, looks quite attractive except for the oxidation resistance at temperature. The second one, the Carpenter-42,

TABLE 27

END BELL MATERIAL COMPARISON

	Required Property	Hastelloy B Ni,2.5Co,28Mo,1Cr,6Fe	Inconel 718 53Ni,20Cr,5Cb,3Mo	B120CVA Ti.13V,11Cr,3Al	Carpenter-42 FE,41.5Ni	Mar-M-302 Co,21.5Cr,10W,9Ta
1. Coeff. Therm. Exp., x 10^{-6} in./in.-°F	4.1-6.4	6.66 (rt-1000°F)	8.0 (rt-1000°F)	5.5 (rt-1000°F)	4.95 (rt-1000°F)	7.6 (rt-1000°F)
2. Temp. Range, °F	rt-890°F					
3. Stress, psi	30,000					
4. Nonmagnetic, μ	1.0-2.0	Paramagnetic, 1.000 and < 1.001	1.001	1.00005	Curie 715°F	Nonmagnetic
5. Properties:						
E, x 10^6		27.8 at 800°F	26 at 890°F	10.7 at 890°F	21 at rt	36 at rt
ρ, lb/in.^{3} at rt		0.334	0.296	0.175	0.293	0.333
K, Btu-in./ft^2-hr-°F		102 at 890°F	97 at 890°F	105 at 890°F	74 at rt	155 at rt
σ_y, psi		39,000 at 890°F	127,000 at 890°F	100,000 at 890°F	40,000 at rt	72,000 at 890°F
σ_t, psi		104,000 at 890°F	159,000 at 890°F	160,000 at 890°F	82,000 at rt	110,000 at rt
Elongation, %		68 percent - 890°F	18 percent - 890°F	20 percent - 890°F	30 percent - rt	2 percent - rt
6. Weldability		All common methods except oxygen/ acetylene	Very good	Excellent	Good	Good
7. Fabricability		Mach. Index 12	Good mach.	Good	Good	Difficult
8. Available Forms		Sheet, Cast, Forge	Sheet, Cast, Bar	Sheet, Bar, Forge	Strip, Bar	Cast
9. K-Resistance, °F		<1100	<1700	<1100	<1100	<1600
10. Oxidation Resistance, °F		<1400	Good	<800	Good	Good

is magnetic up to about 700°F which would preclude the capability of testing the alternator at room temperature; thus, it cannot be seriously considered. The Hastelloy B material has properties which look attractive except the coefficient of thermal expansion is slightly higher than the range specified and the yield strength is only 39,000 psi at temperature.

For purposes of the analytical study, the Inconel 718 alloy was arbitrarily selected* for the representative end-bell material because of the high strength at temperature, reasonably close match to the required thermal expansion, magnetic properties, and excellent fabricability. As shown later, the stresses calculated for the design using the Inconel 718 were sufficiently low to allow eventual use of a weaker structural material such as the Hastelloy B in the final design. As a result of the stress analysis and the review of the material properties of Table 27, it is recommended that Hastelloy B be used as the end-bell material for the final design.

Double cones were used in order to provide bearing housing longitudinal and angular rigidity, while maintaining the bearing housing location and the electrical envelope of the stator (Figure 4, Page 17). Elliptical wire penetrations were provided near the outer edge of the reinforced cones on the antidrive end. The bore seal is welded to the inner cone of this preforated end-bell from the input end of the alternator. Because of the arrangement of the leads through the preforations, this antidrive end-bell becomes a permanent part of the stator assembly and would not ordinarily be removed on a normal teardown disassembly.

---

*It was selected prior to the survey of Table 27 completion. As seen in the table, Inconel 718 cannot be considered one of the better choices due to its high coefficient of expansion.

The end-bell on the drive-end frame is ordinarily removed on disassembly, and provision is allowed by seal welding the bore seal to an axial (tubular) housing extending from the Hiperco-27 frame. Separate bolt circles are provided in the area of the joint between the axial housing and drive end-bell to allow for (1) the attachment of the end-bell and the seal welding of the joint to seal the rotor cavity, and (2) the mounting location for the cold frame truss to the turbine. Separate schemes were devised where these two bolt circles could be combined as one with the requirement that the hermetic sealing of the rotor cavity be combined with the cold-frame mounts. This saves weight but complicates the design in that the cold-frame truss must become a permanent part of the alternator end-bell. Because of the very rigid nature shown by the double-cone configuration, it may be possible to use only one cone and still build the alternator to meet the requirements.

5.2.2.3 Summary of Analysis

The environmental specification supplied by NASA for launch loads indicates that the alternator must withstand very severe sinusoidal vibration with excitation from 5 to 2000 Hz at g-levels up to 15 peak. The shock requirement specified is a 20-g half-sine-pulse of 10-msec duration. The acceleration requirement is less severe than either of these. Orbital operating requirements are also less severe than these launch requirements.

Since it is not practical to design the unit with natural frequencies high enough to avoid resonance, it is recommended that a vibration isolating mount be incorporated into the vehicle interface with the KTA. The mount will tend to amplify loadings at its natural frequency and attenuate loadings at higher frequency. The natural frequency of the mount should be selected to be below all component resonances so that the full input g-level does not excite such resonances.

It is further suggested that a mount be considered to suspend the system at a natural frequency of about 20 Hz with at least 10 percent of critical damping. This mount would amplify the excitation to about 15 g at 20 Hz where resonances can probably be avoided but would attenuate the loadings above 30 Hz where resonances are likely to be encountered. At 100 Hz, for example, the applied loading could be attenuated by about a factor of 10 and at 200 Hz by a factor of 30. This mount system would also attenuate the shock loading below the input pulse level.

The analysis for the stresses in the end-bell structure was performed assuming a g-level of 20, internal pressure difference between the rotor cavity and the environment of 30 psi, and a uniform operating temperature of 850°F. The g-load could, of course, act in any direction. Under the isothermal condition, the bearing center spacing increases 0.103 in. It was assumed that this thermally expanded bearing spacing is the reference point from which the deflections are limited. It should be mentioned that the effect of thermal transients and gradients have not been included at this time since these considerations are beyond the scope of the present conceptual design effort. Now that the thermal analysis has been completed, the gradients in the cones can be included (next design phase). If the gradients cause severe stress increases over those shown, it may be necessary to later use single rather than double cones.

The stress analysis was done using a computer program similar to that for the bore seal stress analysis (Section 5.2.4). The computation technique uses finite element theories requiring large and fast computers.

The results of the analysis are listed below:

(a) Isothermal Heating to 850°F - There are stresses resulting due to differential expansion between the Hiperco-27 and the

Inconel 718*. The maximum effective stress in the Hiperco-27 is 19,700 psi. Since the yield stress is about 55,000 psi and the stress for 1-percent creep in 10,000 hr is about 45,000 psi, this stress level is acceptable. The maximum effective stress in the Inconel 718 is 23,200 psi. Because of the low stresses in the Inconel 718 end-bell, it can be concluded the structural material can be one having lower strength but more compatible properties, especially the coefficient of thermal expansion. The review of materials listed in Table 27 indicates the logical choice of the Hastelloy B material. The analysis was not rerun using the Hastelloy B material since, for all practical purposes, the analysis using the Inconel 718 verified the integrity of the preliminary design. At such time that final design refinements are included into the configuration, the analysis should be re-done using Hastelloy B material.

(b) Rotor Cavity Pressure - The assumed 30-psi rotor cavity pressure produces maximum effective stresses in the Hiperco-27 of 840 psi and in the Inconel 718 of 5500 psi. Both values are negligible. The translation of the bearings (relative to each other) is 0.0013 in. The 30 psi was assumed to act in the direction causing the maximum deflection to the end-bells, i.e., internal pressurization.

(c) 20-g Axial Load - The loading produces a maximum stress of 1050 psi in the Hiperco-27 and 8400 psi in the Inconel 718. Again, the stress levels are low. The relative bearing housing translation is 0.0038 in.

(d) 20-g Lateral Load - This loading produces 920 psi in the Hiperco-27 and 10,000 psi in the Inconel 718. The angular

*For simplifying the following discussion, Inconel 718 will be referred to as the end-bell material, realizing it may be Hastelloy B in the final design.

rotation of the bearing housing is about 0.011 deg. These values are acceptable.

The above deflections can be superimposed directly. The maximum relative translation of the bearings is 0.0051 in. while the maximum rotation is 0.011 deg. These values are well within the desired limits specified at the start of the study. One effect that has not been included is the gyroscopic effect that would exist due to turning of the unit. The specification does not include pitch or yaw velocity requirements which would be needed to determine these effects.

The above stresses do not superimpose directly. In addition, discontinuities complicate the analysis. The maximum stress (approximate) in the Hiperco-27 is an acceptable 20,000 psi. The stress (again approximate) in the end-bell is less than 30,000 psi. The limiting condition in the end-bell is the 10,000-psi compressive stress in the conical members during g-loading. The critical stress is difficult to determine but has been estimated at about 20,000 to 30,000 psi which should provide sufficient margin against buckling.

5.2.3 Rotor Stress Analysis

Although the rotor stress analysis was basically a continuation of the analysis performed in Phase I (except for slight differences in rotor dimensions and for a different rotor temperature distribution), the computation methods were changed as a result of the acquisition of a newer, more powerful digital computer program developed by the Westinghouse Research Laboratories.

The program can be used to solve two-dimensional, plane problems for irregular or arbitrarily shaped bodies in elastic, elastic-plastic, or fully plastic states of stress. The program uses the finite element method and the displacement formulation. The actual experimental

stress-strain curves of the materials comprising the body or any of five common types of stress-strain curves built into the program may be used to solve elastic-plastic problems. The program can accommodate various types of boundary conditions and/or loading, including

(a) Surface tractions of various types
(b) Specified displacements at the boundaries
(c) Body forces (including centrifugal forces)
(d) Thermal stresses

This program made it possible to analyze the complete rotor cross section on a plane through the poles perpendicular to the rotor axis of rotation for the first time (compared to just the core by previous methods). In addition, the effects of stress concentrations due to fillets and the combined effects of thermal stresses, rotation, and partially plastic-deformation could be determined in one solution.

The rotor stress was determined for a symmetrical section normal to the center line through a section consisting of one-half pole pitch. The radial temperature profile according to Figure 115 was included to take into account the thermal stresses. As part of the computer program output, several stress maps are machine-plotted. A portion of these are presented in Figures 118 through 121 to illustrate the conditions of rotor stress. The first two figures present the equivalent (Von Mises) stress for normal speed and 20-percent overspeed. The latter two present the maximum principal stresses and their direction (flow lines). The jaggedness of the plotted lines is due to machine plotter routines (interpolations) rather than actual operating stresses. Note that the majority of the rotor core is below 55 psi at design-speed.

At 20-percent overspeed, the stress at the center bore is beyond the proportional limit of the H-11 steel, indicating the material

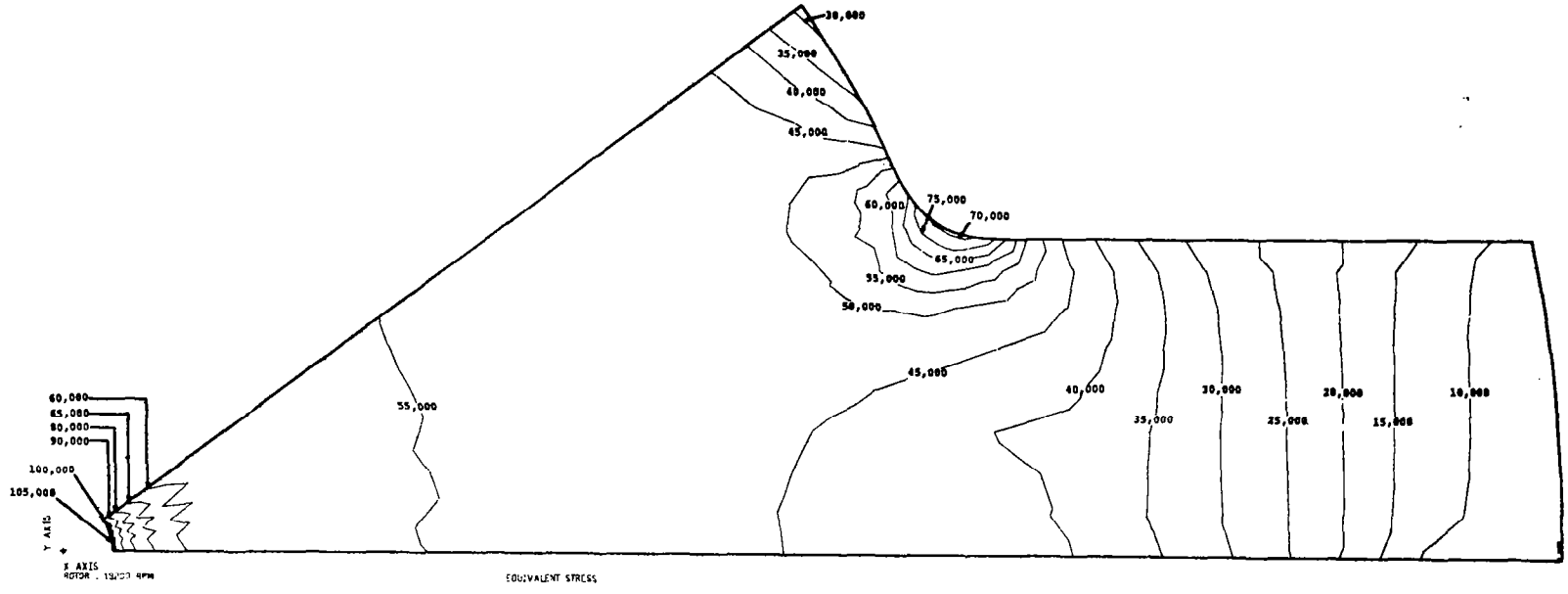

EQUIVALENT STRESS, DESIGN SPEED

FIGURE 118

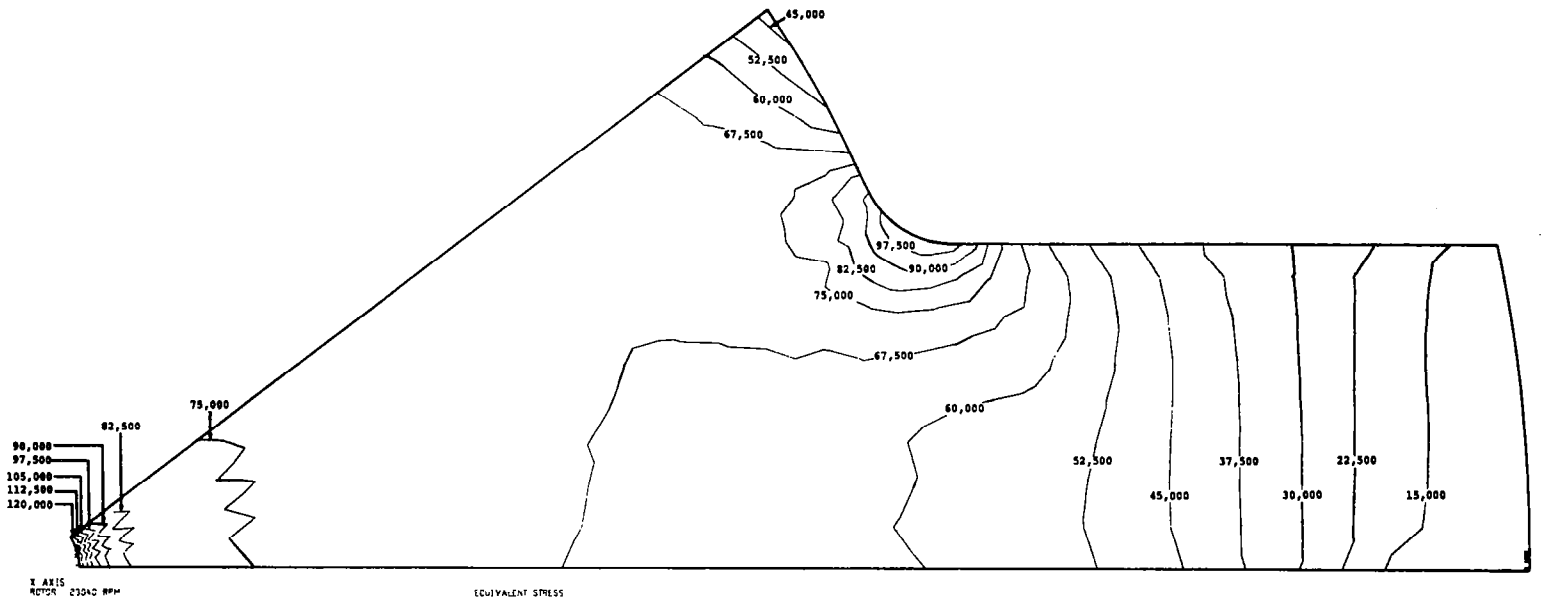

EQUIVALENT STRESS, 20 PERCENT OVERSPEED

FIGURE 119

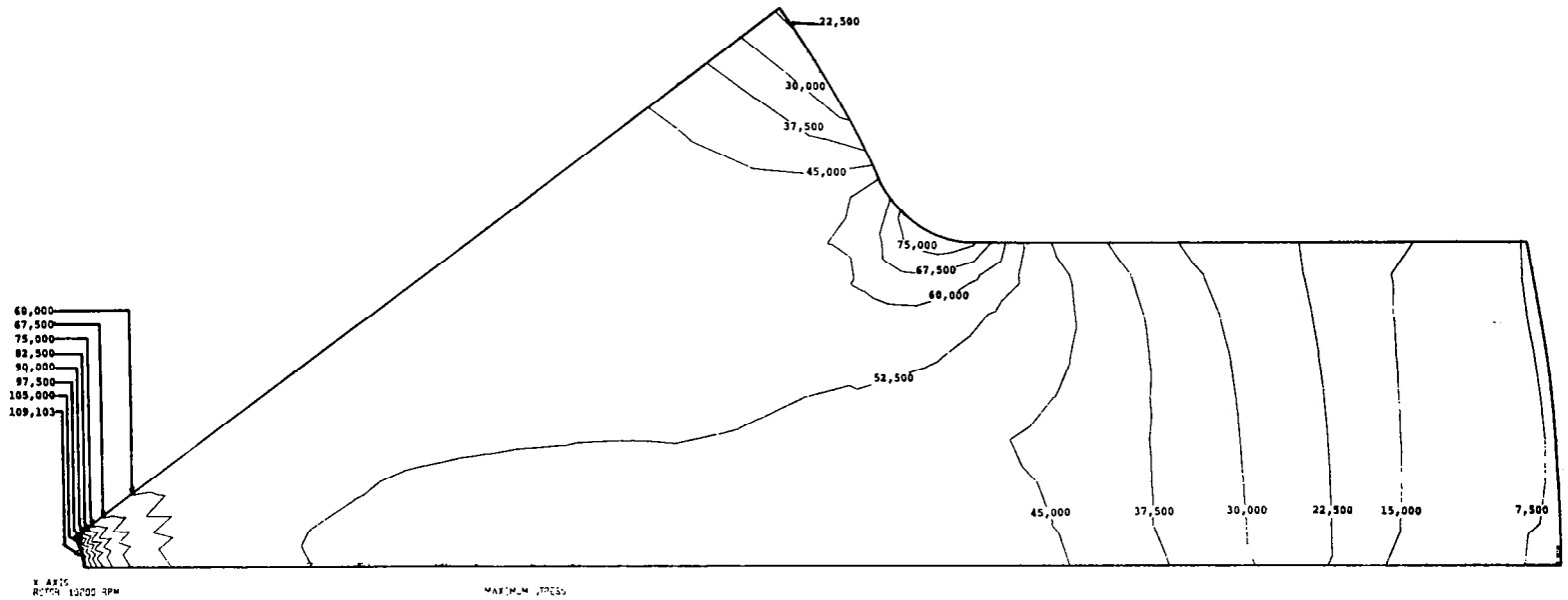

MAXIMUM PRINCIPAL STRESSES, DESIGN SPEED

FIGURE 120

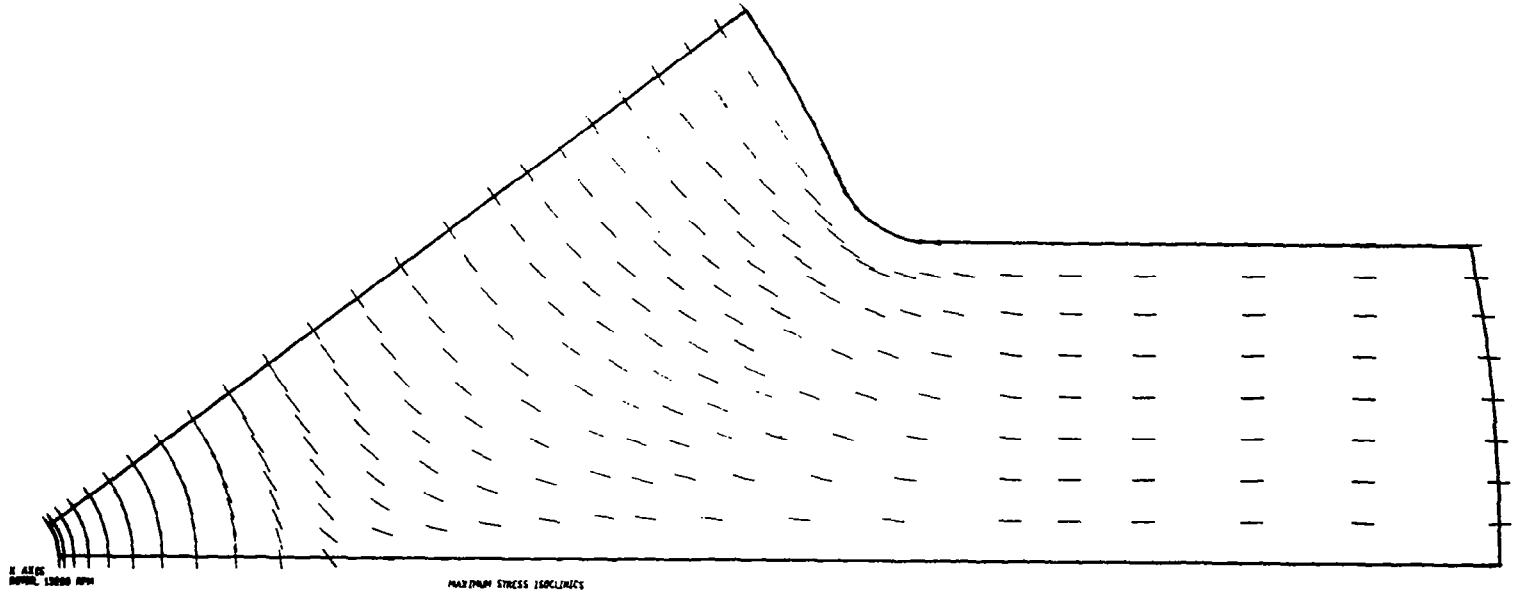

MAXIMUM PRINCIPAL STRESS ISOCLINICS, DESIGN SPEED

FIGURE 121

around the bore will undergo a permanent deformation. However, the integrated creep rate over the rotor radius at design-speed and over-speed is below 0.1 percent, which essentially eliminates creep growth as a critical design criterion. However, to be conservative, the radial gap is sized to absorb at least 0.1-percent creep strain without rubbing. Only at very small radii around the bore are the creep rates in excess of 0.1 percent (Figure 122).

The combined dynamic and thermal growth of the pole tips and 1/2-in. rotor bore are 0.1006 and 0.0046 in. for 19,200 rpm operation at full-load. The combined growths at 20-percent over-speed are 0.1084 and 0.0054 in.

Because of the low stresses and correspondingly low creep strains, it should not be mandatory to prespin the rotor to either prestrain it or to check for internal flaws or integrity. In Phase I, analytical studies indicated critical size flaws could be detected by nondestructive methods.

Although the design is based on a 1/2-in. diameter rotor bore, the final design could be made with any size bore desired. The 1/2-in. hole was sized as an approximation of the minimum that might be needed for bore heat-transfer surface area (0.419-in. diameter). Increasing the diameter to 1 in. would only slightly increase the rotor OD (a few mils) but would double the bore surface area and provide more room for the coolant-flow ducting to be placed in the center.

5.2.4 Bore Seal Assembly

A basic bore seal assembly design concept was derived near the end of Phase I which satisfied two contradictory design requirements--rigidity and flexibility. However, it was recognized and stated in Phase I that design refinements and detailed stress analyses would have

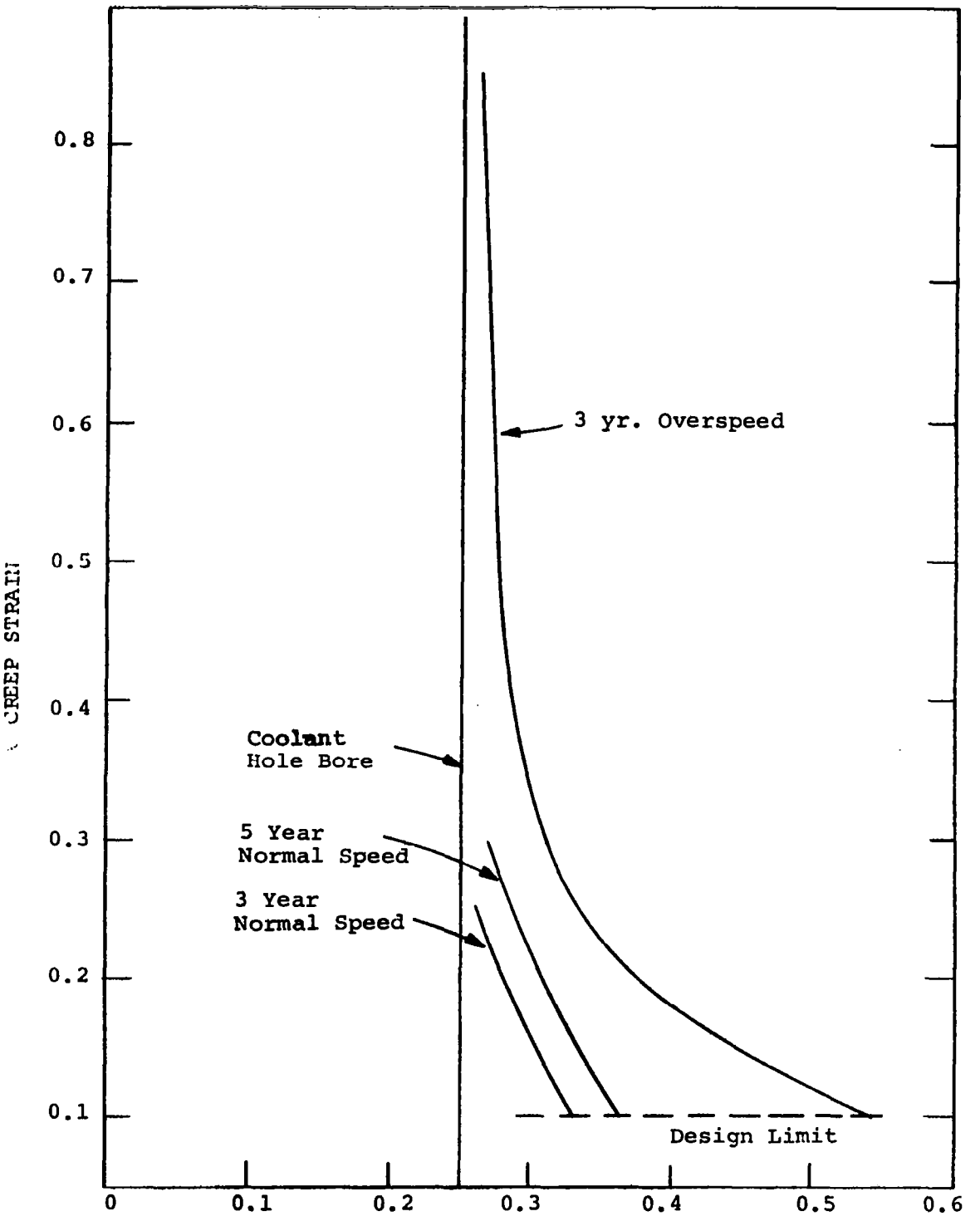

KTA ALTERNATOR ROTOR CREEP

FIGURE 122

to be performed in Phase II because of the complexities introduced by the curvic-type couplings and because of the lack of recognition of bimetallic joint technology requirements and limitations at that time.

The plan for Phase II consisted of, first, familiarizing the bore seal assembly designer with Cb-1Zr-to-steel bimetallic joint technology, and secondly, feeding this into an improved design. As a result of defining the bimetallic joint technology, a much simpler end-member assembly was configured which should give greater reliability over that proposed in Phase I. Once the basic design was derived, stress analyses were run to determine the basic stresses and stress problem areas remaining as well as to identify the solutions.

The above point of only analyzing the "basic stresses" warrants explanation before proceeding further. As part of the studies for designing the KTA alternator bore seal, a rather clear-cut definition of the task to develop the bore seal began to emerge. Also, it became very apparent that the bore seal must include all the assembly components from the radial air-gap to the stator end-bell and that the design must be compatible with all the separate component requirements. This puts a special requirement on the assembly in that its development must be closely coordinated from a central point, preferably at the alternator designer. The desirability for placing this responsibility with the alternator designer is best illustrated by one of the points in this emerging definition; namely, there is a definite need for very thorough analytical treatment (well beyond the scope of Phase II) of all possible conditions of the bore seal assembly from the time it is in fabrication to the end of its life in the alternator. This is because the defined operating conditions are the easiest to design and the undefinable, off-design conditions are the most difficult but are the most likely to cause failures.

If off-design conditions causing failures can be defined and automatic controls to prevent their catastrophic effects can be

included in the system, then the probability of survival should be enhanced. Since it is possible to identify off-design or abnormal conditions numbering in the hundreds, the scope of such an analytical study is necessarily extensive. Compound this with a complex irregular cross section requiring the latest, most powerful computer programs and you have a very comprehensive task. The basic stresses of the Phase II are just one set of stresses for a more-than-likely off-design condition--design temperature with 20-psi (external) pressure difference across the seal. In addition, the lightweight end-bell structure designed in Phase II has the effect of further compounding the task by readily transmitting the rotor vibratory effects into the stator housing near the bore seal ends. While one might balk at the initial cost of such an extensive analytical task, one must note it is easy to prove that it will pay for itself many times over if such an analysis leads to preventing just one off-design bore seal failure in the first-test alternator.

The overall development plan that emerged from the studies is depicted on Figure 123 with the present status. The next step in the development plan, prior to initiating the analysis discussed above, is to reach agreement among the various technologies concerned--alumina body, ceramic-to-metal joint, bimetallic joint, high-temperature preload spring, assembly welds--to verify that the Phase II configuration is indeed compatible with each individual component requirement. After the analysis and process development, this mutual agreement stage must be repeated because beyond that point, the test samples, test programs, and any set-backs or failures can become relatively costly. The remainder of the steps on Figure 123 are self-explanatory with an emphasis noted on the thorough test of the first full-size bore seals.

As indicated above, one of the principal steps in the Phase II bore seal design study involved familiarization with bimetallic joint technologies. The technology required for bimetallic joints on the

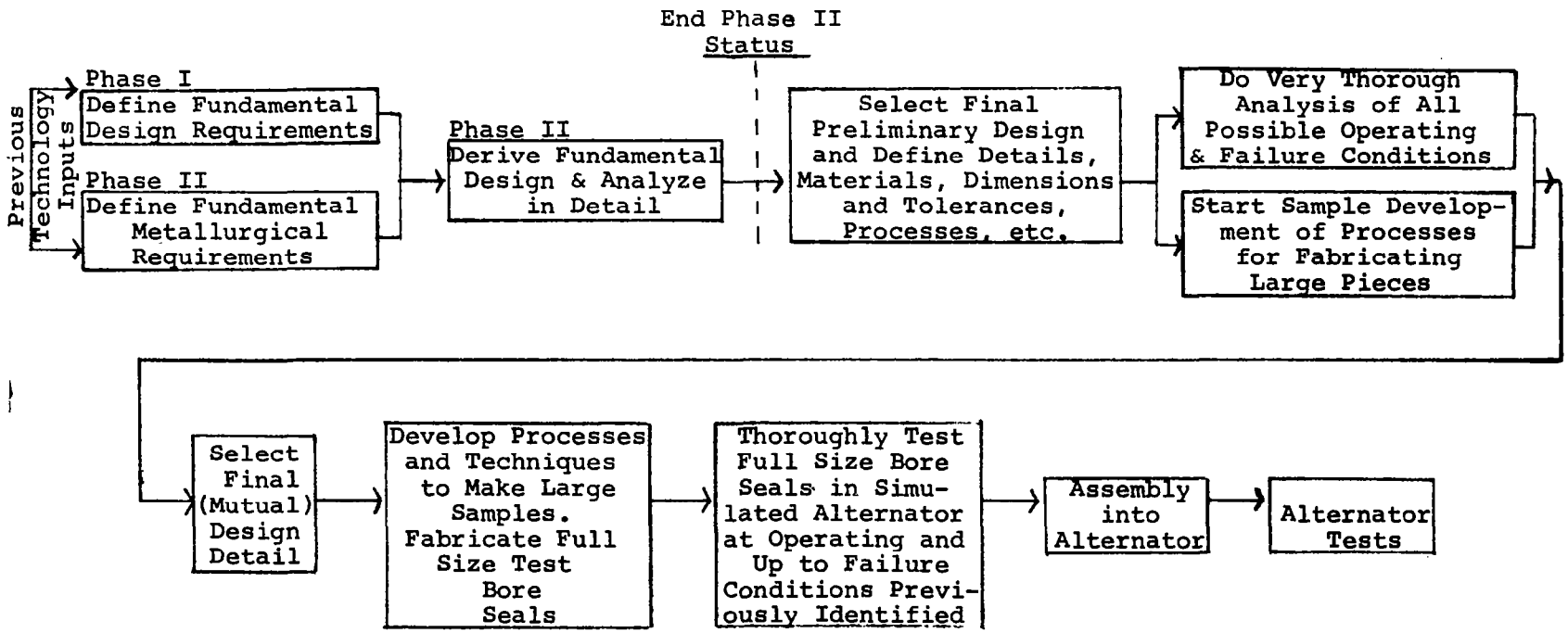

BORE SEAL DESIGN/DEVELOPMENT PROGRAM

FIGURE 123

bore seal assembly was reviewed extensively with Westinghouse Astronuclear Laboratories personnel experienced in the fabrication of bimetallic bonds for adverse environments. It was concluded that large diameter joints could be made if proper configurations and fabrication techniques were used. Both explosive and gas pressure bonding techniques could be used to make a metallurgical bond between a columbium alloy (Cb-1Zr) and a steel which has low nickel content. A joint consisting of concentric rings appears to be the best configuration from the standpoint of minimum space requirements. However, an explosive bond of two concentric rings is difficult to fabricate because the bond must be made on two sheets which are later formed into concentric rings. Gas pressure bonding appears to be a better approach since a bond between concentric rings can be made easily. In this process, the joint is formed at operating temperature (or slightly higher) so that the joint is stressed at room temperature and has a low locked-in stress intensity at operating temperature. Autoclaves capable of forming such a joint on rings 18 in. in diameter are available through Batelle Memorial Institute. This diameter is sufficient for the KTA design.

Once the joint is formed, however, it must survive the several hundred thermal cycles it will have to undergo over its lifetime. Proper design and materials choice can eliminate this problem rather easily. Tests on a quantity of samples at Westinghouse Astronuclear Laboratories show that the joint will not become brittle if the interdiffusion zone of the bimetal joint is less than 1/2-mil (0.0005 in.) thick. These same samples show this zone will not grow that thick over the life of the alternator at the less than 1000°F alternator temperatures. These conclusions are based on Inconel 600 to Cb-1Zr samples at 1250°F for 20,000 hr.

A low-nickel-content (e.g., 20 percent) steel must be used to minimize the rate of interdiffusion. If a steel with low nickel content and a coefficient of thermal expansion near the Cb-1Zr could be

found, the joint strains on each thermal cycle are minimized. Eighteen-percent nickel has an expansion coefficient so that strains will be less than 0.2 percent. The desirability of having elastic strains only on each thermal cycle is obvious to enhancing reliability.

This latter point is one of the key elements in designing the end-member assembly to survive a relatively large number of thermal cycles over its lifetime. In going from the Cb-1Zr end-members to the Hastelloy B end-bells, the end-member assembly must absorb a total of 0.25-percent relative strain. If this can be broken into smaller strains and distributed throughout the materials in the end-member assembly, elastic strains are all that will be prevalent. As indicated in Table 28, materials can be selected to accomplish this. The reader is referred to the footnotes of the table for the reasons for not recommending the desired configuration shown.

With the selection of the basic design materials and concepts, the proposed design of Figure 124 was developed. The design contains the same features of the Phase I design except the concentric piloting of the cylinder is maintained by snug-fitting concentric diametral fits and square shoulders rather than the curvic-type couplings. The various functions and operating characteristics of the assembly are summarized briefly below:

(a) Alumina Body - Pure material (99.8 percent), approximately 15-in. diameter; 0.090-in. minimum thick, maximum thickness decided by that allowed when all assembly tolerances, growths, etc., are figured into detail design drawings; sandwich construction for ceramic-to-metal joint; necked-down configuration details to be defined by ceramic body developer prior to finalizing design, necked-down section is to provide a mirror image (rather than inverted image) of end-member configuration on each end and a 1/2-in. clearance around armature coils.

TABLE 28

RELATIVE STRAINS

No.	Material	Coef. of Thermal Expansion x 10^6 at 875°F, in./in./°F	Material combination and Relative Strain at 875° F, %	
			Desired*	Recommended
1	Al_2O_3 (body)	4.6		
			Mtl 1 and 3	Mtl 1 and 2
2	Cb-1Zr	3.54	0.043	0.093
3	B-33	4.06	Mtl 3 and 4	Mtl 2 and 4
			0.124	0.180
4	18% Ni Maraging ** (steel part of bimetallic)	5.60	Mtl 4 and 5	Mtl 4 and 5
			0.088	0.088
5	Hastelloy B (end-bell)	6.60		

* The B-33 alloy is more compatible from the standpoint of relative strains but introduces new unknowns in the ceramic to metal joint and the bimetal joint. Besides that, there may be a bigger question of its availability and potassium resistance. The latter could possibly be improved with the addition of 0.5- to 1.0-percent zirconium or hafnium.

**The choice of 18-percent Ni maraging steel was made based upon low-nickel content, desirable coefficient of thermal expansion and high strength. The material choice must be approved yet by the bimetal joint developer since the 18-percent Ni maraging steel undergoes a phase transformation at about the operating temperature, thereby introducing a new unknown into the joint design. There is strength data to indicate the transformed steel still has sufficient strength.

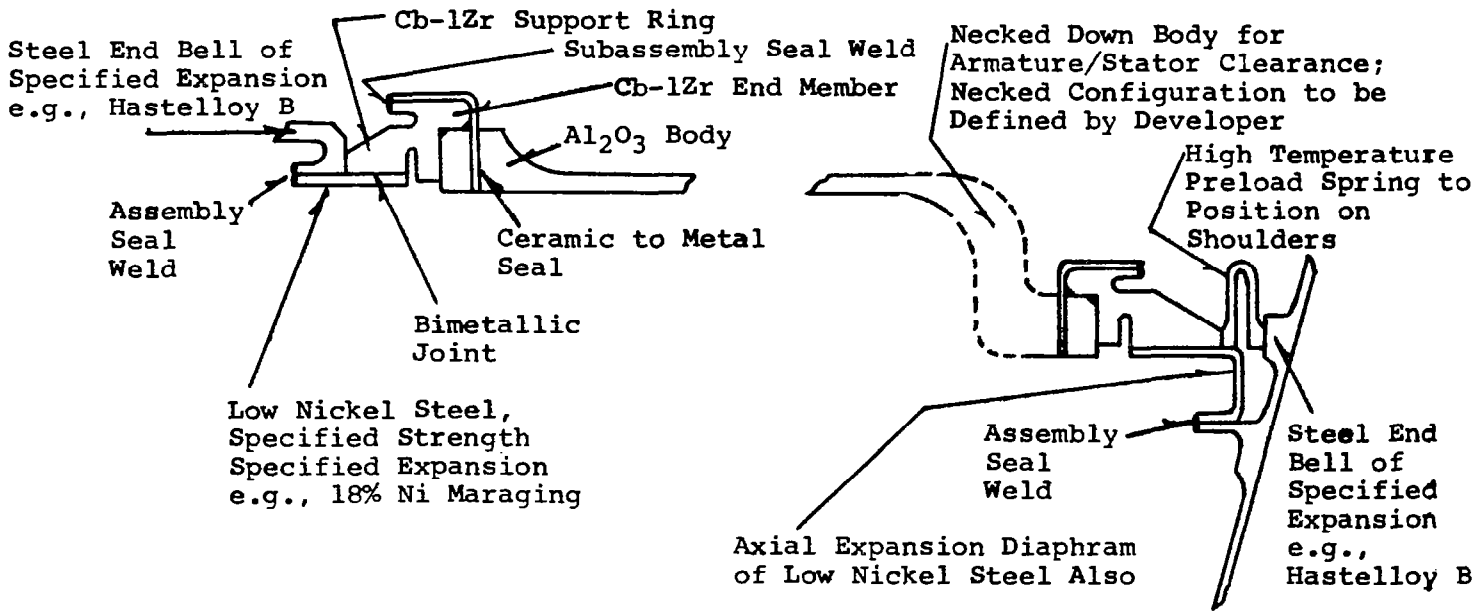

PHASE II BORE SEAL ASSEMBLY

FIGURE 124

(b) Ceramic-to-Metal Joint - Same as Phase I (and prior) except now have mirror image of each end; 0.017-in. thick Cb-1Zr, selected as result of successful previous developments, has short radial height of metal end-member after leaving joint to minimize stresses and liberal braze alloy fillet to minimize stress concentration; uses active metal braze; is a major development item.

(c) Cb-1Zr Support Ring - Provides alignment function, not as precise as curvic couplings but should be adequate (e.g., as much as 0.010 TIR) even though it is a weld joint, back-up pilot fit, not fused with weld, is included; weld has undercut to limit depth of penetration; ring shoulders squarely against alumina body and supports 0.017-in. metal end-member; seal welds to Cb-1Zr, 0.017-in. metal end-member as subassembly, Cb-1Zr subassembly anneal process development required; has relatively large undercut to isolate stresses between Cb-1Zr end-member side and bimetallic joint side; one of two basic parts for fabrication of the bimetallic joint.

(d) Bimetallic Joint - Gas diffusion bonded; starts as two plain concentric rings less than 18-in. in diameter and machined to configuration shown after bonding; steel material is on ID of Cb-1Zr ring to keep joint in compression at temperature; joint is minimum of 1/2-in. long; steel must be low nickel with specific thermal expansion values to keep joint strains in elastic region and to prevent interdiffusion zone from exceeding 0.0005 in. and becoming brittle; should survive hundreds of thermal cycles; is a major development item.

(e) Low-Nickel Steel - Should be on order of 20-percent nickel; must have reasonably high strength; e.g., 100,000-psi yield; coefficient of expansion must provide step to absorb relative thermal strain between Cb-1Zr support ring and steel end-bell; must be readily weldable alloy; weld to end-bell, has undercut

to limit depth of penetration; piece on right end must also absorb axial expansion of at least 0.0131 in. (operating expansion); final selection subject to metallurgists approval because of its influence on the bimetallic joint.

(f) High Temperature Preload Spring - Must maintain compressive force for life of machine to isolate radial and axial relative thermal expansions and to shoulder the alumina cylinder squarely between end-bells (aids concentricity); gives bonus of keeping ceramic-to-metal joint in compression.

The assembly welds are made with the bore seal compressing the high-temperature inverted "U" preload spring (Figure 124). Compression is a specific amount required to maintain axial compression when relative axial thermal expansion takes place. The compression load at 0.0131-in. relative expansion (operating condition) must be greater than 308 lb. With the assembly in compression from one Cb-1Zr supporting shoulder and bimetallic to the opposite supporting shoulder and bimetallic, the bore seal body and Cb-1Zr end-member do not "see" any of the relative axial movement between the bore seal and stator frame. Thus, these members need only be designed to absorb radial differential expansion and pressure differential forces. The only axial relative expansion each end-member sees is that which occurs within its own assembly boundaries.

The majority of the differential radial expansion is absorbed in the low-nickel steel pieces; the rest is absorbed in the various materials and interfaces. As previously discussed, design materials are selected so that the extent of the strain in each of these locations is kept as low as possible in a step-wise fashion.

Random radial motion between the stator punching bore and bore seal OD is minimized by the Cb-1Zr support shoulders on each end (piloting off the end of the alumina body) and by snug fits between

the members at the seal weld assembly joints. The loosest link in this fit-up occurs when the latter fit loosens upon heating to temperature. Locked-in weld stresses may cause some radial movement but should not cause "cocking" due to the bore seal (square) shouldering concept above. The design should absorb at least 0.010 TIR radial movement (if not twice as much) without jeopardizing the radial running clearances. Conical-shaped support shoulders might be possible to minimize the amount of radial motion to less than the 0.010 TIR.

The design should not be temperature-sensitive except when extreme gradients occur to shift differential expansion in opposite directions relative to those which occur at operating or uniform temperatures. This could upset the shouldering concept or over-stress joints due to the fact that relative movements are not always free to occur unlimited in the opposite direction; e.g., if the low-nickel piece were considerably hotter than the end-bell on the drive end (an unlikely situation).

The stress analysis of the bore seal end-members was made with the use of two computer programs. The stationary end-member of the bore seal used a recently developed digital computer program called "A Finite Element Computer Program for Axisymmetric Elasticity Problems". It is based on the displacement formulation of finite element theory and can determine the displacements and stresses in arbitrary solids of revolution subject to axisymmetrical tractions, body forces, temperature variations and prescribed displacements. The materials of the solids are assumed to obey Hooke's Law, although the program is capable of solving the elastic-plastic or fully plastic case if stress-strain curves at operating temperature were readily available for all the materials (which they were not). A theoretical model of the end member was calculated with the respective loadings and geometries. This was then broken into a grid-type mesh for computer program input. The computer program output consists of machine-plotted contour stress

maps of the end-member along with the standard digital stress results. The equivalent or Von Mises stress contour map with its respective isostress lines is shown in Figure 125.

A summary of the stresses on the map are given in Table 29. The maximum values are usually associated with stress concentrations that, with later design refinements, can be minimized. For example, the 27,645-psi stress associated with the bimetallic joint occurs because the analytical model placed the corner and the joint line coincident, a situation that should be avoided in actual hardware.

The stress analysis for the bore seal positioning end-member (right end) was calculated with the use of an in-house digital computer program that, while similar to the above program, is easier to use but less versatile. A model similar to the stationary end-member was developed with its respective loadings and geometries. The principal loading of this end-member was the tensile force associated with the differences in thermal expansion between the stator and bore seal. The relative axial expansion of the stator, compared with the bore seal, was 0.0131 in. at operating temperatures. A uniform soak-temperature of 550°F gave the same relative axial expansion. A pressure differential of 20 psi on the external (stator) side of the end-member was also assumed for input to account for any differentials between the rotor and stator cavities. Initial input of a 60-mil wall thickness on the end-member proved too stiff, and the stresses calculated exceeded the material properties. A thinner and hence more flexible wall was then input. With a wall thickness of 30 mils, the maximum bending stresses calculated were approximately 71,000 psi, which is within the property limits.

The 550°F soak-temperature limit introduces a new problem. Since it is reasonable to assume the minimum allowable thermal soak-temperature might be 700°F, the design must be refined to handle it. For the 0.030-in. thick member above, the relative expansion at 700°F

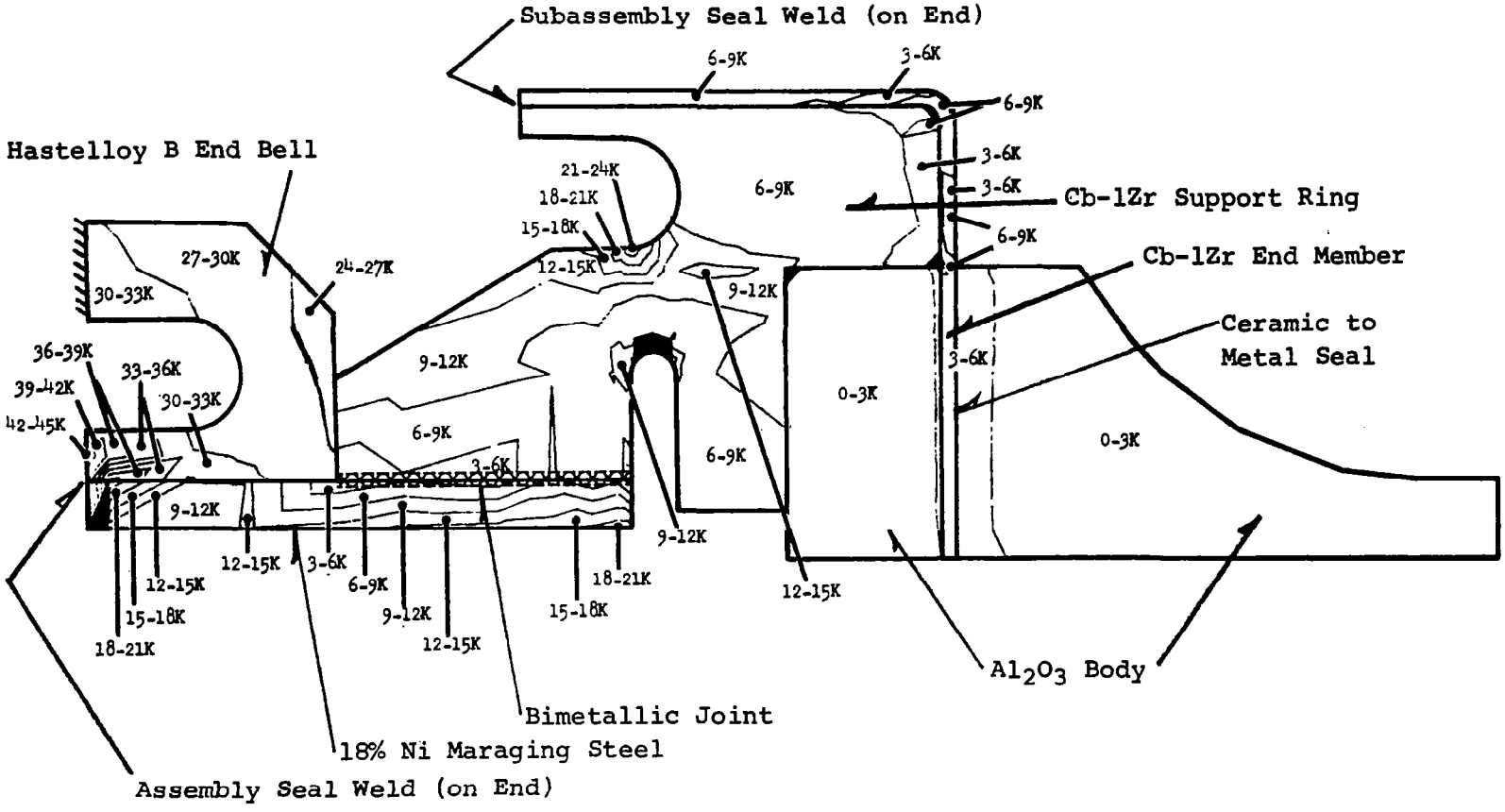

BORE SEAL END MEMBER ASSEMBLY, EQUIVALENT STRESSES

FIGURE 125

TABLE 29

PHASE II BORE SEAL DESIGN DATA EQUIVALENT STRESSES

Component Location	psi		Maximum Stress Location
	Minimum	Maximum	
Ceramic Bore Seal:	582	6946	Top, Cb-1Zr End-Member Interface
Cb-1Zr End-Member:	3032	7209	End-Member Shoulder Piece Weld Joint
Cb-1Zr Shoulder Piece:	3433	30647	Centerline Undercut
Bimetallic Joint:	4095	27645	Hastelloy B, 18% Nickel/Cb-1Zr Shoulder Interface
18% Nickel Piece:	4095	19595	Bottom Edge, Undercut Face
Weld Joint:	10033	44311	Centerline Hastelloy B Piece
Hastelloy B:	3433	30879	Frame Interface

uniform is 0.0167 in. requiring a 2830-lb thrust force from the preload spring. This results in a maximum 90,000-psi bending stress in the end-member.

5.2.5 Seal Design and Performance Analysis

Design, design analyses, and performance computations were performed for the following types of alternator seals:

(a) Viscoseals (noncontacting, hydrodynamic, screw-type liquid shaft seals)
(b) Holweck pump vapor seals (noncontacting, screw-type vapor shaft seals/pumps in the rotor scavenging system)
(c) Static contact seals (basically conventional face contact seals modified for the KTA alternator application, to be used for sealing at start-up until the noncontacting seals become effective). The NASA-type radial, spiral-groove, hydrodynamic, lift-off seal was also considered for the static seal application. Although it is potentially attractive for the application, Westinghouse recommended and AiResearch and NASA jointly concurred that this type of seal not be incorporated in the KTA alternator preliminary design because of the need for a significant amount of additional development and testing.

The design analyses consisted of (a) preliminary heat transfer and temperature distribution analyses and (b) preliminary displacement and stress analyses of the critical heat flow paths and critically stressed seal areas, respectively. The rotating, cupped-shaped, stage of the Holweck pump vapor seal was considered the critical seal design area, and the seal design analyses were performed on this member.

Detailed discussions of the design and analyses of the three seal types are presented in the following paragraphs.

5.2.5.1 Viscoseals

The viscoseals for the Phase II alternator preliminary design were designed and their performance was determined from the results of the design and performance study conducted in Phase I. Therefore, viscoseal design and performance will not be discussed in detail except with regard to effects on static seal design requirements. For a comprehensive presentation of viscoseal design and performance see Appendix B of Volume II. For quick reference, the basic viscoseal design requirements and conditions are summarized below:

(a) The required lengths for the seals were based on the condition that complete sealing of the liquids would be accomplished at 50 percent of the alternator design speed with maximum pressure differential across the seal. Maximum pressure differential was 25 psi.

(b) The wetted-length of the seal at the 50-percent speed-point was made equal to 60 percent of the overall length of the seal. The remaining 40 percent of the seal length is required for dams at the ends of the seal and for scavenging of any liquid which may break away from the interface.

(c) Radial clearance was made 0.3 percent of seal diameter.

(d) Double helical groove geometry was assumed, i.e., helical grooves on the rotating and stationary components.

(e) Sealing capacity per unit length = $7.8 \times 10^{-4} \rho v^2$ N/C where

ρ = density of the fluid

v = peripheral velocity of the rotating part (shaft)

N = 2 for double helical thread geometry

C = radial clearance

5.2.5.2 Holweck Pump Vapor Seal Design Study

5.2.5.2.1 Introduction

The purposes, theory, and function of the Holweck pump in the alternator were previously explained in Volume II and will not be repeated here. See Appendix C to Volume II for a review of the discussion on the basics of the Holweck pump.

The only major difference between the present design concepts and those in Phase I are in the staging of the (cantilevered) pump impellers. It was pointed out in Phase I that multiple staging can be built into the design by using the underside and outside of the Holweck pump impellers with one exception, and that was that the underside of the first stage was not available. With the present design, the underside of this first stage impeller is no longer needed for the scavenge system and is available to act as an impeller surface for a Holweck pump. This is important to the Phase II study because a single impeller having two stages is adequate for the design. In Phase I, where 800°F potassium was being used, it appeared that at least three to four stages would be needed with two impellers.

The preliminary conclusion that a single impeller with two stages would be adequate was based on a review of the parametric performance data of the Phase I study. There, for a two-stage single-impeller configuration of the approximate size used in Phase I, one can see that this single impeller should suffice for 700°F potassium vapor at 19,200 rpm in the envelope of dimensions required for the bearing and seal housings. As discussed below, a single-stage impeller design was evolved which meets the desired goals of performance for the alternator Holweck pumps.

5.2.5.2.2 Summary of Analysis

The schematic configuration for the design is shown in Table 30 and Figure 126. The fixed dimensions and dimensionless parameters determined as a result of the Phase I parametric study are also listed. The values of radial clearance shown are nominal values at the 19,200-rpm design-speed. As shown on Figure 126, the radial clearance varies with speed and the design takes advantage of these changing clearances, as discussed later.

With the fixed-ratio of root width-to-depth (SA/SB) determined in Phase I, the tools required to cut thread-root widths of two different values would necessarily be different. These would correspond to the axial-root widths shown of 0.220 and 0.192. For the sake of commonality, the root width was made the same for both pumps and was taken as 0.210 in. (axial dimension). The resulting width-to-depth ratio (and pitch angles) shown in Table 30 are not exactly the optimum values but are close enough to give negligible differences in the final performance.

Because the Holweck pump impeller shell grows with speed and the underside of the impeller is to be used, it is advantageous to find optimum clearances on both the underside and outside surfaces. For purposes of the Holweck pump performance calculations, it was assumed that the impeller would deform like a spinning, free cylinder. Based on the analysis of a spinning, free cylinder, the underside of the impeller will grow radially 0.0037 and 0.0058 in. for design speed and 20-percent overspeed, respectively. Likewise, the outer surface grows 0.0032 and 0.0050 in. in the radial direction for design-speed and 20-percent overspeed, respectively. These radial displacements are only the portion of the total radial displacements of the impeller due to rotation; they do not include the portion due to thermal expansion. Relative thermal expansion between the rotating impeller and the stationary pump components was ignored in the analysis because the

TABLE 30

HOLWECK PUMP DATA

	Impeller Surface 1	Impeller Surface 2
Fixed Parameters		
Radius R =	3.16 in.	3.29 in.
Length L =	1.62 in.	1.68 in.
Phase I Dimensionless Parameters		
No. Threads G =	2	2
SB/S =	12.5	12.5
SA/SB =	1.5	1.5
XLPR/SA =	1.0	1.0
Calculated Parameters		
Radial Clearance S =	0.0117* in.	0.0102* in.
Thread Root Depth SB =	0.1465 in.	0.1275 in.
Axial Thread-Root Width SA = (based on optimum SA/SB)	0.220 in.	0.192 in.
Axial Thread-Root Width SA = (common width used)	0.210 in.	0.210 in.
Pitch Angle =	2.4224°	2.3267°
Miscellaneous Parameters		
Fluid = 700°F saturated potassium vapor off viscoseal interface; P_{sat} = 0.0452 psi, M = 0.0285 lb/ft-hr		
Speed = 19,200 rpm (23,040 rpm at 20% overspeed)		
Desired Rotor Cavity Pressure at Speed = 0.004 psia		

*Nominal value at design speed only, see discussion and Figure 126.

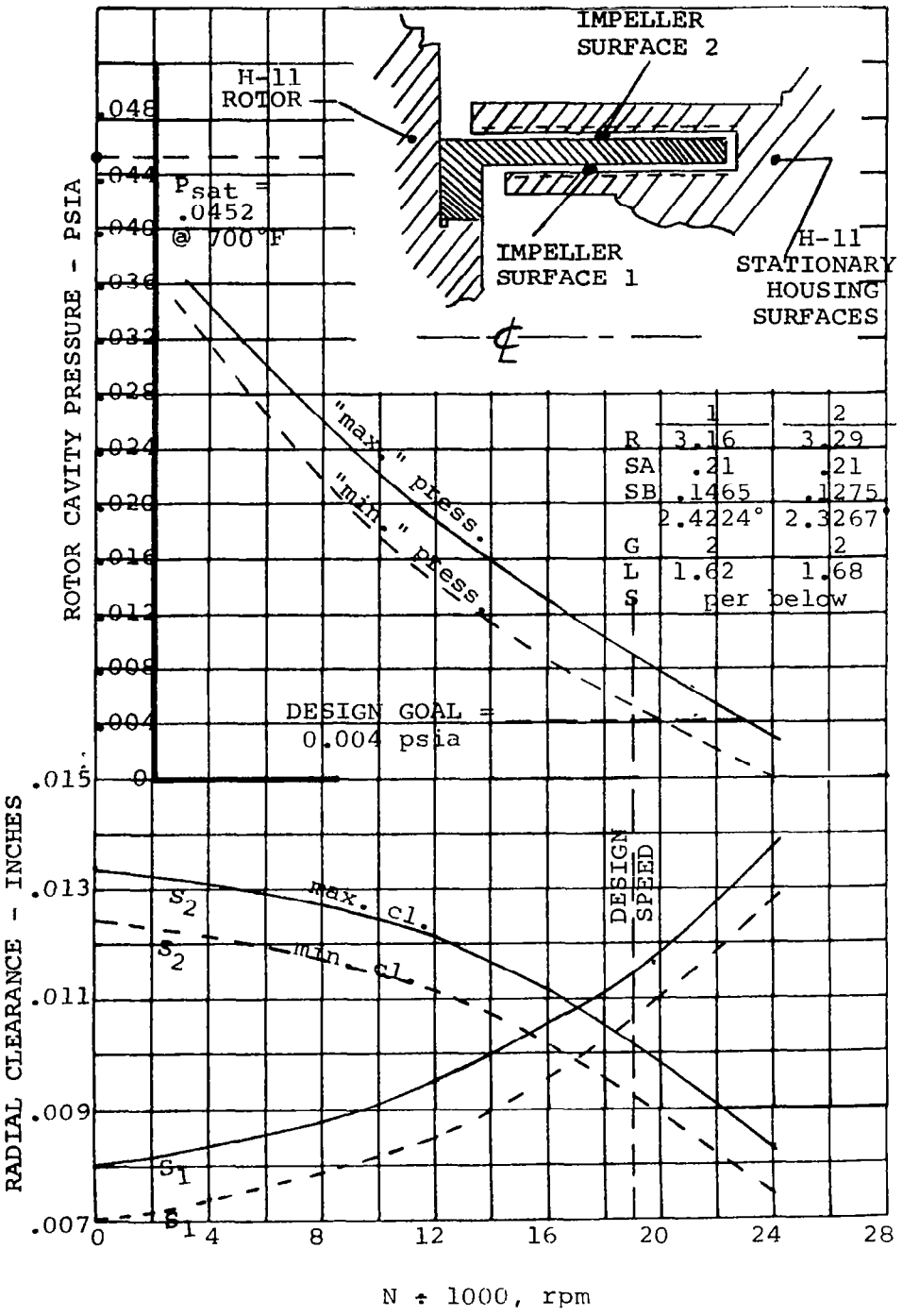

HOLWECK PUMP PERFORMANCE

FIGURE 126

rotating and stationary parts are made of the same material (H-11) (with the same coefficients of thermal expansion). Temperatures of the rotating and stationary parts will be very nearly the same; therefore, relative thermal expansion will be very small, particularly in the radial direction. This means that relative displacement because of rotation will be the most critical to clearances between the impeller and the stationary pump parts.

After the Holweck pump performance analysis was completed, a detailed stress and displacement analysis of the actual Holweck pump impeller geometry was performed to determine the effect of the impeller-mounting flange. The radial displacements obtained from the analysis for a spinning, free-cylinder agreed very closely with the displacements obtained in the computer solution (differences were less than 0.0005 in.). The computer analysis also showed that there was less than 0.001-in. difference in radial displacement over the axial length of the impeller. Based on comparison of the results between the two analyses, it was concluded the analysis based on a spinning, free-cylinder was sufficient for the Holweck pump performance calculations discussed in the next paragraphs. The computer analysis will be discussed further in subsequent paragraphs.

Added to the above radial displacements from rotation are the clearance values that must be allowed for rotor excursion about the journal center, the radial tolerance build-up between and within the rotor and stator assemblies, and the angular misalignment of the rotor associated with radial run-out of the opposite journal bearings. These are summarized below.

(a) Maximum excursion of shaft at bearing = 0.005 in. per AiResearch specification.
(b) Radial tolerance build-up between rotor bearing surface and Holweck pump surfaces = 0.0004 TIR (0.0002 in. radial).

(c) Radial tolerance build-up between stationary bearing surface and stationary Holweck pump surface:

Surface No. 1 (Figure 126)

Bearing ID to bearing OD tolerance = 0.0004 TIR =	0.0002
Slip fit of bearing in bearing housing = 0.0003 x 2 =	0.0006
Bearing housing ID to Holweck surface No. 1 OD = 0.0004 TIR =	0.0002
Total =	0.0010 in.

Surface No. 2 (Figure 126)

Bearing ID to bearing OD tolerance = 0.0004 TIR =	0.0002
Slip fit of bearing in bearing housing = 0.0003 x 2 =	0.0006
Bearing housing ID to Holweck ID pilot for surface No. 2 = 0.0004 TIR =	0.0002
Holweck ID pilot surface to surface No. 2 = 0.0004 TIR =	0.0002
Distortion due to welding after grinding = 0.0004 TIR =	0.0002
Total =	0.0014 in.

(d) Alignment between two journal bearings: use 0.0008-in. radial clearance at each seal. Allows the two bearing centers to have 0.0064 TIR run out between them (including the 0.0048 run-out already associated with Item c above).

The clearance must be sized to obviate a rub at the worst-case. For the underside of the impeller, this is at 0 rpm; for the outside of the impeller, this is at 23040 rpm. Thus, the boundary conditions of radial clearance must be:

$$s_1 = 0.005 + 0.0002 + 0.0010 + 0.0008 = 0.007 \text{ in.}$$

and,

$$s_2 = 0.005 + 0.0002 + 0.0014 + 0.0008 + 0.0050 = 0.0124 \text{ in.}$$

Now, if 0.001 in. is arbitrarily added to each of these values to allow for a worst-case clearance of 0.001 in. at operating speed, we can arrive at a set of working nominal radial clearances for the two stages. They are: s_1 = 0.007/0.008 in. and s_2 = 0.0124/0.0134 in., both at 0 rpm. Ratioing these clearances to 20-percent overspeed will give the clearance as a function of speed for the two stages. This is shown in Figure 126. The nominal clearances at design-speed are indicated, and these are the values that were used to arrive at the thread geometry shown in Table 30. The nominal clearance on the underside of the impeller increases from 0.007/0.008 to 0.0138/0.0128 at 20-percent overspeed. The nominal clearance of the outside surface of the impeller decreases from 0.0134/0.0124 to 0.0083/0.0073 at 20-percent overspeed.

The results of the finite element computer stress analysis of the Holweck pump impeller are displayed graphically in Figures 127, 128, and 129.

Figure 127 is a machine plot of lines of constant-equivalent (Von Mises) stress in the impeller. The maximum equivalent stress which occurs in the cantilevered portion of the impeller or in the bend between the cantilevered shell and the mounting flange (which are critical to the performance of the Holweck pump) is 32,481 psi, which is much less than the yield strength of H-11 at temperature and less than the stress to give 0.1-percent creep in 3 years.

Figure 128 is a machine plot of the radial displacement contour (shown in dashed lines) of the cantilevered portion of the impeller. The displacements are plotted to a scale approximately 2.6 times the

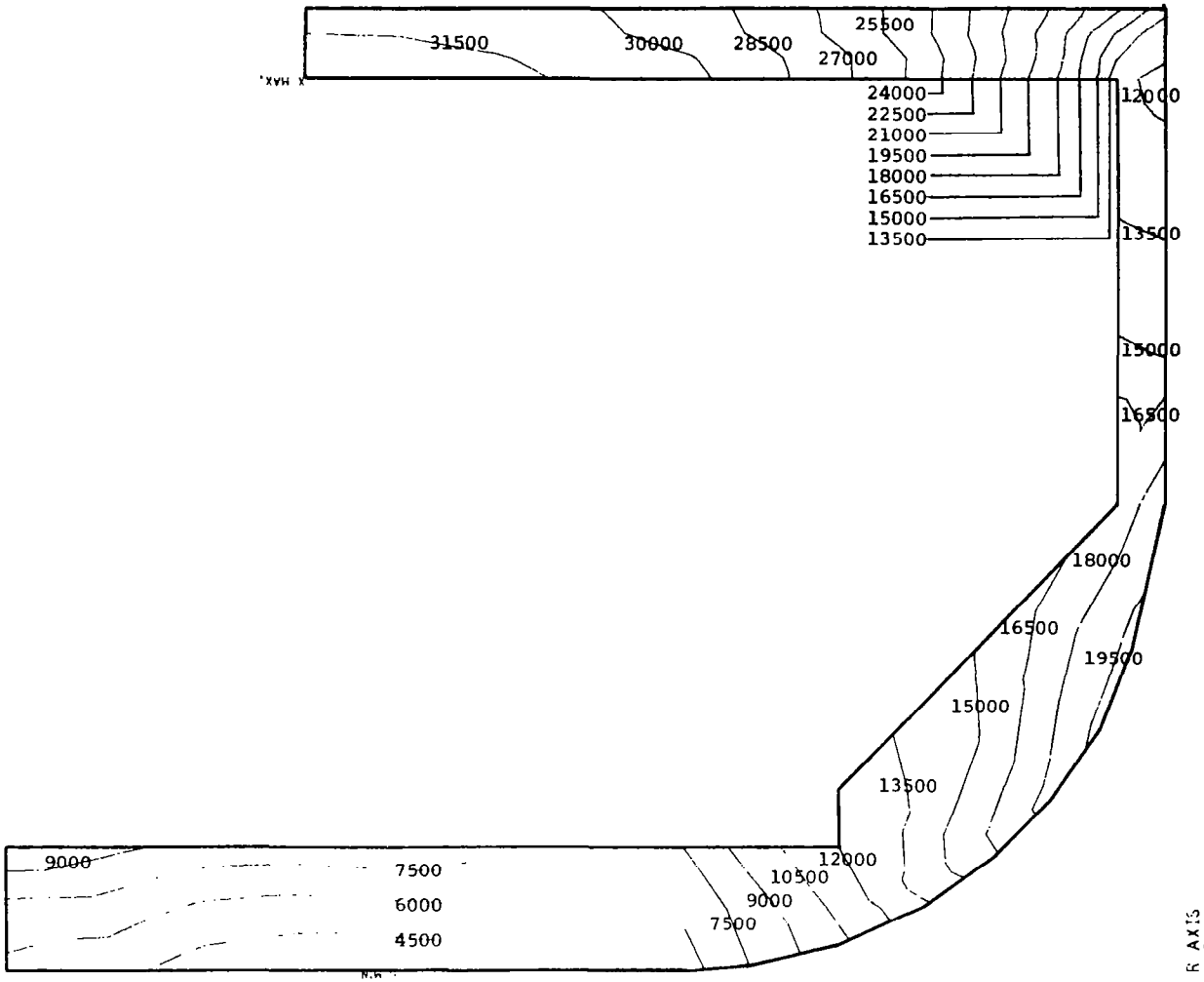

HOLWECK PUMP IMPELLER EQUIVALENT STRESS DISTRIBUTION

FIGURE 127

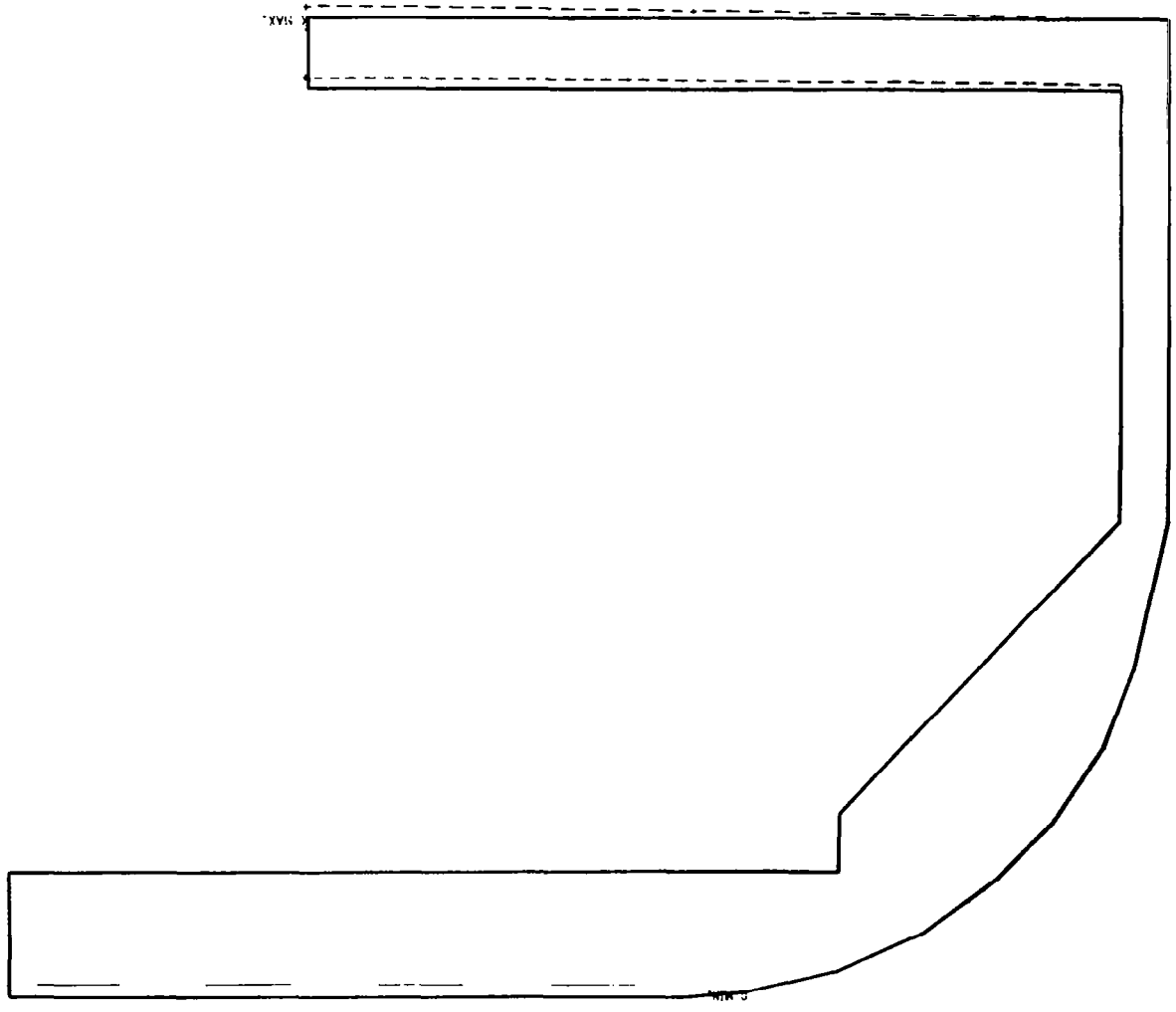

DISPLACEMENT CONTOUR OF HOLWECK PUMP IMPELLER
AT DESIGN SPEED AND TEMPERATURE

FIGURE 128

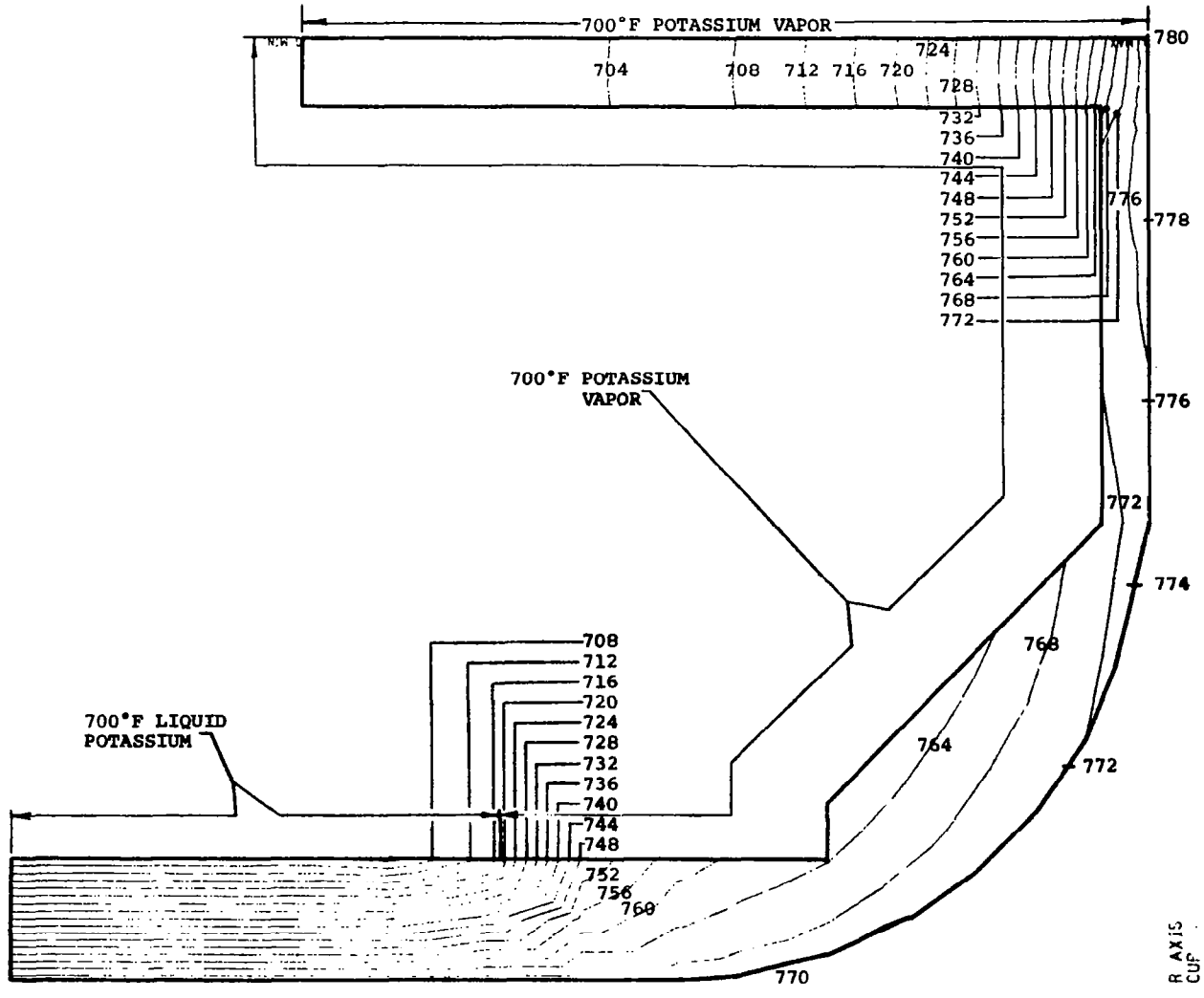

HOLWECK PUMP IMPELLER TEMPERATURE DISTRIBUTION

FIGURE 129

true scale for purposes of better illustration. The maximum radial displacement of the impeller at the outside diameter at the free end of the cantilevered section (as shown in the figure) was computed at 0.0197 in., which includes displacement from rotation and thermal expansion. The displacement of the adjacent stationary portion was not computed because the magnitude of the required analysis was outside the scope of the study. This analysis must be left to later studies.

Figure 129 is a machine plot of the temperature distribution of the impeller in terms of isothermal lines. It was assumed that no heat was generated in the impeller, and the assumed thermal boundary conditions were as illustrated in the figure.

This analysis must be considered preliminary because the effects of adjacent parts and other boundary conditions could not be adequately treated. The objective was to perform a preliminary evaluation of the impeller design which is a critical seal component. Based on these preliminary results, it may be concluded that the impeller design has adequate strength, and critical displacements are acceptable.

The pump performance was calculated using the computer program as described in Volume II of this report. The resulting pump performance is shown on Figure 126. As shown on the figure, 0.0088-psia rotor cavity pressure is all that is reached for the maximum clearance values. For the minimum clearance values (where a rub is imminent--worst eccentricity case) the pressure is 0.0045 psia. While both these pressures are sufficiently low for minimizing windage, it is important to note the desirability of building an additional allowance for 0.001-in. radial clearance into the final hardware design. This will give ample clearance to obviate rubs while giving 0.0045 psia as the largest rotor cavity pressure instead of 0.0088.

The effect of the closing and opening clearances for the two stages is important to the design for the following reasons. At the low speeds, Stage 1 is providing most of the pumping; at greater speeds, Stage 2 provides most of the head. The crossover speed, where both are equally effective, is about 19,500 to 19,000 rpm. This is not surprising in that the pumps were optimized for 19,200-rpm conditions. For maximum effectiveness, however, it is desirable that Stage 1 reach its peak pumping head just at the crossover point. Synthesis of the data shows that Stage 1 reaches its peak pumping head at 16,800 to 17,200 rpm which is close to the crossover speed. Naturally, Stage 2 never reaches a peak value as the clearance decreases continually as the speed increases. The conclusion drawn from this is that the pump staging is well balanced but could be improved with design refinements in the final design. This could be done by decreasing the minimum clearances at 0 rpm. The source of the reduced values of "s" would have to come from the allowable tolerance build-ups or the bearing excursion run out, preferrably the latter since it is the largest of the two (0.005 in.).

5.2.5.2.3 Conclusions

The design shown is adequate for the purposes it is intended to serve--lowering rotor cavity pressure and minimizing windage losses. However, as pointed out by the design summary, if as little as 0.001 in. more were allowable for closing down on radial clearances, the performance and margin of safety could be enhanced significantly. During detailed design every effort must be made to reduce this clearance to the minimum consistent with expected shaft excursions.

5.2.5.3 Static/Start-Up Face Contact Seals

The flow of lubricant from the bearing compartments is prevented by using a pressure-generating viscoseal on each side of the bearing

compartments. The necessary back-pressure is generated by relative motion of helical threads on the shaft and in the housing, and sealing the liquid is produced at a liquid-vapor interface within the seal. This type of seal is inherently stable since a change of pressure on the high- or low-pressure side of the seal immediately results in a change of the liquid engagement within the helical threads which, in turn, produces a stable pressure gradient. Other advantages offered by the viscoseals are:

(a) They perform a radial bearing function as well as a sealing function and allow axial displacement between the rotor and stator.
(b) They provide minimal power losses when compared with slinger types of pressure-generating seals.
(c) Sealing of the bearing lubricant can be performed adjacent to and on the same diameter as the bearing journal which minimizes the friction and viscous losses at other positions along the shaft.

The inherent problem of the viscoseals is that they do not seal when the shaft is not rotating or when the shaft speed is low. To overcome this problem, it is necessary to incorporate contact seals with lift-off provisions. A combined version of a contact seal and a viscoseal applied between the bearing and rotor cavity is shown in Figure 130.

The contact seals consist of a pressure divider "A" between two diaphragms "B" and "C" which move the nosepiece. Leakage between the high- and low-pressure chambers is minimized by using a piston ring seal "D" between the pressure divider and the viscoseal. The contact seal is designed so the nosepiece "E" is normally in the ON position; that is, the nosepiece is normally in contact with the seal seat. This is accomplished by incorporating a 0.030-in. deflection within each of

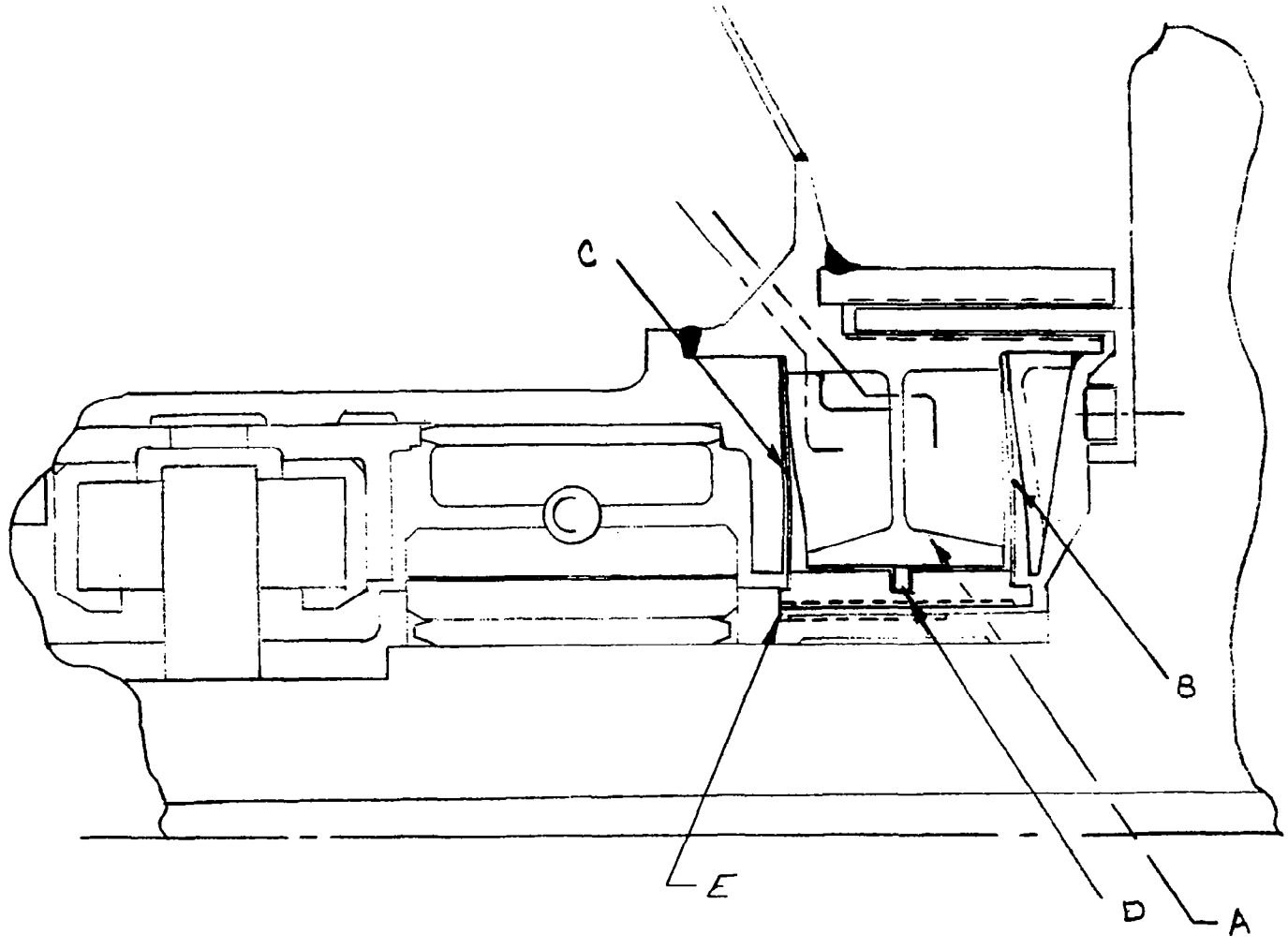

COMBINED CONTACT AND VISCOSEAL ARRANGEMENT

FIGURE 130

the diaphragms at the operating temperature for start-up (approximately 700°F) and with equal pressures in the bearings, seal chambers, and rotor cavity. Figure 131a illustrates the state of the seal for this mode of operation. This state represents the conditions which would exist before liquid potassium is introduced into the bearings and the pressures would be a hard vacuum. The second mode of operation of interest is illustrated in Figure 131b. This state represents the system with the bearings pressurized and with a vacuum in the rotor cavity, or the condition of the system prior to the initial acceleration of the rotor. During start-up, pressures P_1, P_3, and P_4 will remain fairly constant, and P_2 will decrease as the speed increases. This causes the force between the seal rubbing faces to decrease too. The state of the system at lift-off of the seal surfaces is illustrated in Figure 131c. In this mode of operation, the viscoseal is capable of sealing the liquid potassium by virtue of a liquid-vapor interface within the helical threads that occurs after lift-off of the contact seal. For this case the viscoseal is capable of sealing the liquid at 6530 rpm (34 percent of the design-speed with 15 psia bearing pressure). The point of lift-off of the seal surface for the assumed bearing pressure (15 psia) is controlled by the pressure, P_2, within the low-pressure compartment of the static seal. Lift-off occurs when P_2 equals the vapor pressure of the potassium.

An essential feature of the combined sealing system is that the pressure in the low-pressure chamber cannot reach the lift-off point before the viscoseal is capable of sealing the liquid within the bearing. This is accomplished by venting the low-pressure chamber into a viscoseal on the antidrive end of the shaft as shown in Figure 132. The vent port within the auxiliary viscoseal is located at a point where the liquid-vapor interface exists for zero leakage. The auxiliary seal is identical to the bearing seal and is subjected to the same liquid and pressure as the bearing seal. Thus, when zero leakage occurs in the auxiliary seal as indicated by vapor pressure of the liquid at

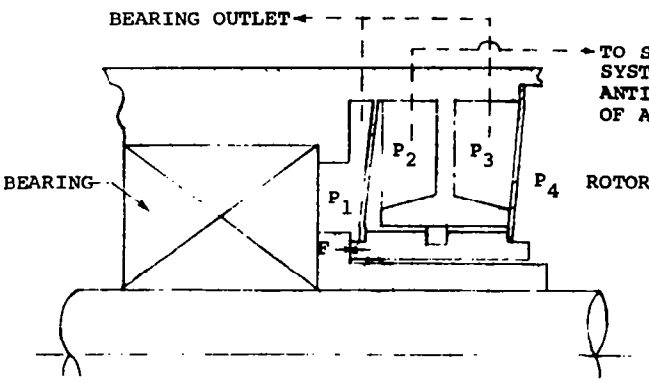

$P_1 = P_2 = P_3 = P_4 = 0$
F = 170 LBS
N = 0

a. SEAL STATE BEFORE POTASSIUM IS INTRODUCED

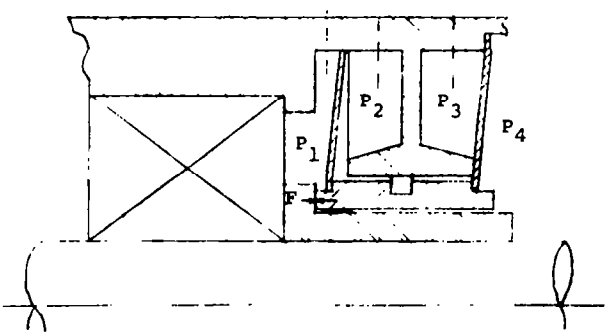

$P_1 = P_2 = P_3 = 15$ PSIA
$P_4 = 0$
F = 85.4 LBS
N = 0

b. SEAL STATE PRIOR TO INITIAL ACCELERATION

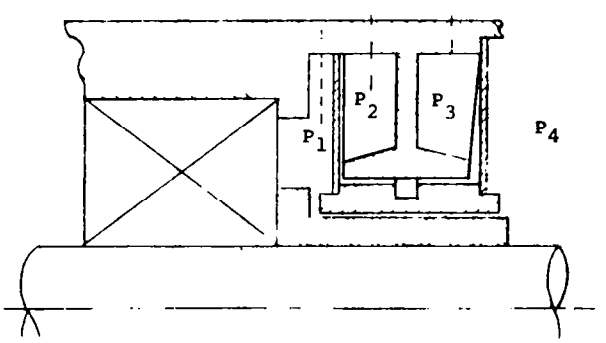

$P_1 = P_3 = 15$ PSIA
$P_2 = P_4$ = VAPOR PRESS OF K
F = 0
N = 6530 RPM

c. SEAL STATE AT LIFT-OFF

OPERATION OF CONTACT SEAL

FIGURE 131

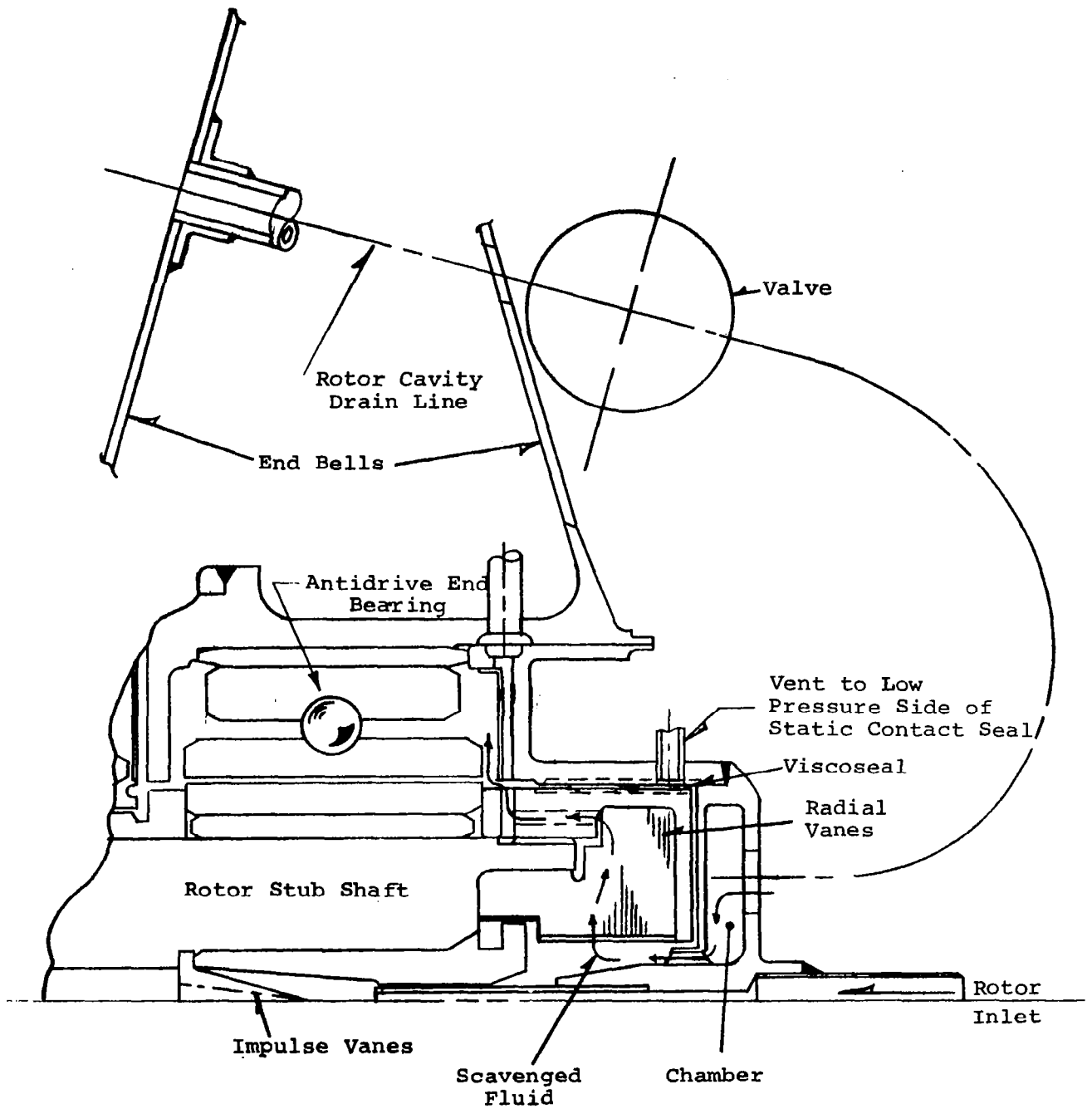

ROTOR CAVITY SCAVENGE SYSTEM DETAILS

FIGURE 132

the vent port, the same condition will be true for the bearing seal, and lift-off of the contact seal is permissible.

Venting the low pressure chamber of the static seal into the auxiliary viscoseal produces a system of seals which is semiautomatic. In order to make the system automatic, a way to control the bearing pressure after lift-off of the face seal has occurred is required. This conclusion is based upon the premise that a bearing pressure of 15 psia would not be adequate for continuous operation near the design-speed (19,200 rpm). Thus, an increase of bearing pressure would be required after the rotor accelerated near the design-speed. An adjustment of the bearing pressure after a steady speed near the design-point is obtained is not a difficult task. The problem arises when it is necessary to shut down in an emergency situation and manual control of the bearing pressure is not warranted. In this situation, the speed could decrease with an excessive pressure in the bearing. This would cause the face seal to remain in the off position over a speed range for which the viscoseal is not capable of sealing the liquid potassium in the bearing.

5.2.6 Scavenge System

The alternator is equipped with a scavenge system which is used to scavenge liquid potassium from various compartments within the assembly. These compartments are (1) the enclosure around the drive shaft coupling, (2) the rotor cavity, and (3) the low pressure chamber within the static bearing seals.

Liquid potassium will leak into the enclosure around the drive shaft before start-up and during the initial acceleration of the rotor since the liquid within the bearings is confined by dynamic seals. These seals will not become effective until the rotor is accelerated. The point at which the seals will become effective depends upon the

pressure within the bearing compartment. For example, if the unit was started with approximately 5-psia pressure in the bearing compartments, the liquid would be effectively confined at 4000 rpm. Nevertheless, it is reasonable to assume that the coupling enclosure will be filled with liquid before the seals become effective. This liquid must be removed before the rotor is accelerated to design-speed in order to prevent damage of the coupling from hydrodynamic forces.

Liquid will flow into the rotor cavity if the face seals between the bearings and rotor cavity are less than perfect. These face seals will be designed only to prevent a large volume of liquid potassium from leaking into the rotor cavity. The rotor could not be accelerated without damage to the bore seal if a large volume of liquid were present within the rotor cavity. Any liquid which passes through the face seal must be removed as vapor through the molecular pump or as liquid through the auxiliary scavenge system. Since the pumping speed of the molecular pumps is very low, the pumps will be unable to remove the vapor associated with a significant amount of liquid. Thus, the liquid which flows into the rotor cavity must be removed, for the most part, by the auxiliary scavenge system.

The liquid which passes through the seal between the high- and low-pressure compartment within the static seal can be scavenged by the auxiliary system. The operation of the static seals for various modes of operation is described in Section 5.2.5.3.

The scavenge scheme for the various compartments consists of a dynamic slinger in the antidrive end of the rotor as illustrated in Figure 132. The slinger contains equally spaced chambers which are vented into the bearing. These chambers produce solid-body rotation of the liquid which, in turn, produces large centrifugal forces upon the dense liquid. The centrifugal head generated in the slinger is sufficient to overcome the pressure within the bearing even with the

vapor pressure of the liquid at the central portion of the slinger, as illustrated in Figure 133. The low pressure in the central portion of the slinger provides a sink for the liquid within the rotor cavity, coupling enclosure, and the low-pressure chamber in the static seals. A head is necessary to circulate the liquid from the drain port on the coupling enclosure and the rotor cavity and into the scavenge ports on the antidrive end of the alternator. This can be accomplished by operating the assembly in a vertical position with the antidrive end down and by using gravitational forces to circulate the liquid. Such an arrangement would not work unless gravitational forces exist. For this case, a dynamic slinger can be incorporated on the rotating parts to provide sufficient velocity head to circulate the liquid from the various drain ports to the scavenge ports in the antidrive end of the alternator.

The rotor cavity cannot be vented into the scavenge system before the central portion of the slinger is empty. If this occurred, liquid would flow into the rotor cavity. Thus, the drain line from the rotor cavity must contain a valve which can be opened and closed at the proper time during the start-up procedure. The valve would be closed after the rotor cavity is drained so the molecular pump can reduce the pressure within the rotor cavity.

5.3 Preliminary Design Data

A summary of performance data, including a loss and weight breakdown, are presented in Tables 31 and 32, respectively. Bearing losses and weights were provided by AiResearch.

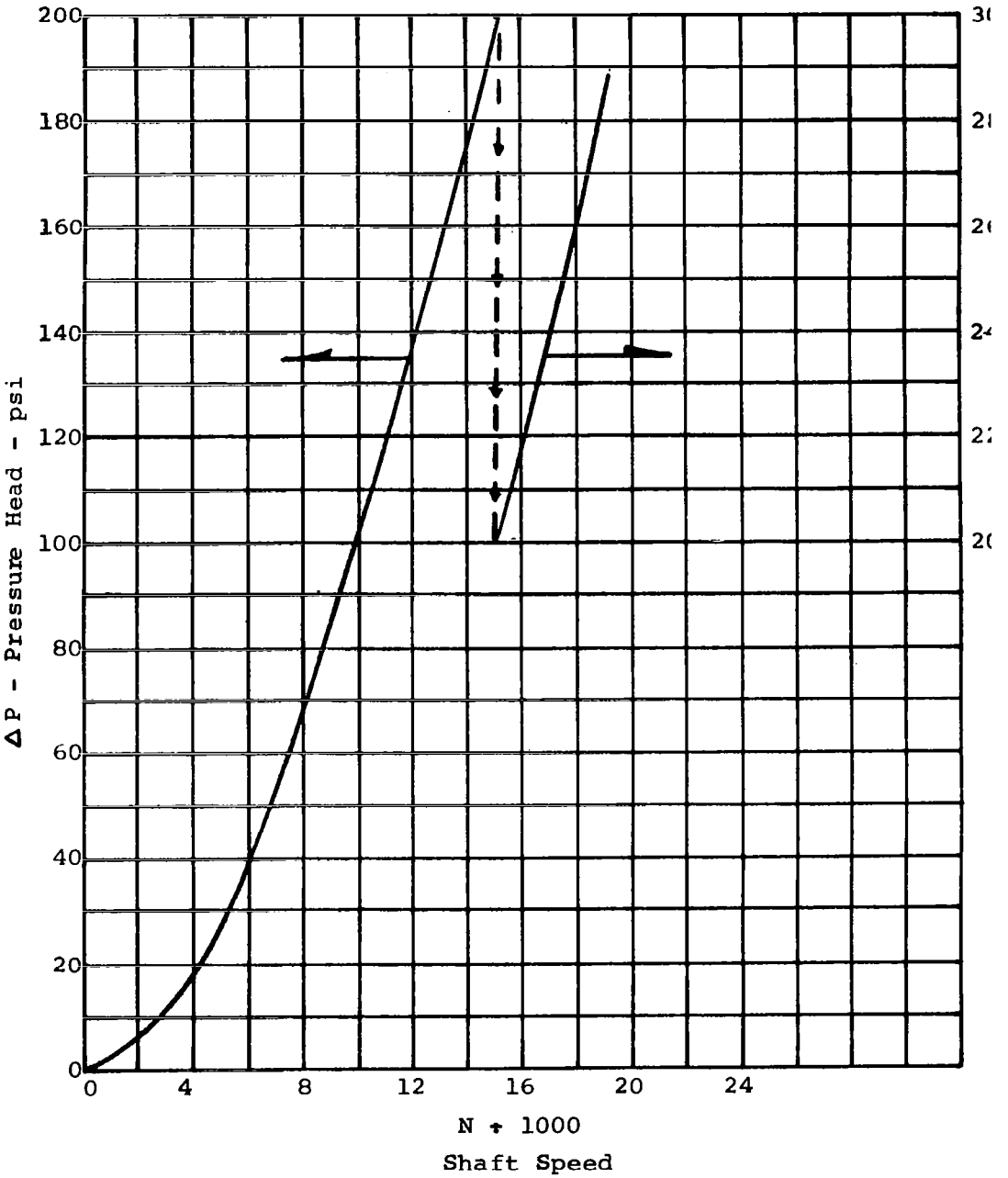

SLINGER CENTRIFUGAL HEAD

FIGURE 133

TABLE 31

PERFORMANCE SUMMARY

Lubricant:	Potassium, 700°F (inlet)
Speed/Frequency:	19,200 rpm, 1600 Hz
Voltage:	480/832 v
Rated Output:	450 kw at 0.75 pf
Alternator Losses:	
Stator	25.6
Rotor (including windage)	1.1
Bearings and seals	11.3
	38.0 kw
Alternator Shaft Power:	488.0 kw
Alternator Electrical Efficiency:*	94.4%
Alternator Overall Efficiency:*	92.2%

*Based on 450-kw rated output.

TABLE 32

ALTERNATOR WEIGHT SUMMARY

Electrical Weight (1.08 lb/kva)			
Stator		343.4	
Rotor		303.5	
			646.9 lb
Inert Hardware Weight			
Bearings		16.7	
Stub Shafts and Seal Components	DE 28		
	ADE 26		
		54	
Bearing and Seal Housings	DE 4		
	ADE 2.1		
		6.1	
End-Bells	DE 25		
	ADE 21		
		46	
Hermetic Shroud		29	
Bus-Rings, Terminals, Bore Seal Assembly, Miscellaneous		62	
			213.8 lb
Total Weight (1.43 lb/kva)			860.7 lb

5.4 Materials Summary

Selection of materials for the KTA alternator were based on results of the extensive work performed under NASA Contracts NAS 3-4162[33, 34, 35] and NAS 3-6465[36], a research and development program on magnetic, electrical conductor, electrical insulation, and bore seal materials, and on results of the KTA Phase I design studies. The selection of H-11 alloy (AMS 6487) rotor material from the several material candidates examined in the Phase I studies was based on the established parametric trends and detail stress and thermal analyses performed on the various alternator configurations. Other electromagnetic component materials selections were based on an investigation of individual material properties relative to application requirements. Table 33 lists the generator electromagnetic materials and the general basis for their selection.

TABLE 33

ALTERNATOR MATERIALS

Component	Material	Selection
Stator Frame	Hiperco-27	Based on results of work presented in Reference 3. Has high-magnetic induction at elevated temperatures, high-thermal conductivity, good magnetic stability, adequate mechanical strength.
Armature Laminations	Hiperco-27	Based on results of work presented in Reference 3. Thermal expansion characteristics same as mating frame.
Lamination Insulation	Plasma-Arc Sprayed Alumina	Based on results of work presented in Reference 1. Good stability and minimum outgassing at high-temperature levels.
Armature Conductor	Nickel-Clad Silver	Based on results of work presented in Reference 1.
Armature Conductor Insulation	Anadur-refractory oxide and glass frit over S-glass fiber serving with silicone resin bonding	Based on results of work presented in Reference 1.
Field Conductor	CUBE Copper - BeO dispersion strengthened copper	Based on results of work presented in Reference 1. Good high-temperature stability, high-electrical conductivity, joints do not require cladding protection. Poor coil-forming characteristics judged adequate for simple field coil configuration.
Field Conductor Insulation	Synthetic mica paper	Based on results of work presented in Reference 1. Low outgassing at field coil temperature, good abrasion resistance.
Armature Slot Liners and Wedges	Alumina, 99.5% purity	Based on results of work presented in Reference 2. Good stability at high temperature, high thermal conductivity, minimum outgassing.
Bus Rings	CUBE Copper	Same as "Field Conductor" above.
Bore Seal	Alumina, 99.8% purity	Based on results of work presented in Reference 2. Alkali metal compatibility with high electrical resistance.
Bore Seal End-Member	Cb-1Zr	Based on results of work presented in References 2 and 6. Alkali metal and braze joint compatibility.
Bimetallic Joint Steel	18% Ni maraging steel	Coefficient of expansion, low Ni content, weldability, strength, potassium resistance.
Rotor Forging	H-11 (AMS 6487)	Based on results of Phase I studies and work presented in References 4 and 5.
End-Bells	Hastelloy B	Coefficient of expansion, nonmagnetic, oxidation and potassium resistant, adequate strength, readily available; can be readily fabricated in complex end-bell shapes
Hermetic Shroud and Cooling Ducts	L-605	Coefficient of expansion, nonmagnetic, oxidation and potassium resistant, adequate strength, readily available and fabricable.

6. REFERENCES

1. Kearton, W.J., "Flow of Air Through Radial Labyrinth Glands", Institution of Mechanical Engineering, AD 8531

2. "Analytical Investigation of Turbine Erosion Phenomena", Interim Technical Report No. 1, Westinghouse Electric Corporation, Astronuclear Laboratory, Contract NAS 7-390, WANL-PR(DD)-014, November 1, 1966.

3. Pouchot, W.D. (Ed.), "Comparison of the Erosion Potential for a Potassium Vapor Turbine and a Cesium Vapor Turbine", Westinghouse Electric Corporation, Astronuclear Laboratory, Contract NAS 7-390, WANL-TME-1730, February 9, 1968.

4. Katz, J.L., H. Saltsburg, and H. Reiss, "Nucleation in Associated Vapors", North American Aviation Science Center, SCPP-65-32, May 18, 1965.

5. Ewing, C.T., et al., "High Temperature Properties of Potassium", U.S. Naval Research Laboratory, Report NRL6233, September 24, 1965.

6. Whitney, W.J., W.T. Stewart, and J.W. Miser, "Experimental Investigation of Turbine-Stator-Blade Outlet Boundary Layer Characteristics and Comparison with Theoretical Results", NACA RME55K24, March 1956.

7. Stewart, W.T., "Analysis of Two-Dimensional Compressible Flow Loss Characteristics Downstream of Turbomachine Blade Rows in Terms of Basic Boundary Layer Characteristics", NACA TN 3515, July 1955.

8. Zweifel, O., "Optimum Blade Pitch for Turbomachines with Special Reference to Blades of Great Curvature", Brown Boveri Review, Vol. 37, No. 12, December 1945, pp. 436-444.

9. Tsien, H.S., "Two-Dimensional Subsonic Flow of Compressible Fluids", Journal Aeronautical Science 6, 399, 1939.

10. Martensen, E., Berechnung der Druckverteilung an Gitterprofilm in ebener Potentials Fromung, Archive for Rational Mechanics and Analysis, Vol. 3, 1959.

11. Gill, W.N., et al., "Mass Transfer in Liquid Lithium System", American Institute Chemical Engineering Journal Vol. 6, No. 1, 1960.

12. Kothmann, R.E., "Condensation in Wet Vapor Turbines", Astronuclear Laboratory, Westinghouse Electric Corporation, Contract NAS 7-390, WANL-TME-1668, October 15, 1967.

13. Hoffman, H.W. and B. Cox, "A Preliminary Collation of the Thermo-dynamic and Transport Properties of Potassium", Oak Ridge National Laboratory, ORNL-TM-2126, NASA Order W-12,353, July 1968.

14. Goldman, L.J., and S.M. Nosek, "Experimental Nozzle Expansion and Flow Characteristics of Potassium Vapor", NASA TND-3209.

15. Katsanis, T., "A Computer Program for Calculating Velocities and Streamlined for Two-Dimensional, Incompressible Flow in Axial Blade Rows", NASA Lewis Center, NASA TND-3762, January 1967.

16. Varljen, T.C., "The Transport of Atomized Drops in Wet Vapor Turbines", Astronuclear Laboratory, Westinghouse Electric Corporation, Contract NAS 7-390, WANL-TME-1836, August 5, 1968.

17. Zimmerman, W.F. and R.J. Rossbach, "Limited Impact Erosion and Metal Losses in Two-Stage Potassium Turbines", JPL Technical Memo 33-354, Section 3, June 15, 1967.

18. Rossbach, R.J., Three-Stage Potassium Test Turbine Review Meeting, General Electric Co., Evandale, Ohio, October 15, 1968.

19. "Basic Investigation of Turbine Erosion Phenomena", Quarterly Progress Report, July-September 1968, Westinghouse Electric Corporation, Astronuclear Laboratory, Contract NAS 7-390, WANL-PR (DD)-038, October 28, 1968.

20. Epstein, L.F., "Static and Dynamic Corrosion and Mass Transfer in Liquid Metal Systems", Chemical Engineering Progress Symposium Series, Vol. 53, No. 20, 1957.

21. Ginell, W.S. and R.J. Teitel, "Determination of the Solubility of Transition Elements in Molten Potassium", Douglas Aircraft, SM 48883, 1965.

22. Climax Molybdenum Co., Spec No. CMX-WB-TZM-2, May 1964.

23. Hays, Lance G. (Ed.), Summary of Turbine Erosion Meeting Held at Jet Propulsion Laboratory, December 29-30, 1966, NASA, JPL Technical Memo 33-354, June 15, 1967.

24. Schnetzer, E. (Ed.), "Two-Stage Potassium Test Turbine", Quarterly Progress Report No. 15, Period: November 8, 1964 through February 8, 1965, Contract NAS 5-1143 NASA-CR-54392.

25. Potassium test turbine review meeting at General Electric Co., Cincinnati, Ohio, October 15, 1968.

26. Rossbach, R.J., "Critical Flow of Potassium Vapor Through Instrumented Converging-Diverging Nozzle", ASME Preprint 65-GTP-22, presented at the Gas Turbine Conference and Product Show, Washington, D.C., February 28-March 4, 1965.

27. Lindhardt, Hans D., "Potassium Erosion Experiments" Ibid., Section 9, pp. 115-127.

28. Baker, D.W.C., K.H. Jolliffee, and D. Pearson, "The Resistance of Materials to Impact Erosion Damage", Phil Trans. Royal Society, London, Series A. No. 1110, Vol. 260, July 28, 1966, pp. 193-203.

29. Hancox, N.L. and J.H. Brunton, "The Erosion of Solids by the Repeated Impact of Liquid Drops", Phil Trans. Royal Society, London, Series A, No. 1110, Vol. 260, July 26, 1966, pp. 121-139.

30. Kovacevich, E.A., "Erosion Properties of Selected Turbine Materials in Water and Potassium", The Garrett Corporation, AiResearch Manufacturing Division, Technical Report AFAPL-TR-65-130, AF 33(675)-8954, et al., January 1966.

31. Stefanov, B.I., et al., Teplofizika Vysokikh Temperature Vol. 4, No. 1, 1966, pp. 141-142.

32. Touloukian, Y.S., "Thermophysical Properties of High Temperature Solid Materials", Thermophysical Properties Research Center, Prudue University, MacMillan Company, New York, 1967.

33. Kays, W.M., "Convective Heat and Mass Transfer", McGraw-Hill, 1966.

34. Cobb, E.C. and O.A. Saunders, "Heat Transfer from a Rotating Disk", Proc. Royal Society of London, Vol. 236, 1956, pp. 343-351.

35. Gazley, Jr., C., "Heat Transfer Characteristics of the Rotational and Axial Flow between Concentric Cylinders", Transactions of the ASME, January 1958.

36. Jakob, M., "Elements of Heat Transfer", John Wiley & Sons, Third Edition, 1957.

37. Meyrial, P.M., M.L. Marin, and W.M. Robsenow, "Heat Transfer During Film Condensation of Potassium Vapor on a Horizontal Plate", MIT Engineering Projects Laboratory.

38. Millensen, M.B. and S.S. Manson, "Determination of Stresses in Gas-Turbine Disks Subjected to Plastic Flow and Creep", NACA Report No. 906, 1948.

39. "Electrical Conductor and Electrical Insulation Materials Topical Report", NASA Lewis Research Center Report, NASA-CR-54092, October 1964. Prepared by Westinghouse Electric Corporation, Aerospace Electrical Division, Lima, Ohio.

40. "Bore Seal Technology Topical Report", NASA Lewis Research Center Report NASA-CR-54093, December 1964. Prepared by Westinghouse Electric Corporation, Aerospace Electrical Division, Lima, Ohio.

41. "Magnetic Materials Topical Report", NASA Lewis Research Center Report, NASA-CR-54091, September 1964. Prepared by Westinghouse Electric Corporation, Aerospace Electrical Division, Lima, Ohio.

42. "High Temperature Magnetic Materials", Westinghouse Electric Corporation, Aerospace Electrical Division, Lima, Ohio. Report No. WAED 67.34E, October 1967. Prepared on "Contract for Development and Evaluating Magnetic and Electrical Materials Capable of Operating in the Temperature Range from 800° to 1600°F", Contract No. NAS3-6465.

43. "AC Generator Rotor Materials Topical Report", USAF Systems Command Report AFAPL-TR-66-127, January 1967. Prepared by Westinghouse Electric Corporation, Aerospace Electrical Division, Lima, Ohio.

44. "SPUR Generator Stator Seal Development, Topical Report", USAF Systems Command Report ASD-TDR-63-677; Part I, August 1963; Part II, February 1967. Prepared by Westinghouse Electric Corporation, Aerospace Electrical Division, Lima, Ohio.

45. "SNAP 50/SPUR 467 kVA Experimental Generator Design Summary", USAF Systems Command Report AFAPL-TR-67-7, May 1967. Prepared by Westinghouse Electrical Corporation, Aerospace Electrical Division, Lima, Ohio.

46. "Topical Report, Experimental Verification", U.S. Atomic Energy Commission Research & Development Report SAN 679-7, February 1968. Prepared by Westinghouse Electric Corporation, Aerospace Electrical Division, Lima, Ohio.

APPENDIX A

TURBINE MATERIALS*

by G. G. Lessmann, R. E. Gold, F. G. Arcella, and F. Reed
Westinghouse Astronuclear Laboratory

I. SUMMARY

A comprehensive review of potential alloys for the KTA turbine was conducted to permit selection of alloys, to establish design properties, and to identify material related problem areas.

The molybdenum base forging alloy TZM was selected for rotating hardware, and the highly fabricable tantalum base alloy T-111 was selected for the stationary hardware. For non-critical low temperature components of the housing Cb-1Zr will be used to reduce turbine weight. These basic selections promote a simple uncluttered turbine design and, hence, enhance system reliability. Both high temperature alloys have growth potential in that complementary alloy systems having improved properties are in an advanced state of development. This increases the attractiveness of T-111 and TZM as selections for this application since design technology will be directly applicable using the advanced alloys. Consequently, a future potential exists for a higher performance turbine through alloy substitution without penalty in terms of lost fabrication experience. A columbium modified TZM offers considerable promise of higher performance as rotating hardware, while ASTAR-811C will eventually provide extended performance for stationary hardware.

---

*Recommendations for selection and application of materials in the KTA turbine are reviewed in this appendix. This work was accomplished under AiResearch Contract P711340. The material in this appendix was originally issued as Westinghouse Astronuclear Laboratory report WANL-TME-1889, 1969.

The only additional material requirement in the turbine are the pads for the potassium lubricated bearings. For bearing temperatures less than 1000°F a number of materials are satisfactory. The best combination of low friction, good wear resistance and low density is provided by a refractory metal bonded titanium carbide (TiC-10%Cb, Reference 1). This material is therefore the preferred choice although an alternate choice has also been identified. This is a refractory metal bonded tungsten carbide (Grade 7178-Reference 1) which is attractive on the basis of strength and ductility but is otherwise inferior.

The selection of alloys, particularly for the rotating components, required considerable discretion in selection and interpretation of data. In addition, extensive extrapolation was required for the 30,000 hour design life and stress state (longitudinal uniaxial data is available whereas the disc stresses are predominantly transverse and biaxial). Discretion in data selection and extrapolation were both necessary but the risk involved was recognized. To partially circumvent this problem, major material development requirements were identified. If these development requirements were to be satisfied, definition of system design reliability could be accomplished. In this respect the conduct of these or similar developmental programs is considered essential. Briefly, major development requirements in support of a detailed turbine design and fabrication exist in the following areas:

1. TZM Disc Forgings: Creep strength of TZM is developed during forging using particular high temperature thermal-mechanical processing schedules. It is necessary to demonstrate that the desired properties can be achieved in complex disc forgings. The central portion of the discs are critical in this respect since stresses are highest there but the ability to work this portion of the disc during processing is most difficult.

2. Disc Forging Directionality: Assuming an adequate forging schedule is developed in terms of thermal-mechanical processing history, there will remain a considerable doubt about the performance of the optimum disc under the complex stress state within the turbine. The best method of correlation between design (and destructive test results) can be achieved by

running a hot spin test. This would provide realistic loading and provide a definition of the effects of directionality in the forging which could not be achieved by conducting individual uniaxial tests. Proper conduct of this test would seem to dictate the use of a vacuum or potassium vapor environment. Consequently, potassium bearing tests could be performed simultaneously as a portion of the same test. Adequate bearing design requires use of tensile or modulus of rupture data for bearing material which is presently not available and would have to be obtained to incorporate a bearing evaluation in this test.

3. Housing Fabrication: The turbine housing will be fabricated from T-111 by making extensive use of welding. Underbead cracking tendencies have been recently observed in multi-pass manual GTA weldments in thick plate of this alloy. Since this joining process offers the greatest flexibility for repair as well as fabrication, this problem requires resolution. Perhaps it can be resolved through the substitution of ASTAR-811C. If this does not work, however, then some further development will be required. Alternatively, the turbine housing would have to be designed for single pass EB welding but repair techniques would still be required. For minimum weight the rear low temperature sections of the housing will be Cb-1Zr requiring evaluation of the structural weld between T-111 and Cb-1Zr. Satisfactory welds between these materials have been made.

II. TECHNICAL APPROACH

Materials support for the KTA design study was entirely consultative. This permitted development of a turbine design which is, as nearly as possible, representative of the state-of-the-art. The three primary functions provided in satisfying the materials support requirements of this program were:

1. Material Selection: This required a comprehensive review of available data for candidate refractory metal alloys. The review was restricted to this class of materials to satisfy corrosion and erosion requirements of the potassium environment. Comparisons among the established alloy systems were developed. Also, projections and extrapolations were made

to demonstrate growth potential based on current programs in which advanced alloys are being developed.

2. Design Integration: Liaison between design and materials personnel was established and maintained to assure integration of current technology into the turbine design. The emphasis was naturally on mechanical and thermal properties with particular emphasis on the relationship between metallurgical structure, high temperature strength, and long time structural stability.

3. Identification of Material Development Requirements: The designs contemplated in this study represent an advance in the state-of-the-art with respect to the application of the selected materials into turbine hardware. This stems primarily from the scarcity of applicable data, and consequently, an inadequate current definition of material reliability. To accommodate this situation, a flexible technical approach was adopted. Quite simply, since existing data would require extrapolation on a technical rather than statistical basis, the risk of extrapolation would have to be recognized. Once recognized the risk can be reduced through effective applied development programs at some future time. The most critical of these were identified during the material review.

Since the required extrapolations are based on a basic appreciation of structural interactions, a logical extension of this approach is the ability to recognize growth potential, (i.e., establishing that improved properties in the selected or similar alloy systems might be achieved in the near future). Identification of growth potential supports the logic used in extrapolations. This approach was particularly useful in supporting an optimistic selection of achievable creep strength levels for TZM. This approach also permitted identification of optimum return-on-investment areas of materials development.

III. TURBINE CRITERIA AND POTENTIAL TURBINE ALLOYS

A general limitation of materials support was that it be non-experimental. Hence, support was confined to data compilation, analysis and reduction. In conducting this review, and ultimately in selecting these alloys, a practical perspective was maintained by emphasizing the major KTA design priorities of high reliability and ease of development.

From a materials standpoint the most pertinent design specifications were the following:

- operating temperatures to 2150°F
- the use of potassium vapor as the turbine working fluid
- minimum design life of three years

Refractory metal alloys were considered exclusively for this application to assure high temperature strength coupled with potassium corrosion resistance. Two general types of materials were considered: fabricable structural alloys and high-strength forging alloys. Fabricable alloys are defined for this program as those alloys displaying a high degree of formability and weldability while retaining considerable high temperature strength. The most important consideration for the high-strength forging alloy, intended for use as turbine wheel and blade material is a high elevated-temperature creep strength/density ratio combined with adequate low temperature ductility consistent with turbine starting conditions.

Mechanical properties represent only one general aspect of alloy selection. The final selection process included an integrated engineering appraisal of the following factors:

- Short-time tensile properties.
- Time-dependent mechanical properties, preferably long-time creep data or extrapolated stress-rupture data if actual long-time data is unavailable.

- Thermal stability of mechanical properties following long-time exposures at elevated temperatures. This data is desirable since it increases confidence in establishing design data.

- Accumulated manufacturing experience. An index of this factor is provided by the relative commercial status of a specific alloy. Again, this is a confidence index.

- Requirements and limitations of forming, machining and welding processes.

- Complexity of processing schedules required to achieve desired properties.

- Compatibility of candidate alloys with alkali metal environments at high temperatures.

- Density of candidate alloys, particularly those intended for applications in rotating members of the turbine assembly.

The general perspective achieved in integrating these factors for alloy selection is discussed below. This includes consideration of developmental alloys which provides a necessary long range perspective for potential turbine applications. The major categories reviewed in detail for the point-in-time recommendations are discussed later. These include mechanical property and supplemental design data for the selected and growth alloy systems, review of potassium corrosion of the selected alloys, and initial turbine fabrication review based on the selected alloys.

The fabricable alloys for which data was compiled are listed below. Due to the importance of weight as a design factor for space electric power conversion systems the density of the various alloys is included.

FABRICABLE ALLOYS

Alloy	Nominal Compositions(w/o)	Density(lb/in^3)	Status
T-111	Ta-8W-2Hf	0.604	Commercial
ASTAR-811C	Ta-8W-1Re-0.7Hf-0.025C	0.604	Scale-up
FS-85	Cb-27Ta-10W-1Zr	0.383	Commercial
D-43	Cb-10W-1Zr-0.1C	0.326	Commercial
Cb-1Zr	Cb-1Zr	0.31	Commercial

This list represents only those fabricable alloys which merited serious consideration and for which reasonably complete property data are available. Initial screening evaluations eliminated several potential alloys on the basis they offered essentially no advantages over the selected candidate alloys while suffering disadvantages in certain aspects. An example of this is the solid-solution alloy Ta-10W which is quite comparable to T-111 in many respects but, lacking a reactive metal addition, is subject to intergranular attack in boiling potassium[2].

The tantalum-base T-111 and the columbium-base FS-85, D-43, and Cb-1Zr alloys have all achieved commercial status. Of these, T-111 and Cb-1Zr are particularly advanced being available in a wide variety of rolled, forged or drawn products. The tantalum-base ASTAR-811C alloy is a recently developed material. It is similar in short-time strength to T-111 but has considerably more creep resistance. This is one of a series of precipitation strengthened alloys developed specifically for long life applications requiring fabricable alloys for containment of alkali metal working fluids[3].

Welding of refractory metals and their alloys must be done observing stringent environmental controls. This is necessitated by the detrimental effects on ductility and corrosion resistance which result from the absorption of interstitial elements during welding operations. While this was a difficult problem in the past, procedures have been established whereby components and hardware assemblies can be welded observing the necessary controls[4,5]. Hence, structures

fabricated by welding can be readily incorporated into the turbine design.

The use of potassium as the working fluid in the turbine requires a consideration of the compatibility of candidate alloys with this environment for long-time high temperature exposures. Experience has shown refractory metal alloys to be subject to intergranular corrosion and premature failure under these conditions if certain precautions are not taken. Strict control of oxygen level in the alkali metal must be maintained. In addition, experience has shown that those refractory metals which contain a reactive metal such as Zr or Hf have performed satisfactorily at temperatures up to at least 2200°F[4]. This has been attributed to the reaction of the reactive metal additions with the oxygen present in the refractory metal alloys and the alkali metal to form stable oxides. This effectively getters the oxygen and eliminates the corrosion associated with high oxygen. Virtually all present-generation refractory metal alloys satisfy this requirement because significant strengthening is also realized by the addition of reactive elements.

The forging alloys for which data was compiled are listed below.

FORGING ALLOYS

Alloy	Nominal Composition(w/o)	Density (lb/in^3)	Status
TZM	Mo-0.5Ti-0.08Zr-0.02C	0.36	Commercial
TZC	Mo-1.2Ti-0.2Zr-0.12C	0.36	Semi-commercial
Cb-TZM	Mo-1.5Cb-0.5Ti-0.3Zr-0.07C	0.36	Scale-up
B-88	Cb-28W-2Hf-0.07C	0.373	Scale-up
NASVF-1	Ta-13W-1.5Re-0.7Hf-0.025C	0.60	Development
NASVF-2	Ta-16W-2Re-0.7Hf-0.025C	0.60	Development
NASVF-3	Ta-13W-1.5Re-0.7Hf-0.03N	0.60	Development

Of the forging alloys, only molybdenum-base TZM and TZC have achieved any significant degree of commercial status. These alloys derive most of their elevated temperature strength from the precipitation of stable Ti and Zr carbides during processing. These carbides tend to impede recovery processes and thus provide stability of strain-hardened structures to high temperatures as well as providing dispersion strengthening. The Cb-TZM alloy was originally developed as a modification of TZC. The Cb addition was found to reduce the tendency toward ingot cracking. While not generally considered a commercial alloy, considerable knowledge has been accumulated with regard to developing high mechanical strength and identifying strengthening mechanisms operative in this alloy.

The columbium-base alloy B-88 combines both solid-solution strengthening and carbide-precipitation strengthening to achieve the highest elevated-temperature strength of any columbium-base alloy yet developed. By reason of its recent development, property data are somewhat limited, particularly the time-dependent properties. The NASVF-series of tantalum-base alloys are the first forging alloys developed in a continuing NASA-sponsored alloy development program[6]. Again, elevated-temperature strength is realized by both solid-solution and precipitation strengthening. The data provided is included to indicate growth potential in this general area. Any attempt to use this data for design purposes would be premature.

IV. ALLOY PROPERTIES

The data and discussion of the fabricable alloys is presented separately from that of the forging alloys since different perspectives must be employed in evaluating data for the two types of alloys.

A. FABRICABLE ALLOYS

For those applications where fabrication requirements are most demanding, the tantalum-base alloy T-111 is recommended. As an alternate selection the tantalum-base ASTAR-811C is chosen. Both of these alloys combine high temperature strength with excellent formability and weldability. T-111 is essentially a solid-solution strengthened alloy, particularly with respect to long time mechanical strength, realizing only a modest strength increment due to precipitation effects, while ASTAR-811C combines both solid-solution and carbide-precipitation strengthening. At this time, based on a consideration of the significantly greater commercial experience, T-111 is a clear choice. However, an adequate background in the use of ASTAR-811C will develop in the near future permitting its reconsideration for prime selection in this application.

The Cb-1Zr alloy could also be considered in the overall assembly for applications such as general plumbing and those components where temperatures and stresses are not beyond its limited range of performance. Its chief assets are its low density (0.31 lb/in^3) and cost. Extensive testing has shown it to perform well as an alkali metal containment material and to possess extremely good welding and forming characteristics. In addition the commercial status of this alloy is unmatched by that of any other refractory metal alloy.

Tensile data for the fabricable alloys is plotted in Figures 1 and 2 to provide a comparison of the elevated temperature ultimate and yield tensile strengths of these alloys.

Thermal stability data for T-111, FS-85 and D-43 alloys are shown in Figures 3, 4, and 5 respectively. On these curves the stability is reflected by the behavior of the ultimate tensile strength at test temperatures to 2400°F following long-time aging at elevated temperatures. Similar plots of the tensile yield strength show the same trend. This data is from one phase of an extensive NASA-sponsored program to evaluate the weldability and stability of

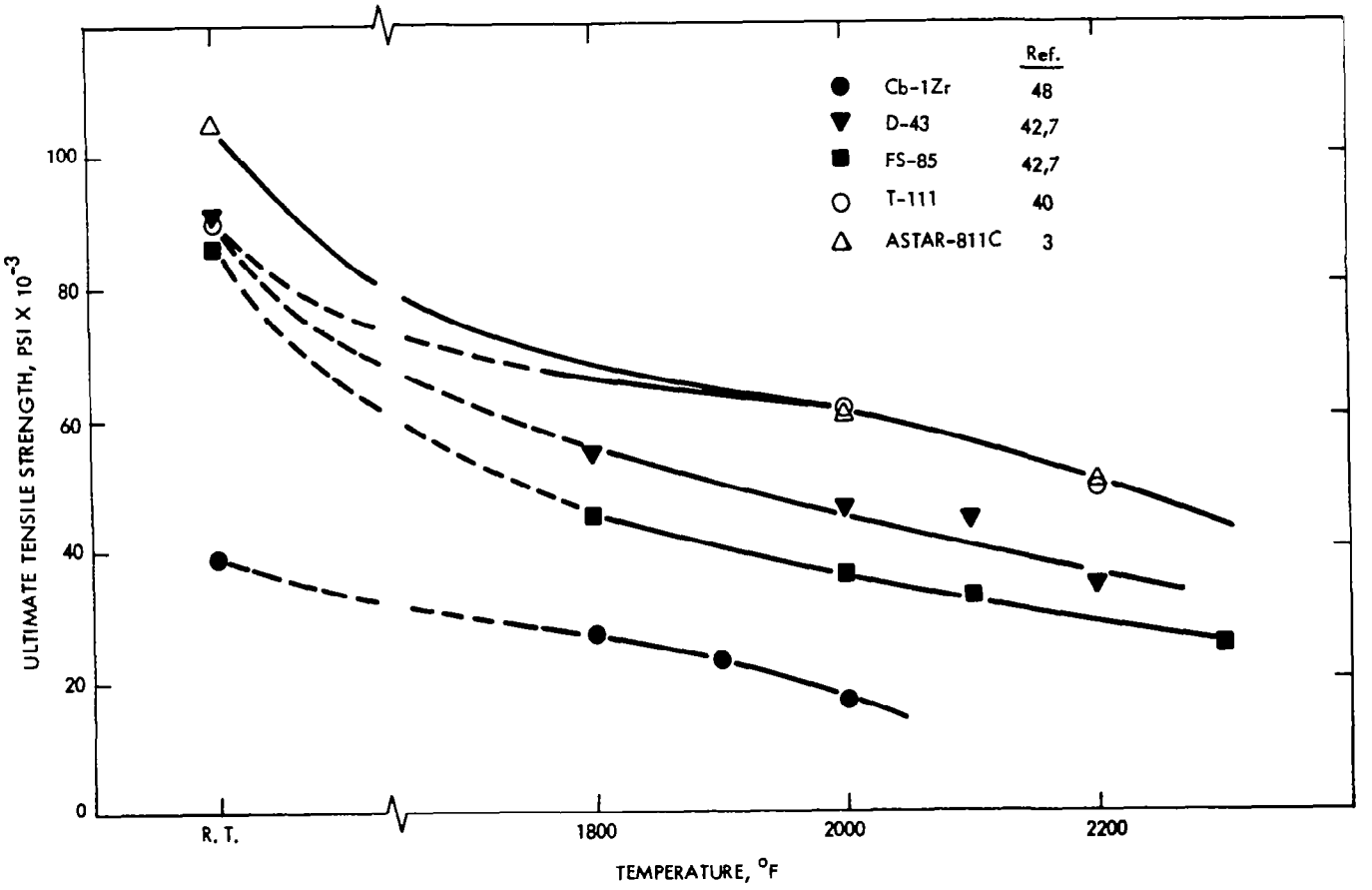

FIGURE 1 - Ultimate Tensile Strength vs. Temperature for Fabricable Alloys

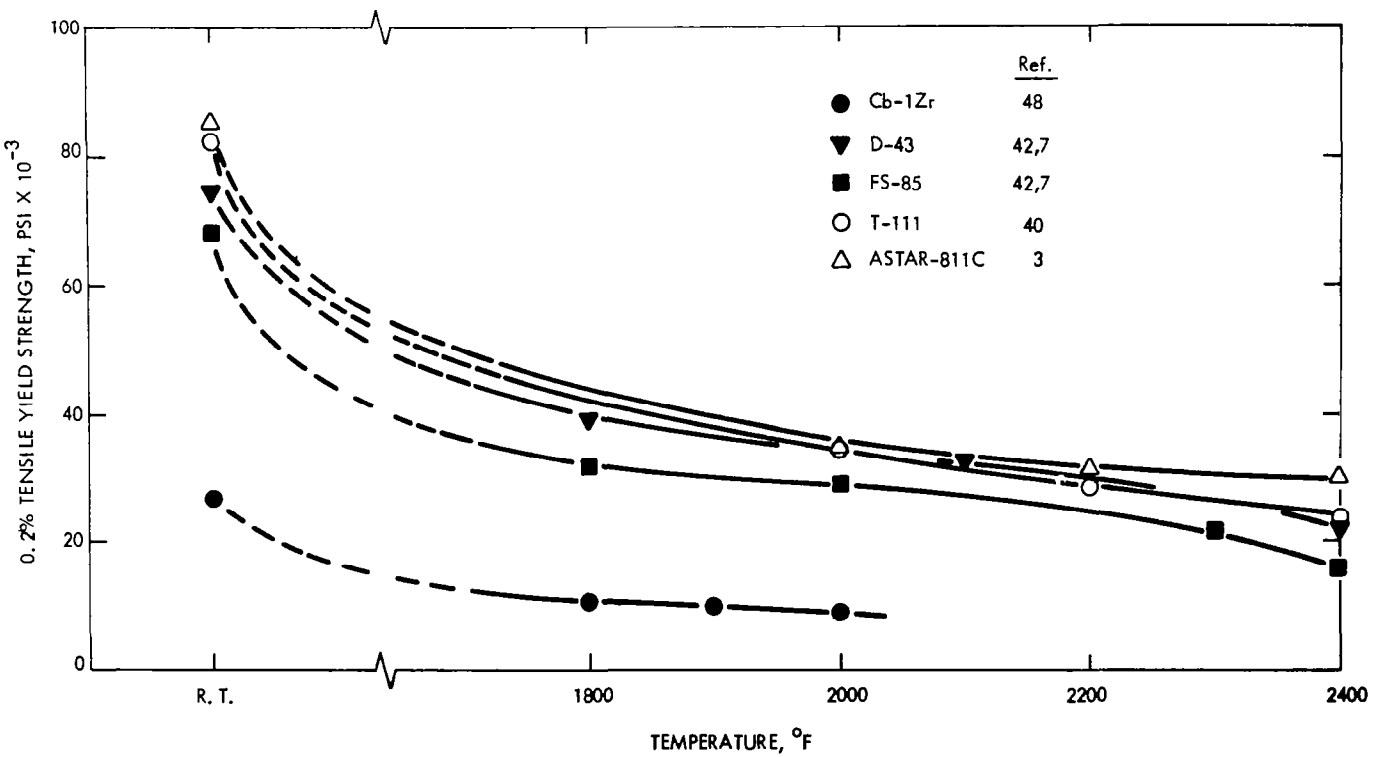

FIGURE 2 - Tensile Yield Strength vs. Temperature for Fabricable Alloys

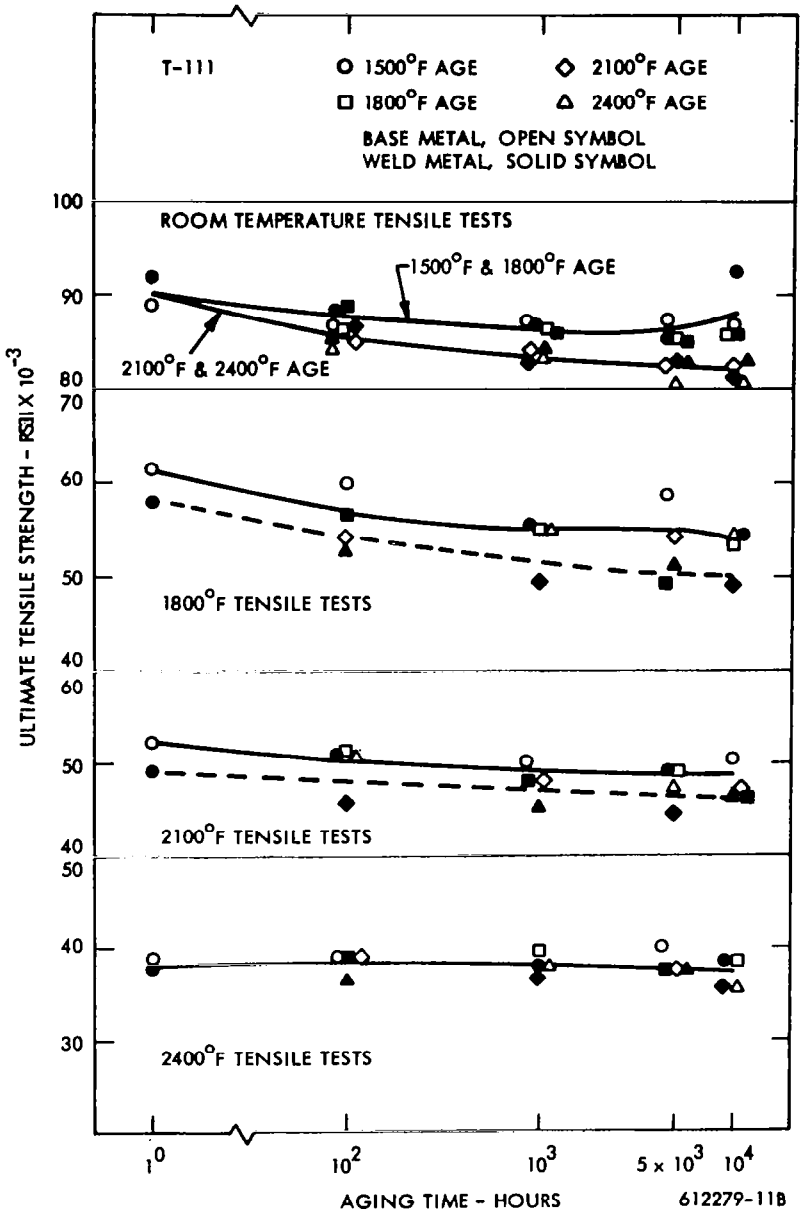

FIGURE 3 - Effect of Aging on the Ultimate Tensile Strength of T-111 (Ref. 7)
All Specimens Annealed 1 Hour at 2400°F Before Aging

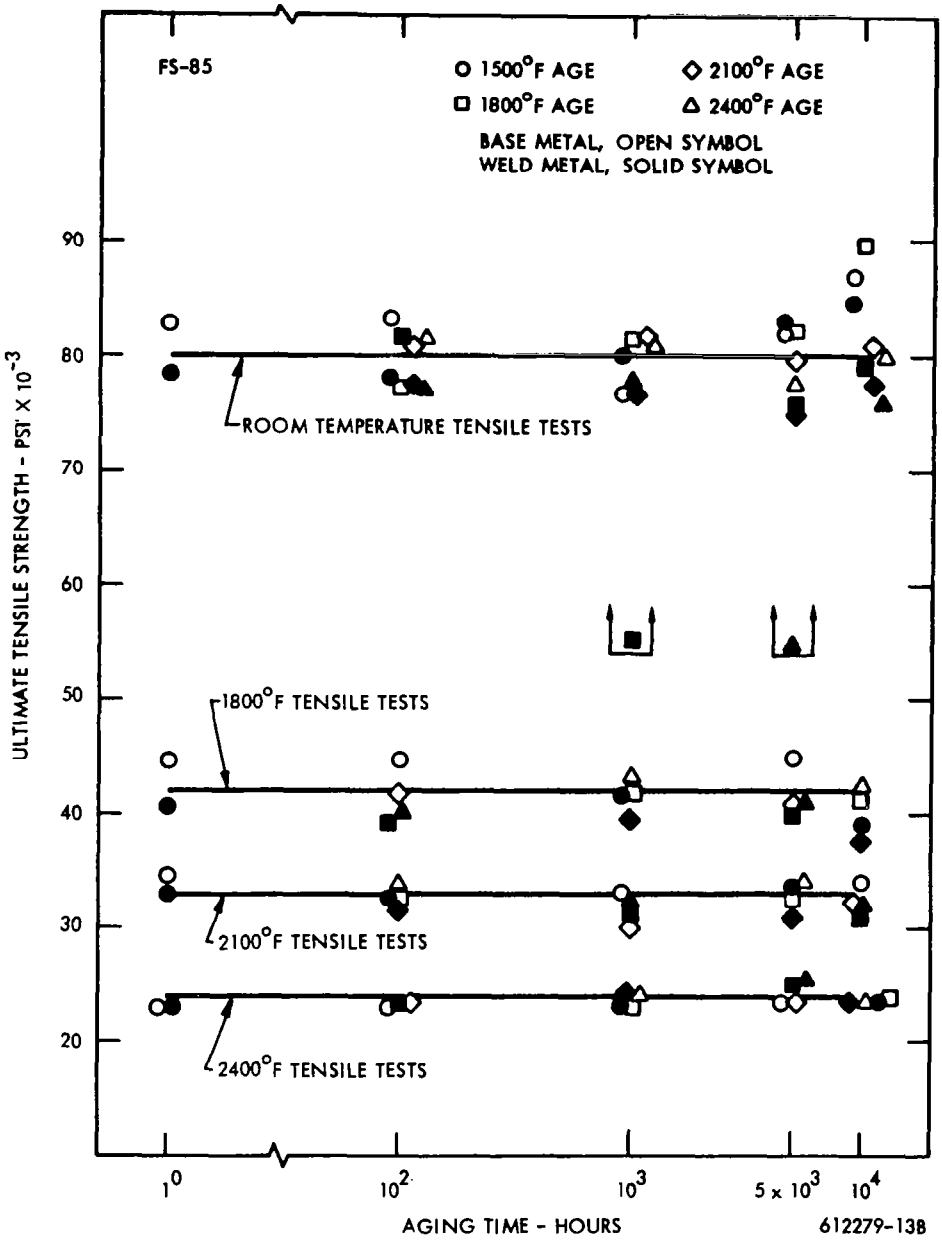

FIGURE 4 - Effect of Aging on the Ultimate Tensile Strength of FS-85 (Ref. 7)
All Specimens Annealed 1 Hour at 2400°F Before Aging

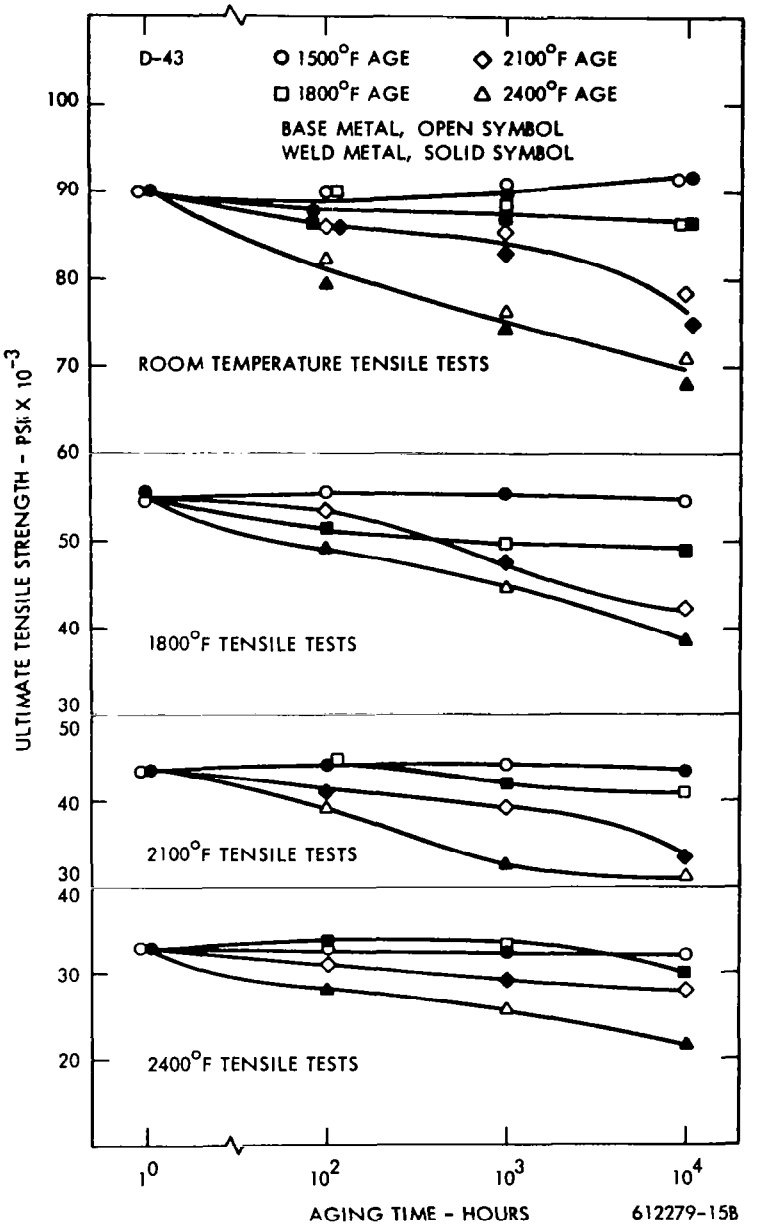

FIGURE 5 - Effect of Aging on the Ultimate Tensile Strength of D-43 (Ref. 7)
All Specimens Annealed 1 Hour at 2400°F Before Aging

promising refractory metal alloys during long-time exposures at elevated temperatures[7]. The aging and test parameters investigated were:

Parameter	Parameter Variations
Aging Time	100,1000,5000 and 10,000 hrs.
Aging Temp.	1500,1800,2100, and 2400°F
Test Temp.	R. T. ,1800,2100, and 2400°F

Only the most promising alloys were aged for times greater than 1000 hours. In addition to the tensile data presented in Figures 3 through 5, aged alloys were evaluated for ductility impairment as reflected by bend transition temperature behavior. Analysis of this data is not yet complete and, as a result, is not included here. Complete tensile data on all alloys, aged to 1000 hours, has been published previously[8].

From the curves in Figures 3-5 it is seen that the tensile properties of the essentially solid-solution strengthened T-111 and FS-85 alloys are exceptionally stable. Conversely, D-43 which is a carbide-precipitation strengthened alloy is subject to overaging at the exposure conditions of this program.

In Figure 6 a parametric representation of the 1% creep data for the fabricable alloys is given. For the applications intended for these alloys 1% creep strain is a reasonable design limitation. Where possible, only data from ultra-high vacuum creep tests were used.

The Larson-Miller parameter, with a value of 15 for the constant, was used for Figure 6. Selection of the constant is normally made to provide a consistent plot of the experimental data. For any given set of data some specific value other than 15 might be better but the need for a common rationale to evaluate material performance dictates the selection of a single constant. From the plot of Figure 6 the value 15 is seen to allow a reasonable fit to the data points for these alloys. The two curves shown for T-111 represent data from creep tests performed at two different laboratories[9,10]. The main differences in these tests were

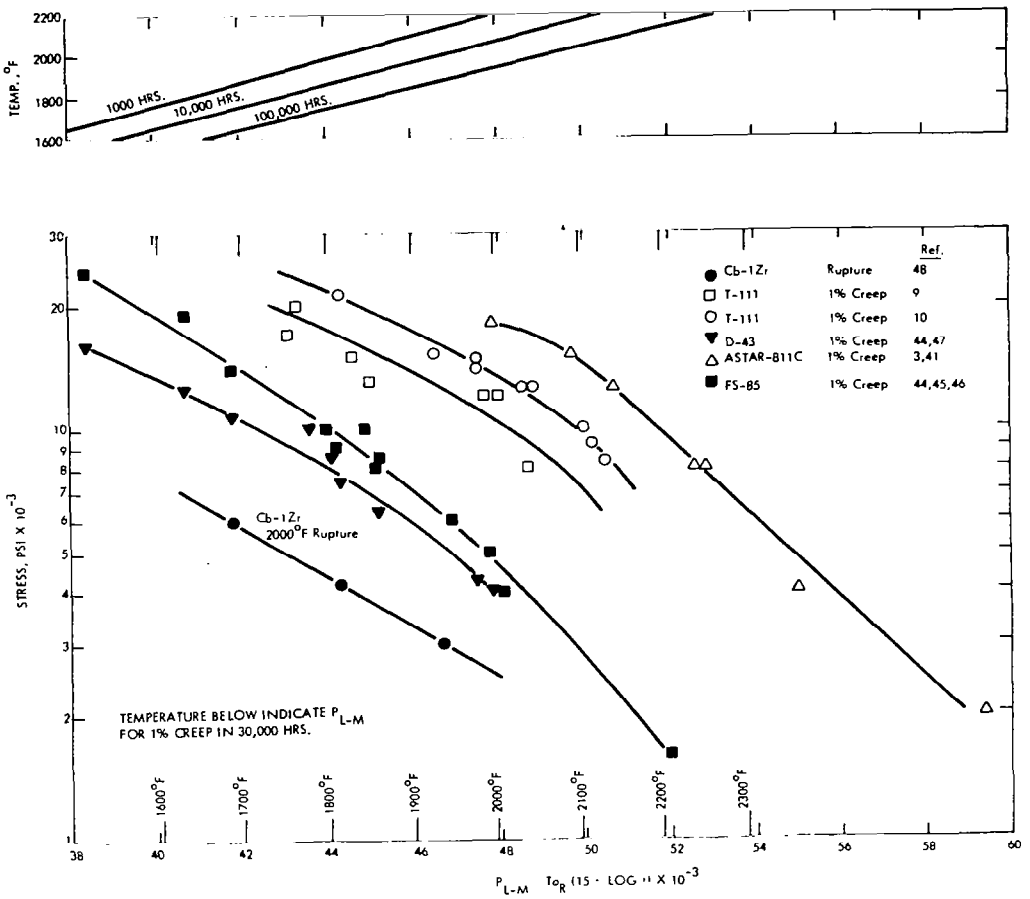

FIGURE 6 - Larson-Miller Plot of 1% Creep Data for the Fabricable Alloys

the temperatures used and the test duration. This apparent difference is the result of using a Larson-Miller constant of 15. A more discriminating choice would provide superimposed data. Hence, no real difference in creep performance is represented by these data.

The superiority of the tantalum-base alloys T-111 and ASTAR-811C is evident, particularly at the higher temperatures. Although not shown here, despite the high density of tantalum-base alloys, strength superiority over other fabricable alloys persists even when the data is compensated on a stress/density basis. The test temperature ranges selected in evaluating these alloys reflect to some degree the elevated temperature potential of the alloys. Hence, the tantalum-base alloys have been tested at higher temperatures than the columbium-base alloys.

The data shown in Figure 6 for T-111 are only a small portion of the creep data available for this alloy. The total data could be reasonably represented by a band between the two curves. Tests on T-111 at TRW[11] have been made on numerous heats over a broad range of temperatures and stresses. As a result of this program more long-time ultra-high vacuum creep data is available for T-111 than for any other refractory metal alloy. The lack of appreciable spread in these test data is of particular interest. Except for the conditions of the final recrystallization anneal, slight variations in processing details do not appreciably affect the creep behavior. This is a considerable advantage realized by using T-111.

Due to its selection as the prime material for these applications, additional, more complete, mechanical and thermophysical property data for T-111 are provided in the Appendix. The data used in preparing Figures 1, 2 and 6 are listed in Tables A1 through A10 of the Appendix.

B. FORGING ALLOYS

The molybdenum-base TZM alloy is recommended for use as the material for the rotating components. These components must withstand higher stresses, at the same high temperatures, as those parts to be made of the fabricable alloys. While fabricability is not a primary design

requirement, some ductility must be present at low temperatures to avoid failures during starting operations. TZM appears to be an excellent choice in this respect, Table A11. The reference design turbine rotor is mechanically assembled rather than fabricated so that the poor weldability of these alloys is not a limiting factor.

At the beginning of this program a review of available data indicated emphasis should be directed toward molybdenum-base alloys for these applications. Little evidence has been found to warrant changing this position. The operating stress-temperature conditions are too severe to allow more serious consideration of commercial columbium and tantalum base alloys. Tungsten and tungsten-base alloys display exceptional strength but are seriously handicapped by a general lack of ductility and their high density. High density is a significant disadvantage in rotating machinery where stresses are essentially proportional to the material density. Hence, a further advantage is realized by using molybdenum alloys which have a density of about 0.36 lb/in^3.

A general appreciation of the metallurgical and processing aspects of developing high creep strength in candidate forging alloys has not attained the status of the fabricable alloys. This stems from the fact that some are developmental while the better known ones were developed primarily for short time applications. Also, because they have been very sensitive to thermal-mechanical processing, they have been more difficult to use. Most of the forging alloys utilize a precipitation (dispersion) strengthening mechanism to achieve long-time creep strength. Thermal-mechanical processing variables are of extreme importance and there is considerably less flexibility in process schedules than is available for the fabricable alloys.

Tensile and creep properties are tabulated for the forging alloys in Tables A11 through A20 of the Appendix. For the recently developed B-88 (Table A17) and the experimental Ta-base forging alloys (Table A19) relevant processing data are included at the bottom of the tables. Ultimate and yield tensile strengths are shown in comparative plots in Figures 7 and 8, respectively. As shown in the tables, very limited data is available for the tensile properties of most of these alloys at temperatures below 1800°F.

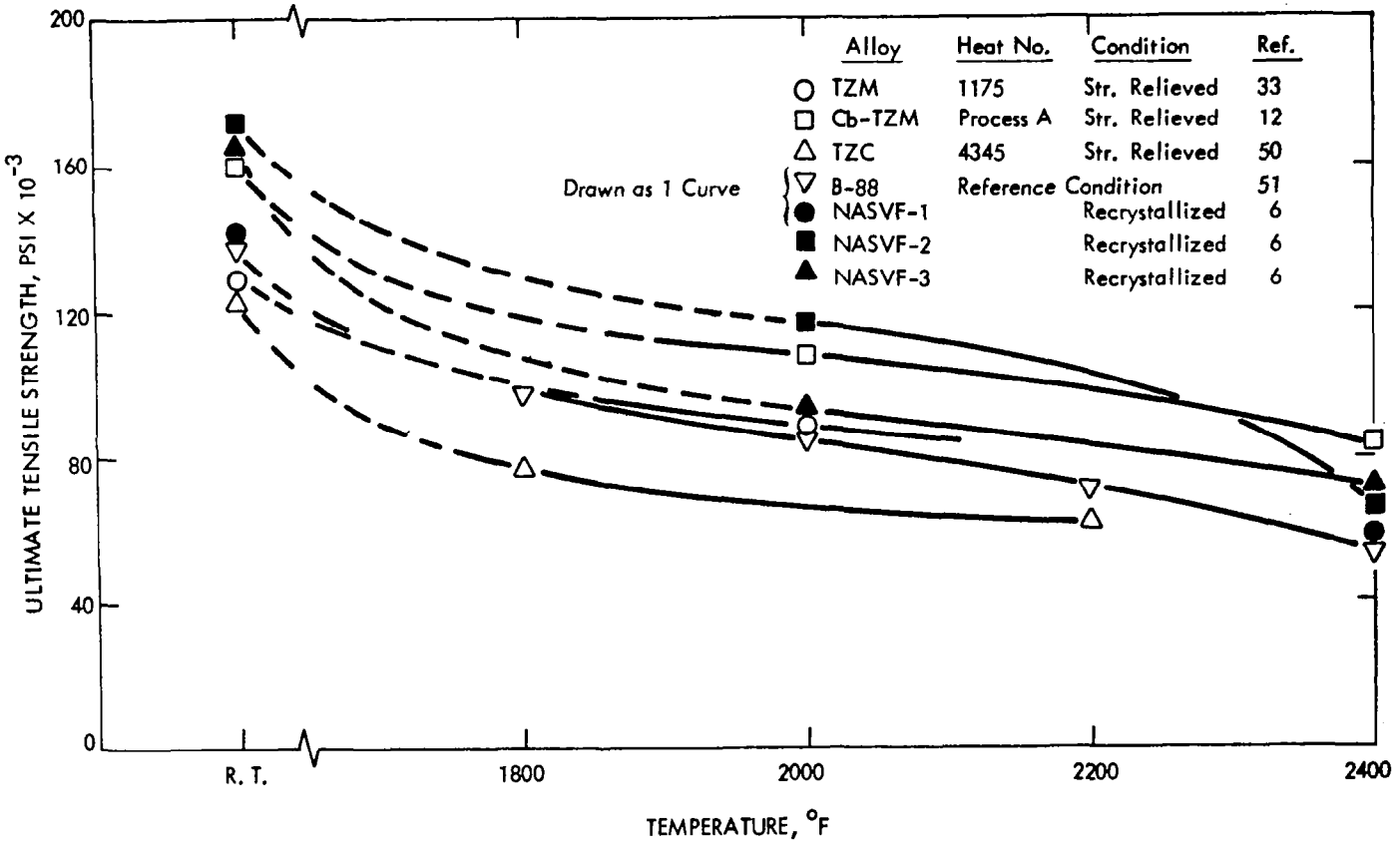

FIGURE 7 - Ultimate Tensile Strength vs. Temperature for Forging Alloys

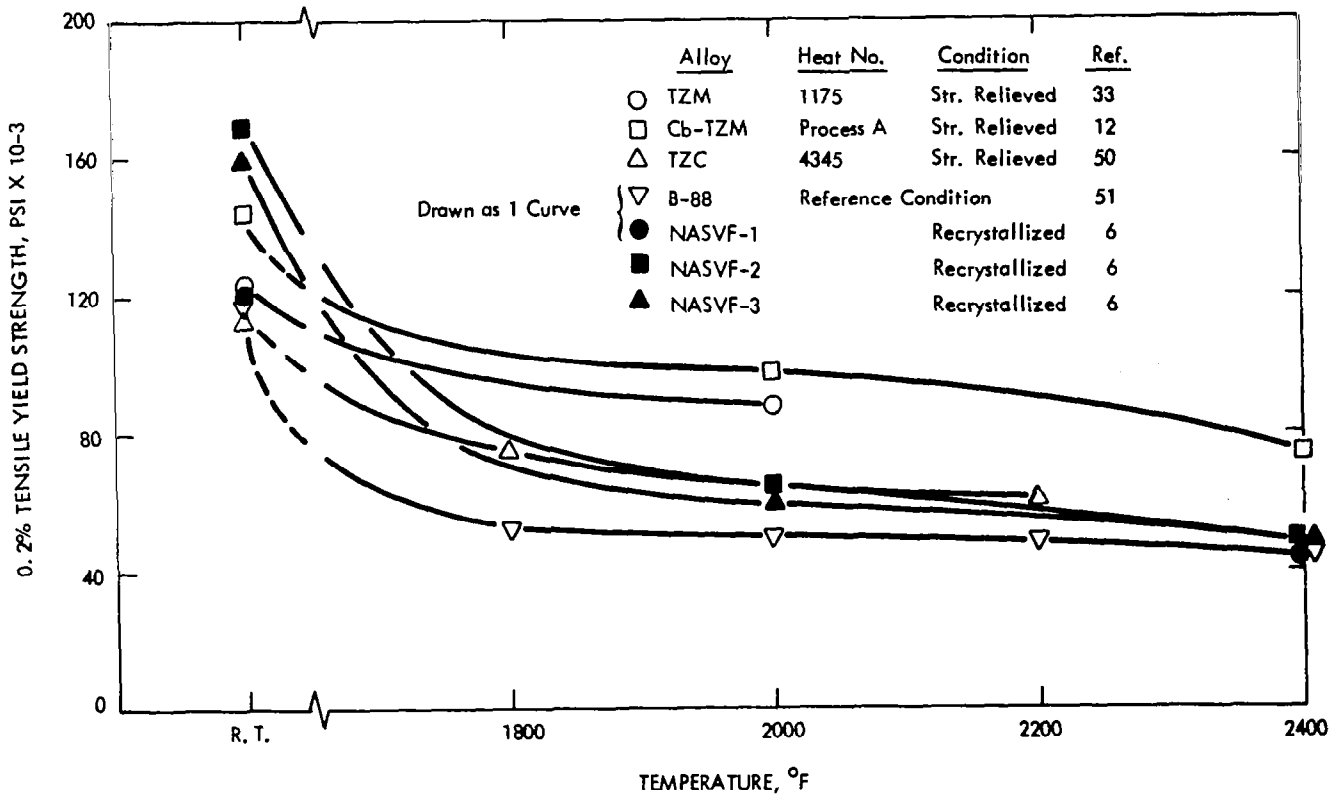

FIGURE 8 - Tensile Yield Strength vs. Temperature for Forging Alloys

Creep data for these alloys, again using the Larson-Miller parameter, is shown in Figure 9. For similar reasons to those previously discussed for the fabricable alloys a common parameter constant of 20 was chosen for this plot. Considerable difficulty was encountered in reducing this data to a form which provides some measure of comparison. Hence, both 0.5% and 1.0% creep data are represented in Figure 9 for ease of comparison even though the 0.5% value is the design criterion. Of the data shown in Figure 9 only TZM and TZC data points are from tests greater than a few hundred hours duration. Pertinent comments on this data follows for the various alloys.

TZM: Only long time test data for heat KDTZM 1175 is plotted. This heat was specially processed as a pancake forging to develop exceptional creep strength. In analyzing data for TZM alloy this heat consistently displayed superior properties. The fact that this data is for a forging enhances its value. However, the general scarcity of pertinent long-time data is evident.

TZC: Only data for stress-relieved TZC is shown. Although partially recrystallized TZC alloy tended to display a slightly better creep strength than stress-relieved material it is not plotted in Figure 9 due to its extremely low ductility. The data on Table A14 is from a program being conducted by TRW, Inc.[11] and represents material with wide variations in thermal-mechanical treatment. Hence, discretion must be exercised in evaluating this data. Again, the scarcity of data is apparent. Although reasonable strength is developed in this alloy, commercial background is lacking and is apparently not forthcoming.

B-88: The 1.0% creep data of Table A18 and Figure 9 was taken from short-time (under 100 hours usually) creep-rupture tests. These tests were on swaged rod processed to give a good combination of mechanical strength and ductility. The lack of long time data is representative of the developmental nature of this alloy.

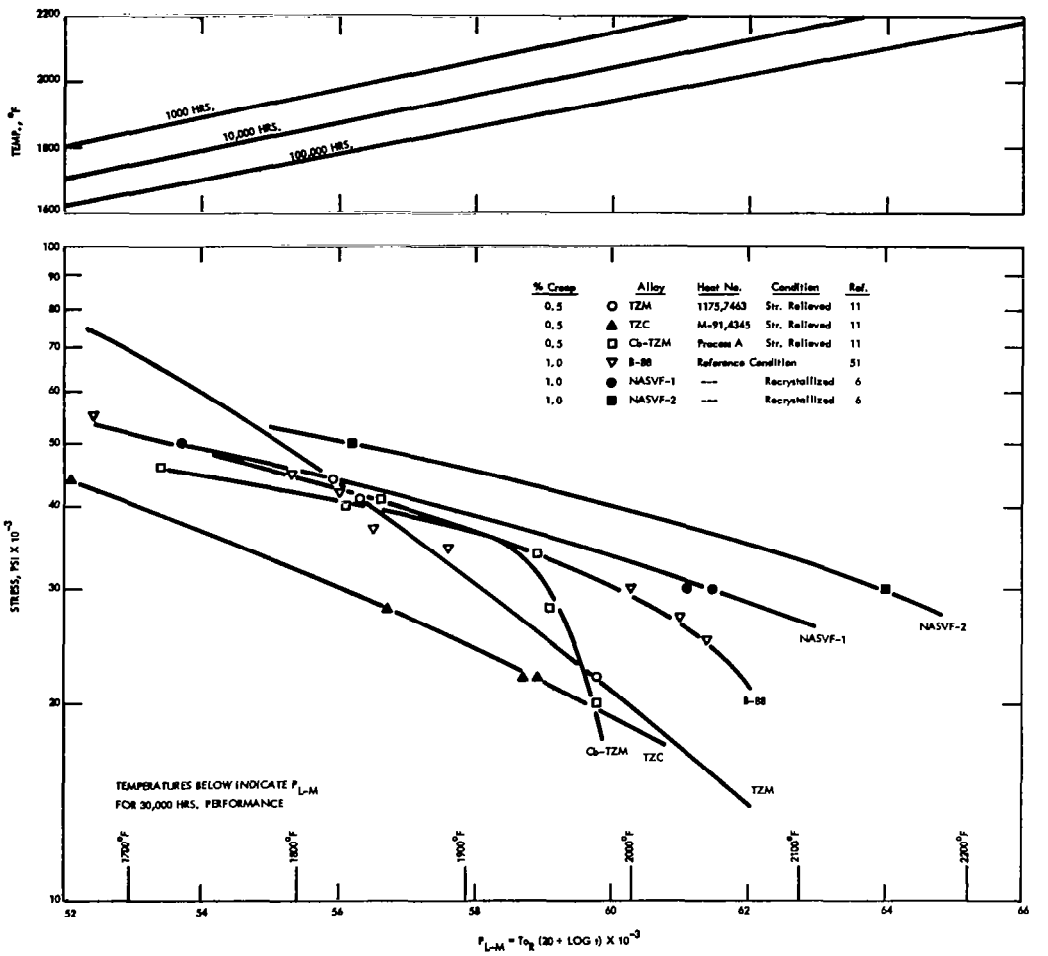

FIGURE 9 - Larson-Miller Plot of Creep Data for Forging Alloys

Cb-TZM: The 0.5% creep data shown in Figure 9 and given in Table A16 is from the TRW program and are the only creep data available for this alloy. The tests were made on stress-relieved swaged bar obtained commercially from Climax Molybdenum Co. of Michigan. Due to a limited amount of material the same specimen was tested at five different stress-temperature conditions and extrapolations to 0.5% creep were made based on observed secondary creep rates. No tensile data are available for this material and it is difficult to relate this creep data to the tensile data generated by Perkins and Lytton[12] which is given in Table A15 and Figures 7 and 8. Perkins and Lytton have demonstrated the profound influence of processing variables on this alloy and have also contributed considerably to an understanding of the strengthening mechanisms involved. This work should provide extremely useful information on the future development of this alloy for long-time applications. Again, it is important to keep in mind the dynamic nature of the state-of-the-art for this and similar alloys with respect to applications of this type.

Other data that has been generated on the mechanical properties of this alloy can be found in the Appendix. Due to the critical nature of variations in thermal-mechanical history and the fact these data represent material having a broad range of process histories, discretion is to be exercised in its use. It is pertinent to note that even where no attempt has been made to optimize the materials being tested, comparisons of strength, creep-rupture, secondary creep rate, etc. indicate that Cb-TZM will be an extremely promising alloy.

Ta-Base Alloys (NASVF-Series): As mentioned previously, data for these alloys have been included to show their growth potential. The 1% creep data of Figure 9 were extrapolated from relatively short-time tests. Due to the necessarily limited amount of material available in a development program, the same specimens were tested at several different temperatures.

Based on an overall evaluation of the data it is felt that TZM, if properly processed, is capable of performing at a level consistent with the requirements of the turbine design.

Additional design data is provided for this alloy in the Appendix. The columbium modification (Cb-TZM) displays considerable promise for future potential. Its potential has been considerably enhanced recently by the appreciation of strengthening mechanisms (and structures) which can be achieved through proper processing.

V. LIQUID METAL COMPATIBILITY

SUMMARY: Liquid metal-refractory metal corrosion and compatibility tests were reviewed and summaries of those studies conducted under conditions comparable to the proposed KTA system operating conditions are presented. Potassium-refractory metal alloy system studies in solubility, corrosion, and mass transport are compared, and extrapolations to the KTA system are made. In summary, potassium corrosion of selected KTA refractory metal alloys will be negligible if (1) gettered refractory metal alloys are employed, and (2) if oxygen concentration levels in the system are kept low (i.e., less than 10 ppm in potassium). The effects of liquid and vapor potassium on the mechanical properties of the chosen KTA turbine materials, T-111 and TZM, will be negligible.

A. ALLOY SELECTION

Material choices for the AiResearch Potassium Turbo-Alternator System turbine have been resolved to the gettered refractory metal alloys, primarily TZM and T-111. TZM will be employed for the tie-bolt and forged rotor discs and blades. T-111 will be used for stationary hardware particularly in the first five stages with a temperature range of 2150 to 1800°F across these stages. Portions of the remainder of the stationary structure could be made of Cb-1Zr to save weight although the present design is for T-111 only. Stationary foil laminate assemblies will be used as interstage seals. The foil will be T-111 or Cb-1Zr. Choice of a bearing material (950°F potassium environment) depends upon the outcome of property analyses and compatibility analyses of several material choices, the most promising of which are the refractory metal bonded carbides such as TiC-Cb and WC-Mo[1].

Of particular concern in liquid metal compatibility are the following considerations:

- Will the chosen turbine alloys resist excessive dissolution corrosion and material loss? Grain boundary corrosion in particular could seriously weaken the alloys. Liquid metal solubility analyses should reveal the relative susceptibility of individual alloy constituents to preferential leaching from the alloy base. If more soluble alloy constituents collect at grain boundaries, serious structural weakening could result from their preferred dissolution.

- Mass transport of dissimilar metals via the interconnecting liquid metal couple by activity gradient or compositional gradient forces could seriously alter alloy properties. Especially detrimental effects would result from the migration of carbon, oxygen, titanium, or zirconium constituents.

- The presence of high oxygen levels in liquid metals seriously influences the compatibility (corrosion characteristics) of the refractory metal alloys. Tests should illustrate which alloys are least affected and to what level oxygen can be safely tolerated.

B. SOLUBILITY TESTS

The dangers of high alloy constituent solubilities has already been mentioned. A high solubility could lead to rapid material removal in a closed loop due to a dissolution/precipitation mechanism between the hot and cold legs of the loop. Also, solubility differences could lead to preferential and discriminatory dissolution of individual alloy constituents and result in severe strength losses.

The attainment of accurate solubility information in liquid metal systems is difficult. The diversity of data for similar systems attests to this difficulty. Elemental solubilities in potassium are affected by the presence of oxygen, other constituents, flow rates, etc., and experimental techniques are deficient. Analysis at reasonable temperatures requires cooled and quenched samples. During cooling solute precipitation results from temperature dependent

solubilities. Thus, solutions must be decanted prior to cooling so that precipitates can be collected in a container of a second material. Dissimilar metal effects can occur. Oxygen levels raise or lower solubilities proportionately. Centrifuging the liquid solvent at temperature is also performed prior to decanting in order to remove particulate solutes. Such problems illustrate the difficulty of attaining precise solubility information. Consequently, such information that is available should be regarded with proper skepticism.

Several investigators have pursued solubility information pertinent to the KTA system. Litman[13] has found the solubility of Mo and Zr in potassium at 815°C to be 10 ppm or less for oxygen levels of less than 1000 ppm. This compares with the work of Cleary et al[14] who found Mo solubility in potassium to be less than 1 ppm at temperatures below 1200°C for oxygen levels below 25 ppm. Cleary et al also found, however, that Mo solubility in potassium increased to 500 ppm in the 700-1200°C range if the oxygen level in the potassium was increased to 500 ppm. McKisson et al[15] also found the Mo solubility in potassium to be less than 14 ppm between 1000-1200°C for oxygen levels less than 15 ppm.

The solubilities of other refractory metal alloy gettering constituents such as Ti and Zr in potassium were found by Ginell and Teitel[16] to range from 40 to 130 ppm in the 1200-1300°C range for less than 10 ppm oxygen in potassium. General trends from these and other studies indicate that the getter additions to refractory metal alloys are slightly more soluble than their alloy base constituents.

Refractory metals are the least soluble metals in alkali liquid metals[17]. If the oxygen content of liquid metals is low (<10 ppm), then the solubilities of the refractory metals will be inconsequential in terms of corrosion considerations.

C. CAPSULE TESTS

Capsule tests are employed to survey the general corrosion tendencies and characteristics of selected materials by liquid metals. These tests are economical alternatives to full system

studies and are used to qualitatively screen material choices for alkali metal systems. Gross corrosion effects as well as dissimilar metal mass transport, grain boundary corrosion, and effects of oxygen can be determined by this test method. Materials which appear compatible with liquid metals by capsule testing may still be incompatible in a full system (because of fluid flow rates, hot and cold loop legs, etc.). However, instances of this reversal in compatibility are the exception.

Capsule tests investigating the compatibility of KTA materials with potassium have been performed. Hoffman[18] reports the testing of TZM inserts in two Cb-1Zr refluxing capsules in potassium at 1100°C for 2500 and 5000 hours. Although the TZM was slightly decarburized, there was no evidence of corrosion or activity gradient mass transfer between the Cb-1Zr and the TZM. Simons and Lagedrost[19] refluxed boiling potassium in TZM capsules from 815 to 1260°C for 5000 hours. The oxygen content of the potassium varied from 20 to 500 ppm. There was no attack of the TZM with low oxygen potassium. Mass transfer of Mo and Ti occurred at the liquid-vapor interface as the oxygen content of the potassium was increased.

Scheuerman and Barrett[20] investigated the compatibility of Cb-1Zr, T-111, and T-222 capsules from 900 to 1300°C for 4000 to 10,000 hours with refluxing potassium. No corrosive attack was noted in any of the refractory alloys investigated. Ta-10W capsules tested from 980 to 1200°C (with the same 20 ppm or less oxygen liquid potassium) showed intergranular attack to 16 mils. Alloys with oxygen getters (Ti, Zr, Hf) were concluded to be more resistant to attack by potassium because of their ability to tie up the oxygen and prevent it from entering the corrosion reactions. Concurrence with these observations has also been expressed by other investigators[21,22,23].

Chandler[24] has shown pure Cb to possess excellent compatibility with boiling potassium to 2400°F. Pure Ta, however, was found to lose weight in liquid potassium in direct proportion to the amount of oxygen present in the potassium (50-3000 ppm)[25]. At temperatures above 600°C and with oxygen levels greater than 20 ppm, Ta was found to suffer intergranular attack.

In general, capsule tests show that TZM, Cb-1Zr, and T-111 have acceptable compatibility with refluxing and boiling potassium for the temperature conditions that will be present in the KTA turbine. Again, this is with the reservation that the oxygen contamination of the potassium be confined to amounts less than 10 ppm. Ungettered refractory metals and alloys (such as pure Ta, or Ta-10W) should be avoided.

D. LOOP TESTS

Natural convection and pumped two phase loops simulate actual applications for refractory metal-alkali liquid metal systems to a greater extent than capsule tests. Materials that exhibit good liquid metal compatibility in the capsule tests are used for loop studies.

A Cb-1Zr loop with Cb-1Zr simulated turbine blades was operated at ORNL[26] for 3000 hours. The potassium vapor varied from 83 to 96% quality and flowed at 33 lb/hr (3100/1300 ft/sec). The liquid temperature varied from 1075 to 355°C and the vapor temperature from 1100 to 690°C. No corrosion or erosion was detected in the system except for a 1 mil deep roughening found in a second stage blade specimen. This erosion was believed to be the result of low quality potassium vapor impinging on the blade leading edge.

A Cb-1Zr two phase forced loop with TZM simulated turbine blades was operated for 5000 hours at G. E.[25]. The TZM blades and nozzle operated at 1100°C in 20-40 lb/hr (830-1350 ft/sec) potassium vapor (1100°C) of 88% quality. Post test examination of the TZM blades revealed no signs of attack, interstitial migration, or liquid metal-caused material degradation.

The effect of high velocity flow rates on TZM simulated turbine blades was studied in potassium vapor at 1385°F at 535 ft/sec in a 3000 hour test[27]. The maximum corrosion/erosion found was less than 1 mil. Conclusions were that the corrosion by potassium vapor would be negligible in such systems if the vapor quality could be kept high. This finding together with Janson and DeVan's[26] observations for low quality potassium vapor in the Cb-1Zr turbine simulator recommend interspool moisture removal and/or an interspool reheating to prevent turbine blade erosion due to low quality vapor.

These studies plus others[28] indicate that TZM, Cb-1Zr, and T-111[29] will exhibit no serious incompatibility with potassium liquid or vapor under the operating conditions proposed for the KTA turbine. Serious dissolution corrosion or dissimilar metal coupling should not be expected if oxygen levels in the system are kept low (less than 10 ppm in the potassium). The only notable metal removal found in potassium vapor turbine simulation studies has been when low quality vapor was used. Although TZM-316 SS systems have exhibited temperature gradient and activity gradient mass transport[25] above 2200°F (Zr, N, O, and C), no such effects have been noted for TZM in an all refractory metal system.

E. MECHANICAL PROPERTIES IN POTASSIUM

Extensive mechanical property analysis of stainless steels in liquid sodium have been performed[30]. Unfortunately, little information is available on the mechanical properties of refractory metal alloys in liquid potassium. The yield strengths of TZM test pieces after 3000 hours exposure in 730-1070°C boiling potassium were not seriously different from those of TZM pieces exposed to the same temperature in argon[31]. Creep rupture tests of TZM in saturated potassium vapor for periods to 1539 hours at 1100°C reveal no significant effects by the potassium vapor over non-potassium conditions[32]. Other investigators report the same findings[33]. The fatigue properties of TZM have also been reported as being unaffected by potassium[34].

F. BEARING MATERIALS

Several programs have investigated the effects of alkali liquid metal environments on bearings and seals[1,35,36,37]. The most exhaustive is that reported by Frank[1,38] in which the compatibility of several bearing materials with potassium is considered. The materials were: (1) Non-refractory metals and alloys; (2) Refractory metals and alloys; (3) Fe-Ni-Co bonded carbides; (4) Carbides; (5) Oxides; (6) Borides; and (7) Refractory metal bonded carbides. The bearing materials for the KTA design must operate at temperatures up to 1000°F. In the work reported by Frank potassium compatibility test temperatures to 1600°F were evaluated in order to further state-of-the-art experience.

Cb-1Zr capsule potassium compatibility tests at 1600°F showed that the oxides (Lucalox, Zircoa 1027), the non-refractory metals and alloys (Star J), and the Fe-Ni-Co bonded carbides all incurred serious weight and dimensional changes. Oxygen in the potassium varied from 11 to 32 ppm. TiC (Cb binder) appeared to possess stability in liquid potassium to 1600°F. WC (Grade 7178) was suspect to corrode in potassium at 1200°F (but did not corrode at 1000°F or less). A weight loss through carbon migration was noted.

Liquid potassium friction and wear tests were conducted[1] between the most promising high temperature bearing material combinations at 400 and 800°F. The combinations were TZM-7178, 7178-7178, and TiC(10%Cb)-TiC(10%Cb). Although the data are still preliminary, results indicate that the TiC(10%Cb)-TiC(10%Cb) test incurred the lowest weight loss, wear rate and displayed the lowest friction of the three combinations.

Although the bearing tests of Reference 1 have not been completed, tentative results indicate that the materials of the three tests mentioned above would serve well at the design rated temperature of 1000°F. Mechanical compression tests conducted in this program indicated that the 7178 grade has a ductility advantage over the TiC(10%Cb) which is of considerable importance in designing the turbine bearings.

G. FABRICATION REQUIREMENTS

Requirements for proper handling of refractory metals and their alloys from the standpoint of cleanliness, both for general handling and for liquid metal service, have received wide acknowledgement[4,5,7,25,59,60]. Proper handling to maintain uncompromised cleanliness is essential to avoid metallurgical degradation before or during service and also to assure adequate corrosion resistance. Specifically, oxygen contamination degrades corrosion resistance, and oxygen which has not been fixed by reaction within the gettered alloy can promote corrosion. Welds are particularly susceptible since thermal disturbance or slight surface contamination during welding results in the presence of uncombined oxygen. This is alleviated by post weld annealing. Hence, welded assemblies must be designed to permit post weld annealing.

VI. TURBINE FABRICATION REVIEW

The preliminary turbine design incorporating the selected structural alloy T-111 and rotor alloy TZM was reviewed to assure that the design approach was reasonably representative of the state-of-the-art for these materials. This was done in some detail, but, recognizing that this function must be repeated in a very thorough manner during the future detail design study, only the most important manufacturing aspects are discussed briefly in this section. Detailed manufacturing plans were beyond the scope of this program.

The basic ground rule for the proposed design is that the stationary structure of T-111 be fabricated while the rotating hardware of TZM be machined from individual forgings and assembled mechanically. This doesn't preclude using forged T-111 components as indicated for several specific instances below. However, to satisfy design requirements the T-111 can be welded whereas the TZM may not be welded. The only restriction in welding T-111 is that it has recently demonstrated a tendency toward underbead cracking in multipass GTA plate welds[39]. This problem may be resolved directly in the near future or can be averted entirely by electron beam welding. Hence, no restrictions have been placed on welding of

T-111 at this point in time in the design study.

A. ROTATING HARDWARE

As previously indicated in the alloy selection discussion, the use of TZM for rotating hardware in this application requires development of precise techniques for achieving the required metallurgical structure. This stems from the fact that optimum creep properties must be obtained in the highest temperature components. These include the first three rotor discs which will be machined with integral blades to minimize service stresses, the front bearing stub shaft, and the tie bolt. The remainder of the discs are operating at lower temperatures for which the design becomes yield strength limited.

To achieve adequate creep strength TZM must be processed to provide a highly worked and stress relieved structure in which a fine carbide dispersion is developed. This has been done in a pancake forging using the following schedule:[33]

1. Ingot extrusion at 2250°F with a 3:1 reduction followed by recrystallization for 4 hours at 2800°F.
2. Swage forging at 3400°F (2800°F finish) for a 60 percent reduction followed by a 2 hour recrystallization at 2950°F.
3. Upset forge 4.75:1 at 2800°F(2160°F finish) and stress relieve at 2300°F.

The final upsetting operating in particular represents a considerable reduction. This will require use of intricate forging techniques. The permissible reheat, if any, between steps during final forging will have to be established. Development of an adequate forging schedule appears to be technically feasible. The general approach which would probably be taken in providing front and rear bearing stub shafts is shown in the following sketches. The sections on the left show approximately the manner in which the stub shaft would be machined from the final forging. The remaining numbered sketches depict the final forging sequence. The flared ends of these components contain the Gleason Curvic clutches which

engage the end rotor discs and hence are the most highly stressed area of the stub shafts. The forging sequence envisioned provides the greatest amount of working in the most highly stressed clutch area. It also provides structural flow lines properly oriented for maximum strength and toughness with respect to axial bending and rotational loads.

Front Bearing Stub Shaft:

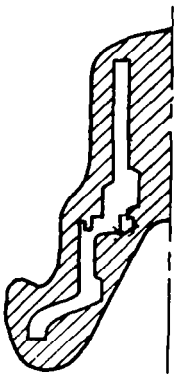

Closed Die Upset Forge

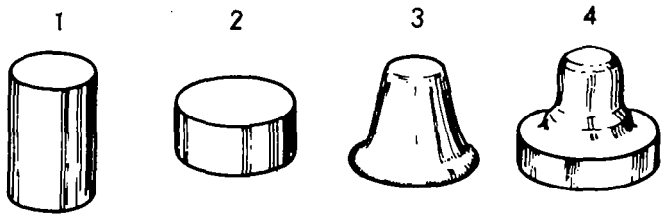

Rear Bearing Stub Shaft:

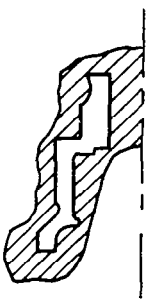

Upset

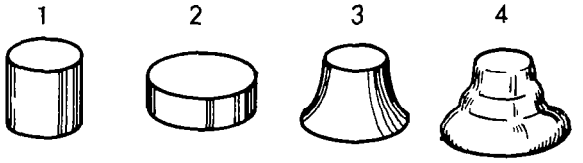

Step 1 represents the swage forged extrusion as recrystallized. This would be upset (Step 2) and then be closed die forged (Steps 3 and 4) to develop the final level of work and directional structure. As indicated, in this approach the final worked structure would be achieved in part by upsetting and in part by a combination of reversed upsetting and partial piercing in closed dies.

Rotor disc forging requires that special techniques be employed which achieve high strength in the area of the blades, hub and clutches. This likewise will require a complex forging schedule for the first five discs. One approach which might be taken is sketched below. Upsetting to partially work the blade area (Step 2) could be followed by piercing to work the hub area (Step 3) and closed die forging (Steps 4, 5, and 6) to further work the hub, blade, and clutch areas by reverse forging while simultaneously developing a favorable flow pattern.

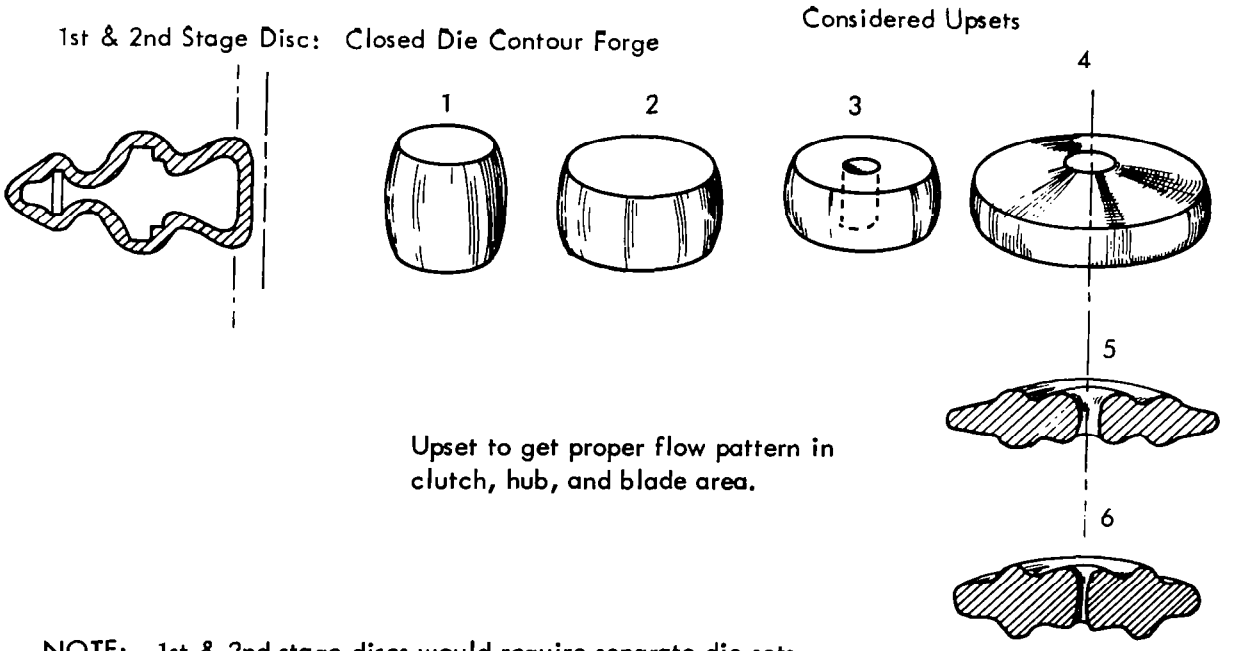

NOTE: 1st & 2nd stage discs would require separate die sets. Work and contour forge lines put into each are considered critical.

3-4-5 Stage Disc
Closed Contour Forged

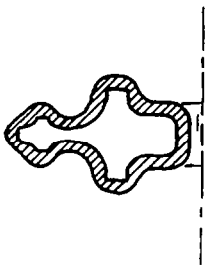

NOTE:

1. Contour discs for stages 3-4-5 could come from common set of dies. Forging shape each stage being the same.

2. It would be preferred to follow pattern of upsets similar to those developed for stage 1 and 2 dies. With exception of:
   2.1 Center may not have to be pierced and reverse upset.

The sixth through tenth stage discs could be forged using standard contour die forging practice:

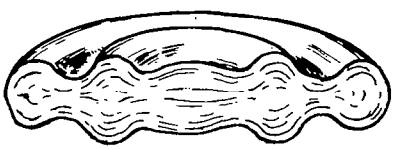

6th through 10th Stage Disc

1. Standard practice contour forge dies. Work material to get flow lines into clutch and tip area.

2. Should not have to pierce center as part of forge operations.

Finally, no particular difficulty is anticipated in achieving the proper amount of work and simple axial flow pattern required for the rotor tie bolt.

The general forging practice required for fabrication of the type of rotor components required appears to be practically the state-of-the-art. However, forging practice for TZM in this application is in the developmental stage. Hence, actual fabrication of TZM hardware should be preceeded with a development program for disc forgings coupled with a detailed disc design stress analysis and hot spin test. This would permit evaluation of the disc processing schedule, the effect of directionality in the disc structure, and adequacy of the design analysis for TZM.

B. STATIONARY HARDWARE

The basic turbine design was reviewed to assure that all stationary components, sub-assemblies and assemblies could be made from T-111 by forming, machining, welding or mechanically fastening. Cast components were not considered in this application since this process is not practiced with the fabricable refractory metal alloys. Since this necessitates extensive welding for sub-assembly fabrication, consideration was also given to the need for post weld annealing to assure corrosion resistance in potassium.

Although not applicable in this turbine design, casting is an ideal process for producing some of the intricate configurations required for stationary turbine hardware. Consequently, some of the assemblies will require quite complex handling to functionally replace components which would normally be made from castings. An example of this is the vaned inlet housing which would require fabrication using at least two complex machined components to replace one casting. The type of assembly which will probably be required for the inlet housing is shown in the following sketch of the turbine inlet in the vicinity of a vane:

Inlet Housing Fabrication

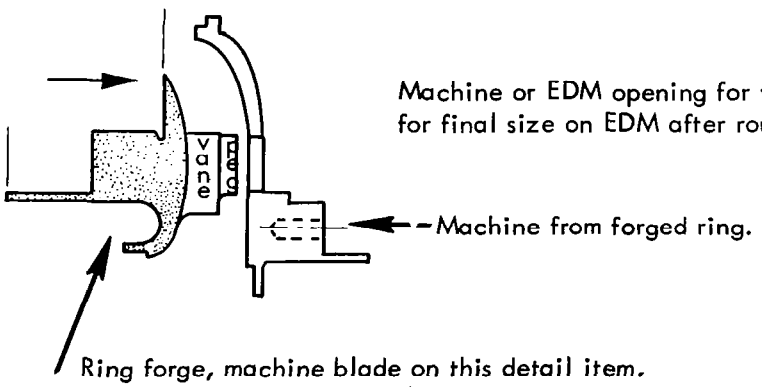

Modifications of this scheme can be readily visualized. Similarly, the exit housing of the turbine and interstage moisture removal inlet and exit will require adaptation of a combination of machined and welded components.

Many of the components of the turbine housing, the diaphragms and outer shrouds will be machined from large diameter T-111 rings. Selection of the process for obtaining these rings will be largely a matter of convenience and conservation of material. Ring forgings, fabricated rings (welded), or combination welded and forged (or rolled) rings could be used. As an example, the curvic clutched diaphragm outer shrouds each might require somewhat different processing either individually or in groups as illustrated below:

Diaphragm Outer Shrouds: (Gleason Curvic Clutched)

Inlet Guide Vane	-	Forge ring. (May be able to EDM in vanes).
1st Stage	-	Rolled & welded ring/alternate forged ring.
2nd Stage	-	Rolled & welded ring
3rd Stage	-	Rolled & welded ring
4th Stage	-	Rolled & welded ring

NOTE: Stage 2 thru 4 might be cut from a rolled and welded pot.

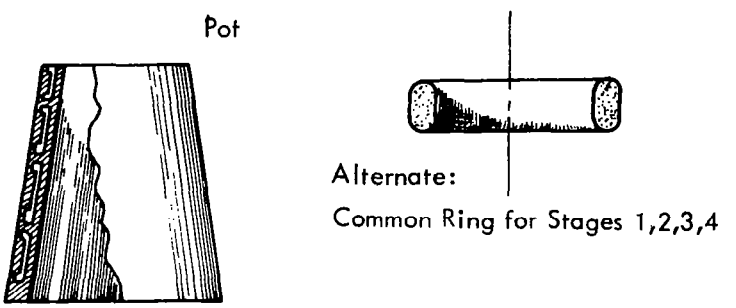

5th Transition Stage - Similar to inlet housing and guide vanes.
6th, 7th, and 8th Stage - Similar to Stages 1 thru 4.

In general, the detailed fabrication review demonstrated that no difficulties are anticipated which cannot be overcome by employing adequate precautions for machining, handling and fabrication of T-111. Difficulty can be expected in machining some of the complex contours required for the stator blades and vanes. Some experimental machining may be required in support of the design program in this area.

Since stress relief of weldments will be required for dimensional stability, no additional problems are introduced by the post weld annealing requirement for corrosion resistance. The proposed turbine design is uncluttered in this respect particularly in its use of a minimum number of dissimilar materials. Only TZM, T-111, and a special bearing material are definitely required in this turbine. It is anticipated that the tight tolerance requirements on this apparatus will pose some difficult handling problems. These will be associated with requirements for machining stacked and assembled components and subsequent disassembly for cleaning and final reassembly. The general problems of integration of the required machining sequences with turbine cleanliness requirements must be resolved at the initiation of the detailed design study.

VII. APPENDIX

The data provided in this Appendix is supplementary to that of the text and was compiled in support of the conclusions presented in the text and as general design data. Apparent contradictions will be noted in the data in some cases due to variations in processing and/or chemistry of tested materials. For this reason, wherever possible, pertinent process histories are included along with complete references.

A. Data Supplementary to Figures 1-9 in Text

1. Tensile and Creep Data for the Fabricable Alloys

2. Tensile and Creep Data for the Forging Alloys

3. Process History of Forging Alloys Tensile Specimens

4. Process History of Forging Alloys Creep Specimens

B. Additional Mechanical Property Data

1. Stress-Rupture Data for Molybdenum Base Alloys

2. Additional Creep Property Data for T-111 Alloy

C. Thermophysical and Miscellaneous Data for T-111 and TZM Alloys

1. T-111 Data

2. TZM Data

TABLE A1 - Tensile Properties of T-111

Test Temperature (°F)	0.2% Yield Strength (ksi)	Ultimate Tensile Strength (ksi)	Total Elongation (%)	Strain Rate (in/in/min)	Comments
-452	---	187.7	17.5	0.005	Reference (40)
-320	145.2	150.6	27.0	0.005	0.028 inch sheet;
-100	93.8	108.8	24.0	0.005	cold rolled 90% and
75	82.5	90.4	29.0	0.005	recrystallized 1 hr.
400	57.0	68.0	23.0	0.005	3000°F
800	43.2	57.2	15.5	0.005	
2000	34.9	61.1	18.0	0.050	
2200	28.6	49.3	25.0	0.050	
2400	23.5	37.3	36.0	0.050	
2700	24.4	30.9	30.0	0.050	
3000	11.9	14.8	48.0	0.050	
3500	12.6	13.0	34.0	0.050	

TABLE A2 - Creep Properties of T-111

Test Temp. (°F)	Stress (ksi)	Time and Corresponding Larson-Miller Parameter for 1% Creep		Heat No.	Test Material	Comments
		t(hrs.)	P_{L-M}[(a)]			
2200	8.0	2000	48.7	70616	0.030" Sheet	Reference (9)
2200	12.0	1140	48.0			
2120	12.0	3130	47.7			
1860	20.0	4800*	43.3			
2000	15.0	1350	44.6	D-1670		
1800	17.0	12000*	43.1			
2000	13.0	1900*	45.0	1102		
2200	21.3	45	44.3	DX-570	0.040" Sheet	Reference (10)
2500	8.3	117	50.5			
2500	9.2	93	50.2			
2400	10.0	300	50.0	NASV-1		
2400	12.7	119	48.8			
2400	14.1	42	47.5			
2400	14.7	42	47.5			
2400	15.2	18	46.5			
2500	12.7	26	48.6			

*Extrapolated

All material recrystallized 1 hr. at 3000°F prior to testing.

(a) $P_{L-M} = To_R\ (15 + \log t) \times 10^{-3}$

TABLE A3 - Tensile Properties of ASTAR-811C

Test Temperature (°F)	0.2% Yield Strength (ksi)	Ultimate Tensile Strength (ksi)	Total Elongation (%)	Comments
-320	147.7	165.3	26.3	Reference (3)
-150	111.0	130.3	28.5	0.040 inch sheet
R.T.	85.0	105.4	25.9	1 hr - 3000°F prior to testing
600	53.7	75.5	24.5	(Heat NASV-20)
1500	41.3	79.6	18.8	" "
2000	35.0	60.9	24.0	" "
2200	31.6	49.9	28.8	" "
2400	30.4	40.9	35.0	" "
2600	29.5	35.3	34.8	" "
2800	23.0	28.4	49.5	" "

TABLE A4 - Creep Properties of ASTAR-811C

Test Temp. (°F)	Stress (ksi)	Time & Corresponding Larson-Miller Parameter for 1% Creep		Comments
		t(hrs.)	P_{L-M} (a)	
2200	18.0	1,017	47.9	Reference (3)-0.040" Sheet
2400	15.0	262	49.7	1 hr. -3000°F prior to testing Heat NASV-20
2400	12.5	570	50.7	" "
2600	8.0	159	52.6	" "
2600	8.0	188	52.8	" "
2800	4.0	78	55.0	" "
2600	2.0	25,000*	59.4	Reference (41)-0.030" Sheet 1/2 hr. -3600°F prior to testing

* Extrapolated

(a) $P_{L-M} = To_R\ (15 + \log t) \times 10^{-3}$

TABLE A5 - Tensile Properties of FS-85

Test Temp. (°F)	0.2% Yield Strength (ksi)	Ultimate Tensile Strength (ksi)	Total Elongation (%)	Comments
R. T.	69.4	85.9	22.5	Reference (42)
400	52.5	68.0	20.9	0.030 inch sheet
800	39.9	54.1	18.6	1 hr. -2300°F prior to testing
1200	42.5	62.5	14.2	0.020 min^{-1} strain rate
1600	33.9	52.4	16.8	" " "
1800	32.3	44.9	16.9	" " "
2000	29.4	36.2	26.8	" " "
2300	21.7	25.0	36.5	" " "
2500	16.0	17.0	53.9	" " "
R. T.	84.3	98.2	18.0	Reference (43)
1800	59.5	71.2	7.0	Strain rates:
2000	45.3	52.9	19.0	0.005 min^{-1} to yielding
2200	---	40.8	38.0	0.05 min^{-1} to failure
2400	21.7	25.8	55.0	Stress relieved
				" " "

TABLE A6 - Creep Properties of FS-85

Test Temp. (°F)	Stress (ksi)	Time and Corresponding Larson-Miller Parameter for 1% Creep		Comments	Ref.
		t(hrs.)	P_{L-M} [a]		
2000	10.0	775	44.0	0.030 inch sheet; 1 hr. -2600°F tested in $<10^{-8}$ torr vacuum	44
2200	5.0	960	47.8	" " "	"
2000	10.0	835	44.0	" " "	45
2000	8.5	2480	45.2	" " "	"
2100	10.0	355	44.9	" " "	"
2200	4.0	1140	48.0	" " "	"
2200	6.0	425	46.9	" " "	"
1800	24.0	100	38.4	Creep-rupture data	46
1800	19.0	1000	40.7	1 hr. -2500°F prior to testing $<2 \times 10^{-7}$ torr vacuum	"
2000	14.0	100	41.8	" " "	"
2000	9.0	1000	44.2	" " "	"
2200	8.3	100	45.2	" " "	"
2200	2.0	1000	47.8	" " "	"
2600	1.6	100	52.0	" " "	"
2600	0.45	1000	55.1	" " "	"

(a) $P_{L-M} = To_R\ (15 + \log t) \times 10^{-3}$

TABLE A7 - Tensile Properties of D-43

Test Temp. (°F)	0.2% Yield Strength (ksi)	Ultimate Tensile Strength (ksi)	Total Elongation (%)	Comments
R. T.	75	95	14	Reference (42)
2000	39	46	14	0.040 Inch Sheet
2200	23	34	14	Stress Relieved 1 hr. -2200°F
2400	20	24	25	
2600	11.7	12	27	Strain Rate: 0.05 in/in/min.

TABLE A8 - Creep Properties of D-43

Test Temp. (°F)	Stress (ksi)	Time and Corresponding Larson-Miller Parameter for 1% Creep		Comments
		t (hrs.)	P_{L-M}(a)	
2000	10.0	530	43.6	Reference (44)
2000	8.52	900	44.1	Heat 43-387
2200	4.27	775	47.5	1 hr. -2600°F prior to testing Cb-9.59W-0.98Zr-0.107C
1800	12.5	1000	40.7	Reference (47)
1800	16.0	100	38.4	1 hr. -2200°F prior to testing
2000	7.3	1000	44.3	Cb-9.4W-0.95Zr-0.93C
2000	10.8	100	41.8	Creep Rupture Data
2200	4.0	1000	47.9	
2200	6.3	100	45.2	

(a) $P_{L-M} = To_R\ (15 + \log t) \times 10^{-3}$

TABLE A9 - Tensile Properties of Cb-1Zr

Test Temp. (°F)	0.2% Yield Strength (ksi)	Ultimate Tensile Strength (ksi)	Total Elongation (%)	Comments
R. T.	27.0	39.0	36	Reference (48) Recrystallized Sheet 1 hr. -2500°F
400	16.5	28.0	33	
800	12.5	29.0	32	
1200	12.5	32.0	24	
1600	12.0	30.5	26	
1800	10.5	27.0	22	
1900	10.0	23.0	26	
2000	9.0	17.5	37	

TABLE A10 - Stress Rupture Properties of Cb-1Zr

Test Temp. (°F)	100 Hr. Rupture Stress (ksi)	1000 Hr. Rupture Stress (ksi)	10,000 Hr. Rupture Stress (ksi)	Comments
1600	18.0	15.0	12.5	Reference (48)
1800	10.0	8.2	6.5	
2000	6.0 (41.8)	4.2 (44.3)	3.0 (46.7)	
2200	3.9	2.4	1.3	

Values in parentheses are Larson-Miller Parameter (P_{L-M}) where,
$P_{L-M} = To_R\ (15 + \log t) \times 10^{-3}$

TABLE A11 - Tensile Properties of TZM Forgings

Test Temp. (°F)	0.2% Yield Strength (ksi)	Ultimate Tensile Strength (ksi)	Total Elongation (%)	Comments
1400	63.1	66.3	12.8	Reference (49) 1 Hr. -2300°F prior to test Heat KDTZM 1312
1600	62.1	64.3	12.8	
1800	58.6	60.0	12.8	
1900	59.1	61.0	11.6	
2000	58.8	61.3	13.6	
				Reference (33)
R.T.	112.7	120.2	18.6	1 Hr. 2200°F Disc No. 1
2000	70.9	72.3	12.7	" " " "
R.T.	121.3	129.9	14.7	1 Hr. 2300°F Disc No. 3 (KDTZM 1175)
2000	87.5	88.3	12.2	" " " "
R.T.	121.9	127.9	17.4	1 Hr. 2200°F Disc No. 6
2000	77.1	78.8	11.5	" " " "

All tests in 10^{-5} torr vacuum

Strain Rates:

$0.005\ min^{-1}$ to 0.6% offset

$0.05\ min^{-1}$ to failure

TABLE A12 - Creep Properties of TZM Forgings

Test Temp. (°F)	Stress (ksi)	Time and Corresponding Larson-Miller Parameter for 0.5% Creep		Test Conditions		Comments
		t (hrs.)	P_{L-M} (d)	Heat No.	Pre-Test Heat Treatment	
2130	12.55	605	59.0	7502	1 Hr. 2200°F: Stress Relief	Reference (11)
2000	10.0	14,200*	59.3	7502	1 Hr. 2200°F: Stress Relief	
2000	10.0	25,000*	60.0	7502	1 Hr. 2850°F: Recrystallized	
2000	41.0	115	54.3	7502	1 Hr. 2200°F: Stress Relief	
1800	44.0	7,000	53.9	7502	1 Hr. 2200°F: Stress Relief	
1855	23.4	(a)	(a)	1175	1 Hr. 2300°F: Stress Relief	
1600	55.0	(b)	(b)	1175	1 Hr. 2300°F: Stress Relief	
1600	65.0	(c)	(c)	1175	1 Hr. 2300°F: Stress Relief	
1800	44.0	50,000*	55.9	1175	1 Hr. 2300°F: Stress Relief	
2000	22.0	20,000*	59.8	1175	1 Hr. 2300°F: Stress Relief	
2000	41.0	800	56.3	7463	1/2 Hr. 2250°F: Stress Relief	(Swaged bar)

*Extrapolated (based on secondary creep rate)

(a) Final 2600 hrs. showed - 0.002% creep strain: no extrapolation made

(b) Final 1250 hrs. showed 0.000% creep strain: no extrapolation made

(c) Only 0.030% Strain (after primary creep) during duration of test: no attempt made to extrapolate

(d) $P_{L-M} = T_{o_R} (20 + \log t) \times 10^{-3}$

TABLE A13 - Tensile Properties of TZC Plate

Test Temp. (°F)	0.2% Yield Strength (ksi)	Ultimate Tensile Strength (ksi)	Total Elongation (%)	Comments
R. T.	117.0	123.0	12.0	Reference (50) Heat 4345 1 Hr. 2500°F
1800	75.0	77.0	17.0	" "
2200	61.0	62.0	18.0	" "
R. T.	50.0	88.0	19.0	1 Hr. 3092°F
1800	27.0	63.0	29.0	" "
2000	24.0	61.0	28.0	" "
2200	25.0	54.0	29.0	" "
R. T.	99.0	106.0	4.0	Reference (50) Heat M-91 1 Hr. 2500°F
R. T.	49.0	85.0	7.0	1 Hr. 3092°F
1800	29.0	45.0	34.0	" "
2000	25.0	41.0	43.0	" "
2200	24.0	35.0	42.0	" "
R. T.	68.0	69.0	1.0	Reference (50) Heat M-80 1 Hr. 3092°F

TABLE A14 - Creep Properties of TZC Plate

Test Temp (°F)	Stress (ksi)	Time and Corresponding Larson-Miller Parameter for 0.5% Creep		Test Conditions		Comments
		t (hrs)	P_{L-M} (b)	Heat No.	Pre-Test Heat Treatment	
2200	18.0	1,225	61.4	M-80	1 Hr 3092°F: Partial RX	Reference (11)
2200	17.0	2,940*	62.4	M-80	1 Hr 3092°F: Partial RX	Heat M-80: Rolled Plate
1856	25.0	(a)	(a)	M-80	1 Hr 3092°F: Partial RX	Heat M-91: Rolled Plate
2056	19.0	50,000*	62.1	M-80	1 Hr 3092°F: Partial RX	Heat 4345: Forged Plate
2000	20.0	12,400	59.2	M-80	1 Hr 3092°F: Partial RX	
2200	22.0	70	58.1	M-91	1 Hr 2500°F: Partial RX	
1935	20.0	17,000*	58.1	M-91	1 Hr 2500°F: Partial RX	
1900	22.0	9,700	56.6	M-91	1 Hr 2500°F: Partial RX	
1800	44.0	1,100	52.1	M-91	1 Hr 2300°F: St. Relief	
2000	28.0	1,200	56.7	M-91	1 Hr 2300°F: St. Relief	
2000	22.0	7,740	58.7	4345	1 Hr 2500°F: St. Relief	
2000	22.0	9,100*	58.9	4345	1 Hr 2400°F: St. Relief	

* Extrapolated (based on secondary creep rates)

(a) Only 0.004 percent creep strain during final 7400 hours of test: therefore, no attempt was made to extrapolate.

(b) $P_{L-M} = T_{o_R} \ (20 + \log t) \times 10^{-3}$

TABLE A15 - Tensile Properties of Cb-TZM

Test Temp. (°F)	0.2% Yield Strength (ksi)	Ultimate Tensile Strength (ksi)	Total Elongation (%)	Comments
-72	160.5	175.0	11.5	1 Hr 2400°F prior to testing
-22	158.1	171.7	10.4	
77	144.6	160.3	9.8	
2000	97.4	107.5	10.4	
2400	73.0	82.3	12.5	
2600	58.9	67.5	15.6	
3000	18.6	26.7	25.0	
-49	119.8	123.7	10.0	1 Hr 3100°F prior to testing
-13	106.8	119.5	12.5	
77	85.1	106.2	19.0	
2400	26.0	41.3	25.0	
3000	10.8	19.8	26.5	

Reference (12)

Process A 0.040 in. sheet

TABLE A16 - Creep Data for Cb-TZM

Test Temp. (^{o}F)	Stress (ksi)	Time and Corresponding Larson-Miller Parameter for 0.5% Creep		Comments
		t (hrs.)	P_{L-M}[(a)]	
2000	20.0	20,000*	59.8	Reference (11) 5/8" Diameter swaged bar 1 hr. -2500^{o}F prior to testing Heat 4305 - 4
2000	28.0	10,000*	59.1	
2000	40.0	630*	56.1	
1800	46.0	4,000*	53.4	
2100	34.0	1,000*	58.9	
2000	41.0	1,090	56.6	

*Extrapolated

(a) $P_{L-M} = To_{R} (20 + \log t) \times 10^{-3}$

TABLE A17 - Tensile Properties of B-88

Test Temp. (°F)	0.2% Yield Strength (ksi)	Ultimate Tensile Strength (ksi)	Total Elongation (%)	Comments
-110	146.6	151.0	1.0	Reference (51) Strain Rate: $0.05\ min.^{-1}$
R.T.	119.3	137.3	11.3	
200	102.0	107.0	16.7	
600	80.0	98.0	19.3	
1200	59.8	97.0	16.0	
1400	53.5	99.7	17.0	
1600	51.4	95.7	17.0	
1800	52.5	97.0	17.0	
2000	50.2	86.0	16.0	
2200	48.8	71.3	14.0	
2400	45.0	53.4	19.0	
2500	43.2	46.8	22.0	

Processing Data: (Reference Condition)
Double Vacuum Arc Melted
Extruded at 3500°F, 5.5:1 Reduction Ratio
Swaged at 2370°F to 0.440" Dia. Bar Stock: 85% Reduction in Area
1 Hr. at 3090°F (Helium gas quench)

TABLE A18 - Creep-Rupture Properties of B-88

Test Temp. (°F)	Stress (ksi)	Time and Corresponding Larson-Miller Parameter for 1% Creep		Comments
		t(hrs.)	P_{L-M}[(a)]	
2000	55	18.5	52.4	Reference (51) Data taken from creep-rupture tests of swaged rod in reference condition (see processing data at bottom of Table A17)
2200	45	6.0	55.3	
2200	42	11.2	56.0	
2200	37	18.5	56.5	
2200	34.5	47.0	57.6	
2400	30	12.4	60.3	
2400	27	21.0	61.0	
2400	25	27.0	61.4	

(a) $P_{L-M} = To_R\ (20 + \log t) \times 10^{-3}$

TABLE A19 - Tensile Data for Ta-Base Forging Alloys
(NASVF-Series)

Test Temp. (°F)	0.2% Yield Strength (ksi)	Ultimate Tensile Strength (ksi)	Total Elongation (%)	Comments
R. T.	119.2	139.9	28.0	NASVF-1 Ta-13W-1.5Re -0.7Hf-0.025C
2400	44.0	58.3	29.0	
R. T.	170.0	172.0	1.85	NASVF-2 Ta-16W-2Re -0.7Hf-0.025C
2000	72.7	115.6*	8.7*	
2400	49.5	65.6	31.5	
R. T.	160.1	166.0	16.0	NASVF-3 Ta-13W-1.5Re -0.7Hf-0.03N
2000	61.0	92.3	14.0	
2400	49.6	72.4	8.0	

*No fracture - reached load limit of machine.

Reference (6)
Processing Data (all compositions):
Double Arc Melted (1.25 to 1.40 inch dia. ingots)
Extruded in moly cans to approximately 0.6 inch dia.
Annealed 1 hr. at 3000°F
Swaged (2200-2550°F) to 3/8 inch dia. rod
Annealed 1 hr. at 3270°F prior to tensile testing

TABLE A20 - Creep Data for Ta-Base Forging Alloys (NASVF-Series)

Test Temp. (°F)	Stress (ksi)	Time and Corresponding Larson-Miller Parameter for 1% Creep		Comments
		t (hrs.)	P_{L-M}[(a)]	
2250	30.0	380	61.1	NASVF-1 1 hr. -3270°F prior to testing
2300	30.0	185	61.5	
2400	30.0	52	62.0	
1850	50.0	965	53.1	
1900	50.0	1110	54.4	
2000	50.0	13	52.0	
2350	30.0	450	63.6	NASVF-2 1 hr. -3630°F prior to testing
2400	30.0	384	64.5	
1950	50.0	1600	55.6	
2000	50.0	1340	56.9	
2050	50.0	825	57.5	

Reference (6)

(a) $P_{L-M} = To_R\ (20 + \log t) \times 10^{-3}$

NOTE: Data based on one specimen per stress level per alloy. Each tested as listed, lowest temperatures first.

TABLE A21 - TZM Tensile Specimen Process History

Heat KDTZM 1312 (See Table A11)

Mo-0.42Ti-0.085Zr-0.014C (Reference 49)

1. Machine arc-cast ingot to 5" diameter by 8" long billet
2. Forge at 2830°F (finishing temperature 2200°F) to 9-1/2" diameter by 1-3/4" thick pancake
3. Stress relieve 1 hour at 2300°F and air-cool

Heat KDTZM 1236B - Disc No. 1 (See Table A11)

Mo-0.46Ti-0.09Zr-0.022C (Reference 33)

1. Vacuum arc cast ingot and machine to 8" diameter
2. Extrude at 2200°F to 4-1/4" diameter by 4" long billet
3. Recrystallize 4 hours at 2800°F
4. Forge at 2200°F (finishing temperature 1800°F) to yield 9" diameter by 3/4" thick pancake
5. Stress relieve 1 hour at 2300°F

Heat KDTZM 1175 - Disc No. 3 (See Table A11)

Mo-0.61Ti-0.12Zr-0.035C (Reference 33)

1. Vacuum arc-cast 11-3/4" diameter ingot
2. Machine to 10-3/4" diameter
3. Extrude to 6-1/2" diameter at 2250°F (3:1 reduction)
4. Recrystallize 4 hours at 2800°F
5. Forge at 3400°F (finishing temperature 2800°F) to 4-1/8" diameter
6. Recrystallize 2 hours at 2950°F
7. Forge at 2800°F (finishing temperature 2160°F) to yield 9" diameter by 3/4" thick pancake
8. Stress relieve 1 hour at 2300°F

TABLE A21 Continued

Heat TZM 7492 - Disc No. 6 (See Table A11)

Mo-0.43Ti-0.10Zr-0.014C (Reference 33)

1. Extrude 12" diameter ingot at 2000°F to 7-1/4" diameter
2. Recrystallize 1 hour at 3000°F
3. Solution treat (in Argon) 1 hour at 3800°F and water quench
4. Extrude at 2250°F to 4-1/4" diameter x 4" long billet
5. Stress relieve 1 hour at 2250°F
6. Forge at 2200°F (finishing temperature 1915°F) to yield 9" diameter by 3/4" thick pancake
7. Stress relieve 1 hour at 2200°F

TABLE A22 - TZC Tensile Specimen Process History

Heat TZC M-80 (See Table A13)

Mo-1.02Ti-0.170Zr-0.080C (Reference 50)

1. Vacuum arc cast 5.88" diameter ingot
2. Machine to 5" diameter
3. Extrude at 3092°F to 4-1/8" x 2.22" plate (2.3:1 reduction)
4. Cross-roll at 2925°F in hydrogen atmosphere to 0.740" thick; 4% reduction per pass

Heat TZC M-91 (See Table A13)

Mo-1.17Ti-0.270Zr-0.046C (Reference 50)

1. Vacuum arc cast 5.88" diameter ingot
2. Machine to 5" diameter
3. Extrude at 3092°F to 4-1/8" x 2.22" plate (2.3:1 reduction)
4. Cross-roll at 2912°F in hydrogen atmosphere to 1.435" thick
5. Cross-roll at 2372°F in hydrogen atmosphere to 0.714" thick

Heat TZC 4345 (See Table A13)

Mo-1.19Ti-0.16Zr-0.075C (Reference 50)

1. Machine vacuum arc cast ingot to 5.85" diameter
2. Extrude to 3" diameter (3.8 reduction)
3. Vacuum heat treat at 3000°F
4. Machine to 2.4/2.8" diameter
5. Upset forge 40% at 2400°F
6. Broad forge to 0.825" thick at 2400°F
7. Vacuum heat treat 1 hour at 2400°F
8. Machine to 0.70" thick

TABLE A23 - Cb-TZM Tensile Specimen Process History

Process A Sheet (See Table A15)

Mo-1.51Cb-0.38/0.41Ti-0.21/0.26Zr-0.077/0.081C (Reference 12)

1. Vacuum arc-cast ingot
2. Homogenize 2 hours at 3000°F
3. Extrude at 3000°F
4. Solution anneal 10 min. at 3800°F + 2 hours at 2900°F
5. Forge at 2900°F to 1/2" sheet bar
6. Solution anneal 10 min. at 3800°F + 2 hours at 3000°F
7. Cross-roll 69% at 2000°F
8. Stress relieve 1 hour at 2400°F
9. Straight roll 70% to 0.040" sheet at 1832°F:
   total 91% cold work from last recrystallization anneal

TABLE A24 - TZM Creep Specimen Process History

Heat TZM 7502 (See Table A12)

Mo-0.44Ti-0.10Zr-0.010C (Reference 11)

1. Vacuum arc cast 11-1/2" diameter ingot
2. Machine to 10-3/4" diameter
3. Extrude to 6-1/4" diameter (3:1 reduction)
4. Heat treat at 2700°F
5. Upset forge at 2200°F to 3/4" thick pancake
6. Stress relieve 1 hour at 2200°F

Heat KDTZM 1175 (See Table A12)

Mo-0.48Ti-0.114Zr-0.024C (Reference 11)

1. Vacuum arc cast 11-3/4" diameter ingot
2. Machine to 10-3/4" diameter
3. Extrude to 6-1/2" diameter at 2250°F (3:1 reduction)
4. Recrystallize 4 hours at 2800°F
5. Forge at 3400°F (finishing temperature 2800°F) to 4-1/8" diameter
6. Recrystallize 2 hours at 2950°F
7. Forge at 2800°F (finishing temperature 2160°F) to yield 9" diameter by 3/4" thick pancake
8. Stress relieve 1 hour at 2300°F

Heat TZM 7463 (See Table A12)

Mo-0.48Ti-0.08Zr-0.016C (Reference 11)

1. Vacuum arc cast 11-1/2" diameter ingot
2. Machine; extrude to 6" diameter
3. Recrystallize
4. Roll to 2" diameter (9:1 reduction)
5. Recrystallize
6. Roll to 1" diameter (4:1 reduction)
7. Swage to 5/8" diameter
8. Stress relieve 1/2 hour at 2250°F

(Above processing is normal commercial practice as used by Climax Molybdenum Company, Coldwater, Michigan in the production of swaged TZM alloy)

TABLE A25 - TZC Creep Specimen Process History

Heat TZC M-80 (See Table A14)

Mo-1.02Ti-0.170Zr-0.080C (Reference 11)

1. Vacuum arc cast 5.88" diameter ingot
2. Machine to 5" diameter
3. Extrude at 3092°F to 4-1/8" x 2.22" plate (2.3:1 reduction)
4. Cross-roll at 2925°F in hydrogen atmosphere to 0.740" thick; 4% reduction per pass

Heat TZC M-91 (See Table A14)

Mo-1.17Ti-0.270Zr-0.046C (Reference 11)

1. Vacuum arc cast 5.88" diameter ingot
2. Machine to 5" diameter
3. Extrude at 3092°F to 4-1/8" x 2.22" plate (2.3:1 reduction)
4. Cross-roll at 2912°F in hydrogen atmosphere to 1.435" thick
5. Cross-roll at 2372°F in hydrogen atmosphere to 0.714" thick

Heat TZC 4345 (See Table A14)

Mo-1.19Ti-0.16Zr-0.075C (Reference 11)

1. Machine vacuum arc cast ingot to 5.85" diameter
2. Extrude to 3" diameter (3.8 reduction)
3. Vacuum heat treat at 3000°F
4. Machine to 2.4/2.8" diameter
5. Upset forge 40% at 2400°F
6. Broad forge to 0.825" thick at 2400°F
7. Vacuum heat treat 1 hour at 2400°F
8. Machine to 0.70" thick

TABLE A26 - Cb-TZM Creep Specimen Process History

Heat No. 4305-4 (See Table A16)

Mo-1.00Cb-0.48Ti-0.095Zr-0.015C (Reference 11)

1. Vacuum arc-cast ingot and machine to 3-1/8" diameter
2. Extrude to 1-3/8" diameter
3. Recrystallize
4. Swage to 5/8" diameter rod
5. Stress relieve 1 hour at 2500°F

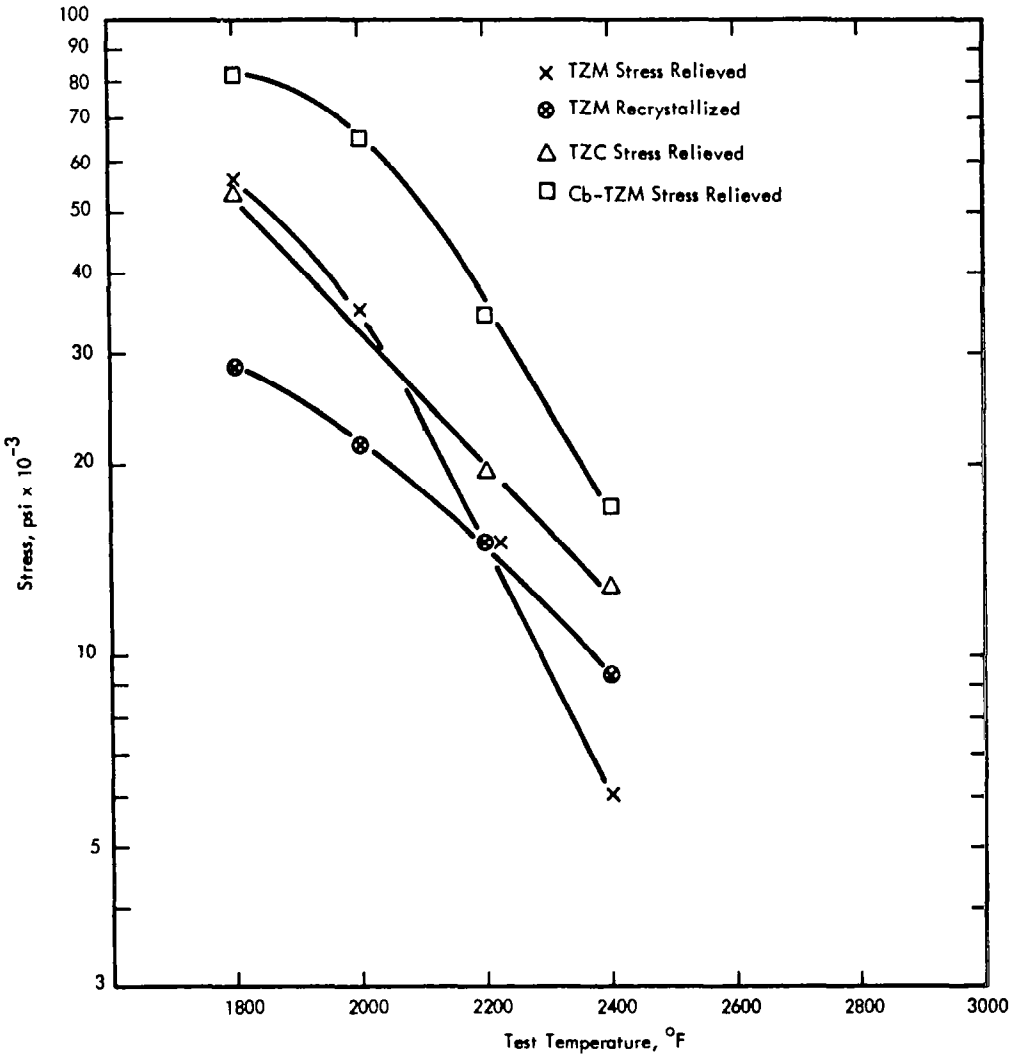

FIGURE A1 - Stress to Produce Rupture in 1000 Hours vs Temperature for Molybdenum Base Alloys (See Table A27)

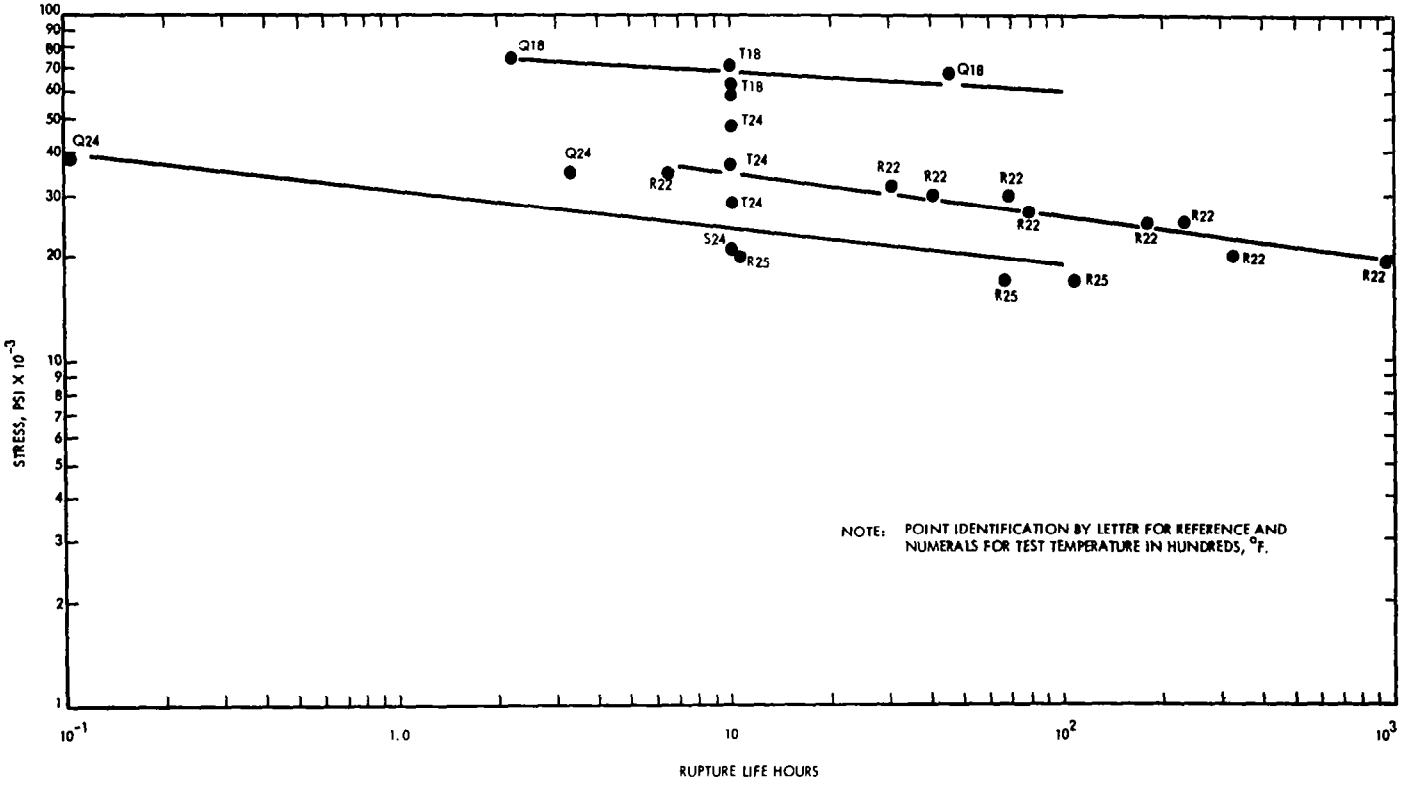

FIGURE A2 - Rupture Life of Stress Relieved TZC (See Table A27)

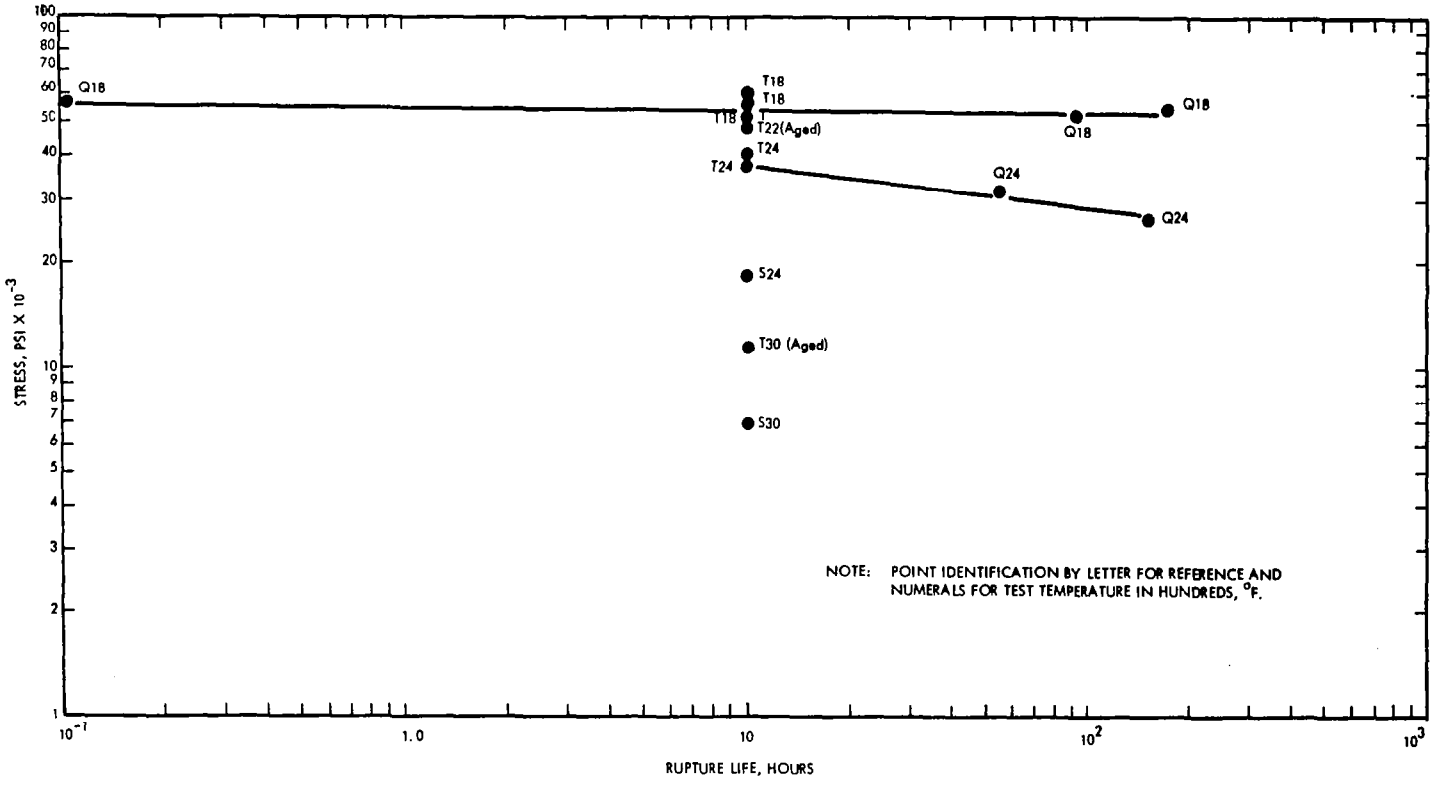

FIGURE A3 - Rupture Life of Recrystallized TZC (See Table A27)

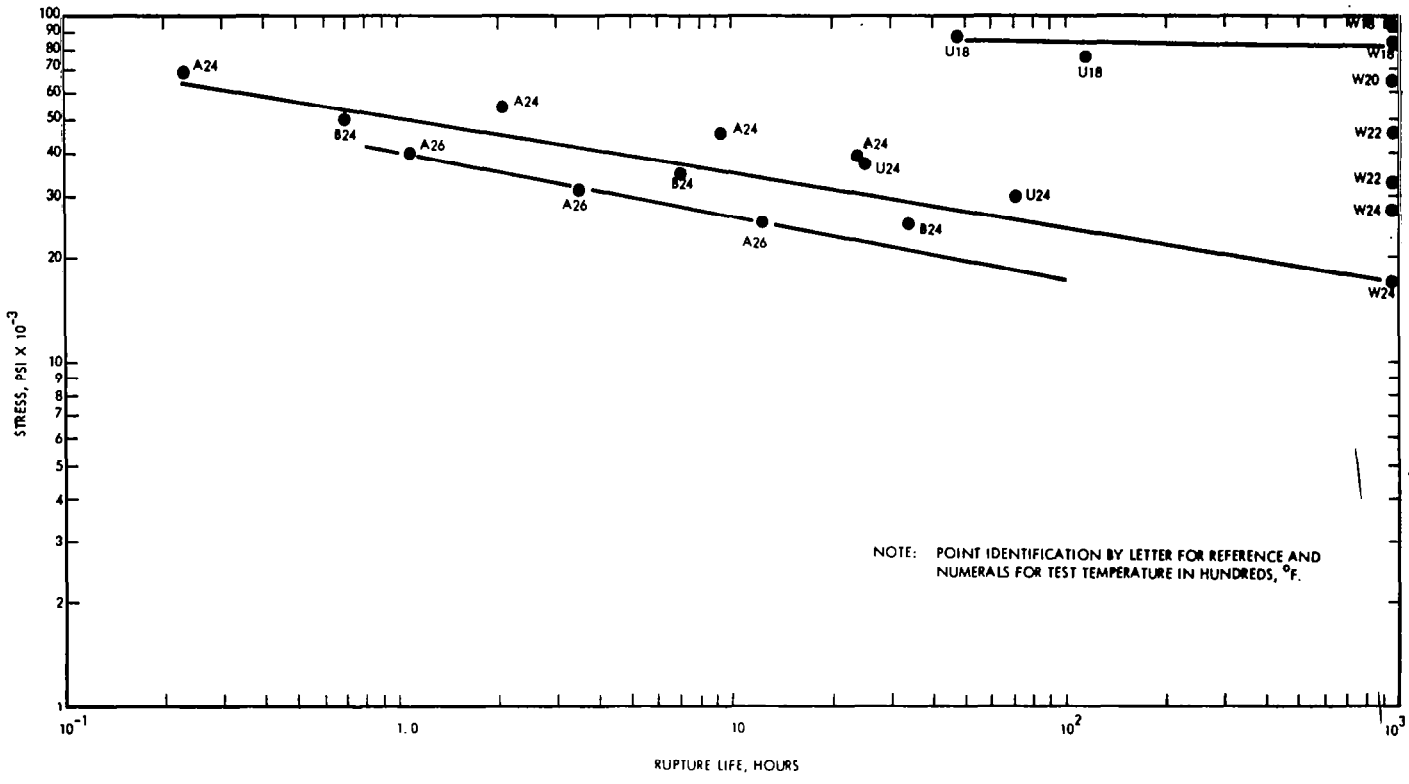

FIGURE A4 - Rupture Life of Stress Relieved Cb-TZM (See Table A27)

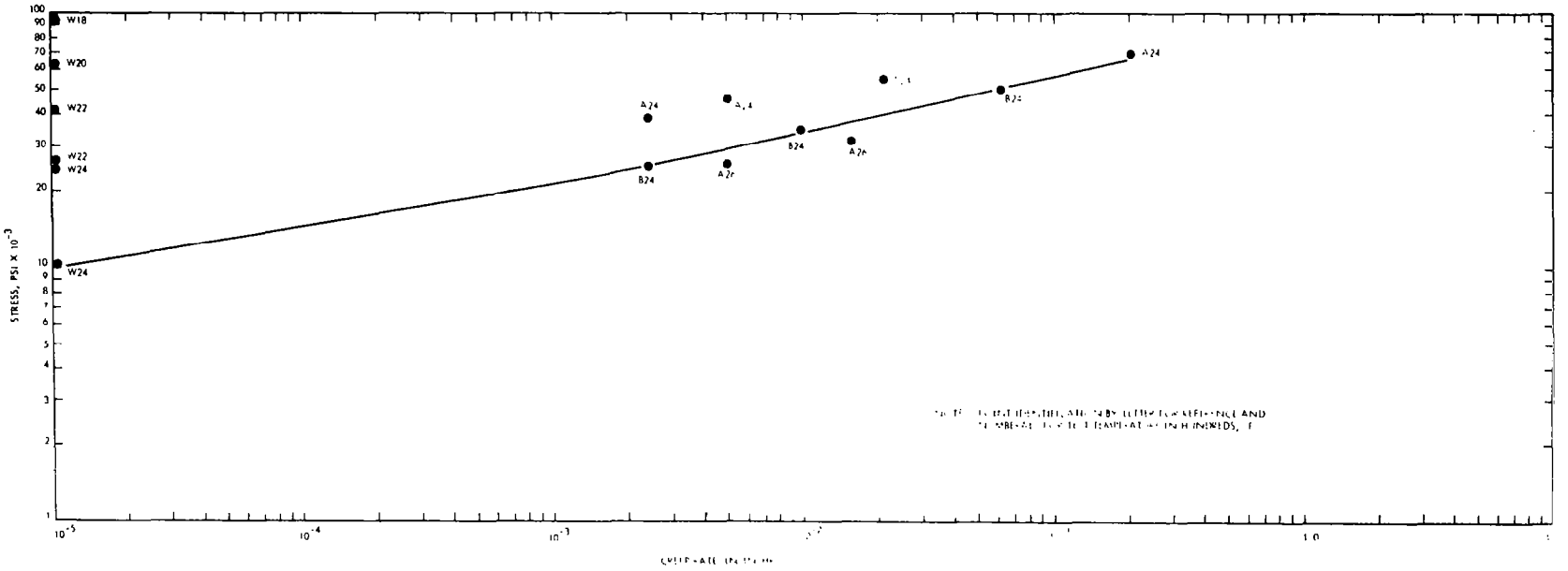

FIGURE A5 - Minimum Stress Rupture Test Creep Rates of Stress Relieved Cb-TZM
(See Table A27)

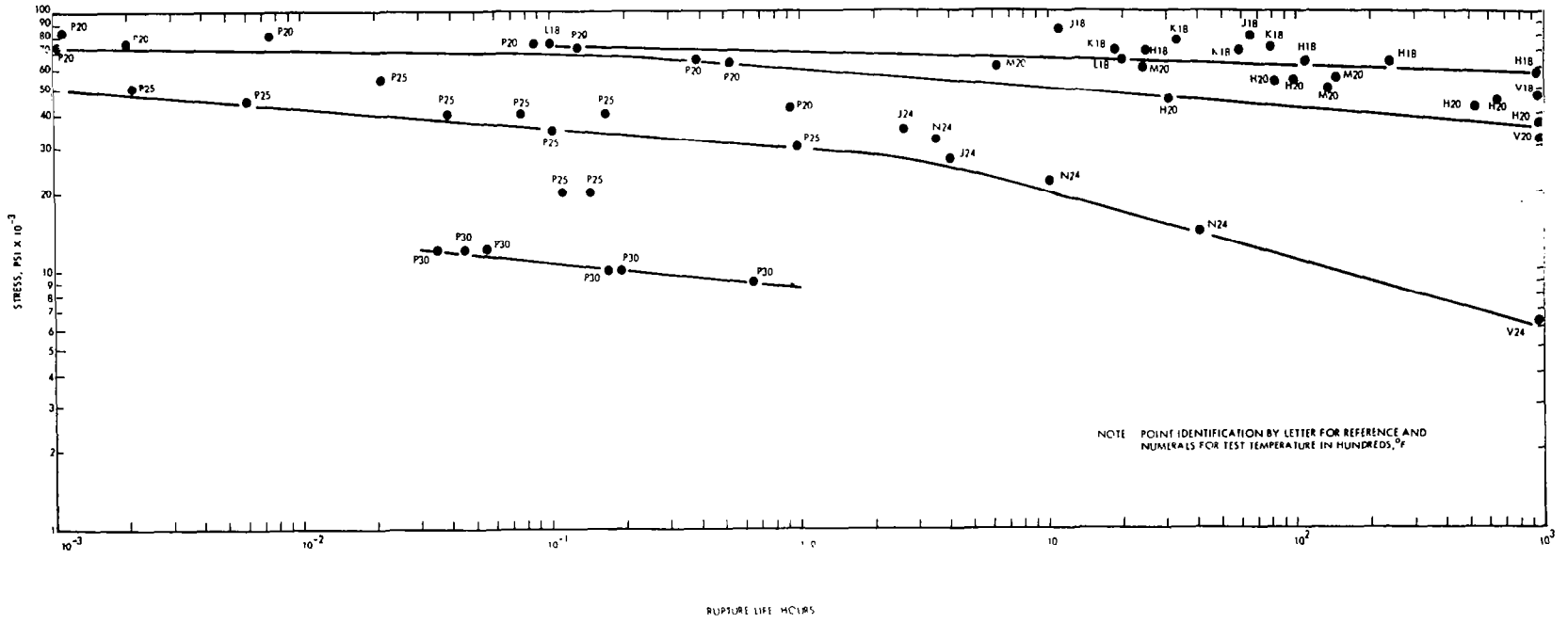

FIGURE A6 - Rupture Life of Stress Relieved TZM (See Table A27)

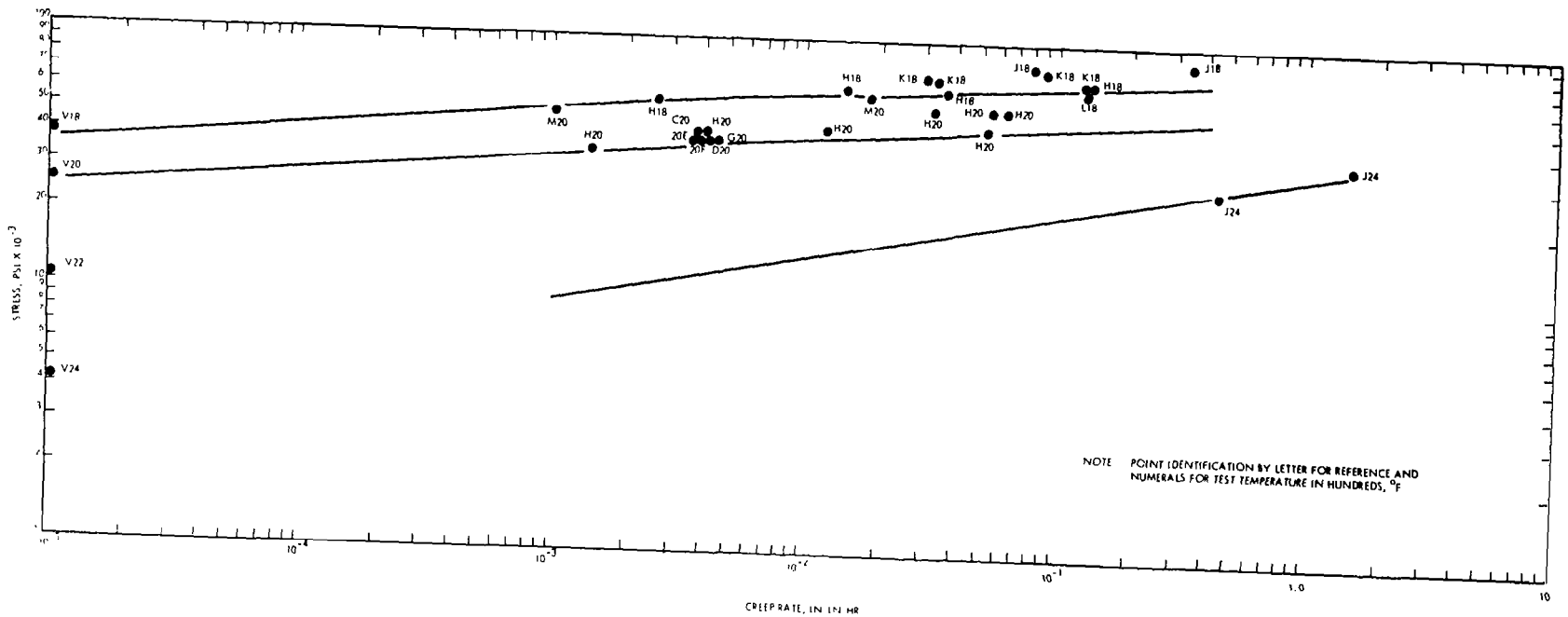

FIGURE A7 - Minimum Stress Rupture Test Creep Rates of Stress Relieved TZM
(See Table A27)

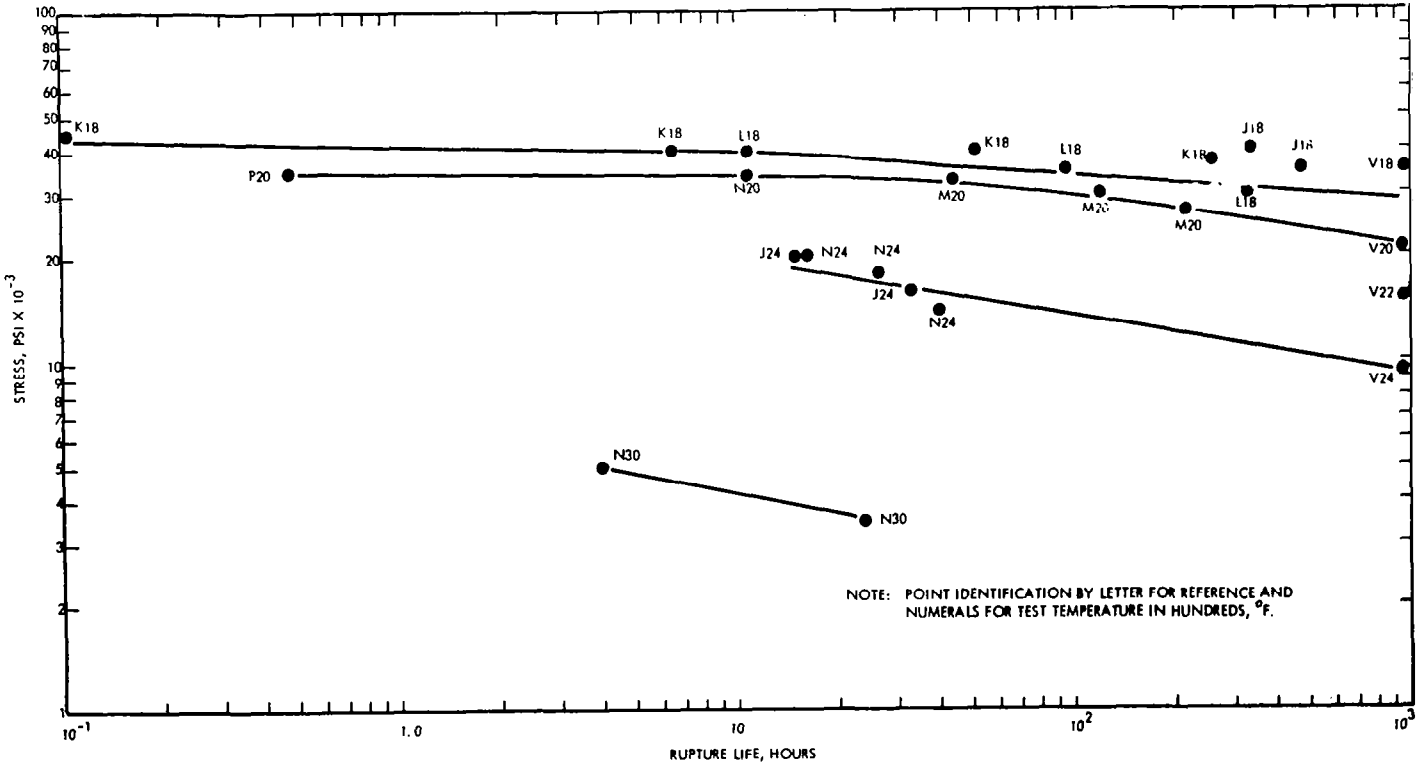

TABLE A8 – Rupture Life of Recrystallized TZM (See Table A27)

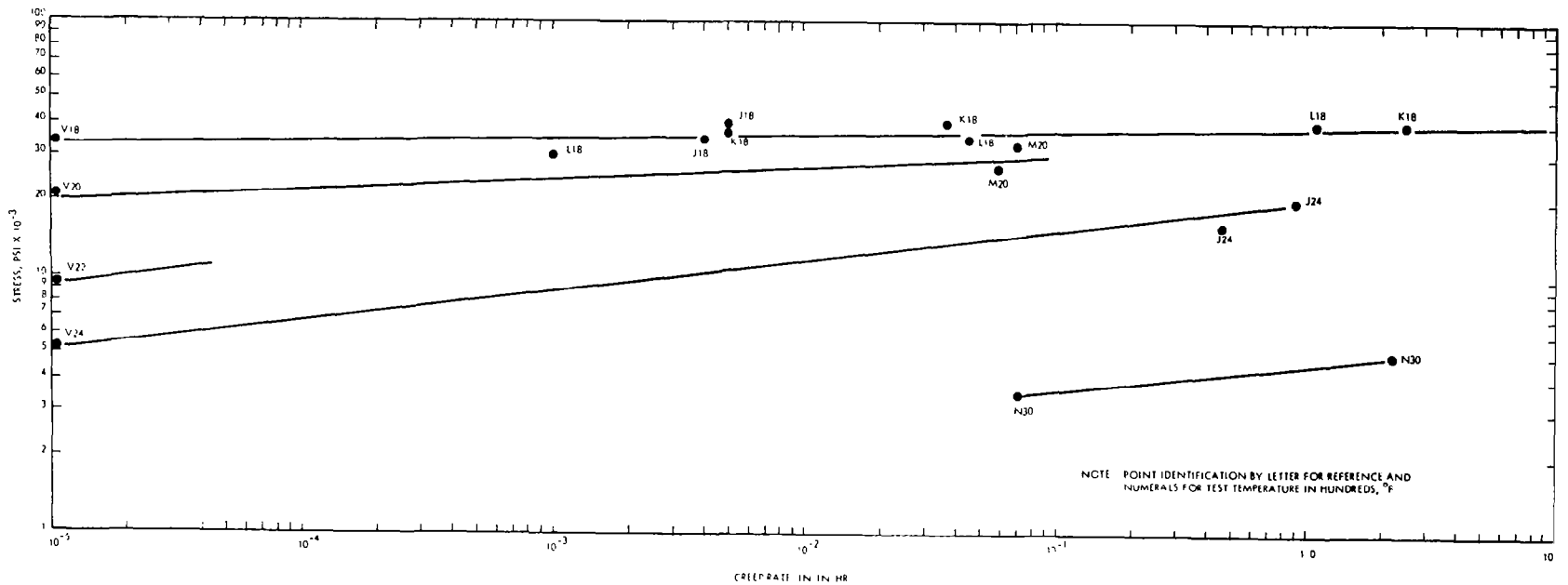

FIGURE A9 - Minimum Stress Rupture Test Creep Rates of Recrystallized TZM
(See Table A27)

TABLE A27 - Molybdenum Alloys, Materia

Spec. Code	Ref. Code	Alloy	Composition Ti	Zr	Cb	C	Ingot	Processing to last reduction
A	12	TZM+Cb	.38/.41	.21/.26	1.51	.077/.081	5" dia. x 32" long. Vacuum arc cast.	Machine to 3" dia. Extrude to 1.39" dia. Forge to .5" flat b (Recrystallize 2850F)
B	12	TZC+Cb	.41	.22/.27	1.51/1.55	.071/.073	5" dia. x 32" long. Vacuum arc cast.	Same processing. (Recrystallize 2600F)
C	33	TZM	.46/.49	.09/.114	-	.014/.022	8" dia. Vacuum arc cast. (two ingots)	Machine surface, extrude to 4¼" dia., and upset forge 2200-1815F to discs
D	33	TZM	.48	.114	-	.024	11 3/4" dia. Vacuum arc cast. (three ingots)	Machine to 10 3/4", extrude to 6 1/2" dia.
E	33	TZM	.43	.10	-	.014	13¼" dia. Vacuum arc cast. (One ingot)	Machine to 12", extrude to 7¼" dia. recrystallize and sol. treat at 3800F, re-extrude to 4¼" dia.
F	33	TZM	.43	.10	-	.014	Same	Same
G	33	TZM	.43	.10	-	.014	Same	Same
H	52	TZM	.50	.09	-	.027	Size not reported. Vacuum arc cast.	Universal Cyclops furnished hot-rolled 3/4" rounds stress-relieved at 2200F.
J	54 (53)	TZM	.46	.08	-	.08	5" dia. arc cast in vacuum or helium.	Machined to 4" round, extruded to about 1¼" round.
K	56 (53)	TZM	.40/.55*	.06/.12*	-	.01/.04*	Not reported.	Not reported
L	55 (53,56)	TZM	.50	.07	-	.019	Arc-cast. Size not reported.	Machined to 6.6" or 7.7" rounds, extruded to 4" rd. at 2300F, forged or rolled to 1" thick x 4" wide sheet b
M	56 (53)	TZM	.40/.55*	.06/.12*	-	.01/.04*	Not reported.	Not reported
N	56 (53)	TZM	.40/.55*	.06/.12*	-	.01/.04*	Not reported.	Not reported
P	53 Ref. 11	TZM	.04/.55*	.06/.12*	-	.01/.04*	Not reported.	Forge to slab, roll in steps : 2100F to final thickness with intermediate anneals at 2900F
Q	57 Table 17 (53)	TZC	1.23	.27	-	.14	Vacuum arc cast ia. not given.	Machined to 3" dia. Extrude at 2600F to 1 3/8" dia.
R	53 Table A107	TZC	1.2/1.25	.13/.15	(two analyses)	.13/.15	Not reported.	Not reported.
S	53 Table A108	TZC	1.17	.27	-	.14	Not reported.	Not reported except recryst. before final rolling
T	53 Table A108	TZC	1.22/1.30	.27/.31	(Four analyses of four samples)	.12/.23	Not reported.	Same
U	58 Table 22	TZM+Cb	.55	.28	1.47	.10	Vacuum arc cast 4" dia.	Machined to 3" dia. Extruded at 3000F to 1½" dia. Rolled at 2400F to ½" dia. bar.
V		TZM	Data from ORNL					
W		TZM+Cb	Data from ORNL					

* Exact Analysis Not Reported.

ieference Data for Figures A1 thru A9

Reduction - ngot to size ested	Last reduction and treatment of final size	Specimen Size	Test temperature and atmosphere
∿99%	Cross roll 69% and str. roll 70% = 91% cold work. Str. rel. 2400F	.040 x .160 x .75 gage	2400 and 2600F in vacuum.
∿99%	Roll: Cross -45%, str. - 44% anneal 3000, cross -45% str. -45% = 69% C.W. Str. rel. 2400F	Same	2400F in vacuum
∿75% to billet 80% to forging	Upset forge 2200 - 1815F to 3/4" discs, Str. rel. 2200F	¼" dia. gage	2000F in argon
∿60% to billet ∿90% to forging	Upset forge 2800-3400F to 3/4" discs in two steps. Str. rel. -2300F	Same	Same
∿90% to second xtrusion + 80% to orging	Upset forge 2200 to 3/4" disc and str. rel. 2300°F	Same	Same
ame	Same except str. rel. 1600°F	Same	Same
ame	Same except str. rel. 2300F + age 2700F for 2 hr.	Same	Same
ot reported	Bored 1/4" hole length wise. Potassium added to cavity in 7 of 12 specimens	Tube: .250 I.D. .330 O.D.	1800 and 2000F in vacuum
∿98%	Roll to ½" round St. rel. 2200F - one hour or recryst. 2950F one hour.	3/16" dia. x one inch gage	1800 and 2400F in vacuum at Battelle
t reported	Rolled or extruded to bar. Str. rel. 2200F or recryst.	.250 dia. gage	1800F-atmosphere not reported
+ %	Recrystallised rolled to 1/16" sheet in several passes, Str. rel. at 2200F or recryst. at 2650-1 hr.	1/16" x.4" wide x 2 in. gage	1800F in vacuum at Battelle
t reported	Rolled or extruded to bar. Str. rel. 2200 or 2300F, or recryst.	.250 dia. gage	2000F-atmosphere not reported
t reported	2400F tests - ¼" round and 3000F tests - 3/4" rounds. Str. rel. 2300F or recryst.	Same	2400 or 3000F-atmosphere not reported
t. 95% min.	Roll to sheets .040 to .088 thick. Str. rel. at 1900 to 1920F or recryst. 2500 to 2550F	Not given	2000, 2500 or 3000F. 93% argon, 7% hydrogen
	Rolled to ½" dia. Str. rel. 2200F, 1 hr. or recryst. 3400F, 1 hr.	¼" dia. x 1" gage	1800 and 2400F, 90% argon, 10% hydrogen
t reported	Not reported - except stress relieved.	Not reported	2200 and 2500F atmosphere not reported
t reported	Rolled to .050" sheet. Str. rel. or recryst.	Not reported	1800, 2200, 2400 or 3000F. Atmosphere not reported
t reported	Rolled to ½" or 5/8" rounds. Str. rel. or recryst.	Not reported	Same
.4%	½" dia., bar str. rel. at 2300F, 1 hr. or recryst. at 3100F, 1 hr.	.250 x 1.00" gage	1800 and 2400F in vacuum of 10^{-4} torr
	Str. rel. at 2245° F or recryst. at 2800F		
	Warm working at 2400 or 2500F considered equivalent to str. rel.		

TABLE A28 - Creep Properties for T-111 (See Figures A10 and A11)

Temperature (°R)	Stress psi(x10^{-3})	Time and Corresponding Larson-Miller Parameter for Indicated Creep $P_{L-M}=(To_R)(15+\log t) \times 10^{-3}$						Test Conditions			Reference
		0.1%		0.5%		1.0%		Heat Number	Specimen Form	Pre-Test Recrystallization	
		t(hrs)	P	t(hrs)	P	t(hrs)	P				
2660	8.0	250	46.3	1220	48.0	2000	48.7	70616	0.030" sheet	1 hr. at 3000°F	9
2660	12.0	125	45.5	650	47.4	1140	48.0	"	" "	" " "	9
2580	12.0	400	45.4	1750	47.1	3130	47.7	"	" "	" " "	9
2320	20.0	500	41.1	3000	42.9	4800*	43.3	"	" "	" " "	9
2460	15.0	160	42.3	700	43.9	1350	44.6	D-1670	" "	" " "	9
2260	17.0	1900	41.3			12000*	43.1	"	" "	" " "	9
2460	13.0	200	42.6	1060*	44.3	1900*	45.0	1102	" "	" " "	9
2460	15.9			200	42.6	340	43.1		Cold rolled 80%	1 hr. at 2600°F	44
2660	7.9			100	45.2	300	46.5		to 0.030" sheet	" " "	44
2660	21.3			24	43.6	45	44.3	DX-570	0.040" sheet	1 hr. at 3000°F	10
2960	8.3			72	49.9	117	50.5	"	" "	" " "	10
2960	9.2			67	49.8	93	50.2	"	" "	" " "	10
2860	10.0					300	50.0	NASV-1	" "	" " "	10
2860	12.7			76	48.2	119	48.8	"	" "	" " "	10
2860	14.1					42	47.5	"	" "	" " "	10
2860	14.7			27	46.9	42	47.5	"	" "	" " "	10
2860	15.2					18	46.5	"	" "	" " "	10
2960	12.7					26	48.6	"	" "	" " "	10

*Extrapolated

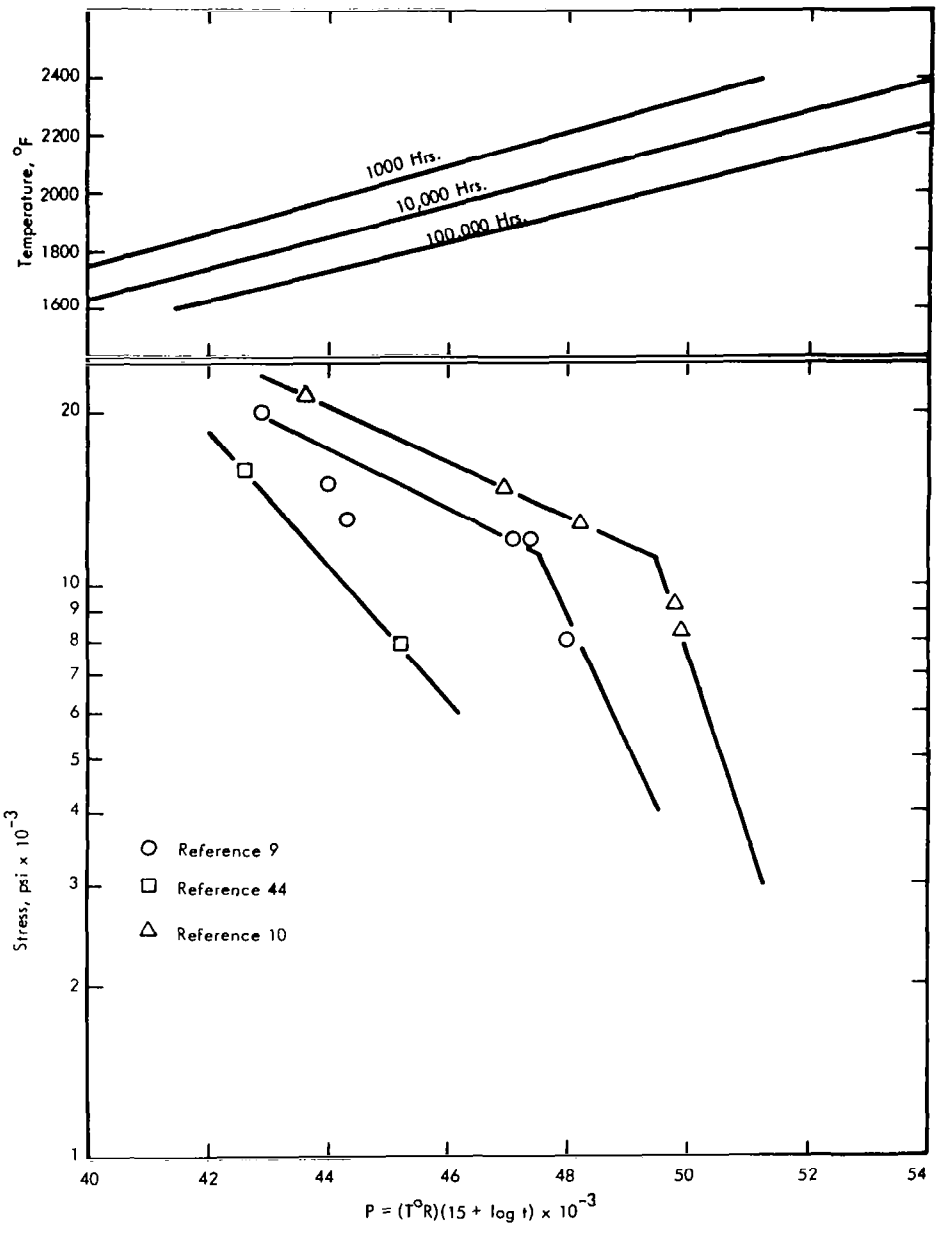

FIGURE A10 - Larson-Miller Plot for 0.5% Creep in T-111

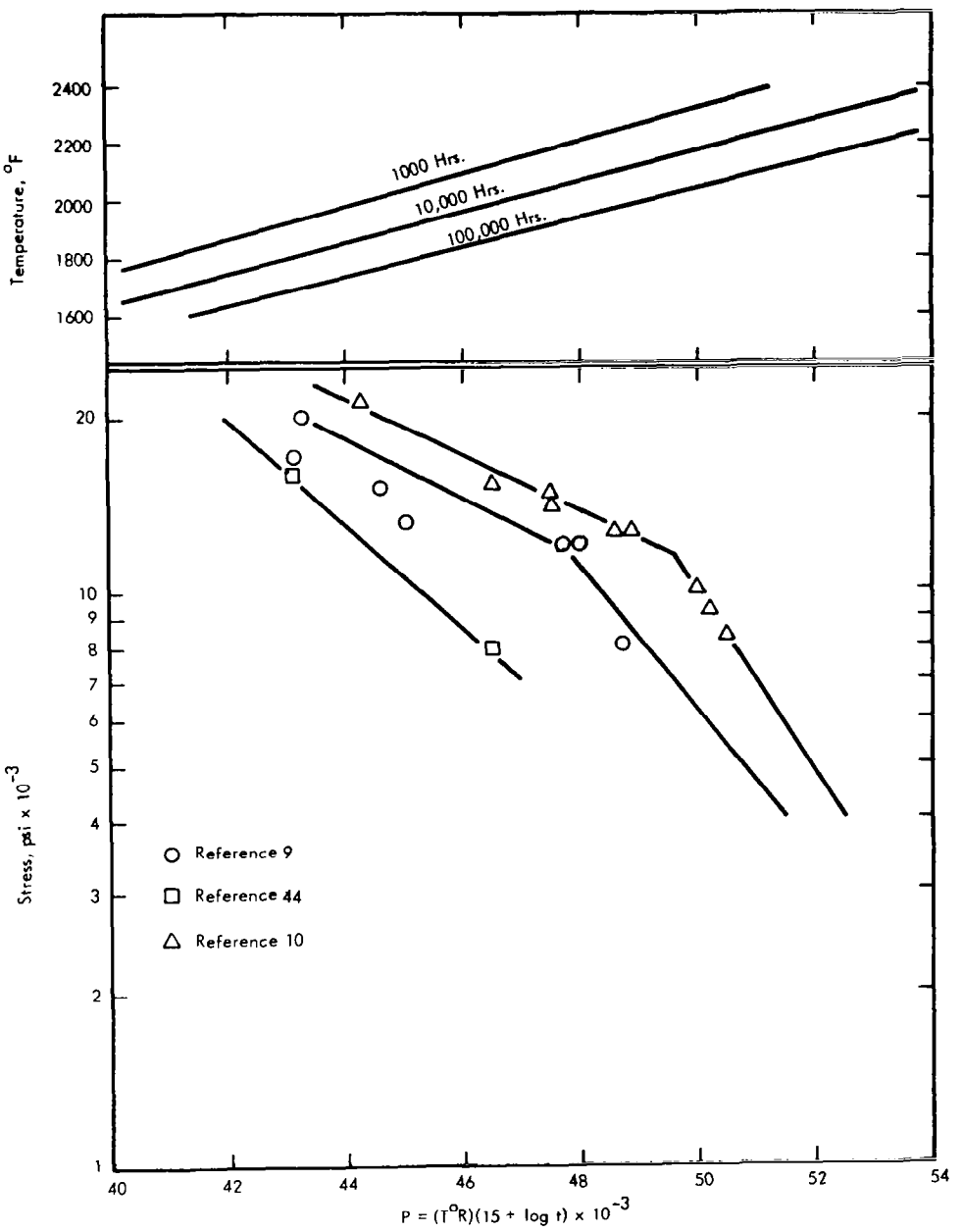

FIGURE A11 - Larson-Miller Plot for 0.1% Creep in T-111

TABLE A29 - Coefficient of Thermal Expansion of T-111

Temperature (°F)	Average Coefficient (in/in °F x 10^6)	Remarks
80 - 500	3.1	Reference 61
80 - 1000	3.5	Dilatometric technique in vacuum.
80 - 1500	3.9	Specimens recrystallized prior to testing.
80 - 2000	3.9	
80 - 2500	4.0	
80 - 3000	4.2	

TABLE A30 - Electrical Resistivity of T-111

Temperature (°F)	Resistivity (micro-ohm-cm)	Remarks
-320	10.7	Reference 61
78	22.2	Measurements made on recrystallized
212	24.5	0.057 inch diameter wire using a
765	41.2	Kelvin-Bridge.
1475	53.0	
2160	64.0	

TABLE A31 - Elastic Modulus of T-111

Temperature (°F)	Modulus (psi x 10^{-6})	Remarks
77	26.0	Reference 62
750	24.8*	Values are for dynamic
1110	24.2*	measurements.
1470	23.6*	
1830	23.0*	
2190	22.4*	
2550	21.8	
2910	21.1	
3270	20.2	
3630	19.1	

*Interpolated

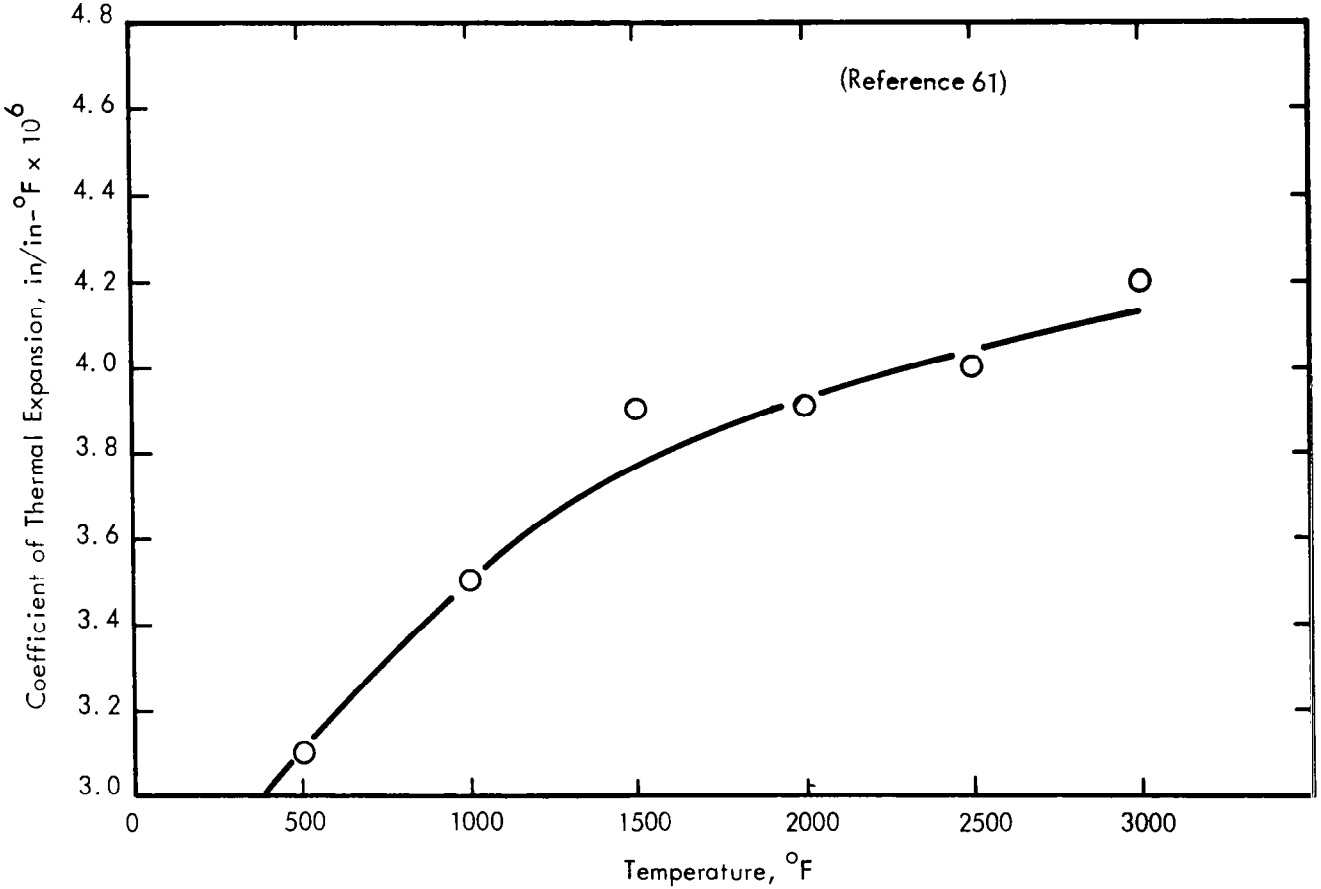

FIGURE A12 - Thermal Coefficient of Expansion of T-111

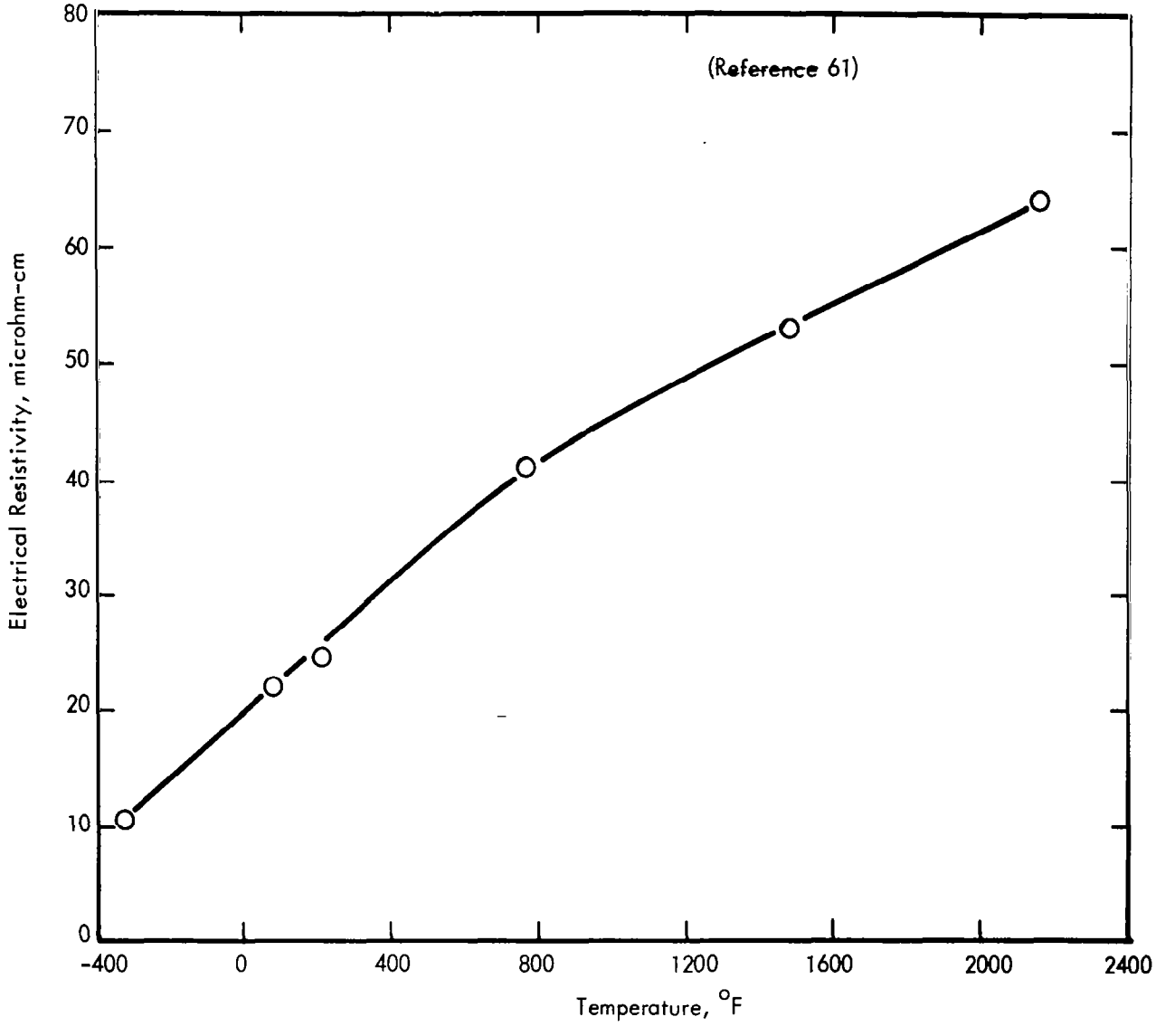

FIGURE A13 - Electrical Resistivity of T-111

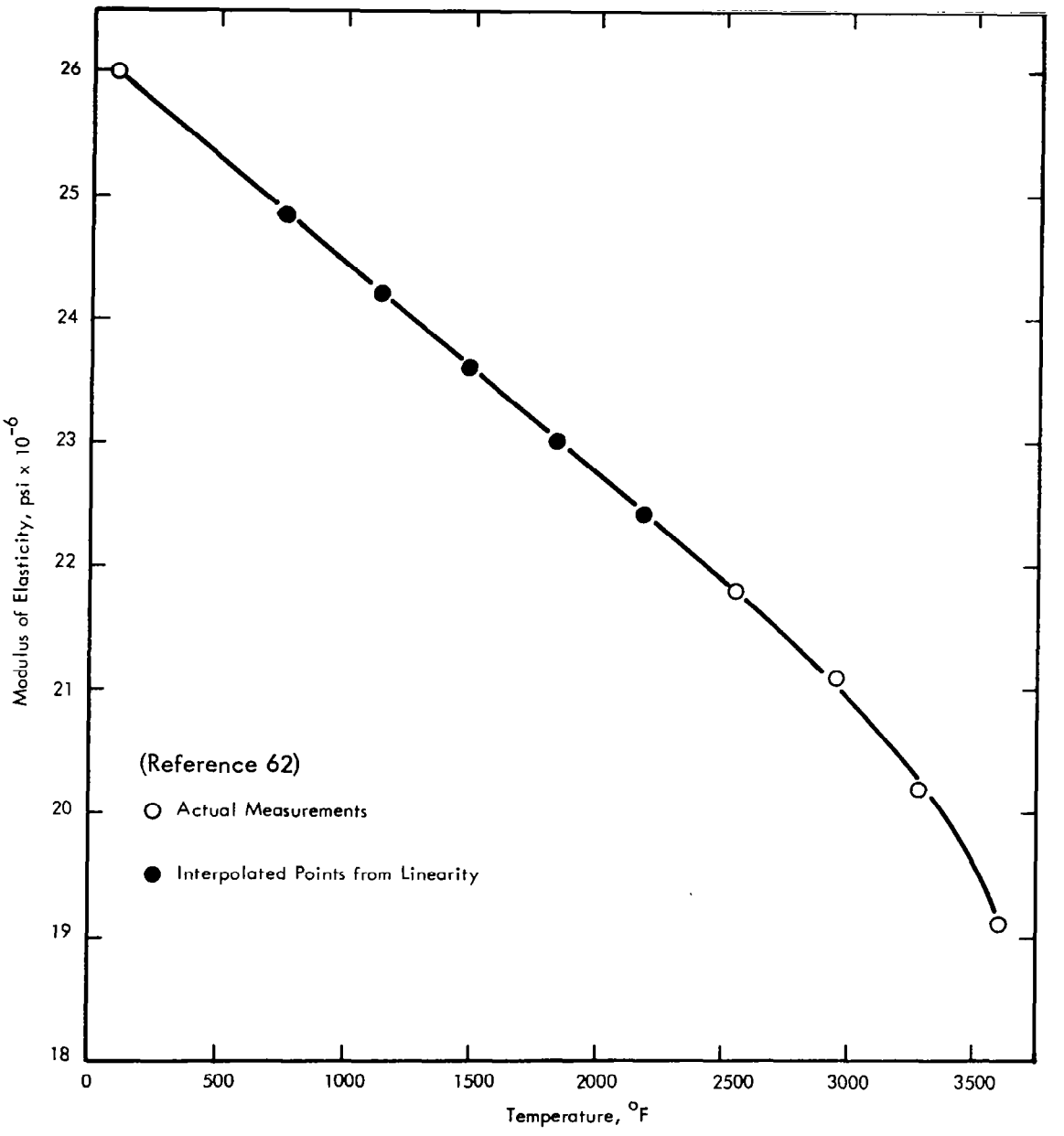

FIGURE A14 - Elastic Modulus of T-111

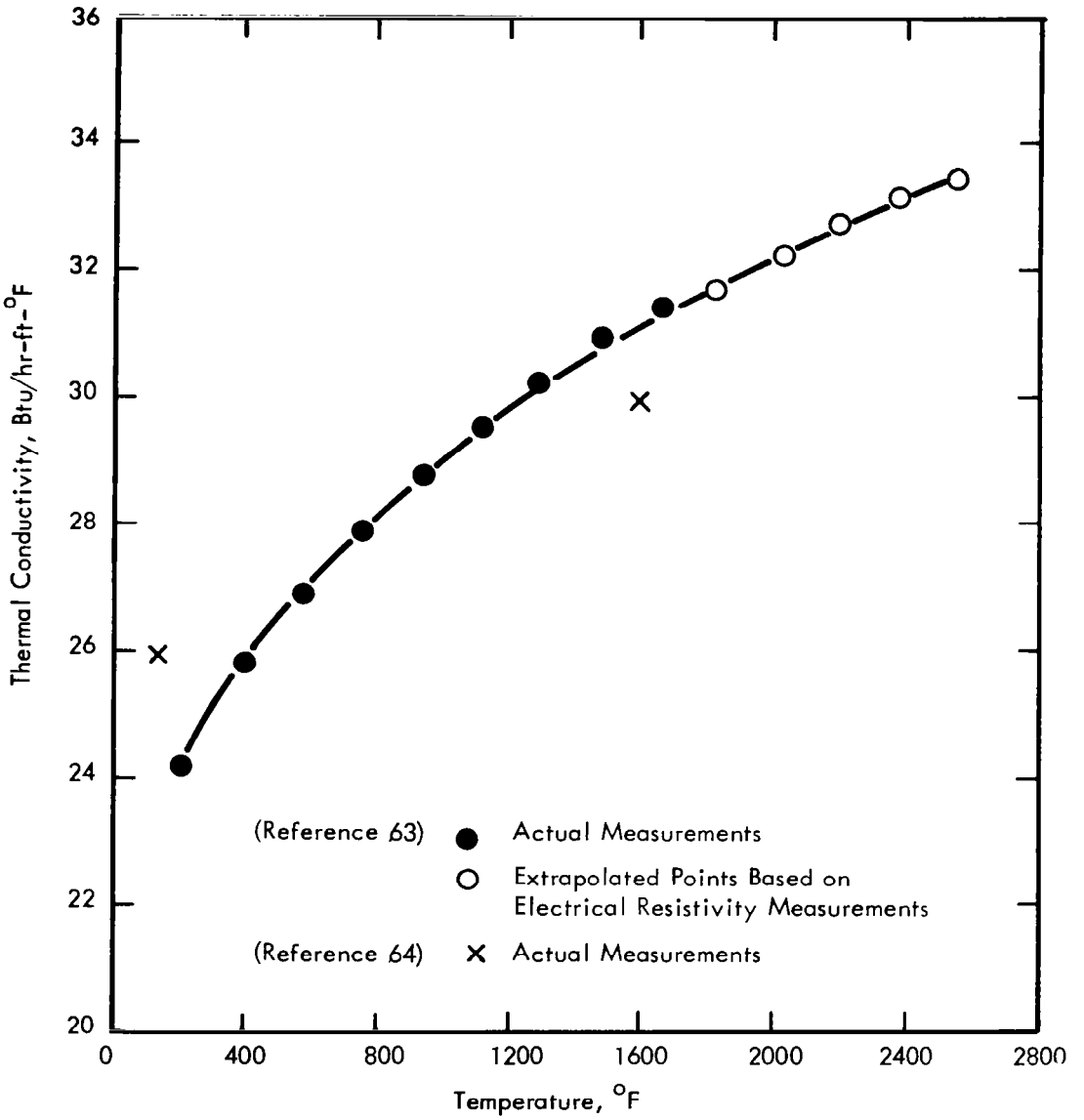

FIGURE A15 - Thermal Conductivity of T-111 .

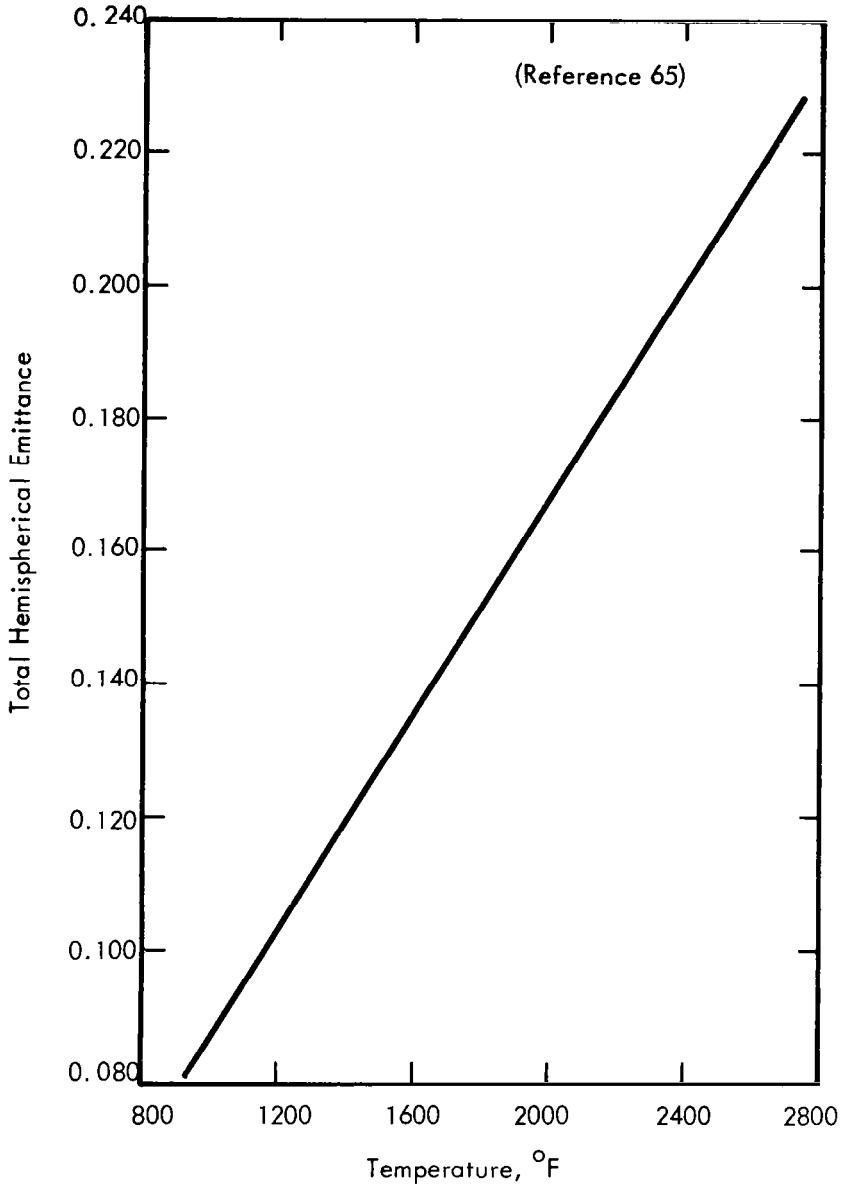

FIGURE A16 - Total Hemispherical Emittance of T-111

TABLE A32 - Linear Thermal Expansion of TZM

Temperature (°F)	Thermal Expansion ($\Delta L/L$, %)	Remarks
80	0.000	Reference (66)
222	0.043	Mo-0.50Ti-0.07Zr-0.019C
326	0.074	
538	0.129	
736	0.189	
903	0.240	
1008	0.282	
1093	0.304	
1241	0.371	
1459	0.451	
1633	0.521	
1773	0.580	
1967	0.662	
2137	0.727	
2400	0.841	
2589	0.928	
2713	0.963	
2801	1.032	
2974	1.131	
3312	1.272	

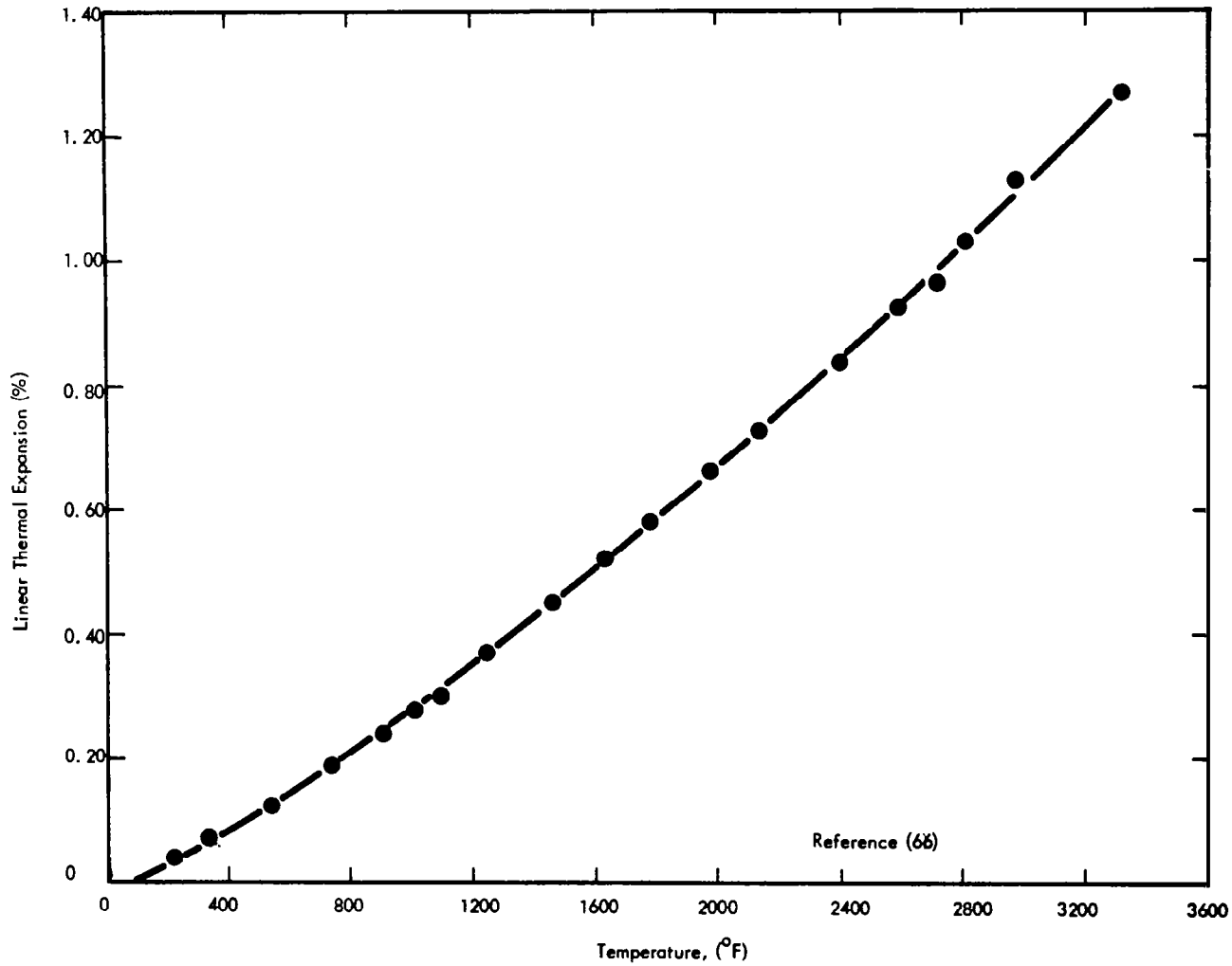

FIGURE A17 - Linear Thermal Expansion of TZM

TABLE A33 - Specific Heat and Thermal Conductivity of TZM

Temperature (°F)	Specific Heat (BTU/lb-°F)	Thermal Conductivity (BTU/Hr-ft-°F)	Remarks
160		73.5	Reference (66)
310		72.0	Mo-0.50Ti-0.07Zr-0.019C
600		70.0	
945	0.0668	67.5	Specific heat values were experimentally determined
1295	0.0684	64.2	
1520	0.0698	61.6	Thermal conductivity values were calculated from measurements of thermal diffusivities
1915	0.0739	58.0	
2230	0.0761	54.0	
2605	0.0805	51.0	
3065	0.0875	47.1	
3570	0.0968	43.1	
4180	0.1100	39.2	

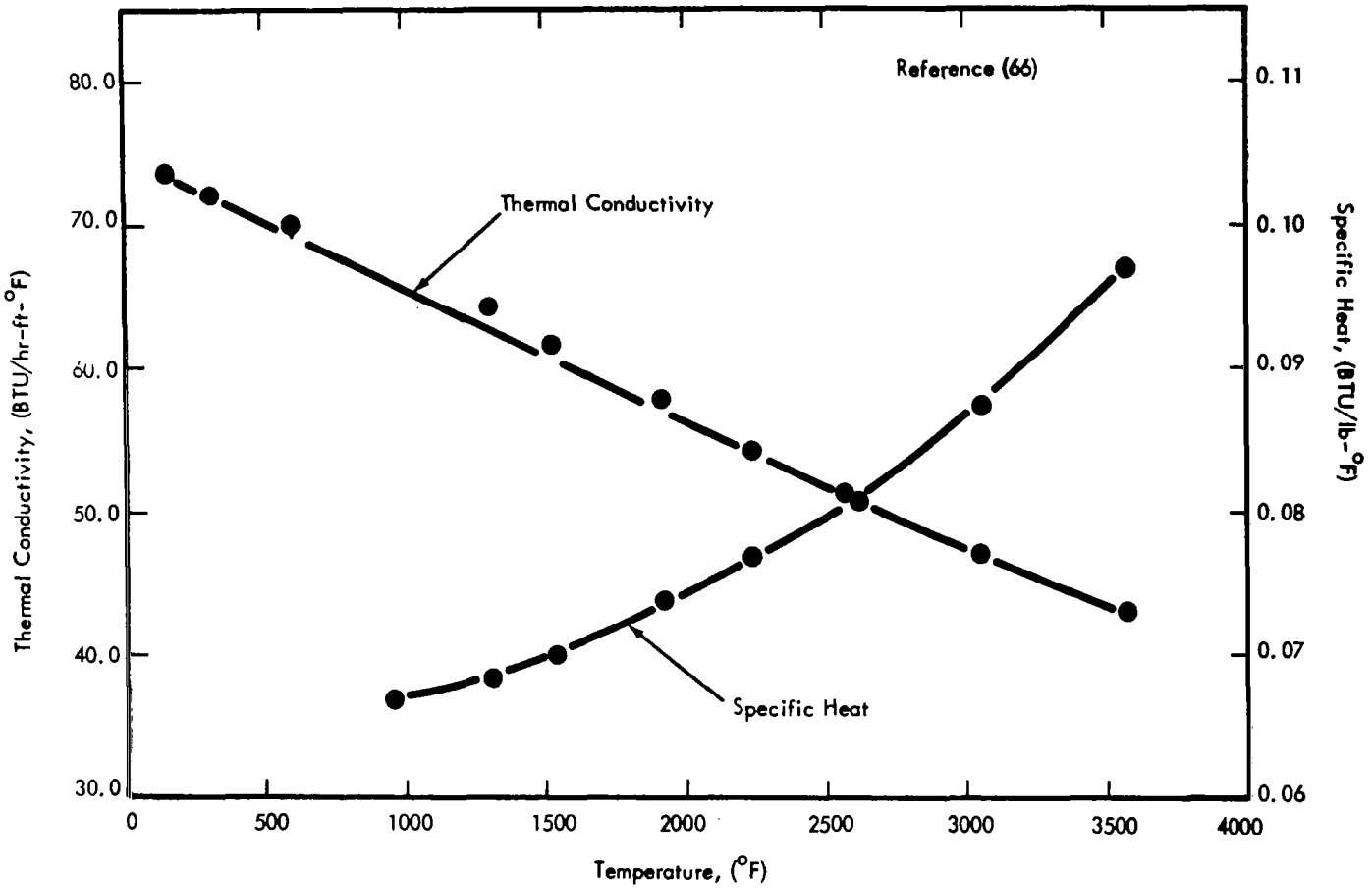

FIGURE A18 - Specific Heat and Thermal Conductivity of TZM

TABLE A34 - Transition Temperature Data for TZM

Material Identity	Material Form	Thermal Condition	Test Method	Transition Temperature Range (°F)	Composition	Ref.
KDTZM 1236B	Forging	S.R. 1 hr. 2200°F	Unnotched Charpy	-25 to +25	Mo-0.46Ti-0.09Zr-0.022C	33
KDTZM 796	Forging	S.R. 1 hr. 2200°F	"	100 to 175	Mo-0.49Ti-0.114Zr-0.014C	33
KDTZM 1175	Forging	S.R. 1 hr. 2300°F	"	150 to 200	Mo-0.48Ti-0.114Zr-0.024C	33
TZM 7492	Forging	S.R. 1 hr. 2200°F	"	50 to 75	Mo-0.43Ti-0.10Zr-0.014C	33
KDTZM 1312	Forging	S.R. 1 hr. 2300°F	"	200 to 250	Mo-0.42Ti-0.085Zr-0.014C	49
KDTZM 1196	0.040" sheet	S.R. 1 hr. 2300°F	Notched Tensile(a)	-175 to -150	Mo-0.42Ti-0.088Zr-0.032C	67
KDTZM 1196	0.040" sheet	Rx 1 hr. 2475°F	"	-125 to -100	Mo-0.42Ti-0.088Zr-0.032C	67
KDTZM 1196	0.040" sheet	S.R. 1 hr. 2300°F	4t Bend Tests	-200 to -137	Mo-0.42Ti-0.088Zr-0.032C	67
KDTZM 1196	0.040" sheet	Rx 1 hr. 2475°F	"	-137	Mo-0.42Ti-0.088Zr-0.032C	67
KDTZM 1233A,B	0.040" sheet	S.R. 1 hr. 2100°F	2t to 3.5t Bend Tests	-125 to -75	Mo-0.48Ti-0.099Zr-0.022C	68
KDTZM 1233A,B	0.020" sheet	S.R. 1 hr. 2100°F	3.2t to 4t Bend Tests	-200 to -100	Mo-0.48Ti-0.099Zr-0.022C	68

(a) Stress concentration factor, K_t, was 4.2. Strain rate was 0.005 min^{-1}.

TABLE A35 - Recommended Machining Practices for TZM Alloy

Operation	Tool Material*	Tool Geometry*	Test Tool**	Depth of Cut	Feed	Wear-land	Cutting Speed	Tool Life
Turning	C2	BR: 0°; SR: 20°; SCEA: 15° ECEA: 15°; Relief: 5°; NR: 0.030"	5/8" square brazed	0.060"	0.009 in/rev	0.010"	350 ft/min	20 min
Face milling	C2	AR: 0°; RR: 0°; CA: 45°; TR: 0°; Incl: 0°; ECEA: 5°; Cl: 10°	4" dia. single tooth face mill	0.060 (2" width)	0.005 in/tooth	0.015	350	100 in/tooth
Face milling	T15	AR: 0°; RR: 20°; CA: 45°; TR: 14°; Incl: —14°; ECEA: 10°; Cl: 15°	4" dia. single tooth face mill	0.060 (2" width)	0.010 in/tooth	0.015	100	70 in/tooth
End milling	T15	30°RH helix; RR: 10°; CA: 45° x 0.060"; ECEA: 3°; Cl: 10°	3/4" dia., 4 tooth end mill	0.125 (3/4" width)	0.004 in/tooth	0.012	190	78"
Drilling	M1	118° point angle; helix angle: 29°; Cl: 7°; split point	0.250" dia. drill 2-1/2" long	1/2" (thru hole)	0.005 in/rev	0.015	100	110 holes
Reaming	M2	Helix angle: 0°; CA: 45° Cl: 10°	0.272" dia. 6 flute chucking reamer	1/2" (thru hole)	0.015 in/rev	0.012	60	51 holes
Tapping	M10	4 flute plug tap; 75% thread	5/16-24NF tap	1/2" (thru hole)	---	---	70	100+ holes

* BR = back rake; SR = side rake; SCEA = side cutting edge angle; ECEA = end cutting edge angle; NR = nose radius; AR = axial rake; RR = radial rake; CA = corner angle; TR = resultant rake; Incl = inclination; Cl = clearance; RH = right hand; C2 = carbide; M1, M2, M10, and T15 = high speed steels.

** NF = National Fine. Cutting fluids: soluble oil, 20:1, for turning and milling; highly chlorinated oil for other operations. Source: Metcut Research Associates, Inc., Cincinnati, Ohio, and Air Force Materials Laboratory, Dayton, Ohio.

VIII. REFERENCES

1. "Materials for Potassium Lubricated Journal Bearings", Quarterly Progress Reports 1-13, Contract NAS 3-2534, Edited by R. G. Frank, General Electric Company, Missiles and Space Division.

2. Devan, J. H. , Litman, A. P., DiStefano, J. R. and Sessions, C. E., "Lithium and Potassium Corrosion Studies with Refractory Metals", ORNL-TM-1673, December, 1966.

3. Contract NAS 3-2542, "Development of Dispersion Strengthened Tantalum Base Alloy", Westinghouse Astronuclear Laboratory.

4. Semmel, J. W., Jr., "Refractory Metals in Space Electric Power Conversion Systems", Paper Presented at AIME Symposium on Metallurgy and Technology of Refractory Metal Alloys, Washington, D. C., April 25-26, 1968.

5. Stoner, D. R. and Lessmann, G. G., "Measurement and Control of Weld Chamber Atmospheres", Welding Journal Research Supplement, Vol. 44, No. 8, pp. 337S-346S, August, 1965.

6. Preliminary Results, Contract NAS 3-10939, "Development of High Strength Tantalum Base Alloys", Westinghouse Astronuclear Laboratory.

7. Preliminary Results, Contract NAS 3-2540, "Determination of the Weldability and Elevated Temperature Stability of Refractory Metal Alloys", Westinghouse Astronuclear Laboratory.

8. Lessmann, G. G., "Effect of 1000 Hour Thermal Exposures on Tensile Properties of Refractory Metal Alloys", NASA-CR-72095, Westinghouse Report No. WANL-PR-(P)-012.

9. Sawyer, J. C. and Steigerwald, E. A., "Generation of Long Time Creep Data of Refractory Alloys at Elevated Temperatures", 13th Quarterly Report, Contract NAS 3-2545.

10. Buckman, R. W., Jr. and Goodspeed, R. C., "Development of Dispersion Strengthened Tantalum Base Alloy", 11th Quarterly Report, WANL-PR(Q)-012, NASA-CR-72094.

11. Sawyer, J. C. and Steigerwald, E. A., "Generation of Long Time Creep Data of Refractory Alloys at Elevated Temperatures", Final Report on Contract NAS 3-2545, 6 June 1967.

12. Perkins, R. A. and Lytton, J. L., "Effect of Processing Variables on the Structure and Properties of Refractory Metals", AFML-TR-65-234, Part I, Lockheed Missiles and Space Company, July, 1965.

13. Litman, A. P., "The Effect of Oxygen on the Corrosion of Niobium by Liquid Potassium", ORNL-3751 (1965).

14. Cleary, R. E., Blecherman, S. S., and Corliss, J. E., "Solubility of Refractory Metals in Lithium and Potassium", TIM-850 (1965).

15. McKisson, R. L., et al, "Solubility Studies of Ultra-Pure Transition Elements in Ultra-Pure Alkali Metals", NASA-CR-610, Oct. 1966

16. Ginell, W. S. and Teitel, R. J., "Determination of the Solubility of Transition Elements in Molten Potassium", Douglas Aircraft Corp., SM-48883 (1965).

17. Swisher, J. H., "Solubility of Fe, Ni and Co in Liquid Potassium and the Effect of Oxygen Gettering Agents", CONF-650411, AEC-NASA Liquid Metals Information Meeting, April (1965).

18. Hoffman, E. E., (Ed.), "Potassium Corrosion Test Loop Development", NASA-CR-54843 (1965).

19. Simons, E. M. and Lagedrost, J. F., "Mass Transfer of TZM Alloy by Potassium in Boiling-Refluxing Capsules", CONF-650411 (1966), AEC-NASA Liquid Metals Information Meeting, April (1965).

20. Scheuerman, C. M. and Barrett, C. A., "Compatibility of Columbium and Tantalum Tubing Alloys with Refluxing Potassium", NASA TN-D-3429 (1966).

21. DeVan, J. H., DiStefano, J. R. and Jansen, D. H., "Compatibility of Refractory Metals with Boiling Alkali Metals", Trans. Amer. Nucl. Soc., 8 ,2 (1965).

22. Engel, L. B., Jr. and Frank, R. G., "Evaluation of High-Strength Columbium Alloys for Alkali Metal Containment", NASA-CR-54226 (1964).

23. Semmel, J. W., et al, "Alkali Metals Boiling and Condensing Investigations, Vol. II, Materials Support", Final Report from January 1, 1961 to June 30, 1962. G. E. -63-FPD-66, June (1963).

24. Chandler, W. T., "Alkali Metal Corrosion Studies at Rocketdyne", AEC-NASA Liquid Metals Corrosion Meeting, TID-7626 (Part 1), April, 1962.

25. Hoffman, E. E. and Harrison, R. W., "The Compatibility of Refractory Metals with Liquid Metals", pp. 251-288, in Refractory Metal Alloys, Metallurgy and Technology by Machlin, I., Begley, R. T., and Weisert, E. D. (Eds.) TMS AIME, Plenum Press, New York (1968).

26. Jansen, D. H. and DeVan, J. H., "Niobium-1% Zirconium Boiling Potassium Forced-Convection Loop Test", ORNL-4301, December, 1968.

27. Schnetzer, E. (Ed.), "3000-Hour Test Two-Stage Potassium Turbine", NASA-CR-72273, July, 1967.

28. Young, H. G. and Grindell, A. G., "Summary of Design and Test Experience with Cesium and Potassium Components and Systems for Space Power Plants", ORNL-TM-1833, June, 1967.

29. DeVan, J. H., et al, "Compatibility of Boiling Potassium with Refractory Metal Alloys", pp. 124-129 in ORNL-3870, Metals and Ceramics Division Annual Progress Report for Period Ending June 30, 1965. November, 1965.

30. Andrews, R. C., "The Effect of Sodium on the Mechanical Properties of Austenitic and Ferritic Steels", In AEC-NASA Liquid Metals Information Meeting, Gatlinburg, Tennessee, April, 1965, CONF-650411, p. 108 (1966).

31. Blecherman, S. S. and Hodel, J., "The Compatibility of Structural and Turbo-Machinery Alloys in Boiling Potassium", AEC Report PWAC-501 (1965).

32. Kelly, K. J., Blecherman, S. S., and Hodel, J. E., "Corrosion Studies of Refractory Metal Alloys in Boiling Potassium and Liquid NaK", AEC Report CNLM-6246 (1965).

33. Kovacevich, E. A. and Salley, R. L., "Materials Investigation, SNAP 50/SPUR Program, Mechanical Properties of TZM", AFAPL-TR-65-51, June, 1965.

34. Kovacevich, E. A., "Materials Investigation, SNAP 50/SPUR Program, Elevated-Temperature Fatigue Studies of Wrought, Stress-Relieved TZM Alloy", AFAPL-TR-66-134, December, 1966.

35. Degner, V. R., "Research in the Field of Liquid-Metal-Lubricated Bearings", Rocketdyne Report R-5086-7, June, 1965.

36. Burton, R. A., et al, "Fundamental Investigation of Liquid-Metal Lubricated Journal Bearings", Southwest Research Institute, SWRI-1228-60, April, 1965.

37. Arwas, E. B. (Ed.), "Proceedings of the Technical Meeting on: Super-Laminar Flow Bearings and Seals for Process Fluid Lubricated Turbomachinery", Report No. NYO-3363-6 and MTI-66TR66, December, 1966.

38. Frank, R. G., "Potassium Corrosion Studies", in AEC-NASA Liquid Metals Information Meeting, Gatlinburg, Tennessee, April, 1965, CONF-650411, p. 302 1966.

39. Preliminary Data from Contract NAS 3-10602, "Development of Large Diameter T-111 Alloy Tubing", Westinghouse Astronuclear Laboratory.

40. Ammon, R. L. and Begley, R. T., "Pilot Production and Evaluation of Tantalum Alloy Sheet", Summary Phase Report, WANL-PR-M-004, June 15, 1963.

41. Sheffler, K. D. and Steigerwald, E. A., "Generation of Long Time Creep Data on Refractory Alloys at Elevated Temperatures, "Fifteenth Quarterly Report on Contract NAS 3-9439, NAS-CR-72431, April 14, 1968.

42. Schmidt, F. F. and Ogden, H. R., "The Engineering Properties of Columbium and Columbium Alloys", DMIC Report 188, September 6, 1963.

43. Fansteel Corporation, Technical Data Bulletin, "Fansteel 85 Metal", TD 823C.

44. Titran, R. H. and Hall, R. W., "Ultra-High-Vacuum Creep Behavior of Columbium and Tantalum Alloys at 2000° and 2200°F for Times Greater than 1000 Hours", NASA-TN D-3222, January, 1966.

45. Titran, R. H. and Hall, R. W., "High-Temperature Creep Behavior of a Columbium Alloy, FS-85", NASA-TN D-2885, June, 1965.

46. Stephenson, R. L., "Creep-Rupture Properties of FS-85 Alloy and Their Response to Heat Treatment", ORNL-TM-1456, July, 1966.

47. Stephenson, R. L. and Donnelly, R. G., "Effect of Aging on the Creep-Rupture Properties of D-43 Welds", ORNL-TM-1708, January, 1967.

48. Wah Chang Corp., "Columbium, Tantalum and Tungsten Alloys, Technical Information", Volume III, January, 1968.

49. Kovacevich, E. A., "Materials Investigation, SNAP 50/SPUR Program, Elevated-Temperature Tensile Properties and Ductile-Brittle Transition Temperature of Forged TZM Alloy", AFAPL-TR-66-133, Garrett Corp., AiResearch Mfg. Division, December, 1966.

50. Preliminary Results, Contract NAS 3-2545, TRW, Inc.

51. Begley, R. T., Cornie, J. A. and Goodspeed, R. C., "Development of Columbium Base Alloys", AFML-TR-67-116, November, 1967.

52. Salley, R. L. and Kovacevich, E. A., "Materials Investigation, SNAP 50/SPUR Program, Creep-Rupture Properties of Stress-Relieved TZM Alloy", Report APL-TDR-64-116, Part I, Garrett Corporation, AiResearch Mfg. Division, October, 1964.

53. Schmidt, F. F. and Ogden, H. R., "The Engineering Properties of Molybdenum and Molybdenum Alloys", DMIC Report 190, September 20, 1963.

54. Semchyshen, M., McArdle, G. D., and Barr, R. Q., "Development of High Strengths and High Recrystallization Temperatures in Molybdenum-Base Alloys", Report WADC TR 48-551, Climax Molybdenum, February, 1959.

55. Semchyshen, M., McArdle, G. D., and Barr, R. Q., "Development of Molybdenum-Base Alloys", WADC TR 59-280, October, 1959.

56. Climax Molybdenum Co., "Developmental Data, Climelt TZM," January, 1962.

57. Semchyshen, M. and Barr, R. Q., "Extrusion and Mechanical Properties of Some Molybdenum- and Tungsten-Base Alloys", Report ASD TR 61-193, Climax-Molybdenum Co., May, 1961.

58. Semchyshen, M., Barr, R. Q. and Chesmar, G. G., "Development of Workable Molybdenum- and Tungsten-Base Alloys", Report NR ASD-TDR-62-508, April, 1962.

59. Lessmann, G. G., "The Comparative Weldability of Refractory Metal Alloys", The Welding Journal, Research Supplement, 45 (12), December, 1966.

60. Stoner, D. R. and Lessmann, G. G., "Operation of 10^{-10} Torr Vacuum Heat Treating Furnaces in Routine Processing", Trans. of the 1965 Vacuum Metallurgy Conference of the American Vacuum Society.

61. Westinghouse Electric Corp., "T-111, Tantalum Base Alloy Refractory Metal", Special Technical Data 52-365 (March, 1963).

62. Armstrong, P., Table SVS 3-63-1 (Communication to R. L. Ammon, Westinghouse Astronuclear Lab.), Los Alamos Scientific Laboratory, March 28, 1963.

63. Private Communication to General Electric, October 27, 1966, McElroy, D. L. and Moore, J. P., Metals and Ceramics Division, Oak Ridge National Laboratory.

64. Private Communication, October 3, 1967, R. L. Ammon, Westinghouse Astronuclear Laboratory.

65. Oak Ridge National Laboratory, Metals and Ceramics Division, Annual Progress Report for Period Ending June 30, 1964, ORNL-3670, p. 109.

66. Hedge, J. C., Kostenko, C. and Lang, J., "Thermal Properties of Refractory Alloys", ASD-TDR-63-597, June, 1963.

67. Southern Research Institute, "Report on the Mechanical and Thermal Properties of Tungsten and TZM Sheet Produced on the Refractory Metal Sheet Rolling Program - Part I", AD 638631, Contract No. N600(19)-5930, 31 August 1966.

68. Bonchak, J., Mueller, C. P. and McNeish, W. A., "Infab Processing of TZM Sheet", AFML-TR-67-298, Universal-Cyclops Division, Cyclops Corp., September, 1967.

APPENDIX B

EXISTING METHODS FOR ESTIMATING TURBINE AERODYNAMIC EFFICIENCY

In general, turbine-blade losses can be categorized as two-dimensional profile losses and three-dimensional losses. The two-dimensional losses consist of surface friction losses due to boundary layers and downstream mixing losses due to boundary-layer and trailing-edge wakes. The three-dimensional losses consist of end-wall boundary layers, secondary flow and shroudline curvature, and tip clearance losses. Two-dimensional profile losses can be predicted with reasonable accuracy as long as the wake region is so thin that it has no effect on the profile velocity distribution. Three-dimensional profile losses present a more difficult problem, and experimental data are required.

For a wide variety of turbine blading, Stewart, Whitney, and Wong[1] have shown that the trailing-edge momentum thickness can be correlated with total blade surface diffusion by the following equation:

$$\frac{\theta_t}{\ell} = \left(\frac{0.003}{1 - 1.4D_t}\right)\left(\frac{3 \times 10^5}{Re_\ell}\right)^{0.2}$$

where

θ_t = total trailing-edge momentum thickness

ℓ = mean chamber line length of blade section

Re_ℓ = blade row Reynolds number based on camber line length

D_t = total surface diffusion parameter

The total diffusion parameter is the sum of the suction surface and pressure surface diffusion parameters defined by:

$$D_t = D_s + D_p$$

$$D_s = 1 - \frac{V_{exit}}{V_{max}}$$

$$D_p = 1 - \frac{V_{min}}{V_{inlet}}$$

where

D_t = total diffusion parameter

D_s = suction side diffusion parameter

D_p = pressure side diffusion parameter

V_{exit} = average exit velocity

V_{max} = maximum velocity on the suction side

V_{min} = minimum velocity on the pressure side

These parameters are related to the blade loading diagram, as shown in Figure 1.

Detailed testing has indicated that turbines designed with zero or minimum suction surface diffusion, D_s, have the best performance. For this situation, an idealized loading is indicated in Figure 1.

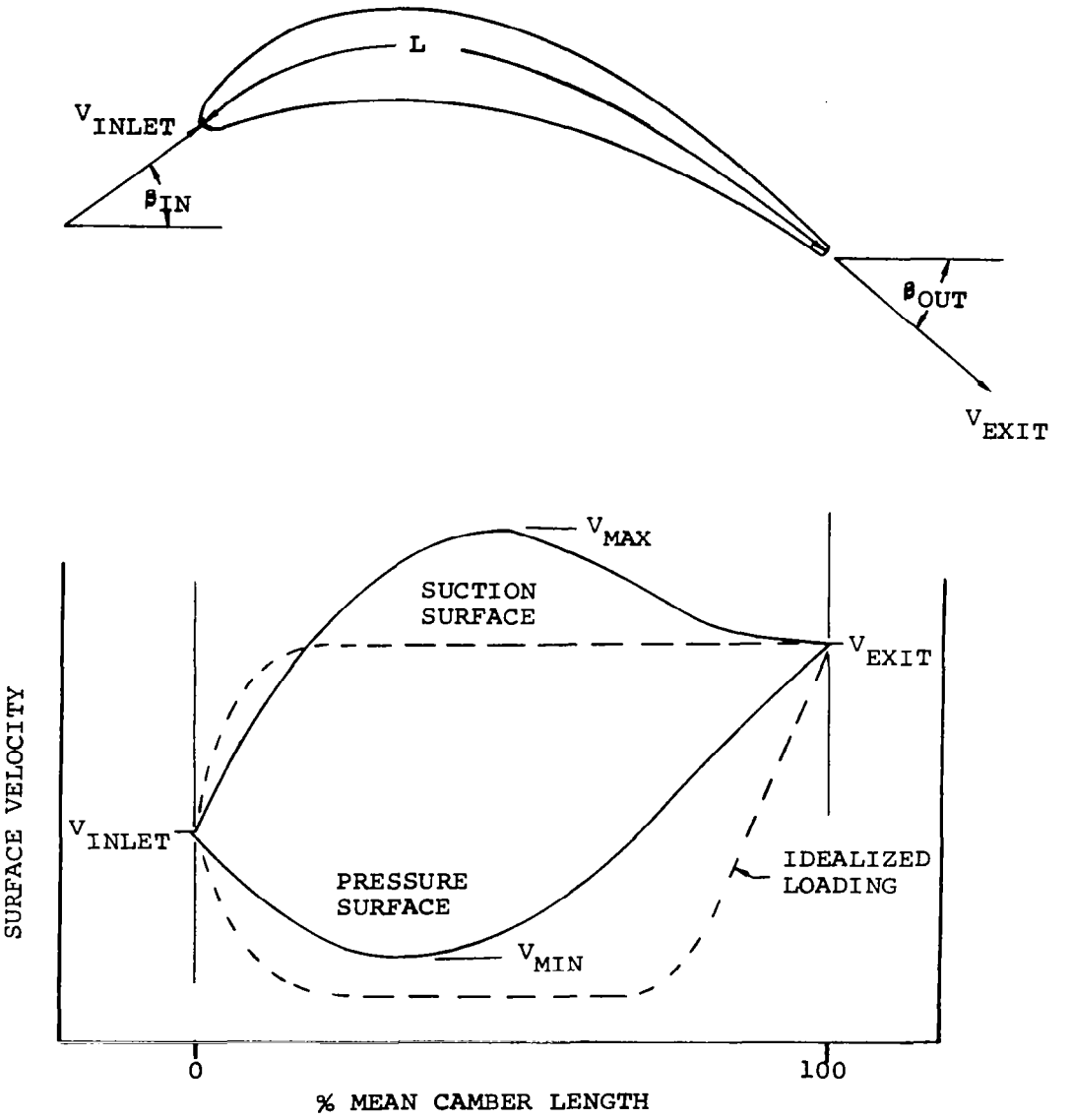

FIGURE 1 BLADE AERODYNAMIC LOADINGS

In the case of the idealized loading, the amount of pressure surface diffusion which can be tolerated is dependent on many factors, but mainly it is limited by the onset of boundary layer separation in the blade passage. If pressure surface diffusions large enough to trigger boundary layer separation in the blade passage are considered, the idealized loading cannot be expected to approximate the actual flow through the blade passage.

Nevertheless, for a specified pressure surface diffusion conforming to the above limitations, the requirements of the upstream and downstream vector triangles will determine, for the idealized loading, a solidity requirement which should be close to optimum. The upstream and downstream vector triangles determine the required blade row calculation, Γ_{REQ}.

$$\frac{\Gamma_{REQ}}{s} = V_{in} \sin\beta_{in} - V_{out} \sin\beta_{out}$$

Contour integration of the idealized loading around the profile determines the blade calculation, Γ_{BLADE}.

$$\frac{\Gamma_{BLADE}}{s} = \left\{ \int_{\text{Suction surface}} V_s \frac{dl}{L} - \int_{\text{Pressure surface}} V_p \frac{dl}{L} \right\} \frac{L}{s}$$

L = mean chamber length

s = blade pitch

However, $\Gamma_{BLADE} = \Gamma_{REQ}$ since the flow through the blade passage can be considered frictionless outside the surface boundary layers. Thus, L/s is determined to satisfy the specified idealized loading. The axial solidity C_x/s is then determined from a geometric correlation of L and C_x using circular arc approximations to the blade profile.

$$\frac{C_x}{s} = \frac{L}{s} \frac{C_x}{L}$$

where

$$\frac{C_x}{L} = F\left(\beta_{in}, \beta_{out}, \frac{L}{s}\right)$$

Optimum blade and vane numbers are determined from the optimum solidity and specified axial chord, C_x.

Local two-dimensional surface friction losses are determined by analysis of the specified idealized surface velocity distributions, using the turbulent boundary layer calculations described in Reference (2).

The calculation determines the trailing edge boundary layer parameters, momentum thickness, θ/L, and displacement thickness, δ^*/L, by integrating a momentum integral equation over the blade surface. Alternately, the correlation of Stewart, Whitney and Wong, presented on Page 1 can be used to determine these parameters from the specified diffusion ratio.

Wake mixing losses are calculated using the methods of Reference (3). The calculation solves the equations of continuity and momentum for compressible flow between the blade trailing edge plane and a plane downstream where mixing is complete.

The analysis described to this point provides estimates of the two-dimensional blade row losses as a function of radius. However, the method is only as valid as the correlations employed; and since these relationships are strictly applicable only to blade sections having small trailing-edge blockage ratios, the results may not reflect the real situation for higher trailing-edge blockage ratios.

Integration of the estimated two-dimensional blade section losses over the entire blade height and correction of the results for end-wall boundary layers provide an estimated loss for the blade row. The end-wall boundary layer correction is described by Stewart, Whitney, and Wong[1]. Combining stator and rotor loss estimates results in a predicted aerodynamic stage efficiency, $\eta_{3D,A}$. A loss correlation for the secondary flow and shroud line curvature is then made, based on test data of numerous AiResearch axial turbines.

Tip-clearance losses in the rotor are correlated by the following equation:

$$\eta_{3D} = \eta_{3D,A} \left[1 - \frac{r_t}{r_m} K \frac{c}{h}\right]$$

where

η_{3D} = stage efficiency for rotor-tip clearance equal to c

$\eta_{3D,A}$ = predicted three-dimensional aerodynamic efficiency at zero clearance

r_t, r_m = rotor-tip and mean radius, respectively

c = rotor-tip clearance

h = rotor-blade height

k = constant, depending on tip-shroud geometry

Figures 2 and 3 indicate the accuracy of the turbine efficiency prediction method described above. The analysis technique was used to

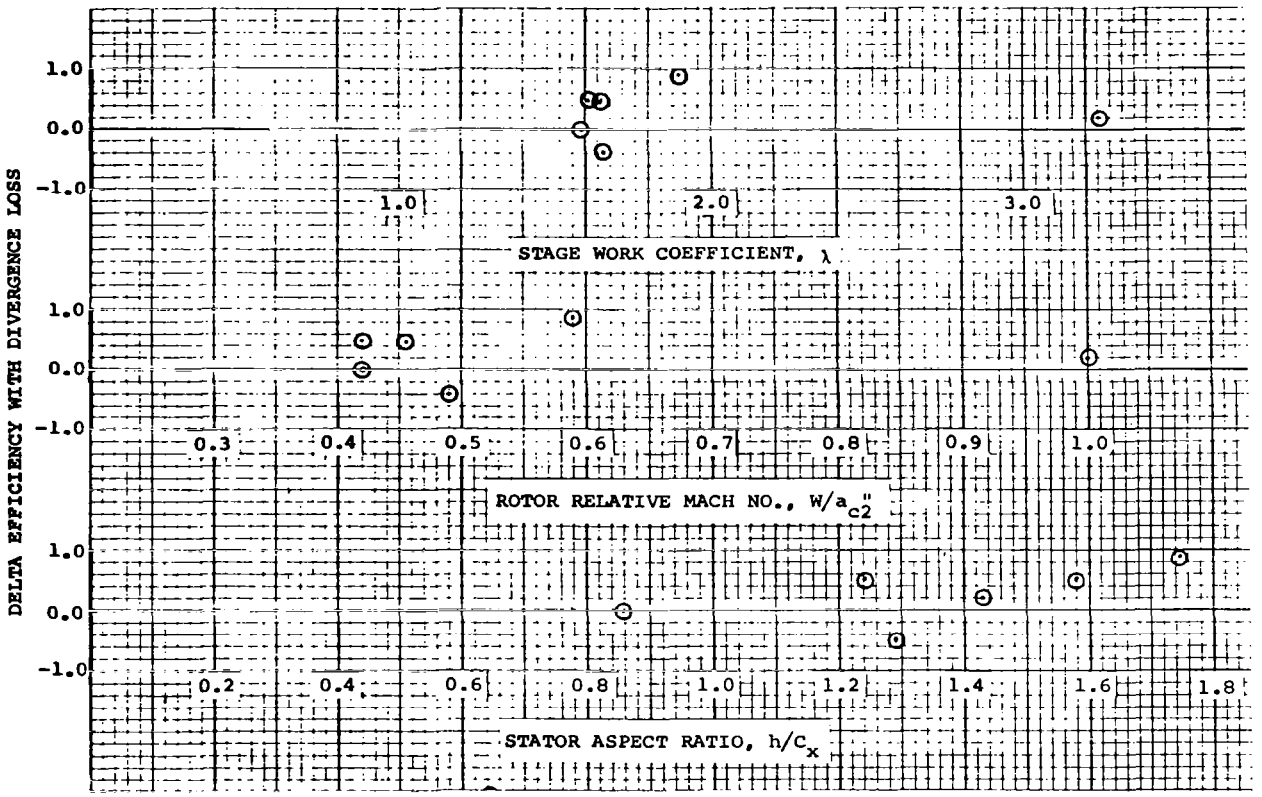

FIGURE 2 PERFORMANCE PREDICTABILITY

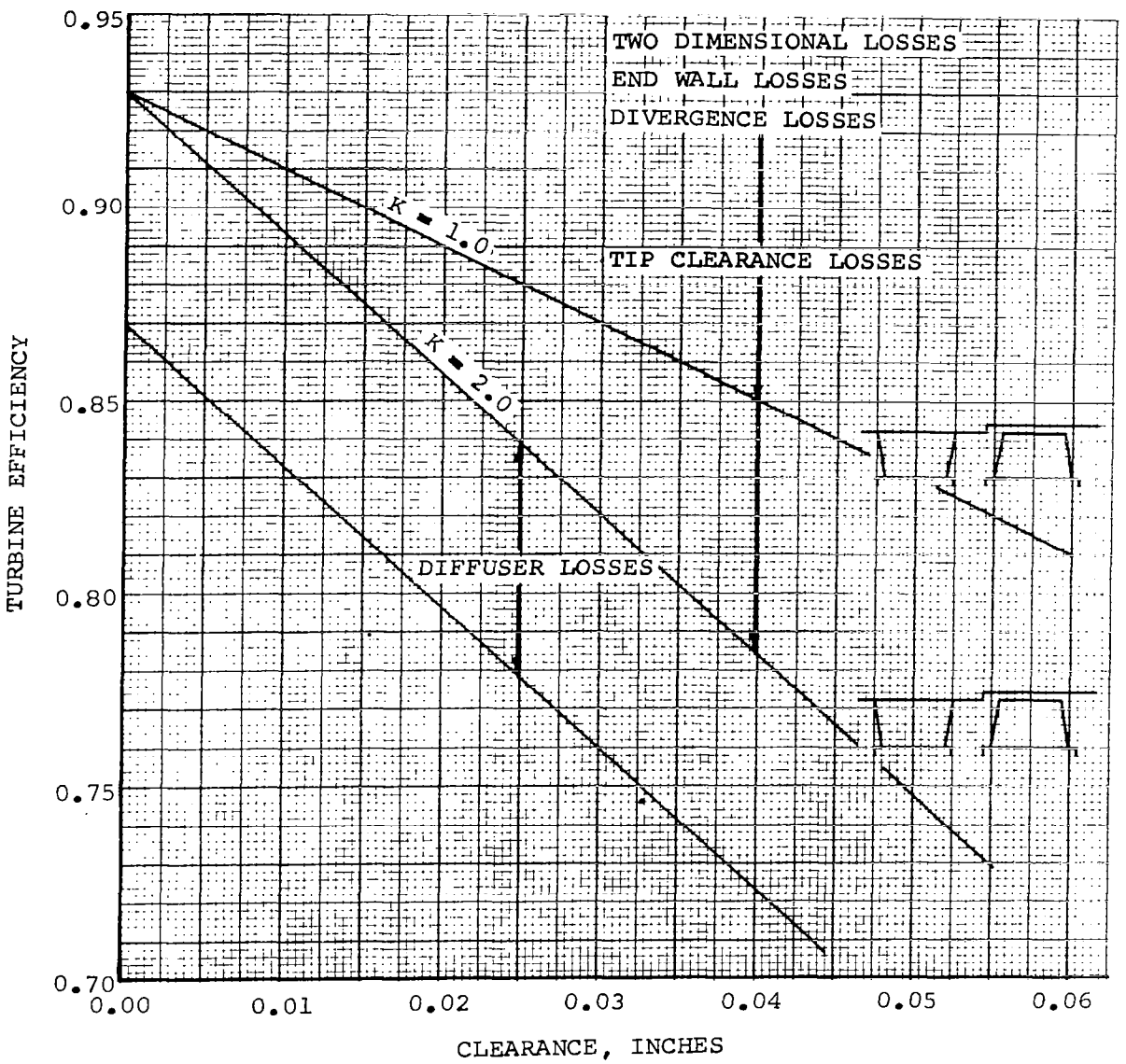

FIGURE 3. ATTAINABLE TURBINE EFFICIENCY

estimate the efficiency levels of several single-stage axial flow turbines designed at AiResearch and NASA. These estimates, including tip clearance and aspect ratio effects, are compared to measured efficiency levels obtained in cold air rig tests. The first figure gives the discrepancy, in percentage points, between the predicted and measured efficiencies for each turbine as a function of:

(a) Stage work coefficient

(b) Rotor inlet relative critical velocity ratio

(c) Stator aspect ratio

The second curve shows a typical loss breakdown for a single-stage turbine for varying rotor clearance and tip-shroud geometry.

REFERENCES

1 Stewart, W. L., W. Whitney, and R. Y. Wong, "A Study of Boundary Layer Characteristics of Turbomachine Blade Rows and Their Relation to Overall Blade Loss," ASME Transactions, Journal of Basic Engineering, Paper No. 59-A-23, 1959.

2 Whitney, W. J., W. L. Stewart, and J. W. Miser, "Experimental Investigation of Turbine-Stator-Blade Outlet Boundary Layer Characteristics and Comparison with Theoretical Results," NACA RM E55K24, March 1956.

3 Stewart, W. L., "Analysis of Two-Dimensional Compressible Flow Loss Characteristics Downstream of Turbomachine Blade Rows in Terms of Basic Boundary Layer Characteristics," NACA TN 3515, July 1955.

APPENDIX C

DERIVATION OF LABYRINTH SEAL LEAKAGE EQUATIONS

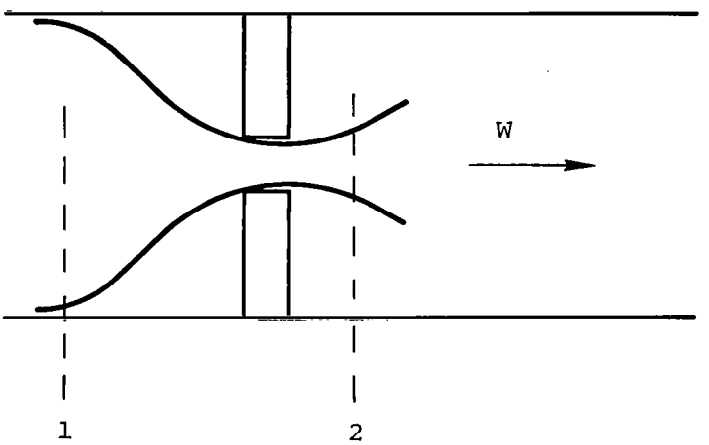

Assuming an isentropic expansion in the region of converging flow, a local mechanical energy balance requires that:

$$\frac{udu}{g} = -VdP \qquad (1)$$

where:

u = local axial velocity, ft/sec

P = static pressure, lb/ft^2

V = specific volume, ft^3/lb

The specific volume varies with static pressure in the following manner:

$$PV^n = P_1 V_1{}^n = \text{constant} \tag{2}$$

where:

$$n = \text{isentropic exponent} = -\frac{V}{P}\left(\frac{\partial P}{\partial V}\right)_s$$

Although n varies with both temperature and pressure in the case of potassium vapor, it can be assumed to remain constant during a single expansion if the pressure ratio is not too large. Since the overall throttling process is one of constant enthalpy, the vapor specific volume in each pocket of the seal becomes a function of either total temperature or total pressure alone. Likewise, the local isentropic exponent can be functionally related to either temperature or pressure along the seal.

After substituting Equation 2 in Equation 1 and integrating:

$$\frac{U_2{}^2}{2g} = -\int_{P_1}^{P_2} V_1 \left(\frac{P_1}{P}\right)^{1/n} dp$$

$$= \frac{nP_1V_1}{n-1}\left[1-\left(\frac{P_2}{P_1}\right)^{(n-1)/n}\right] \tag{3}$$

$$U_2 = \sqrt{\frac{2gnP_1V_1}{n-1}\left[1-\left(\frac{P_2}{P_1}\right)^{(n-1)/n}\right]} \tag{4}$$

where:

U_2 = gas velocity in vena contracta, ft/sec

P_2 = vena contracta static pressure, lb/ft^2

P_1 = total pressure, lb/ft^2

From the continuity equation, the mass flow rate is:

$$W = \frac{U_2\ CA}{V_2} = \frac{U_2\ CA}{V_1}\left(\frac{P_2}{P_1}\right)^{1/n} \tag{5}$$

where:

C = discharge coefficient

A = orifice geometric area, ft^2

Substituting Equation 4 in Equation 5:

$$W = \frac{CA}{V_1}\left(\frac{P_2}{P_1}\right)^{1/n}\sqrt{\frac{2gnP_1V_1}{n-1}\left[1-\left(\frac{P_2}{P_1}\right)^{(n-1)/n}\right]} \tag{6}$$

$$= CA\sqrt{\left(\frac{2gn}{n-1}\right)\frac{P_1}{V_1}\left[\left(\frac{P_2}{P_1}\right)^{2/n}-\left(\frac{P_2}{P_1}\right)^{(n+1)/n}\right]}$$

The pressure ratio corresponding to choked flow can be estimated by differentiating Equation 6 with respect to pressure ratio and setting the derivative equal to zero.

Assuming a constant discharge coefficient and letting $X = P_2/P_1$:

$$\frac{dW}{dX} = \frac{CA\sqrt{\left(\frac{2gn}{n-1}\right)\frac{P_1}{V_1}}\left[\frac{2}{n}X^{2/n} - \frac{n+1}{n}X^{(n+1)/n}\right]}{2X\sqrt{X^{2/n} - X^{(n+1)/n}}}$$

$$= \frac{W}{2X}\left[\frac{\frac{2}{n}X^{2/n} - \frac{n+1}{n}X^{(n+1)/n}}{X^{2/n} - X^{(n+1)/n}}\right] \qquad (7)$$

$$\frac{dW}{dX} = 0 \quad \text{when} \quad X^{2/n}\left[\frac{2}{n} - \frac{n+1}{n}X^{(n-1)/n}\right] = 0$$

Hence, a choked flow condition is reached when:

$$X = \frac{P_2}{P_1} = \left(\frac{2}{n+1}\right)^{n/(n-1)} \qquad (8)$$

Substitution in Equation 4 yields the sonic velocity:

$$U_2 = \sqrt{\frac{2gnP_1V_1}{n-1}\left[1-\left(\frac{2}{n+1}\right)\left(\frac{n}{n-1}\right)\left(\frac{n-1}{n}\right)\right]}$$

$$= \sqrt{\left(\frac{2gnP_1V_1}{n-1}\right)\left(1-\frac{2}{n+1}\right)} \qquad (9)$$

$$= \sqrt{\left(\frac{2gn}{n+1}\right)P_1V_1}$$

Substitution of Equations 8 and 9 in Equation 5 yields the mass flow rate for a choked orifice:

$$W = \frac{CA}{V_1}\left(\frac{2}{n+1}\right)^{\frac{1}{n-1}}\sqrt{\left(\frac{2gn}{n+1}\right)P_1V_1}$$

$$= CA\sqrt{gn\,\frac{P_1}{V_1}\left(\frac{2}{n+1}\right)^{\frac{n+1}{n-1}}} \qquad (10)$$

In the case of a perfect gas PV = RT, and the flow rate equations reduce to the more familiar form:

$$\frac{W\sqrt{RT_1}}{CAP_1} = \sqrt{\left(\frac{2g\gamma}{\gamma-1}\right)\left[\left(\frac{P_2}{P_1}\right)^{2/\gamma} - \left(\frac{P_2}{P_1}\right)^{\frac{\gamma+1}{\gamma}}\right]} \quad \text{(unchoked flow)}$$

$$\frac{W\sqrt{T_1}}{CAP_1} = \sqrt{\frac{\gamma g}{R}\left(\frac{2}{\gamma+1}\right)^{\frac{\gamma+1}{\gamma-1}}} \quad \text{(choked flow)}$$

where:

$\gamma = C_P/C_V$

C_P = specific heat at constant pressure, Btu/lb°F

C_V = specific heat at constant volume, Btu/lb°F

APPENDIX D

POTASSIUM THERMODYNAMIC PROPERTY AND FLOW EQUATIONS

Figure 1 presents the thermodynamic property equations as used by the turbine design program. Figure 2 shows the flow equations which are consistant with the thermodynamic property equations and accurately account for supersaturated vapor flow.

1. Vapor Specific Volume

$$V_v = \left(\frac{R_o}{144M}\frac{T}{P}\right)\left[1 + \frac{B}{V_v} + \frac{C}{V_v^2} + \frac{D}{V_v^3}\right]$$

2. Second Virial Coefficient

$$B = B_1 \, T \, e^{\left(B_2/T\right)}$$

For Potassium

$$B_1 = -3.38156 \times 10^{-6}$$

$$B_2 = 11{,}261.3$$

3. First Derivative of Second Virial Coefficient

$$\frac{dB}{dT} = \left[1 - \frac{B_2}{T}\right]\frac{B}{T}$$

4. Second Derivative of Second Virial Coefficient

$$\frac{d^2B}{dT^2} = \left[\frac{B_2}{T^2}\right]^2 B$$

5. Third Virial Coefficient

$$C = C_1 e^{\left(C_2/T\right)}$$

$$C_1 = 2.52903 \times 10^{-3}$$

$$C_2 = 14{,}703.7$$

6. First Derivative of Third Virial Coefficient

$$\frac{dC}{dT} = -\frac{C_2}{T^2} C$$

FIGURE 1

7. Second Derivative of Third Virial Coefficient

$$\frac{d^2C}{dT^2} = \left[2 + \frac{C_2}{T}\right]\left[\frac{C_2}{T}\,\frac{C}{T^2}\right]$$

8. Fourth Virial Coefficient

$$D = D_1 e^{\left(D_2/T\right)}$$

$$D_1 = -4.81912 \times 10^{-4}$$

$$D_2 = 18{,}107.2$$

9. First Derivative of Fourth Virial Coefficient

$$\frac{dD}{dT} = -\left[\frac{D_2}{T^2}\right]D$$

10. Second Derivative of Fourth Virial Coefficient

$$\frac{d^2D}{dT^2} = \left[2 + \frac{D_2}{T}\right]\left[\frac{D_2}{T}\right]\frac{D}{T^2}$$

11. Saturation Pressure

$$P_{sat} = CPS_1 T^{-CPS_2}\, e^{\left(-CPS_3/T\right)}$$

$$CPS_1 = 1.9714 \times 10^{7}$$

$$CPS_2 = 0.53299$$

$$CPS_3 = 18{,}717.22$$

FIGURE 1 (Contd.)

12. Saturated Liquid Specific Volume

$$v_\ell = \left[VL_1 + VL_2\left(\frac{T_\ell}{1000}\right) + VL_3\left(\frac{T_\ell}{1000}\right)^2 + VL_4\left(\frac{T_\ell}{1000}\right)^3 \right]^{-1}$$

$VL_1 = 56.099$

$VL_2 = -6.9828$

$VL_3 = -0.5942$

$VL_4 = 0.0498$

13. Liquid Phase Enthalpy

$$h_\ell = CH_1 + CH_2 T_\ell + CH_3 T_\ell^2 + CH_4 T_\ell^3 + CH_5 T_\ell^4$$

$CH_1 = 394.2209$

$CH_2 = -0.609266$

$CH_3 = 6.05836 \times 10^{-4}$

$CH_4 = -2.009 \times 10^{-7}$

$CH_5 = 2.481349 \times 10^{-11}$

14. Ideal Gas Enthalpy

$$h^\circ = AHG_1 + AHG_2 T + AHG_3 e^{-\left(AHG_4/T\right)}$$

$AHG_1 = 998.95$

$AHG_2 = 0.127$

$AHG_3 = 24,836$

$AHG_4 = 39,375$

FIGURE 1 (Contd.)

15. Ideal Gas Entropy

$$s^\circ = CS_1 + CS_2 \ln_e T + CS_3 e^{-\left(CS_4/T\right)}$$

$CS_1 = 0.18075$

$CS_2 = 0.127$

$CS_3 = 0.7617$

$CS_4 = 31{,}126$

16. Ideal Gas Specific Heat

$$C_p^\circ = ACP_1 + ACP_2 e^{-\left(ACP_3/T\right)}$$

$ACP_1 = 0.127$

$ACP_2 = 2.888$

$ACP_3 = 28{,}070$

17. Vapor Enthalpy

$$h_v = h^\circ + \left[\frac{R_o}{MJ}\right] T \left\{\frac{1}{V_v}\left[B - T\frac{dB}{dT}\right] + \frac{1}{V_v^2}\left[C - \frac{T}{2}\frac{dC}{dT}\right] + \frac{1}{V_v^3}\left[D - \frac{T}{3}\frac{dD}{dT}\right]\right\}$$

18. Vapor Entropy

$$s_v = s^\circ - \left[\frac{R_o}{MJ}\right]\left\{\ln_e\left[\frac{P}{P_{atm}}\right] - \ln_e\left[\frac{PV_v}{\left(\frac{R_o}{144M}\right)T}\right] + \frac{1}{V_v}\left[B + T\frac{dB}{dT}\right] + \frac{1}{2V_v^2}\left[C + T\frac{dC}{dT}\right] + \frac{1}{3V_v^3}\left[D + \frac{dD}{dT}\right]\right\}$$

FIGURE 1 (Contd.)

19. Vapor Specific Heat

$$C_{P_v} = C_p^\circ - \left[\frac{R_o}{MJ}\right]\left\{1 - \frac{\left[1 + \frac{1}{V_v}\left(B + T\frac{dB}{dT}\right) + \frac{1}{V_v^2}\left(C + T\frac{dC}{dT}\right) + \frac{1}{V_v^3}\left(D + T\frac{dD}{dT}\right)\right]^2}{\left[1 + 2\frac{B}{V_v} + 3\frac{C}{V_v^2} + 4\frac{D}{V_v^3}\right]}\right.$$

$$\left. - \frac{T}{V_v}\left[\left(T\frac{d^2B}{dT^2} + 2\frac{dB}{dT}\right) + \frac{1}{2V_v}\left(T\frac{d^2C}{dT^2} + 2\frac{dC}{dT}\right) + \frac{1}{3V_v^3}\left(T\frac{d^2D}{dT^2} + 2\frac{dD}{dT}\right)\right]\right\}$$

20. Mixture Specific Volume

$$V_m = xV_v + (1 - x)V_\ell$$

21. Mixture Enthalpy

$$h_m = xh_v + (1 - x)\left[h_l + C_{p_l}\left(T_l - T\right)\right]$$

$$C_{p_l} = 0.190$$

22. Mixture Entropy

$$s_m = s_v - (1 - x)\frac{\left[h_v - h_l\right]}{T} + (1 - x)C_{p_l}\ln_e\left[\frac{T_l}{T}\right]$$

FIGURE 1 (Contd.)

a. Energy Equation

$$h + \frac{w^2}{2gJ} = \text{const.} \tag{1}$$

Equation (1) in differential form is

$$\frac{w^2}{gJ}\left(\frac{1}{w}\frac{dw}{dz}\right) + x\frac{dh_v}{dz} + y\frac{dh_\ell}{dz} + yC_{p_\ell}\frac{d\left(T_\ell - T\right)}{dz} + h_v\frac{dx}{dz} + \left[h_\ell + C_{p_\ell}\left(T_\ell - T\right)\right]\frac{dy}{dz} = 0 \tag{2}$$

but since $y = 1 - x$

$$\frac{dy}{dz} = -\frac{dx}{dz}$$

thus

$$\frac{w^2}{gJ}\left(\frac{1}{w}\frac{dw}{dz}\right) + x\frac{dh_v}{dz} - \left[h_v - h_\ell - C_{p_\ell}\left(T_\ell - T\right)\right]\frac{dy}{dz} + y\left[\frac{dh_\ell}{dz} + C_{p_\ell}\frac{d\left(T_\ell - T\right)}{dz}\right] = 0 \tag{3}$$

b. Momentum Equation

$$\rho w\frac{dw}{dz} = -\frac{dP}{dz} - \left(\frac{\delta T_{xx}}{\delta x} + \frac{\delta T_{yz}}{\delta y} + \frac{\delta T_{zz}}{\delta z}\right) \tag{4}$$

let

$$F = \frac{\delta T_{xx}}{\delta x} + \frac{\delta T_{yz}}{\delta y} + \frac{\delta T_{zz}}{\delta z}$$

then

$$w\frac{dw}{dz} = -V_m\frac{dP}{dz} - V_mF \tag{5}$$

For a reversible, adiabatic expansion process

$$\frac{dh}{dz} = V\,dP \tag{6}$$

let

$$V_mF = -\left(1 - \eta_p\right)\left.\frac{dh}{dz}\right|_{s\,=\,c} \tag{7}$$

FIGURE 2

That is for $\eta_p = 1$, there is no friction loss. Thus $(1 - \eta_p)$ is the fraction of the isentropic enthalpy drop that goes to frictional heating.

Equations (5) and (7) combine to form

$$\frac{w}{g}\frac{dw}{dz} = -\eta_p V_m \frac{dP}{dz} \tag{8}$$

c. Continuity Equation

$$\frac{Aw}{\bar{V}} = \text{const.} \tag{9}$$

In differential form, Equation (9) is written

$$\frac{1}{A}\frac{dA}{dz} + \frac{1}{w}\frac{dw}{dz} + \frac{1}{x}\frac{dy}{dz} - \frac{1}{V_v}\frac{dV_v}{dz} = 0 \tag{10}$$

d. State Equation

$$\frac{PV_v}{RT} = \left[1 + \frac{B}{V_v} + \frac{C}{V_v^2} + \frac{D}{V_v^3} + \frac{E}{V_v^4}\right] \tag{11}$$

let

$$Z_c = \left[1 + \frac{B}{V_v} + \frac{C}{V_v^2} + \frac{D}{V_v^3} + \frac{E}{V_v^4}\right] \tag{12}$$

then

$$\ln P + \ln V_v - \ln R - \ln T = \ln Z_c \tag{13}$$

$$\frac{1}{P}\frac{dP}{dz} + \left[1 - \frac{V_v}{Z_c}\frac{\delta Z_c}{\delta V_v}\right]\frac{1}{V_v}\frac{dV_v}{dz} = \left[1 + \frac{T}{Z_c}\frac{\delta Z_c}{\delta T}\right]\frac{1}{T}\frac{dT}{dz} \tag{14}$$

Equations (3), (8), (10) and (14) are rearranged to the following forms

$$\frac{1}{V_v}\frac{dV_v}{dz} = \frac{1}{w}\frac{dw}{dz} + \frac{1}{A}\frac{dA}{dz} + \frac{1}{x}\frac{dy}{dz} \tag{15}$$

FIGURE 2 (Contd.)

$$\frac{1}{T}\frac{dT}{dz} = \frac{\frac{1}{P}\frac{dP}{dz} + \left[1 - \frac{V_v}{Z_c}\frac{\delta Z_c}{\delta V_v}\right]\left[\frac{1}{V_v}\frac{dV_v}{dz}\right]}{\left[1 + \frac{T}{Z_c}\frac{\delta Z_c}{\delta T}\right]} \tag{16}$$

$$\frac{1}{P}\frac{dP}{dz} = -\frac{\frac{w^2}{g}\left(\frac{1}{w}\frac{dw}{dz}\right)}{PxV_v\eta_p} \tag{17}$$

$$\frac{w^2}{gJ}\left(\frac{1}{w}\frac{dw}{dz}\right) + x\frac{\delta h_v}{\delta T}\frac{dT}{dz} + x\frac{\delta h_v}{\delta V_v}\frac{dV_v}{dz} - \left[h_v - h_\ell - C_{p_\ell}\left(T_\ell - T\right)\right]\frac{dy}{dz} + y\frac{\delta h_\ell}{\delta T}\frac{dT}{dz} + yC_{p_\ell}\frac{dT_\ell}{dz} - yC_{p_\ell}\frac{dT}{dz} = 0 \tag{18}$$

It is convenient to further rearrange the energy equation (18) to the following form

$$\frac{1}{w}\frac{dw}{dz} = \frac{\Delta W}{\Delta\theta} \tag{19}$$

where

$$\Delta W = \left(PxV_v\eta_p\right)\left\{\left(1 + \frac{T}{Z_c}\frac{\delta Z_c}{\delta T}\right)\left[\left[h_v - h_\ell - C_{p_\ell}\left(T_\ell - T\right)\right]\frac{dy}{dz} - yC_{p_\ell}\frac{dT_\ell}{dz}\right] - \phi x\left(\frac{1}{A}\frac{dA}{dz} + \frac{1}{x}\frac{dy}{dz}\right) + \left(1 - \frac{V_v}{Z_c}\frac{\delta Z_c}{\delta V_v}\right)\left(\frac{1}{A}\frac{dA}{dz} + \frac{1}{x}\frac{dy}{dz}\right)Ty\left(C_{p_\ell} - \frac{\delta h_\ell}{\delta T}\right)\right\} \tag{20}$$

$$\Delta\theta = \left(PxV_v\eta_p\right)\left[\frac{w^2}{gJ}\left(1 + \frac{T}{Z_c}\frac{\delta Z_c}{\delta T}\right) + x\phi\right] - \frac{w^2}{g}xT\frac{\delta h_v}{\delta T} + yT\left(C_{p_\ell} - \frac{\delta h_\ell}{\delta T}\right)\left[\frac{w^2}{g} - \left(PxV_v\eta_p\right)\left(1 - \frac{V_v}{Z_c}\frac{\delta Z_c}{\delta V_v}\right)\right] \tag{21}$$

FIGURE 2 (Contd.)

$$\phi = Ta\frac{\delta h_v}{\delta T} + V_v\, b\, \frac{\delta h_v}{\delta V_v} \tag{22}$$

$$a = \left(1 - \frac{V_v}{Z_c}\frac{\delta Z_c}{\delta V_v}\right) \tag{23}$$

$$b = \left(1 + \frac{T}{Z_c}\frac{\delta Z_c}{\delta T}\right) \tag{24}$$

FIGURE 2 (Contd.)

The flow equations of the Westinghouse Condensation Model require a value of η_p which appears in the momentum equation. This friction factor may be obtained by first postulating a polytropic expansion process described by:

$$PV^n = \text{constant} \tag{23}$$

The integration of equation (23) over the range of end states across a blade row yields for the polytropic exponent.

$$n = \frac{\ln\left(P_1/P_2\right)}{\ln\left(V_2/V_1\right)} \tag{24}$$

The polytropic path equation (23) may be combined with the momentum equation to form:

$$\frac{1}{g}\int wdw = -\eta_p \int \left(\frac{\text{Const}}{P}\right)^{\frac{1}{n}} dP \tag{25}$$

The integration of equation (25) across a blade row yields for η_p

$$\eta_p = \frac{\left(\frac{n-1}{n}\right)\left(\frac{w_2^2 - w_1^2}{2g}\right)}{\left(P_1V_1 - P_2V_2\right)} \tag{26}$$

Thus, if the end states across a blade row are known, the polytropic expansion exponent is known from equation (24) and the friction factor is obtained from equation (26).

The procedure for finding a value of η_p for a stator blade row differs from the procedure for a rotor blade row. A choice of work

coefficients and blade flow angles for a stage combined with the radial equilibrium equation determines the velocity vector diagrams for that stage. Thus, across a blade row the static radial enthalpy distribution can be calculated from the energy equation. The entropy at the exit of a blade row is determined from a nozzle efficiency for a stator and the aerodynamic efficiency for a rotor. Thus, the mean line thermodynamic states can be calculated for stator and rotor blade rows before it is necessary to apply the flow equations for the integration of condensation phenomena across a blade row. In the AiResearch design program the use of the condensation subroutine is an iterative process in which the row exit diameter is varied until the required velocity vector diagram is satisfied. Thus it is only necessary to approximate η_p for a starting value and as the iterations are performed the correct value is determined from Equations (24) and (26).

APPENDIX E

MECHANICAL DESIGN ANALYTICAL METHODS FOR HIGH-SPEED TURBOMACHINERY

1. INTRODUCTION

This appendix contains a compilation of the analytical procedures and computer programs available at AiResearch which were used for the mechanical analysis of the KTA turbine.

2. TEMPERATURE ANALYSIS

2.1 Transient and Steady-State Temperature Distribution

Digital computer programs have been developed at AiResearch to compute the transient as well as the steady-state temperature distributions for any two- or three-dimensional problem. The conduction heat transfer within a body must satisfy the Fourier conduction equation.

$$\frac{\partial}{\partial x}\left[K\frac{\partial T}{\partial x}\right] + \frac{\partial}{\partial x}\left[K\frac{\partial T}{\partial y}\right] + \frac{\partial}{\partial z}\left[K\frac{\partial T}{\partial z}\right] = \rho\, C_p\, \frac{\partial t}{\partial \theta}$$

The computerized method of solution used at AiResearch for the transient temperature distributions is analogous to the lumped-parameter method. With the lumped-parameter method, the system to be analyzed is divided up into a finite number of small volumes connected together by a network of conductance paths. When the volumes and conductance paths are considered as discrete lumps of capacitance coupled by lumps of resistance, a thermal circuit results.

An energy balance at each volume or node is formed by setting the net rate of heat flow into the point from all sources equal to the rate of thermal energy storage at the node. This results in an ordinary first-order differential equation at each node.

NOMENCLATURE

T_i = current temperature at a node

T_g = gas temperature adjacent to the node

θ = time

C = thermal capacitance of an element

$R_{j,i}$ = thermal resistance between nodes

R_s = thermal resistance between surface exposed to gas and node point

R_B = thermal resistance of boundary layer

$A_{j,i}$ = area for heat flow between nodes

A_g = area exposed to gas

$\Delta L_{j,i}$ = distance between nodes

ΔLg = distance of node from boundary of body

C = specific heat of metal

γ = density of metal

h = heat-transfer coefficient

k = thermal conductivity of metal

V = volume of element

Q = heat source or sink, Btu per sec

For example, consider a typical node of the thermal circuit, as shown below:

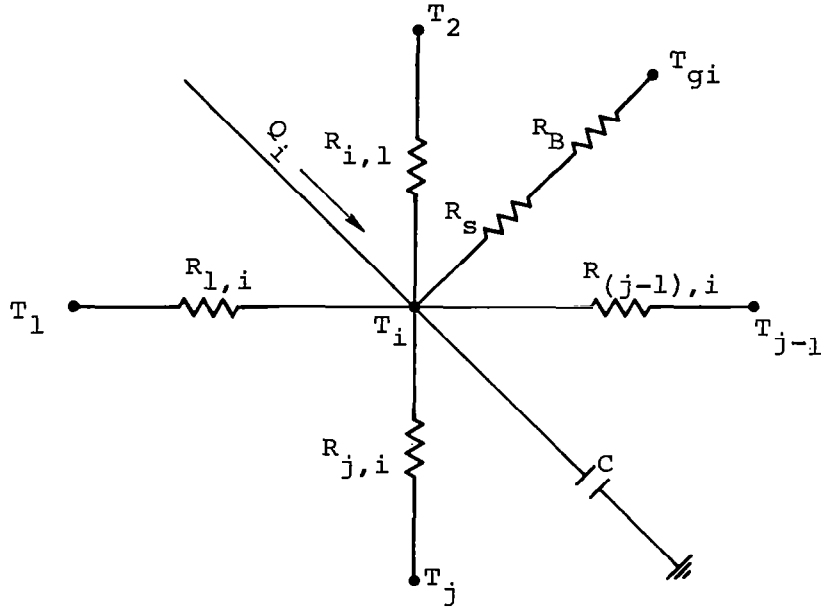

An energy balance for this node gives the following differential equation:

$$\frac{T_1 - T_i}{R_{1,i}} + \frac{T_2 - T_i}{R_{2,i}} + \ldots + \frac{T_{j-1} - T_i}{R_{(j-1),i}} + \frac{T_j - T_i}{R_{j,i}} + Q_i + \frac{T_{gi} - T_i}{R_{si} + R_{Bi}} = C \frac{d\,T_i}{d\theta}$$

NOTE: (1) For a two-dimensional problem, j is normally 4 or less, while for a three-dimensional problem, j could have a value of 6.

(2) The resistances between points are expressed as $R_{j,i} = [\Delta L/KA]_{j,i}$ and the capacitance at each point as $C_i = \gamma c V_i$.

The above type of equation would result at each node, giving a set of n differential equations where the maximum value of i would be determined by n, the number of nodes in the problem. A method of numerical integration is then used to solve this set of differential equations simultaneously to give the temperature distribution at any time.

For the steady-state solution the equations reduce to a set of algebraic equations that are solved simultaneously to give the steady-state temperature distribution.

Both transient and steady-state analysis include the changes in material thermal conductivity and specific heat with temperatures. Up to nine materials have been considered in a single problem, each one having a different variation of its thermal properties with temperature. The present transient-temperature computer programs will handle up to four different variations of heat-transfer coefficient and gas temperatures with time in a single problem. There is virtually no restriction on the type of variation that can be considered.

In many of the temperature problems at AiResearch the presence of a small cooling flow must be included in the analysis, and the thermal capacitance of the coolant must be a part of the analysis to accurately determine the coolant temperature at each node. This has been included in both transient and steady-state temperature programs at AiResearch.

2.2 Gas Temperatures and Heat Transfer Coefficients

The boundary conditions for heat transfer analyses include the distribution of gas temperatures and heat transfer coefficients. These properties must be accurately determined.

Temperatures of the high velocity gases are determined by thermodynamic calculations that include the effects of heat transfer, pumping, recovery, and relative velocities. A variety of techniques

have been developed for predicting heat transfer coefficients for ducts, nozzles, rotating disks, and blades. Computer programs are available for determining the heat transfer coefficients around bodies of arbitrary shape.

3. STRESS ANALYSIS

3.1 Stress Analysis of Symmetrical Disks

The stress analysis of axial flow disks is usually performed using a symmetrical disk program.

This program utilizes the method of analysis described in NACA Report No. 871 to calculate elastic stresses, growth and physical properties for a symmetrical disk. The program calculates centrifugally and thermally induced stresses using input material properties as functions of temperature.

The method of analysis is essentially a finite difference solution of the following equations:

EQUILIBRIUM EQUATION

$$\frac{d}{dr}(rh\delta r) - h\delta t + \rho w^2 hr^2 = 0$$

COMPATIBILITY EQUATION

$$\frac{d}{dr}\left(\frac{\delta t}{E}\right) - \frac{d}{dr}\left(\frac{\mu \delta r}{E}\right) + \frac{d}{dr}(\alpha \Delta T) - \frac{(1 + M)(\delta r - \delta t)}{Er} = 0$$

3.2 Elastic-Plastic Symmetrical Disk

An elastic-plastic symmetrical disk program which utilizes the method of analysis described in NACA Report No. 906 is available.

This program provides the stress distribution of a thin symmetric disk after plastic flow or elastic creep has occurred. The following assumptions are made in the analysis:

(a) The disk material is linearly elastic up to the proportional limit; and above this limit, plastic flow occurs.

(b) All variables of material properties and operating conditions are symmetrical about the axis of rotation.

(c) Axial stress may be neglected and the stress and temperature distribution is uniform across the thickness.

(d) The volume of the disk material above the elastic limit remains constant.

Since the axial stresses have to be neglected, the complete state of stress is defined when the two principal stresses, radial and tangential, are known. These may be determined from the equations of equilibrium and compatibility. The first of these equations involves no properties of the material and may be written

$$\frac{d}{dr}\left(rh\sigma_r\right) - h\sigma_t + \rho w^2 r^2 h = 0 \qquad (1)$$

The compatibility equations, however, must be modified to take into account any deviation from Hooke's law:

$$\varepsilon_r = \frac{du}{dr} = \frac{\sigma_r - \nu\sigma_t}{E} + \alpha\Delta T + \Delta_r + \delta_r$$

$$\varepsilon_t = \frac{u}{r} = \frac{\sigma_t - \nu\sigma_r}{E} + \alpha\Delta T + \Delta_t + \delta_t$$

The parameter u may be eliminated resulting in:

$$\frac{d}{dr}\left(\frac{\sigma_t}{E} - \frac{\nu\sigma_r}{E} + \alpha\Delta T + \Delta_t + \delta_t\right) = \frac{1+\nu}{E}\left(\sigma_r - \sigma_t\right) + \frac{\Delta_r - \Delta_t}{r} + \frac{\delta_r - \delta_t}{r} \quad (2)$$

This equation, together with the equation of equilibrium, is then solved by means of finite difference equations as outlined in NACA Reports Nos. 871 and 906.

Yielding is assumed to occur if the equivalent stress based on Von Mise's criterion exceeds the proportional limit at a given temperature, where

$$\sigma_e = \frac{1}{\sqrt{2}}\left[\left(\sigma_1 - \sigma_2\right)^2 + \left(\sigma_2 - \sigma_3\right)^2 + \left(\sigma_3 - \sigma_1\right)^2\right]^{1/2}$$

For a biaxial state of stress, however, the above relationship simplifies to

$$\sigma_e = \left(\sigma_r^2 - \sigma_r\sigma_t + \sigma_t^2\right)^{1/2}$$

If σ_e > proportional limit, the total equivalent strain based on σ_e and the initial value of plastic strain (ε_p on Figure 1) are taken as the difference between the total strain and the elastic strain based on σ_{p_1} where σ_{p_1} lies on the stress-stain curve for T_n which is interpolated between the two chosen temperatures T_j and T_{j+1} entered in the input. Now ε_p is the minimum plastic strain, which when used in the solution of the equilibrium and compatibility equations results in an equivalent stress σ_{p_2}, but σ_{p_2} does not necessarily lie in the stress-stain curve. If it does not, the plastic strain is increased slightly until the above condition is satisfied.

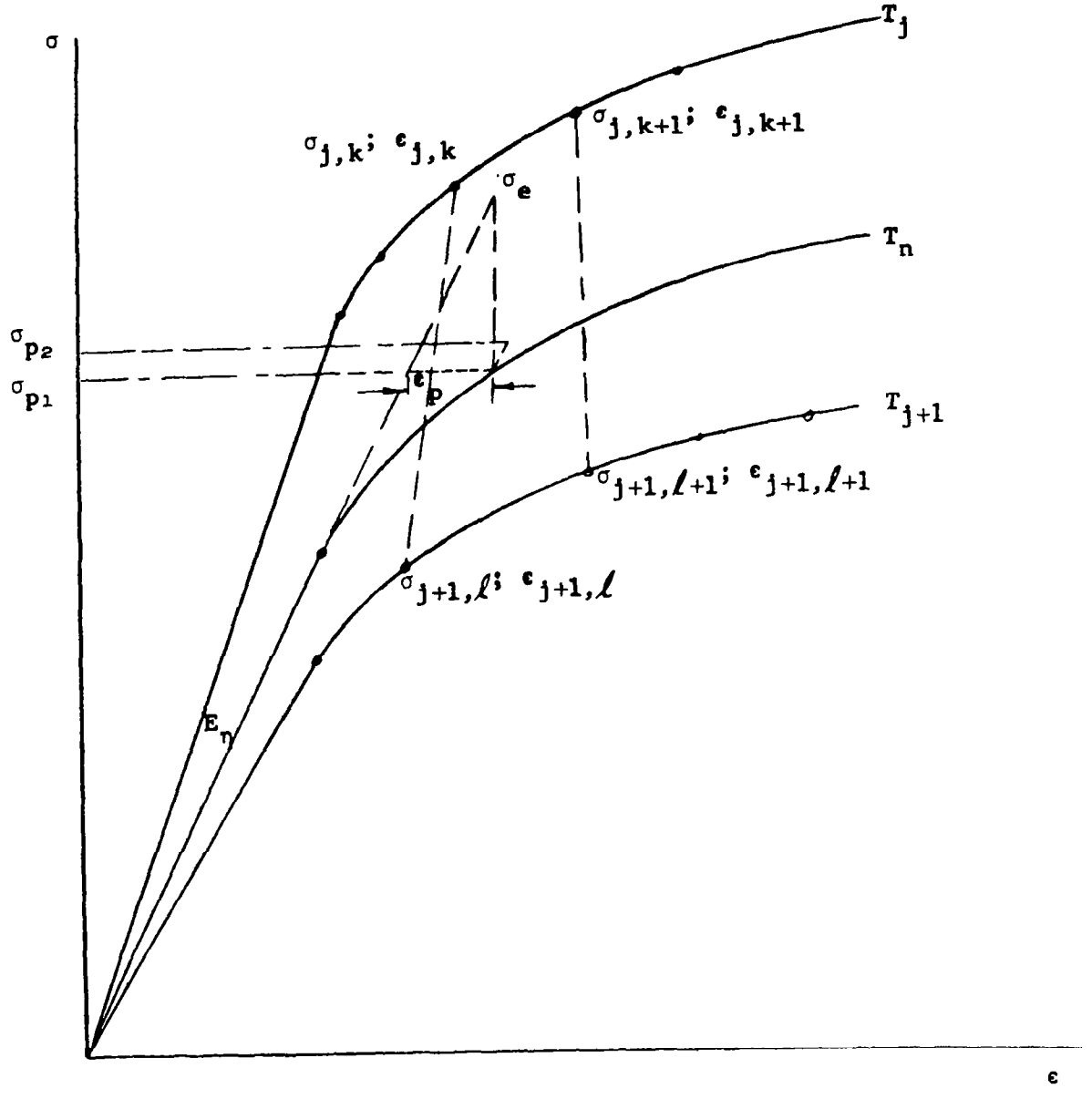
σ
T_j
$\sigma_{j,k+1}$; $\epsilon_{j,k+1}$
$\sigma_{j,k}$; $\epsilon_{j,k}$
σ_e
T_n
σ_{p2}
σ_{p1}
ϵ_p
T_{j+1}
$\sigma_{j+1,\ell+1}$; $\epsilon_{j+1,\ell+1}$
$\sigma_{j+1,\ell}$; $\epsilon_{j+1,\ell}$
E_η
ε

FIGURE 1

Creep rate may be input to the program by the expression:

$$\text{Creep rate} = K\delta_e^{\,n}$$

where

K = constant (in./in./hr)

n = constant (dimensionless)

3.3 Centrifugal Blade Stresses

The stress levels in a rotating beam may be determined numerically by various methods.

In such methods, it is assumed that the mass of the blade is concentrated at discrete points along its axis and that the section of beam between two points is massless but possesses the elastic properties of the real beam.

The method is used to determine forced-vibration amplitude ratios and, as a special case, may be used to determine "static" deflections and stress levels.

In general, it is assumed that the blade is a straight radial beam and that bending takes place in a plane perpendicular to the plane of rotation.

The stress levels in an axial turbine or compressor blade can be adequately determined only if the following factors are considered:

(a) Initial curvature of blade centroidal axes. The curvature may be large.

(b) Unequal bending stiffness and twist of the principal axes with respect to the centroidal axes.

(c) Aerodynamic loading producing bending in two planes, and torsion.

(d) A complete range of permissible boundary values at the blade root.

(e) For vibration stresses to be determined, damping must be included in the analysis.

AiResearch has developed a digital program which is based on the above mentioned assumptions, for the determination of blade stresses.

3.4 Blade Attachment Stress

The life of blade fasteners at elevated temperatures is not readily predictable by rigorous analytical means; however, two empirically based analyses which bracket blade attachment lives have been developed.

The first analysis is based upon test results presented in ASME Paper No. 55-A-122 entitled "Correlation of Fir-Tree Type Turbine-Blade Fastening Strength with Mechanical Properties of Materials". Test data presented in this paper indicates a good correlation between fir tree life, in the absence of vibration, and notched stress-rupture life for fasteners subjected to centrifugal forces. To determine lower limit a proprietary computer analysis is employed.

In this analysis six loads, 3 mutually perpendicular forces and moments, may be applied to the platform of the fastener; thus, both aerodynamic and centrifugal blade loadings may be considered.

The platform loadings are assumed to be reacted by linear loads along the "contact" patches of each of the lobes - the location of this contact line is dependent upon geometry and modulus of elasticities of the mating parts. The eccentricity of the assumed line load results in both tensile and bending stresses within the fillet of the fastener.

Appropriate stress concentration factors, determined experimentally, are then applied to each of these stresses.

At this point another empirical factor, used to correct for vibration, is applied - its value was determined from correlation of analytical results to experimental data.

The result is a combined stress. To determine the lower limit of the fastener life, the combined stresses are compared to a design stress based upon the stress rupture strength of the material used.

3.5 Advanced Analytical Techniques

A finite element program is in use for the stress analysis of elastic axisymmetric bodies. The program permits external, thermal and rotational loadings as well as prescribed boundary displacements anywhere within or on the boundary of the body.

Bladed disks can be analyzed, the blades being approximated by plane stress elements with stiffness assumed uniformly distributed in the circumferential direction. The analysis has been extended to bladed disks with anisotropic elements, e.g., filament reinforced regions. Currently under development are extensions of the program to include force-fits, plasticity, and creep. These more modern methods, having had substantial experimental verification, are now supplementing programs which have been in use a number of years and include plasticity and creep.

Additional programs are available for blade analysis including plane stress or plane strain, thermal stresses and creep effects.

APPENDIX F

ANALYSIS OF POTASSIUM LIQUID VISCOSEAL FOR THE KTA TURBINE

It is desirable to optimize the viscoseal thread geometry to secure the maximum pressure rise per unit length of the seal. Assuming a given shaft diameter, radial clearance, and shaft speed, the design variables to be investigated include thread depth, pitch angle, ratio of channel width to land width, and number of thread starts. An optimization study of viscoseals was conducted, based on equations developed in Reference 1, but modified to include an end effect correction similar to that described in Reference 2.

The pressure rise for a 2-in.-diameter viscoseal is plotted versus thread depth in Figures 1 through 4 to illustrate the effect of various parameters on seal performance. The particular seal chosen for this example is the one adjacent to the KTA turbine thrust bearing. It is a double-thread seal (identical threads on both rotor and housing), with an actual radial clearance of 0.005 in. In accordance with the procedure discussed in Appendix B of Volume II, an equivalent single-thread clearance of 0.0025 in. was used in the analysis.

Examination of the figures reveals that the optimum channel width is approximately 60 percent of the combined channel and land width, independent of the other variables. Also, the optimum pitch angle decreases as the channel depth increases, and at least 20 interlaced threads are needed to obtain a close approach to the maximum theoretical pressure rise. The latter condition arises due to end effects associated with the relatively short seal lengths assumed in the analysis.

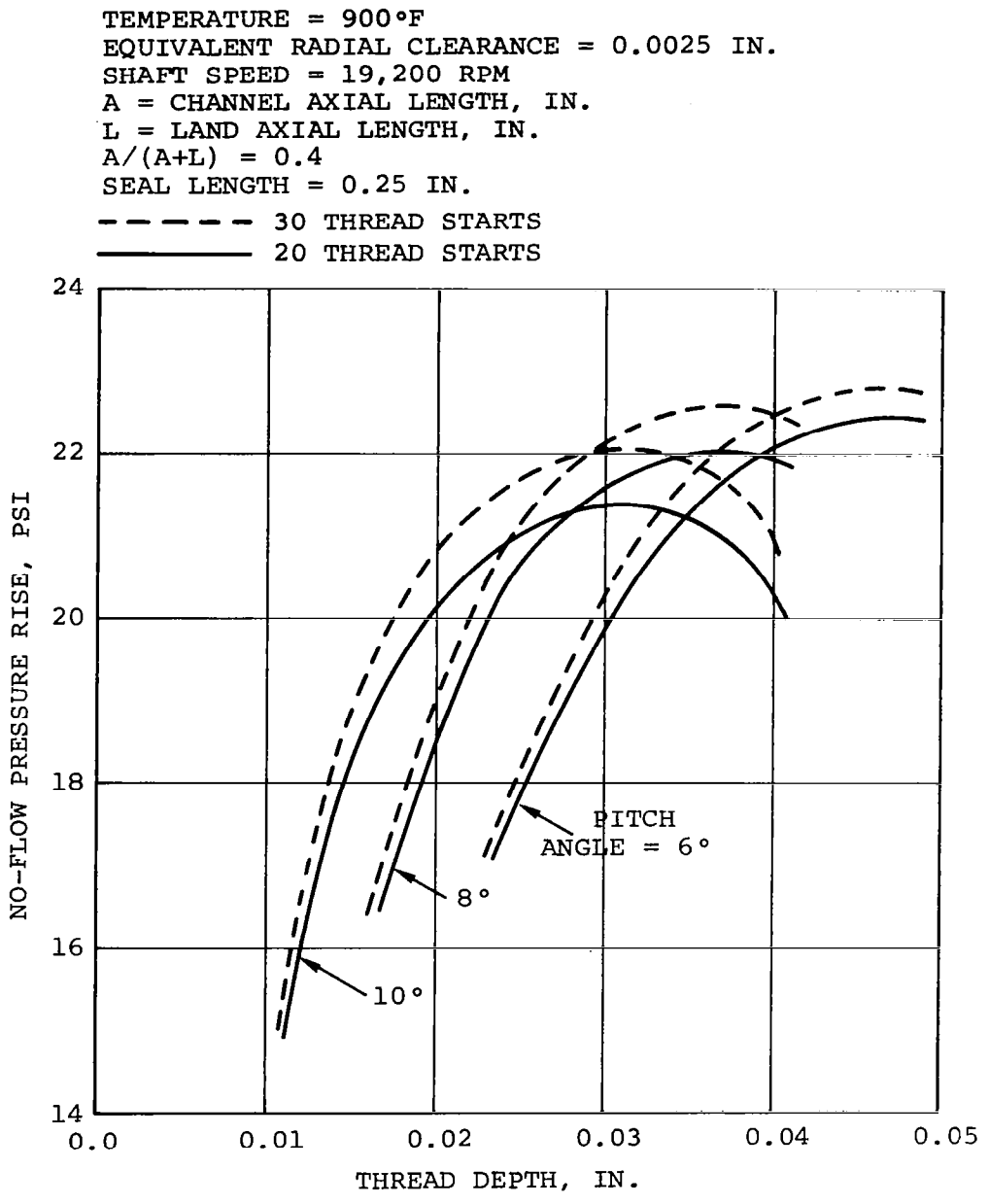

OPTIMIZATION OF POTASSIUM

LIQUID VISCOSEAL GEOMETRY

FIGURE 1

TEMPERATURE = 900°F
EQUIVALENT RADIAL CLEARANCE = 0.0025 IN.
SHAFT SPEED = 19,200 RPM
A = CHANNEL AXIAL LENGTH, IN.
L = LAND AXIAL LENGTH, IN.
A/(A+L) = 0.5
SEAL LENGTH = 0.25 IN.
— — — - 30 THREAD STARTS

———— 20 THREAD STARTS

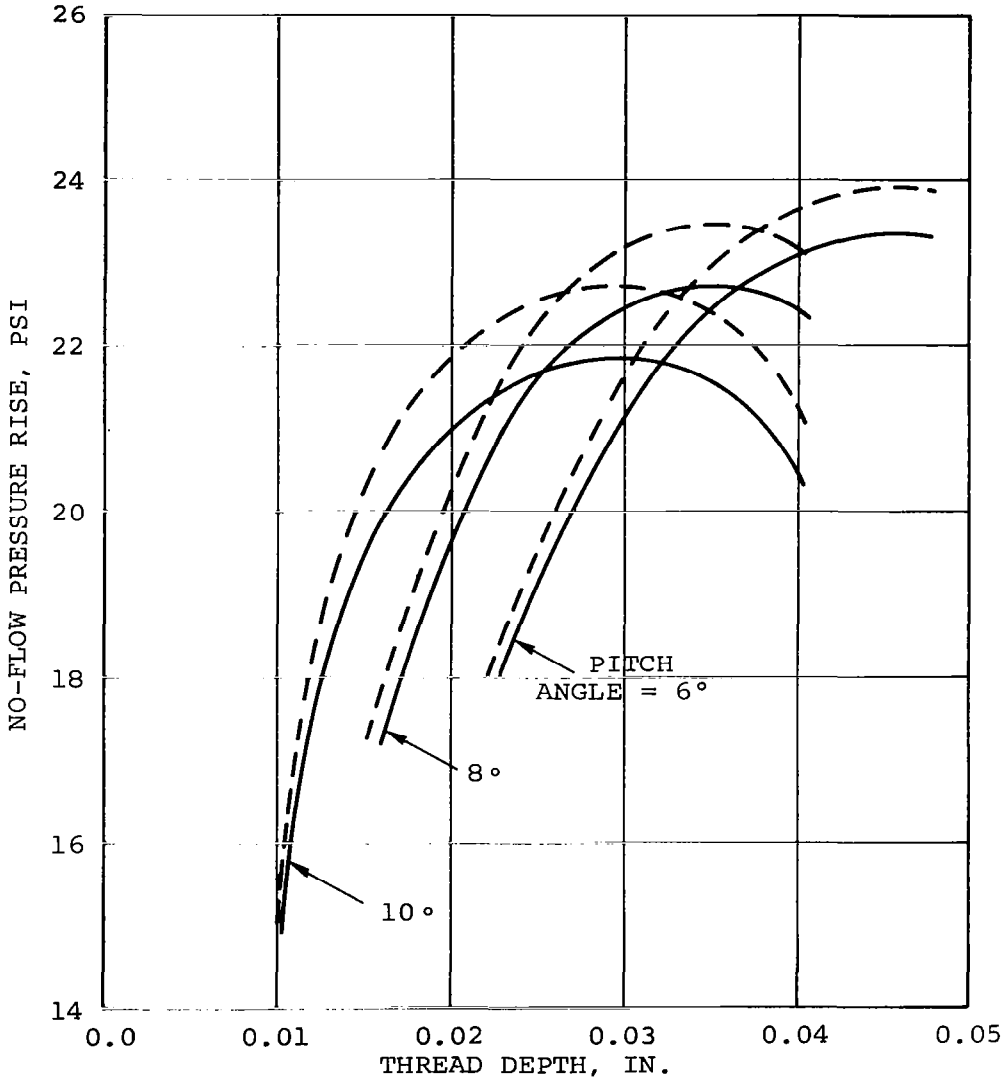

OPTIMIZATION OF POTASSIUM

LIQUID VISCOSEAL GEOMETRY

FIGURE 2

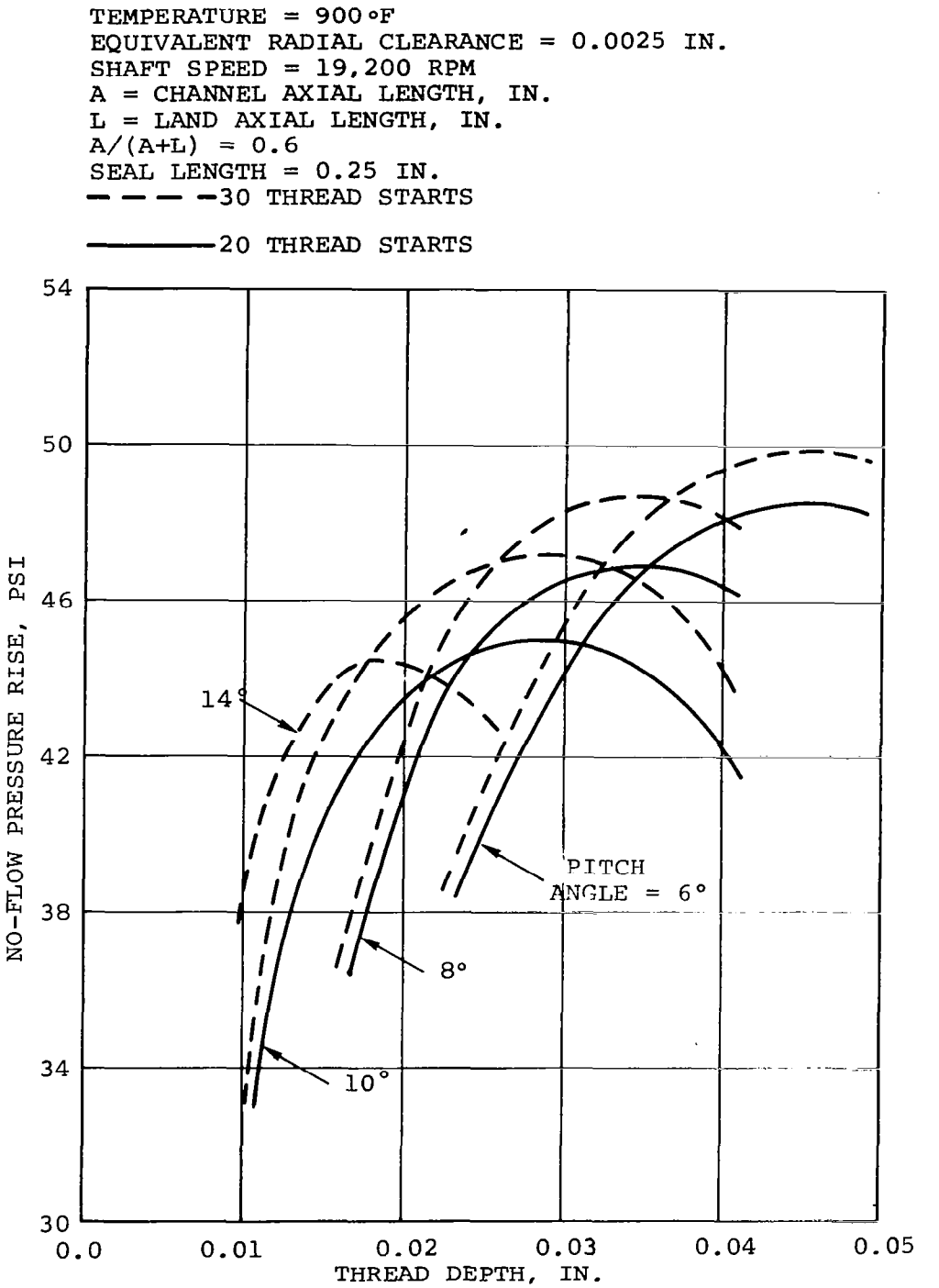

OPTIMIZATION OF POTASSIUM

LIQUID VISCOSEAL GEOMETRY

FIGURE 3

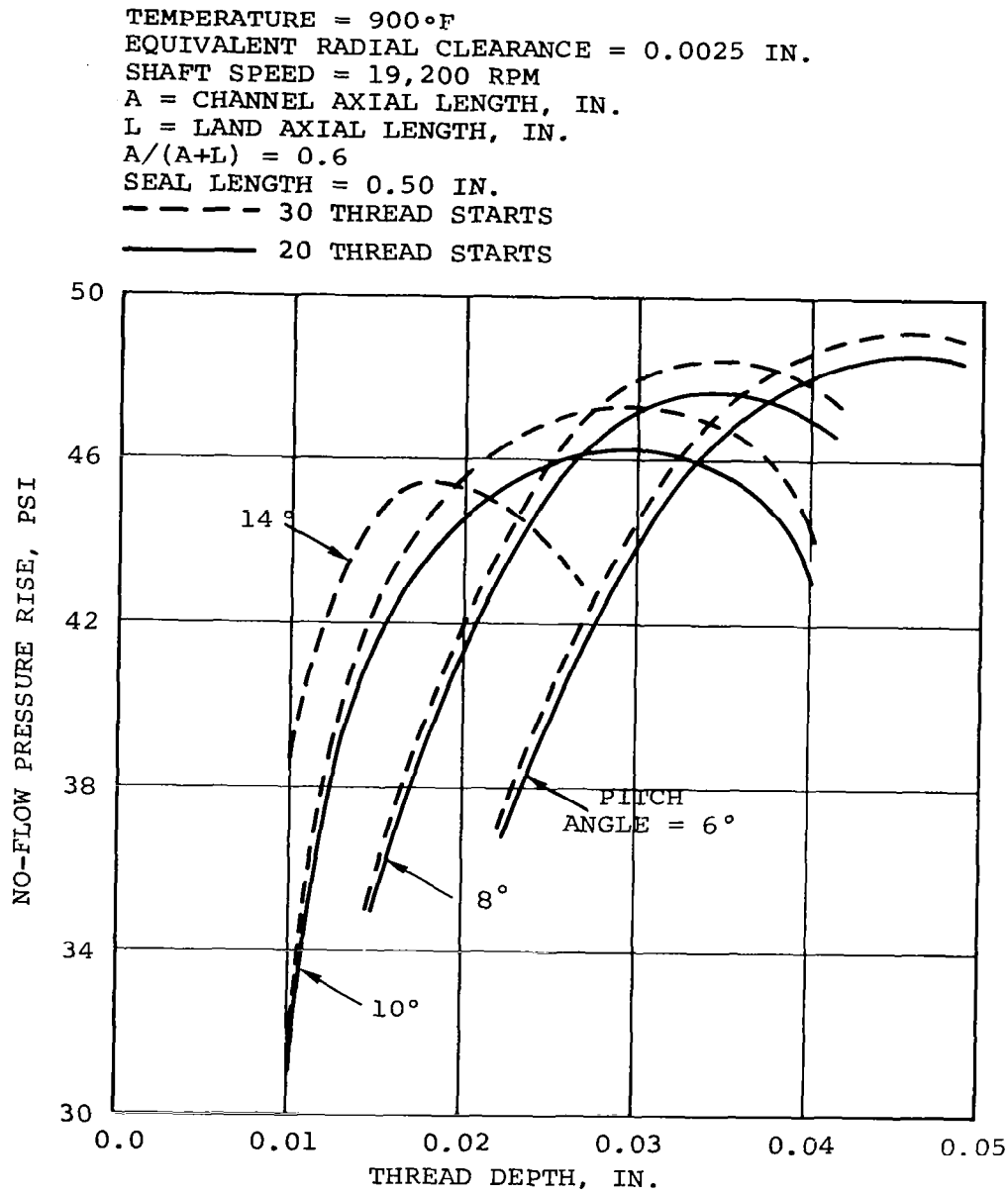

OPTIMIZATION OF POTASSIUM

LIQUID VISCOSEAL GEOMETRY

FIGURE 4

Increasing the thread depth and number of thread starts may be of less benefit than the analysis would seem to indicate, since this causes the channel aspect ratio (ratio of depth to width) to increase beyond the point where the basic assumptions of Reference 1 apply. The effect of increased channel aspect ratio on the performance of a double-thread seal configuration can best be established through actual testing with potassium or other fluids.

It is conceivable that the optimum thread geometry will differ for the rotor and housing surfaces of a double-thread viscoseal. A better mathematical model for such a configuration can possibly be established in conjunction with a test program.

Test data to verify the indicated optimum configurations is not available. Thus, a smaller thread depth (0.018 in.) and a larger pitch angle (14 deg) were specified for the KTA design. This configuration is in the range of viscoseal designs that have been verified by other investigations. Figures 3 and 4 show the selected configuration compared to the others used in the analysis.

REFERENCES

1. Ketola, H. N. and McGrew, J. M., "Turbulent Operation of The Viscoseal," ASLE/ASME Report No. 66LC-12, 1966.

2. King, A.E., "A Holweck Type Molecular Vacuum Pump Used as a Shaft Seal for Alkali Metal Vapors," Report No. WAED 63.10E, 1963.

APPENDIX G

ANALYSIS OF ALTERNATE REAR TURBINE SEAL

An analysis of the potassium evaporation rate from the rear turbine viscoseal to the alternator scavenge system is presented herein. The rate was excessive, and a molecular pumping seal was designed to reduce this leakage and change the leakage direction from the alternator toward the turbine.

The problem is not the leakage, per se, but the required inventory control. If the leakage is a vapor from the turbine to the alternator, the inventory control requires the introduction of iron-contaminated liquid potassium from the alternator loop to the refractory turbine loop. However, if the vapor leakage (without contamination) is from the alternator loop to the turbine loop, then the liquid inventory control is from the clean turbine loop to the alternator loop.

Figure 1 shows the calculated leakage rate for the rear turbine viscoseal as a function of interface temperature. Since the reference design interface temperature is 920°F, the leakage will be very large (1.43 lb/hr) with choked flow (see Appendix C for equations used). The results of this analysis indicated the need for the Holweck pump alternate seal system.

The Holweck molecular pump is schematically shown in Figure 2. The subsequent calculation of pressure rise is based on the techniques discussed by A. E. King* and utilized the following simplifying assumptions:

*King, A. E., "A Holweck-Type Molecular Vacuum Pump Used As A Shaft Seal for Alkali Metal Vapors", Report No. WAED G3.10E, 1963.

SHAFT DIAMETER, IN. = 2.75
RADIAL GAP, IN. = 0.005
DISCHARGE COEFFICIENT = 0.8
DOWNSTREAM PRESSURE, PSIA = 0.0449

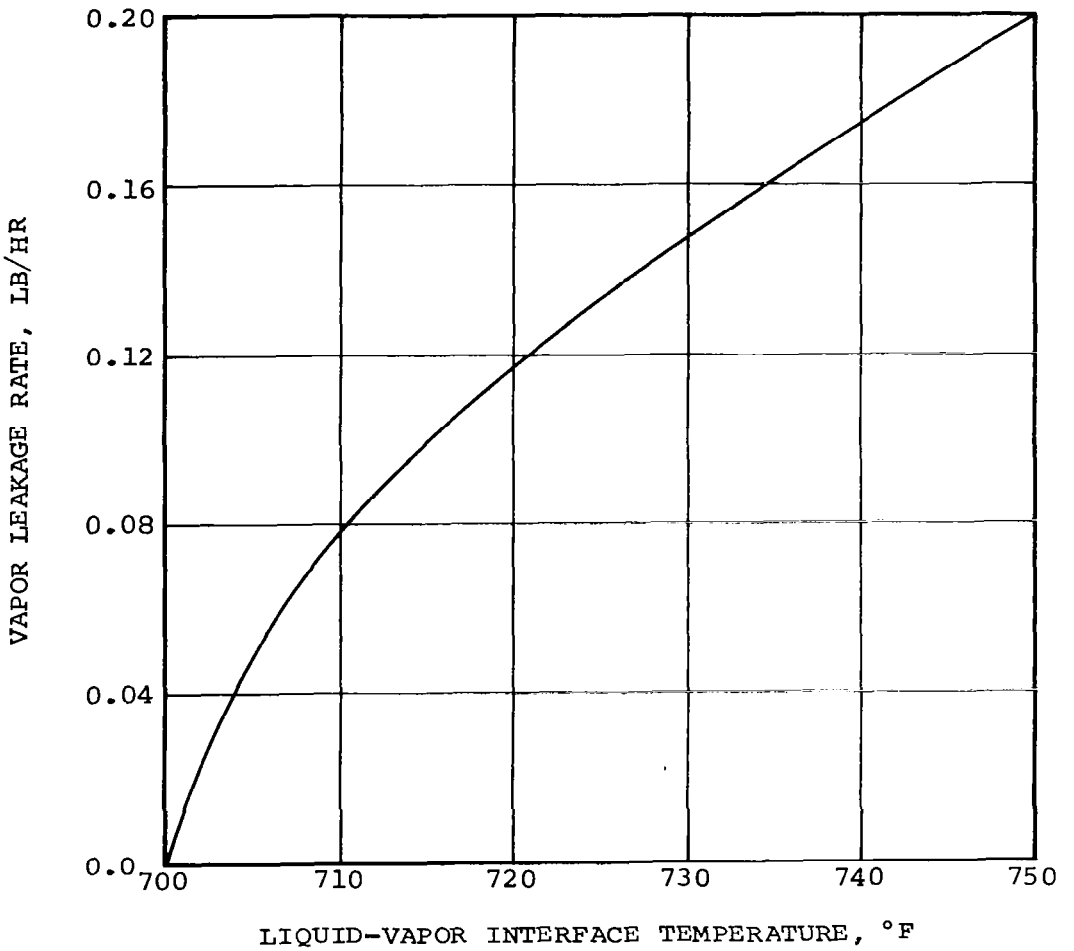

SEAL LEAKAGE IN THE ABSENCE OF PUMPING

FIGURE 1

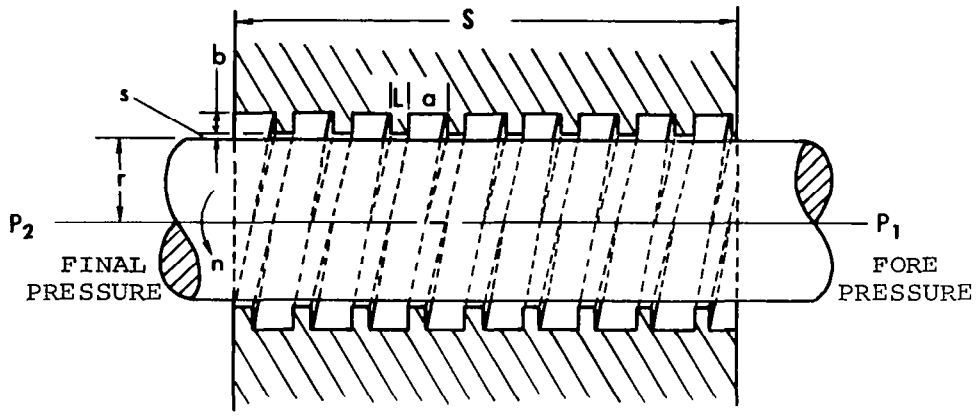

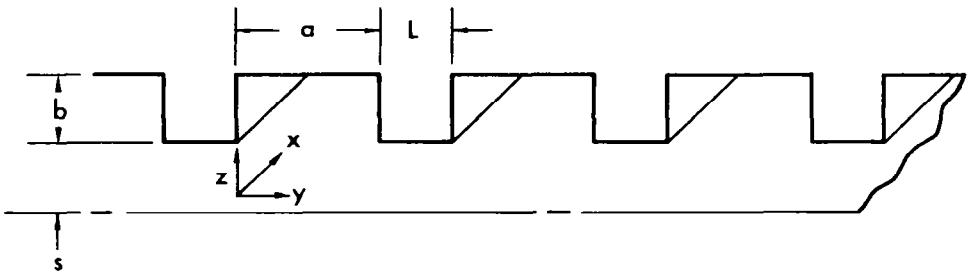

HOLWECK MOLECULAR PUMP SCHEMATIC

FIGURE 2

(a) Steady-state isothermal flow through the seal

(b) Negligible gas velocities in the y and z directions

(c) Velocity gradient with respect to x negligible compared to velocity gradient with respect to y and z

(d) Concentric smooth rotor and threaded housing

(e) Negligible radial pressure gradient induced by high-speed rotor

(f) Local Mach number, less than one

(g) Laminar or transition slip flow, using appropriate value for slip factor

It is desirable to optimize the internal thread dimensions to secure the maximum pressure rise for a given seal length. This was restricted to 1 in. due to the clearance between the turbine and the coupling. Hence, certain restraints on the pitch angle must be observed in order to assure that the entire bore circumference is occupied by at least one thread.

The maximum allowable pitch angle is thus given by

$$\alpha_{max} = \tan^{-1} (N\ S/\pi\ D)$$

where

α_{max} = maximum allowable pitch angle

N = number of thread starts

S = seal length = 1.0 in.

D = shaft diameter, in.

For a given seal length, shaft diameter, number of thread starts, and pitch angle, the remaining variables to be optimized are the thread depth and ratio of thread width to land width.

Figure 3 shows the maximum no-flow pressure rise as a function of thread depth and the ratio of thread width to land width for a 3-in. shaft diameter with a fore-pressure corresponding to 800°F saturated potassium vapor. A single thread start and a thread width of 40-percent of the seal length is the best geometry in conjunction with the maximum allowable pitch angle (α_{max}). Similar information for shaft diameters of 4 and 5 in. is shown in Figures 4 and 5. The optimum thread depth increased slightly with increasing diameter while the optimum thread width was constant.

The effect of pitch angle on seal performance is shown in Figures 6, 7, and 8 for a single-thread start and the same range of shaft diameters. The highest pressure rise is obtained with the maximum pitch angle in each case. This same trend was noted for two thread starts, but the two starts gave lower pressure rise than the one start.

In order to make certain that any net flow of vapor is in the desired direction (away from the low-pressure cavity), the molecular

FORE PRESSURE, PSIA = 0.1547
RADIAL CLEARANCE, IN. = 0.005
SHAFT SPEED, RPM = 19,200

A = THREAD AXIAL LENGTH, IN.
L = LAND AXIAL LENGTH, IN.

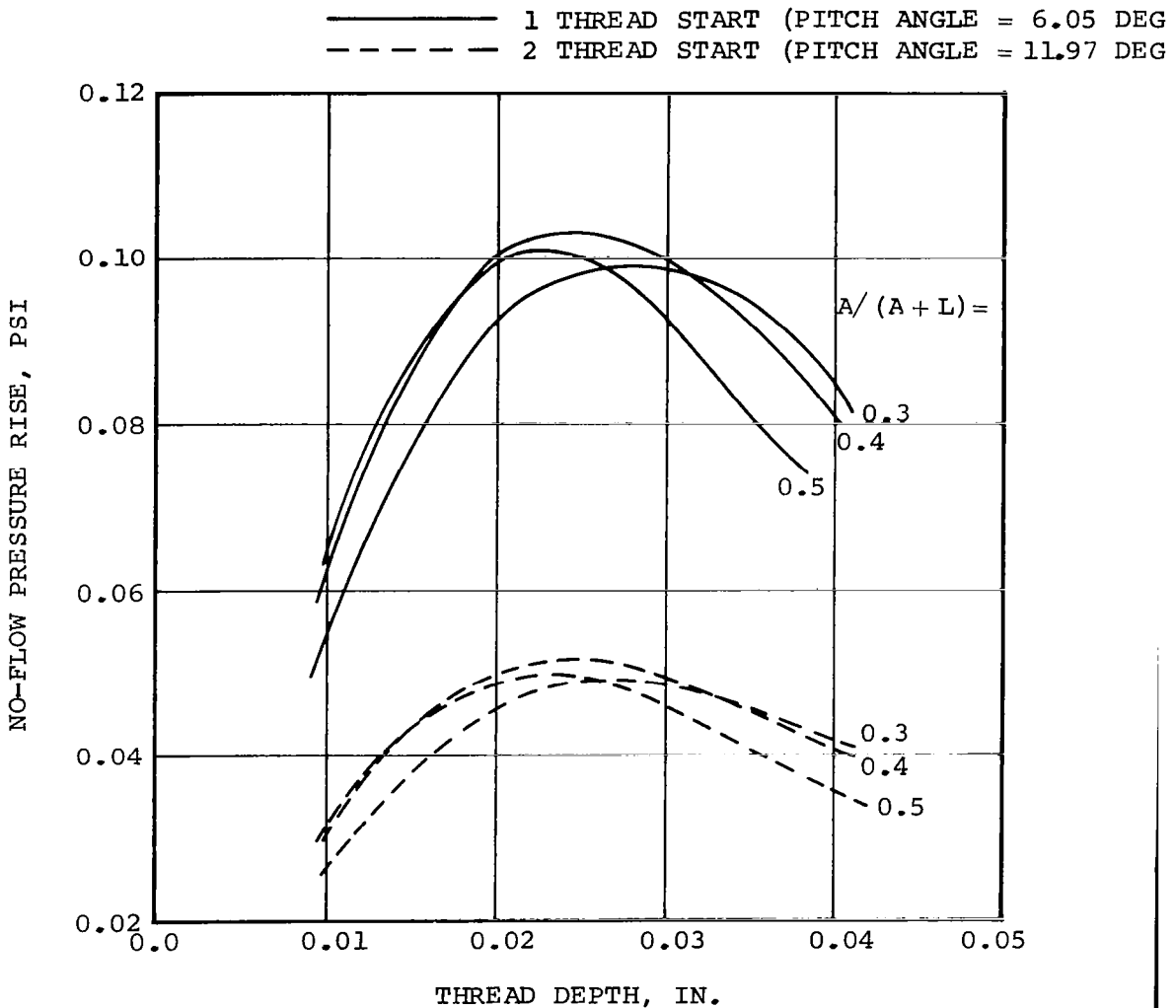

OPTIMIZATION OF 3-IN. DIA. POTASSIUM HOLWECK PUMP

FIGURE 3

FORE PRESSURE, PSIA = 0.1547
RADIAL CLEARANCE, IN. = 0.005
SHAFT SPEED, RPM = 19,200

A = THREAD AXIAL LENGTH, IN.
L = LAND AXIAL LENGTH, IN.

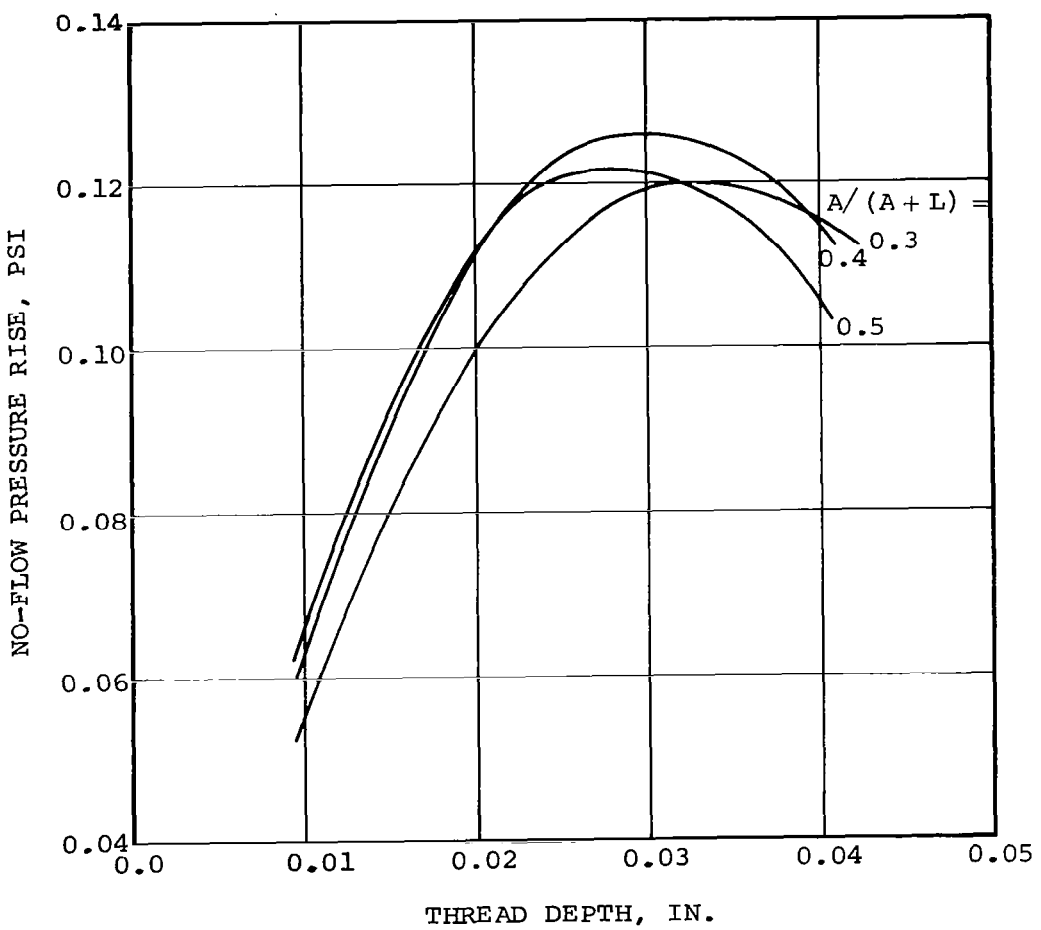

OPTIMIZATION OF 4-IN. DIA. POTASSIUM HOLWECK PUMP

FIGURE 4

FORE PRESSURE, PSIA = 0.1547
RADIAL CLEARANCE, IN. = 0.005
SHAFT SPEED, RPM = 19,200

A = THREAD AXIAL LENGTH, IN.
L = LAND AXIAL LENGTH, IN.

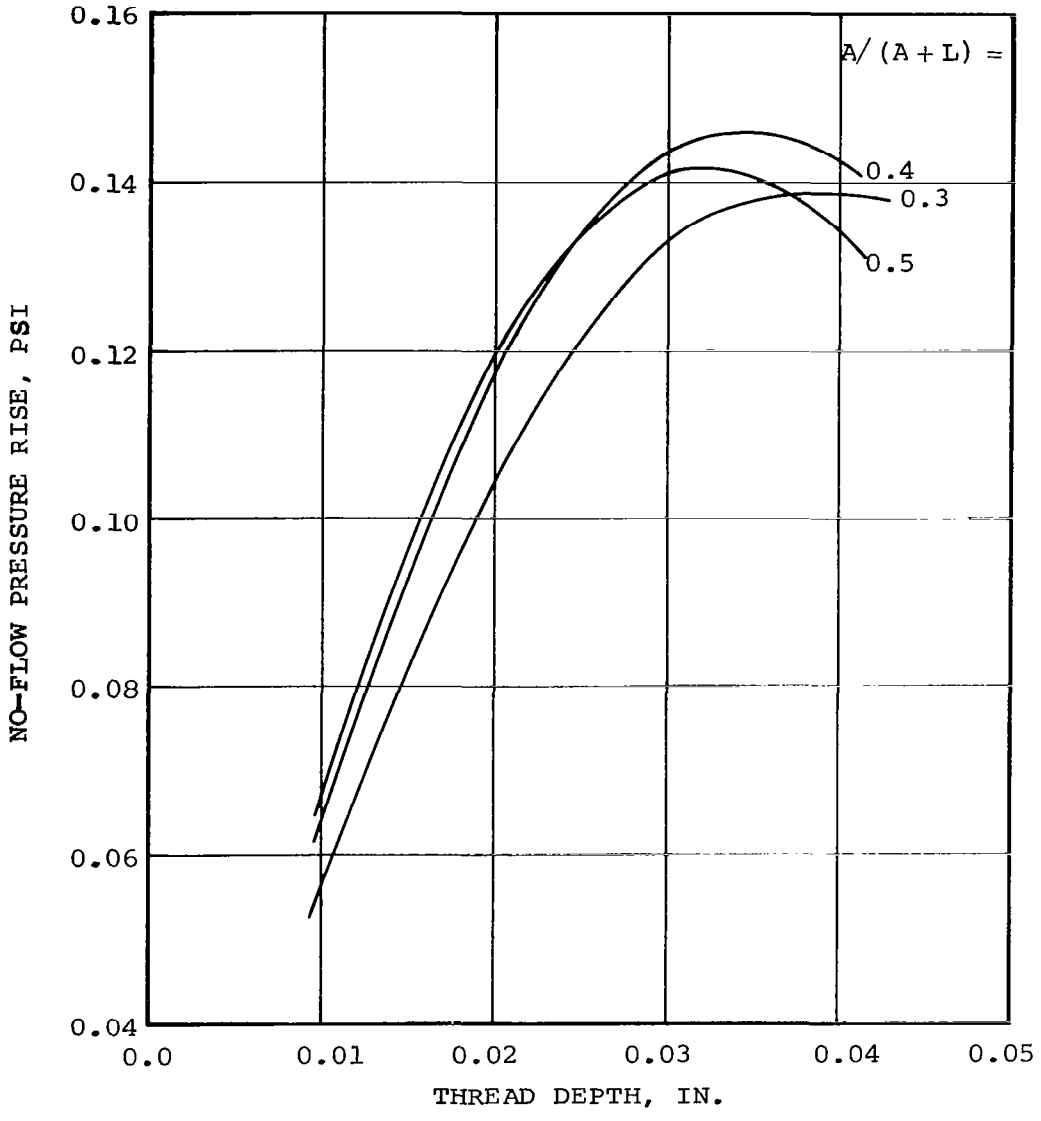

OPTIMIZATION OF 5-IN. DIA. POTASSIUM HOLWECK PUMP

FIGURE 5

FORE PRESSURE, PSIA = 0.1547
RADIAL CLEARANCE, IN. = 0.005
SHAFT SPEED, RPM = 19,200

1 THREAD START (α_{max} = 6.05 DEG)

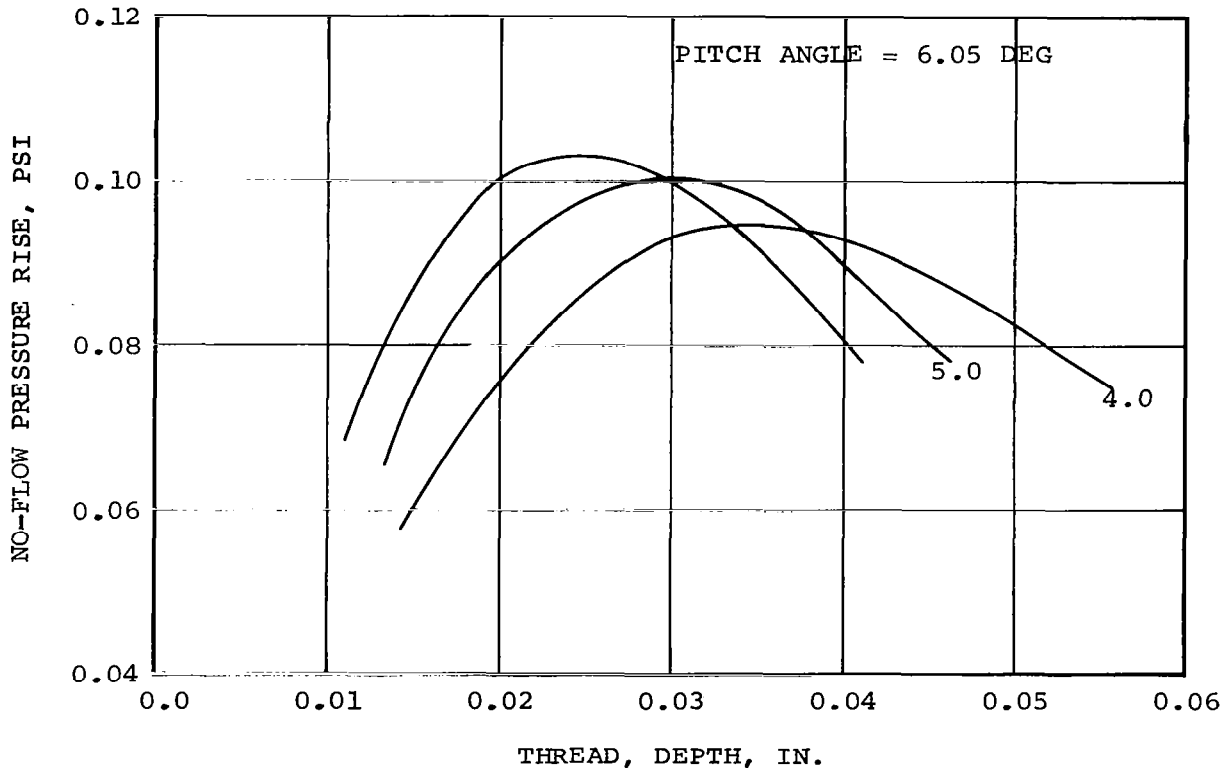

OPTIMIZATION OF 3-IN. DIA. POTASSIUM HOLWECK PUMP

FIGURE 6

FORE PRESSURE, PSIA = 0.1547
RADIAL CLEARANCE, IN. = 0.005
SHAFT SPEED, RPM = 19,200

1 THREAD START (α_{max} = 4.55 DEG)

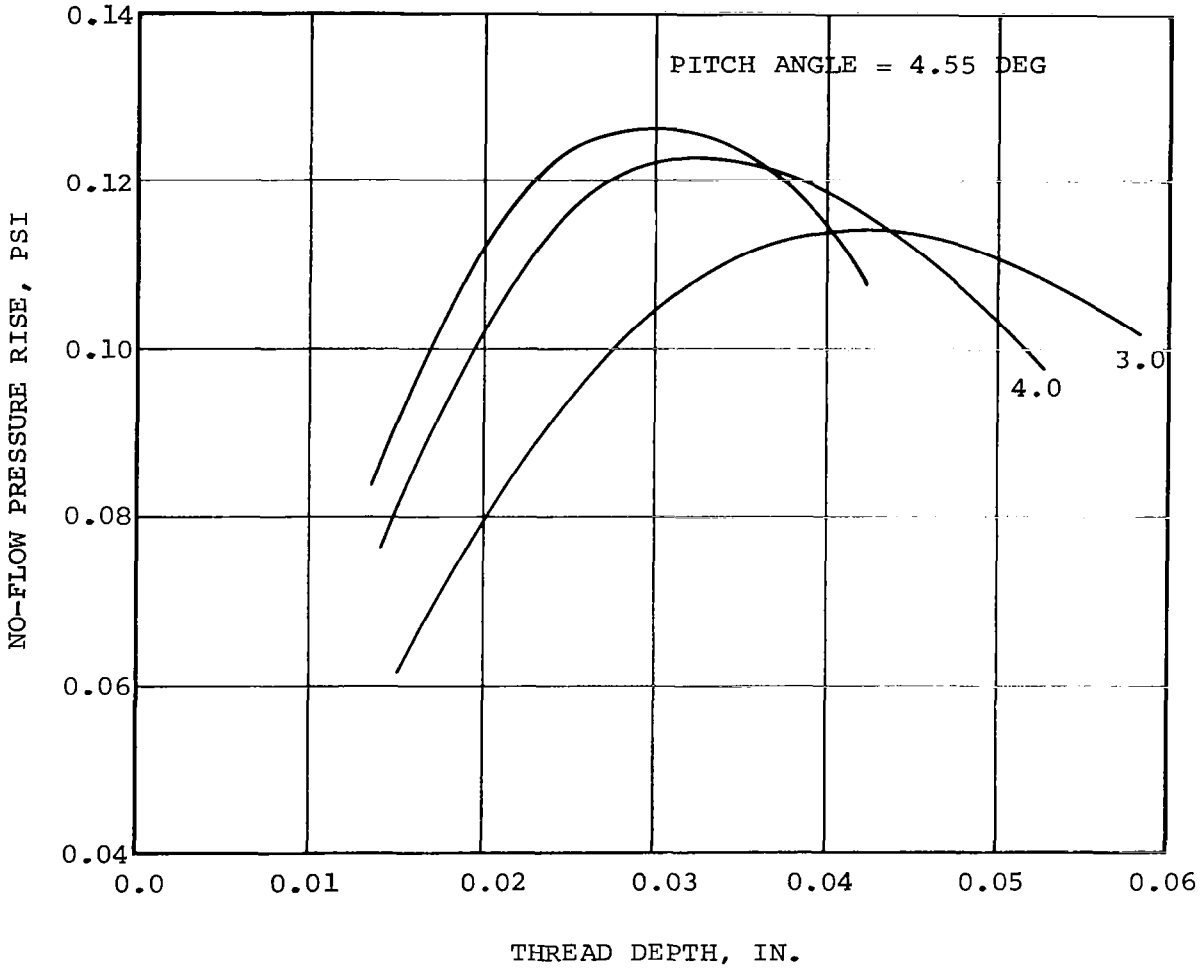

OPTIMIZATION OF 4-IN. DIA. POTASSIUM HOLWECK PUMP

FIGURE 7

FORE PRESSURE, PSIA = 0.1547
RADIAL CLEARANCE, IN. = 0.005
SHAFT SPEED, RPM = 19,200

1 THREAD START (α_{max} = 3.65 DEG)

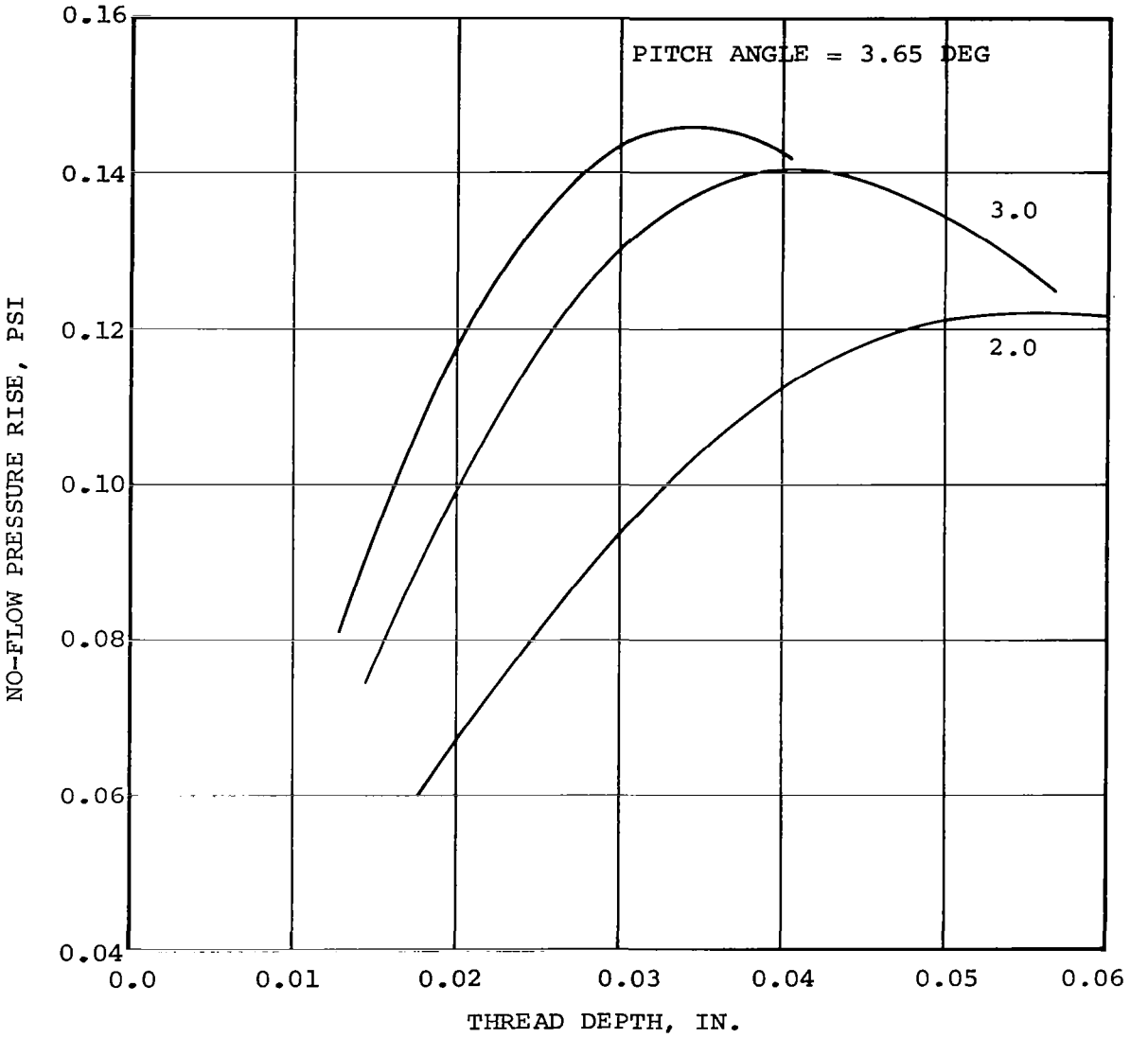

OPTIMIZATION OF 5-IN. DIA. POTASSIUM HOLWECK PUMP

FIGURE 8

pump pressure rise was also computed as a function of flow rate at various fore pressures. Pressure rise is plotted versus flow rate in Figure 9, assuming a 4-in-diameter pump. Liquid viscoseal cooling down to about 800°F is necessary with the vapor molecular pump characteristics depicted in Figure 9, at which point the set vapor flow is approximately 12 lb/yr toward the turbine viscoseal. This is a substantial reduction over the 1.43 lb/hr predicted without the Holweck vapor pump.

The selected Holweck pump geometry is a 4-in-diameter shaft with a pitch angle of 6 deg, a thread depth of 0.029-in., and a land width of 0.4 in.

SHAFT DIAMETER, IN. = 4.0
RADIAL CLEARANCE, IN. = 0.005
SEAL LENGTH, IN. = 1.0
SHAFT SPEED, RPM = 19,200
THREAD AXIAL LENGTH, IN. = 0.4
THREAD DEPTH, IN. = 0.029

T = TEMPERATURE, °F
P = FORE PRESSURE, PSIA

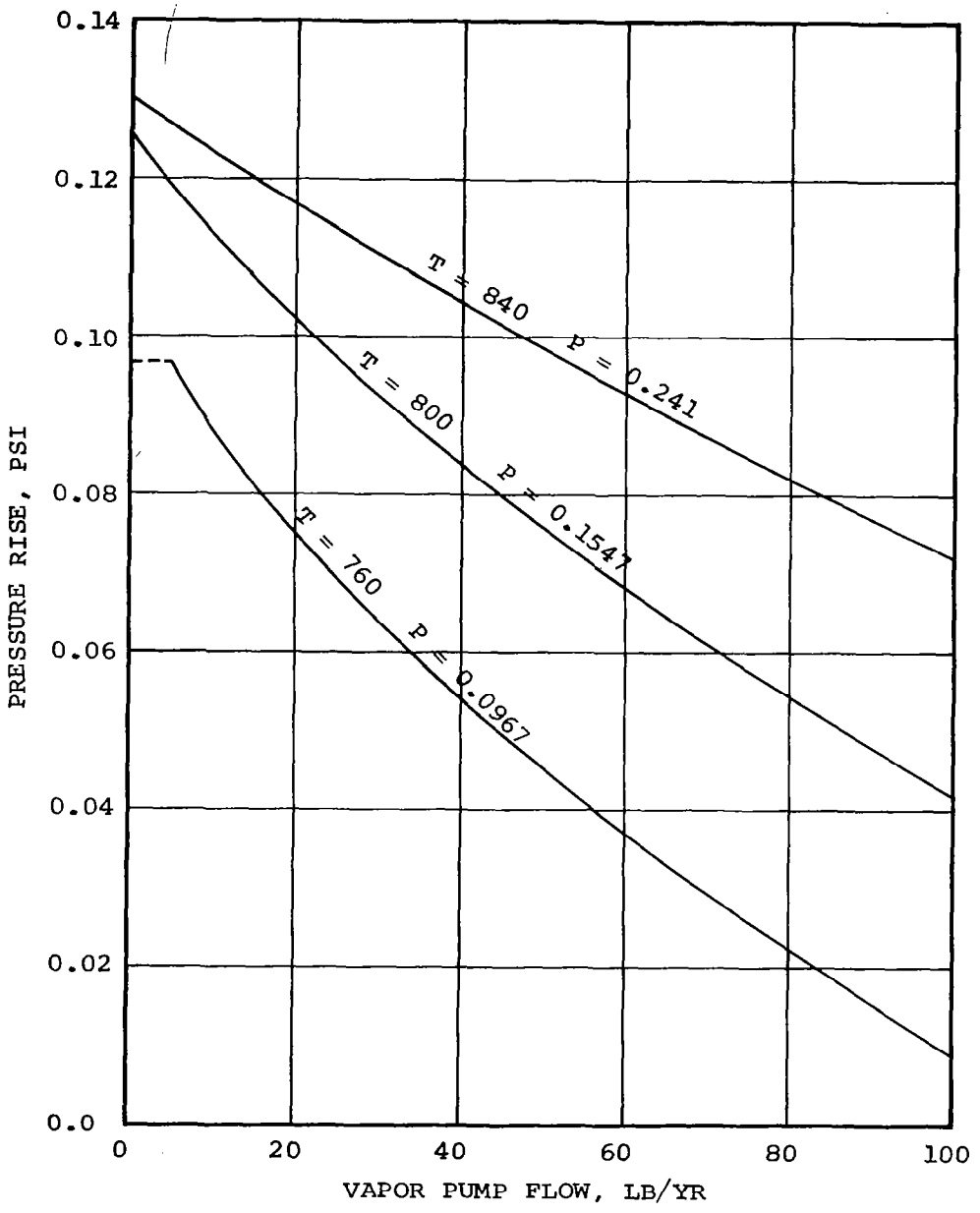

KTA TURBINE HOLWECK PUMP CHARACTERISTICS

FIGURE 9

E-5329

NASA-Langley, 1970 —— 3